Journal of Experimental and Theoretical Physics, Vol. 94, No. 2, 2002, pp. 217–221.
Translated from Zhurnal Éksperimental'noĭ i Teoreticheskoĭ Fiziki, Vol. 121, No. 2, 2002, pp. 260–265.

NUCLEI, PARTICLES, AND THEIR INTERACTION

Ionization Loss of Relativistic Structural Heavy Ions in Collisions with Atoms

V. I. Matveev
Lomonosov Pomorskiĭ State University, Arkhangel'sk, 163006 Russia
e-mail: matveev.victor@pomorsu.ru
Received June 18, 2001

Abstract—A nonperturbative theory of energy loss in collisions between structural, highly charged heavy ions moving at relativistic velocities and atoms is developed. A simple formula for effective deceleration is derived. By structural ions are meant ions containing partially filled electron shells. It is such ions characterized, as a rule, by a significant charge (for example, partially "stripped" uranium ions) that are used in numerous experiments involving the use of modern heavy-ion accelerators. *© 2002 MAIK "Nauka/Interperiodica".*

1. INTRODUCTION

It is known that inelastic processes, which accompany collisions of relativistic ions of fairly high charges with atoms, cannot be described [1, 2] within perturbation theory however high the collision energy may be. A consistent nonperturbative theory of loss of energy by relativistic "bare" heavy ions at free electrons has been developed by Lindhard and Sorensen [3]. However, experiments often involve partially stripped ions; in addition, when a fast ion moves in a medium, some equilibrium ion charge, which is less than the bare ion charge sets in, as a result of processes of charge exchange and electron loss. In calculations of deceleration, the field of a screened ion is usually described as the field of a point charge, although it is, in principle, clear that, during collisions with low impact parameters or high transferred momenta, the ion behaves as a bare unscreened charge, and, in collisions with high impact parameters or low transferred momenta, the ion behaves as a screened charge. In other words, it appears necessary to treat a decelerated ion as an extended structural particle with the size of the order of electron shells on which electrons are located with a steady equilibrium ion charge, rather than as a point particle. Some researchers (see, for example, [4–6]) treated such effects within perturbation theory, whose range of applicability calls for the validity of the inequality $Z/v \ll 1$, where Z is the incident particle charge and v is the relative velocity of collision (here and below, use is made of the atomic units $\hbar = m_e = e = 1$). For consistent inclusion of the presence of an electron "coat" of a heavy relativistic ion, nonperturbative treatment is required. Recent experiments (see, for example, [7–10] and the references cited there) have involved the investigation of energy loss by ions whose charges are so high that the range of applicability of the Born approximation, strictly speaking, cannot be attained [1] even at $v \approx c$ (c is the velocity of light), so that it often turns out that $Z/v \sim 1$.

This paper deals with a nonperturbative theory of energy loss in collisions between structural, highly charged heavy ions moving at relativistic velocities and nonrelativistic atoms. A simple formula for effective deceleration is derived.

2. ENERGY LOSS IN COLLISIONS WITH INDIVIDUAL ATOMS

For simplicity, we will first treat a collision between a relativistic heavy ion and a hydrogen atom. According to [11], the entire range $0 < b < \infty$ of possible values of the impact parameter b may be divided into three regions, namely,

$$(A)\ \ 0 < b < b_0,\ \ (B)\ \ b_0 < b < b_1,\ \ (C)\ \ b_1 < b < \infty, \tag{1}$$

which correspond to low, moderate, and high values of the impact parameter. We will calculate the effective deceleration [12] κ in each one of regions (1) to derive the total effective deceleration on adding up the contributions by three regions. The exact values of the boundaries are of no importance to us, because the dependence of κ in each region on the parameters b_1 and b_0 turns out to be logarithmic, which results in the joining of the contributions by adjacent regions and eliminates the dependence on the parameters of joining b_1 and b_0 in the final answer. One must bear in mind that the cancellation of logarithmic terms is a necessary, but far from sufficient, condition of correctness of joining. In each one of the three regions, we will apply an approximation that is specific to the given region, and different approximations will correspond to different regions. Then, the condition of sufficient correctness of joining will be the condition of equal validity of the approxima-

tions employed in adjacent regions, in some neighborhood containing a parameter of joining.

(A) The region of low values of the impact parameter: $0 < b < b_0$. In collisions with low impact parameters or high transferred momenta, one can assume [13] atomic electrons to be free and at rest until scattering and describe an ion as a bare unscreened charge Z. This enables one to use the result of Lindhard and Sorensen [3]; in so doing, according to numerical calculation results, the effective deceleration (up to $\gamma \le 10$ and up to ion charges of ≤ 92) may be represented in the frequently used form

$$\kappa(b < b_0) = \frac{4\pi Z^2}{v^2} \times \left(\ln(b_0 \gamma v \eta) - \frac{1}{2}\beta^2 + \Delta L_{\text{Bloch}} + \Delta L_{\text{Mott}} \right), \quad (2)$$

where

$$\gamma = \frac{1}{\sqrt{1-\beta^2}}, \quad \beta = \frac{v}{c}, \quad \eta = 1.781,$$

and ΔL_{Bloch} and ΔL_{Mott} are Bloch [14] and Mott [15] corrections which are effectively other than zero [3] only in the case of low values of the impact parameter. The inclusion of the Mott correction only in the region of low values of the impact parameter calls for additional comments. The Mott correction arises due to the difference between the Rutherford cross section and the exact cross section [16] of quantum relativistic scattering in the Coulomb field. In our case, an atomic electron prior to collision is always nonrelativistic, and a relativistic velocity in collision with an ion may be acquired by such an electron only in the region of low values of the impact parameter (see detailed estimates for this and other sections in Section 3).

(B) The intermediate region: $b_0 < b < b_1$. We will restrict ourselves to treatment of collisions with light (nonrelativistic) atoms. In this case, as in [4–6], one can ignore the processes of excitation of electron shells of an ion and treat an incident structural ion as an extended charge. We will follow [4–6, 17] and assume that the nucleus of an incident ion has the charge Z, and its N_i electrons are distributed around the nucleus with the density

$$\rho(r) = -\frac{N_i}{4\pi\lambda^3}\frac{\lambda}{r}\exp\left(-\frac{r}{\lambda}\right),$$

where λ is the screening length. The Coulomb interaction between an ion located at point $\mathbf{R}$ and an atomic electron located at point $\mathbf{r}$ has the form

$$U(\mathbf{R}; \mathbf{r}) = -\frac{Z(1-\nu)}{|\mathbf{r}-\mathbf{R}|} - \frac{Z\nu}{|\mathbf{r}-\mathbf{R}|}\exp\left(-\frac{1}{\lambda}|\mathbf{r}-\mathbf{R}|\right), \quad (3)$$

where we introduced the relative number of electrons $\nu = N_i/Z$ in the ion. In writing the ion and electron coordinates, the impact parameter $\mathbf{b}$ and the projection $\mathbf{s}$ of coordinates $\mathbf{r}$ of an atomic electron on the impact parameter plane are usually introduced,

$$\mathbf{R} = (X, \mathbf{b}), \quad \mathbf{r} = (x, \mathbf{s}).$$

The transition cross section of a nonrelativistic hydrogen atom from the $|0\rangle$ state to the $|n\rangle$ state as a result of collision with a relativistic ion has the following form in an eikonal approximation (see, for example, [11]):

$$\sigma_n = \int d^2b \times \left| \langle n | 1 - \exp\left\{ -\frac{i}{v}\int dX U(\mathbf{R}; \mathbf{r}) \right\} | 0 \rangle \right|^2. \quad (4)$$

This formula is valid if, in the impact parameter range of $b_0 < b < b_1$, an atomic electron as a result of collision is imparted a momentum that is much less than c and may be regarded as nonrelativistic before and after collision. It is this fact that enables one to use (see also [18, 19]) formula (4) for cross sections, with the potential in the form of a static Coulomb potential (and disregard the Mott correction in this region and in region C).

The standard technique [20, 21] in calculating the eikonal phase for the Coulomb potential consists in the following:

$$U(\mathbf{R}; \mathbf{r}) = U((X, \mathbf{b}); (x, \mathbf{s}))$$

is replaced by

$$U'((X, \mathbf{b}); (x, \mathbf{s})) = U((X, \mathbf{b}); (x, \mathbf{s})) - U((X, \mathbf{b}); (x, 0)),$$

and the integral of U' over dX is written with the prime omitted. As a result of integration, we have

$$\frac{i}{v}\int_{-\infty}^{+\infty} U dX = 2i\frac{Z^*}{v}\ln\frac{|\mathbf{b}-\mathbf{s}|}{b} + 2i\nu\frac{Z}{v}\left[K_0\left(|\mathbf{b}-\mathbf{s}|\frac{1}{\lambda}\right) - K_0\left(\frac{b}{\lambda}\right)\right], \quad (5)$$

where $Z^* = Z(1-\nu)$, and $K_0(x)$ and $K_1(x)$ are Macdonald functions. The specific feature of collisions of highly charged ions with atoms consists in that the cross sections of inelastic processes are, as a rule, fairly large and exceed considerably the atomic dimensions. In view of this circumstance, we will assume that $s/b \ll 1$; then, Eq. (5) may be rewritten as

$$\frac{i}{v}\int_{-\infty}^{+\infty} U dX = i\mathbf{q}\cdot\mathbf{s}, \quad (6)$$

where the vector

$$\mathbf{q} = \frac{2Z(1-\nu)}{vb}\left[1 + \frac{\nu}{1-\nu}\frac{b}{\lambda}K_1\left(\frac{b}{\lambda}\right)\right]\frac{\mathbf{b}}{b} \quad (7)$$

apparently has the meaning of momentum transferred to an atomic electron upon its collision with an ion at the impact parameter **b**. The limiting values of **q** have a transparent physical meaning,

$$\mathbf{q} \longrightarrow \frac{2Z(1-\nu)\mathbf{b}}{v b^2} \quad \text{for} \quad b \longrightarrow \infty,$$

which corresponds to scattering from a screened ion of charge $Z(1-\nu)$, and

$$\mathbf{q} \longrightarrow \frac{2Z\mathbf{b}}{v b^2} \quad \text{for} \quad b \longrightarrow 0,$$

which corresponds to scattering from a bare ion of charge Z. Therefore, the cross section (4) of the inelastic process for the orthogonal $|n\rangle$ and $|0\rangle$ states takes the form

$$\sigma_n = \int d^2b |\langle n| \exp(-i\mathbf{q}\cdot\mathbf{r})|0\rangle|^2 = \int d^2b |f_{0n}|^2,$$

where the generalized inelastic form factor is

$$f_{0n} = \langle n| \exp(-i\mathbf{q}\cdot\mathbf{r})|0\rangle.$$

The effective deceleration [12] is

$$\kappa = \sum_n (\epsilon_n - \epsilon_0)\sigma_n = \sum_n (\epsilon_n - \epsilon_0)\int d^2b |f_{0n}|^2, \quad (8)$$

where ϵ_n and ϵ_0 denote the energy of the $|n\rangle$ and $|0\rangle$ states, and $f = \exp(-i\mathbf{q}\cdot\mathbf{r})$. In following Landau and Lifshitz [12], one can readily find that the effective deceleration in the $b_0 < b < b_1$ range is represented in the form

$$\kappa(b_0 < b < b_1) = \frac{1}{2}\int_{b_0}^{b_1} q^2 2\pi b db. \quad (9)$$

The integral appearing here is readily calculated analytically, and, given the validity of the conditions

$$\frac{b_0}{\lambda} \ll 1, \quad \frac{b_1}{\lambda} \gg 1, \quad (10)$$

the contribution made to effective deceleration by the region of intermediate values of the impact parameter depends logarithmically on the parameters of joining (b_0 and b_1) and is

$$\kappa(b_0 < b < b_1) = \frac{4\pi Z^2(1-\nu)^2}{v^2}\ln b_1 + \frac{4\pi Z^2}{v^2}\ln\left[\frac{1}{b_0}\left(\frac{2\lambda}{\eta}\right)^{\nu(2-\nu)}\right]. \quad (11)$$

(C) The region of high values of the impact parameter: $b_1 < b < \infty$. Here, the ion–atom interaction may be included using perturbation theory; in the case of high values of the impact parameter, the atom is acted upon by the field of a screened ion; i.e., the apparent ion charge is $Z^* = Z(1-\nu)$. The respective effective deceleration is [11]

$$\kappa(b > b_1) = 4\pi\frac{(Z^*)^2}{v^2}\left\{\ln\frac{2v}{\eta I b_1\sqrt{1-\beta^2}} - \frac{\beta^2}{2}\right\}. \quad (12)$$

Here, we followed [13] and introduced the "mean" atomic energy I.

The total deceleration is derived by summing up the contributions made by the three regions,

$$\kappa = \kappa(b < b_0) + \kappa(b_0 < b < b_1) + \kappa(b > b_1).$$

As a result, we have

$$\kappa = \frac{4\pi Z^2(1-\nu)^2}{v^2}\left(\ln\frac{2v}{\eta I\sqrt{1-\beta^2}} - \frac{\beta^2}{2}\right) + \frac{4\pi Z^2}{v^2}\left(\ln\frac{v\eta}{\sqrt{1-\beta^2}} - \frac{\beta^2}{2} + \ln\left[\left(\frac{2\lambda}{\eta}\right)^{\nu(2-\nu)}\right] + \Delta L_{\text{Bloch}} + \Delta L_{\text{Mott}}\right). \quad (13)$$

This formula is generalized to the cases of collisions between relativistic structural heavy ions and complex atoms using a standard [12] method; namely, the right-hand side of the formula is multiplied by the number N_a of atomic electrons, and the respective atomic characteristic I in Eq. (12) is calculated for a complex atom. In addition, one can readily see that, within the suggested approach, it is possible to directly take into account the fact that, when the processes of trapping and loss are included, the number N_i of ion electrons (and, consequently, $\nu = N_i/Z$) turns out to be dependent on the target parameters, the ion charge, and the relative velocity of collision.

3. RANGE OF VALIDITY OF THE APPROACH

The values of the boundaries of regions (1) and the conditions of validity of the developed approach call for additional comments. The division of all possible values of the impact parameter into three regions corresponds to three different approximations. The region A of low values of the impact parameters is the region of validity of the method of Lindhard and Sorensen [3] with the following reservations. Atomic electrons may be assumed to be free if the collision time

$$\tau \sim \frac{b\sqrt{1-\beta^2}}{v} \ll 1$$

is the characteristic atomic time, whence $b \ll v\gamma$. When this inequality is valid, atomic electrons are scattered as free electrons from an unscreened ion nucleus, if $b \ll \lambda$, the characteristic size of the electron "coat" of the ion.

The main contribution to the Bloch correction is made [3] by the angular momenta l (connected to the impact parameter b through the conventional relation $l = v\gamma b$) such that $0 \le l^2 \le (Z/2v)^2$ or by the impact parameters such that $0 \le b \le Z/2v\gamma$. The Mott correction is significant if an atomic electron, as a result of collision with a relativistic ion, acquires the velocity in the Coulomb field of $\Delta v \sim 2Z/(vb) \sim c$ and becomes relativistic, or in the case of collisions with impact parameter values of

$$0 \le b \le \frac{2Z}{vc}.$$

Note that, in our case,

$$\frac{2Z}{vc} < \frac{Z}{2v\gamma}.$$

Therefore, strictly speaking, it must be pointed out that the region A is located in the range of $0 < b < b_0'$, where $b_0' \gg Z/2v\gamma$. The region B of moderate values of the impact parameter is the range of validity of the eikonal approximation in the form of Eq. (4) and is located [11, 18, 19] in the range of $b_0'' < b < b_1'$, where

$$b_0'' \gg \frac{2Z}{vc}, \quad b_1' \ll \frac{v}{\sqrt{1-\beta^2}}.$$

The region C of high values of the impact parameter is the region of validity of perturbation theory, which corresponds to the smallness of the eikonal phase given by Eq. (6), which, for high values of b, is estimated as

$$qs \sim \frac{2Z^*}{vb} d \ll 1,$$

where $d \sim 1$ is the characteristic size of an atom. Therefore, the region C is located within the boundaries $b_1'' < b < \infty$, where $b_1'' \gg 2Z^*/v$.

Thus, the values of b_0 and b_1 in (1) lie in the ranges of overlapping of adjacent regions and satisfy the following inequalities:

$$b_1'' < b_0 < b_0', \quad b_1'' < b_1 < b_1'$$

or

$$\frac{2Z}{vc} \ll b_0 \ll \frac{Z}{2v\gamma}, \quad \frac{2Z^*}{v} \ll b_1 \ll v\gamma. \tag{14}$$

In addition, in order to perform a correct joining with the values of the region boundaries dropping out of the final formula (13), the validity of inequalities (10) was required; these inequalities may now be rewritten in a more convenient form,

$$\frac{1}{\gamma v} \ll \lambda \ll \gamma v, \quad \gamma = \frac{1}{\sqrt{1-\beta^2}}. \tag{15}$$

One can readily see that inequalities (14) and (15) (along with the conditions $b_0 < b_1$ and $b_0 < \lambda$) are compatible, and valid in numerous cases of practical importance, when the collisions between relativistic heavy ions and light (nonrelativistic) atoms are investigated, including the cases treated by us, where $Z \le 92$ and $\gamma \le 10$. Note further that condition (15) is valid in a fairly wide range of variation of the screening length λ; at the same time, this condition does not make it possible to perform a direct limiting transition $\lambda \longrightarrow 0$ or $\lambda \longrightarrow \infty$ in formula (13)

4. RESULTS AND ESTIMATES

In order to describe the correction due to the extent of the ion charge and to clarify the importance of different regions of the impact parameters, we will introduce relative corrections χ_1 and χ_2. The correction

$$\chi_1 = \frac{\kappa - \kappa_{\text{point}}(Z^*)}{\kappa_{\text{point}}(Z^*)},$$

where

$$\kappa_{\text{point}}(Z^*) = \frac{4\pi(Z^*)^2}{v^2} \times\left(\ln\frac{2v^2}{I(1-\beta^2)} - \beta^2 + \Delta L_{\text{Bloch}} + \Delta L_{\text{Mott}}\right) \tag{16}$$

is the effective deceleration [22] of a point nucleus of charge Z^*, and the correction

$$\chi_2 = \frac{\kappa - \kappa_{\text{point}}(Z)}{\kappa_{\text{point}}(Z)}$$

is similar to the correction χ_1 with the difference that $\kappa_{\text{point}}(Z)$ is the effective deceleration of a point bare nucleus of charge Z. The behavior of the relative corrections χ_1 and χ_2 is given in the figure. We followed [4, 17] (see also [5, 6]) and calculated the screening length λ by the formula

$$\lambda = g\frac{\nu^{2/3}}{1-\nu/7}\frac{a}{Z^{1/3}}, \quad g = 0.3\frac{3\pi^2}{50}\Gamma\left(\frac{1}{3}\right) \approx 0.48,$$

where a is the Bohr radius (although, in principle, a may be treated as a parameter describing the effective ion size in the presence of excited electron shells of an ion).

In the frequently encountered cases of $Z \gg 1$ and $Z^* \gg 1$ corresponding to $\nu \ll 1$, only the terms linear

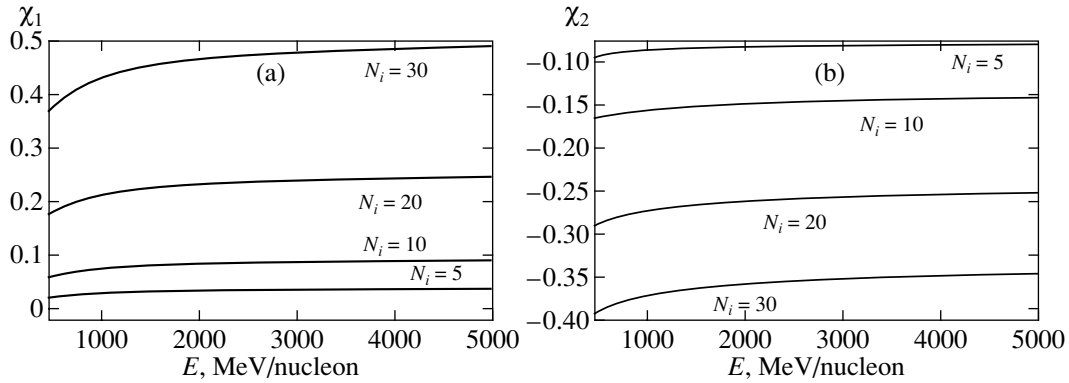

The relative corrections (a) χ_1 and (b) χ_2 as functions of the incident ion energy for the ion nucleus charge $Z = 92$ with different numbers of screening electrons $N_i = 5, 10, 20, 30$.

with respect to $\nu \ll 1$ may be retained; then,

$$\kappa = \frac{4\pi(Z^*)^2}{v^2}\left(\ln\frac{2v^2}{I(1-\beta^2)} - \beta^2 + \Delta L_{\text{Bloch}} + \Delta L_{\text{Mott}}\right) + \frac{8\pi(Z^*)^2}{v^2}\nu\left(\ln\frac{2v\lambda}{\eta\sqrt{1-\beta^2}} + \Delta L_{\text{Bloch}} + \Delta L_{\text{Mott}} - \frac{Z^*}{2}\frac{d}{dZ^*}(\Delta L_{\text{Bloch}} + \Delta L_{\text{Mott}})\right). \quad (17)$$

In the right-hand side of formula (17) (as in Eq. (16)), the values of ΔL_{Bloch} and ΔL_{Mott} and of their derivatives are calculated for the point charge Z^*. The first term in this formula represents the effective deceleration of a point ion of charge Z^*, while the second term is a correction due to the finite size of the ion. The following conclusions may be made. The inclusion of the extent of the ion charge brings about a considerable increase in the effective deceleration κ of the ion compared with the deceleration κ_{point} of a point nucleus of the same charge Z^*. The order of the energy loss increase may be estimated as

$$(\kappa - \kappa_{\text{point}})/\kappa_{\text{point}} \geq \nu,$$

where $\nu = N_i/Z$ is the relative number of electrons on the ion shells. For example, a uranium ion with ten electrons in bound states experiences a deceleration that is approximately 10% higher than that experienced by a bare point nucleus of charge 82 and of the same mass moving with the same energy.

ACKNOWLEDGMENTS

I am grateful to the Ministry of Education of the Russian Federation (project no. E00-3.1-390) and to the Russian Foundation for Basic Research (project no. 01-02-17047) for the financial support of this study.

REFERENCES

1. J. Eichler and W. E. Meyrhof, *Relativistic Atomic Collisions* (Academic, New York, 1995).
2. J. Eichler, Phys. Rep. **193**, 167 (1990).
3. J. Lindhard and A. Sorensen, Phys. Rev. A **53**, 2443 (1996).
4. G. L. Yudin, Zh. Tekh. Fiz. **55**, 9 (1985) [Sov. Phys. Tech. Phys. **30**, 4 (1985)].
5. G. Maynard, D. Gardes, M. Chabot, *et al.*, Nucl. Instrum. Methods Phys. Res. B **146**, 88 (1998).
6. G. Maynard, M. Chabot, and D. Gardes, Nucl. Instrum. Methods Phys. Res. B **164/165**, 139 (2000).
7. E. E. Zhurkin and S. D. Bogdanov, Nucl. Instrum. Methods Phys. Res. B **164/165**, 230 (2000).
8. H. Weick, H. Geissel, and C. Scheidenberger, Nucl. Instrum. Methods Phys. Res. B **164/165**, 168 (2000).
9. C. Scheidenberger and H. Geissel, Nucl. Instrum. Methods Phys. Res. B **135**, 25 (1998).
10. C. Scheidenberger, H. Geissel, H. H. Mikelsen, *et al.*, Phys. Rev. Lett. **77**, 3987 (1996).
11. V. I. Matveev and S. G. Tolmanov, Zh. Éksp. Teor. Fiz. **107**, 1780 (1995) [JETP **80**, 989 (1995)].
12. L. D. Landau and E. M. Lifshitz, *Course of Theoretical Physics*, Vol. 3: *Quantum Mechanics: Non-Relativistic Theory* (Nauka, Moscow, 1989, 4th ed.; Pergamon, New York, 1977, 3rd ed.).
13. V. B. Berestetskii, E. M. Lifshitz, and L. P. Pitaevskii, *Course of Theoretical Physics*, Vol. 4: *Quantum Electrodynamics* (Nauka, Moscow, 1989; Pergamon, New York, 1982).
14. F. Bloch, Ann. Phys. (Leipzig) **16**, 285 (1933).
15. N. F. Mott, Proc. R. Soc. London, Ser. A **124**, 425 (1929).
16. J. A. Doggett and L. V. Spenser, Phys. Rev. **103**, 1597 (1956).
17. W. Brandt and M. Kitagawa, Phys. Rev. B **25**, 5631 (1982).
18. V. I. Matveev and Kh. Yu. Rakhimov, Zh. Éksp. Teor. Fiz. **114**, 1646 (1998) [JETP **87**, 891 (1998)].
19. V. I. Matveev, Kh. Yu. Rakhimov, and D. U. Matrasulov, J. Phys. B **32**, 3849 (1999).
20. J. Eichler, Phys. Rev. A **15**, 1856 (1977).
21. V. I. Matveev, Fiz. Élem. Chastits At. Yadra **26**, 780 (1995) [Phys. Part. Nucl. **26**, 329 (1995)].
22. S. P. Ahlen, Rev. Mod. Phys. **52**, 121 (1980).

Translated by H. Bronstein

Journal of Experimental and Theoretical Physics, Vol. 94, No. 2, 2002, pp. 222–227.
Translated from Zhurnal Éksperimental'noĭ i Teoreticheskoĭ Fiziki, Vol. 121, No. 2, 2002, pp. 266–273.

NUCLEI, PARTICLES, AND THEIR INTERACTION

Generation of a Fast-Ion Beam upon the Interaction of a Multiterawatt Picosecond Laser Pulse with a Solid Target

A. A. Andreev[a], V. M. Komarov[b], A. V. Charukhchev[b], I. M. Litvinenko[c], and K. Yu. Platonov[d, *]

[a]*Research Institute of Laser Physics, Vavilov State Optical Institute All-Russia Scientific Center, St. Petersburg, 199034 Russia*

[b]*Federal Scientific and Production Center, Research Institute of Complex Testing of Optoelectronic Devices, Sosnovyĭ Bor, Leningrad oblast, 188537 Russia*

[c]*All-Russia Research Institute of Technical Physics, Snezhinsk, Chelyabinsk oblast, 456770 Russia*

**e-mail: platonov@quark.stu.neva.ru*

[d]*St. Petersburg State Technical University, St. Petersburg, 195251 Russia*

Received July 12, 2001

Abstract—The parameters of fast particles generated upon the interaction of 10^{19} W/cm^2 laser pulses with solid targets are studied. The spatial and energy parameters of fast ions are investigated. It is found that approximately 1–3% of the laser energy is transformed to the energy of mega- and submegaelectronvolt ions at laser pulse intensities $\geq 10^{18}$ W/cm^2. It is shown experimentally that an ion beam is directed perpendicular to the target surface. The analytic and numerical simulations agree with experimental results and predict the propagation of fast electrons in the mirror direction with respect to the incident laser beam and of ions perpendicular to the target. The theoretical calculations are compared with the experimental output and spectra of fast electrons and ions. © *2002 MAIK "Nauka/Interperiodica".*

1. INTRODUCTION

The recent development of the laser technique resulted in the building of high-power laser systems providing the radiation intensity on a target of $\leq 7 \times 10^{20}$ W/cm^2 [1]. At such ultrahigh intensities and the optimal choice of the parameters of a laser pulse and targets, a plasma can become a powerful source of hot electrons, fast ions, and hard X-rays and gamma rays in the megaelectronvolt energy range [2, 3]. The creation of a laser plasma source of particles and quanta with such parameters opens up unique possibilities for initiating various nuclear reactions for producing compact neutron sources, obtaining a variety of isotopes, and generation of artificial radioactivity. Due to its small size (of the order of 10 μm) and ultrashort pulse duration (of the order of 1 ps), such a source can have a brightness that is much greater than that of all known sources, which opens up wide prospects for its applications in nuclear physics, medicine, and accelerators [2, 4].

In the case of relativistic intensities, the conversion of laser energy to the energy of fast electrons is determined by the known nonlinear mechanisms, the value of the conversion coefficient being quite large [4]. At the same time, to increase the efficiency of conversion of laser energy to the energy of fast ions, it is necessary to study first of all the mechanisms of acceleration of ions by electrostatic fields induced in a solid-target plasma. This would allow the optimization of the parameters of laser pulses and the configuration of targets for increasing the yield of nuclear reactions because the advantage of ions is that they have much higher (compared to electrons and gamma quanta) cross sections for nuclear reactions.

The generation of fast ions by solid targets irradiated by picosecond laser pulses was observed in earlier experiments [5, 6] where submegaelectronvolt and megaelectronvolt ions were detected and rather high conversion coefficients were obtained. The detection of protons with energies up to 55 MeV at a laser pulse intensity $\leq 3 \times 10^{20}$ W/cm^2 was recently reported in papers [7, 8]. A collimated beam of fast 1.5-MeV protons within an angle of 40° was obtained in experiments [9]. In this paper, we performed more detailed theoretical and experimental studies of the energy and angular characteristics of electrons and ions escaping to vacuum and inside the target upon the interaction of an ultrashort high-power ($\leq 10^{19}$ W/cm^2) laser pulse with a solid target.

2. EXPERIMENTAL RESULTS

Experiments were performed on the picosecond channel of a Progress-II neodymium-glass laser setup [10, 11]. The laser pulse duration was of about 1.5 ps. The experimental studies were carried out in two steps. In the first stage, when the laser energy was up to 1 J (the laser power of the order of 1 TW) for a beam diameter of 35 mm, the radiation was focused with a lens with the aperture ratio f/4 (f is the focal distance) [10]. As the beam energy increased up to 16 J and its power

increased approximately up to 10 TW, it was difficult to provide the near-diffraction-limited size of the focal spot. For this reason, we used an axial parabolic mirror with the aperture ratio f/1.1 for focusing laser radiation instead of the lens. The measurements of the focal spot of the laser beam on the target showed that approximately 50% of laser energy was contained in the spot of diameter $d \le 7$ μm [11]. The experiments were performed with both *p*-polarized and *s*-polarized radiation with targets made of optically polished Al and Sn at angles of incidence of the laser beam on the target $\theta = 33°$ and 45°.

Upon the interaction of picosecond pulses with solid targets, a prepulse, whose parameters can strongly affect the interaction, plays an important role. For this reason, we measured the energy and shape of a pulse of amplified spontaneous emission (ASE) behind an aperture located in the focal plane of a long-focus (90 m) optical system and having an equivalent diameter of 7 μm in the target plane [11]. The duration of the ASE prepulse was approximately 5 ns at half maximum. The pulse energy was measured with a calorimeter with a sensitivity threshold of 2 nJ. The measurements showed that the ASE prepulse energy did not exceed 0.5 mJ and its power was less than 5×10^{-9} of the main picosecond pulse, which is well below the plasma formation threshold [12]. The measurements performed in the interval from 10 to 100 ps before the main single pulse showed that the prepulse intensity was lower than the sensitivity threshold of the method ($\le 10^{-3}$). To find out whether the prepulse noticeably affects the size of the plasma spot formed in a real laser beam with a nominal power of about 10 TW, we photographed the plasma spot in soft 0.25- to 1.5-keV X-rays with the help of a pinhole camera of diameter 5 μm (twelvefold magnification). We found that the focal spot size did not exceed 8 μm and its shape was close to that obtained by optical methods. Therefore, the prepulse power is too low to affect noticeably the interaction process.

We determined the absorption coefficient of the target irradiated by 10^{17}-W/cm^2 pulses by measuring the energy of scattered light using the Ulbricht sphere. A focusing lens was simultaneously used as an entrance window of a vacuum chamber. The target in the form of a polished plate of size 5×5 mm and thickness of several hundred microns was placed at the center of the sphere. In experiments with the use of a parabolic focusing mirror, calorimeters were placed around the target. One of the calorimeters completely picked up the radiation reflected from the target in the mirror direction, while the rest of the calorimeters were placed around the target, both in the plane of incidence and perpendicular to it. The energy reflected backward to the aperture of the focusing optical system was measured separately. All the components of scattered and incident energy were detected with a multichannel measuring system [13].

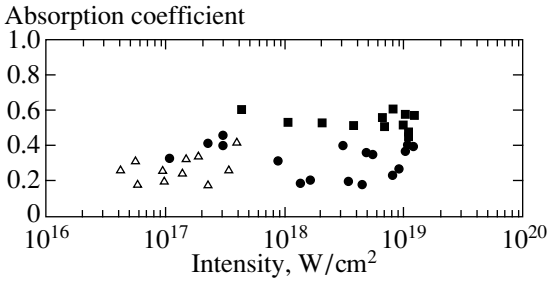

Fig. 1. Absorption coefficients of *s*- and *p*-polarized laser radiation as functions of the laser intensity for Al [(●) *p* polarization, (△) *s* polarization] and Sn [(■) *p* polarization] targets.

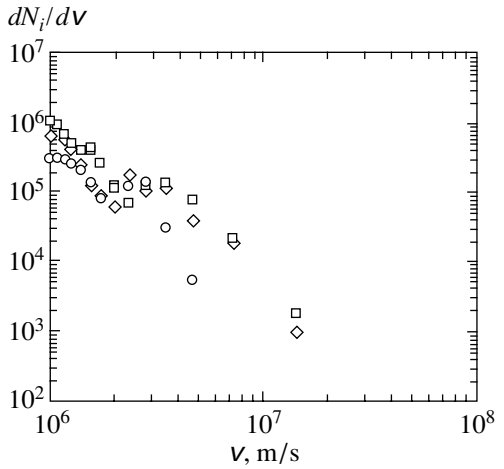

Fig. 2. The velocity distribution of all fast ions for different escape angles: 0° (□), 20° (◇), and mirror direction (○). The proton velocity $v \approx (5.4\text{–}10) \times 10^{18}$ cm/s corresponds to the energy $\varepsilon_i = 150\text{–}550$ keV. The velocity of the carbon ion C^{+2} $v \approx 3.3 \times 10^{18}$ cm/s corresponds to the energy $\varepsilon_i = 0.8$ MeV.

The velocity distributions of ions were measured by the time-of-flight method using ion collectors and a 60-MHz-bandwidth multichannel computer-controlled digital oscilloscope. The detectors were arranged around the target so that at least one of them detected ions leaving the target in a direction close to the normal, as well as ions escaping in the mirror direction with respect to the incident beam. Collectors were used in the experiments to study the spatial distribution of the scattered ions and to estimate, in combination with plasma calorimeters, the charge state *Z*/*A* of the plasma [14].

The experimental dependences obtained in this study are presented in Figs. 1–4.

Figure 1 shows the absorption coefficients of *p*- and *s*-polarized laser radiation measured as functions of the laser intensity for Al and Sn targets. We have found the following properties. The target with a higher *Z* (Sn) has a higher absorption. As the laser intensity increases, absorption becomes the same for *s*- and *p*-polarized

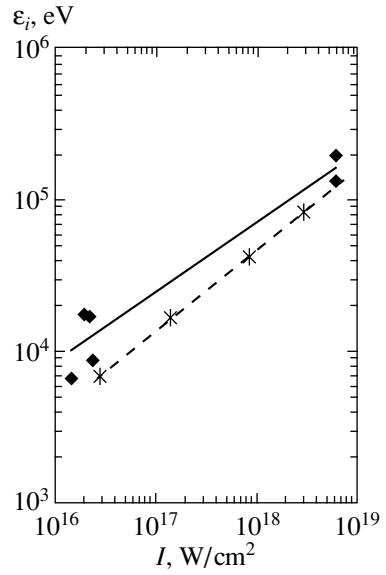

Fig. 3. Dependence of the mean energy ε_i of the hydrogen ion on the laser-radiation intensity I. The experimental curve (solid line) corresponds to the dependence $\varepsilon_i = 0.0003I^{0.46}$, and the theoretical curve (dashed line) is plotted according to (1).

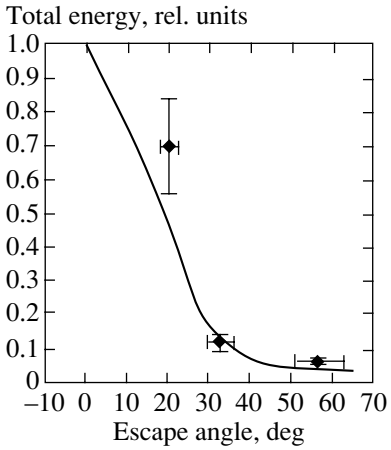

Fig. 4. Dependence of the total energy carried away by hydrogen ions into vacuum on the escape angle for an intensity of 10^{18} W/cm^2. The *PIC* code calculation is shown by the solid curve; dots are the experimental data. The total energy carried away is about 1.2×10^{16} eV.

laser pulses and only weakly depends on the laser intensity in the range from 10^{17} to 5×10^{18} W/cm^2.

Figure 2 presents the velocity distribution for high-energy ions for different angles of escape from the target plasma. The laser pulse intensity on the target made of polished Al was approximately 5×10^{18} W/cm^2. The dependence of dN_i/dv on v is linear at the logarithmic scale, indicating a power distribution of high-energy ions over velocities. The preliminary mass spectrometric measurements showed that the main part of the ions are protons with energies up to ~550 keV ($v = 10^9$ cm/s). A small amount of carbon ions were also detected with the maximum velocity of 4.5×10^8 cm/s ($\varepsilon_i = 1.5$ MeV). At the same time, no Al ions with velocities higher than 10^8 cm/s were detected [15]. The estimates based on the assumption that the main part of fast ions are protons give the total number of fast ions escaping during the laser pulse of about 10^{11}.

Figure 3 shows the dependence of the average energy ε_i of fast ions on the laser intensity I. The experimental curve corresponds to the power dependence $\varepsilon_i = 0.0003I^{0.46}$, where ε_i is measured in eV and I in W/cm^2.

Figure 4 presents the angular distribution of the total energy of all ions that escaped. The ions escaped perpendicular to the target with an angular dispersion of ~30°.

The total energy of escaping ions estimated in the experiments for the laser intensity of about 5×10^{18} W/cm^2 amounts to 0.01–0.03 of the laser pulse energy.

To analyze our further measurements, we will use the results obtained in our paper [15], where we have measured the spectrum of hard X-rays under the same experimental conditions in the energy range from 15 to 1000 keV and estimated the yield of hot 2.7- to 22-MeV electrons leaving the plasma. The method and results of these measurements are described in detail in paper [15], so we point out here only the main features. The spectrum of hard X-rays was measured in the 15- to 90-keV region by the method of selective filters [16] and at higher energies, up to 1.0 MeV, by the method of neutral filters. The selective filters were made of Zr, Rh, Cd, Gd, and Pb, and neutral filters were made of Pb. The detectors of hard X-rays were protected from hot electrons leaving the plasma with a Be filter of thickness 3.5 g/cm^2, which was placed at a distance of 10–20 cm from the detector. This filter reduces the X-ray signal by a factor of 1.5–2 and completely absorbs electrons with energies up to 10 MeV. All the detectors were protected from scattered quanta and particles by a lead case.

The spectra of fast electrons were measured simultaneously with the measurement of hard X-rays by the method of neutral Pb filters. A detector with the same filter but without Be protection was placed near the hard X-ray detector. Thus, the detector with the Pb filter measured the total signal from electrons and X-rays, whereas the detector additionally shielded with the Be filter measured only X-rays.

In experiments with the laser pulse intensity on the Al target of about 5×10^{18} W/cm^2, we detected 8- to 10-MeV electrons leaving the target in the near mirror direction. Our estimated showed that the number of hot electrons leaving the plasma in the energy range from 2.7 to 10 MeV was approximately 10^9. The spectra of hard X-rays emitted by the plasma have a characteristic

two-temperature shape. The higher temperature was 200–400 keV, and the lower one was 20–30 keV [15].

3. ANALYSIS OF EXPERIMENTAL DATA AND THE THEORETICAL ESTIMATES

Consider processes resulting in the absorption of laser radiation and generation of fast particles. For $I \geq 10^{16}$ W/cm^2, collisionless absorption occurs because the plasma temperature becomes rather high. Since the prepulse intensity in our experiments is low, we deal with a sufficiently sharp plasma boundary, when the scale of the plasma inhomogeneity L in less than the wavelength. It is known that the laser-field amplitude is reduced at the sharp boundary by ω_p/ω times. Therefore, we can roughly estimate the absorption coefficient η equal to the ratio of the absorbed energy to the laser pulse energy ε_L,

$$\eta = \frac{\int_0^{\tau_i} jE dV\, dt}{\varepsilon_L},$$

for these intensities by using the expression for collisionless absorption in the regime of high-frequency anomalous skin effect [17] or sheath inverse bremsstrahlung (SIB) [18] obtained in the approximation linear in the laser field:

$$\eta \approx \eta_{SIB} = \frac{4}{\sqrt{\pi}}\left(\frac{v_T}{c}\right)^3 \frac{\omega_{pe}^2}{\omega^2}. \quad (1)$$

In this case, thermal electrons moving deep in the plasma are accelerated by the laser-wave field over the skin-layer length by absorbing the laser radiation energy. This process is physically analogous to the Landau damping of a plasma wave. Expression (1) is valid for $v_T\omega_p/c\omega \leq 1$ (in our case, ~1), and it follows from it that the absorption coefficient is proportional to the number Z^*n_i of electrons in plasma. Note that the "vacuum heating" [19] and "pondermotive absorption" [20] have, under our conditions, an effect on the absorption coefficient that is comparable with the SIB effect, so that expression (1) is valid with an accuracy to a factor of the order of unity. When the laser pulse intensity is very high, the absorption coefficient η is no longer dependent on θ and I and is of the order of 0.3–0.4 [4, 21]. The velocity v_e of electrons in the plasma skin layer is determined by the laser-field strength. For this reason, for comparable values of v_e, the electron current density $\mathbf{j} = en_e\mathbf{v}_e$ entering the expression for η becomes greater for a materials with a higher concentration of electrons in the plasma. One can see from Fig. 1 that absorption in the Sn target is approximately 1.5–1.7 times higher than that in the Al target in the intensity range in vacuum from 10^{18} to 5×10^{18} W/cm^2. Let us estimate the ratio of electron concentrations in these materials taking into account the effective degree of their ionization. The electron temperature T_e of the plasma, which determines the degree of ionization of the target atoms at this intensity, is several keV [2]. This is sufficient for full ionization of an Al atom and provides the effective degree of ionization $Z^* \approx 25$ for Sn because $Z^* \approx (2/3)(AT_e)^{1/3}$ [22]. Therefore, according to our estimates, the absorption coefficient of the Sn target at $I \leq 5 \times 10^{18}$ W/cm^2 is approximately two times higher than that of the Al target.

Let us analyze the energy distribution of fast electrons in the target, which follows from the shape of the X-ray spectrum [15]. We will need the number of hot electrons and their energy for analysis of the ion acceleration. The bremsstrahlung intensity of fast electrons is described by the expression [23]

$$\frac{d\varepsilon}{d\varepsilon_\gamma} = \frac{8\sqrt{2}e^6 Z^2 n_i n_{eh}}{3\pi\sqrt{\pi m_e T_e} m_e c^3 \hbar}\exp\left(-\frac{\varepsilon_\gamma}{T_e}\right). \quad (2)$$

It is obvious that the dependence of the intensity on the photon energy at the logarithmic scale is a straight line with a slope determined by temperature, while the point of intersection of the straight line with the ordinate axis gives the logarithm of the concentration n_{eh} of fast electrons. The estimate of the concentration of fast electrons gives $n_{eh} \sim 10^{18}$ cm^{-3}, while the total number of fast electrons produced during the laser pulse is 10^{11}. The temperature of fast electrons is determined by the characteristic energy

$$\varepsilon_h = m_e c^2(\sqrt{1 + (2-\eta)I_{18}} - 1), \quad (3)$$

which is acquired by an electron in the field of laser waves. Here, I_{18} is the laser radiation intensity in units of 10^{18} W/cm^2. The appearance of the second group of electrons with a lower temperature [15] is probably explained by the countercurrent of plasma electrons compensating for the fast-electron current [24]. Without such compensation, the fast-electron current would exceed the Alfven current, which is physically impossible.

Let us now analyze the mechanisms of the escape of electrons and ions from a target into vacuum. A greater part of fast electrons are accelerated deep into the plasma by the pondermotive pressure force. However, electrons located in the outer plasma layer near its surface leave the plasma under the action of the reflected part of the laser pulse at an angle to the normal close to the mirror angle. Due to the escape of electrons into vacuum and their penetration inside the target, the near-surface plasma region becomes depleted of electrons. The appearing ambipolar field and a positive spatial discharge eject the near-surface part of the ions into vacuum and deep into plasma in a direction close to the normal to the target surface. Assuming that photons impart their momentum ε_L/c and energy ε_L with the conversion coefficient $\eta_v \ll \eta$ to a group of electrons

and ions escaping into vacuum, we obtain from the conservation laws the equation

$$\sin\theta_e + \frac{p_i}{Z^*\gamma}\sin\theta_i = \sin\theta\frac{\eta_v\varepsilon_L}{N_e\gamma}$$

for the conservation of the transverse component of the momentum and the equation

$$\gamma - 1 + \frac{\varepsilon_i}{Z^*} = \frac{\eta_v\varepsilon_L}{N_e}$$

for the energy conservation.

Here, η_v is a part of the absorption coefficient corresponding to the particles escaping into vacuum; γ and N_e are the Lorentz factor and the number of electrons; and ε_L, ε_i, and p_i are measured in units m_ec^2 and m_ec. Because the system is inhomogeneous in the longitudinal direction, the longitudinal component of the field momentum and of particles escaping into vacuum is not conserved. By combining two conservation laws, we obtain the relation

$$\sin\theta_e = \sin\theta\frac{\gamma - 1 + \varepsilon_i/Z^*}{\gamma} - \frac{p_i}{Z^*\gamma}\sin\theta_i, \qquad (4)$$

between the escape angles of the particles. Two important conclusions follow from expression (4).

(1) The escape angle of the high-energy group of electrons with $\gamma \gg 1$ is close the mirror angle, $\theta_e \approx \theta$, while electrons with lower energies leave the target in a direction close to the normal. The highest energy electrons are formed in the region of plasma transparency, where electrons are subjected to the action of the most intense field. The energy of such fast electrons in the electromagnetic wave is

$$\varepsilon_{uh} = m_ec^2(\gamma - 1) \approx \frac{p_0}{mc}\left(\frac{v_E}{c}\right)^2, \qquad (5)$$

where $v_E = eE/m\omega$ is the oscillation velocity of electrons, and the initial momentum of an electron along the laser beam is $p_0 \approx mv_E$ because it is determined by the acceleration in the laser field E at the wavelength $\lambda = 2\pi c/\omega$. From here, we obtain for $I \approx 10^{19}$ W/cm^2 the value $\varepsilon_{uh} \approx 10$ MeV, in accordance with the experiment. We emphasize that this concerns a small number of electrons belonging to the "tail" of the distribution function. The main part of electrons has a lower characteristic energy (3). Thus, electrons leave the target in a range of directions from normal to mirror.

(2) The escape angle of ions, obtained from (4), cannot obviously exceed

$$\theta_i \le \sin\theta\frac{Z^*(\gamma - 1) + \varepsilon_i}{\sqrt{2\mu_i/m_e}\sqrt{\varepsilon_i}} \ll 1. \qquad (6)$$

Thus, the ions escape on average virtually along the normal to the target. We estimate the energy of a fast ion from the law of conservation of momentum in the differential form, i.e., of conservation of the flux density for the longitudinal component of the ion pulse and of electrons pulling the ions:

$$n_im_iv_i^2 = \cos^2\theta_e\frac{n_e\varepsilon_ev_e^2}{c^2},$$

where $n_{i,e}$ are the concentrations of ions and electrons in the near-surface plasma layer (the transparency region of scale L) and

$$n_e < n_i \approx \frac{n_{cr}}{Z^*}$$

(n_{cr} is the critical concentration). The characteristic energy of fast electrons in the field of the incident and reflected laser pulses is estimated as (3). Then,

$$\varepsilon_i = \cos^2\theta_eZ^*\frac{n_e}{n_{cr}}\frac{(2-\eta)I_{18}}{\sqrt{1 + (2-\eta)I_{18}}}. \qquad (7)$$

For $I_{18} \ge 1$, we find from (7) that $\varepsilon_i \sim I_{18}^{0.5}$, in accordance with the experimental dependence $\varepsilon_i \sim I_{18}^{0.46}$ in Fig. 3. To determine the ratio Z^*n_e/n_{cr}, in the near-surface plasma we will use the results of X-ray measurements presented in the previous section. By substituting the value of n_{eh} instead of n_e, we obtain $Z^*n_e/n_{cr} \sim 0.1$. Let us plot the theoretical dependence $\varepsilon_I(I)$ in Fig. 3, by substituting the values $Z^*n_e/n_{cr} \sim 0.1$, $\theta_e \approx \theta$, and $\eta = 0.4$ because absorption weakly depends on I (Fig. 1). One can see from Fig. 3 that the theoretical dependence (the dashed curve) is close to the experimental dependence, indicating the validity of the model.

Along with simple estimates, we simulated the escape of particles using the relativistic *PM2*D *PIC* code [25]. The theoretical dependence of the total energy (in eV) carried away by hydrogen ions to vacuum on the escape angle for the intensity equal to 10^{18} W/cm^2 is shown in Fig. 4 (the solid curve) together with experimental data. As in the experiment, the ions leave the target mainly along its normal, with an angular dispersion of ~15°. The difference in the angular widths of the theoretical and experimental dependences in Fig. 4 is probably explained by the use of the one-dimensional spatial model in calculations. The escape angle of ions predicted by the two-dimensional model can be substantially larger than (6).

Let us also compare the energy carried away by fast ions calculated using the *PIC* code with the experimental value. It follows from the numerical calculation presented in Fig. 4 that the ions carry away the energy 1.2×10^{16} eV in the direction along the normal to the target when the irradiation intensity is 10^{18} W/cm^2. By integrating the experimental velocity distribution of ions escaping along the normal (Fig. 2) and multiplying by the average energy of ions taken from Fig. 3, we obtain the experimental result 7×10^{15} eV. Thus, the calculations and experimental data are consistent.

The main part of ions leaving the target are protons with a small amount of C^+ and C^{2+}. The hydrogen and carbon ions appear in the aluminum target due to adsorption of water vapor on the target surface and as chemical traces of the target surface polishing. Therefore, in the absence of hydrogen and carbon on the target surface, according to (7), the energy of Al ions with high Z^* should be $\varepsilon_i \geq 1$ MeV for $Z^* \geq 6$.

Note that, according to our calculations, the fast-ion beam of approximately the same angular width propagates deep into the target from the near-surface region of volume $V = \pi(d/2)^2 L$ due to the charge-separation potential $e\varphi = \varepsilon_{eh}$ produced owing to the escape of fast electrons with the energy $\varepsilon_{eh} \approx \eta I/cn_{eh}$ from the surface region deep into the target. Assuming that the fast ion acquires the energy $Z^* e\varphi \approx \varepsilon_{ih}$ and

$$\varepsilon_{eh} \geq e^2 n_{eh} \pi L d\left(1 - \frac{L}{d}\right)$$

is the Coulomb barrier energy, we obtain, similarly to [9],

$$\varepsilon_{ih} \approx 3Z^* mc^2\left(\eta I_{18}\frac{dL}{\lambda^2}\right)^{1/2},$$

where the dependence on I corresponds to (7) and coincides with (7) for $((d/\lambda)^{1/2} \approx n_e/n_{cr}$. The number of such ions in the Al target for the intensity 5×10^{18} W/cm^2 is of the order of 10^7, and the coefficient of conversion to the energy of fast ions achieves ~1%. This fast-ion beam can be used for the generation of nuclear reactions inside the target (similarly to [26]), in particular, as a high-power pulsed neutron source.

4. CONCLUSIONS

We have obtained the following results in this paper.

(i) Megaelectronvolt ions, submegaelectronvolt protons, and fast electrons with an energy above 10 MeV have been detected by irradiating targets by ~10^{19} W/cm^2 *p*-polarized laser pulses.

(ii) The spectral, spatial, and energy parameters of the fast-ion beam have been determined for $I > 10^{17}$ W/cm^2.

(iii) The two-dimensional *PIC* calculations have shown that the main part of fast ions leave the target within a narrow solid angle normally to the target surface upon its oblique irradiation (unlike fast electrons), in accordance with the experimental results obtained for $I > 10^{17}$ W/cm^2; in addition, the fast-ion beam also propagated deep into the target.

(iv) The coefficient of conversion of the laser-pulse energy into the energy of fast ions (of about 1%) obtained by us confirms the outlook for using the laser for acceleration of particles and generation of nuclear reactions.

ACKNOWLEDGMENTS

This study was partly supported by the Russian Foundation for Basic research, project no. 00-02-17288.

REFERENCES

1. M. D. Perry, D. Pennington, B. C. Stuart, *et al.*, Opt. Lett. **24**, 160 (1999).
2. A. A. Andreev, A. I. Zapysov, A. V. Charukhchev, and V. E. Yashin, Izv. Akad. Nauk, Ser. Fiz. **63**, 1239 (1999).
3. P. L. Shkolnikov, A. E. Kaplan, A. Pukhov, *et al.*, Appl. Phys. Lett. **71**, 3471 (1997).
4. A. A. Andreev, A. A. Mak, and V. E. Yashin, Kvantovaya Élektron. (Moscow) **24**, 99 (1997).
5. A. P. Fews, P. A. Norreys, F. N. Beg, *et al.*, Phys. Rev. Lett. **73**, 1801 (1994).
6. F. N. Beg, A. R. Bell, A. E. Dangor, *et al.*, Phys. Plasmas **4** (2), 447 (1997).
7. K. Krushelnick *et al.*, Phys. Plasmas **7**, 2055 (2000).
8. S. P. Hatchett, C. G. Brown, T. E. Cowan, *et al.*, Phys. Plasmas **7**, 2076 (2000).
9. A. Maksimchuk, S. Gu, K. Flippo, *et al.*, Phys. Rev. Lett. **84**, 4108 (2000).
10. V. G. Borodin, V. M. Komarov, S. V. Krasov, *et al.*, Kvantovaya Élektron. (Moscow) **25**, 115 (1998).
11. V. G. Borodin, V. M. Komarov, V. A. Malinov, *et al.*, Kvantovaya Élektron. (Moscow) **29**, 101 (1999).
12. J. M. Auerbach, N. C. Holmes, J. T. Hunt, and G. L. Linford, Appl. Opt. **18**, 2495 (1979).
13. V. V. Il'in, V. M. Komarov, A. V. Charukhchev, *et al.*, Prib. Tekh. Éksp., No. 4, 113 (1997).
14. A. A. Andreev, V. M. Komarov, A. G. Samsonov, *et al.*, Kvantovaya Élektron. (Moscow) **19**, 709 (1992).
15. V. G. Borodin, O. N. Gilev, A. L. Zapysov, *et al.*, Pis'ma Zh. Éksp. Teor. Fiz. **71**, 354 (2000) [JETP Lett. **71**, 246 (2000)].
16. V. G. Borodin, F. L. Zapysov, O. N. Gilev, *et al.*, Fiz. Plazmy **24**, 157 (1998) [Plasma Phys. Rep. **24**, 136 (1998)].
17. E. M. Lifshitz and L. P. Pitaevskiĭ, *Physical Kinetics* (Nauka, Moscow, 1979; Pergamon, Oxford, 1981).
18. T.-Y. Briang Yang, W. L. Kruer, R. M. More, and A. B. Langdon, Phys. Plasmas **2**, 3146 (1995); T.–Y. Brian Yang *et al.*, Phys. Plasmas **3**, 2702 (1996).
19. F. Brunel, Phys. Rev. Lett. **59**, 52 (1987).
20. K. Estabrook and W. L. Kruer, Phys. Rev. Lett. **40**, 42 (1978).
21. T. E. Cowan *et al.*, in *Technical Digest of the International Conference "Lasers'97", New Orleans, Louisiana, 1997.*
22. M. Muruane, H. Kapteyn, M. Rosen, and R. Falcone, Science **251**, 531 (1991).
23. V. L. Ginzburg, *Theoretical Physics and Astrophysics* (Nauka, Moscow, 1981; Pergamon, Oxford, 1979).
24. A. R. Bell and J. R. Davies, Phys. Rev. E **58**, 2471 (1998).
25. A. A. Andreev, I. A. Litvinenko, and K. Yu. Platonov, Zh. Éksp. Teor. Fiz. **116**, 1184 (1999) [JETP **89**, 632 (1999)].
26. V. Yu. Bychenkov, V. T. Tikhonchuk, and S. V. Tolokonnikov, Zh. Éksp. Teor. Fiz. **115**, 2080 (1999) [JETP **88**, 1137 (1999)].

Translated by M. Sapozhnikov

Journal of Experimental and Theoretical Physics, Vol. 94, No. 2, 2002, pp. 228–238.
Translated from Zhurnal Éksperimental'noĭ i Teoreticheskoĭ Fiziki, Vol. 121, No. 2, 2002, pp. 274–285.

NUCLEI, PARTICLES, AND THEIR INTERACTION

Self-Oscillatory Heterogeneous Recombination of Hydrogen Atoms and Nonequilibrium Desorption of Molecules from the Surface (Teflon)

V. P. Grankin[a, *], V. V. Styrov[a, **], and Yu. I. Tyurin[b, *]**

[a]*Azov State Technical University, Mariupol', Donetsk oblast, 87500 Ukraine*
**e-mail: grankin@pstu.edu*
***e-mail: svv@pstu.edu*
[b]*Tomsk Polytechnical University, Tomsk, 634034 Russia*
****e-mail: tyurin@fnsm.tpu.edu.ru*
Received August 1, 2001

Abstract—The channel of the accommodation of the energy of a heterogeneous chemical reaction (recombination of hydrogen atoms) related to vibrational *V–V* exchange between excited chemical reaction products and adsorption layer molecules (H_2O, HDO, D_2O, and H_2) was studied by the method of modulated molecular beams. The chemical reaction was found to proceed in an oscillatory mode caused by the nonequilibrium character of its elementary steps. The participation of adsorbed molecules in accommodation was studied by analyzing nonequilibrium desorption of these molecules. An isotope effect was observed in nonequilibrium desorption. The kinetic mechanism of the reaction and the micromechanism of elementary reaction events, which determine the "physical" mechanism of catalysis in the system under study, are discussed. © *2002 MAIK "Nauka/Interperiodica".*

1. INTRODUCTION

Reactive collisions of atomic particles with the surface of a solid (adsorption, recombination of atoms, etc.) are often accompanied by considerable energy liberation, up to several electronvolts per elementary event. Usually, this energy first concentrates on the newly formed chemical bond in the form of high-excitation motions of nuclei. Nonequilibrium vibrational states with large quantum numbers then relax by transferring excess energy to various degrees of freedom of the solid and, possibly, reaction product (accommodation process). At high reaction heats (of the order of 1 eV) and usual Debye temperatures of solids, the energy released in the reaction is large compared with the energy even of phonons with the highest frequency (of about 10^{-2} eV), and exchanging the heat of the reaction into phonons is seriously hindered. Long-lived (on the time scale of one-phonon excitation lifetimes) nonequilibrium vibrational states (vibratons) with lifetimes $\tau_v \gg 10^{-13}$ s can then form on the surface. If the vibrational spectrum of the surface contains frequencies (for instance, adsorption layer frequencies) coinciding with or close to vibraton frequencies, a vibraton can move over the surface with insignificant damping and display the properties of a usual quasi-particle (in two dimensions). In addition to its high-frequency character, the simplicity of reaction product structures contributes to the long lifetime of vibratons, because a small number of internal vibrational (and other) degrees of freedom in the product impedes the decay of vibratons to its "internal" excitations. Such conditions, for instance, characterize heterogeneous recombination of hydrogen atoms, when the $H + H_{ads} = H_{2(ads)}$ recombination event causes the appearance on the surface of a "giant" high-frequency vibraton H_2^v, which has an energy of about 4 eV and $\hbar\omega_0 \approx 0.5$ eV and is bound to the very simple H_2 molecule.

Note that, generally, a vibraton interacts with both the atomic (lattice) and the electronic subsystem of crystals (reaction products) and causes transitions of these subsystems into excited vibrational and electronic states. Even comparatively recently, the latter ("electronic") accommodation channel has been totally rejected in view of the drastically different masses of the electron and atomic particles [1]. In a strongly vibrationally nonequilibrium state, we cannot, however, independently consider the "heavy" (lattice) and "light" (electronic) crystal subsystems in the Born–Oppenheimer approximation, because electron-vibrational coupling caused by motions of nuclei mixes electronic states and can initiate nonadiabatic electronic transitions. Other electron-vibrational interaction mechanisms that cannot be disregarded in the problem under consideration are also known [2]. Electronic accommodation is observed in several physical phenomena related to electronic excitation of solids as a result of heterogeneous chemical reactions. These phenomena include nonequilibrium conductivity of crys-

tals on whose surface reactions occur [3, 4], transverse chemomagnetoelectric effect (similar to the Kikoin–Noskov effect in photoexcitation) [5], longitudinal chemical valve effect similar to the generation of photoelectromotive force [6], luminescence of crystals in the visible and other spectral regions [7], and electronic emission from the surface [8, 9].

The lattice accommodation channel also leads to several physical effects unknown earlier, such as emission from the surface of crystal lattice components (atoms and ions) during reactions [8] and reaction-induced diffusion of impurity atoms from the surface into the bulk of the crystal [10]. All these effects have been discovered comparatively recently.

To summarize, an elementary exothermic chemical reaction event is nonequilibrium in principle from the physical point of view. The evolution of primary excitations (vibratons) that arise in electronic configuration (chemical bond) rearrangements can determine the fine features and the most important characteristics of reactions including reaction rates, as will be shown below.

As concerns practical applications, solving the problem under consideration opens up possibilities for controlling many important technological processes such as growth of crystals and epitaxial layers, catalysis, adsorption separation of isotopes (including adsorption separation under laser actions), and thermal protection of descending spacecraft.[1]

The problem of accommodation has not been rigorously formulated in the theory of adsorption and heterogeneous reactions, in particular, because the microscopic paths and mechanisms of accommodation on the surface have scarcely been studied theoretically and experimentally.

In this work, we consider the poorly studied accommodation channel, which is of importance for gas–solid systems when the surface of the solid has a noticeable adsorbate coverage. The participation of adsorbed molecules in accommodation can be traced by studying the effect of nonequilibrium desorption of these molecules ("own" or "foreign") as a result of absorbing the energy of reactive vibratons. The gas–adsorption layer interaction was found to cause the appearance of an oscillatory reaction mode in the system under study. The observation of a real oscillatory chemical process is always a striking event, although such phenomena are becoming common in modern physics.

2. EXPERIMENTAL RESULTS

The object of study was the Teflon (with some adsorbate)–atomic hydrogen system. Teflon is characterized by very low heats of adsorption of H_2O and H_2 molecules and H atoms (adsorbate particles of our experiments), which favors nonequilibrium desorption of such particles caused by the energy effect of the reaction. The nonequilibrium desorption effect in this system is also favored by substantial energy release in the recombination of H atoms (above 4 eV per recombination event). The electronic accommodation channel is of no importance in the system under consideration because the lowest electronically excited Teflon and reaction product (H_2 molecules) states lie much higher than the heat effect of the reaction on the energy scale.

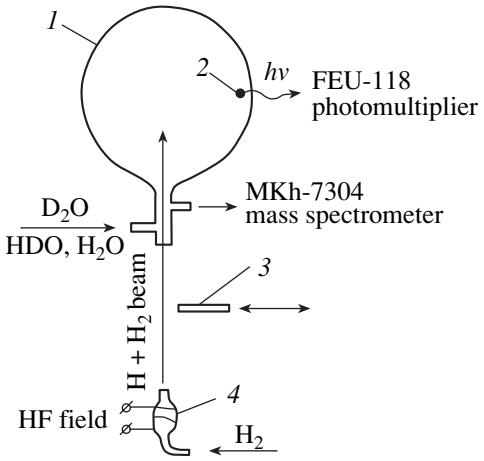

Fig. 1. Scheme of experimental unit (see text for explanation).

Virtually the only effective accommodation channel under these conditions is vibrational *V–V* relaxation in the adsorption layer (this process can occur under conditions close to resonance) and the accompanying *V–T* relaxation (nonequilibrium desorption). At low adsorbed particle concentrations, there is no conditions favoring accommodation. The Teflon–atomic hydrogen system is therefore characterized by exceptionally low atomic recombination coefficients (this is one of the reasons for using this system in hydrogen masers [11]).

Measurements were taken on a unit with molecular beams. The experimental procedure was described in [12]. Here, we only give the basic scheme of measurements (Fig. 1). An atomic–molecular beam of hydrogen (H_2 + H) formed by a source of a special design was directed into accumulating quartz flask *1* (15 cm in diameter), such as usually employed in hydrogen masers. The flask walls were coated by a Teflon film (F-10). The densities of the flows of H atoms and H_2 molecules were $j_1^0 \approx 5 \times 10^{14}$ cm^{-2} s^{-1} and $j_2^0 \approx 2 \times 10^{15}$ cm^{-2} s^{-1}, respectively. Preliminarily, heavy water D_2O molecules with HDO and H_2O admixtures were adsorbed on flask walls (adsorption time $t \approx 1$ min, $P_{D_2O,\,HDO,\,H_2O} = 18$ Torr, $T = 300$ K). Starting with the moment of switching on the H + H_2 beam, the following kinetic dependences were recorded by independent methods: (1) the intensity of desorption of particles from the surface of Teflon

[1] Spacecraft are heated both because of air friction and because of the recombination on their surfaces of free atoms (O and N) formed from molecules in the Earth's atmosphere dissociated under the shock wave action.

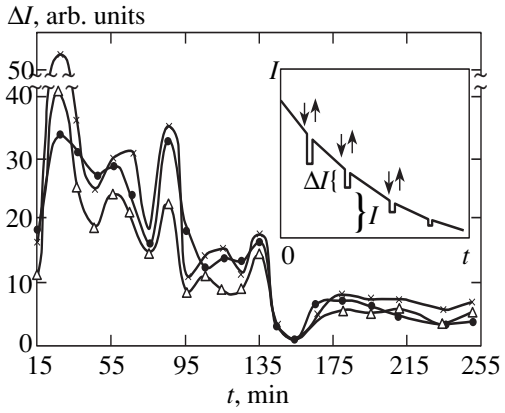

Fig. 2. Dependences of the intensity of nonequilibrium desorption of D_2O (●), HDO (×), and H_2O (△) from the surface of Teflon F-10 on the time of exposure to H + H_2 beams. The experimental schedule is shown in the inset, where marked by arrows are time moments of switching off (↓) and on (↑) H + H_2 beams during measurements of intensity I of desorption of water molecules as a function of time at $T = 295$ K and $j_1 = 5 \times 10^{14}$ cm^{-2} s^{-1}.

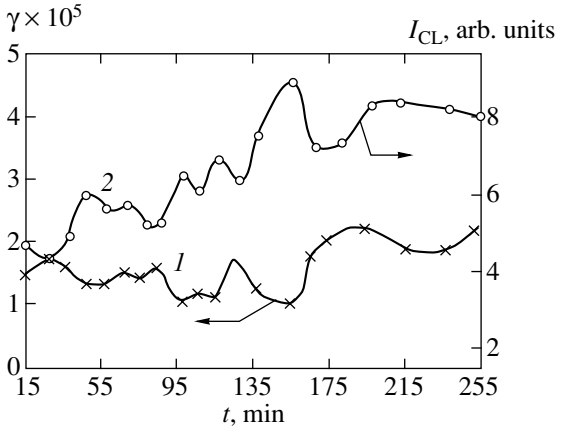

Fig. 3. Heterogeneous recombination coefficient of H atoms (curve *1*) and heterogeneous chemiluminescence intensity of a probe within the flask (curve *2*) as functions of the time of exposure to H + H_2 beams at $T = 295$ K and $j_1 = 5 \times 10^{14}$ cm^{-2} s^{-1}.

was determined mass spectrometrically on an MKh-7304 mass spectrometer; (2) concentration n of hydrogen atoms in the flask was monitored by observing the chemiluminescent response of a small luminophor *2* sample, which luminesced because of the recombination of H atoms on it; the intensity of chemiluminescence (I_{CL}, recorded using an FEU-118 photomultiplier) at the moment of switching on the beam of atoms was strictly proportional to n; (3) the recombination coefficient of H atoms on Teflon (γ) was determined from the rate of decreasing the concentration of H atoms in the flask, $n(t)$, after switching off the atomic beam with the use of the same chemiluminescent sensor and photomultiplier. Recombination coefficient γ is the ratio between the number of incident atoms that recombine on the surface to the total number of atoms colliding with the surface (for instance, in unit time). The recombination of atoms incident from the gas phase with atoms adsorbed on the surface is characterized by $\gamma = \sigma_2 N_1$, where N_1 is the surface concentration of adsorbed atoms and σ_2 is the recombination reaction cross section. When the beam is switched off, the concentration of atoms in the flask (n) decreases because of their recombination on flask walls by the law [13]

$$n = n_0 \exp\left(-\gamma \frac{v_a k S}{4V} t\right),$$

from which the γ value is calculated (v_a is the thermal velocity of atoms). The time taken by γ measurements was small (5 s), which allowed us to study long-term kinetics $\gamma(t)$ determined by slow changes in the conditions on the surface.

Along with usual equilibrium (thermal) desorption of water molecules (D_2O, HDO, and H_2O), we observed nonequilibrium desorption when the surface was subjected to bombardment by H + H_2 beams. We were able to separate the equilibrium and nonequilibrium contributions by applying a modulation procedure. When beam atoms were switched off (HF discharge generating atoms was switched off or modulator shutter *3* closed the beam), we observed a jump decrease (ΔI) in the intensity of D_2O, HDO, and H_2O peaks in the mass spectrum. The residual intensity (I) was used as a measure of the equilibrium desorption flow, whereas the ΔI value characterized the nonequilibrium desorption component (Fig. 2, inset). The $\Delta I/(I + \Delta I)$ ratio, or the fraction of nonequilibrium desorption, increased during H atomic beam action from zero to 30–40% at $t > 30$ min. An H_2 purely molecular beam (free of atoms) did not cause the nonequilibrium desorption effect.

The $\Delta I(t)$ and $\Delta I(t)/I(t)$ time dependences were unusual (the latter value can be selected as a measure or effectiveness of nonequilibrium desorption of water molecules). The ΔI intensity of nonequilibrium desorption (like the $\Delta I/I$ ratio) was an oscillatory function of time (Fig. 2) at a constant beam intensity. In addition, the $\gamma(t)$ recombination coefficient of atoms on the surface of Teflon (Fig. 3) and the $n(t)$ concentration of H atoms in the flask (as mentioned, $n(t)$ was measured by the intensity of luminescence from the chemiluminescent sensor) also exhibited oscillations. The ΔI nonequilibrium desorption flow, the $\Delta I/I$ relative flow, and the γ value oscillated almost in phase with each other but in antiphase to $n(t)$. According to our hypothesis, the nonequilibrium component of the desorption of molecules is due to transfer of vibrational energy from H_2^v–L (vibratons)[2] to preliminarily adsorbed water molecules (V–V exchange in the adsorption layer) fol-

[2] Here, L (from lattice) is the symbol of the surface of a solid.

lowed by their nonequilibrium desorption (*V–T* exchange). As the γ value characterizes the intensity of the reaction ($cm^{-2}\ s^{-1}$) of the recombination of atoms on the surface (the reaction intensity equals γj_1, where j_1 is the flow density of atoms H that reach flask walls), this hypothesis directly explains the synchronous character of γ, ΔI, and $\Delta I/I$ variations in time, because the last two values are also proportional to the intensity of the reaction. At time moments corresponding to the highest reaction intensity on the surface (to maximum ΔI, $\Delta I/I$, and γ values), the concentration of atoms in the flask is minimum (at a constant j_1^0 flow of H atoms into the flask from the source of atoms).

Oscillations themselves can also be explained by *V–V* exchange on the assumption that the probability of recombination of atoms (and, therefore, the rate of the reaction) is determined by the probability of stabilizing H_2^v–L molecules formed in recombination events by means of vibrational energy loss. This probability in turn depends on surface coverage by water molecules, which absorb energy in excess of the equilibrium energy. It follows that we discuss an unusual catalytic action of a substrate with an adsorbate which is "physical" catalysis involving the accommodation of reaction heat by an adsorbate (catalyst); this catalyst increases the σ_2 recombination reaction cross section in the $\gamma = \sigma_2 N_1$ formula, where N_1 is the surface concentration of adsorbed atoms. The "naked" substrate itself much less effectively stabilizes the H_2^v–L reaction product (less effectively absorbs vibratons), because this product is a carrier of large vibrational quanta (in the free H_2 molecule, $\hbar\omega_0 \approx 0.5$ eV at the lower vibrational levels). The accommodation "through a substrate" is an essentially multiphonon (and therefore low-probability) process; Teflon is known as one of the worst catalysts of the recombination of H atoms, $\gamma \sim 10^{-6}$. Conversely, H_2O, H_2, etc., adsorbates containing "light" atoms may have frequencies with a small "resonance defect" with respect to the H_2^v–L vibraton, which favors effective accommodation "through the adsorbate."[3] Surface coverage by an adsorbate should not be too large, because, for the recombination of atoms on the surface to occur, the surface should contain a fairly large number of free adsorption centers for H atoms (the N_1 value in the $\gamma = \sigma_2 N_1$ formula should be fairly large). From this point of view, vibrational development of the recombination of H atoms on the surface of Teflon with an adsorbate can qualitatively be described as follows. At large surface coverages by water molecules, the surface concentration of adsorbed atoms (N_1) is low. The γ value and the intensity of recombination γj_1 are therefore also low. As water molecules undergo desorption (both equilibrium and nonequilibrium), surface coverage by H atoms (that is, N_1) increases, and surface coverage by water molecules approaches the value optimal for effective *V–V* exchange between the H_2^v–L and H_2O–L systems. An increase in N_1 and σ_2 leads to an increase in γ and, therefore, the rate of the reaction accompanied by an increase in the intensity of nonequilibrium desorption (the $\Delta I(t)$ and $\Delta I/I$ values increase). At the same time, the volume concentration of atoms (n) decreases and that of water molecules increases.[4] However, simultaneously, the mechanism of reaction deceleration begins to operate; namely, because of nonequilibrium desorption of water as a result of *V–V* exchange, surface coverage by the adsorbate (water molecules) decreases and increasingly deviates from optimal (the σ_2 and γ values decrease). The γj_1 reaction intensity and, accordingly, the ΔI and $\Delta I/I$ values also decrease. The amplitude of ΔI oscillations should lessen as time passes, because the concentration of water molecules in the flask and on the surface decreases as a result of evacuation from cycle to cycle. This conclusion is in agreement with the experimental data (Fig. 2). Conversely, the amplitude of $\Delta I/I$ oscillations increased in our experiments because the relative contribution of nonequilibrium desorption grew larger. Interestingly, contrary to our expectations, the amplitude of $\gamma(t)$ oscillations did not decrease to zero even at very long times (more than 4 hours) of Teflon surface exposure to H + H_2 beam action, when water molecule lines disappeared from the mass spectra (Fig. 4). This led us to conclude that the adsorption of foreign molecules (water in our experiments) is not a necessary condition for the appearance

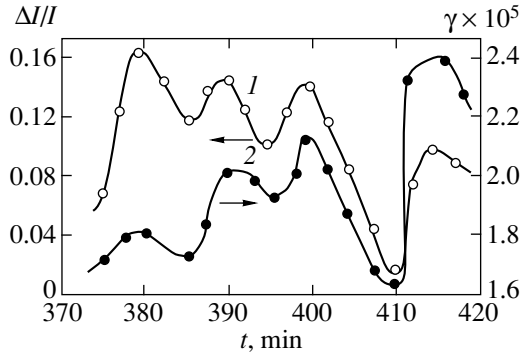

Fig. 4. (*1*) Relative nonequilibrium desorption of H_2 and (*2*) recombination coefficient of H atoms on the surface of Teflon F-10 as functions of the time of exposure to H + H_2 beams at $j_1 = 2.5 \times 10^{14}$ $cm^{-2}\ s^{-1}$ and $T = 298$ K.

[3] According to [14], excited $H_2^{v=1}$ molecules incident on the Teflon surface from the gas phase were also successfully accommodated in the presence of specially preadsorbed molecules on the surface.

[4] The concentration of water increases because of the design of the unit. Although molecules are continuously evacuated from the flask, they are evacuated through a narrow capillary, which makes the process inertial. Any adsorption–desorption equilibrium violation therefore causes pressure changes in the flask.

of recombination coefficient oscillations, which can also result from the adsorption and subsequent nonequilibrium desorption of its own molecules (H_2). We performed special experiments following the same procedure with H + H_2 atom–molecular beams but without preliminarily adsorbing water. The surface of the Teflon was made free of adsorbed impurities by heating in a high vacuum and pretreating with an intense flow of hydrogen atoms ($j_1 = 10^{18}$ cm^{-2} s^{-1}) for an hour (the gas was supplied by diffusion). As with water adsorption, we used independent techniques to simultaneously measure the intensity of nonequilibrium desorption of H_2 molecules $\Delta I/I$ (mass spectrometrically), the intensity of chemiluminescence of the luminescent probe $I_{CL} \sim n$ (by a photomultiplier), and the recombination coefficient of H atoms on Teflon. According to Fig. 4, the $\Delta I/I$ and $\gamma(t)$ values oscillated in time in phase with each other, as in experiments with water. It can be suggested that the mechanism of oscillations had the same nature in both experiments, and that, in the absence of foreign (water) molecules in the adsorbate, the role of the adsorbate–catalyst was played by its own H_2 molecules; that is, the process occurred under autocatalytic oscillation conditions. Autocatalytic oscillations were caused by oscillations of surface coverage by adsorbate particles (H_2 and H). The effectiveness of *V–V* exchange with H_2–L molecules in the adsorption layer was even higher than with H_2O–L because these molecules best satisfied the resonance conditions for vibrational energy transfer.

Let us estimate the effectiveness of nonequilibrium desorption of H_2, that is, the number of desorbed molecules per one recombination event on the surface, from the experimental data. If J_{H_2} is the flow of molecules from the accumulating flask to the mass spectrometer and ΔJ_{H_2} is the nonequilibrium contribution to this flow, then, clearly,

$$\Delta J_{H_2} = \frac{\Delta I}{I} J_{H_2}. \quad (1)$$

The lifetime of molecules in flask volume determined by the probability of their gas kinetic escape through the narrow orifice equaled 15 s in our experiments, which was much less than the period of $\Delta I/I$ oscillations. It follows that quasi-stationary conditions were maintained in the flask, and the flow of molecules into the flask from the H + H_2 beam equaled the outflow of molecules from the flask; that is,

$$J_{H_2} = j_2^0 S_0,$$

where j_2^0 is the density of the flow of molecules incident on the flask inlet hole of area S_0. Substituting this J_{H_2} value into (1) yields

$$\Delta J_{H_2} = \frac{\Delta I}{I} j_2^0 S_0. \quad (2)$$

The flux of H atom recombination events on the Teflon flask surface is

$$J = \frac{1}{2}\gamma j_1 S, \quad (3)$$

where j_1 is, as previously, the density of the flow of H atoms onto flask walls of area *S*. The effectiveness of nonequilibrium desorption is determined by the ratio between (2) and (3),

$$\alpha \equiv \frac{\Delta J_{H_2}}{J} = \frac{\left(\frac{\Delta I}{I}\right) j_2^0 S_0}{\frac{1}{2}\gamma j_1 S}. \quad (4)$$

The above relations allow estimates to be made. Under the experimental conditions, $j_2^0 S_0 = 4 \times 10^{14}$ s^{-1}, $j_1 = 3 \times 10^{15}$ cm^{-2} s^{-1}, $S = 706$ cm^2, and $(\Delta I/I)_{max} = 0.16$ (Fig. 4, curve *1*). The corresponding γ value is $\gamma = 1.8 \times 10^{-5}$ (Fig. 4, curve *2*). Substituting these values into (4) yields

$$\left(\frac{\Delta J_{H_2}}{J}\right)_{max} \approx 3.$$

The minimum value is

$$\left(\frac{\Delta J_{H_2}}{J}\right)_{min} \approx 0.2.$$

It follows that one H_2^v–L molecule formed on the surface causes nonequilibrium desorption of up to 3 H_2 molecules. Clearly, if $\Delta J_{H_2}/J > 1$, the flow of molecules that experience nonequilibrium desorption (ΔJ_{H_2}) exceeds the flow of molecules that replenish the surface as a result of the recombination of atoms (these molecules in the form of vibratons have fairly long lifetimes on the surface; otherwise, they would not be able to participate in *V–V* exchange). Under these conditions, surface coverage decreases as time passes. If the opposite inequality holds, that is, $\Delta J_{H_2}/J < 1$, surface coverage by molecules increases (this is the effect of dynamic blocking of the surface by molecules formed on the surface during the reaction). Oscillations of the $\Delta J_{H_2}/J$ ratio between values larger and smaller than one is precisely what signifies the occurrence of heterogeneous recombination in the accumulating flask in an oscillatory regime.

Qualitative considerations concerning the appearance of oscillations are substantiated by a strict kinetic analysis of the problem (see Section 3).

Similar experimental estimates for nonequilibrium desorption of water molecules during the recombination of H atoms on the surface also give $\Delta J_{H_2O}/J$ ratios that oscillate between values larger and smaller than

one. In these experiments also, the maximum $\Delta J_{H_2O}/J$ value reached three.

In the experiments that we describe, we observed the isotope effect in nonequilibrium desorption; namely, the relative probability θ of nonequilibrium desorption of water molecules caused by the recombination of H atoms depended on the isotope composition of molecules. The probabilities determined experimentally for the D_2O, HDO, and H_2O molecules were related as $\theta_1 : \theta_2 : \theta_3 = 1.6 : 1.8 : 2.0$. Light water molecules with vibrational quanta highest in energy (as compared with D_2O and HDO), which, therefore, exhibited the smallest resonance defect in *V–V* exchange with H_2^v–L vibratons, most readily underwent nonequilibrium desorption.

The isotope effect in nonequilibrium desorption is one of the direct arguments of the validity of the model under consideration. Under certain conditions, an adsorption layer provides an effective channel for the accommodation of the energy of the heterogeneous chemical reaction. The adsorption layer necessary for energy accommodation can be either created from the outside or formed automatically by the reaction itself (from reagents and reaction products). No matter what the origin of the adsorbate on the surface, the catalytic efficiency of the surface and the rate of the reaction are functions of surface coverage, and the coverage in turn depends on the rate of the reaction. Under these conditions, manifestations of various nonlinear effects in the kinetics of the reaction can be expected.

3. KINETIC MECHANISM OF THE RECOMBINATION OF H ATOMS AND NONEQUILIBRIUM DESORPTION OF ADSORBED MOLECULES

In what follows, we consider the problem in the most general form taking into account that, in the recombination of H atoms, the surface can contain both foreign molecules (water, etc.) and its own particles (H and H_2) and that all of them can participate in nonequilibrium desorption. The kinetic mechanism of reactions in the flask includes the following steps:

$$H + L \underset{\nu_1'}{\overset{\nu_1}{\rightleftarrows}} HL\text{—adsorption (desorption) of atoms,}$$

$$H + HL \xrightarrow{\nu_2} H_2^v L\text{—recombination of atoms,}$$

$$H_2^v L \longrightarrow \begin{cases} (+L) \xrightarrow{\mu} 2(HL)\text{—nonequilibrium dissociation,} \\ \xrightarrow{\Gamma_1} H_2^{v-1}L + \text{phonons—multiphonon relaxation,} \\ (+H_2L) \xrightarrow{\sigma\Gamma_2} H_2^{v_1}L + H_2^{v-1}L\text{—relaxation } (V\text{–}V \text{ exchange}), \\ \xrightarrow{\Gamma_3} H_2 + L\text{—nonequilibrium desorption of } H_2 \text{ molecules,} \\ (+HL) \xrightarrow{\sigma_4\Gamma_4} H + L + H_2^{v-1}L\text{—nonequilibrium desorption of atoms,} \\ (+H_2OL) \xrightarrow{\sigma_5\Gamma_5} H_2O + L + H_2^{v-1}L\text{—nonequilibrium desorption of } H_2O \text{ molecules.} \end{cases}$$

Further, the process is repeated with a decrease in the number of the occupied vibrational level,

$$H_2^{v-m+1}L \longrightarrow \begin{cases} \xrightarrow{\Gamma_1} H_2^{v_1}L + \text{phonons,} \\ (+H_2L) \xrightarrow{\sigma\Gamma_2} H_2^{v_1}L + H_2^{v_1}L, \\ \xrightarrow{\Gamma_3} H_2 + L, \\ (+HL) \xrightarrow{\sigma_4\Gamma_4} H + L + H_2^{v_1}L, \\ (+H_2OL) \xrightarrow{\sigma_5\Gamma_5} H_2O + L + H_2^{v_1}L, \end{cases}$$

and so on until

$$H_2 + L \underset{\nu_3'}{\overset{\nu_3}{\rightleftarrows}} H_2L\text{—adsorption (desorption) of } H_2,$$

$$H_2OL \xrightarrow{\nu'} H_2O + L\text{—desorption of } H_2O.$$

Probabilities ν_i referred to unit time, Γ_i, and cross sections σ_i of the corresponding reactions are given above the arrows. The vibrational quantum number $v - m + 1$ corresponds to $v = 2$, and v_1 labels molecules at the first vibrational level $v = 1$. For simplicity, the model includes adsorbed water without heavy water admixtures, and $\sigma_i\Gamma_i$-type values are the rates of exchange of vibrational quanta.

The system of kinetic equations that corresponds to this model [with the corresponding surface concentrations[5] $L \longrightarrow N(t)$, $HL \longrightarrow N_1(t)$, $H_2L \longrightarrow N_2(t)$,

[5] For instance, the concentration of free surface centers $L(t)$ is denoted by $N(t)$.

$H_2^\nu L \longrightarrow N_2^\nu(t)$, $H_2^{\nu-k}L \longrightarrow N_2^{\nu-k}(t)$, and $H_2OL \longrightarrow N_3(t)$] is as follows:

$$\dot N = -\nu_1 N - \nu_3 N + \nu_1' N_1 + \nu_3' N_2 - \mu N_2^\nu + (\sigma_4\Gamma_4 N_1 + \Gamma_3 + \sigma_5\Gamma_5 N_3) \times (N_2^\nu + N_2^{\nu-1} + \ldots + N_2^{\nu_1}) + \nu' N_3,$$

$$\dot N_1 = \nu_1 N - \nu_1' N_1 - \nu_2 N_1 + 2\mu N_2^\nu - \sigma_4\Gamma_4 N_1 (N_2^\nu + N_2^{\nu-1} + \ldots + N_2^{\nu_1}),$$

$$\dot N_2^\nu = \nu_2 N_1 - (\mu_1 + \Gamma_1 + \Gamma_3 + \sigma\Gamma_2 N_2 + \sigma_4\Gamma_4 N_1 + \sigma_5\Gamma_5 N_3) N_2^\nu,$$

$$\dot N_2^{\nu-1} = N_2^\nu(\Gamma_1 + \sigma\Gamma_2 N_2 + \sigma_4\Gamma_4 N_1 + \sigma_5\Gamma_5 N_3) - (\Gamma_1 + \sigma\Gamma_2 N_2 + \Gamma_3 + \sigma_4\Gamma_4 N_1 + \sigma_5\Gamma_5 N_3) N_2^{\nu-1},$$

and so on according to

$$\dot N_2^{\nu-m+1} = \dot N_2^{\nu-m+2} \times (\Gamma_1 + \sigma\Gamma_2 N_2 + \sigma_4\Gamma_4 N_1 + \sigma_5\Gamma_5 N_3) - (\Gamma_1 + \sigma\Gamma_2 N_2 + \Gamma_3 + \sigma_4\Gamma_4 N_1 + \sigma_5\Gamma_5 N_3) N_2^{\nu-m+1},$$

$$\dot N_2^{\nu_1} = N_2^{\nu-m+1}(\Gamma_1 + \sigma\Gamma_2 N_2 + \sigma_4\Gamma_4 N_1 + \sigma_5\Gamma_5 N_3) + \sigma\Gamma_2 N_2 (N_2^\nu + N_2^{\nu-1} + \ldots + N_2^{\nu-m+1}) - (\Gamma_1 + \Gamma_3 + \sigma_4\Gamma_4 N_1 + \sigma_5\Gamma_5 N_3) N_2^{\nu_1},$$

$$\dot N_2 = \nu_3 N - \nu_3' N_2 + (\Gamma_1 + \sigma_4\Gamma_4 N_1 + \sigma_5\Gamma_5 N_3) N_2^{\nu_1} - \sigma\Gamma_2 N_2 (N_2^\nu + N_2^{\nu-1} + \ldots + N_2^{\nu-m+1}),$$

$$\dot N_3 = -\nu' N_3 - \sigma_5\Gamma_5 N_3 (N_2^\nu + N_2^{\nu-1} + \ldots + N_2^{\nu_1}).$$

Note that the surface processes under consideration are characterized by a certain hierarchy of times. For instance, the $\Gamma_i \sim 10^3$–10^8 s^{-1} values are much larger than the characteristic rates of adsorption, desorption, and recombination ν_i. The system is then in a quasi-equilibrium state; that is,

$$\dot N_2^\nu = \dot N_2^{\nu-1} = \ldots = \dot N_2^{\nu_1} = 0.$$

The quasi-equilibrium condition yields

$$N_2^\nu = \frac{\nu_2 N_1}{a_1},$$

$$a_1 = \mu + \Gamma_1 + \Gamma_3 + \sigma\Gamma_2 N_2 + \sigma_4\Gamma_4 N_1 + \sigma_5\Gamma_5 N_3,$$

$$N_2^{\nu-1} = N_2^\nu \delta,$$

$$\delta = \frac{\Gamma_1 + \sigma\Gamma_2 N_2 + \sigma_4\Gamma_4 N_1 + \sigma_5\Gamma_5 N_3}{\Gamma_1 + \sigma\Gamma_2 N_2 + \Gamma_3 + \sigma_4\Gamma_4 N_1 + \sigma_5\Gamma_5 N_3},$$

$$N_2^{\nu-m+1} = N_2^\nu \delta^{m-1},$$

$$N_2^{\nu_1} = N_2^\nu \delta^m + (A-1)BN_2^\nu,$$

$$N_2^\nu + N_2^{\nu-1} + \ldots + N_2^{\nu_1} = N_2^\nu AB,$$

$$A \equiv 1 + \frac{\sigma\Gamma_2 N_2}{\Gamma_1 + \Gamma_3 + \sigma_4\Gamma_4 N_1 + \sigma_5\Gamma_5 N_3},$$

$$B \equiv \frac{1-\delta^{m+1}}{1-\delta}.$$

Substituting these relations into the initial system of equations, we obtain

$$\begin{aligned} \dot N_1 &= \nu_1 N - \nu_1' N_1 - \nu_2 N_1 + (2\mu - \sigma_4\Gamma_4 N_1 BA) N_2^\nu, \\ \dot N_2 &= \nu_3 N - \nu_3' N_2 + \nu_2 N_1 - (\mu + \Gamma_3 AB) N_2^\nu, \\ \dot N_3 &= -\nu' N_3 - \sigma_5\Gamma_5 N_3 BA N_2^\nu. \end{aligned} \qquad (5)$$

Here,

$$N_1 + N_2 + N + N_3 = N_0$$

is the total number of adsorption sites per unit surface,

$$\mu = \mu_0\left(1 - \frac{N_1 + N_2 + N_3}{N_0}\right).$$

The flow of H_2O molecules that undergo nonequilibrium desorption from the surface is proportional to the N_2^ν concentration and depends on the rate of the recombination of H atoms,

$$\Delta I = \sigma_5\Gamma_5 N_3 BA\left(\frac{\nu_2 N_1}{a_1}\right).$$

H_2O molecules (or other admixtures) may be (preliminarily) adsorbed predominantly on surface sites M different from H atom adsorption sites L. The recombination of H atoms can then also stimulate desorption of H_2O (or other admixtures) from sites M by the mechanism described above. In addition, stimulated surface diffusion of H_2O molecules adsorbed on sites M to sites L, on which H atoms recombine, can occur,

$$H_2^{\nu-k}L + H_2OM + L \xrightarrow{\Gamma_m\sigma_m} H_2^{\nu-k-1}L + M + H_2OL, \quad 0 \le k \le \nu - 1,$$

$$H_2^\nu L + H_2OM \xrightarrow{\Gamma_5\sigma_5} H_2^{\nu-1}L + M + H_2O.$$

The above system of equations then takes the form

$$\dot N_1 = \nu_1 N - \nu_1' N_1 - \nu_2 N_1 + (2\mu - \sigma_4\Gamma_4 N_1 BA) N_2^\nu,$$

$$\dot N_2 = \nu_3 N - \nu_3' N_2 - (\mu + \Gamma_3 AB) N_2^\nu,$$

$$\dot{N} = -\nu_1 N - \nu_3 N + \nu_1' N_1 + \nu_3' N_2 - \mu N_2^\nu + (\sigma_4\Gamma_4 N_1 + \Gamma_3 + \sigma_5\Gamma_5 N_3) BA N_2^\nu - N_2^\nu AB\Gamma_m\sigma_n N_m \frac{N}{N_0} + \nu' N_3,$$

$$\dot{N}_m = -\nu_m' N_m - N_2^\nu AB\Gamma_m\sigma_m N_m \frac{N}{N_0} - \sigma_5\Gamma_5 N_m AB N_2^\nu,$$

$$\dot{N}_3 = -\nu' N_3 - \sigma_5\Gamma_5 BA N_2^\nu + N_2^\nu AB\Gamma_m\sigma_m N_m \frac{N}{N_0}.$$

Here, H_2O–M $\longrightarrow N_m$, and ν_m' is the probability of desorption of H_2O from site M per unit time.

The complete scenario of surface processes should take into account the possibility of preliminary adsorption on sites M of not only foreign (water molecules) but also its own molecules (H_2). The recombination of H atoms on surface sites L then can cause stimulated transfer of H_2 molecules from sites M to L,

$$H_2^{\nu-k}L + H_2M + L \xrightarrow{\Gamma_M\sigma_M} H_2^{\nu-k-1}L + M + H_2L.$$

For simplicity, let there be no adsorbed water molecules, $N_3 = N_m = 0$.

The kinetic equations for this model have the form

$$\dot{N}_1 = \nu_1 N - \nu_1' N_1 - \nu_2 N_1 + (2\mu - \sigma_4\Gamma_4 N_1 BA) N_2^\nu,$$

$$\dot{N}_2 = \nu_3 N - \nu_3' N_2 + \nu_2 N_1 - (\mu + \Gamma_3 BA) N_2^\nu + N_2^\nu AB\Gamma_M\sigma_M N_{2M}\frac{N}{N_0}, \quad (6)$$

$$\dot{N}_{2M} = \sigma_{2M} j_2 N_M - \nu_M' N_{2M} - N_2^\nu AB\left(\Gamma_M\sigma_M\frac{N}{N_0} + \Gamma_3\right) N_{2M}.$$

Here, the surface concentrations are denoted as M $\longrightarrow N_M$ and H_2 – M $\longrightarrow N_{2M}$, σ_{2M} is the cross section of adsorption of H_2 on sites M, and j_2 is the density of the flow of H_2 molecules onto flask surface.

It is also necessary to write the kinetic equations that determine the densities of H atom and H_2 molecule flows in the accumulating flask. Under kinetic conditions ($\sigma_2 N_1 R/2D < 1$, where R is the flask radius and D is the diffusion coefficient of atoms) characteristic of units with molecular beams, we have, for instance, for atoms,

$$\frac{4R}{3\nu_a}\frac{\partial j_1}{\partial t} = \left(\frac{S_0}{4\pi R^2} j_1^0 + \nu_1' N_1\right) + \left(\sigma_4\Gamma_4 AB\frac{\sigma_2 N_1^2}{a_1} - \sigma_2 N_1 - \sigma_1 N - P\frac{S_0}{4\pi R^2}\right) j_1. \quad (7)$$

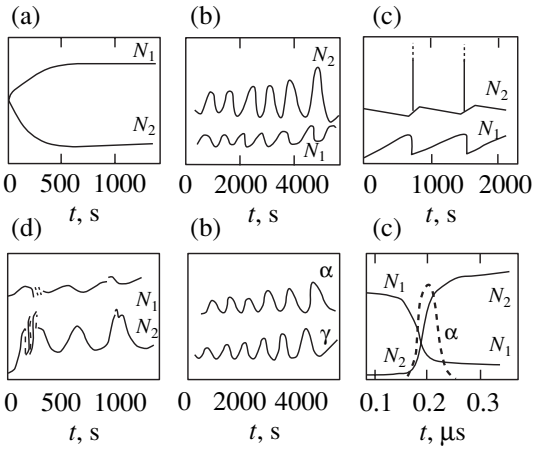

Fig. 5. Changes in surface coverage by atoms N_1 and molecules N_2, in recombination coefficient γ, and in number α of molecules undergoing nonequilibrium desorption per one recombination event: (a) in the absence of oscillations, (b) periodic changes with increasing amplitudes, (c) relaxation oscillations ("recombination explosion"), and (d) stochastic oscillations. Computer simulations.

As $3\nu_a/4R \sim 10^5\ s^{-1}$, there is quasi-equilibrium between surface coverage and the concentration of atoms in the accumulating flask,

$$j_1 = \left(\frac{S_0}{4\pi R^2} j_1^0 + \nu_1' N_1\right) \times \left(P\frac{S_0}{4\pi R^2} + \sigma_1 N + \sigma_2 N_1 - \sigma_4\Gamma_4 AB\frac{\sigma_2 N_1^2}{a_1}\right)^{-1}. \quad (8)$$

Here, P is the probability of escape of an atom from the flask when the atom is in the supplying channel of the accumulating flask of the maser.

The obtained system of kinetic equations (5)–(7) was numerically solved by the Runge–Kutta method with a $\Delta t = 10^{-9}$–10 s step over the time mesh; it was taken into account that the criterion of stability of the solution to the system should be satisfied.

A computer study of the model revealed self-oscillatory variations in time of the N_1 and N_2 concentrations, the heterogeneous recombination coefficient γ, and the intensity of nonequilibrium desorption of water molecules, H_2, and H atoms (Fig. 5). The effectiveness of nonequilibrium desorption (the number of particles that underwent nonequilibrium desorption as a result of one H atom recombination event) was close to that observed experimentally. Taking into account the total probability of gas kinetic escape of desorbed particles from the reaction volume [see (7)] also leads to the time dependence of the concentrations of hydrogen atoms and molecules in the reaction volume.

The period of oscillations is determined by the densities of the flows of atoms and molecules, the cross sections of adsorption σ_1 and recombination σ_2, and the initial conditions. An analytic (sufficient) condition of

the appearance of oscillations, which follows from the obtained kinetic mechanism, is given by the following inequalities:

$$\frac{2\mu - a_1}{a_1}\nu_2 - (\nu_1 + \nu_1' + \nu_3 + \nu_3') \geq 0,$$

$$\frac{a_2 - \mu + \Gamma_M \sigma_M N_{2M}}{a_1}\nu_1\nu_2 - \nu_3\nu_1 - (\nu_3 + \nu_3')^2 > 0.$$

In the problem under consideration, the necessary condition for the appearance of oscillations is nonequilibrium desorption of H_2^v ($\mu \neq 0$) and stimulated diffusion of H_2M ($\Gamma_M \neq 0$).

We found by numerically solving (5)–(7) that imposing nonlinearities of various types resulted in a complex behavior of the system. Several types of qualitatively different solutions are possible. These are monotonic time dependences of γ, α, and surface coverages N_1 and N_2 (Fig. 5a), as well as periodic oscillations and quasi-periodic behavior. Periodic oscillations can, in turn, have a constant amplitude or an increasing (Fig. 5b) or decreasing amplitude. More complex behaviors of surface coverages N_1 and N_2 and the γ and α values were also obtained. For instance, periodic oscillations of the type of relaxation oscillations ("recombination explosion") shown in Fig. 5c are possible. Recombination explosion is a sharp change in the N_1, N_2, and α parameters during a very short time (less than 10^{-6} s in the problem under consideration). For such an explosion to occur, the stimulated recombination reaction

$$H_2^v - L + 2(H - L) \xrightarrow{\Gamma_6} 2(H_2^v - L) + L$$

with the rate constant Γ_6 of the order of 10^{-19} cm^2 s^{-1} is additionally introduced into the scheme of processes. At large Γ_2 values, model behavior variants corresponding to multiplicity of solutions with the transition to stochastic oscillations are possible (Fig. 5d).

The rates of the corresponding processes can be estimated based on their microscopic models.

4. MICROMECHANISMS OF NONEQUILIBRIUM DESORPTION CAUSED BY VIBRATIONAL EXCITATION OF INTRAMOLECULAR BONDS (*V–V* AND *V–T* EXCHANGE)

Consider vibrational quantum transfer from an adsorbed H_2^v–L molecule (vibraton) to a water molecule H_2O–L (or to another recipient) on the surface. In first-order perturbation theory, the rate of a multiquantum transition with transfer of k vibrational quanta from H_2^v–L and excitation of H_2O–L from the zero to the $k' - k_0$ vibrational level is

$$\nu^* = \frac{2\pi}{\hbar}|\langle v - k, k'|W|v, 0\rangle|^2 \rho(E),$$

where $\rho(E)$ is the energy density of final states.

The interaction between H_2^v–L and H_2O–L is, in all probability, quadrupole–dipole interaction. The interaction energy then equals

$$W = \frac{\chi}{\varepsilon R^4}\dot{D}(r_0)\dot{\mu}(Q_0) r Q = W_0 r Q,$$

where R is the distance through which energy is transferred, r and Q are the displacements in the quadrupole and the dipole from the equilibrium position, χ is the orientation factor, and $\dot{D}$ and $\dot{\mu}$ are the derivatives of the dipole and quadrupole moments at equilibrium,

$$W_0 = \frac{\chi}{\varepsilon R^4}\dot{D}(r_0)\dot{\mu}(Q_0).$$

Let us calculate the matrix element for the transition rate. Substituting W into the expression for $\langle \text{final}|W|\text{initial}\rangle$ yields

$$\langle v - k, k'|W|v, 0\rangle = W_0 \langle v - k|r|v\rangle \langle k'|Q|0\rangle.$$

Consider relaxation in the H_2^v–L molecule through one or two vibrational levels. For oscillations in the Morse anharmonic potential, we have

$$\langle v - k|r|v\rangle = \begin{cases} \left(\frac{\hbar v}{2m\omega_0}\right)^{1/2}, & k = 1, \\ \left(\frac{\hbar v}{2m\omega_0}\right)^{1/2}\left(\frac{v-1}{4S}\right)^{1/2}, & k = 2. \end{cases}$$

Accordingly, let us find the second multiplier of the interaction matrix element for the excitation of H_2O–L from the zeroth to the first vibrational level,

$$\langle k' = 1|Q|0\rangle = \left(\frac{\hbar}{M\omega}\right)^{1/2}.$$

Here, m and M are the reduced masses of the oscillators, and ω and ω_0 are their cyclic frequencies.

The energy density of final states $\rho(E)$ in H_2O can be estimated as

$$\rho(E) = (\hbar\omega)^{-1}.$$

The rate of quadrupole–dipole exchange of vibrational quanta then equals

$$\nu^* = \frac{\pi|W_0|^2 v}{mM\omega^2\omega_0}.$$

For H_2, $\dot{D}(r_0) = 2.9$ D/Å. For estimation purposes, set $\dot{\mu}(Q_0) = 1$ D and $R \approx 10$ Å for water (coverage by H_2O equals 10^{14} cm^{-2}). This gives $\nu^* = 10^5$ s^{-1}. Generally, $\nu^* = 10^5(N'/10^{14})^4$ s^{-1}, where N' is the sum of the concentrations of H_2O and H_2 adsorbed molecules. The rate of the transfer rapidly increases as the surface is

filled by H_2O–L and H_2–L molecules. The probability of desorption of a vibrationally excited molecule (H_2O–L or H_2–L) from the adsorption potential of depth q as a result of intramolecular nonequilibrium vibrations of frequency ω will also be estimated in first-order perturbation theory. The potential including correlation of internal (coordinate Δr) and adsorption (Δz) vibrations will be written in the form

$$U = 2\alpha^2 q \Delta z \Delta r$$

(this is a linear approximation to the Morse potential). The rate of nonequilibrium desorption of a molecule into a continuous spectrum of free states is

$$\Gamma = \frac{2\pi}{\hbar}(2aq)^2 \int dE F(E) |\langle 0|\Delta r|1\rangle|^2 \frac{3U}{(2\pi\hbar)^3}$$

$$\times \int 4\pi p^2 \delta(E-q) \frac{(\hbar\alpha)^2 |\langle \exp(i\mathbf{p}\cdot\mathbf{r}/\hbar)|\hat{\mathbf{p}}|i\rangle|^2}{M^2(E+q)^2} dp$$

$$\approx 192\pi^{3/2}\left(\frac{\omega_i}{\omega}\right)^3 \omega_i (2S+1)^{1/2}.$$

Here, ω_i is the vibrational frequency of the molecule as a whole in the adsorption potential of depth q, ω is the intramolecular vibration frequency, $\hat{\mathbf{p}}$ is the operator of momentum, $\mathbf{p}$ is the momentum of the desorbing molecule, and $2S + 1$ is the number of levels in this potential up to the continuous spectrum boundary. The rate of nonequilibrium desorption at $\omega = 10^{13}$ s^{-1}, $\omega_i = 10^{12}$ s^{-1}, and $2S + 1 \approx 10$ equals $\Gamma \approx 10^6$ s^{-1}. This desorption rate value is quite measurable and agrees with our experimental data in order of magnitude.

5. CONCLUSION

In this work, we used a modified variant of the Ramsey unit with molecular beams to study nonequilibrium processes on the surface. The original version was designed to accumulate atomic particles in the required quantum state in the flask volume for creating hydrogen masers. The accumulation effect is observed because a hydrogen atom from a beam that enters the flask occurs as though in a trap: it does not perish in collisions with flask walls (a small recombination coefficient) and cannot escape the flask because the inlet hole is small. During its lifetime, the atom collides with flask walls 10^5 times, and the lifetime itself of atomic particles that are short-lived under usual conditions increases to macroscopic values and amounts to several seconds. This allowed us to increase the accuracy of measurements to five orders of magnitude. We were able not only to reveal nonequilibrium processes at the interphase boundary but also to develop a method, which is likely to be the most sensitive and accurate at present, for determining the recombination coefficient of atoms γ on the surface necessary for studying inelastic collisional processes at the gas–solid interface. This method is free of instrumental interference in the system under study and, because of its low inertial characteristics, allows the time dependence of γ to be measured by physical methods as the reaction proceeds [we know no other method for measuring $\gamma(t)$ kinetic dependences]. Precisely $\gamma(t)$ kinetic measurements allowed us to observe oscillatory variations in the rate of the recombination reaction. The reliability of recording oscillations was ensured by simultaneous measurements of several values that underwent oscillatory changes, namely, the concentration of hydrogen atoms in the accumulating volume, the recombination coefficients of atoms on flask walls, and the intensity of nonequilibrium desorption of molecules from the surface of Teflon. These measurements were performed using independently operating instruments.

The system considered in this work (Fig. 1) is the simplest open dissipative system far from thermodynamic equilibrium. This system, which in many respects can be considered a model one, possesses all the remarkable properties of dissipative systems. In conformity to the synergistic principles [15, 16], we observed self-organization elements in this system under the experimental conditions described above; namely, when substances and energy were continuously supplied to the system, a time structure in the form of undamped self-oscillations spontaneously formed in it (the system as though became animated). Energy supplied from an external (nonoscillatory) source then compensated dissipative loss in the system.[6] For the limiting cycle (oscillatory process) to arise, the level of energy supply ("pumping" level) should exceed some critical value.

This simple model system can be used to study various regimes of its behavior (from fully stochastic to coherent) and, in particular, observe the development of fluctuations leading to the loss of system stability and to bifurcation transitions to one of the set of possible system states in computer experiments (see Fig. 5). This is to be done in full measure in our further studies.

In some sense, the dynamic system under consideration can serve as a prototype of more complex open systems (for instance, biological systems) because the general characteristics of oscillatory chemical processes ("chemical clock") model those of the corresponding biological processes ("biological clock"), where undamped self-oscillations are also sustained by the energy of a nonoscillatory external source which feeds biological organisms. This results in the mutual synchronization of the behavior of many oscillators (cells). As in the system under consideration, there exists a hierarchy of times of various processes in biological systems, from fairly slow processes that manifest themselves in exchange with the environment (in our unit, this corresponds to escape of molecules from

[6] It would be an exaggeration to claim that we *a priori* expected to observe this effect.

the flask, 15 s) to very fast processes responsible for internal transformations in the system.

Lastly, the system under consideration allowed us to separately consider a purely "physical" catalysis mechanism, probably, for the first time. In this mechanism, the rate of the recombination of atoms is limited by energy accommodation, that is, by the physical conditions of the relaxation of highly excited reaction products.[7] The catalysis mechanism under consideration is fairly general (at least, in simple heterogeneous reactions), although, in complex reactions, it can be obscured by other factors that contribute to reaction rates. This does not decrease its value, because the number of practically important "simple reactions" is fairly large, from growth of epitaxial layers in the production of semiconductors to reactions determining heating of descending spacecraft in the atmosphere of planets (see Introduction).

The system studied in this work complements the list of systems with oscillatory chemical reactions (e.g., see [17–21]) studied since the discovery of the Belousov–Zhabotinskii reaction [22].

REFERENCES

1. K. V. Shaĭtan, Zh. Fiz. Khim. **51**, 586 (1977).
2. Yu. I. Tyurin, Poverkhnost, No. 9, 115 (1986).
3. V. V. Styrov and V. M. Tolmachev, Dokl. Akad. Nauk SSSR **218**, 1150 (1974).
4. V. P. Grankin and V. V. Styrov, Pis'ma Zh. Éksp. Teor. Fiz. **31**, 403 (1980) [JETP Lett. **31**, 375 (1980)].
5. A. E. Kabanskiĭ and V. V. Styrov, Zh. Éksp. Teor. Fiz. **76**, 1803 (1979) [Sov. Phys. JETP **49**, 916 (1979)].
6. A. E. Kabanskiĭ, V. V. Styrov, and Yu. I. Tyurin, Pis'ma Zh. Tekh. Fiz. **5**, 833 (1979) [Sov. Tech. Phys. Lett. **5**, 343 (1979)].
7. F. F. Vol'kenshteĭn, A. N. Gorban', and V. A. Sokolov, *Radical-Recombination Luminescence of Semiconductors* (Nauka, Moscow, 1976), p. 278.
8. V. V. Styrov, Pis'ma Zh. Éksp. Teor. Fiz. **15**, 242 (1972) [JETP Lett. **15**, 168 (1972)].
9. V. P. Grankin, N. A. Savinkov, V. V. Styrov, and Yu. I. Tyurin, Zh. Éksp. Teor. Fiz. **98**, 226 (1990) [Sov. Phys. JETP **71**, 125 (1990)].
10. V. I. Menyaĭlo and O. M. Gorban', Ukr. Fiz. Zh. **44**, 375 (1989).
11. N. F. Ramsey, *Molecular Beams* (Clarendon, Oxford, 1985), p. 466.
12. V. P. Grankin, N. A. Savinkov, V. V. Styrov, and Yu. I. Tyurin, Zh. Fiz. Khim. **68**, 2032 (1994).
13. V. V. Styrov, Yu. I. Tyurin, and N. N. Govorunov, Dokl. Akad. Nauk SSSR **228**, 652 (1976).
14. O. V. Krylov and B. R. Shub, *Nonequilibrium Processes in Catalysis* (Khimiya, Moscow, 1990), p. 288.
15. G. Nicolis and I. Prigogine, *Self-Organization in Non-Equilibrium Systems* (Wiley, New York, 1977; Mir, Moscow, 1979).
16. H. Haken: *Advanced Synergetics: Instability Hierarchies of Self-Organizing Systems and Devices* (Springer-Verlag, New York, 1983; Mir, Moscow, 1985).
17. A. I. Ivanova, G. A. Furman, V. I. Bykov, and G. S. Yablonskiĭ, Dokl. Akad. Nauk SSSR **242**, 872 (1978).
18. V. V. Barelko and Yu. E. Volodin, Dokl. Akad. Nauk SSSR **211**, 1373 (1973).
19. M. G. Slin'ko and M. M. Slin'ko, Usp. Khim. **49**, 561 (1980).
20. G. S. Yablonskiĭ, V. I. Bykov, and A. N. Gorban', *Kinetic Models of Catalytic Reactions* (Nauka, Novosibirsk, 1983), p. 254.
21. D. A. Frank-Kamenetskiĭ, *Diffusion and Heat Transfer in Chemical Kinetics* (Nauka, Moscow, 1967), p. 491.
22. A. M. Zhabotinskiĭ, *Concentration Self-Oscillations* (Nauka, Moscow, 1974).

[7] The usual chemical catalysis mechanism is known to increase the rate of the reaction (thermodynamically possible under given conditions) by decreasing the height of energy barriers along the reaction path (by decreasing the activation energy).

Translated by V. Sipachev

Journal of Experimental and Theoretical Physics, Vol. 94, No. 2, 2002, pp. 239–243.
Translated from Zhurnal Éksperimental'noĭ i Teoreticheskoĭ Fiziki, Vol. 121, No. 2, 2002, pp. 286–290.

NUCLEI, PARTICLES, AND THEIR INTERACTION

The Bremsstrahlung of Electrons on Atoms Calculated in a Broad Range of Photon Energies

V. P. Romanikhin

All-Russia Institute of Experimental Physics, Russian Federal Nuclear Center, Sarov, Nizhni Novgorod oblast, 607190 Russia

e-mail: zvenigorod@expd.vniief.ru

Received September 4, 2001

Abstract—The total bremsstrahlung spectra for electrons colliding with atoms have been calculated for krypton atoms in a photon energy range from 10 eV to 25 keV and for lanthanum atoms in the vicinity of the 4*d* shell ionization energy. The generalized atomic polarizabilities were calculated using a simple semiclassical local energy density approximation and experimental data on the photon absorption. The results are compared to those obtained using the distorted partial wave approximation for Kr and to the experimental data available for La. © *2002 MAIK "Nauka/Interperiodica".*

1. INTRODUCTION

The bremsstrahlung radiation arising upon collision of a charged particle with an atom is generated via two different mechanisms. The first is related to the particle acceleration in a static atomic field [1], and the second, to a dynamic polarization of the target atom in the electromagnetic field of the impinging particle [2]. The spectral distribution of photons with the energies ω emitted by charged particles decelerated in the static atomic field is described by a smooth curve decreasing approximately as 1/ω. In contrast to the static field effect, the polarization mechanism usually leads to the appearance of rather intense maxima and minima in the emission spectra in the vicinity of ionization potentials of the atomic shells.

Calculations of the electron bremsstrahlung spectra with an allowance for the polarization mechanism were performed for a number of atoms (see, e.g. [3–6]. An analysis of the obtained results leads to the conclusion that a contribution of the polarization channel to the total bremsstrahlung cross section requires the knowledge of generalized polarizabilities of the target atoms. Since the exact quantum-mechanical calculation of this quantity encounters extremely large computational difficulties, the development of simple approximate calculation methods is still an important task.

In this study, the generalized polarizabilities of the target atoms are calculated using a simple semiclassical local energy density approximation [7, 8] and experimental data on the photon absorption. This approach eliminates cumbersome calculations taking into account the electron–electron correlations. All calculations will be performed in the atomic system of units ($e = m = \hbar = 1$).

2. BASIC RELATIONSHIPS

In the dipole approximation, the spectral intensity of emitted photons with an energy of ω can be described in terms of the particle acceleration and averaged over the photon polarization [1, 9]:

$$\omega\frac{d\sigma}{d\omega} = \frac{4p_2}{3(2\pi c)^3 p_1}\int|\langle\psi_2^*|\mathbf{a}|\psi_1\rangle|^2 d\Omega_2. \quad (1)$$

Here, p_1 and ψ_1 are the electron momentum and wave function before the photon emission, p_2 and ψ_2 are the electron momentum and wave function after the photon emission, $d\Omega_2$ is the element of a solid angle of the electron scattering, and **a** is the electron acceleration operator. The wave functions ψ are normalized to a single particle per unit volume.

Let us assume that the spatial orientation of atoms in the target is arbitrary and, hence, the electron scattering can be considered as axially symmetric. In this case, the electron wave function can be expanded as follows [9]:

$$\psi(r, \theta) = \sum_{l=0}^{\infty} i^l(2l+1)P_l(\cos\theta)\frac{R_l(r, p)}{r}, \quad (2)$$

where θ is the angle between vectors **p** and **r**, $R_l(r, p)$ is the radial wave function of an electron with the momentum p and the angular moment l, and P_l are Legendre polynomials. Upon substituting expression (2) into Eq. (1) and integrating with respect to angles, we obtain

$$\omega\frac{d\sigma}{d\omega} = \frac{32p_2}{3c^3 p_1}\sum_{l=0}^{\infty}(l+1)(|M_{l,l+1}|^2 + |M_{l+1,l}|^2), \quad (3)$$

1063-7761/02/9402-0239$22.00

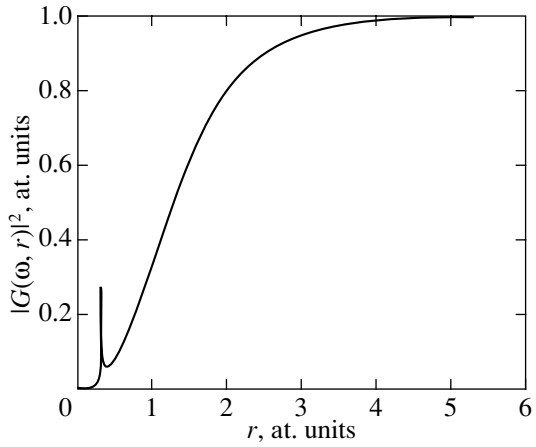

Fig. 1. The $|G(\omega, r)|^2$ function calculated in the local electron density approximation for Kr atom at a photon energy of $\omega = 500$ eV.

where

$$M_{l,l'} = \int_0^\infty R_l(r, p_1) a R_{l'}(r, p_2) dr. \quad (4)$$

The acceleration operator a can be written as a sum of the static and polarization components [8],

$$a = a_{\text{st}} + a_{\text{pol}},$$
$$a_{\text{st}} = \frac{\partial U(r)}{\partial r}, \quad a_{\text{pol}} = -\frac{\omega^2}{r^2}\alpha(\omega, r), \quad (5)$$

where $U(r)$ is the atomic potential and $\alpha(\omega, r)$ is the generalized polarizability in a coordinate form. Since $\alpha(\omega, r)$ is a complex quantity, relationship (3) also describes the interference between the static and polarization emission channels.

As was mentioned in the Introduction, calculation of the generalized polarizability $\alpha(\omega, r)$ is a very complicated quantum-mechanical problem. In order to simplify the calculations, we have used a semiempirical approach similar to that proposed by Korol' *et al.* [5]. According to this, the function $\alpha(\omega, r)$ is presented in the form of a product

$$\alpha(\omega, r) = \alpha(\omega) G(\omega, r), \quad (6)$$

where $\alpha(\omega)$ is the usual dipole polarizability of an atom. In [5], where it was demonstrated that all information about the electron–electron correlations is contained in the factor $\alpha(\omega)$, the function $G(\omega, r)$ was calculated in the Hartree–Fock approximation. We have used a simpler model of the local spin density [7, 8], according to which the target atom was considered as an inhomogeneous plasma formation with an electron density distribution $\rho(r)$ and the plasma frequency $\omega_p(r)$ obeying the relationship

$$\omega_p^2(r) = 4\pi\rho(r). \quad (7)$$

Within the framework of this model, radiation with the frequency ω is absorbed provided that the resonance condition $\omega = \omega_p(r)$ is satisfied. An expression for the generalized polarizability is as follows:

$$\alpha_L(\omega, r) = \int_0^r \frac{\omega_p^2(r') r'^2 dr'}{\omega_p^2(r') - \omega^2} + i\frac{\pi\omega^2 r_p^2(\omega)}{2d\omega_p^2(r)/dr}\Theta(r - r_p(\omega)), \quad (8)$$

where $r_p(\omega)$ is the function inverse to (7) and Θ is the Heaviside function.

An analysis performed in [8] showed that the local spin density model provides for a quite reasonable approximation for the atomic polarizabilities. Using expression (8), we readily obtain an approximated formula for the function $G(\omega, r)$:

$$G(\omega, r) \approx \frac{\alpha_L(\omega, r)}{\alpha_L(\omega, \infty)}. \quad (9)$$

Figure 1 shows the results of calculations of the function $G(\omega, r)$ for a Kr atom at a photon energy of $\omega = 500$ eV. Note a resonance peak at a distance determined by the condition $\omega = \omega_p(r)$.

In contrast to the $G(\omega, r)$ function, the usual dipole polarizability $\alpha(\omega)$ has to be determined as precisely as possible. For this reason, we have calculated this quantity by the OPTCON program (Moxgraf Company) using a compilation of the empirical data. The dipole polarizability can also be calculated using experimental values of the photon absorption cross section $\sigma_\gamma(\omega)$, a dispersion relationship, and the optical theorem [2, 5]

$$\alpha(\omega) = \frac{c}{2\pi^2}\int_0^\infty d\omega' \frac{\sigma_\gamma(\omega')}{\omega'^2 - \omega^2} + i\frac{c}{4\pi\omega}\sigma_\gamma(\omega). \quad (10)$$

3. SOME FEATURES OF THE POLARIZABILITY CALCULATION

The radial wave functions $R_l(r, p)$ were calculated by the phase method [10]. This technique provides for a convenient parameterization, thus simplifying taking the integrals in expression (4). We employed the following representation of the wave function:

$$R_l(r, p) = \exp(A_l) pr[j_l(pr)\cos\delta_l - n_l(pr)\sin\delta_l], \quad (11)$$

where j_l and n_l are spherical Bessel functions and δ_l are the partial phase shifts. The amplitude functions $A_l(r)$ and phase shifts $\delta_l(r)$ were determined from the differential equations

$$\frac{d\delta_l}{dr} = -2pr^2 U(r)[j_l(pr)\cos\delta_l - n_l(pr)\sin\delta_l]^2, \quad (12)$$

$$\frac{dA_l}{dr} = -2pr^2U(r)[j_l(pr)\cos\delta_l - n_l(pr)\sin\delta_l] \times [j_l(pr)\sin\delta_l + n_l(pr)\cos\delta_l]. \quad (13)$$

For large values of the angular moment l, the radial wave functions $R_l(r, p)$ differ but little from the undistorted wave functions of the free electron. Therefore, the phase shifts for $l > l_{max}$ can be taken equal to zero, and the $R_l(r, p)$ values can be replaced by the spherical Bessel functions $j_l(pr)$. The value of l_{max} can be roughly estimated from the relationships

$$l_{max} \approx pr_{max}, \quad U(r_{max}) \approx \varepsilon\frac{p^2}{2}, \quad (14)$$

where ε is a certain small value characterizing the degree of distortion of the wave function.

The atomic potential $U(r)$ was described using a simple approximated analytical expression [11] obtained by fitting to an exact Hartree–Fock potential

$$U(r) = -\frac{Z}{r}\sum_{j=1}^{3} A_j\exp(-\alpha_j r), \quad (15)$$

where A_j and α_j are the fitting coefficients and Z is the charge of the atomic nucleus. Using this approximation, we can also readily calculate the plasma frequency using relationship (7):

$$\omega_p^2(r) = \frac{Z}{r}\sum_{j=1}^{3} A_j\exp(-\alpha_j r)\alpha_j^2. \quad (16)$$

Our experience showed that using the analytical potential (15) considerably reduces the computational time, while not introducing significant errors in the results.

4. CALCULATION RESULTS

The results of our calculations of the total bremsstrahlung cross sections for electrons with an energy of 1, 5, 10, and 25 keV scattered on the krypton atom are presented in Figs. 2–5 (thin solid curves) in comparison with the same values (thick solid curves) calculated [6] within the framework of the distorted partial wave approximation (DPWA).

On the whole, our results satisfactorily agree with those obtained in [6]. A peak observed in the region of photon energies ω = 10–100 eV reflects the contribution of virtual dipole excitations from the 4*s* and 4*p* subshells. For photon energies of ω = 100–1000 eV, the total bremsstrahlung spectrum exhibits the second maximum related to the dipole excitation of electrons in the intermediate 3*s*, 3*p*, and 3*d* subshells. For photons with energies exceeding 2000 eV, the total cross section varies rather monotonically with the energy ω, except for a region near the ionization potentials of the 2*s* and 2*p* subshells of the krypton atom.

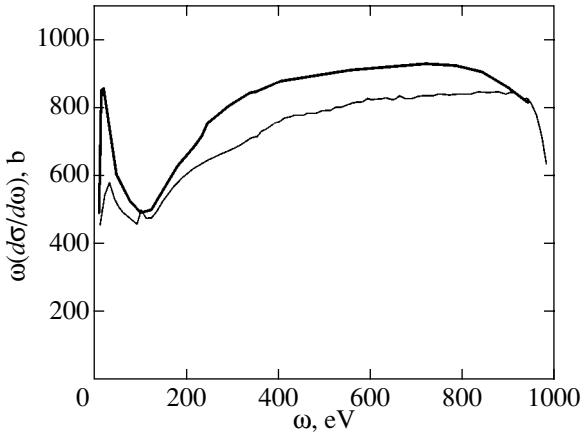

Fig. 2. The total bremsstrahlung cross sections for electrons with an energy of 1 keV scattered on the krypton atom, calculated using the DPWA method [6] (thick solid curve) and the local electron density approximation (thin solid curve).

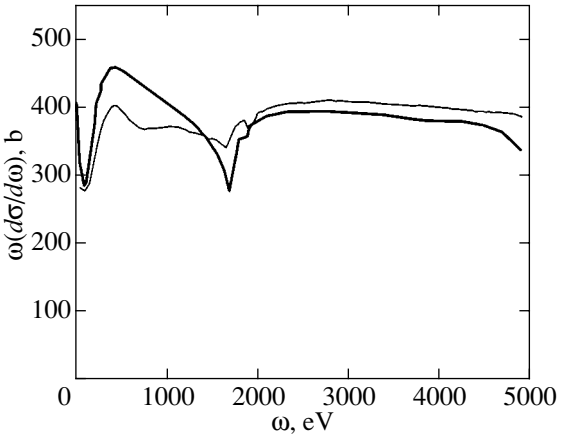

Fig. 3. The total bremsstrahlung cross sections for electrons with an energy of 5 keV scattered on the krypton atom, calculated using the DPWA method [6] (thick solid curve) and the local electron density approximation (thin solid curve).

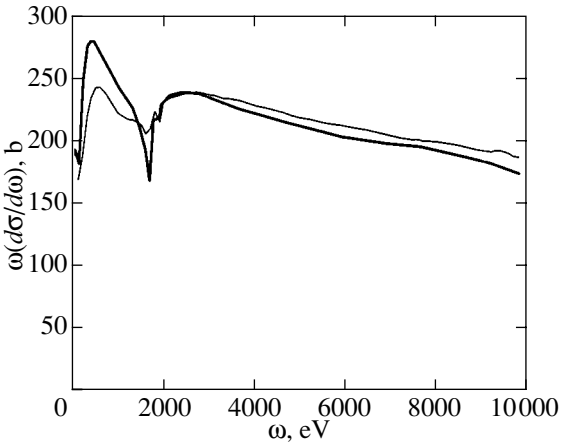

Fig. 4. The total bremsstrahlung cross sections for electrons with an energy of 10 keV scattered on the krypton atom, calculated using the DPWA method [6] (thick solid curve) and the local electron density approximation (thin solid curve).

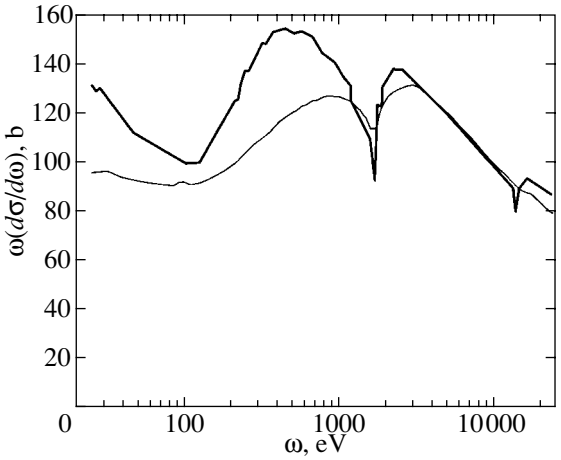

Fig. 5. The total bremsstrahlung cross sections for electrons with an energy of 25 keV scattered on the krypton atom, calculated using the DPWA method [6] (thick solid curve) and the local electron density approximation (thin solid curve).

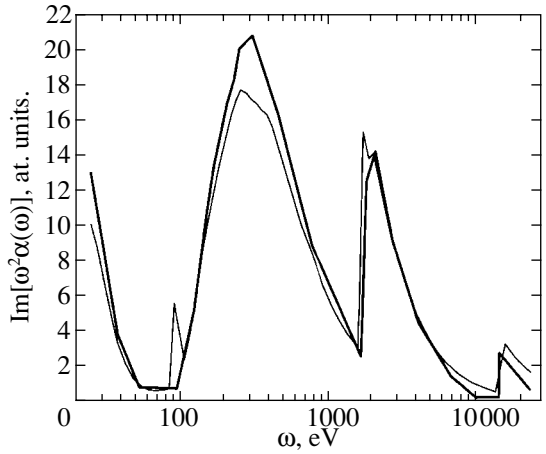

Fig. 6. The spectrum of the imaginary part of the dipole polarizability: (thick solid curve) DPWA calculation method [6]; (thin solid curve) experimental data compiled using the OPTCON program.

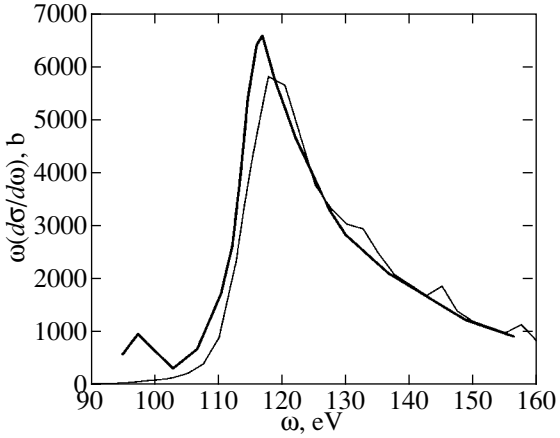

Fig. 7. The polarization bremsstrahlung cross sections for electrons with an energy of 500 keV scattered on the lanthanum atom: (thick solid curve) experiment [12]; (thin solid curve) calculation using the local electron density approximation.

Differences between the bremsstrahlung spectra calculated by the two methods are manifested predominantly in the low-energy spectral region. As a rule, the maxima and minima calculated using the local energy density approximation are smaller than those calculated by DPWA. One possible reason for these discrepancies is a difference between the experimental values of the dipole polarizability of Kr atoms used in our calculations and the $\alpha(\omega)$ values calculated by the DPWA method. Indeed, the dependence of the polarization radiation spectrum on ω can be estimated as

$$\left(\omega\frac{d\sigma}{d\omega}\right)_{\text{pol}} \approx \left|\omega^2\alpha(\omega)\right|^2 g(\omega), \qquad (17)$$

where $g(\omega)$ is a certain smooth monotonically decreasing function. As can be seen from relationship (17), the $\alpha(\omega)$ value significantly influences the polarization component of the bremsstrahlung spectrum.

Figure 6 shows the plots of $\mathrm{Im}[\omega^2\alpha(\omega)]$ predicted by the DPWA method [6] (thick solid curve) in comparison with the compilation of experimental data (thin solid curve) processed using the OPTCON program. As can be seen, the difference between the two plots in the low-energy spectral region actually amounts to 15–20%, which may account for the difference observed in the bremsstrahlung spectra.

Another possible reason for the observed discrepancy can be the use of the electron wave functions calculated for the unperturbed atomic potential in the Hartree–Fock approximation. As is known [2], somewhat different results can be obtained for the bremsstrahlung cross sections calculated in terms of the acceleration and length.

Figure 7 shows the results of calculations of the polarization component of the bremsstrahlung radiation for lanthanum in the vicinity of the 4*d* subshell ionization potential (thin solid curve) in comparison to the experimental data [5, 12] (thick solid curve) As can be seen, the proposed method provides for a quite satisfactory coincidence of the calculation and experiment.

5. CONCLUSION

We have proposed a semiempirical method for theoretical description and calculation of the total bremsstrahlung spectrum, which offers a simple means of taking into account the phenomena related to the electron–electron correlations. The bremsstrahlung spectra were calculated for krypton atoms in the energy range from 10 eV to 25 keV and for lanthanum in the vicinity of the 4*d* subshell ionization energy. Despite the relative simplicity of the models used in the theoretical description of the polarization radiation, the results show satisfactory agreement with the values calculated by a different method (DPWA) and with the available experimental data. It should be noted that this approach can also be used to calculate the bremsstrahlung spectra

of electrons colliding with more complicated objects such as molecules.

ACKNOWLEDGMENTS

This study was supported by the International Scientific-Technical Center, project no. 1126.

REFERENCES

1. V. B. Berestetskiĭ, E. M. Lifshitz, and L. P. Pitaevskiĭ, *Quantum Electrodynamics* (Nauka, Moscow, 1989; Pergamon, Oxford, 1982).
2. M. Ya. Amus'ya, *Bremsstrahlung* (Énergoatomizdat, Moscow, 1990).
3. A. V. Korol, A. G. Lyalin, and A. V. Solov'yov, J. Phys. B **28**, 4947 (1995).
4. N. B. Avdonina, M. Ya. Amus'ya, M. Yu. Kuchiev, and L. V. Chernysheva, Zh. Tekh. Fiz. **56**, 246 (1986) [Sov. Phys. Tech. Phys. **31**, 150 (1986)].
5. A. V. Korol', A. G. Lyalin, A. V. Solov'ev, and A. S. Shulakov, Zh. Éksp. Teor. Fiz. **109**, 1174 (1996) [JETP **82**, 631 (1996)].
6. A. V. Korol', A. G. Lyalin, O. I. Obolenskiĭ, and A. V. Solov'ev, Zh. Éksp. Teor. Fiz. **114**, 458 (1998) [JETP **87**, 251 (1998)].
7. W. Brandt and S. Lundqvist, Phys. Rev. A **139**, 612 (1965).
8. V. A. Astapenko, L. A. Bureeva, and V. S. Lisitsa, Zh. Éksp. Teor. Fiz. **117**, 496 (2000) [JETP **90**, 434 (2000)].
9. V. P. Zhdanov and M. I. Chibisov, Zh. Tekh. Fiz. **47**, 1804 (1977) [Sov. Phys. Tech. Phys. **22**, 1045 (1977)].
10. V. V. Babikov, *Phase Function Method in Quantum Mechanics* (Nauka, Moscow, 1988).
11. F. Salvat, J. D. Martinez, *et al.*, Phys. Rev. A **36**, 467 (1987).
12. T. M. Zimkina, A. S. Shulakov, and A. P. Braĭko, Izv. Akad. Nauk SSSR, Ser. Fiz. **48**, 1263 (1984).

Translated by P. Pozdeev

Journal of Experimental and Theoretical Physics, Vol. 94, No. 2, 2002, pp. 244–251.
Translated from Zhurnal Éksperimental'noĭ i Teoreticheskoĭ Fiziki, Vol. 121, No. 2, 2002, pp. 291–298.

PLASMA, GASES

The Effect of Excited Atomic States on the Harmonic Generation in a Photoionized Plasma

V. P. Silin

Lebedev Institute of Physics, Russian Academy of Sciences, Moscow, 117991 Russia
e-mail: silin@sci.lebedev.ru

Received July 13, 2001

Abstract—Owing to the conservation by the electrons of the memory of their intra-atomic states, a photoionized plasma arising in the mode of suppression of the ionization barrier exhibits a pronounced dependence of the efficiency of generation of the third and fifth harmonics of the pumping field on such states of electrons. For the maximal values of generation efficiency, this dependence is directly proportional to the tenth power of the principal quantum number of excited *ns* states of electrons. © *2002 MAIK "Nauka/Interperiodica".*

1. The generation of higher harmonics under the effect of coherent radiation on matter was treated in 1964 using plasma as an example. The physical pattern of this phenomenon was associated with the coherent bremsstrahlung of electrons oscillating in the pumping field and scattered by plasma ions [1]. Later on, the harmonic generation in a plasma came to be associated with the ponderomotive effect of radiation on plasma (see, for example, [2]). Relevant experimental studies were performed in parallel with studies into controlled laser fusion (see, for example, [3]). More recently, rather intensive experiments in generation of higher harmonics of laser pumping radiation were performed with gas targets (see, for example, [4]). The results of such experiments brought about the accumulation of a large body of experimental data, as well as the development of new concepts of the manifestation of the properties of atomic electrons in the generation of higher harmonics. It must be emphasized that the theory of such concepts is associated with computer development of physical models; as a result, it is not always that physical phenomena may be thoroughly treated in full detail. However, in this respect as well, certain progress was made recently thanks to the development of analytical description [5].

Note that, more often than not, the harmonic generation in experiments involving gas targets is actually caused by the bremsstrahlung of harmonics by electrons moving in the pumping field; i.e., the cause is the same as that initially used to predict the generation of higher harmonics in a fully ionized plasma [1]. Plasma theory is largely analytical and relatively descriptive. Its development for the case of pumping radiation of elliptic polarization [6] revealed, in particular, the possibility of an anomalous increase in the efficiency of harmonic generation with the degree of circular polarization of radiation in the region of small values of this degree [7]. This phenomenon was previously detected experimentally [8].

The results of experiments involving gas targets indicate that the gas is ionized under the effect of laser pumping radiation [9–11]. Therefore, there is good reason to understand the behavior of such plasmas arising as a result of photoionization and the regularities characterizing the harmonic generation in these plasmas. Of special interest is the photoionization of gas in the mode of suppression of the ionization barrier, when the Bethe condition is valid [12],

$$E \geq \frac{I_Z^2}{4Z}. \tag{1.1}$$

This formula is written in atomic units. Here, E is the electric field intensity of pumping radiation, I_Z is the ionization potential, and Z is the charge of the atomic nucleus. The importance of excited states will be apparent if one uses the formula

$$I_Z = Z^2/2n^2, \tag{1.2}$$

which holds for electrons in the Coulomb field and for excited states with the principal quantum number n. The latter formula, after being substituted into Eq. (1.1), leads to the following condition for the energy flux density of pumping radiation:

$$q \geq \frac{Z^6}{256n^8} \longrightarrow q\ [\mathrm{W/cm^2}] \geq 1.37 \times 10^{14}\ \frac{Z^6}{n^8}. \tag{1.3}$$

Hence, it follows, in particular, that, for fairly high values of the principal quantum number and not very high values of Z, the ionization in the mode of barrier suppression may turn out to be determining in a wide range of relatively easily accessible experimental values of the laser energy flux density.

1063-7761/02/9402-0244$22.00

The brief communication [13] contains a reference to the physical possibilities of theoretical determination of regularities of generation of higher harmonics in a photoionized gas, when the ionization proceeds in the mode of suppression of the ionization barrier. In [14], the possibilities referred to in [13] are substantiated, and examples of plasmas arising as a result of ionization of a gas consisting of hydrogen-like atoms in some quantum states are used to determine asymptotic dependences characterizing the generation of higher harmonics of pumping radiation. The next step (which is important from the standpoint of our treatment) was made in [15], where, firstly, the general form of the distribution function of photoelectrons arising as a result of their ionization from the *ns* state of a hydrogen-like atom was determined for the case of the mode of suppression of the ionization barrier,

$$f_{ns}(p) = \frac{N_e}{4\pi^2(mV_Z)^3} \times \frac{8n[\sin(2n\arctan(np/mV_Z))]^2}{(p/mV_Z)^2[1+(np/mV_Z)^2]^2}. \quad (1.4)$$

Here, N_e is the electron number density, p is the electron momentum, m is the electron mass, n is the principal quantum number, $V_Z = Ze^2/\hbar$ is the Coulomb unit of velocity [16], e is the electron charge, and $\hbar$ is Planck's constant. Secondly, the importance of excited atomic states with respect to the generation of higher harmonics of pumping radiation in a photoionized plasma was revealed in [15]. It was found that the presence of atoms in excited states in a photoionized gas may bring about an increase in the efficiency of generation of higher harmonics by several orders of magnitude.

Of considerable importance in understanding the urgency of the present investigation is the study [17] involving experimental investigation of the generation of the third harmonic in a gas with preexcited atoms. It has been shown that the generation efficiency increases by orders of magnitude compared with the generation from a gas without such preexcitation of atoms. The experimental data of [17] were not sufficient for uniquely determining the mechanism of harmonic generation. On the other hand, the results of the theoretical study [15] apply to the case of very high harmonics, and the experimental investigation [17] was performed for a lower, third, harmonic. In view of this, for better understanding of experiments in generation of relatively lower harmonics, it appeared urgent to develop the theory of generation of such harmonics that would enable one to perform the necessary comparison with the results of detailed experimental investigations, including investigations of the dependence of the generation efficiency on the pumping intensity. This is especially urgent under conditions in which it is possible to somehow control the excitation of atoms of a photoionized gas. Therefore, presented below is the theory of generation of the third and fifth harmonics, the results of which supplement substantially the results of the asymptotic theory of generation of very high harmonics given in [15], first of all, for the region which is not described by the asymptotic theory of higher harmonics and, second, for the region which is more open to investigation. Here, all of our treatment concerns the effects of the mechanism of generation of higher harmonics, which came to be known as the mechanism of coherent bremsstrahlung (see, for example, [1, 15]).

2. In order to describe the coherent bremsstrahlung of lower harmonics in a plasma, we will use the simplest model of this phenomenon based on the kinetic equation for electrons with the electron–ion collision integral in the Focker–Planck–Landau form [18]. In this approach, as was demonstrated even in [1] (see also, for example, [15]), a relatively simple relation holds for the perturbation of electron current $\delta\mathbf{j}$, which is due to the pumping field and defines the harmonics field,

$$\frac{\partial\delta\mathbf{j}}{\partial t} = -\frac{4\pi e^2 e_i^2 N_i\Lambda}{m^2} \times \int (d\mathbf{V})\frac{e\mathbf{V}}{V^3} f_e(\mathbf{V}-\mathbf{u}_E(t)). \quad (2.1)$$

Here, e_i is the ion charge, N_i is the ion density, Λ is the Coulomb logarithm, $\mathbf{V} = \mathbf{p}/m$ is the electron velocity, $\mathbf{u}_E(t)$ is the rate of electron oscillation in the pumping field, and $f_e(\mathbf{V})$ is the electron distribution function. For the simplest case of monochromatic pumping field with linear polarization that is treated here, the electric field intensity may be represented as

$$\mathbf{E} = (E_x(t), 0, 0), \quad E_x(t) = E\cos(\omega t - \phi_x), \quad (2.2)$$

where E is the amplitude of the electric field of the pumping wave, ω is the pumping frequency, and ϕ_x is the phase that is independent of time but capable of being dependent on coordinates. The dipole approximation is sufficient for the theory of harmonics generation in a nonrelativistic plasma. In this approximation, the following approximate expression is sufficient for the rate of electron oscillations in the pumping field:

$$\mathbf{u}_E(t) = (u_{Ex}(t), 0, 0), \quad u_{E_x}(t) = -V_E\sin(\omega t - \phi_x), \quad (2.3)$$

where

$$V_E = |e|E/m\omega \quad (2.4)$$

is the amplitude of the rate of electron oscillations; the dependence on this amplitude plays a decisive part in

our theory. It is appropriate to note that the Bethe condition given by Eq. (1.3) in view of (2.4) has the form

$$\frac{V_E}{V_Z} \geq \frac{Z^2}{8n^4}\frac{I_\mathrm{H}}{\hbar\omega} \approx 1.7\frac{Z^2}{n^4}\frac{1}{\omega[\mathrm{eV}]}, \tag{2.5}$$

where I_H is the ionization potential of a hydrogen atom and ω is the pumping frequency measured in electron volts. The right-hand side of relation (2.5) indicates that the Bethe condition of photoionization of atoms in the mode of barrier suppression for excited states may also arise in the case when the rate of electron oscillations in the pumping field does not significantly exceed the unit of Coulomb velocity V_Z.

The substitution of relations (1.4) and (2.3) into formula (2.1) enables one to derive the following expression for the perturbation of electron current:

$$\delta j_x = \sum_{N=1}^{\infty} \sigma_{xx}^{(2N+1)} E\cos[(2N+1)(\omega t - \phi_x)]. \tag{2.6}$$

This formula describing the generation of odd harmonics is general (see, for example, [1]). It is our objective to determine the explicit form of partial nonlinear conductivities for which we use the notation

$$\sigma_{xx}^{(2N+1)} = \frac{e^2 N_e}{m\omega^2}\nu_{xx}^{(2N+1)}(n, E), \tag{2.7}$$

where the effective nonlinear collision frequencies are defined by the formulas

$$\nu_{xx}^{(2N+1)}(n, E) = \nu_Z n^3 A_n^{(2N+1)}\left(\frac{nV_E}{V_Z}\right). \tag{2.8}$$

Here,

$$\nu_Z = \frac{16e^2 e_i^2 N_i \Lambda}{m^2 V_Z^3} \tag{2.9}$$

is the effective frequency of electron–ion collisions for electrons, related to the unit of Coulomb velocity. The functions $A_n^{(2N+1)}$ depend both on the number of the harmonic being generated and on the principal quantum number n. These functions may be represented in a form which considerably simplifies the theory, where the dependences on the harmonic number and on the quantum number are separated. Namely, we derive

$$A_n^{(2N+1)}(x) = \frac{1}{x^3}\left[D_n \alpha^{(2N+1)}\left(\frac{b}{x}\right)\right]_{b=1}. \tag{2.10}$$

Here, after using the operator D_n, we must assume $b = 1$. In this case, D_n for different values of the principal quantum number represents different differential operators which have the following form, for example, for the first five values of $n = 1, 2, 3, 4, 5$ used below:

$$D_1 = 1 - \frac{d}{db} + \frac{1}{3}\frac{d^2}{db^2},$$

$$D_2 = 1 - \frac{d}{db} + \frac{1}{3}\frac{d^2}{db^2} + \frac{1}{15}\frac{d^4}{db^4},$$

$$D_3 = 1 - \frac{d}{db} + \frac{1}{3}\frac{d^2}{db^2} + \frac{1}{15}\frac{d^4}{db^4} + \frac{2}{45}\frac{d^5}{db^5} + \frac{2}{315}\frac{d^6}{db^6},$$

$$\begin{aligned} D_4 = {} & 1 - \frac{d}{db} + \frac{1}{3}\frac{d^2}{db^2} + \frac{1}{5}\frac{d^4}{db^4} + \frac{2}{15}\frac{d^5}{db^5} \\ & + \frac{2}{45}\frac{d^6}{db^6} + \frac{2}{315}\frac{d^7}{db^7} + \frac{1}{2835}\frac{d^8}{db^8}, \end{aligned} \tag{2.11}$$

$$\begin{aligned} D_5 = {} & 1 - \frac{d}{db} + \frac{1}{3}\frac{d^2}{db^2} + \frac{4}{15}\frac{d^4}{db^4} + \frac{4}{15}\frac{d^5}{db^5} \\ & + \frac{44}{315}\frac{d^6}{db^6} + 105\frac{4}{315}\frac{d^7}{db^7} + \frac{16}{2835}\frac{d^8}{db^8} \\ & + \frac{2}{4725}\frac{d^9}{db^9} + \frac{2}{155925}\frac{d^{10}}{db^{10}}. \end{aligned}$$

The function $\alpha^{(2N+1)}(Y)$, which is common for all atomic states and different for different harmonics, may be represented in the form of the following integral:

$$\alpha^{(2N+1)}\left(\frac{b}{x}\right) = \frac{2}{\pi}\int_0^{\pi/2} d\theta \frac{Q_{N+1/2}(\zeta) + Q_{N-1/2}(\zeta)}{\zeta + 1}, \tag{2.12}$$

where $Q_\nu(\zeta)$ denotes Legendre functions. Under the integral given by Eq. (2.12), the variables ζ and θ are related by

$$\zeta = 1 + \frac{2b^2}{x^2\sin^2\theta}. \tag{2.13}$$

Before proceeding to the determination of the form of functions defined by the integral given by Eq. (2.12), note that, as is demonstrated below, a simple scaling dependence proportional to n^2 is present for the functions $A_n^{(2N+1)}(x)$ in the region of not very high values of the argument in the vicinity of their maximal values. This points to the efficiency of using the functions

$$\Psi_n^{(2N+1)}\left(\frac{V_E}{V_Z}\right) = \frac{1}{n^2}A_n^{(2N+1)}\left(\frac{nV_E}{V_Z}\right). \tag{2.14}$$

For effective nonlinear collision frequencies, one can write

$$\nu_{xx}^{(2N+1)}(n, E) = \nu_Z n^5 \Psi_n^{(2N+1)}\left(\frac{V_E}{V_Z}\right). \quad (2.15)$$

The fifth power of the principal quantum number in formula (2.15) is one of the main new regularities revealed below.

3. This section will be devoted to the theory of third harmonic generation. For this purpose, we must first treat formula (2.12), which, in the case of interest to us and in view of relation (2.13), may be represented as

$$\alpha^{(3)}(Y) = \frac{Y\sqrt{2}}{\pi}\int_{1+2Y^2}^{\infty} d\zeta \frac{Q_{3/2}(\zeta) + Q_{1/2}(\zeta)}{(\zeta^2-1)\sqrt{\zeta-(1+2Y^2)}}. \quad (3.1)$$

One of the possible ways of transforming this expression is associated with the use of an integral representation for Legendre functions [19, 8.713, p. 1015],

$$Q_\nu(\zeta) = \frac{1}{2^{\nu+1}}\int_{-1}^{+1} dt \frac{(1-t^2)^\nu}{(\zeta-t)^{\nu+1}}.$$

This representation enables one to write, in the form convenient for further computations,

$$Q_{3/2}(\zeta) + Q_{1/2}(\zeta) = \frac{1}{\sqrt{2}}\int_{-1}^{+1}\frac{dt}{\sqrt{\zeta-t}}\Theta_3(t), \quad (3.2)$$

where

$$\Theta_3(t) = \sqrt{\frac{1+t}{1-t}}(2t-1). \quad (3.3)$$

As a result of these transformations, formula (3.1) may be represented as

$$\alpha^{(3)}(Y) = \frac{2}{\pi}\int_{-1}^{+1} dt \Theta_3(t) I(t), \quad (3.4)$$

where

$$I(t) = \frac{Y}{2} \times \int_{1+2Y^2}^{\infty} \frac{d\zeta}{(\zeta^2-1)(\zeta-t)^{1/2}(\zeta-(1+2Y^2))^{1/2}}$$

or

$$I(t) = \frac{1}{2^{3/2}}\left(\frac{1}{\sqrt{1-t}}\arctan\frac{\sqrt{1-t}}{Y\sqrt{2}} - \frac{Y}{2(1+t^2)^{1/2}(1+Y^2)^{1/2}}\ln\frac{2^{1/2}(1+Y^2)^{1/2}+(1+t)^{1/2}}{2^{1/2}(1+Y^2)^{1/2}-(1+t)^{1/2}}\right). \quad (3.5)$$

Formulas (3.3)–(3.5) enable one to write expression (3.1) in the following explicit form:

$$\alpha^{(3)}\left(\frac{b}{x}\right) = \operatorname{arcsinh}\left[\frac{x}{b}\right] + \frac{1}{3}\left(\frac{8b}{x} - \frac{8b^2+7x^2}{\sqrt{x^2+b^2}}\right), \quad (3.6)$$

which makes it possible, in accordance with Eqs. (2.10) and (2.11), to represent the functions $A_n^{(3)}(x)$ for five *ns* states $n = 1, 2, 3, 4, 5$ in the form

$$A_n^{(3)}(x) = \frac{1}{x^3}\{\operatorname{Arcsinh}[x] + a_n^{(3)}(x)\}, \quad (3.7)$$

where

$$a_1^{(3)}(x) = \frac{-3x-7x^3-3x^5}{3(1+x^2)^{5/2}}, \quad (3.8)$$

$$a_2^{(3)}(x) = \frac{-x(15+65x^2+44x^4+38x^6+9x^8)}{15(1+x^2)^{9/2}}, \quad (3.9)$$

$$a_3^{(3)}(x) = \frac{1}{105(1+x^2)^{13/2}}\{-x(105+665x^2-77x^4 + 2062x^6+663x^8+327x^{10}+53x^{12})\}, \quad (3.10)$$

$$a_4^{(3)}(x) = -\frac{1}{63(1+x^2)^{17/2}} \times (63x+525x^3-1302x^5+7596x^7-2830x^9 + 3314x^{11}+696x^{13}+236x^{15}+29x^{17}), \quad (3.11)$$

$$a_5^{(3)}(x) = -\frac{1}{495(1+x^2)^{21/2}}(495x+5115x^3-35541x^5 + 268\,092x^7-426\,118x^9+482\,664x^{11}-120\,750x^{13} + 54\,400x^{15}+8475x^{17}+2175x^{19}+215x^{21}). \quad (3.12)$$

Figure 1 gives five functions $A_n^{(3)}$ ($x = nV_E/V_Z$). At high values of the argument, all of these functions come closer together. On the contrary, in the region of their maxima, these functions differ strongly. It turns out with a high accuracy that this difference is given by n^2. In view of this, five functions $\Psi_n^{(3)}(V_E/V_Z)$ are given in Fig. 2 for describing the third harmonic generation using the effective nonlinear collision frequency $\nu_{xx}^{(3)}(n, E)$. One can see that, while the curve for the 1*s* state falls out somewhat from the general pattern, the remaining curves, first, differ little from one another and, second, come closer together as the principal quantum number increases. For all of the curves which have thus come closer together, their maxima are reached at $V_E = (1.2–1.5)V_Z$, with the maximal values being approximately 0.13.

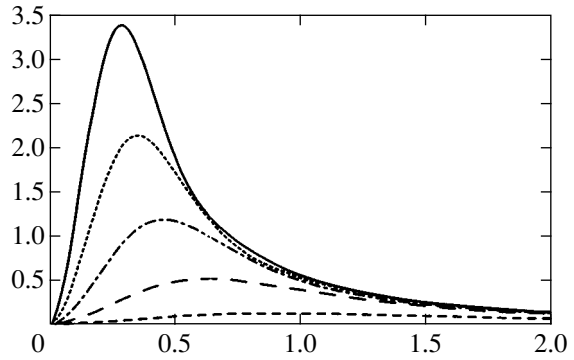

Fig. 1. Graphs of the functions $A_n^{(3)}(x = nV_E/V_Z)$ for five *ns* states corresponding to $n = 1, 2, 3, 4, 5$. Here and in subsequent drawings, the dashed curve with short dashes corresponds to $n = 1$, the dashed curve with long dashes corresponds to the 2*s* state, the dot-and-dash curve corresponds to the 3*s* state, the dotted curve corresponds to the 4*s* state, and the solid curve corresponds to $n = 5$.

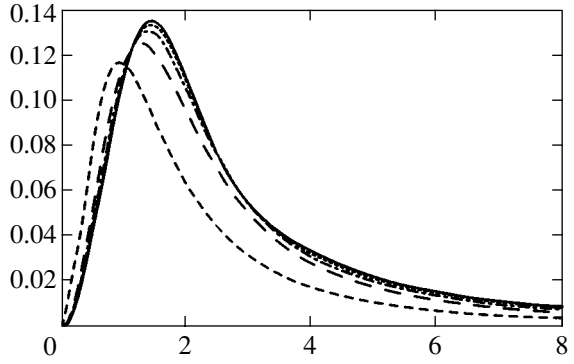

Fig. 2. Graphs of the functions $\Psi_n^{(3)}(V_E/V_Z)$ for the first five *ns* states.

Formula (2.15), on the one hand, and the virtually coinciding maxima of the $\Psi_n^{(3)}$ curves, on the other hand, lead one to conclude that the real scaling of the effective frequencies $\nu_{xx}^{(3)}$ on the principal quantum number is given by approximately n^5.

4. We will now treat the effective nonlinear collision frequencies $\nu_{xx}^{(5)}$ describing the nonlinear conductivity of plasma responsible for the generation of the fifth harmonic of the pumping field. Similar to Eq. (3.1), the input relation is

$$\alpha^{(5)}(Y) = \frac{Y\sqrt{2}}{\pi} \times \int\limits_{1+2Y^2}^{\infty} d\zeta \frac{Q_{5/2}(\zeta) + Q_{3/2}(\xi)}{(\zeta^2-1)(\zeta-(1+2Y^2))^{1/2}}. \quad (4.1)$$

The integral representation of Legendre functions makes it possible to write the relation

$$Q_{5/2}(\zeta) + Q_{3/2}(\zeta) = \frac{1}{\sqrt{2}}\int\limits_{-1}^{+1}\frac{dt}{\sqrt{\zeta-1}}\Theta_5(t), \quad (4.2)$$

where

$$\Theta_5(t) = \sqrt{\frac{1+t}{1-t}}(4t^2-2t-1). \quad (4.3)$$

Accordingly, formula (4.1) may be represented as

$$\alpha^{(5)}(Y) = \frac{2}{\pi}\int\limits_{-1}^{+1} dt\Theta_5(t)I(t). \quad (4.4)$$

In the latter relation, the integral may be taken in an explicit form, so that

$$\alpha^{(5)}\left(\frac{b}{x}\right) = \mathrm{Arcsinh}\left[\frac{x}{b}\right] + \frac{24b}{5x} + \frac{64b^3}{15x^3} - \frac{64b^4 + 104b^2x^2 + 43x^4}{15x\sqrt{x^2+b^2}}. \quad (4.5)$$

This is the key formula in our theory of fifth harmonic generation. We use the procedure of (2.10) and formula (4.5) to find

$$A_n^{(5)}(x) = \frac{1}{x^3}\{\mathrm{Arcsinh}[x] + a_n^{(5)}(x)\}, \quad (4.6)$$

where

$$a_1^{(5)}(x) = -\frac{15x + 35x^3 + 23x^5}{15(1+x^2)^{5/2}}, \quad (4.7)$$

$$a_2^{(5)}(x) = -\frac{15x + 65x^3 + 108x^5 + 54x^7 + 17x^9}{15(1+x^2)^{9/2}}, \quad (4.8)$$

$$a_3^{(5)}(x) = -\frac{1}{105(1+x^2)^{13/2}}(105x + 665x^3 + 1771x^5 + 1166x^7 + 1783x^9 + 551x^{11} + 109x^{13}), \quad (4.9)$$

$$a_4^{(5)}(x) = -\frac{1}{315(1+x^2)^{17/2}}(315x + 2625x^3 + 9618x^5 + 1692x^7 + 37\,594x^9 + 5818x^{11} + 9528x^{13} + 2188x^{15} + 313x^{17}), \quad (4.10)$$

$$a_5^{(5)}(x) = -\frac{1}{495(1+x^2)^{21/2}}(495x + 5115x^3 + 23\,859x^5 - 32\,868x^6 + 331\,562x^9 - 195\,288x^{11} + 245\,154x^{13} + 12\,610x^{15} + 23\,259x^{17} + 4287x^{19} + 479x^{21}). \quad (4.11)$$

These formulas give an exhaustive analytical answer to the question of the effective nonlinear collision frequency responsible for the generation of the fifth harmonic of the pumping field.

To continue our discussion, consider the attached figures. Figure 3 shows graphs of five functions $A_n^{(5)}(nV_E/V_Z)$ which come closer together at high values of the argument. This is associated with the fact that, at high values of the argument, formula (4.6) takes the form

$$A_n^{(5)}(x) = \frac{1}{x^3}\{\ln(2x) + a_n^{(5)}(\infty)\}, \qquad (4.12)$$

where $a_1^{(5)}(\infty) = -1.533$, $a_2^{(5)}(\infty) = -1.133$, $a_3^{(5)}(\infty) = -1.038$, and $a_5^{(5)}(\infty) = -0.978$. In the region of their maxima, the functions $A_n^{(5)}(x)$ differ markedly from one another. With a high accuracy, this difference is given by n^2. All of the foregoing lends support to the above-mentioned advisability of using the functions $\Psi_n^{(2N+1)}$ in the region of moderate values of pumping intensity to describe the harmonic generation.

Figure 4 gives five functions $\Psi_n^{(5)}$. The graphs of functions in this figure are qualitatively similar to those in Fig. 2. Here, the curve corresponding to the ground 1*s* state likewise falls somewhat out of the pattern. As the principal quantum number increases, the curves corresponding to excited state come closer together. The maximal values of the curves corresponding to the 2*s*, 3*s*, 4*s*, and 5*s* states are approximately four times less than the values corresponding to Fig. 2 and lie in the range from 0.03 to 0.033, and the values (V_E/V_Z) corresponding to such maxima lie in the range from 2.2 to 2.5. Figure 4 leads one to assume that the dependence of the nonlinear effective collision frequency on the principal quantum number is given by approximately n^5, which is analogous to the above-identified law for the third harmonic. On comparing the curves of Figs. 4 and 2, one can see that the ratio of the values (V_E/V_Z) corresponding to the maxima of the curves in these figures approximately follows the law

$$(V_E/V_Z)_{\max} \approx 2N + 1.$$

In other words, the pumping field at which the maximal value of the effective nonlinear collision frequency is attained increases with the harmonic number.

5. In order to gain an impression of the order of magnitude of the effects being discussed, we will turn to the case of the simplest geometry of the pumping field. Namely, we will assume that the pumping field is described by a traveling plane wave along the *z* axis with the wave vector *k*. Then, $\phi_x = kz$, and the wave vector of the pumping field is defined by the relation

$$\omega^2 = 4\pi e^2 N_e/m + k^2c^2.$$

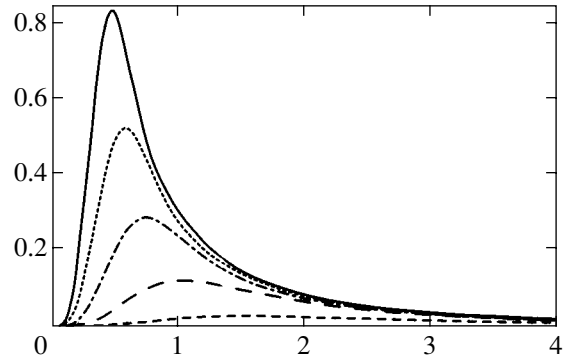

Fig. 3. Graphs of the functions $A_1^{(3)}$ ($x = V_E/V_Z$), $A_2^{(3)}$ ($x = 2V_E/V_Z$), $A_3^{(3)}$ ($x = 3V_E/V_Z$), $A_4^{(3)}$ ($x = 4V_E/V_Z$), and $A_5^{(3)}$ ($x = 5V_E/V_Z$).

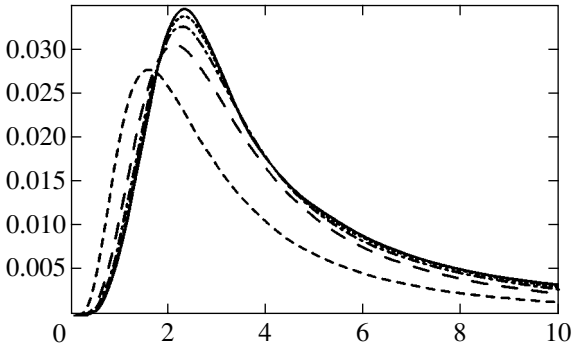

Fig. 4. Graphs of the functions $\Psi_n^{(5)}(V_E/V_Z)$ characterizing the generation of the fifth harmonic.

According to formula (2.6), in this case, the harmonics field also has the form of plane waves with frequencies $(2N + 1)\omega$ and wave vectors $(2N + 1)k$. We define the efficiency of harmonic generation as the ratio of the flux density of its energy to the energy flux density of the pumping field to derive (cf. [15])

$$\eta^{(2N+1)}(n, E) = \left[\frac{(2N+1)}{4N(N+1)}\frac{\nu_{xx}^{(2N+1)}}{\omega}\right]^2. \qquad (5.1)$$

For the treated case of generation of the third and fifth harmonics, the following expressions may be written in accordance with formula (2.15):

$$\eta^{(3)}(n) = \frac{9}{64}\left(\frac{\nu_Z}{\omega}\right)^2 n^{10}\left[\Psi_n^{(3)}\left(\frac{V_E}{V_Z}\right)\right]^2, \qquad (5.2)$$

$$\eta^{(5)}(n) = \frac{25}{576}\left(\frac{\nu_Z}{\omega}\right)^2 n^{10}\left[\Psi_n^{(5)}\left(\frac{V_E}{V_Z}\right)\right]^2. \qquad (5.3)$$

We will use these expressions to treat the maximal values of the harmonics generation efficiency. Note, first of all, that, because the peaks on the curves in Figs. 2

and 4 are observed at $V_E \sim 2V_Z$, they are realized at the energy flux density of the pumping field:

$$q \sim 3 \times 10^{14} Z^2 (\omega[\text{eV}])^2, \quad (5.4)$$

where the energy flux density is measured in W/cm^2 and the pumping frequency is measured in electron volts. Then, in accordance with the results given in Sections 3 and 4 for the maximal efficiency of generation of the third and fifth harmonics, the following estimates may be written:

$$\eta^{(3)}_{\max}(n) \approx 0.057 (y/\omega[\text{eV}])^2 (n/10)^{10}, \quad (5.5)$$

$$\eta^{(5)}_{\max}(n) \approx 0.002 (y/\omega[\text{eV}])^2 (n/10)^{10}, \quad (5.6)$$

where

$$y = \frac{\Lambda Z_i^2}{10 Z^3} \frac{N_i}{10^{17}\ \text{cm}^{-3}}. \quad (5.7)$$

The tenth power of the principal quantum number is a very clearly defined dependence of the maximal generation efficiency described by formulas (5.5) and (5.6). The parameter given by Eq. (5.7) for dense plasmas may considerably exceed unity. We will not assume this in our estimate which is clearly not overstated. Namely, we will assume that $\Lambda \sim 10$, $Z_i^2/Z^3 \geq 0.1$, and $N_i \leq 10^{18}$ cm^{-3}, which leads one to take the parameter $y \approx 1$. We will further assume that $\omega[\text{eV}] \approx 1$. Then, in accordance with Eqs. (5.5) and (5.6) for the generation of the third and fifth harmonics by the plasma produced during ionization of atoms in the 5*s* state, we derive

$$\eta^{(3)}_{\max}(5) \sim 5.6 \times 10^{-5}, \quad \eta^{(5)}_{\max}(5) \sim 2 \times 10^{-6}.$$

These values are ten million times higher than the efficiency of harmonic generation by the plasma arising during ionization of atoms in the ground 1*s* state,

$$\eta^{(3)}_{\max}(1) \sim 5.7 \times 10^{-12}, \quad \eta^{(5)}_{\max}(1) \sim 2 \times 10^{-13}.$$

The foregoing estimates enable one to sum up. The theoretical treatment of coherent bremsstrahlung of the third and fifth harmonics of pumping radiation in a photoionized plasma formed in the mode of suppression of the ionization barrier helped reveal a very strong dependence of the efficiency of harmonics generation on the principal quantum number of atoms of the gas from which the plasma is formed. Therefore, the presence in the gas of a small percentage of atoms in excited states may bring about a considerable increase in the generation of the third and fifth harmonics in a photoionized plasma. It was such an increase in the efficiency of third harmonic generation that was observed in [17]. At the same time, it must be emphasized that, as is demonstrated in [15], the importance of excited states discussed by us decreases if the duration of the pumping radiation pulse exceeds the time of electron–electron collisions. This time is given by the estimate

$$t_{ee} \approx \frac{1}{n^3}\left(\frac{10}{\Lambda}\right)\frac{Z^3}{Z_i}\frac{10^{-13}\ \text{s}}{N_i/10^{18}\ \text{cm}^{-3}}.$$

With longer times, when the velocity of electrons approaches a Maxwellian distribution, the n^{10} law of formulas (5.5) and (5.6) changes, according to [15], to the n^6 law. In addition, the harmonics generation increases considerably owing to the presence of excited states in the gas being ionized. The effect of excited atomic states on the harmonics generation in plasma ceases when the duration of the pumping pulse is such that the electrons are heated so that their temperature exceeds their intra-atomic energy.

ACKNOWLEDGMENTS

I am deeply grateful to Mr. W. Kruer (USA) and Mr. P. Mulser (Germany) for valuable discussions of the material of this paper. This study received partial financial support from the International Scientific and Technical Center (project no. 1253), from the Russian Foundation for Basic Research (project no. 99-02-18075), and from the Program of State support for leading scientific schools (project no. 00-15-96720).

REFERENCES

1. V. P. Silin, Zh. Éksp. Teor. Fiz. **47**, 2254 (1964) [Sov. Phys. JETP **20**, 1510 (1964)].
2. Yu. V. Afanas'ev, N. G. Basov, O. N. Krokhin, *et al.*, *Interaction of High-Power Laser Radiation with Plasma* (VINITI, Moscow, 1979), Itogi Nauki Tekh., Radiotekh. **17**.
3. R. L. Carman, C. K. Rhodes, and R. F. Benjamin, Phys. Rev. A **24**, 2649 (1981).
4. A. L'Huiller and Ph. Balcou, Phys. Rev. Lett. **70**, 774 (1993).
5. V. T. Platonenko and V. V. Strelkov, Kvantovaya Élektron. (Moscow) **30**, 236 (2000).
6. V. P. Silin, Zh. Éksp. Teor. Fiz. **114**, 864 (1998) [JETP **87**, 468 (1998)].
7. K. N. Ovchinnikov and V. P. Silin, Kvantovaya Élektron. (Moscow) **29**, 145 (1999).
8. N. H. Burnett, C. Kan, and P. B. Corkum, Phys. Rev. A **51**, R3418 (1995).
9. C.-G. Wahlstroem, J. Larsson, A. Person, *et al.*, Phys. Rev. A **48**, 4709 (1993).
10. K. Kondo, T. Tamida, Y. Nabekawa, and S. Watanabe, Phys. Rev. A **49**, 3881 (1994).
11. S. G. Preston, A. Sanpera, M. Zepf, *et al.*, Phys. Rev. A **53**, R31 (1996).
12. H. A. Bethe, in *Handbuch der Physik*, Bd. 1, 24/1: *Quantenmechanik der Ein- und Zwei-Electronenprobleme* (Berlin, 1933; ONTI, Moscow, 1935).
13. V. P. Silin, Pis'ma Zh. Éksp. Teor. Fiz. **69**, 486 (1999) [JETP Lett. **69**, 521 (1999)].

14. V. P. Silin, Kvantovaya Élektron. (Moscow) **29**, 49 (1999).
15. V. P. Silin, Zh. Éksp. Teor. Fiz. **117**, 926 (2000) [JETP **90**, 805 (2000)].
16. L. D. Landau and E. M. Lifshitz, *Course of Theoretical Physics*, Vol. 3: *Quantum Mechanics: Non-Relativistic Theory* (Fizmatgiz, Moscow, 1963; Pergamon, New York, 1977).
17. A. B. Fedotov, A. N. Naumov, V. P. Silin, *et al.*, Phys. Lett. A **271**, 407 (2000).
18. V. P. Silin, *Introduction to the Kinetic Theory of Gases* (Fiz. Inst. Ross. Akad. Nauk im. P. N. Lebedeva, Moscow, 1998).
19. I. S. Gradshteyn and I. M. Ryzhik, *Table of Integrals, Series, and Products* (Fizmatgiz, Moscow, 1962; Academic, New York, 1980).

Translated by H. Bronstein

Journal of Experimental and Theoretical Physics, Vol. 94, No. 2, 2002, pp. 252–259.
Translated from Zhurnal Éksperimental'noĭ i Teoreticheskoĭ Fiziki, Vol. 121, No. 2, 2002, pp. 299–307.

PLASMA, GASES

Enhanced Superdiffusion and Finite Velocity of Levy Flights

V. Yu. Zaburdaev and K. V. Chukbar*
Russian Research Center Kurchatov Institute, Moscow, 123182 Russia
**e-mail: chukbar@dap.kiae.ru*
Received August 16, 2001

Abstract—A fractional differential equation is derived that describes the transformation of a stochastic transport from fast spreading ($\bar{x} \propto t^{\alpha}$, $\alpha > 1$) to a pseudowave regime ($\alpha = 1$) due to the finiteness of the velocities of individual particles. Qualitative features of the new regime are discussed. © *2002 MAIK "Nauka/Interperiodica".*

1. INTRODUCTION

In this paper, we consider the diffusion, in a homogeneous and isotropic medium, of a macroscopic cloud of microscopic passive particles (i.e., those that do not affect the medium) characterized by a certain internal random-walk law. The latter circumstance relates this process to the class of stochastic transports, which is very popular in modern physics (see, for example, surveys [1–3] or the recent papers [4–9]). Depending on the features of the random walk at the microscopic level, macroscopic transport equations for the cloud density $n(x, t)$ may strongly differ from classical diffusion equations (while including the latter as a particular case) and involve, as a rule, fractional derivatives (see [10]) with respect to the space and/or time variables.

The standard random-walk model is as follows. Consider one-dimensional motion of a particle along a straight line x (multidimensional analogues will be considered at the end of this paper) that is characterized by the probability laws $g(|x|)$ and $f(t)$: the particles situated at any point (say, at x_0) may instantaneously jump to neighboring points, so that the probability that a particle occurs within the interval $(x_0 + x, x_0 + x + dx)$ is equal to $g(x)dx$; this jump occurs after a certain waiting period, so that the probability that a particle leaves its original position (the same point x_0) within the interval $(t, t + dt)$ (after arriving at this point) is equal to $f(t)dt$. It is the random character of the microscopic law of motion that is responsible for the stochastic character of the corresponding macroscopic transport: during this process, the initial state $n_0(x) = n(x, 0)$ is forgotten, and the distribution $n(x, t)$ attains a universal self-similar profile (see the cited literature and the reasoning below).

Historically, the first analyzed example of such walks was a crowd of drunk sailors with rather primitive g and f (see [1]); however, the model described here is fairly universal and admits a wide variety of physical interpretations. For example, we are especially interested in the resonance radiative transfer in a coronal plasma [11, 12]. In this case, the mean free path of a microscopic particle (a photon or a γ quantum) depends on whether this particle is emitted at the center or on the wing of a line, so that $g(x)$ is uniquely determined by the shape of the line contour, whereas $f(t)$ describes a spontaneous radiative decay of the excited state of the ion into which a quantum is transformed after its absorption. Of course, the actual process of radiative transfer is more complicated than the model under consideration (in particular, it requires that the plasma characteristics, such as the concentration and temperature, should be homogeneous and stationary); nevertheless, this model reflects many features of actual processes.

A specific problem to the solution of which this paper is devoted is the determination of the effect of the finiteness of a fixed velocity v of particles on the spreading of a cloud of excitations, i.e., taking into account the deviation from the standard model. However, a better understanding of the arising problems requires a brief account of the specific character of the process in the classical statement, i.e., with $v = \infty$. We will mainly follow [5], although there are many other works devoted to similar problems.

2. SPECIFIC FEATURES OF THE DESCRIPTION OF A STOCHASTIC TRANSPORT

The spreading of a cloud of particles is determined by the following important characteristics of the space and time distribution functions: the mean square of displacement (mean free path) and the mean expectation time

$$\langle x^2 \rangle = \int_{-\infty}^{+\infty} x^2 g(x)dx, \quad \langle t \rangle = \int_0^{\infty} t f(t)dt. \qquad (1)$$

When these parameters are finite, the effective transport equation asymptotically (i.e., for macroscopic time

$t \gg \langle t \rangle$ and spatial scales $|x| \gg \sqrt{\langle x^2 \rangle}$) reduces to the classical diffusion equation

$$\frac{\partial n}{\partial t} = D\frac{\partial^2 n}{\partial x^2}, \quad D = \frac{\langle x^2 \rangle}{2\langle t \rangle}.$$

When these expressions are divergent (due to the slowly decaying power tails of g and f), the situation changes drastically. The case $\langle x^2 \rangle = \infty$ of the so-called Levy flights leads to the spatial nonlocality of the transport process (a fractional power of a Laplacian—a convolution-type integral operator with a certain power function of x—appears in the equation) and a faster spreading of the cloud, whereas the case with $\langle t \rangle = \infty$ (which is characterized by the term "traps") gives rise to the time nonlocality (a fractional time derivative of a certain different type!) and decelerates the macroscopic motion. In the general case, the asymptotic transport equation is expressed as

$$\frac{\partial^\gamma n}{\partial t^\gamma} = -K(-\Delta)^\beta n, \tag{2}$$

where the constant K and the exponents $\gamma \le 1$ and $\beta \le 1$ are related to the powers of the tails of f and g, so that the evolution of the cloud width $n(x, t)$ is described by

$$\bar{x} \propto t^\alpha, \quad \alpha = \frac{\gamma}{2\beta}. \tag{3}$$

The redundant minuses of the Laplacian are attributed to the form of the corresponding operator in the Fourier space (see below).

The standard terminology classifies any stochastic processes described by (3) with $\alpha > 1/2$ and $\alpha < 1/2$ as super- and subdiffusion processes.[1] Here, the stochasticity, or forgetting the initial conditions mentioned above, consists in ascribing the self-similarity of the Green's function,

$$G(x, t) = (1/t^\alpha)\Phi(x/t^\alpha),$$

of Eq. (2) to the general solution of this equation; namely, as soon as the characteristic width of G, which increases according to (3), becomes greater than the initial size of the cloud (one often speaks of the sufficiency of the doubling of the scale during the spreading process), the density distribution

$$n(x, t) = \int_{-\infty}^{+\infty} n_0(x')G(x - x', t)dx' \tag{4}$$

becomes more and more universal:

$$n(x, t)|_{t \to \infty} \longrightarrow G(x, t)\int_{-\infty}^{+\infty} n_0 x' dx'$$

(see below). In other words, the self-similarity, which generally facilitates the analysis of the properties of mathematical physics equations, in this case is "attracting" in addition; this considerably simplifies the analysis of the possible behavior of such physical systems. Interestingly, the specific form of $G(\Phi)$ depends on β and γ separately, rather than on α.

Thus, it is the Levy flights that are responsible for the superdiffusion behavior in this model.[2] Depending on a specific physical problem (for example, depending on the shape of the line contour), the parameter α may take any value. Here, the case $\alpha > 1$ is of greatest interest (when $\langle t \rangle \ne \infty$, the boundary of α is associated with the divergence of the moment $\langle |x| \rangle$ of g) when the spreading of the cloud occurs at increasing rate. There is no established term for this situation; the term "enhanced superdiffusion" used in the title sounds fairly natural.

As we mentioned above, the problems presented in this section were analyzed from various viewpoints and to different degrees of comprehensiveness in many studies. Nevertheless, the question concerning such an important generalization of the random-walk model as the consideration of the finiteness of the velocities of microscopic particles as they move to neighboring points (which is certainly inherent in real physical situations) has scarcely been analyzed. As applied to nondiffusion equations, this question has been raised quite recently in [6, 7]; however, one can hardly agree with all the assertions made in those works.

3. THE EFFECT OF THE FINITENESS OF FLIGHT VELOCITIES: PRIMARY CONSIDERATIONS

In fact, even a qualitative analysis of the arising new situation (cf. [7]) allows one to make important assumptions about the expected phenomena. First of all, we have to realize what we are going to find out. The obvious effect of the finiteness of the flight velocity is the fact that the Green's function of the effective equation (which represents the density distribution $n(x, t)$ in (2) with $n_0 = \delta(x)$; see (4)) identically vanishes for $|x| > vt$. This fact may be very important, for example, in physical problems that require a rigorous consider-

[1] In fact, here we implicitly assume that physical systems are spatially and temporally homogeneous, as was mentioned in the Introduction, since a conventional diffusion process with $\bar{x} \sim \sqrt{Dt}$ in the case of $D = D(x, t)$ can guarantee the fulfillment of (3) for any α (which frequently occurs).

[2] In general, the converse is not true: the fact that a transport equation contains the operator $(-\Delta)^\beta$ does not always guarantee that there are Levy flights in the physical phenomenon described by this equation. For example, in the problems of skin effect [13] or the Maxwell relaxation of charge [14] in thin films, the operator $(-\Delta)^{1/2}$ is attributed to purely geometric reasons, and there are no microscopic particles at all; in these problems, n plays the role of the component of a magnetic (electric) field normal to the film.

ation of the relativistic causality principle, and does not always strongly influence the behavior of the main group of particles. When $\alpha < 1$, the boundary $G \equiv 0$ moves faster than the characteristic self-similar parameter (3), so that the old Green's function is formed asymptotically (Eq. (2) also makes sense only asymptotically) with the distortion of $\Phi(\xi)$ only on "far" tails (the boundary of these distortions being such that $\xi_{\text{bound}}|_{t \to \infty} \longrightarrow \infty$). We will not consider this phenomenon. A sufficiently detailed discussion of this phenomenon as applied to the conventional diffusion equation (the Gaussian profile $\Phi(\xi)$) was given, for example, in [15].

The situation is entirely different for the enhanced superdiffusion. Here, in contrast, the evolution of the self-similar width of the cloud is faster; therefore, the asymptotic condition $|x| < vt$ substantially changes the form of G and the structure of Eq. (2) itself. The present paper is devoted precisely to the derivation of this equation with allowance for these new circumstances.

It is fair to say that, when $\alpha < 1$, the finiteness of v may change the value of the coefficient K, while leaving unchanged (in the above sense) the fractional exponents of (2). It seems sufficiently obvious that, when $\langle t \rangle$ and $\langle |x| \rangle$ are finite, the following change is made in K:

$$\langle t \rangle \longrightarrow \langle t \rangle + \frac{\langle |x| \rangle}{v}. \tag{5}$$

This fact is well known for a diffusion process. However, the change (5) should also be valid for infinite values of the mean expectation time (in the sense that finite values of $\langle |x| \rangle$ do not influence the value of K any longer).

The earlier works [6, 7] shed light differently on the v phenomena discussed. There is a rather enigmatic assertion in [6] that the finiteness of v reduces any equations of type (2) (with any β and γ) to a diffusion equation. This error was corrected in [7], which was only partly concerned with this problem; however, the authors of [7] restricted themselves to the derivation and analysis of the type (2) equations with regard to (5). As for the enhanced superdiffusion (recall that $\langle |x| \rangle = \infty$ in this case), a strange result was obtained in [7] that, since the finiteness of v for $\alpha > 1$ qualitatively changes the Green's function of the initial equation (2), this equation is "absolutely inapplicable to the description of real processes"; as a result, the strongest effect due to the finite particle velocity ($v \neq \infty$) was left unstudied.

In fact, the more a power function with a large exponent leads a linear function for large values of the argument, the more it falls behind it for small values of the argument. Under enhanced superdiffusion, a cloud first spreads rather slowly, so that the constraint $|x| < vt$ starts to influence the self-similarity (3) not very soon and, for sufficiently large values of v, the transformation of the process, which occurs for $t \propto v^{1/(\alpha-1)}$, may leave enough time for the initial macroscopic evolution by the law (2), (3) (intermediate asymptotics).

A clear physical example of such a possibility is provided by a radiative transfer in a coronal plasma. This phenomenon is characterized by considerable values of α and huge values of v (it is the velocity of light!). The latter fact allows one to set v equal to infinity in the majority of plasma problems; however, technically, this is not always correct. Moreover, this simply may prove to be incorrect even in the present statement, let alone in other possible physical realizations of the model; this fact stimulates the analysis of the transformation described. The mathematical procedures involved will be based on the approach used in [5].

4. INITIAL EQUATIONS

An adequate description of the kinetics of a transport process requires the introduction of several new parameters N, F, and Q in addition to n, g, and f. As we noted in the Introduction, the particles located at a given point x remember the moment when they arrived at this point; therefore, their spatial density n represents an integral of a certain distribution N with respect to lifetime τ:

$$n(x, t) = \int_0^\infty N(x, t, \tau) d\tau.$$

It is more convenient to express the transition to further motion in terms of the probability to survive until τ,

$$F(\tau) = 1 - \int_0^\tau f(t) dt,$$

rather than directly in terms of f. Finally, we can denote by $Q(x, t)$ a flow emanating from a given point and directed to either side and reaching any distance. According to the definition, f characterizes the escape rate in terms of particles that have initially arrived at this point, of which only a part determined by $F(\tau)$ remain by the moment τ. Therefore, by the conditional probability formula (see [5]), we have

$$Q(x, t) = \int_0^\infty \frac{N(x, t, \tau)}{F(\tau)} f(\tau) d\tau. \tag{6}$$

Thus, we obtain the following compact expression for the equation of balance for the particles that are located at a given point at a given moment (for resting particles):

$$n(x, t) = \int_{-\infty}^{+\infty} g(x')\theta\left(t - \frac{|x'|}{v}\right) \times \int_0^{t-|x'|/v} Q\left(x - x', t - \frac{|x'|}{v} - t'\right)F(t')dt'dx' + \int_t^{\infty} \frac{N_0(x, \tau - t)}{F(\tau - t)}F(\tau)d\tau, \quad (7)$$

where $N_0(x, \tau) \equiv N(x, 0, \tau)$ is the initial lifetime distribution of particles. Equations (6) and (7) provide a full description of the situation.

It is easily seen that, while the parameters F and Q are only needed to make the expression more compact, the introduction of the distribution N is essential in the sense that the equation for n cannot be expressed only in terms of the density n of particles; i.e., in general, the macroscopic kinetics depends on the microscopic details in a rather awkward way. Unfortunately, this technical feature is not properly reflected in the literature; as a rule, one immediately writes only a microscopic transport equation (see, for example, [7]), which is actually valid only in a certain asymptotic sense.

One meets no problems only in the case

$$f = \mu\exp(-\mu t), \quad \mu = 1/\langle t\rangle,$$

when F and f (and, consequently, Q and n) are just proportional to each other. This law is encountered quite frequently in physical applications; for example, it is typical of the radiative decay of excited states. For other f (which are also encountered in practice), the features of the function of N versus its arguments make their own contributions. The point is that the newly arriving particles form a self-similar profile

$$N_{\text{new}} = \theta(t - \tau)P(t - \tau)F(\tau)$$

with a correlated dependence on t and τ, where P is an incoming flow. The old initial distribution is shifted to the domain $\tau > t$ and monotonically decreases due to the flights to the neighboring points (see (7)). When such self-similarity occupies a greater part of the profile $N(\tau)$ and starts to dominate in Q, the integrals in dt' and $d\tau$ (the latter integral enters the definition of Q (6)) in (7) can be interchanged, and, instead of N, one obtains its integral—the macroscopic density n. For simplicity, one can choose N_0 as a shifted Dirac's delta function (as proposed in [5]):

$$N_0 = n_0\delta_+(\tau), \quad \int_0^{\infty} \delta_+(\tau)d\tau = 1.$$

This provides a self-similar relation between the functions of N versus t and τ from the very beginning of the process. Then, instead of (6) and (7), one obtains a single basic equation (cf. [5] with $v = \infty$ and [7]):

$$n(x, t) = \int_{-\infty}^{+\infty} g(x')\theta\left(t - \frac{|x'|}{v}\right) \times \int_0^{t-|x'|/v} f(t')n\left(x - x', t - \frac{|x'|}{v} - t'\right)dt'dx' + F(t)n_0(x). \quad (8)$$

In the general case, this equation is valid only asymptotically; this makes the problem of describing the evolution of a cloud for small time $t \longrightarrow 0$ rather involved but does not influence the present study. In fact, Eq. (8) in the problem considered is not sufficiently asymptotic. For our purposes, we have to make the transition $t \longrightarrow \infty$ (which is accompanied by the transition $\bar{x} \longrightarrow \infty$ due to the spreading phenomenon). The simplest way to do this is to apply the Laplace transform with respect to the time variable and the Fourier transform with respect to the space variable; this will save us from dealing with convolution integrals; calculations with functions are simpler than those with operators.

5. ASYMPTOTIC EVOLUTION

To facilitate intermediate calculations and to make definite certain numerical coefficients, it is desirable to specify the expressions for the distribution functions g and $f(F)$ without losing the possibility to describe a variety of forms of Eq. (2). The following class of functions proves to be very convenient (see [5]; to simplify the cumbersome expressions, everywhere below we use dimensionless variables, so that $x, t \sim 1$ correspond to microscopic scales):

$$g(x) = \frac{\Gamma(\beta + 1/2)}{\sqrt{\pi}\Gamma(\beta)}\frac{1}{(1 + x^2)^{\beta + 1/2}}, \quad f(t) = \frac{\gamma}{(1 + \gamma)^{\gamma + 1}}, \quad F(t) = \frac{1}{(1 + t)^{\gamma}}. \quad (9)$$

Here, Γ is the Euler gamma function, and the numerical coefficients are determined by the normalization of g and f to 1. Only the power exponents of the tails of functions that are parameterized by the positive numbers β and γ are essential for the further analysis. These exponents coincide with those introduced in Eqs. (2) and (3) (variants (9) with $\beta, \gamma > 1$ give standard integral-order derivatives in macroscopic transport equations[3]).

[3] Stochastic transports of type (2) and with a fractional derivative with $\gamma > 1$ are yet possible but in entirely different problems, for example, in a drift of a passive impurity by a turbulent flow of a fluid [16].

As reference information, we present the aforementioned power moments of these distributions (as long as they exist):

$$\langle x^2\rangle = \frac{1}{2(\beta-1)}, \quad \langle |x|\rangle = \frac{\Gamma(\beta-1/2)}{\sqrt{\pi}\Gamma(\beta)},$$

$$\langle t\rangle = \frac{1}{\gamma-1}.$$

Below, we will restrict the analysis to the case $\beta < 1$ (the opposite case is described by analogous formulas) and mainly to $\beta < 1/2$.

The simultaneous application of the above Laplace and Fourier transforms reduces Eq. (8) to

$$n_{pk} = [g(x)\exp(-p|x|/v)]_k f_p n_{pk} + F_p n_{0k} \qquad (10)$$

(here, the symbol $[\cdot]_k$ stands for a Fourier component of an appropriate function). The asymptotic transition $|x|$, $t \longrightarrow \infty$ in (8) corresponds to the dual transition k, $p \longrightarrow 0$ in (10). For the latter transition, it suffices to expand the equation in power series in k and p and retain the first terms in the expansion. Here, it is convenient to subtract the expression $f_p n_{pk}$ from the left- and right-hand sides of (10) simultaneously. Then, for g and f from (9), the original Eq. (10) is transformed to (the appropriate integrals and their series expansions can be found, for example, in [17])

$$\left[p^\gamma\Gamma(1-\gamma) + \frac{p}{\gamma-1}\right]n_{pk} = -\left\{\frac{\Gamma(\beta-1/2)}{\sqrt{\pi}\Gamma(\beta)}\frac{p}{v} + \frac{\Gamma(1-\beta)}{\Gamma(1+\beta)}\frac{1}{2^{2\beta+1}\cos(\pi\beta)} \times\left[\left(\frac{p}{v}+ik\right)^{2\beta} + \left(\frac{p}{v}-ik\right)^{2\beta}\right]\right\}n_{pk} + \left[p^{\gamma-1}\Gamma(1-\gamma) + \frac{1}{\gamma-1}\right]n_{0k} \qquad (11)$$

(cf. [5] and (2) with $v = \infty$).

Actually, for every specific value of β and γ, Eq. (11) has a simpler form. Say, for $\gamma > 1$ (i.e., for finite $\langle t\rangle$), one can neglect $p^{\gamma-1}$ as compared with unity (p^0) in square brackets on both sides of the equation, whereas, for $\gamma < 1$, the situation is opposite. The cases $\beta > 1/2$ and $\beta < 1/2$ give similar results. The "critical" values of the numbers $\beta = 1/2$ and $\gamma = 1$ (as well as $\beta = 1$) yield a slightly more complicated problem (which requires removal of the $\infty - \infty$ uncertainties), since there appear logarithms in addition to the power terms in the equation (see [5]). The terminology of $\partial^\gamma/\partial t^\gamma$ and $(-\Delta)^\beta$ used in (2) is attributed to the coefficients p^γ and $|k|^{2\beta}$ (for $v = \infty$).

The combination containing $(p/v \pm ik)^{2\beta}$ (just as the first term on the right-hand side, where the terms $\pm ik$ are merely canceled out) results from the series expansion of the integral

$$\int_{-\infty}^{+\infty}\frac{\exp(-p|x|/v)\cos(kx)}{(1+x^2)^{\beta+1/2}}dx. \qquad (12)$$

Therefore, we have to single out a branch with real values for real k and positive p; i.e., the above combination can be represented as

$$2\left|\frac{p^2}{v^2}+k^2\right|^\beta\cos(2\beta\varphi), \quad \cos\varphi = \frac{p/v}{\sqrt{(p/v)^2+k^2}}. \qquad (13)$$

It is clear that, for finite values of $\langle |x|\rangle$, the situation actually coincides with the case discussed in Section 3. For example, if $\langle t\rangle$ is also finite, then the first term in curly brackets on the right-hand side of (11) is combined with the expression on the left-hand side to give a term of the form

$$(\langle t\rangle + \langle |x|\rangle/v)pn_{pk}$$

(cf. [7]). It is interesting to note that there is no such a coefficient on the right for n_{0k}; this naturally implies that the number of particles described by Eq. (11) asymptotically decreases by a factor of

$$\langle t\rangle/(\langle t\rangle + \langle |x|\rangle/v)$$

as compared with its initial value. This situation has a simple explanation: The finite velocity of motion results in a natural separation of particles into two types: resting ones, which are described by Eqs. (8), (10), and (11), and flying ones. It is obvious that, on macroscopic temporal and spatial scales satisfying the inequalities

$$t \gg \langle t\rangle, \quad |x| \gg \langle |x|\rangle,$$

the densities of each type of particles are proportional to the time during which they stay in this state; therefore (cf. [7]),

$$n_{\mathrm{fly}}(x,t) = \frac{\langle |x|\rangle}{v\langle t\rangle}n(x,t). \qquad (14)$$

If there are flying particles in the system at the initial moment, then the following change is made in (11):

$$n_{0k} \longrightarrow n_{0k} + n_{\mathrm{fly}0k}.$$

This trivial circumstance results in another (in addition to those discussed in Section 3) nontrivial phenomenon when $\langle |x|\rangle = \infty$. In this case, the number of flying particles should asymptotically increase; in other words, an irreversible transformation of resting particles (whose number asymptotically tends to zero) into flying ones occurs during such a transport. Recall that these two states are actually quite different in a physical problem of radiative transfer through a plasma, so that the total number of excitations in a medium will decrease, while the number of γ quanta will asymptoti-

cally tend to a constant value. Naturally, this fact manifests itself in the structure of the Green's function since

$$\int_{-\infty}^{+\infty} n dx$$

is not an integral of motion any longer in the effective transport equation.

Thus, the problem in question is solved: Eq. (11) represents an asymptotic equation of stochastic transport with the finite velocity of Levy flights. In the next section, we discuss the characteristic features of the equation obtained.

6. TRANSFORMATION OF REGIMES UNDER ENHANCED SUPERDIFFUSION

In addition to the renormalization of the coefficient K in (2), which was pointed out in [7], for finite values of v, the fractional power of the Laplacian is replaced, according to (11), by a slightly more exotic combination

$$|k|^{2\beta} \longrightarrow \frac{(p/v + ik)^{2\beta} + (p - ik)^{2\beta}}{2\cos(\pi\beta)}. \qquad (15)$$

In principle, within the framework of the terminology used, this combination can be expressed in terms of an appropriate sum of fractional derivatives

$$\left(\frac{1}{v}\frac{\partial}{\partial t} \pm \frac{\partial}{\partial x}\right)^{2\beta}$$

(which, possibly, more clearly demonstrates the necessary condition $G \equiv 0$ for $|x| > vt$). However, in contrast to $(-\Delta)^\beta$ or $\partial^\gamma/\partial t^\gamma$, this expression is not widely used. How does such a transformation of operators influence the structure of the Green's function of the transport equation?

Since we are interested in the change of the self-similarity (i.e., in a maximally strong influence; see Section 3), we have to study a self-similar relation between the characteristic scale of the wave vector $\bar{k}$ and p in Eq. (11). Let us rewrite (11) in a more compact form setting, for definiteness, $\gamma > 1$ and $\beta < 1/2$ (cf. (2)),

$$pn_{pk} = -K\frac{\cos(2\beta\varphi)}{\cos(\pi\beta)}\left(k^2 + \frac{p^2}{v^2}\right)^\beta n_{pk} + n_{0k},$$
$$K = \frac{\Gamma(1-\beta)}{\Gamma(1+\beta)}\frac{\gamma - 1}{2^{2\beta}}, \qquad (16)$$

and assume that $v \gg 1$ for transformation of regimes at the stage of macroscopic evolution; formula (16) makes sense only for this stage since we assumed that $\bar{x}, t \gg 1$ when deriving these formulas.

Consider two limit regimes in (16): the old, now intermediate, asymptotics and the new, final, asymptotics. Initially (i.e., for moderately large t and moderately small p), the term $(p/v)^2$ can be neglected as compared with k^2 in the parentheses on the right-hand side of (16) (by setting $\varphi = \pi/2$). Indeed, in this case, (16) reduces to (2) with $\bar{x} \propto t^{1/2\beta}$ (see (3)) or $\bar{k} \propto p^{1/2\beta}$ (see the right- and left-hand sides of (16)), which allows us to neglect $(p/v)^2$ as compared with $p^{1/\beta}$ up to $p \sim v^{-2\beta/(1-2\beta)}$ (or always when $\beta > 1/2$) or $t \sim v^{2\beta/(1-2\beta)}$ ($t \sim v^{1/(\alpha-1)}$ when $\gamma < 1$; cf. Section 3).

However, after a certain period of time, the situation is radically changed, and the new self-similarity $\bar{x} \sim vt$ ($\bar{k} \sim p/v$) is established, so that the entire left-hand side of (16) can be neglected:

$$K\frac{\cos(2\beta\varphi)}{\cos(\pi\beta)}\left(k^2 + \frac{p^2}{v^2}\right)^\beta n_{pk} = n_{0k}.$$

Hence, the required Green's function of the "transformed" equation is expressed as

$$G_{pk} = \frac{\cos(\pi\beta)}{K\cos(2\beta\varphi)(k^2 + p^2/v^2)^\beta}. \qquad (17)$$

This function really satisfies the announced conditions that it should identically vanish at large distances and that the total number of resting particles should asymptotically decrease. Since

$$\int_{-\infty}^{+\infty} n dx = n_k|_{k=0},$$

the effect is determined by the zero harmonic of G. In addition,

$$G_{p0} \propto p^{-2\beta},$$

therefore,

$$\int_{-\infty}^{+\infty} n dx \propto t^{2\beta-1} \quad (\text{or } t^{2\beta-\gamma} \text{ at } \gamma < 1)$$

(recall that this regime is not realized when $\gamma < 2\beta$ or $\alpha < 1$!). This expression coincides with the expression obtained by integrating (14) under the following interpretation:

$$\int_{-\infty}^{+\infty} n_{\text{fly}} dx \longrightarrow \text{const}, \quad \langle |x| \rangle \longrightarrow \int_{-vt}^{vt} g(x)|x| dx \propto t^{1-2\beta},$$
$$\langle t \rangle \longrightarrow \int_0^t f(t) t dt \propto t^{1-\gamma}.$$

Note that, when passing from p to t, the exponents in the expressions for the real function G and the self-similar parameter $\bar{x}$ (cf. conventional diffusion equation) differ by unity.

The transformation of regimes from the conservation of the total number of particles to its decrease occurs, according to the general Eq. (16), by the following law:

$$\int_{-\infty}^{+\infty} n_p dx \propto \frac{1}{p + K(p/v)^{2\beta}}. \quad (18)$$

As is clear from (11), when $\gamma < 1$, the second term in the denominator of this expression is additionally multiplied by $p^{1-\gamma}$.

7. PARTICULAR CASES AND THE DISCUSSION OF GENERAL PROPERTIES

According to (4), asymptotic relation (17) (or its full variant following from (11) or (16)) allows one to obtain a solution to the problem of enhanced superdiffusion with the finite velocity of Levy flights for any initial distribution $n_0(x)$. However, operations in the Laplace–Fourier space prove to be poorly descriptive; therefore, to give an idea of the character of the new form of the Green's function, we present simple expressions for some of these functions in conventional variables.

For the case $\beta = 1/4$ ($\bar{x} \propto t^2$), which corresponds to the frequently encountered Lorentz contour of lines in the physical problem of radiative transfer, we have

$$G \sim \frac{\theta(vt - |x|)}{v^{1/2} t^{3/2}} \quad (19)$$

(recall that this expression is valid only for $t \gg v$). Here, Eq. (17) is inverted completely due to the simple relation between the cosines of a simple and a half angle. In this case, the transformation of regimes (18) occurs by the following law:

$$\int_{-\infty}^{+\infty} n dx \propto \exp\left(K^2 \frac{t}{v}\right) \mathrm{erfc}\left[K\left(\frac{t}{v}\right)^{1/2}\right].$$

Another case corresponds to a whole class of extremely fast transports with $\beta \longrightarrow 0$; here, one can set $\cos(2\beta\varphi) \longrightarrow 1$ (which is not fully rigorous since the questions concerning the convergence rate in dual spaces are rather complicated; nevertheless, $\varphi \sim 1$ in the self-similarity domain $\bar{k} \sim p/v$), and, hence,

$$G \sim \frac{v\theta(vt - |x|)}{(v^2 t^2 - x^2)^{1-\beta}} \quad (20)$$

(for $t \gg v^{2\beta} \gg 1$, this inequality imposes certain constraints on β for a given v).

Despite the fact that the Green's functions obtained are similar to their analogues encountered in wave problems, the process considered possesses all the characteristic features inherent in stochastic transport. Indeed, we still deal with the infinitely spreading function

$$G = \frac{1}{t^{2-2\beta}} \Phi(x/t);$$

therefore, according to (4), any initial profile $n_0(x)$ tends to the following universal distribution involving few parameters (see [5]):

$$n(x, t) \approx AG(x - x_0)[1 + O(1/t^2)],$$

$$A = \int_{-\infty}^{+\infty} n_0 dx, \quad Ax_0 = \int_{-\infty}^{+\infty} x n_0 dx;$$

i.e., the forgetting fully manifests itself (cf. the Hamiltonian problem of a truly wave motion). Note that, since $n(x, t)$ represents a convolution of n_0 with G, the sharp gradients (and even discontinuities) of the latter for $|x| \sim vt$ in the asymptotic profile of the macroscopic concentration are actually smoothed over a distance on the order of the initial width of a cloud.

Nevertheless, variant (17) of the Green's function is different from those obtained in earlier investigations. When $\langle |x| \rangle \neq \infty$, for any velocity v, one can determine the boundaries starting from which the effective transport equation loses its sensitivity to the initial conditions; this occurs for $\bar{x} \gg \langle |x| \rangle$. In fact, we always deal with the transient regime. This fact manifests itself in the following. As was noted above, for $\beta > 1/2$ and $n_{\mathrm{fly}0}(x) \neq 0$, we obtain only a certain renormalization of the initial condition; however, in our case, this function does not fully describe the situation; an adequate description requires the introduction of the distribution n_{fly} at the place where the particles will settle (cf. the introduction of the distribution $N(\tau)$). Therefore, the whole subsequent evolution can be radically changed by an appropriate choice of the function $n_{\mathrm{fly}}(x)$.[4] In this case, the relation between the functions n and n_{fly} is different from a simple proportion even for $n_{\mathrm{fly}0} \equiv 0$ (see [7]):

$$n_{fly} = \frac{1}{2v} \int_{-\infty}^{+\infty} Q\left(x - x', t - \frac{|x'|}{v}\right)$$

$$\times \theta\left(t - \frac{|x'|}{v}\right) \int_{|x'|}^{\infty} g(y) dy dx'.$$

This fact is attributed to the extreme nonlocality of the problem and the asymptotic extinction of resting particles.

[4] Note that, in the case of highly nonequilibrium initial distribution functions $N_0(\tau)$ for $\langle t \rangle = \infty$, the formation of the self-similar "$t - \tau$" profile of N may also take a rather long time.

8. INCREASING THE DIMENSION OF THE PROBLEM

It is well known that, in conventional superdiffusion (with $v = \infty$), the transformation of the effective equation when passing from a one-dimensional problem to a multidimensional problem is trivial: the fractional power of the Laplacian in Eq. (2) corresponds to $-|\mathbf{k}|^{2\beta}$ in space of arbitrary dimension (see [1–7]). The situation is completely different in the present case; it is rather difficult to rewrite (11) or (16) in a new form. Here, the problem is associated with the fact that the simple additivity of p and $\pm ik$ is attributed exclusively to the convenient properties of expression (12), which, in the general case, are not preserved in spaces of other dimensions.

Nevertheless, the situation is quite similar in the most frequently encountered three-dimensional case:

$$\int_{-\infty}^{+\infty} \exp(-pr/v)\exp(-i\mathbf{k}\cdot\mathbf{r})g(r)d\mathbf{r} = -4\pi\int_0^\infty \frac{\exp(-pr/v)\sin(kr)}{k} g(r)r\,dr$$

(in the two-dimensional case, the sine is replaced by a Bessel function). Hence, for $v \neq \infty$, the block of terms containing $k^{2\beta}$ (where k is the modulus of the wave vector) in the effective equation is replaced by

$$\frac{(p/v + ik)^{2\beta+1} - (p/v - ik)^{2\beta+1}}{2ik\cos(\pi\beta)} \qquad (21)$$

and the separation of the required branch yields $\sin[(2\beta + 1)\varphi]$ rather than a cosine. In terms of conventional physical variables, the situation is not so simple as in (15), since, although p/v still corresponds to $\partial/\partial t$, $\pm ik$ is an integral operator of the type $\Delta^{1/2}$ from the very beginning. However, from the mathematical viewpoint, operations with (21) are not substantially more difficult than operations with (15).

9. CONCLUSION

Thus, the solution of the problem on the determination of asymptotic properties of the stochastic transport of microscopic particles has allowed us to derive new macroscopic equations describing the kinetics of this process with allowance for the finiteness of the velocity of particles. Despite a different type of fractional derivatives involved, these equations prove to be very convenient for a sufficiently detailed analysis of the phenomena associated with the finiteness of v: the transformation of the self-similarity of the Green's functions, the extinction of resting particles, and nontrivial dependence of the system evolution on the dimension of the problem. All these questions can find direct practical application, in particular, to the study of radiative transfer in plasma.

ACKNOWLEDGMENTS

The authors are grateful to A.S. Kingsep for valuable remarks.

This work was supported in part by the program "Nonlinear Dynamics" of the Ministry of Science of the Russian Federation and by the INTAS (grant no. 97-0021).

REFERENCES

1. E. W. Montroll and M. F. Schlesinger, in *Studies in Statistical Mechanics*, Ed. by J. Leibowitz and E. W. Montroll (North-Holland, Amsterdam, 1984), Vol. 2, p. 1.
2. J.-P. Bouchand and A. Georges, Phys. Rep. **195**, 127 (1990).
3. M. B. Isichenko, Rev. Mod. Phys. **64**, 961 (1992).
4. G. M. Zaslavsky, Physica D (Amsterdam) **76**, 110 (1994).
5. K. V. Chukbar, Zh. Éksp. Teor. Fiz. **108**, 1875 (1995) [JETP **81**, 1025 (1995)].
6. V. V. Uchaĭkin, Teor. Mat. Fiz. **115**, 154 (1998).
7. V. M. Zolotarev, V. V. Uchaĭkin, and V. V. Saenko, Zh. Éksp. Teor. Fiz. **115**, 1411 (1999) [JETP **88**, 780 (1999)].
8. I. M. Sokolov, Phys. Rev. E **63**, 056111 (2001).
9. E. Lutz, Phys. Rev. Lett. **86**, 2208 (2001).
10. S. G. Samko, A. A. Kilbas, and O. I. Marichev, *Fractional Integrals and Derivatives, Theory and Applications* (Nauka i Tekhnika, Minsk, 1987; Gordon and Breach, Amsterdam, 1993).
11. L. M. Biberman, V. S. Vorob'ev, and I. T. Yakubov, *Kinetics of Nonequilibrium Low-Temperature Plasmas* (Nauka, Moscow, 1982; Consultants Bureau, New York, 1987), p. 1.
12. V. I. Kogan and V. S. Lisitsa, Itogi Nauki Tekh., Fiz. Plazmy **4**, 194 (1983).
13. E. B. Tatarinova and K. V. Chukbar, Zh. Éksp. Teor. Fiz. **92**, 809 (1987) [Sov. Phys. JETP **65**, 455 (1987)].
14. M. I. D'yakonov and A. S. Furman, Zh. Éksp. Teor. Fiz. **92**, 1012 (1987) [Sov. Phys. JETP **65**, 574 (1987)].
15. P. M. Morse and H. Feshbach, *Methods of Theoretical Physics* (McGraw-Hill, New York, 1953; Inostrannaya Literatura, Moscow, 1958), Vol. 1, Para. 7.4.
16. K. V. Chukbar, Zh. Éksp. Teor. Fiz. **109**, 1335 (1996) [JETP **82**, 719 (1996)].
17. A. P. Prudnikov, Yu. A. Brychkov, and O. I. Marichev, *Integrals and Series Elementary Functions* (Nauka, Moscow, 1981; Gordon and Breach, New York, 1986), Chap. 2.

Translated by I. Nikitin

Journal of Experimental and Theoretical Physics, Vol. 94, No. 2, 2002, pp. 260–269.
Translated from Zhurnal Éksperimental'noĭ i Teoreticheskoĭ Fiziki, Vol. 121, No. 2, 2002, pp. 308–319.

FLUIDS

On Mechanisms of the Helix Pitch Variation in a Thin Cholesteric Layer Confined between Two Surfaces

S. P. Palto

Shubnikov Institute of Crystallography, Russian Academy of Sciences, Moscow, 117333 Russia
e-mail: palto@online.ru; lbf@ns.crys.ras.ru

Received September 13, 2001

Abstract—Two possible mechanisms of the temperature-induced variation and jump of the helix pitch in a spatially bounded planar layer of a cholesteric liquid crystal (LC) was considered within the framework of the continuum theory of elasticity. These mechanisms are related to the existence of two configuration curves of the system free energy. The states with local free energy minima on each of the configuration curves correspond to topologically equivalent configurations of the LC director distribution and are quasi-equivalent in this sense. The transitions between such quasi-equivalent states are especially important in the first mechanism of the helix pitch jump proceeding without participation of defects. The second mechanism is related to transitions between the ground states of different configuration curves corresponding to topologically nonequivalent configurations. This mechanism requires either participation of disclination lines or the formation of defects. © *2002 MAIK "Nauka/Interperiodica".*

1. INTRODUCTION

The cholesteric liquid crystals (LCs) occupy a special place among numerous liquid-crystalline materials. The chirality of cholesteric molecules, which is an inherent property of this class of liquid crystals, accounts for a very large number of physical effects important both for practical applications (e.g., in LC display technology) and for the proper understanding of basic problems pertaining to the physics of liquid crystals [1].

The effect of a sharp change in the helix pitch in a spatially bounded cholesteric liquid crystal (CLC) in response to the temperature variation was both experimentally observed and theoretically studied [2–4]. Recently, Belyakov and Kats [2] demonstrated an important role of the cohesive energy in this effect; proposed a mechanism responsible for a change in the helix pitch, according to which the total number of halfturns in the helix changes by one as a result of the LC director slippage on the surface; and introduced a universal parameter playing a special role in this effect:

$$S_d = K_{22}/Wd,$$

where K_{22} is the torsion modulus of the LC, W is the height of the potential of cohesion between LC and the surface, and d is the LC layer thickness. Unfortunately, an analysis of the pitch jump phenomenon performed in [2] was restricted to very large values of this parameter ($S_d \sim 1/2\pi$) for which a change in the helix configuration cannot involve metastable states. According to an estimate obtained using typical values of the LC parameters ($K_{22} = 3$ pN, $d = 5$ μm, and $W \geq 0.1$ mJ/m^2 [5])

$$S_d < 6 \times 10^{-3} \ll 1/2\pi,$$

excluding the metastable states from consideration can only be justified in a special case of extremely small cohesive energies.

In this paper, the notions about the LC director slippage are further developed, but a somewhat different approach to this problem is proposed. In particular, the concept of quasi-equivalent states is introduced, and, according to one of the proposed mechanisms, the transitions involving a change in the helix pitch take place just between such states. The quasi-equivalent states correspond to topologically equivalent configurations of the CLC director distribution, the transitions between which (quasi-equivalent transitions) are allowed both due to deformation of the director field in the bulk and due to a finite cohesive energy at the LC boundaries. For a relatively large energy of cohesion between LC molecules and a surface ($\gg 0.1$ mJ/m^2), this implies configurations differing from one another by an even integer number of halfturns in the cholesteric helix. At a relatively small cohesive energy caused by a deviation of the director from the easy orientation axis, a minimum change in the number of halfturns upon a quasi-equivalent transition can be characterized by an intermediate value between one and two. In contrast to the second mechanism involving transitions between the topologically nonequivalent configurations differing by a halfturn of the cholesteric helix, the quasi-equivalent transitions require no defect formation.

This study is devoted to the general case, whereby the easy orientation axis of LC molecules possesses an initial slope (tilt) at the boundary surfaces and the cohesive energy comprises two components—zenithal and azimuthal. The latter circumstance is of special signifi-

cance from the standpoint of investigations related to the development of oriented coatings of a new type with controlled slope of the LC molecules and controlled components of the cohesive energy. It will be demonstrated that important factors determining the helix pitch variation include, in addition to the temperature dependence of the natural helix pitch considered in [2], the temperature dependence of the elasticity coefficient and the presence of an LC director tilt at the boundaries. With a view to subsequent experimental verification of the proposed mechanisms, the general equations were numerically solved for a particular CLC and the optical transmission spectra in a selective reflection range were calculated.

2. BASIC EQUATIONS

Consider the layer of a cholesteric liquid crystal confined between two surfaces spaced by a distance d. The CLC is assumed to possess a planar texture, whereby the cholesteric helix axis is oriented perpendicularly to the boundary surfaces. For brevity, this system is referred to below as the CLC cell. The right-handed coordinate system is oriented so that the x and y axes are lying in the plane of the first boundary surface and the z axis is directed toward the second surface. Let the easy orientation axes of CLC molecules in both boundary planes belong to the xz plane. The orientation state of CLC molecules in the layer is characterized by a unit vector (director)

$$n = (n_x, n_y, n_z) = (\sin\theta\cos\varphi, \sin\theta\sin\varphi, \cos\theta),$$

where θ and φ are the azimuthal and polar angles measured from the z and x axes, respectively (Fig. 1). When the total number of halfturns in the cholesteric helix is much greater than unity, we can use Frank's general formula [5] for the free energy density and obtain the following expression for the free energy of a CLC per unit area (see Appendix for details):

$$F = \frac{K_{22}d}{2}(q_0 - q)^2 + \sqrt{K_{11}K_{33}}(\cos^2\theta_{s1} + \cos^2\theta_{s2})q + W_1 + W_2, \quad (1)$$

where K_{11}, K_{22}, and K_{33} are the LC constants of elasticity; q is the wavenumber of the cholesteric helix in the cell; q_0 is the wavenumber corresponding to the natural helix pitch $P_0 = 2\pi/q_0$ (attained in the limit of negligibly weak interaction between CLC and the boundary surfaces); and $W_1 = W_1(\varphi_{s1}, \theta_{s1})$ and $W_2 = W_2(\varphi_{s2}, \theta_{s2})$ are the energies of cohesion between CLC and the boundary surfaces, which depend on the director orientation (the subscripts s1 and s2 indicate the director angles on the first and second surfaces, respectively).

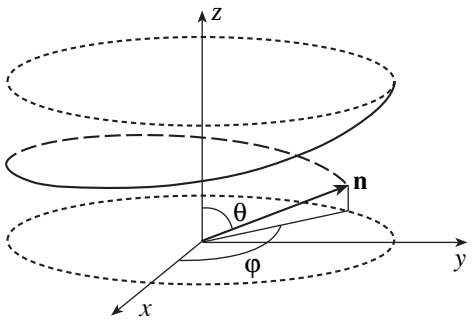

Fig. 1. A schematic diagram of a cholesteric helix in the laboratory coordinate system.

The azimuthal distribution of the CLC director is described by the expressions

$$n_x = \sin\theta\cos(qz + \varphi_{s1}), \quad n_y = \sin\theta\sin(qz + \varphi_{s1}). \quad (2)$$

with the boundary conditions

$$\varphi_{s1} + qd = \varphi_{s2} + \pi k, \quad (3.1)$$

$$-\pi < \varphi_{s1,\,s2} \le \pi, \quad (3.2)$$

where k is an integer. Note that the domain of $\varphi_{s1,\,s2}$ values represents a 2π-wide sector. In the general case of a tilted director, this domain contains no $\varphi_{s1,\,s2}$ values corresponding to like director states on the boundary surfaces. The helix configurations with the same k may differ by a multiple of two halfturns. In the particular case when the director is not tilted at the boundaries, the orientational equivalence of the director states ($\mathbf{n} = -\mathbf{n}$) allows the $\varphi_{s1,\,s2}$ domain to be restricted to a π-wide sector; in this case, the k value corresponds to an integer of the total number of halfturns in the helix. However, for the sake of generality and consistency, we will consider the entire domain of $\varphi_{s1,\,s2}$ values defined in (3.2).

For the subsequent analysis, it is convenient to define the quasi-equivalent states as the states in which the k values either are the same or differ by an even integer. The introduction of this concept be justified below. It should be noted that the quasi-equivalent states correspond to local minima of the free energy of the system on the general configuration curve (representing the free energy as a function of q). Adjacent states with the k values differing by unity belong to a different configuration curve and should be spatially separated by a disclination line.

The equilibrium state of a CLC corresponds to a minimum total free energy of the system. For the extremal values of the function (1), variation of the angles φ_{s1} and φ_{s2} with an allowance of the boundary conditions (3) yields

$$\frac{\partial F}{\partial \varphi_{s1}} = K_{22}(q_0 - q)$$
$$-\frac{1}{d}\sqrt{K_{11}K_{33}}(\cos^2\theta_{s1} + \cos^2\theta_{s2}) + \frac{\partial W_1}{\partial \varphi_{s1}} = 0, \quad (4)$$
$$\frac{\partial F}{\partial \varphi_{s2}} = -K_{22}(q_0 - q)$$
$$+\frac{1}{d}\sqrt{K_{11}K_{33}}(\cos^2\theta_{s1} + \cos^2\theta_{s2}) + \frac{\partial W_2}{\partial \varphi_{s2}} = 0.$$

These equations lead to several important results. The first is the boundary condition

$$\frac{\partial W_1}{\partial \varphi_{s1}} = -\frac{\partial W_2}{\partial \varphi_{s2}}. \quad (5)$$

In the case of identical surfaces ($W_1 = W_2 \equiv W$), this yields

$$\varphi_{s1} = -\varphi_{s2} \equiv \varphi_s. \quad (6)$$

Secondly, substituting relationship (6) into Eqs. (4) and taking into account the boundary condition (3.1), we obtain expressions for the helix wavenumber in a cholesteric layer confined between two like surfaces:

$$q = q_0 - \frac{2\sqrt{K_{11}K_{33}}}{K_{22}d}\cos^2\theta_s + \frac{1}{K_{22}}\frac{\partial W}{\partial \varphi_s}, \quad (7.1)$$

$$\varphi_s = \frac{\pi k - qd}{2}, \quad (7.2)$$

$$\frac{\partial^2 W}{\partial q^2} + \frac{1}{2}K_{22}d > 0, \quad (7.3)$$

where (since the surfaces are identical) we set $\theta_{s1} = \theta_{s2} \equiv \theta_s$. The solutions of the system of Eqs. (7.1) and (7.2) correspond to extremal values of the free energy. Supplementing this system by condition (7.3), we restrict the consideration to solutions representing minima of the energy. Expressions (7.1)–(7.3) are the key relationships in the subsequent analysis.

3. RESULTS AND DISCUSSION

The experimentally observed effect [3, 4] consists in that a change in the temperature leads to a sharp shift of the selective transmission spectrum, which is explained by a jumplike change in the cholesteric helix pitch. The jump takes place over a very narrow temperature interval amounting to a fraction of one kelvin. As can be see from Eq. (7.1), changes in the helix wavenumber for a fixed CLC layer thickness can be due to the temperature dependence of either the quantity q_0 or the elastic constants, tilt angle, and cohesive energy. The temperature dependences of elastic constants for some LC materials were measured with a good accuracy [6], which allows us to perform an analysis based on the particular estimates. Turning to the experiments reported in [3], where the selective reflection band was observed in the visible range ($\lambda \sim 500$–600 nm) for a 4.8-μm-thick CLC cell, we can readily estimate that the change by one in the number of halfturns of a cholesteric helix corresponds to a relative change in the wavenumber by

$$\Delta q/q_0 \sim 1/N = \lambda/2dn \sim 0.03,$$

where $n \sim 1.6$ is the CLC index of refraction and N is the number of halfturns in the cholesteric helix over the cell thickness. According to (7.1), the presence of a finite director tilt at the boundary allows the helix pitch to change as a result of variation of the elastic constants even for infinite cohesive energy. A finite cohesive energy makes the wavenumber q even more sensitive toward the temperature variations because deviations of the director from the easy orientation axis give rise to a nonzero derivative $\partial W/\partial \varphi_s$. In the case of a zero tilt of the director, a relative change in the helix wavenumber due to the temperature variation of K_{22} per one kelvin can be estimated as

$$\frac{1}{q_0}\frac{\partial q}{\partial T} = -\frac{1}{q_0(K_{22})^2}\frac{\partial W}{\partial \varphi_s}\frac{\partial K_{22}}{\partial T}$$
$$\sim \frac{1}{1.5\times 10^7\ \mathrm{m^{-1}} \times 9\times 10^{-24}\ \mathrm{H}^2}\frac{10^{-4}\ \mathrm{J/m^2}}{\pi/4} \quad (8)$$
$$\times 6\times 10^{-14}\ \mathrm{N\,K^{-1}} = 0.06\ \mathrm{K^{-1}}.$$

Here, we took $q_0 = 15\ \mu\mathrm{m}^{-1}$, the elastic constant $K_{22} = 3$ pN, and the temperature coefficient $dK_{22}/dT \approx -0.06$ pN/K for the well-known nematic liquid crystal pentylcyanobiphenyl (5CB) and limited the cohesive energy variation to a typical value of 0.1 mJ/m^2 for the director deviation by an angle of $\pi/4$. As noted above, a change in the number of halfturns by one under the experimental conditions used in [3, 4] requires a relative change in the wavenumber $\Delta q/q_0 \sim 0.03$ (here, we do not specify a mechanism changing the number of halfturns). For the conditions used in the estimate (8), this corresponds to a temperature interval width on the order of 0.5 K.

Thus, typical temperature-induced variations in the elastic constants may introduce, together with the temperature dependence of the natural helix pitch, a significant contribution to the resulting effect of variation of the helix pitch.

3.1. On Mechanisms of the Cholesteric Helix Wavenumber Jump in the Absence of a Director Tilt in the Rapini Model Potential

Let us consider in more detail the possible mechanisms of the temperature-induced jump in the helix pitch, based on the Rapini model—the most popular shape of the surface potential in the absence of a tilt of the CLC director at the boundaries. As will be shown below, there are two basically different mechanisms that may account for the variation and jump in the helix pitch, which are related to the two configuration curves of the free energy as a function of the wavenumber.

In one of these mechanisms, an important role belongs to the temperature dependence of the natural pitch and the ratio of the coefficient of elasticity to the cohesive energy. Unfortunately, precise measurements of the cohesive energy encounter a number of difficulties. In most cases, the experimental data presently available on the cohesive energies at various surfaces can be considered only as estimates. For this reason, we will fix the cohesive energy and consider the influence of the temperature variation of the coefficient of elasticity. However, it should be borne in mind that, in the general case, we imply the temperature dependence of the ratio of the coefficient of elasticity to the cohesive energy. The role of the temperature variation of the wavenumber q_0 requires special analysis.

For certainty, the calculations will be performed for a 5CB liquid crystal, the parameters of which are known in a broad temperature range [6]. The use of such values by no means reduces generality of the analysis, while indicating the boundaries of variation of the parameters that are important in experiment. The liquid crystals of pure 5CB are not cholesteric, but small chiral additives (only slightly affecting the elastic constants of the matrix) render the material cholesteric with a certain natural helix pitch. In our calculations, the natural pitch is assumed to be $P_0 = 2\pi/q_0 = 0.5$ μm. As is commonly known, 5CB possesses a room-temperature ($T = 20°C$) elastic constant $K_{22} \approx 3.3$ pN and the corresponding temperature coefficient $dK_{22}/dT \approx -0.06$ pN/K. For the sake of generality, the layer thickness will be taken somewhat different from a nominal value ($d_0 = 5$ μm).

In the case when the CLC easy orientation axes occur in the boundary planes (e.g., are parallel to the x axis), the Rapini potential is

$$W(\varphi_s) = \frac{1}{2}W_0 \sin^2\varphi_s \qquad (9)$$

and Eqs. (7.1)–(7.3) acquire the following form:

$$q = q_0 + \frac{W_0}{2K_{22}}\sin(\pi k - qd), \qquad (10.1)$$

$$K_{22} + 2W_0 d\cos(\pi k - qd) > 0. \qquad (10.2)$$

Obviously, Eq. (10.1) has a trivial solution $q = q_0$ for a thickness of $d = d_0 = \pi k/q_0$ referred to as the nominal. In the general case, the thickness d differs from d_0 and, hence, the cholesteric helix is ether contracted or extended owing to cohesion between LC and the surface.

The possible mechanisms of a jump in the wavenumber q are most clearly illustrated by a graphical solution of Eq. (10.1) presented in Fig. 2a. The solutions to this equation correspond to the points of intersection of the functions

$$f(q) = W_0\sin(\pi k - qd)/(2K_{22}), \quad g(q) = q - q_0$$

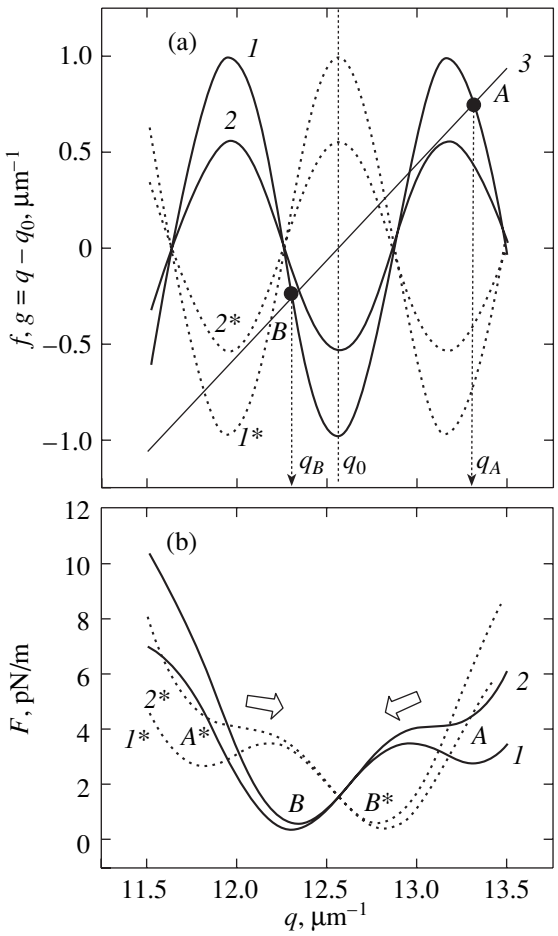

Fig. 2. (a) A graphical solution of Eq. (10.1) for $d = d_0 + P_0/4 = 5.125$ μm and (b) the corresponding configuration curves of the free energy: solid curves *1*, *2* correspond to the states with $k = 20$; dashed curves *1**, *2** represent the adjacent states with $k = 19$ or 21; the pairs of curves *1*, *1'* and *2*, *2'* show the $f(q)$ and $F(q)$ functions calculated for $K_{22} = 1.5$ and 3 pN, respectively; straight line *3* represents the function $g(q) = q - q_0$ (see the text); the minima *A*, *B* and *A**, *B** indicate the quasi-equivalent states on the configuration curves *1* and *1**, respectively; arrows indicate transitions between quasi-equivalent states.

represented by curve *1* (or *2*) and line *3*, respectively. For a set of k values differing by an even integer, $f(q)$ is a common continuous periodic function. By the same token, the free energy function $F(q)$ for the same set of k values is also represented by a common smooth curve (Fig. 2b).

Not all solutions to Eq. (10.1) satisfy the condition (10.2) of the free energy minimum. If there is a family of solutions meeting the condition of minimum for a given set of k values (differing by an even integer), we will speak of a set of the quasi-equivalent states. Here, the prefix "quasi" emphasizes a difference in the free energies for the states corresponding to various local minima, while the term "equivalence" indicates that the states belong to the same configuration curve $F(q)$.

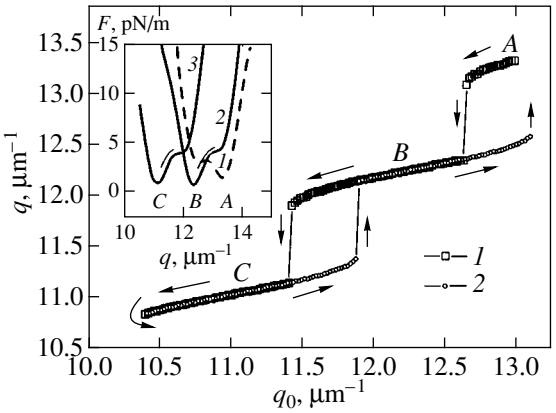

Fig. 3. A plot of the helix wavenumber q in the CLC cell versus the wavenumber q_0 corresponding to the natural helix pitch. Arrows indicate the direction of variation of the parameter q_0. The inset shows the configuration curves of the free energy versus q for various $q_0 = 13$ (*1*), 12.6 (*2*), and 11.4 μm^{-1} (*3*), illustrating the mechanism of jumps in the wavenumber q. Symbols *A*, *B*, and *C* indicate stable states of the system for various q_0. All calculations were performed for $d = 5.125$ μm, $K_{22} = 3$ pN, and $W_0 = 3 \times 10^{-3}$ mJ/m^2.

There are only two sets of integers k—even and odd—which determine two configuration curves of the free energy as a function of q. It is the existence of the two configuration curves that accounts for the two basically different mechanisms of a jump in the helix wavenumber.

In Fig. 2a, solid curves show the functions $f(q)$ for $k = k_0 = 2d_0/P_0 = 20$, while the dashed curves represent the analogous functions for $k = k_0 - 1 = 19$ (the pairs of curves *1*, *1**, and *2*, *2** corresponding to different coefficients of elasticity). First, let us restrict the consideration to the solutions for $k = 20$ at a fixed helix wavenumber q_0. Although there are three points of intersection between curve *1* and line *3*, only two of these solutions (indicated by points *A* and *B*) satisfy the condition (10.2) of minimum free energy (see Fig. 2b). The point *A* corresponds to a metastable quasi-equivalent state, which is separated from the energetically more favorable state *B* by a barrier depending on the cohesive energy and the coefficient of elasticity. Once falling into the state *A*, the system may occur there for a rather long time (in practice, the lifetime of a metastable state may be on the order of tens of minutes). However, a temperature-induced increase in the elastic constant up to a certain level may decrease the amplitude of the $f(q)$ function (Fig. 2, curve *2*), leading to disappearance of the solution *A* (curve *2* intersects with line *3* at a single point *B* corresponding to the free energy minimum). Thus, the local energy minimum corresponding to the metastable quasi-equivalent state *A* disappears and the system exhibits a jumplike transition into state *B* with a sharply different helix wavenumber q (Fig. 2b, curve *2*).

An analogous behavior can be observed on displacing line *3* (representing the function $g(q) = q - q_0$) in Fig. 2a. For example, if the temperature variation leads to a decrease in the wavenumber q_0, the line *3* would shift toward greater values along the ordinate axis and, hence, the solution *A* would disappear. However, there is an essential difference in this scenario from the case of variation of the elastic constant. Indeed, the shift of the $g(q)$ line upward not only leads to disappearance of the solution *A*, but can "create" a new solution *C* on the left (along the q axis) of solution *B*. Moreover, continuing variation of the wavenumber q_0 would render the state *B* metastable, whereas *C* would become the main stable state. Finally, a moment will come when the state *B* disappears (by a mechanism described above for state *A*) and the system passes into state *C* (see the inset in Fig. 3).

If the direction of displacement of the $g(q)$ line is reversed (by inverting the direction of temperature variation), the system would apparently exhibit a hysteresis because the temperature at which state *C* disappears on increasing the q_0 value differs from the temperature of disappearance of state *B* with decreasing q_0. Thus, the variation of the natural helix pitch leads to reversible changes in the wavenumber, albeit with a certain hysteresis. This is illustrated in Fig. 3 showing a plot of the helix wavenumber q versus q_0 corresponding to the natural helix pitch. In contrast to this behavior, the jump in the wavenumber caused by changing the elastic constant is not reversible, since the system always passes into an energetically more favorable state.

Now let us briefly mention the role of other parameters varied at a fixed wavenumber q_0. An increase in the layer thickness d leads to a change in the period of function $f(q)$ and, accordingly, increases the temperature sensitivity of the system with respect to the appearance of local minima in the W_0/K_{22} ratio. In our example, $W_0 = 3 \times 10^{-3}$ mJ/m^2 and one of the two possible jumps in the helix pitch (extremely low cohesive energy of this system results in that only one metastable quasi-equivalent state exists on each configuration curve) can be observed provided that the coefficient of elasticity varies from 2.9 to 3.1 pN, which corresponds to the temperature variation from 21 to 23°C. An increase in the cohesive energy would increase the number of quasi-equivalent states between which the transitions can take place. However, the most sensitive with respect to the temperature still will be the states with deeper local energy minima, that is, with maximum change in the number of halfturns relative to the nominal value $2d_0/P_0$.

It should be emphasized that, in contrast to the approach proposed in [2], we consider the transitions between quasi-equivalent states with the same (or differing by an even integer) k values. The quasi-equivalent character of states is a very important condition, since this mechanism does not require the formation of bulk defects for changing the helix wavenumber. The quasi-equivalent states correspond to topologically equivalent configurations of the LC director distribu-

tion. A continuous transition between these configurations, even for infinite surface energy, can be provided by deformation of the LC director in the bulk. A good illustration is offered by a hydrodynamic bistability phenomenon observed upon application of an electric field pulse to a CLC cell [7, 8]. The physical pattern of this bistability can be clearly described in terms of the mechanism proposed above, by considering the transitions between quasi-equivalent states differing (under conditions of strong cohesion) by two halfturns of the CLC helix.

The considerations above referred to the case of states belonging to the same configuration curve. However, there is a basically different possible mechanism of the helix pitch variation related to the transitions between ground states belonging to the different configuration curves. The states with adjacent values $k = \{19, 21\}$ are characterized by analogous, albeit somewhat shifted, configuration curves of the free energy (see dashed curves *1** and *2** in Fig. 2b) and may equiprobably exist in a real cell with the thickness $d = d_0 + P_0/4$. The configuration with $k = 20$ and any of the adjacent states with $k = \{19, 21\}$ are topologically nonequivalent and, hence, separated by a disclination line. An insignificant energy gain acquired by one of the two configurations would result in movement of the disclination line separating the two states with the k values differing by unity.

In contrast to the quasi-equivalent transitions, for which a minimum change in the helix wavenumber q falls within the interval from π/d to $2\pi/d$ (at higher cohesive energies, the corresponding change in the number of halfturns approaches two), a change in q for the transition between adjacent states does not exceed π/d. This property can serve a criterion for distinguishing the different mechanisms of the helix pitch jump corresponding to the transitions between quasi-equivalent and adjacent states. By leveling the energies of ground states on the two configuration curves (which can be provided by varying the layer thickness or the natural helix pitch so that $d = d_0 + P_0/4$), we may create conditions for the existence of equiprobable adjacent configurations. In the experimental selective reflection spectra, the presence of adjacent configurations should be manifested by superposition of the spectra from two spatially separated regions, which was probably observed in [3]. At the same time, a jump in the wavenumber with the number of halfturns changed by two reported in [4] can be attributed to a quasi-equivalent transition.

For a greater cohesive energy ($\geqslant 0.01$ mJ/m^2), when the amplitude of the $f(q)$ function is sufficiently large, the system possesses a large number of solutions corresponding to deep minima in the free energy. Here, a change in the coefficient of elasticity or the natural helix pitch may be insufficient to eliminate the quasi-equivalent states with the k values close to the nominal number of halfturns $N_0 = 2d_0/P_0$. In this case, a mechanism of the helix wavenumber variation can only be related to a shift of the disclination lines or to the formation of defects (assuming that the LC director in the bulk is not perturbed, e.g., by an applied electric field).

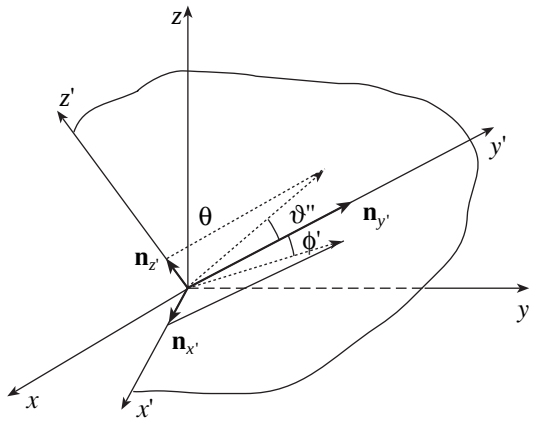

Fig. 4. A schematic diagram illustrating the interaction between the LC director and the surface in a local coordinate system $x'y'z'$. The y' axis coincides with the easy orientation axis; the z axis of the laboratory coordinate system lies in the $y'z'$ plane. Deviation of the LC director from the easy orientation axis is considered as a superposition of deviations in the two orthogonal planes $z'y'$ and $x'y'$, which correspond to the azimuthal and zenithal cohesive energy components, respectively.

3.2. Effects of the Director Tilt and the Cohesive Energy Components

In order to establish the role of the director tilt angle, it is important to take into account that, in the general case, the azimuthal cohesive energy component (i.e., the cohesion related to the director deviation by the angle φ) differs from the zenithal component (involving the director deviation in the θ angle).

At present, there is no commonly accepted form of representation for the potential of interaction between the LC director and the surface, although this problem has been discussed for a long time [9]. In particular, the interaction energy is frequently written in the form of an expansion in Legendre polynomials. However, the mean field distribution at the surface in the general case does not possess a cylindrical symmetry. Mathematically, the mean field asymmetry requires introducing the angular dependence of the cohesive energy with the aid of a set of orthogonal functions ensuring the expansion of dependences defined over the $\{0, 2\pi\}$ interval and possessing a period of 2π. This possibility is offered by the Fourier expansion instead of the Legendre polynomials that can only provide for the expansion of functions defined on the interval of $\cos a = x \in \{-1, 1\}$, $\theta \in \{0, \pi\}$.

The Fourier representation of the cohesive energy can be conveniently written in a local coordinate system $x'y'z'$ in which the y' axis coincides with the easy

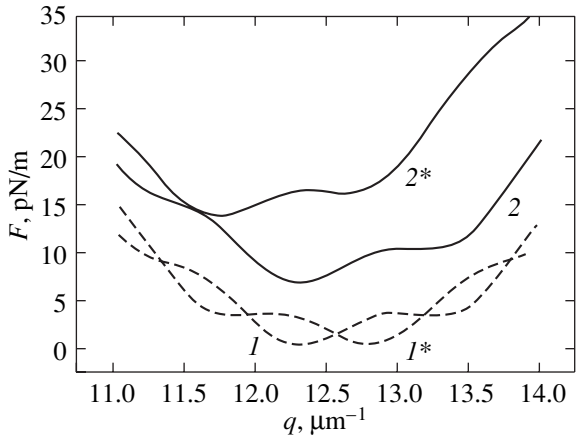

Fig. 5. The configuration curves of the free energy for a CLC layer with the thickness $d = d_0 + P_0/4 = 5.125$ μm (*1*, *1**) in the absence of tilt and (*2*, *2**) in the presence of a 10° director tilt and the anisotropic cohesive energy. The curves were calculated for $k = 20$ (*1*, *2*) and 19 (*1**, *2**); $K_{22} = 2$ pN; $K_{33} = 10$ pN; $K_{11} = 6.4$ pN/m; $W_a = 3 \times 10^{-3}$ mJ/m^2; and $W_z = 0.3$ mJ/m^2. The corresponding director tilt θ_s at the boundaries for $k = 20$ and 19 is 83° and 97°, respectively.

orientation axis (Fig. 4). The concept of the easy orientation axis is very important. By definition, this axis is determined in the laboratory coordinate system *xyz* by a tilt angle relative to the *xy* plane and corresponds to the director orientation on the surface in the absence of elastic deformations in the bulk. If the director field in the LC bulk is deformed, the director orientation on the surface would deviate from the easy orientation axis. The returning force of the surface is determined by the type of the cohesive energy.

In the local coordinate system, the movements of the director in the two orthogonal planes *x'y'* and *y'z'* can be considered as independent (i.e., characterized by independent amplitudes of the harmonics); these movements are defined as corresponding to the azimuthal and zenithal cohesive energy components. In the most general case, each of these components can be represented as a Fourier series in the orthogonal directions corresponding to the rotations with respect to angles ϕ' (for the azimuthal energy) and ϑ' (for the zenithal energy):

$$W_{z'} = \sum_{m=0}^{\infty} (A_{zm}\cos(m\vartheta') + B_{zm}(m\vartheta')), \qquad (11.1)$$

$$W_{x'} = \sum_{m=0}^{\infty} (A_{xm}\cos(m\phi') + B_{xm}\sin(m\phi')), \qquad (11.2)$$

where m is the harmonic number and A_{zm}, B_{zm}, A_{xm}, and B_{xm} are the corresponding harmonic amplitudes. Assuming the presence of a certain symmetry, expansions (11.1) and (11.2) can be simplified. For example, if the system is symmetric relative to the easy orientation axis, the energy function should be even and the Fourier series in both (11.1) and (11.2) would contain only the terms with cosines. An additional symmetry with respect to the *x'z'* plane (orthogonal to the easy orientation axis) would retain only even harmonics in the expansion. In the latter case, the zeroth and second harmonics reflect the widely used Rapini potential. Evidently, no such symmetry takes place in the general case, and, hence, the development of methods for determining the Fourier coefficients in expansions (11.1) and (11.2) would provide an approach to adequate characterization of the cohesive energy. However, since most of the measurements so far were performed for the Rapini model potential, we will restrict the further analysis to a modified form of this potential taking into account an anisotropy in the cohesion and the director tilt.

Retaining only the zeroth and second harmonics in the Fourier expansions (11.1) and (11.2), we can express the total cohesive energy in terms of the director components as follows:

$$W = W_{x'} + W_{z'} = \frac{1}{2}W_a n_{x'}^2 + \frac{1}{2}W_z n_{z'}^2, \qquad (12)$$

where W_a and W_z are the amplitudes of the azimuthal and zenithal components of the cohesive energy, and $n_{x'}$ and $n_{z'}$ are the director components in the local coordinate system (see Fig. 4).

Accomplishing the coordinate transformation and taking into account that easy orientation axis belongs to the *xz* plane, we arrive at an expression for the cohesive energy in the laboratory coordinate system:

$$W = \frac{1}{2}W_a n_{ys}^2 + \frac{1}{2}W_z(n_{zs}\sin\theta_{s0} - n_{xs}\cos\theta_{s0})^2, \qquad (13)$$

where the index *s* indicates the values determined at the surface,

$$\mathbf{n} = (n_{xs}, n_{ys}, n_{zs}) \equiv (\sin\theta_s\cos\varphi_s, \sin\theta_s\sin\varphi_s, \cos\theta_s),$$

and the angle θ_{s0} determines the orientation of the easy orientation axis relative to the *z* axis. Substituting (13) into Eqs. (7.1) and (7.2), we obtain

$$q = q_0 - \frac{2\sqrt{K_{11}K_{33}}}{K_{22}d}\cos^2\theta_s + \frac{(W_a - W_z\cos^2\theta_{s0})\sin^2\theta_s}{2K_{22}}\sin(\pi k - qd) + \frac{W_z\sin 2\theta_s\sin 2\theta_{s0}}{4K_{22}}\sin\left(\frac{\pi k - qd}{2}\right). \qquad (14)$$

Comparing expressions (14) and (10.1), one can readily see that the director tilt could be treated in terms of the effective change in the natural helix pitch and renormalized cohesive energy, if it was not the last term that may give a very significant contribution due to an anisotropic cohesive energy (when $W_z \gg W_a$). These contributions are different for the two adjacent states as a result of the $\pi/2$ phase shift. Should the anisotropic contribution be zero at a certain thickness for the states

with $k = 0$, the adjacent state with $k = 1$ will be characterized by the maximum contribution. This is a consequence of the qualitatively different free energy relationships in the adjacent states. For a comparison, Fig. 5 shows the configuration curves of the free energy for adjacent states in the absence (dashed curves *1* and *1**) and in the presence (solid curves *2* and *2**) of the director tilt. In the absence of tilt, the configuration curves *1* and *1** for the given thickness ($d = d_0 + P_0/4 = 5.125$ μm) are symmetric with respect to the vertical axis drawn at $q = q_0$; in the presence of a 10° tilt, the curves exhibit a strong shift in both ordinate (energy) and abscissa (wavenumber) axes. The latter shift may result in a considerable displacement of the Grangin zones in the Kano wedge, which should be taken into account when this method is used for determining the natural helix pitch.

The presence of a director tilt is a factor important for practical applications, which can be used for introducing asymmetry into the energy of adjacent states in order to inhibit the formation of undesired domains and the transitions between adjacent states in the CLC cell. It is well known that the supertwist nematic (STN) LC display technology employs large tilts (25° for 270° STNs) for avoiding the domain formation.

3.3. Manifestations of the Cholesteric Helix Wavevector Jump in the Selective Optical Transmission Spectra

With a view to the possible experimental verification of the mechanism of variation of the cholesteric helix wavenumber, we have numerically modeled a CLC cell using parameters of the 5CB crystal. In particular, we calculated the optical transmission spectra in a selective reflection range.

The calculation was performed using a two-stage procedure. In the first stage, the general Lagrange equations (derived using expression (A.3) in the Appendix) were solved by the relaxation method and a distribution of the director was determined for a CLC layer with preset boundary conditions. Then, using the 4×4 matrix method with an algorithm proposed in [10], we numerically solved the Maxwell equations for a layered optical system including both the CLC layer and the boundary glass plates. The optical problem was solved for a partly monochromatized (coherence length, 100 μm) nonpolarized light, which is the closest to typical conditions that can be used in the possible experiment.

By properly selecting the φ_{s0} value (0° or 180°) for the easy orientation axis on the second surface, we obtained numerical solutions corresponding to one of the configuration curves (with $k = 19$ or 20) considered above. Examples of the transmission spectra of a CLC cell calculated for $k = 19$, fixed wavenumbers q_0, and various coefficients of elasticity are presented in Fig. 6 (the other parameters corresponded to the values used for calculation of the configuration curves in Fig. 2). As can be seen, the selective transmission band exhibits a sharp displacement within the region of K_{22} between 2.8 and 3.2, which is caused by a change in the helix wavenumber from 11.7 μm^{-1} (curve *3*) to 12.7 μm^{-1} (curve *2*). This behavior is fully consistent with the proposed interpretation of the helix pitch jump as a result of the quasi-equivalent transitions. In this particular case, the system features a transition of the type $A^* \longrightarrow B^*$ as indicated in Fig. 2. Naturally, analogous (but displaced) curves will also be observed for the $A \longrightarrow B$ transition on the other configuration curve. Thus, for any selected layer thickness, the measured spectra can represent a superposition of spectral curves corresponding to various states.

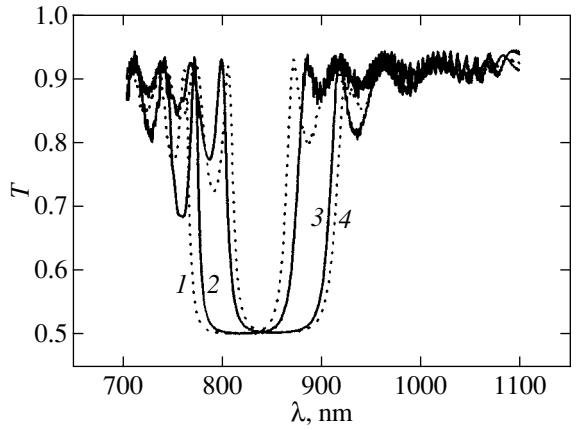

Fig. 6. The optical transmission spectra of a 5.125-μm-thick CLC cell for nonpolarized light, calculated for various values of the elastic constant $K_{22} = 4$ (*1*), 3.2 (*2*), 2.8 (*3*) and 2 pN (*4*) with an allowance for the boundary glass plates (refractive index, $n = 1.5$; thickness, 200 μm). The calculations were performed for a normal dispersion law with the following refractive indices: $n_\parallel$ (λ = 514 nm) = 1.736; $n_\perp$ (λ = 514 nm) = 1.544; $n_\parallel$ (λ = 630 nm) = 1.706; $n_\perp$ (λ = 600 nm) = 1.531.

A real system exhibits the temperature dependence of both the elastic constants and the natural helix pitch. According to the proposed mechanism, the latter factor must result in that the jumplike shift of the selective transmission spectrum would be periodically repeated, for example, on heating, with a hysteresis behavior observed on cooling (see Fig. 3).

In the case of transitions between adjacent states, the spectral shift caused by a jump in the helix pitch will be smaller than that depicted in Fig. 6, because the total number of halfturns in the helix cannot change by more than one. Moreover, since the transition is accompanied by motion of the disclination line separating two states, the transition may be accompanied both by a superposition of the spectral curves from the two spatially separated regions and by increased light scattering.

The presence of a director tilt will affect both the positions of the spectral curves and the period of jumplike spectral shifts. The last term in Eq. (14) accounts for the existence of two different intervals on the wavenumber scale through which the jump of the selective

transmission spectrum takes place in the course of a gradual variation of the natural helix pitch.

4. CONCLUSION

We have considered two possible mechanisms explaining the temperature variation of the helix pitch in the spatially bounded layer of a cholesteric liquid crystal. The two mechanisms are related to the existence of two configuration curves of the free energy as a function of the cholesteric helix wavenumber.

The first mechanism is based on the temperature variation of the positions of quasi-equivalent states on one of the configuration curves. As the CLC parameters or the boundary conditions exhibit temperature-induced variations, solutions of basic equations corresponding to the quasi-equivalent states may disappear. This results in a jumplike transition to another quasi-equivalent state, which is accompanied by a change (ranging from one to two) in the number of halfturns. The transitions between quasi-equivalent states require no defect formation.

The second mechanism is based on the transitions between ground states belonging to different configuration curves. This mechanism implies either the motion of a disclination line or the formation of defects. In this case, the total number of halfturns changes by no more than one.

ACKNOWLEDGMENTS

The author is grateful to L.M. Blinov, M.I. Barnik, V.V. Lazarev, and N.M. Shtykov for fruitful discussions and valuable advice.

This study was supported by the Russian Foundation for Basic Research, project nos. 99-02-16484 and 01-02-16287.

APPENDIX

In the most general case, the free energy density of a CLC is determined by the Frank expression [5] and, with an allowance for the cohesive energy, can be written as

$$f = \frac{1}{2}[K_{11}(\mathrm{div}\mathbf{n})^2 + K_{22}(\mathbf{n}\mathrm{curl}\,\mathbf{n} + q_0)^2 + K_{33}(\mathbf{n}\times\mathrm{curl}\,\mathbf{n})^2] + W_1\delta(z)|_{z=0} + W_2\delta(z-d)|_{z=d}, \quad \text{(A.1)}$$

where $\delta(z)$ is the Dirac delta function.

Restricting the consideration to a practically important case of the director orientation changing only in the z direction, we can use the relationships

$$\mathrm{div}\mathbf{n} = \frac{\partial n_z}{\partial z}, \quad \mathrm{curl}\,\mathbf{n} = \left(-\frac{\partial n_y}{\partial z}, \frac{\partial n_x}{\partial z}, 0\right)^T,$$

$$(\mathbf{n}\times\mathrm{curl}\,\mathbf{n})^2 = (\mathrm{curl}\,\mathbf{n})^2 - (\mathbf{n}\mathrm{curl}\,\mathbf{n})^2 \quad \text{(A.2)}$$

$$= n_z^2\left[\left(\frac{\partial n_y}{\partial z}\right)^2 + \left(\frac{\partial n_x}{\partial z}\right)^2\right] + \left[n_x\frac{\partial n_x}{\partial z} + n_y\frac{\partial n_y}{\partial z}\right]^2,$$

and Eq. (A.1) acquires the following form:

$$f = \frac{1}{2}\left\{K_{11}\left(\frac{\partial n_z}{\partial z}\right)^2 + K_{22}\left(n_y\frac{\partial n_x}{\partial z} - n_x\frac{\partial n_y}{\partial z} + q_0\right)^2 + K_{33}\left[n_z^2\left(\left(\frac{\partial n_y}{\partial z}\right)^2 + \left(\frac{\partial n_x}{\partial z}\right)^2\right) + \left(n_x\frac{\partial n_x}{\partial z} + n_y\frac{\partial n_y}{\partial z}\right)^2\right]\right\} \quad \text{(A.3)}$$

$$+ W_1\delta(z)|_{z=0} + W_2\delta(z-d)|_{z=d}.$$

An analysis of the numerical solution to the Lagrange–Euler equations for the free energy density (A.3) showed that the director distribution can be described with very good accuracy by the expressions

$$n_x = \sin\theta\cos(qz + \varphi_{s1}), \quad n_y = \sin\theta\sin(qz + \varphi_{s1}), \quad \text{(A.4.1)}$$

$$n_z \equiv \cos\theta = A_1\exp(-\xi_1 z) + A_2\exp(\xi_2(z-d)). \quad \text{(A.4.2)}$$

Therefore, the analytical solutions for the CLC director orientations corresponding to the free energy minima can be solved in the form of (A.4.1) and (A.4.2), where the quantities ξ_1^{-1} and ξ_2^{-1} refer to the first and second surfaces and correspond to the characteristic length over which the z component of the director exhibits variation. These quantities can be determined from the condition of minimum for the free energy. The corresponding A_1 and A_2 values are determined from the boundary conditions.

Substituting (A.4.1) and (A.4.2) into (A.3) and integrating with respect to thickness, we obtain the following expressions for the free energy per unit area:

$$F = F_1 + F_2 + F_3 + W_1(\varphi, \theta) + W_2(\varphi, \theta), \quad \text{(A.5)}$$

$$F_1 = \frac{K_{11}}{2}\int_0^d\left(\frac{\partial n_z}{\partial z}\right)^2 dz$$

$$= \frac{K_{11}}{2}\left[A_1^2\xi_1^2(1 - \exp(-2\xi_1 d)) + A_2^2\xi_2^2(1 - \exp(-2\xi_2 d)) + \frac{1A_1A_2\xi_1\xi_2}{\xi_1 - \xi_2}(\exp(-\xi_2 d) - \exp(-\xi_1 d))\right], \quad \text{(A.6)}$$

$$F_2 = \frac{K_{22}}{2}\int_0^d\left(n_y\frac{\partial n_x}{\partial z} - n_x\frac{n_y}{\partial z} + q_0\right)^2 dz$$

$$= \frac{K_{22}d}{2}(q_0 - q)^2 + K_{22}q(q_0 - q) \quad \text{(A.7)}$$

$$\times\left[\frac{A_1^2}{\xi_1}(1 - \exp(-2\xi_1 d)) + \frac{A_2^2}{\xi_2}(1 - \exp(-2\xi_2 d))\right] + O(A_1^4, A_2^4),$$

$$F_3 = \frac{K_{33}}{2}\int_0^d\left[n_z^2\left(n_y\left(\frac{\partial n_x}{\partial z}\right)^2 + \left(\frac{\partial n_y}{\partial z}\right)^2\right) + \left(n_x\frac{\partial n_x}{\partial z} + n_y\frac{\partial n_y}{\partial z}\right)^2\right]dz = \frac{K_{33}}{2}q^2 \times\left[\frac{A_1^2}{\xi_1}(1-\exp(-2\xi_1 d)) + \frac{A_2^2}{\xi_2}(1-\exp(-2\xi_2 d))\right] + O(A_1^4, A_2^4), \quad \text{(A.8)}$$

where $O(A_1^4, A_2^4)$ denotes the fourth-order terms in $A_{1,2}$. Since $A_{1,2} < 1$ (moreover, the tilt at the boundaries is usually small and $A_{1,2} \ll 1$), the fourth-order terms in $A_{1,2}$ can be fully ignored.

The results of numerical modeling of the general problem showed that, in the presence of a director tilt at the boundary and for a large number of halfturns in the helix ($N \gg 1$), the director tilt angle $\vartheta = \pi/2 - \theta$ (measured from the *xy* plane) tends to zero in the majority of the CLC cell (except for a thin near-surface region having a thickness comparable with the helix pitch). Thus, for $N \gg 1$, the exponential terms in (A.6)–(A.8) can be ignored since $\xi_1 d \gg 1$ and $\xi_2 d \gg 1$. Moreover, in this case one can readily derive from the boundary conditions that $A_1 \approx n_{zs1}$ and $A_2 \approx n_{zs2}$, so that the expression for the free energy acquires a still simpler form:

$$F = \frac{K_{22}d}{2}(q_0 - q)^2 + \left[\frac{n_{zs1}^2}{\xi_1} + \frac{n_{zs2}^2}{\xi_2}\right] \times\left(K_{22}q(q_0 - q) + \frac{K_{33}}{2}q^2\right) + \frac{K_{11}}{2}(\xi_1 n_{zs1}^2 + \xi_2 n_{zs2}^2) + W_1(\varphi_{s1}, \theta_{s1}) + W_2(\varphi_{s2}, \theta_{s2}). \quad \text{(A.9)}$$

Varying (A.9) with respect to ξ_1 and ξ_2 and using the condition of minimum free energy (A.9), we obtain

$$\xi \equiv \xi_1 = \xi_2 = \sqrt{\frac{2\left(K_{22}q(q_0 - q) + \frac{K_{33}}{2}q^2\right)}{K_{11}}}. \quad \text{(A.10)}$$

It should be noted that the quantities ξ_1 and ξ_2 are independent of the cohesive energy. However, the weak cohesive energy influences the values of n_{zs1} and n_{zs2}. For this reason, the director slope at the boundaries differs from the initial tilt determining the easy orientation axis. Substituting (A.10) into (A.9), we finally arrive at

$$F = \frac{K_{22}d}{2}(q_0 - q)^2 + (n_{zs1}^2 + n_{zs2}^2) \times\sqrt{2K_{11}\left(K_{22}q(q_0 - q) + \frac{K_{33}}{2}q^2\right)} + W_1(\varphi_{s1}, \theta_{s1}) + W_2(\varphi_{s2}, \theta_{s2}) \approx \frac{K_{22}d}{2}(q_0 - q)^2 + \sqrt{K_{11}K_{33}}(n_{zs1}^2 + n_{zs2}^2)q + W_1(\varphi_{s1}, \theta_{s1}) + W_2(\varphi_{s2}, \theta_{s2}). \quad \text{(A.11)}$$

The approximation in the right-hand part of (A.11) is justified when $|q_0 - q| \ll q_0$, which takes place for $N \gg 1$.

REFERENCES

1. G. S. Chilaya, Kristallografiya **45**, 944 (2000) [Crystallogr. Rep. **45**, 871 (2000)].
2. V. A. Belyakov and E. I. Kats, Zh. Éksp. Teor. Fiz. **118**, 560 (2000) [JETP **91**, 488 (2000)].
3. H. Zink and V. A. Belyakov, Mol. Cryst. Liq. Cryst. **265**, 445 (1995).
4. H. Zink and V. A. Belyakov, Mol. Cryst. Liq. Cryst. **329**, 457 (1999).
5. L. M. Blinov and V. G. Chigrinov, *Electrooptic Effects in Liquid Crystal Materials* (Springer-Verlag, New York, 1994).
6. J. D. Bunning, T. E. Faber, and P. L. Sherrell, J. Phys. (Paris) **42**, 1175 (1981).
7. D. W. Berreman and W. R. Heffner, J. Appl. Phys. **52**, 3032 (1981).
8. P. J. Bos, P. Watson, J. E. Anderson, *et al.*, in *Proceedings of International Display Research Conference "Eurodisplay'99", Berlin, 1999*, p. 397.
9. G. Barbero, N. V. Madhusudana, and G. Durand, Z. Naturforsch. A **39**, 1066 (1984).
10. S. P. Palto, Zh. Éksp. Teor. Fiz. **119**, 638 (2001) [JETP **92**, 552 (2001)].

Translated by P. Pozdeev

Journal of Experimental and Theoretical Physics, Vol. 94, No. 2, 2002, pp. 270–282.
Translated from Zhurnal Éksperimental'noĭ i Teoreticheskoĭ Fiziki, Vol. 121, No. 2, 2002, pp. 320–334.

SOLIDS
Structure

Interference of Instanton Trajectories during Quantum Tunneling in Small Particles of Real Antiferromagnets

B. A. Ivanov and V. E. Kireev*
Institute of Magnetism, National Academy of Sciences of Ukraine, Kiev, 03142 Ukraine
**e-mail: kireev@imag.kiev.ua*
Received May 30, 2001

Abstract—For a two-sublattice antiferromagnet, the Lagrangian is constructed taking into account Berry's phase whose form is matched with the quantum-mechanical Heisenberg Hamiltonian. Tunnel effects are analyzed taking into account the crystallographic symmetry and possible types of Dzyaloshinski interaction. It is shown that, when the real magnetic symmetry and the Dzyaloshinski interaction are taken into consideration, the effects of destructive instanton interference and the suppression of macroscopic quantum tunneling may come into play. This may lead to a periodic dependence of the ground-state level splitting on the Dzyaloshinski interaction constant; the magnitude of this splitting is calculated. © *2002 MAIK "Nauka/Interperiodica".*

1. INTRODUCTION

During the last decade, macroscopic quantum tunneling in macroscopic (or, to be more precise, mesoscopic) magnetic systems has become an object of intense experimental and theoretical investigations [1]. In the physics of magnetism, such systems include small magnetic particles, magnetic clusters, and high-spin molecules. Special attention is paid to coherent macroscopic quantum tunneling (CMQT) between physically different, but energetically equivalent, states in systems with discrete degeneracy of the ground state. A typical CMQT effect in such systems is tunneling between two equivalent classical states corresponding to two minima of the anisotropy energy (see [2]).

The CMQT effects can be observed experimentally from the resonant absorption of electromagnetic waves at tunnel-split energy levels. The interest in this effect is associated with the following two factors. First, mesoscopic objects exhibiting quantum-mechanical properties are interesting as potential elements of quantum computers. Second, fine and elegant effects of interference of instanton trajectories emerge in these problems. For ferromagnetic particles, these effects suppress tunneling for half-integral values of the total spin of the system [3, 4] and lead to oscillatory dependences of the tunnel splitting of energy levels on extrinsic parameters [5]. In addition, in contrast to the effects of quantum runaway from a metastable to a stable state, the manifestations of CMQT effects are not masked by thermal fluctuations.

Initially, the CMQT investigations were carried out for small particles of a ferromagnet [6, 7] under the assumption that all spins in a particle are in fact parallel to one another (high-spin model). The effects of destructive interference of instanton trajectories and interference suppression of tunneling were predicted precisely for such systems [3, 4, 8]. It turned out later that antiferromagnets form a more convenient class for experimental investigations of CMQT. According to calculations [9, 10], the level spitting in an antiferromagnet is stronger than in a ferromagnet and the effects can be observed at a higher temperature. It is not surprising that the CMQT effects were observed for the first time in ferritin particles possessing an antiferromagnetic structure [8]. No interference effects are observed in pure antiferromagnets (i.e., in the case of complete compensation of the spins of sublattices), but such effects may appear upon the application of a magnetic field [5]. It will be shown below that even in zero field, the interference effects may also appear when the real magnetic symmetry of the crystal is taken into account (in particular, in the presence of the Dzyaloshinski–Moriya interaction).

A semiclassical description of magnetic systems is based on the formalism of coherent spin states. In constructing the effective field Lagrangian both for a ferromagnet and for an antiferromagnet, we will proceed from the formula for the Euclidean Lagrangian of an individual spin, which has the form [11]

$$\mathcal{L}_0 = i\hbar s\sum_k \dot{\phi}_k(1-\cos\theta_k) - W(\phi_k, \theta_k). \qquad (1)$$

Here, s is the spin associated with each magnetic moment, ϕ_k and θ_k are the polar coordinates of the kth magnetic moment, and $W(\phi_k, \theta_k)$ is the classical energy of a magnetic material; the dot indicates the differentiation with respect to the imaginary time $\tau = it$. The first term determines the magnetization dynamics (its variation leads to the well-known Landau–Lifshitz equations in angular variables) and also determines the so-called Berry's phase (see [11, 12]). This quantity is associated with the total time derivative which is not

manifested in the equations of motion, but is responsible for the interference of instanton trajectories.

For a macroscopic description, it is natural to use one or several field variables (order parameters) instead of the set of microscopic variables. The determination of the number of order parameters and their transformation properties in magnetic systems is a nontrivial problem. In the approach base on coherent spin states, the order parameter for ferromagnets is the magnetization vector of constant length, which can be parametrized by the angular variables θ and ϕ. In this case, Berry's phase is just the resultant change in angle ϕ along an instanton trajectory [3, 4]. The behavior of an antiferromagnetic system can be correctly described with the help of a three-component vector of a fixed length, viz., the ferromagnetism vector $\mathbf{l}$ [13–15]. The total spin in this case is a subordinate variable and is determined by vector $\mathbf{l}$ and its time derivative $\partial\mathbf{l}/\partial t$. Dynamic equations for the antiferromagnetism vector $\mathbf{l}$ can be either constructed proceeding from the symmetry considerations [13] or derived from the Landau–Lifshitz equations for the magnetizations of sublattices [16, 17]. In both these approaches, the same classical equations of motion for the unit vector $\mathbf{l}$ are obtained, which are usually referred to as the equations of the σ model. The application of such equations considerably simplifies the analysis of both linear and nonlinear dynamic effects in an antiferromagnet (see [18, 19]). However, the advantage of using these equations for describing macroscopic quantum effects is not so obvious. At any rate, the Lagrangian obtained from the classical Landau–Lifshitz equations or from symmetry considerations cannot be used directly for describing the MQT effect taking into account the interference of instanton trajectories. It is probably for this reason that Golyshev and Popkov [5] used in their analysis of the CMQT effects a system of two equations for the magnetizations of sublattices, whose analysis is much more complicated.

As a matter of fact, it is impossible in principle to reconstruct the Lagrangian of a dynamic system from the classical equations of motion. The Lagrangians describing the same classical equations of motion for the system may differ in the term which is the total derivative with respect to time. This term does not affect the classical dynamics of the system, but alters the magnitude of action on trajectories. For this reason, the corresponding terms of the type of total derivatives were lost in the early publications [6, 7]. A consistent quantum-mechanical expression for the spin Lagrangian taking into account the correct equation for the total derivative can be derived using the formalism of coherent states and the analysis of the evolution operator; this expression coincides with formula (1) given above. Topological terms of the form of total derivatives in the effective Lagrangian for vector $\mathbf{l}$ were found to be significant for the quantum theory of 1D antiferromagnets [11]. However, it is impossible in principle to derive their expressions proceeding only from the classical equations of the σ model for vector $\mathbf{l}$.

In the simplest version of the σ model, the derivatives of $\mathbf{l}$ with respect to time appear in the Lagrangian in the trivial form $(\partial\mathbf{l}/\partial\tau)^2$ [13–15]. In this case, the equations of the σ model are Lorentz-invariant, and the description of the dynamics of nonlinear magnetization waves (kink-type solitons in antiferromagnets) is simplified considerably (see [15, 18]). In such a case, the interference effects in MQT are obviously absent. However, the situation changes radically in an analysis of more realistic models.

First, for many antiferromagnetic crystals, there exist terms taking into account interactions of the Dzyaloshinski-Moriya type, which are linear in $\mathbf{l}$ and in magnetization. It was shown in [20, 21] that these interactions are responsible for the terms in the effective Lagrangian which are linear in $\partial\mathbf{l}/\partial t$; this considerably modifies the kink dynamics as compared with the simplest Lorentz-invariant model. Obviously, such interactions may in principle also lead to the emergence of total derivatives (topological phases). The presence of a magnetic field may also lead to similar effects; this was noted in an analysis of the nonlinear dynamics of antiferromagnets [22] as well as for the MQT effect (see [5] and recent publications [23–27]).

In the present work, we will construct the Lagrangian of the σ model on the basis of formula (1) taking into account consistently the sources of the terms with the total derivative, which may lead to nontrivial interference effects. This Lagrangian will be used to study the interference of instanton trajectories for the real models of antiferromagnetic particles of various symmetries and to determine the contribution of these effects to the tunneling probability.

2. LAGRANGIAN OF THE σ MODEL FOR REAL ANTIFERROMAGNETS

Let us consider a system with localized spins, in which nearest neighbors are coupled through the antiferromagnetic interaction. We assume that the lattice has such a structure that the sites with spins can be divided into two groups so that the spins appearing in pairs of nearest neighbors belong to different groups and there are no frustrations in the lattice. For an ideal antiferromagnet, these two groups correspond to two magnetic sublattices. In this case, we can assume that the spins corresponding to each group have parallel orientations and form the total spins $\mathbf{S}_1$ and $\mathbf{S}_2$ of the sublattices. In the exchange approximation for such antiferromagnets, vectors $\mathbf{S}_1$ and $\mathbf{S}_2$ are antiparallel. The total spin $\mathbf{S} = \mathbf{S}_1 + \mathbf{S}_2$ in the ground state can differ from zero in view of a different number of sites in the sublattices (decompensation), $|\mathbf{S}_1| \neq |\mathbf{S}_2|$, and also in the presence of an external magnetic field and/or the Dzyaloshinski interaction, when the antiparallelism of the spins is violated (i.e., $|\mathbf{S}_1 + \mathbf{S}_2| \neq 0$ even for $|\mathbf{S}_1| = |\mathbf{S}_2|$). We will consider only completely compensated antiferromagnets with $|\mathbf{S}_1| = |\mathbf{S}_2|$ since the specific effects

associated with spin decompensation ($|\mathbf{S}_1 + \mathbf{S}_2| \neq 0$, but $|\mathbf{S}_1 - \mathbf{S}_2| \ll |\mathbf{S}_{1,2}|$) in fact reduce the interference effects to those which are well known for ferromagnets (see [28]).

Our goal is the construction of the Lagrangian describing the dynamics of vector $\mathbf{l}$ in the presence of the Dzyaloshinski–Moriya interaction and a magnetic field. Since the tensor of exchange interaction constants J_{ij} may have an antisymmetric component in the nearest neighbor approximation, the Hamiltonian of such a system has the form

$$\mathcal{H}_e = J\sum_{\langle\alpha\beta\rangle}\mathbf{S}_\alpha\cdot\mathbf{S}_\beta + \sum_{\langle\alpha\beta\rangle}\mathbf{d}\cdot[\mathbf{S}_\alpha\times\mathbf{S}_\beta] - g\mu_B\sum_\alpha\mathbf{H}\cdot\mathbf{S}_\alpha. \quad (2)$$

Here, the first term describes the isotropic exchange interaction, and the summation in this term is extended to the pairs of nearest neighbors, and $\mathbf{S}_\alpha$ is the spin at the αth site. The antisymmetric component of the tensor of exchange constants J_{ij} is a microscopic source of the Dzyaloshinski–Moriya interaction (see [29]), corresponding to the dual vector $\mathbf{d}$. The last term describes the interaction of spins with the external magnetic field.

Let us consider the exchange approximation in which the deviation from the conventional Heisenberg model with an isotropic exchange interaction of the type $J\mathbf{S}_\alpha\mathbf{S}_\beta$ is small; i.e., d, $g\mu_B H \ll J$. In this case, we can introduce the spins $\mathbf{S}_1 = \sum\mathbf{S}_{\alpha_1}$ and $\mathbf{S}_2 = \sum\mathbf{S}_{\alpha_2}$ of the sublattices and assume that vectors $\mathbf{S}_1$ and $\mathbf{S}_2$ have a fixed length. It is convenient to put $\mathbf{S}_1 = Ns\boldsymbol{\sigma}_1$ and $\mathbf{S}_2 = Ns\boldsymbol{\sigma}_2$, where s is the spin of a sublattice site and N is the number of sites in each sublattice. We will parametrize the unit vectors $\boldsymbol{\sigma}_1$ and $\boldsymbol{\sigma}_2$ by the polar coordinates (θ_1, ϕ_1) and (θ_2, ϕ_2), respectively. In this case, the classical energy of the antiferromagnet, whose exchange component corresponds to Hamiltonian (2), can be written in the form

$$\mathcal{W}(\boldsymbol{\sigma}_1, \boldsymbol{\sigma}_2) = Js^2zN\boldsymbol{\sigma}_1\cdot\boldsymbol{\sigma}_2 + s^2zN\mathbf{d}\cdot[\boldsymbol{\sigma}_1\times\boldsymbol{\sigma}_2] + w(\boldsymbol{\sigma}_1, \boldsymbol{\sigma}_2) - g\mu_B sN\mathbf{H}\cdot(\boldsymbol{\sigma}_1 + \boldsymbol{\sigma}_2). \quad (3)$$

Here, N is the number of spins in a sublattice, z is the coordination number for a lattice site, and $w(\boldsymbol{\sigma}_1, \boldsymbol{\sigma}_2)$ is the anisotropy energy.

Thus, we arrive at the description of the energy of an antiferromagnet in terms of two vectors of unit length. Their dynamics can be described by a Lagrangian which can be written in the dynamic variables $\boldsymbol{\sigma}_1$ and $\boldsymbol{\sigma}_2$ taking into account relation (3) in the form

$$\mathcal{L} = -i\hbar S_1\mathbf{A}_1(\boldsymbol{\sigma}_1)\cdot\dot{\boldsymbol{\sigma}}_1 - i\hbar S_2\mathbf{A}_2(\boldsymbol{\sigma}_2)\cdot\dot{\boldsymbol{\sigma}}_2 - \mathcal{W}(\boldsymbol{\sigma}_1, \boldsymbol{\sigma}_2). \quad (4)$$

Here, we have chosen a more general form of the kinetic terms as compared to relation (1). These terms can be presented through the vector potential of the field of a magnetic monopole:

$$\mathbf{A}_{1,2}(\boldsymbol{\sigma}) = \frac{\boldsymbol{\sigma}\times\mathbf{n}_{1,2}}{\sigma(\sigma + \boldsymbol{\sigma}\cdot\mathbf{n}_{1,2})}, \quad (5)$$

where $\mathbf{n}_{1,2}$ are the quantization axes of coherent states for each sublattice. This potential has a singularity for $\boldsymbol{\sigma}\cdot\mathbf{n} = -\sigma$, i.e., on a certain half-line in the $\boldsymbol{\sigma}$ space. Usually, the "north pole" gauge with $\mathbf{n} = \mathbf{e}_z$ is used, in which the quantity $\mathbf{A}(\boldsymbol{\sigma})\cdot\dot{\boldsymbol{\sigma}}$ assumes the familiar form (1). The potentials $\mathbf{A}_{1,2}$ of the monopole field permit gauge transformations (such as a change in the position of spin quantization axes and, hence, singularities) which do not change the equations of motion, but make a contribution to the Lagrangian in the form of the total derivative of the function of spins $\boldsymbol{\sigma}_1$and $\boldsymbol{\sigma}_2$ with respect to τ, which may in principle be significant for the description of interference effects. The kinetic term for each sublattice can be written in an individual gauge (in particular, with different directions of $\mathbf{n}_1$ and $\mathbf{n}_2$).

We present the unit vectors $\boldsymbol{\sigma}_1$ and $\boldsymbol{\sigma}_2$ in terms of vectors $\mathbf{l} = (\boldsymbol{\sigma}_1 - \boldsymbol{\sigma}_2)/2$ and $\mathbf{m} = (\boldsymbol{\sigma}_1 + \boldsymbol{\sigma}_2)/2$ which are connected through the relations

$$\mathbf{l}^2 + \mathbf{m}^2 = 1, \quad \mathbf{m}\cdot\mathbf{l} = 0. \quad (6)$$

In the σ-model approximation, when the magnetic moment is small ($|\mathbf{m}| \ll |\mathbf{l}|$), we can use simple transformations to present Lagrangian (4) as a power expansion in $\mathbf{m}$. Confining the expansion to the terms linear in $\mathbf{m}$, we can write the kinetic term in the form

$$\begin{aligned} &-i\hbar\mathbf{A}_1(\boldsymbol{\sigma}_1)\cdot\dot{\boldsymbol{\sigma}}_1 - i\hbar\mathbf{A}_2(\boldsymbol{\sigma}_2)\cdot\dot{\boldsymbol{\sigma}}_2 \\ &= -i\hbar\dot{\mathbf{l}}\cdot[\mathbf{A}_1(\mathbf{l}) - \mathbf{A}_2(-\mathbf{l})] \\ &- i\hbar m_i\left[\dot{\mathbf{l}}\frac{\partial\mathbf{A}_1(\mathbf{l})}{\partial l_i} + \dot{\mathbf{l}}\frac{\partial\mathbf{A}_2(-\mathbf{l})}{\partial l_i}\right] \\ &- i\hbar\dot{\mathbf{m}}\cdot[\mathbf{A}_1(\mathbf{l}) + \mathbf{A}_2(-\mathbf{l})]. \end{aligned} \quad (7)$$

Here, the form of potentials $\mathbf{A}_1$ and $\mathbf{A}_2$ has not been specified as yet; in particular, the quantization axes $\mathbf{n}_1$ and $\mathbf{n}_2$ have not been chosen. It is natural to choose such an arrangement of the quantization axes $\mathbf{n}_1$ and $\mathbf{n}_2$ that $\mathbf{A}_1(\mathbf{l}) = \mathbf{A}_2(-\mathbf{l})$, which is possible for $\mathbf{n}_1 = -\mathbf{n}_2$. In this case, the singular term with $d\mathbf{l}/d\tau$ vanishes, and the dynamic term starts with the term linear in $\mathbf{m}$, which can be written in the form

$$-i\hbar\mathbf{m}\cdot[\mathbf{F}\times\dot{\mathbf{l}}] - i\hbar\frac{d}{d\tau}(\mathbf{m}\cdot\mathbf{A}_1(\mathbf{l})), \quad (8)$$

where

$$F_i = \epsilon_{ijk}\left(\frac{\partial A_j}{\partial l_k} - \frac{\partial A_k}{\partial l_j}\right). \quad (9)$$

Thus, most of the arbitrariness in the choice of the gauge field **A**, which takes place for ferromagnets, does not exist for antiferromagnets. The gauge-invariant quantity F_i, which has the meaning of a formal magnetic field associated with potential **A**, is the magnetic monopole field $\mathbf{F} = \mathbf{l}/|\mathbf{l}|^3$. In the transition from formula (7) to expression (8), the initial gauge arbitrariness turned out to be localized in the term with the total derivative $d(\mathbf{m} \cdot \mathbf{A}(\mathbf{l}))/d\tau$. As regards this quantity, its contribution to the Euclidean action is obviously equal to zero in the case when an instanton trajectory misses the singular point of **A**(**l**). This condition can be satisfied easily if we choose the direction $\mathbf{n} = \mathbf{n}_1 = -\mathbf{n}_2$ along the hard magnetization axis of the antiferromagnet. In this case, the phase for a closed path on the sphere $\mathbf{l}^2 = 1$, which is formed by instanton trajectories, is independent of the position of the quantization axis **n**.

Taking into account the condition $\mathbf{m} \cdot \mathbf{l} = 0$, we eliminate from expression (4) the subordinate variable **m**:

$$\mathbf{m} = \frac{\hbar}{2Jsz}[\gamma(\mathbf{H}^{\text{eff}} - \mathbf{l}(\mathbf{H}^{\text{eff}} \cdot \mathbf{l})) - i\mathbf{l} \times \dot{\mathbf{l}}], \qquad (10)$$

where $\gamma = g\mu_B/\hbar$ is the gyromagnetic ratio and $\mathbf{H}^{\text{eff}}$ is the effective field which is the sum of the external field **H** and the Dzyaloshinski field $\mathbf{H}^D$. In the approximation chosen above, in which the Dzyaloshinski–Moriya interaction can be presented in a purely antisymmetric form $\mathbf{d} \cdot [\boldsymbol{\sigma}_1 \times \boldsymbol{\sigma}_2] \propto \mathbf{d} \cdot [\mathbf{l} \times \mathbf{m}]$, the Dzyaloshinski field can be written as

$$\mathbf{H}^D = zs[\mathbf{d} \times \mathbf{l}]/g\mu_B.$$

The expression for **m** is also valid for more general forms of the Dzyaloshinski interaction, which cannot be reduced to a bilinear form in $\boldsymbol{\sigma}_{1,2}$. In particular, we will consider more general forms of the Dzyaloshinski interaction of the type $D_{ik}(\mathbf{l})m_i l_k$, $H_i^D = D_{ik}(\mathbf{l})l_k$, which are observed for many crystals and are significant for the MQT effects. In this case, the effective field in the expression for **m** assumes the form

$$H_i^{\text{eff}} = H_i^0 + D_{ik}(\mathbf{l})l_k. \qquad (11)$$

In this section, we will not specify the form $D_{ik}(\mathbf{l})$. It follows from formula (10) that the approximation $|\mathbf{m}| \ll |\mathbf{l}|$ used in the derivation of the σ model is satisfied for $\max(H, H^D) \ll H_{\text{ex}}$, where $H_{\text{ex}} = Jsz/\mu_B$ is the exchange field. Substituting **m** into Lagrangian (4), we obtain the effective Lagrangian for vector **l** in the form

$$\mathcal{L} = \frac{\hbar^2 N}{2Jz}\left\{\frac{1}{2}\dot{\mathbf{l}}^2 + i\gamma\mathbf{H}^{\text{eff}} \cdot [\mathbf{l} \times \dot{\mathbf{l}}]\right\} - \mathcal{W}_a(\mathbf{l}) + \frac{2\mu_B^2 N}{Jz}\{(\mathbf{H} \cdot \mathbf{l})^2 - \mathbf{H}^2 + 2\mathbf{H} \cdot (\mathbf{l}(\mathbf{H}^D \cdot \mathbf{l}) - \mathbf{H}^D)\}. \qquad (12)$$

Here, $\mathcal{W}_a(\mathbf{l})$ has the meaning of the effective anisotropy energy in which the additional term $(\mathbf{H}^D \cdot \mathbf{l})^2 - (\mathbf{H}^D)^2$ is taken into account along with the initial energy $w(\mathbf{l}) = w(\boldsymbol{\sigma}_1, \boldsymbol{\sigma}_2)$ introduced above for $\boldsymbol{\sigma}_1 = -\boldsymbol{\sigma}_2 = \mathbf{l}$. The quantity $\mathcal{W}_a(\mathbf{l})$ is obviously the real anisotropy energy determined from static measurements in weak fields, and there is no point in separating these contributions. We must simply use the expression for $\mathcal{W}_a(\mathbf{l})$ which is determined by the crystal symmetry of the magnet. The specific form of the anisotropy energy for various antiferromagnets is given in the table. The terms in the braces describe the variation of the static energy of the antiferromagnet due to the external magnetic field. The first term, which is quadratic in the components of **H**, is quadratic in **l** and can also be presented as the field-induced renormalization of the anisotropy energy. The second term, which is bilinear in the components of the external magnetic field **H** and the Dzyaloshinski field $\mathbf{H}^D$, contains odd powers of the components of **l** and describes the energy of the weak ferromagnetic moment induced by the Dzyaloshinski interaction. (In particular, this term can be reduced to $\mathbf{H} \cdot [\mathbf{d} \times \mathbf{l}]$ for a purely antisymmetric Dzyaloshinski interaction.) This term can completely remove the degeneracy of the classical ground state of the system, and the analysis of the MQT effects becomes meaningless. For this reason, it makes sense to take into account the external magnetic field and the Dzyaloshinski interaction simultaneously only for certain selected orientations of the external field, when this term vanishes for vector **l** directed along the easy magnetization axis of the antiferromagnet. Some of these orientations of the field for orthorhombic antiferromagnets were considered in [5].

Thus, we arrive at the following conclusions. The Lagrangian for vector **l** differs from the Lagrangian in the σ model of an ideal antiferromagnet [11] in the presence of a number of additional terms which play different roles in the description of CMQT. In contrast to the case of a ferromagnet or an antiferromagnet with different spins of the sublattices, the term with the total derivative can easily be eliminated and is immaterial. It is important that the inclusion of the external field and some forms of the Dzyaloshinski interaction leads to the emergence of gyroscopic terms linear in $d\mathbf{l}/d\tau$. The emergence of these terms indicates the lowering of the actual dynamic symmetry of antiferromagnets in the presence of a magnetic field and/or the Dzyaloshinski interaction.

The structure of the Lagrangian is such that the contribution of the Dzyaloshinski interaction to the gyroscopic term can be taken into account simply by adding the Dzyaloshinski field $\mathbf{H}^D$, which is a function of **l**, to the external magnetic field **H**. Gyroscopic terms can make significant contributions to the probabilities of tunneling processes both by affecting the structure of instanton solutions and by creating destructive interference of instanton trajectories. It will be proved below that, in contrast to the case of a ferromagnet or an antiferromagnet with different spins of the sublattices, this interference is not of topologic origin, but can also be

Anisotropy in the basal plane and the Dzyaloshinski interaction for systems with various types of magnetic symmetry

n	$\tilde{w}_a$	Axes	DMI	$\Gamma(\theta, \phi)$		$B(\theta, \phi)$	K
2	$\beta_2\sin^2\theta\sin^2\phi$	$2_z^{(+)}, 2_x^{(-)}, 2_y^{(-)}$	$m_x l_y + m_y l_x$	$3\sin^3\theta\sin 2\phi$	*	$3\sin^2\theta\sin 2\phi$	4
		$2_z^{(-)}, 2_x^{(+)}, 2_y^{(-)}$	$m_y l_z + m_z l_x$	$6\sin^2\theta\cos\theta\sin\phi$	*	$6\sin\theta\cos\theta\sin\phi$	4
		$2_z^{(-)}, 2_x^{(-)}, 2_y^{(+)}$	$m_x l_z + m_z l_x$	$6\sin^2\theta\cos\theta\cos\phi$		$6\sin\theta\cos\theta\cos\phi$	4
4	$\beta_4\sin^4\theta\sin^2 2\phi$	$4_z^{(+)}, 2_x^{(-)}, 2_{xy}^{(-)}$	$\frac{1}{2i}(m_+ l_+^3 - m_- l_-^3)$	$5\sin^5\theta\sin 4\phi$	*	$5\sin^4\theta\sin 4\phi$	16
		$4_z^{(-)}, 2_x^{(+)}, 2_{xy}^{(-)}$	$m_x l_x - m_y l_y$	$3\sin^3\theta\cos 2\phi$		$3\sin^2\theta\cos 2\phi$	16
		$4_z^{(-)}, 2_x^{(-)}, 2_{xy}^{(+)}$	$m_x l_y + m_y l_x$	$3\sin^3\theta\sin 2\phi$	*	$3\sin^2\theta\sin 2\phi$	$8 + 8\cos(sdN/J)$
6	$\beta_6\sin^6\theta\sin^2 3\phi$	$6_z^{(+)}, 2_x^{(-)}, 2_{\pi/6}^{(-)}$	$\frac{1}{2i}(m_+ l_+^5 - m_- l_-^5)$	$7\sin^7\theta\sin 6\phi$	*	$7\sin^6\theta\sin 6\phi$	36
		$6_z^{(-)}, 2_x^{(+)}, 2_{\pi/6}^{(-)}$	$\frac{1}{2i}m_z(l_+^3 - l_-^3)$	$5\sin^4\theta\cos\theta\sin 3\phi$	*	$5\sin^3\theta\cos\theta\sin 3\phi$	36
		$6_z^{(-)}, 2_x^{(-)}, 2_{\pi/6}^{(+)}$	$\frac{1}{2i}m_z(l_+^3 + l_-^3)$	$5\sin^4\theta\cos\theta\cos 3\phi$		$5\sin^3\theta\cos\theta\cos 3\phi$	36

Note: For higher-order axes, the following notation is introduced: $m_\pm = m_x \pm i m_y$ and $l_\pm = l_x \pm i l_y$. Asterisks mark systems for which the exact solution corresponding to the least action exists; DMI stands for the Dzyaloshinski–Moriya interaction.

of fundamental importance. The examples of "pure" antiferromagnets in which tunneling can be completely suppressed due to the interference of instanton trajectories will be given below.

While deriving Lagrangian (12), we disregarded the possibility of inhomogeneous tunneling and, hence, the dependence of **S** and **l** on spatial coordinates was omitted from the very outset. The inclusion of such a dependence leads to the substitution $N \longrightarrow \int dV/a^3$, where a is the lattice constant, and to the emergence of an additional term proportional to $Ja^2(\nabla\mathbf{l})^2$ in the Euclidean action. A comparison of the inhomogeneity energy with the anisotropy energy leads to an estimate of the spatial inhomogeneity size on the order of $\Delta_0 = a\sqrt{H_{ex}/H_{an}}$, where H_{ex} and H_{an} are the exchange field and the anisotropy field and Δ_0 is the domain wall thickness. If the size of a particle is larger than Δ_0, i.e., $N > N_c \approx (\Delta_0/a)^3 \approx (H_{ex}/H_{an})^{3/2}$, we can assume a more advantageous inhomogeneous tunneling scenario, in which the level splitting weakly depends on N (or is even independent of it) for $N > N_c$. Although this question has not been discussed in the literature and its analysis is beyond the scope of the present publication, we will consider it briefly.

The value of N_c is too large for the tunneling effects to be observable for $N > N_c$. As a matter of fact, N in the tunneling exponent is multiplied by the susceptibility of the system, i.e., appears in the combination NH_{an}/H_{ex} (see [10]). The presence of this small parameter actually makes it possible to observe tunneling at ferritin particles with $N \approx 3.5 \times 10^3$ [8, 30]. However, for typical values of $H_{an}/H_{ex} \sim 10^{-3}$–$10^{-2}$, the tunneling exponent $N_c H_{an}/H_{ex} \approx (H_{ex}/H_{an})^{1/2} \gg 1$ is too large and the observation of the transition to the inhomogeneous tunneling mode becomes problematic.

3. SYMMETRY OF INSTANTON SOLUTIONS AND INTERFERENCE OF CONTRIBUTIONS FROM INSTANTON TRAJECTORIES

In accordance with the general rules of the semiclassical approximation formulated in the language of instantons, the amplitude of transition from one state to another is described in the so-called instanton-gas approximation [31]. The level splitting for a system with two equivalent minima can be presented in the form

$$\Delta = 2D\sqrt{K}, \tag{13}$$

where the quantity D is defined as

$$D = (\det'\hat{\Omega})^{-1/2}\left(\frac{\mathrm{Re}\,\mathcal{J}}{\hbar}\right)^{1/2}\exp\left(-\frac{\mathrm{Re}\,\mathcal{J}}{\hbar}\right), \tag{14}$$

$\mathcal{I}$ is the one-instanton action; K is a combinatorial factor emerging due to nonuniqueness of the tunnel path connecting two equivalent minima; and $\det'\hat{\Omega}$ is the fluctuation determinant disregarding the zeroth mode, which is determined by small deviations from an instanton trajectory (see [31] for details). In order to analyze the effects of tunneling between degenerate states corresponding to the ground states of the system and to determine the value of splitting, we must find the one-instanton trajectories connecting these states, calculate the value of the Euclidean action $\mathcal{I}$ on these trajectories, and find the determinant of the operator for the second variation of action. The contribution to the splitting comes only from equivalent trajectories corresponding to the minimum value of the real component of $\mathcal{I}$. The combinatorial factor depending on the phase difference in the trajectories will be calculated below using formula (18). In this section, we concentrate our attention on an analysis of the main contribution which comes only from $\mathcal{I}$ and will not calculate the preexponential factor. Let us see how these calculations can be carried out in actual practice.

For a concrete analysis, it is convenient to write the Lagrangian in the form

$$\mathcal{L} = \frac{\hbar^2 N}{2Jz} \times \left[\frac{1}{2}\left(\frac{d\mathbf{l}}{d\tau}\right)^2 + i[\boldsymbol{\omega}_H \times \mathbf{l}] \cdot \frac{d\mathbf{l}}{d\tau} + \frac{\omega_0^2}{2} w_a(\mathbf{l})\right], \quad (15)$$

where $\boldsymbol{\omega}_H = \gamma \mathbf{H}^{\text{eff}}$, γ is the gyromagnetic ratio, and $\mathbf{H}^{\text{eff}}$ is the effective field. The dimensionless function $w_a(\mathbf{l})$ is proportional to the anisotropy energy, and the value of ω_0 coincides with the frequency of a homogeneous antiferromagnetic resonance in the uniaxial anisotropy field. We parametrize vector $\mathbf{l}$ by the angular variables

$$l_1 = \sin\theta\cos\phi, \quad l_2 = \sin\theta\sin\phi, \quad l_3 = \cos\theta. \quad (16)$$

We assume that we are dealing with an easy-axis anisotropy; consequently, the ground state is doubly degenerate and has two values of $\mathbf{l}$ corresponding to it: $\mathbf{l} = \mathbf{e}_3$ and $\mathbf{l} = -\mathbf{e}_3$, the unit vector $\mathbf{e}_3$ being parallel to the easy magnetization axis. Let us consider the tunneling between these two states. Function $w_a(\mathbf{l})$ for a magnet with the anisotropy axis C_n can be written in the form

$$w_a(\theta, \phi) = \sin^2\theta + \tilde{w}_a(\theta, \phi), \quad (17)$$

where the first term corresponds to easy-axis anisotropy and $\tilde{w}_a(\theta, \phi) \ll 1$ defines anisotropy in the basal plane.

For a magnet with an easy-magnetization axis of symmetry C_n, there exist n instanton trajectories and n anti-instanton trajectories, and the combinatorial factor has the form

$$K = \sum_{k, \bar{k}' = 0}^{n-1} \cos\Phi_{k, k'}, \qquad \Phi_{k, \bar{k}'} = \frac{1}{\hbar}\mathrm{Im}\oint_{k \cup \bar{k}'} d\tau \mathcal{L}(\mathbf{l}, \dot{\mathbf{l}}); \quad (18)$$

i.e., $\Phi_{k, \bar{k}'}$ is the phase difference between the kth instanton and the k'th anti-instanton. The integral defining $\Phi_{k, k'}$ is taken over a closed path formed by the trajectories of the k instanton and the k' anti-instanton. In the Lorentz-invariant σ model, the Lagrangian is real and all $\Phi_{k, k'}$ are equal to zero; consequently, the combinatorial factor K is trivial and equal to n^2. Consequently, $\sqrt{K} = n$; i.e., the total transition amplitude and level splitting for n pairs is just the contribution from one instanton multiplied by the number of paths. It will be shown below, however, that, for $\Phi_{k, \bar{k}'} \neq 0$, the level splitting Δ may contain an oscillatory dependence on the product of the small parameter $|\boldsymbol{\omega}_H|$ and the large quantity N and, hence, requires a more detailed analysis. The nature of its oscillations can be established from symmetry considerations, and the specific form of the function K of the parameters of the problem can be determined even without solving the corresponding the Euler–Lagrange equations.

Lorentz-invariant σ model. It is convenient to consider first the tunneling in the simplest Lorentz-invariant σ model which corresponds to Lagrangian (15) with $\boldsymbol{\omega}_H = 0$. As a matter of fact, for some models of an antiferromagnet with the Dzyaloshinski–Moriya interaction, the results turn out to be the same as in the absence of this interaction (see below). If $H^{\text{eff}} = 0$, the analysis of the problem does not present any difficulty. Indeed, for any form of the anisotropy energy in a uniaxial antiferromagnet with the principal axis C_2, C_4, or C_6 (in the subsequent analysis, we will consider only the type of symmetry that can exist in the crystal lattice), the instanton solution corresponds to the function $\theta = \theta(\tau)$ with the boundary conditions $\theta \longrightarrow 0, \pi$ for $\tau \longrightarrow \pm\infty$ and $\phi = \phi_0 = \text{const}$, where ϕ_0 is defined by the relation

$$\left.\frac{\partial w_a(\theta, \phi)}{\partial \phi}\right|_{\phi = \phi_0} = 0. \quad (19)$$

Let us assume that the ground states $\pm\mathbf{e}_3$ are on the principal axis C_n. In this case, the value of $\widetilde{w_a}(\theta, \phi)$ is proportional to $\sin n\phi$ and there exist $2n$ solutions to this equation:

$$\phi_k^{(0)} = \frac{\pi k}{n}, \quad k = 0, 1, \ldots, 2n-1, \quad (20)$$

from which n solutions $\phi_{k,\min}^{(0)}$ correspond to the minimum of $w_a(\theta, \phi)$, while the remaining n solutions $\phi_{k,\max}^{(0)}$ correspond to the maximum of this function for all $\theta \neq 0, \pi$. Instantons with $\phi_{k,\min}^{(0)}$ correspond to the lower value of the Euclidean action, and we will consider below only these n solutions. Function $\theta(\tau)$ can be determined from the second-order equation for which the first integral is known to be

$$\left(\frac{d\theta}{d\tau}\right)^2 = \omega_0^2[w_a(\theta, \phi_k^{(0)}) - w_a(0, \phi_k^{(0)})]. \quad (21)$$

Henceforth, we assume that $w_a(0, \phi) = w_a(\pi, \phi) = 0$ and that the value of $\phi = 0$ corresponds to the minimum of the function $w_a(\theta, \phi)$. With such a choice of the axes, z is always an easy magnetization axis and x is an intermediate magnetization axis. The Euclidean action on trajectories is real-valued for all values of ϕ and is defined as

$$\mathcal{I} = \frac{\hbar^2\omega_0 N}{2Jz}\int_0^\pi d\theta\sqrt{w_a(\theta, \phi)}. \quad (22)$$

This approximate expression is written in the main approximation in small anisotropy in the basal plane $\tilde{\beta} \ll 1$, where $\tilde{\beta}$ is the characteristic anisotropy constant in the basal plane, i.e., the maximum value of $\widetilde{w_a}$. Thus, the contribution in the given case comes from n instanton trajectories on which vector $\mathbf{l}$ is real and rotates in one of the n planes defined by the condition $\phi = \phi_{k,\min}^{(0)} = \phi_k^{(0)}$. The imaginary component of $\mathcal{I}$ in the Lorentz-invariant model is absent, and the combinatorial factor K in expression (18) is equal to n^2.

Role of $\mathbf{H}^{\text{eff}}$. The inclusion of the terms with $\mathbf{H}^{\text{eff}}$, which destroy the Lorentz invariance, brings about two types of difficulties. First, for $\mathbf{H}^{\text{eff}} \neq 0$, the solution $\phi =$ const is generally inapplicable and the instanton structure is determined by the general system of two second-order equations

$$-\ddot{\theta} + \dot{\phi}^2\sin\theta\cos\theta + \omega_0^2\frac{\partial w_a}{\partial\theta} - i\omega_H\dot{\phi}\Gamma(\theta, \phi) = 0, \quad (23)$$

$$-\ddot{\phi}\sin^2\theta - 2\dot{\phi}\dot{\theta}\sin\theta\cos\theta + \omega_0^2\frac{\partial w_a}{\partial\phi} - i\omega_H\dot{\theta}\Gamma(\theta, \phi) = 0, \quad (24)$$

whose solutions are generally not real-valued. Here, the terms with Γ are determined by the variation of the term with $\mathbf{H}^{\text{eff}} \cdot [(d\mathbf{l}/d\tau) \times \mathbf{l}]$ in Lagrangian (15), and the form of the function $\Gamma(\theta, \phi)$ generated by the Dzyaloshinski interaction for various types of magnetic symmetry is given in column 5 of the table. Second, the imaginary component of the Euclidean action $\mathcal{I}$, which comes from the term proportional to ω_H, may appear even for trajectories with a real $\mathbf{l}$. Let us consider the cases when these situations are realized.

If $\Gamma(\theta, \phi)$ vanishes at the same values of $\phi_k^{(0)}$ as for $\partial w_a(\theta, \phi)/\partial\phi$, Eq. (24) is satisfied identically for the plane trajectories $\phi = 0$, while the first equation in (23) can be reduced to Eq. (21) considered above in the Lorentz-invariant σ model. Consequently, in this case $\Gamma(\theta, \phi_k^{(0)})$ does not affect the form of the function $\theta = \theta(\tau)$ in an instanton, but changes the imaginary component of the action. This effect will be considered in greater detail in Section 4.

If, however, $\Gamma(\theta, \phi_k^{(0)}) \neq 0$, an instanton does not correspond to a plane solution $\phi =$ const any longer, and we must seek the general solution of the system (23), (24) of the form $\theta = \theta(\tau)$, $\phi = \phi(\tau)$. In this case, functions $\theta(\tau)$ and $\phi(\tau)$ may in general turn out to be complex-valued. There are no general analytic methods for constructing such separatrix solutions; an instanton solution of the system of equations (23), (24) can be constructed exactly only in some cases (see [32] and Section 4 in the present paper).

It will be shown below that the effect of the term $\mathbf{H}^{\text{eff}}$ in the Lagrangian on the imaginary component of action $\mathcal{I}$ may lead to nontrivial consequences even for antiferromagnets for which $\Gamma(\theta, \phi) \neq 0$, but $\Gamma(\theta, \phi_k^{(0)}) = 0$, and there exists a real-valued instanton solution $\theta = \theta(\tau)$, $\phi = \phi_k^{(0)}$, or in the case when the value of $H^{\text{eff}}/H_{\text{ex}}$ is negligibly small and its inclusion changes $\theta = \theta(\tau)$ and the real component of $\mathcal{I}$ insignificantly.

In order to explain this, we consider the case when the value of $(\Gamma/H_{\text{ex}}) \ll 1$ is so small that instanton trajectories can be regarded as planar, $\theta = \theta(\tau) \ll 1$, $\phi =$ const. The presence of the term linear in $d\mathbf{l}/d\tau$ leads to the contribution to the imaginary component of the Euclidean action $\mathcal{I}$, which is proportional to the number of spins in a particle. The imaginary component of the Euclidean action $\mathcal{I}$ is of the order of $\text{Im}\,\mathcal{I}/\hbar \propto Nd/J$; i.e., it is proportional to the product of a small and a large parameter. Consequently, it can be appreciable and the effects of destructive interference can be significant. It is well known that the interference effects for an orthorhombic ferromagnet may suppress tunneling completely (see [1–4]). In contrast to the case of an antiferromagnet, the term with $d\mathbf{m}/d\tau$ for a ferromagnet does not contain a small factor of the type of $H^{\text{eff}}/H_{\text{ex}}$, but it is immaterial since the value of $\text{Im}\,\mathcal{I}/\hbar \approx \pi Ns \gg 1$ for a ferromagnet, while tunneling is suppressed completely when $\text{Im}\,\mathcal{I}/\hbar \approx \pi$. This condition can easily be satisfied for a large N. In particular, for an antiferromagnetic particle of the ferritin type with $N \approx 3500$, the tunneling probability in a magnetic field taking interference into account is an oscillating function of the field, and the suppression of tunneling can be observed in fields $H \lesssim 100$ Oe [5, 28, 33], which are much weaker than the characteristic value of the Dzyaloshinski field $H^D = 10^3$–10^5 Oe.

On the other hand, the contribution to the real component of the Euclidean action does not contain the large parameter N. This contribution can be appreciable

(see the next section), but in this case the product of other parameters, namely, the small quantity $d/J \ll 1$ and the large quantity $d/\tilde{\beta} \gg 1$, is significant. Thus, the terms with $d\mathbf{l}/d\tau$ may lead to two types of effects: (1) the emergence of nonplane instanton trajectories and complex values of components of $\mathbf{l}$ on these trajectories; (2) the interference of instantons even in the case of plane trajectories with real $\mathcal{I}$.

First-type effects only take place when the term $\Gamma(\theta, \phi)$ in Eqs. (23), (24) differs from zero. Such terms are always important for the description of domain wall dynamics in an antiferromagnet: they may reduce the limiting velocity of a domain wall to a considerable extent and may also lead to an abrupt change in the wall structure upon a continuous variation of its velocity [20, 21]. The subsequent analysis of concrete instanton solutions will show that the role of such terms in the description of the instanton structure and tunneling is not so important as in the description of the domain wall dynamics. On the other hand, if function $\Gamma(\theta, \phi)$ differs from zero, but the function $\Gamma(\theta, \phi_k^{(0)}) = 0$ for the given solution $\phi = \phi_k^{(0)}$, the domain wall dynamics is trivial and can be described by Lorentz-invariant formulas. In this case, the instanton structure $\theta = \theta(\tau)$ is the same as in the Lorentz-invariant theory. However, the situation with instantons is different: not all features can be described by the function $\theta(\tau)$ and the real component of $\mathcal{I}$ only. It will be shown bellow that the main contribution from the term $\mathbf{H}^{(\text{eff})} \cdot [(d\mathbf{l}/d\tau) \times \mathbf{l}]$ is associated precisely with interference processes and is manifested most clearly exactly when an instanton trajectory is planar; i.e., $\Gamma(\theta, \phi^{(0)}) = 0$.

In the case of real-valued trajectories, it is convenient to use the following approach for calculating the imaginary component of action [34]. We introduce the vector $\mathbf{r} = r\mathbf{l}$ which is not subjected to the condition $\mathbf{r}^2 = 1$ and present the term with the first derivative in expression (15) in the form

$$-i\gamma\mathcal{A}\frac{\partial \mathbf{r}}{\partial \tau}, \quad \mathcal{A} = \frac{\mathbf{r} \times \mathbf{H}^{\text{eff}}}{r^2}. \tag{25}$$

This expression has the same structure as the term in the nonrelativistic Lagrangian describing the interaction of a classical charged particle moving in a 3D space with coordinate $\mathbf{r}$ and velocity $\mathbf{v} = d\mathbf{r}/d\tau$ with a formal magnetic field $\mathbf{B} = \nabla \times \mathcal{A}$ (differentiation is carried out in the $\mathbf{r}$ space). It is well known that the magnetic field appears in the Lagrangian of a charged particle through the vector potential $\mathcal{A}$ at point $\mathbf{r}$, which is defined only to within a certain gauge, while the field $\mathbf{B}$ is gauge-invariant.

Simple but cumbersome calculations proved that, for any ferromagnet, this formal magnetic field $\mathbf{B}$ may be radial and can be presented in the form

$$\mathbf{B} = \frac{\mathbf{r}}{r^2}B(\theta, \phi),$$
$$B(\theta, \phi) = 2(\mathbf{H}^{\text{eff}} \cdot \mathbf{l}) - \frac{\partial H_i^{\text{eff}}}{\partial l_i} + \frac{\partial H_i^{\text{eff}}}{\partial l_k} l_i l_k. \tag{26}$$

In the absence of the Dzyaloshinski interaction, the value of $B(\theta, \phi)$ is determined only by the external field $\mathbf{H}^{(0)}$, $B(\theta, \phi) = 2(\mathbf{H}^{(0)} \cdot \mathbf{l})$. In zero external field, the value of $B(\theta, \phi)$ is determined by the Dzyaloshinski field $H_i^D = D_{ij}(\mathbf{l})l_j$ and can be presented in terms of tensor D_{ij}:

$$B(\theta, \phi) = 3D_{ij}l_i l_j - D_{ii} + D_{ij,k}l_i l_j l_k - D_{ij,i}l_j. \tag{27}$$

Here, the comma in the subscript on D indicates the differentiation of tensor D_{ij} with respect to the corresponding component of $\mathbf{l}$, and the summation is carried out over recurrent indices. The values of $B(\theta, \phi)$ for various types of Dzyaloshinski interaction and of the configurations of axes are given in column 7 of the table.

Phases $\Phi_{k,\bar{k}'}$ defined above (see formula (18)) can be presented in terms of the integrals $\int \mathcal{A} d\mathbf{r}$ taken over instanton–anti-instanton pairs forming closed contours. Using the Stokes theorem, we can present the phase difference $\Phi_{k,k'}$ as the magnetic flux of vector $\mathbf{B}$ through a part of the unit sphere bounded by such a contour. Obviously, individual phases are determined by the vector potential $\mathcal{A}$, i.e., depend on the gauge, but the phase differences are gauge-invariant for all pairs of trajectories.

It is important that the structure of $B(\theta, \phi)$ for all possible types of Dzyaloshinski interaction is such that the total flux of field $\mathbf{B}$ through the unit sphere,

$$\Phi_{\text{tot}} = \int_0^{\pi} \sin\theta d\theta \int_0^{2\pi} d\phi B(\theta, \phi), \tag{28}$$

is equal to zero and the value of $\cos \Phi_{k,\bar{k}'}$ is independent of the total time derivative in the Lagrangian (gauge invariance).[1]

[1] It should be noted that the situation in this case is basically different from the case of a particle with an uncompensated total spin S, where we have the potential of field of a magnetic monopole for $\mathcal{A}$ (see formula (4) above). This vector potential $\mathcal{A}$ can be written only in singular form with a singularity on the half-line emerging from the point of location of the monopole (Dirac string). The total flux Φ_{tot} through the sphere is equal to $4\pi S$, and, hence, the phase difference $\Delta\Phi$ for two diametrically positioned trajectories is equal to $2\pi S$. For this reason, the phase factor $\cos(\Delta\Phi/2) = 0$ for half-integral values of S, and tunneling is forbidden. It should also be noted that, having repeated Dirac's analysis concerning the uniqueness of the electron wave function is the monopole field, we can derive the condition $\cos(\Phi_{\text{tot}}/2) = 0$ leading to the half-integral quantization of uncompensated spin (an example of quantization of parameters; see [35]). In our case of an uncompensated antiferromagnetic particle in the presence of an external field and/or Dzyaloshinski interaction, $\Phi_{\text{tot}} = 0$ and, naturally, no quantization of parameters takes place.

This approach enables us to calculate specifically without any difficulty the phase difference of integral trajectories and the combinatorial factor K in formula (13). We begin with the simplest case of an orthorhombic antiferromagnet for which there are only two pairs of instanton trajectories. It can easily be verified that the Dzyaloshinski interaction of any type (see table) makes zero contribution to the phase difference for two diametrically opposite trajectories [34]. For this reason, the required phase factor can be determined only by the external field and can be written in the form

$$\cos\Phi = \cos\left(\frac{g\mu_B H^{(0)} Ns}{Jz}\cos\alpha\right), \qquad (29)$$

where α is the angle between the plane containing the instanton trajectories and the external field $\mathbf{H}^{(0)}$. This result was obtained by Chiolero and Loss [33] in particular cases when $\alpha = 0$ and $\alpha = \pi/2$. Thus, for instanton trajectories lying in the same plane, all possible types of Dzyaloshinski–Moriya interaction given in the table do not affect the tunneling. This results does not contradict the analysis carried out by Golyshev and Popkov [5], who studied tunneling in small completely compensated particles of an orthorhombic antiferromagnet with the orthoferrite structure and discovered no interference effects in zero magnetic field. The approach used by us here enabled us to obtain this result without resorting to the Euler–Lagrange equations. Thus, we have proved that the conclusion that no interference takes place for diametrically opposite trajectories can be extended to more general cases of the Dzyaloshinski interaction. It is important that this conclusion is drawn without resorting to any approximation, which is inevitable in the solution of a complex system of equations describing the instanton structure.

Thus, in the case of orthorhombic antiferromagnets with two instanton trajectories, none of the types of Dzyaloshinski interaction presented in the table leads to destructive interference. However, this result is different for uniaxial antiferromagnets with an easy magnetization axis C_n, $n > 2$. In this case, there exist n pairs of instanton trajectories. Obviously, here we also have pairs of trajectories lying in the same plane, for which $\Phi_{k,\bar{k}'} = 0$ and interference is trivial, but interference can be manifested for pairs of trajectories with $\phi_k^{(0)} - \phi_{\bar{k}'}^{(0)} \neq \pi$. It will be shown below that the value of combinatorial factor in this may be reduced considerably in this case from its maximum value n^2 to zero; i.e., both partial and complete suppression of interference is possible.

Tetragonal antiferromagnets. Let us demonstrate this using specific examples of particles with a tetragonal easy magnetization axis and binary axes in the perpendicular plane (crystallographic class $4_z2_x2_{xy}$), when the minimum of the real component of action corresponds to four instanton and four anti-instanton trajectories. In order to describe tetragonal antiferromagnets, we choose the polar axis $\mathbf{e}_3$ along the tetragonal easy magnetization axis 4_z. Anisotropy in the basal plane is determined by the fourth-order invariant (see table). We assume that $\beta_4 > 0$; i.e., instanton trajectories correspond to the rotation of $\mathbf{l}$ in the equivalent planes zx and zy. Depending on the magnetic parity of the principal axis (according to Turov; see [36]) and of the binary axes 2_x, 2_y or 2_{xy}, 2_{yx}, basically different versions of the behavior can be observed. We will consider them separately.

Axes $4_z^{(+)}$, $2_x^{(-)}$, and $2_{xy}^{(-)}$. With such a structure of axes in an antiferromagnet, only the antisymmetric invariant $d(m_x l_y - m_y l_x)$ is usually considered, which can be obtained from the antisymmetric component of the tensor of exchange constants. The value of d is on the order of $\sqrt{\beta J}$ (see [29]). This invariant determines the weak isotropic ferromagnetic moment when $\mathbf{l}$ is oriented in the basal plane. However, it is of no interest to us since it can be reduced to the total derivative in the Lagrangian and, hence, gives $\Gamma(\theta, \phi) = 0$ in the equations of motion and $B(\theta, \phi) = 0$ in the imaginary component of the Euclidean action. In addition, there exist a number of invariants of relativistic origin (see [37]), which give a nonzero value of $\Gamma(\theta, \phi)$. The simplest of these invariants has the form $2(l_x^2 - l_y^2)(m_x l_y + m_y l_x)$, which coincides (except for the total derivative) with the invariant $(m_+ l_+^3 - m_- l_-^3)/2i$ presented in the table. It can easily be seen, however, that in this case $\Gamma(\theta, \phi_k^{(0)}) = 0$ and the instanton solution has the form $\theta = \theta(\tau)$, $\phi = \phi_k^{(0)} = \pi k/2$ for integral k. The value of $B(\theta, \phi)$ is such that

$$B \propto \sin^4\theta \sin 4\phi, \qquad (30)$$

and, hence, all phases $\Phi_{k,\bar{k}'}$ are equal to zero (see table). An analysis of other invariants, e.g., of the type $l_z^2(m_x l_y - m_y l_x)$, leads to the same result (namely, the Dzyaloshinski interaction does not affect tunneling in any way). This result is apparently independent of the model and is determined only by the type of magnetic symmetry (the model independence for dynamic effects in domain walls having the same origin, i.e., the Dzyaloshinski interaction, was demonstrated in [20, 21]). Thus, the case of an even principal axis $4_z^{(+)}$ may serve as an example that nonzero terms which are linear in $d\mathbf{l}/d\tau$ and cannot be reduced to the total derivative are not manifested in the separatrix solution and do not affect tunneling in any way.

A different situation takes place for an antiferromagnet with an odd principal axis $4_z^{(-)}$. In this case, two versions are possible: when the intermediate anisotropy axes through which tunneling takes place are odd and when these axes are even.

Axes $4_z^{(-)}$, $2_x^{(-)}$, and $2_{xy}^{(+)}$. In this case, $\Gamma(\theta, \phi) = 0$ for $\phi = \phi_k^{(0)} = \pi k/2$ and the presence of the Dzyaloshinski interaction does not affect the instanton trajectories with the minimum action, which correspond to $\phi = \phi_k^{(0)}$, $\theta = \theta(\tau)$. However, in contrast to the system with $4_z^{(+)}$, the contribution of the Dzyaloshinski interaction is significant for calculating the combinatorial factor K in formula (13). It can be seen from the explicit expression $B(\theta, \phi) \propto \sin^2\theta \sin 2\phi$ that the phase difference for adjacent trajectories (with $\phi = \phi_k^{(0)}$ and $\phi = \phi_{k\pm1}^{(0)}$) differs from zero.

Thus, the phase factor for the tunneling probability is given by

$$K = 16\sin^2\left(\frac{sdN}{J}\right). \tag{31}$$

It is an oscillating function of the Dzyaloshinski interaction constant d and assumes the values from 0 to 16. For realistic values of N on the order of 10^3–10^5, the period is not large; the value of $\Delta H^D/H^D \approx 10^{-3}$–$10^{-1}$ for characteristic values of $H^D \approx 10^4$ Oe and $H_{ex} \approx 10^6$ Oe. Since the value of the Dzyaloshinski field is very sensitive to extrinsic parameters (e.g., the value of pressure or the addition of a small amount of an impurity to the crystal), these oscillations can be observed and monitored. An additional opportunity for observing interference effects appears when the magnetic field is taken into consideration.

Axes $4_z^{(-)}$, $2_x^{(+)}$, and $2_{xy}^{(-)}$. Such a symmetry group is typical of the extensively studied weak antiferromagnet MnF_2 (see [38]). In this case, $\Gamma(\theta, \phi) \propto \sin^3\theta\cos 2\phi$ and $\Gamma(\theta, \phi) \neq 0$ for all values of $\phi = \phi_k^{(0)}$, corresponding to the minimum of anisotropy in the basal plane and describing instanton trajectories for $d = 0$. For $d \neq 0$, instanton solutions cannot be written in the simple form $\theta = \theta(\tau)$, $\phi = \pi k/2$, $k = 0, 1, 2, 3$. On the other hand, if we assume that the value of d is very small, we can easily find, applying the approximation of planar rotation and using the formula $B(\theta, \phi) \propto \sin^2\theta\cos 2\phi$ (see table), that the difference in the imaginary components of $\mathcal{J}$ for pairs of trajectories lying in the same plane as well as for adjacent instanton trajectories is equal to zero and no interference effects take place. We will consider the solution for this case in the next section and prove that these simple regularities are preserved in a more rigorous analysis also, when we do not require that $\phi = \pi k/2$. We will also consider general mechanisms of tunneling in the case when $\Gamma(\theta, \phi_{\min}^{(0)}) \neq 0$ and the instanton solution is not real-valued.

Hexagonal antiferromagnets. Let us briefly consider the case of a hexagonal principal axis. Here, we again have three cases presented in the table. For a system with an even principal axis $6_z^{(+)}$, $2_x^{(-)}$, and $2_{\pi/6}^{(-)}$, there exists the invariant $m_x l_y - m_y l_x$, and the Dzyaloshinski interaction, which cannot be reduced to a total derivative, appears only in the fifth order in $\mathbf{l}$. The analysis is similar to that for the system $4_z^{(+)}$, $2_x^{(-)}$, and $2_{xy}^{(-)}$. In this case also, nonzero terms which are linear in $d\mathbf{l}/d\tau$ and cannot be reduced to a total derivative do not affect tunneling in any way. It can be verified that such a behavior is the same as for an antiferromagnet with the even principal axis $n_z^{(+)}$.

For systems with an odd principal axis, the Dzyaloshinski interaction is a cubic function of $\mathbf{l}$, but it makes zero contribution to the imaginary component of the Euclidean action under the assumption of planar real trajectories. In the system $6_z^{(-)}$, $2_x^{(-)}$, and $2_{\pi/6}^{(+)}$, minimal instanton trajectories have an imaginary component, but this only changes the real component of the Euclidean action. The analysis of this system is similar to that which will be carried out in Section 4 for the system $4_z^{(-)}$, $2_x^{(+)}$, and $2_{xy}^{(-)}$. Consequently, the combinatorial factor K in all the three cases has the maximum value equal to 36.

4. INSTANTON SOLUTION FOR AN ANTIFERROMAGNET WITH SYMMETRY $4_z^{(-)}$, $2_x^{(+)}$, AND $2_{xy}^{(-)}$

It was noted above that, in the case of an antiferromagnet with symmetry $4_z^{(-)}$, $2_x^{(+)}$, $2_{xy}^{(-)}$, there is no exact solution of the type $\phi = \pi k/2$, $\theta = \theta(\tau)$ for trajectories with the rotation of $\mathbf{l}$ in the vicinity of the easy plane $\phi \approx \pi k/2$, and we have to analyze the complete system of two equations (23), (24). The situation is complicated even further since these equations have complex-valued coefficients and, in general, their complex solutions of the type $\theta = \theta_1(\tau) + i\theta_2(\tau)$, $\phi = \phi_1(\tau) + i\phi_2(\tau)$ must be considered. As a result, system (23), (24) is equivalent to a dynamic system with four degrees of freedom and is not integrable. No general method exists for an analysis of such systems; however, a comprehensive analysis can be carried out in the given case as well as for magnets with other types of symmetry, which are listed in the table.

In the case of an antiferromagnet with an odd tetragonal axis, the equations for the angular variables θ and ϕ have the form

$$-\ddot{\theta} + \dot{\phi}^2\sin\theta\cos\theta + \omega_0^2\sin\theta\cos\theta(1 + \beta_4\sin^2\theta\sin^2 2\phi) + 3i\omega_D\dot{\phi}\sin^3\theta\cos 2\phi = 0, \tag{32}$$

$$-\ddot{\phi}\sin^2\theta - 2\dot{\phi}\dot{\theta}\sin\theta\cos\theta + \beta_4\omega_0^2\sin^4\theta\sin 2\phi\cos 2\phi - 3i\omega_D\dot{\theta}\sin^3\theta\cos 2\phi = 0. \tag{33}$$

The quantity ω_0 defines the height of the potential barrier through which tunneling occurs, and β_4 is the dimensionless parameter of anisotropy in the basal plane. We assume that $\beta_4 > 0$, which corresponds to instantons in the Lorentz-invariant σ model ($\omega_D = 0$), passing through the even axes x or y; $\beta_4 \ll 1$ corresponds to the easy-axis limit, and ω_D is proportional to the Dzyaloshinski interaction constant, $\omega_D = \gamma|\mathbf{H}^D| = zd/\hbar$.

It can easily be seen that this system has the exact solution $\phi = \pi(2k + 1)/4$, $\theta = \theta(\tau)$ which was considered in the previous section. It determines tunneling for $\beta_4 < 0$, but in the case of $\beta_4 > 0$ we are interested in now, it corresponds to the rotation of $\mathbf{l}$ in hard planes, does not ensure the minimum value of the real component of the Euclidean action, and makes zero contribution to tunneling in the instanton approximation. The exact solution $\phi = \pi k/2$ does not exist in this case; it can be seen, however, that the substitution $\phi = \pi k/2 + if(\tau)$ and $\theta = \theta(\tau)$ with the real functions $f(\tau)$ and $\theta(\tau)$ does not contradict this system and leads to the following system of two equations for functions f and θ:

$$-\ddot{\theta} - \dot{f}^2\sin\theta\cos\theta + \omega_0^2\sin\theta\cos\theta(1 - \beta_4\sin^2\theta\sinh^2 2f) - 3(-1)^k\omega_D\dot{f}\sin^3\theta\cosh 2f = 0, \tag{34}$$

$$\ddot{f}\sin^2\theta + 2\dot{f}\dot{\theta}\sin\theta\cos\theta - \beta_4\omega_0^2\sin^4\theta\sinh 2f\cosh 2f + 3(-1)^k\omega_D\dot{\theta}\sin^3\theta\cosh 2f = 0. \tag{35}$$

In addition, such a substitution renders the Lagrangian real-valued:

$$\mathcal{L} = \frac{\hbar^2 N}{2Jz}\left[\frac{\dot{\theta}^2 - \dot{f}^2\sin^2\theta}{2} + (-1)^k\omega_D\dot{f}\cosh 2f\cos\theta(2 + \sin^2\theta) + \frac{\omega_0^2}{2}\sin^2\theta - \frac{\omega_0^2\beta_4}{4}\sin^4\theta\sinh^2 2f\right]. \tag{36}$$

It can be seen that the imaginary component $f = \mathrm{Im}\,\phi$ of the instanton solution affects only the real part of the action. The system of equations (34), (35) is equivalent to a mechanical system with two degrees of freedom, and only one first integral is known for it:

$$\mathcal{E} = \frac{\hbar^2 N}{2Jz}\left[\frac{\dot{\theta}^2 - \dot{f}^2\sin^2\theta}{2} - \frac{\omega_0^2}{2}\sin^2\theta + \frac{\omega_0^2\beta_4}{4}\sin^4\theta\sinh^2 2f\right] \tag{37}$$

($\mathcal{E} = 0$ for the separatrix solutions we are interested in); for this reason, this system cannot be analyzed exactly. However, an approximate solution can be constructed in the physically interesting case, when $\omega_D \ll \omega_0$, $\beta_4 \ll 1$ and for any relation between ω_D and $\omega_0\beta_4$. In order to find such a solution, we note that Eq. (34) from system (34), (35) is transformed into $\dot{\theta}^2 \approx \omega_0^2\sin^2\theta$ in the zeroth approximation in the small parameters ω_D/ω_0 and β_4. In this case, the constant solution $f = f_0 = \text{const}$ satisfies Eq. (35) and gives

$$\sinh 2f_0 = \omega_D/\beta_4\omega_0. \tag{38}$$

It should be noted that the value of f_0 is determined by the ratio of two small parameters and can be appreciable. Using this fact, we can write a refined equation for $\theta(\tau)$:

$$\ddot{\theta} = \omega_0^2\sin\theta\cos\theta\left(1 - \frac{\omega_D^2}{\beta_4\omega_0^2}\sin^2\theta\right). \tag{39}$$

The approximate solution constructed by us is valid if $\dot{\theta} \approx \omega_0\sin\theta$; i.e.,

$$\omega_D^2 \ll \omega_0^2/\beta_4. \tag{40}$$

This condition may also hold for $\sinh 2f_0 = \omega_D/\beta_4\omega_0$ of the order of unity, but is still violated for $\beta_4 \longrightarrow 0$. In this case, the situation is similar to that observed for the domain wall dynamics (see [21]): the limiting velocity of a domain wall in a tetragonal antiferromagnet with an odd axis, the limiting velocity of a wall with $\phi \neq \text{const}$ tends to zero as $\beta_4 \longrightarrow 0$, and no dynamic solution exists for $\beta_4 = 0$.

The value of the Euclidean action for the obtained solution is real and is defined by the formula

$$\mathcal{I} = \frac{\hbar^2 N\omega_0}{Jz}\left(1 + \frac{\omega_D^2}{3\beta_4\omega_0^2}\right). \tag{41}$$

Thus, in the range of applicability of the constructed solution, i.e., when ω_D and β_4 are small and when inequality (40) is satisfied, the inclusion of the Dzyaloshinski interaction leads only to a small correction to the real component of the Euclidean action, the imaginary component being identically equal to zero.

For models of an antiferromagnet with binary and hexagonal symmetry axes, such an approximate solution cannot be constructed, but an analysis of these models is even simpler than in the case of an antiferromagnet with a tetragonal symmetry axis. In these cases, we can also verify that, if the exact solution $\phi = \phi_k^{(0)} = 2\pi k/n$, $\theta = \theta(\tau)$ does not exist, the solution has the same form as before:

$$\phi = \frac{2\pi k}{n} + if(\tau), \quad \theta = \theta(\tau), \tag{42}$$

and the term in the Lagrangian which is linear in $d\mathbf{l}/d\tau$ contributes only to the real component of $\mathcal{J}$. It can be proved, however, that function $f(\tau)$ is antisymmetric and proportional to the parameter $\omega_D/(\beta\omega_0)$, which is always small (in contrast to the case of a tetragonal antiferromagnet, in which there appears the parameter $\omega_D/\beta_4\omega_0$, whose value may be appreciable). Consequently, we can seek the quantity $f \ll 1$ using virtually the same perturbation theory as for the domain wall dynamics in such antiferromagnets (see [21]). As a result, we obtain the following expression for the real component of the Euclidean action:

$$\mathcal{J} = \frac{\hbar^2 N\omega_0}{Jz}\left(1 + \xi\frac{\omega_D^2}{\omega_0^2}\right), \qquad (43)$$

where the numerical factor ξ is of the order of unity. Thus, the correction to the result typical of the Lorentz-invariant model is always small. Considering that no interference effects take place in this case, we arrive at the conclusion that the Dzyaloshinski interaction hardly affects the tunneling probability in hexagonal and orthorhombic antiferromagnets.

5. CONCLUDING REMARKS

The analysis of antiferromagnetic particles with a tetragonal symmetry axis indicates the existence of three possible versions of the effect of the Dzyaloshinski interaction on tunneling processes. The investigation of the remaining cases important for an analysis of crystalline antiferromagnets (orthorhombic or uniaxial with a hexagonal symmetry axis; see table) proved that these versions include all possible cases for antiferromagnetic systems with a doubly degenerate ground state. In fact, all cases can be reduced to the following three versions of the behavior.

1. The principal axis is even, e.g., $4_z^{(+)}$ or $6_z^{(+)}$. In this case, vector $\mathbf{l}$ is real on all instanton trajectories and the trajectories are planar ($\phi = 2\pi k/n$, $\theta = \theta(\tau)$). The real part of the Euclidean action is independent of the Dzyaloshinski interaction constant, the imaginary component is equal to zero, and destructive interference effects are absent. In this case, tunneling can in fact be described without taking into account the Dzyaloshinski interaction.

2. The principal axis is odd, and there exists an exact real solution with the rotation of $\mathbf{l}$ in the easy plane determined by anisotropy. An example is a system of the type $4_z^{(-)}$ or $2_x^{(-)}$, in which the instanton trajectory is plane and the Dzyaloshinski constant does not appear in the real component of the Euclidean action. In this case, however, the inclusion of the Dzyaloshinski interaction leads to the emergence of the imaginary component of the Euclidean action and may affect the tunneling probability due to the interference of instanton trajectories lying in different planes. Since the corresponding phase factor contains the large factor N, tunneling can be suppressed completely due to destructive interference even for small values of the Dzyaloshinski constant.

3. The principal axis is odd and the simple solution $\phi = 2\pi k/n$ does not exist. In this case, vector $\mathbf{l}$ has both real and imaginary components, but all types of Dzyaloshinski interaction change only the real component of the Euclidean action, this change being small in view of the smallness of the parameter $d^2/J\beta$. The imaginary component of the Euclidean action is equal to zero and destructive interference effects are absent in this case.

Thus, the only important effect produced by the Dzyaloshinski interaction is associated with the possibility of the interference of instanton trajectories in the case when their number is greater than two (an antiferromagnetic particle with the easy magnetization axis approximately corresponds to $n > 2$). This effect can be observed for an antiferromagnet with an odd principal axis in the case when the rotation of $\mathbf{l}$ on the instanton trajectory also occurs through the odd axis. It is associated with the interference of pairs of instanton trajectories lying in different planes. Since $\mathbf{l}$ is real in this case and all instanton trajectories are plane, an exact analysis can easily be carried out and the description of tunneling is reduced to the geometrical analysis described in Section 3.

ACKNOWLEDGMENTS

The authors thank A.K. Kolezhuk for fruitful discussions.

This work was supported financially by Volkswagen Stiftung (grant no. I/75895).

REFERENCES

1. E. M. Chudnovsky and J. Tejada, *Macroscopic Quantum Tunneling of the Magnetic Moment* (Cambridge Univ. Press, Cambridge, 1998).
2. *Quantum Tunneling of Magnetization*, Ed. by L. Gunter and B. Barbara (Kluwer, Dordrecht, 1995), NATO ASI Series E, Vol. 301.
3. D. Loss, D. P. DiVincenzo, and G. Grinstein, Phys. Rev. Lett. **69**, 3232 (1992).
4. J. von Delft and C. L. Henley, Phys. Rev. Lett. **69**, 3236 (1992).
5. V. Y. Golyshev and A. F. Popkov, Europhys. Lett. **29**, 327 (1995).
6. E. M. Chudnovskiĭ, Zh. Éksp. Teor. Fiz. **77**, 2157 (1979) [Sov. Phys. JETP **50**, 1035 (1979)].
7. E. M. Chudnovsky and L. Gunter, Phys. Rev. B **37**, 9455 (1988).
8. D. D. Awschalom, J. F. Smyth, G. Grinstein, *et al.*, Phys. Rev. Lett. **68**, 3092 (1992).
9. B. Barbara and E. M. Chudnovsky, Phys. Lett. A **145**, 205 (1990).
10. I. V. Krive and O. B. Zaslavskii, J. Phys.: Condens. Matter **2**, 9457 (1990).

11. E. Fradkin, *Field Theories in Condensed Matter* (Addison-Wesley, Reading, 1991), Chap. 5.
12. M. V. Berry, Proc. Roy. Soc. London **392**, 45 (1984).
13. A. F. Andreev and V. I. Marchenko, Usp. Fiz. Nauk **130**, 39 (1980) [Sov. Phys. Usp. **23**, 21 (1980)].
14. A. M. Kosevich, B. A. Ivanov, and A. S. Kovalev, *Nonlinear Waves of Magnetization. Dynamic and Topological Solitons* (Naukova Dumka, Kiev, 1983).
15. V. G. Bar'yakhtar and B. A. Ivanov, *Solitons and Thermodynamics of Low-Dimensional Magnets* (Harwood, Amsterdam, 1992).
16. V. G. Bar'yakhtar and B. A. Ivanov, Fiz. Nizk. Temp. **5**, 759 (1979) [Sov. J. Low Temp. Phys. **5**, 361 (1976)].
17. H.-J. Mikeska, J. Phys. C **13**, 2913 (1980).
18. V. G. Bar'yakhtar, B. A. Ivanov, and M. V. Chetkin, Usp. Fiz. Nauk **146**, 417 (1985) [Sov. Phys. Usp. **28**, 563 (1985)].
19. V. G. Bar'yakhtar, M. V. Chetkin, B. A. Ivanov, and S. N. Gadetskii, *Dynamics of Topological Magnetic Solitons. Experiment and Theory* (Springer-Verlag, Berlin, 1994), Springer Tracts in Modern Physics, Vol. 129.
20. E. V. Gomonaĭ, B. A. Ivanov, V. A. L'vov, and G. K. Oksyuk, *Symmetry and Dynamics of Domain Walls in Weak Ferromagnets*, Preprint ITF-89-40R (Kiev, 1989).
21. E. V. Gomonaĭ, B. A. Ivanov, V. A. L'vov, and G. K. Oksyuk, Zh. Éksp. Teor. Fiz. **97**, 307 (1990) [Sov. Phys. JETP **70**, 174 (1990)].
22. B. A. Ivanov, A. K. Kolezhuk, and G. K. Oksyuk, Europhys. Lett. **14**, 151 (1991).
23. B. A. Ivanov and V. E. Kireev, Pis'ma Zh. Éksp. Teor. Fiz. **69**, 369 (1999) [JETP Lett. **69**, 398 (1999)].
24. R. Lü, J.-L. Zhu, X.-B. Wang, and L. Chang, Phys. Rev. B **58**, 8542 (1998).
25. R. Lü, H. Hu, J.-L. Zhu, *et al.*, Phys. Rev. B **61**, 14581 (2000).
26. R. Lü, S.-P. Kou, J.-L. Zhu, *et al.*, Phys. Rev. B **62**, 3346 (2000).
27. R. Lü, J.-L. Zhu, Y. Zhou, and B.-L. Gu, Phys. Rev. B **62**, 11 661 (2000).
28. A. Chiolero and D. Loss, Phys. Rev. B **56**, 738 (1997).
29. T. Moriya, Phys. Rev. **120**, 91 (1960).
30. J. Tejada, X. X. Zhang, E. del Barco, *et al.*, Phys. Rev. Lett. **79**, 1754 (1997).
31. A. I. Vaĭnshteĭn, V. I. Zakharov, V. A. Novikov, and M. A. Shifman, Usp. Fiz. Nauk **136**, 553 (1982) [Sov. Phys. Usp. **25**, 195 (1982)].
32. B. A. Ivanov and V. E. Kireev, Fiz. Nizk. Temp. **25**, 1287 (1999) [Low Temp. Phys. **25**, 966 (1999)].
33. A. Chiolero and D. Loss, Phys. Rev. Lett. **80**, 169 (1998).
34. B. A. Ivanov, in *Path Integrals from peV to TeV: 50 Years after Feynman's Paper*, Eds. by R. Casalbuoni, R. Giachetti, V. Tognetti, R. Vaia, and P. Verrucchi (World Scientific, Dordrecht, 1999), p. 410.
35. R. Jackiw, Comments Nucl. Part. Phys. **13**, 141 (1984).
36. E. A. Turov, *Physical Properties of Magnetically Ordered Crystals* (Akad. Nauk SSSR, Moscow, 1963; Academic, New York, 1965).
37. I. E. Dzyaloshinskiĭ, Zh. Éksp. Teor. Fiz. **32**, 1547 (1957) [Sov. Phys. JETP **5**, 1259 (1957)].
38. Y. Shapira and T. Zak, Phys. Rev. **170**, 503 (1968).

Translated by N. Wadhwa

Journal of Experimental and Theoretical Physics, Vol. 94, No. 2, 2002, pp. 283–292.
Translated from Zhurnal Éksperimental'noĭ i Teoreticheskoĭ Fiziki, Vol. 121, No. 2, 2002, pp. 335–346.

SOLIDS
Structure

Crossover between the Thermodynamic and Nonequilibrium Scenarios of Structural Transformations of H_2O I*h* Ice during Compression

A. G. Lyapin*, O. V. Stal'gorova, E. L. Gromnitskaya, and V. V. Brazhkin

Institute of High-Pressure Physics, Russian Academy of Sciences, Troitsk, Moscow oblast, 142190 Russia
**e-mail: alyapin@hppi.troitsk.ru*

Received June 19, 2001

Abstract—A detailed investigation of different scenarios of structural transformations of H_2O I*h* ice during compression to a pressure of 2 GPa in the temperature range from 77 to 200 K is performed. In the range of temperatures and pressures being treated, detailed data are obtained for the density and the shear modulus for different phases of ice including the *hda*, IX, and XII phases. The experimentally obtained correlations for the density and ultrasonic velocities, with due regard for the available data of structural investigations, are used to identify the transformation sequences I*h* ⟶ *hda* (below 135 K), I*h* ⟶ II ⟶ VI (above 165 K), and I*h* ⟶ IX ⟶ VI (from 155 to 180 K). In the vicinity of the crystallization temperature of amorphous ice, i.e., at about 140 K, an anomalous transformation pattern is observed, which is interpreted as predominantly the I*h* ⟶ XII phase transition. The temperature crossover is discussed between the mode of solid-phase amorphization (I*h* ⟶ *hda*) and crystal–crystal transitions, as well as the metastable nature of IX ice and the mechanism of solid-phase amorphization. © *2002 MAIK "Nauka/Interperiodica".*

1. INTRODUCTION

The investigation of the properties of water and ice at high pressures is of great importance for astrophysics, geophysics of planets and their satellites [1–5], and cryobiology [6]. H_2O ice is characterized by one of the most complex phase diagrams: at least 16 different crystalline and amorphous modifications are observed at different pressures P and temperatures T [7–13]. Many of these ice phases are apparently present in quantity in satellites of giant planets such as Europa, Callisto, and Ganymede, as well as in the nuclei of comets and in interstellar dust [1–5].

As in the case of other substances, the phase diagram of ice may be conventionally divided into a high-temperature part, in which phase transitions occur in the vicinity of the lines of thermodynamic equilibrium of the respective phases, and a low-temperature part, in which unusual structural transformations may be observed such as the solid-phase amorphization of ice [12–16]. If we restrict ourselves to the regular diffusion mechanism of phase transitions, then, at fairly high temperatures (at approximately $T \geq (2/3)T_m$, where T_m is the respective melting temperature), phase transitions proceed through the stage of formation of nuclei of a new phase and their further growth [17], while, at low temperatures (conventionally, at $T \leq (1/3)T_m$, the diffusion of atoms and molecules is frozen, and the transformation may occur away from the line of equilibrium. In the latter case, phase transformations may be defined by the singularities of the lattice dynamics rather than by the thermodynamic relations. This means that nonequilibrium scenarios of phase transitions are possible, which are associated with the softening of certain phonon modes or elastic moduli [18, 19]. The intermediate temperature range estimated at $(1/3)T_m < T < (2/3)T_m$ is a transition region corresponding to the crossover between the thermodynamic and nonequilibrium (kinetic) scenarios of phase transformations. For H_2O ice at pressures of up to 2 GPa, the range of crossover between those two modes of structural transformations may be estimated at $120 < T < 200$ K.

A diffusion mechanism and a martensite mechanism exist in accordance with the standard classification of phase transitions of the first order. In the case of martensite transitions, the atomic displacement occurs coherently over the entire lattice (or in a macroscopically extended region), and the transition is associated with the softening of certain elastic moduli [17]. It is natural that, for martensite transitions, the division into the thermodynamic and nonequilibrium modes of phase transformations makes no sense, as a rule. Martensite phase transitions are usually accompanied by a small jump in volume. At the same time, many phase transitions under conditions of low-temperature compression occur with a considerable variation of volume, which makes difficult the realization of coherent transition in the entire crystal; as a result, a lamellar substructure is formed [20]. In addition to ice, a spontaneous solid-phase amorphization (SPA) is observed for a number of crystals upon low-temperature compression (naturally, the low-temperature condition is individual for each substance) [21–25] (see also the references

cited in [18, 19, 23–25]); this may apparently be treated as the limiting case of nonequilibrium transformations controlled by the softening of certain phonon modes in the absence of diffusion [18, 19, 21, 26–30].

In the equilibrium part of the phase diagram for H_2O ice, the compression of the I*h* phase brings about the realization of sequences of phase transitions such as I*h* ⟶ III ⟶ V ⟶ VI, I*h* ⟶ II ⟶ V ⟶ VI, and I*h* ⟶ II ⟶ VI, depending on temperature, which are well studied using different procedures [7–9] including the ultrasonic method [31–33]. In the case of low-temperature compression of ice (77–120 K), its solid-phase amorphization occurs (I*h* ⟶ *hda* transformation) [12–16], whose structural and thermodynamic aspects have also been studied fairly well [12–16, 34–36]. Recently, ultrasonic investigations of this transformation were performed, which revealed a considerable softening of the shear modulus prior to amorphization [37, 38].

Almost no studies have been made of the intermediate region of temperature at which the mechanism of structural transformations changes from equilibrium to nonequilibrium. In the case of compression of I*h* ice, IX ice [16, 39] and XII ice [40, 41] were observed in the temperature range of crossover of $120 < T < 200$ K, which apparently had no regions of thermodynamic stability. Few attempts at studying phase transitions in this temperature range involved structural investigations and measurements of the specific volume of phases at certain pressures and temperatures [11, 14–16, 40, 41]. As to the behavior of elastic moduli, which is extremely important from the standpoint of understanding the mechanism of phase transitions, it was not previously investigated in this range of temperatures and pressures.

It was the objective of our study to investigate in detail the transition (crossover) from the thermodynamic to nonequilibrium scenario of transformations of I*h* ice during compression in the temperature range from 77 to 200 K, by way of measuring the elastic properties and density.

2. EXPERIMENTAL PROCEDURE

The elastic characteristics of H_2O ice were measured in the pressure range from zero to 2.0 GPa and in the temperature range from 77 to 300 K by the pulsed ultrasonic method [42]. Samples of ice were prepared from distilled water by rapid cooling using liquid nitrogen. Cylindrical ice samples 8–10 mm high and 16–17 mm in diameter in thin-walled lead sheaths (~0.4 mm) were placed in a high-pressure chamber of the cylinder-piston type. Thin (0.02 mm) layers of copper foil were placed between the sample and pistons to protect the latter from destruction due to diffusion of the substance being investigated into the material of the chamber. Ultrasonic measurements were performed using piezoelectric transducers which generated a transverse or longitudinal oscillation at a resonance frequency of 5 MHz. During the experiment, the variation of the time of travel of an ultrasonic signal in the sample $t(p, T)$ and of the travel path length $\Delta l(p, T)$ under the effect of pressure and temperature was determined. The typical rate of pressure variation was 0.02–0.05 GPa/min. Corrections for the deformation of the chamber with the variation of pressure and temperature were determined in special experiments. The error of pressure measurement did not exceed 0.03 GPa. The temperature in the working volume was measured with the aid of four copper–constantan thermocouples located in the immediate vicinity of the sample; the temperature gradient across the sample did not exceed 1 K. The measurements at 77 K were performed with the high-pressure unit fully immersed in a container filled with liquid nitrogen. In this case, the temperature was maintained constant throughout the experiment. At higher temperatures, use was made of a system of cooling the high-pressure chamber and stabilizing the temperature, which was based on controlling the velocity of flow of liquid nitrogen vapor through bores in the top and bottom supports of the high-pressure unit, as well as through the shell of the working chamber. In this case, the temperature was determined within 1–2 K. A more detailed description of the experimental equipment and procedure is found in [43]. In order to calculate the shear modulus G and the bulk modulus B, we used the approximation of homogeneous isotropic medium, i.e., the relations $G = \rho V_t^2$ and $B + (4/3)G = \rho V_t^2$, where ρ is the density, and V_t and V_l denote the velocity of transverse and longitudinal ultrasonic waves, respectively.

3. NONEQUILIBRIUM PHASE DIAGRAM OF I*h* ICE

The points of phase transitions and structural transformations, determined in our experiments by jumps in density and ultrasonic velocity, are given in the phase diagram (Fig. 1). This diagram may be treated as nonequilibrium because, on the one hand, it includes the lines of phase transitions observed under concrete kinetic conditions ($dP/dt \sim 0.02$–0.05 GPa/min, and so on) with a certain experimental hysteresis and, on the other hand, structural transformations of the type of solid-phase amorphization of ice I*h* ⟶ *hda* bear no relation whatsoever to the thermodynamic phase diagram. The presented diagram is in fact the main experimental result and will be discussed in detail as the study is described. The coordinates of the points of phase transitions in Fig. 1 are, in general, consistent with the previously published data of low-temperature structural investigations performed under pressure [12, 14, 16]. In particular, the curve of amorphization of I*h* ice (Fig. 1) fits nicely the curve determined by Mishima [16].

The advantage of our investigations consists in that the parameters being measured were monitored continuously, whereby we could accurately determine the

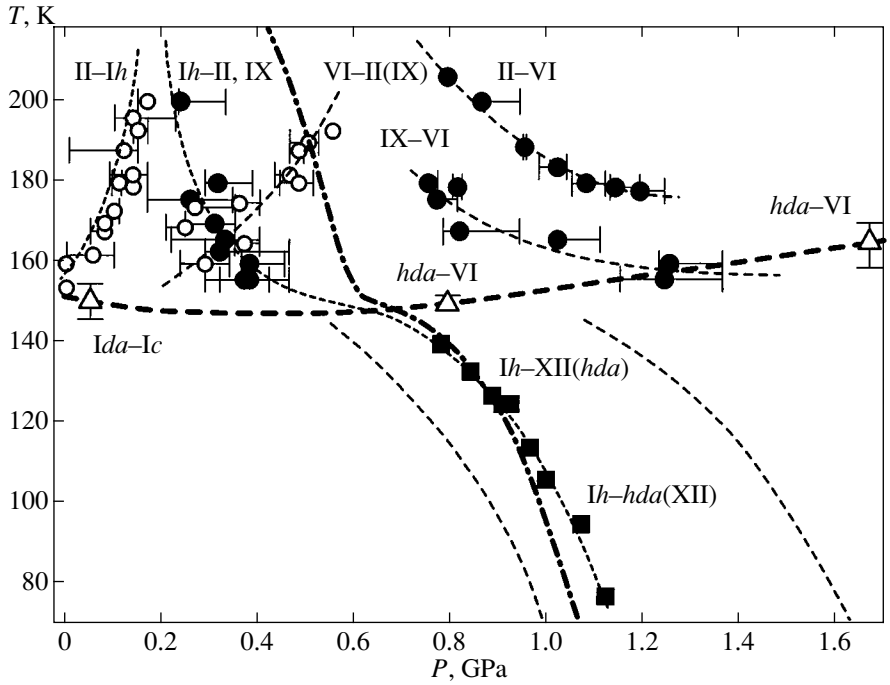

Fig. 1. A nonequilibrium phase diagram for ice, in which the experimental points of structural transformations are marked: ●, crystal–crystal transitions during compression; ■, solid-phase amorphization of I*h* ⟶ *hda*; and ○, crystal–crystal transitions upon pressure release from the VI phase. The dashed curves indicate the interpolation of phase transformations, as well as the position of the beginning and completion of solid-phase amorphization of I*h* ⟶ *hda*. The bold dashed curve indicates the crystallization curve of amorphous ice (*lda* or *hda*), with △ indicating the experimental data. The bold dot-and-dash curve indicates the interpolation of the experimental data for transformation of I*h* ice emulsion [16].

pressure P and the temperature T of phase transitions. At the same time, the absence of direct structural measurements obviously made it difficult for us to interpret the fairly complex pattern of phase transitions. Nevertheless, the use of the available data of direct structural and Raman investigations under pressure [12, 14, 16, 39, 41] and the measurements of density during the experiments enabled us, in all cases being treated, to highly reliably interpret the observed anomalies and identify most of the structural transformations (special cases will be discussed separately).

The crystallization curve of amorphous *lda* and *hda* ice (see Fig. 1, as well as [14, 16]) divides the phase diagram of ice into two parts corresponding to low-temperature nonequilibrium transformations and to high-temperature transitions between crystal phases. Below, we will treat the variation of the elastic properties of ice during compression of the I*h* phase in the above-identified two temperature regions.

3.1. Crystal–Crystal Phase Transitions

As was already mentioned, the high-temperature part of the phase diagram of H_2O (T = 150–300 K) has been well studied using different methods [5–7]. As to the variation of the elastic properties during I*h* ⟶ III ⟶ V ⟶ VI and I*h* ⟶ II ⟶ V ⟶ VI phase transitions, it was investigated using the ultrasonic technique and Brillouin scattering [31–33] only at temperatures above the triple points $T_{\text{II–V–VI}} \approx 213$ K, $T_{\text{II–III–V}} \approx 249$ K, and $T_{\text{Ih–II–III}} \approx 238$ K [7–9].

We have determined fairly accurately (Fig. 1) the values of pressure for direct and inverse phase transitions I*h*–II and II–VI in the range of 175–200 K, i.e., below the triple point $T_{\text{II–V–VI}} \approx 213$ K. The obtained lines of phase transitions fit well the data of Mishima [14]. X-ray investigations [16] and Raman scattering [39] were used to find that the I*h* ⟶ IX phase transition is observed in the range of 155–180 K, where IX ice is a proton-ordered analog of III ice [44–46] and may be obtained by cooling III ice below 170 K [44]. However, the exact positions of the I*h* ⟶ IX phase transition were registered on the pressure–temperature plane either sporadically [39] or only qualitatively [16, 41].

Our measurements help complete the pattern in this temperature range (Fig. 1). Two clearly defined anomalies were observed in the density and elastic properties at temperatures above 175 K, which obviously corresponded to the sequence of phase transitions I*h* ⟶ II ⟶ VI. As the temperature decreased, the points of phase transitions shifted to the right (Figs. 1 and 2) in accordance with the increase in kinetic hysteresis for the transitions. However, the pattern changed abruptly below 175 K: the position of the second anomaly of ρ and V_t shifted in a jump to the left with respect to pressure, and, for intermediate temperatures of 166–175 K,

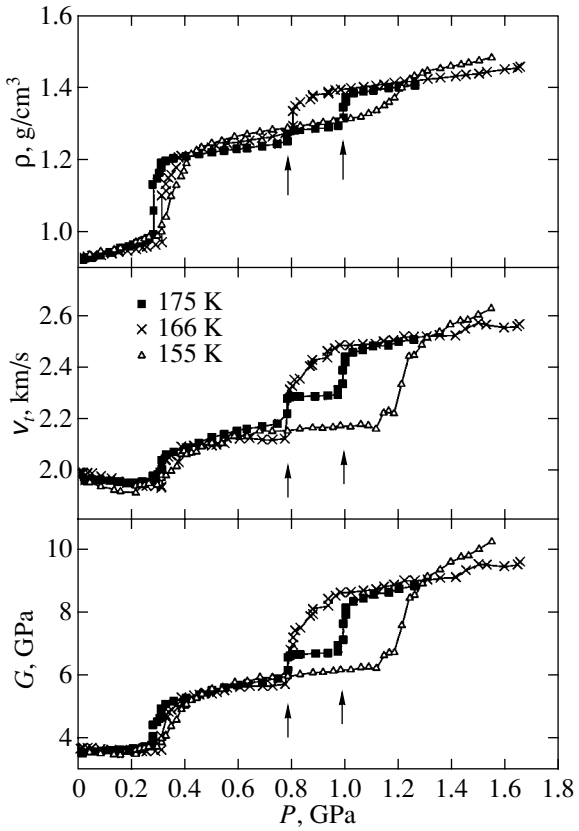

Fig. 2. Typical experimentally obtained dependences of the density, of the rate of transverse ultrasound, and of the shear modulus during compression of I*h* ice in the temperature range from 150 to 200 K. The arrows indicate the jumps corresponding to the IX ⟶ VI and II ⟶ VI transitions for the curve at $T = 175$ K.

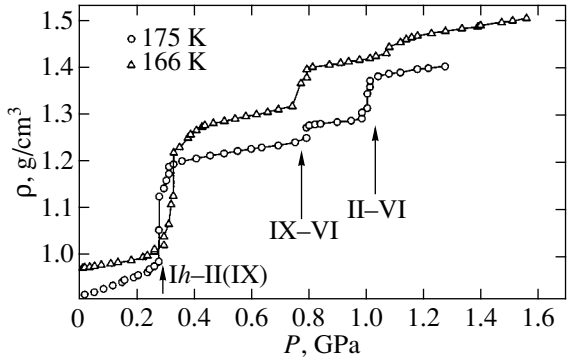

Fig. 3. Dependences of the density of I*h* ice upon compression for experiments in which a mixture of phases of II and IX ice was observed.

curves with three anomalies of ρ and V_t were observed (Figs. 2 and 3). It is natural to relate the observed pattern to the change from the sequence of phase transitions I*h* ⟶ II ⟶ VI to the sequence I*h* ⟶ IX ⟶ VI. In view of the fact that the densities of the II and IX phases of ice are very close to one another, the curves with three anomalies of ρ and V_t during transition to the VI phase must apparently correspond to the mode of mixture of the II and IX phases. The amplitudes of the second and third anomalies are defined by the fraction of the II and IX phases (Fig. 3). Note that, in the temperature range corresponding to the transition region between the II ⟶ VI and IX ⟶ VI transformations, the pattern of variation of ρ and V_t might differ strongly for the same temperatures (compare the curves for $T = 166$ K in Figs. 2 and 3) depending, apparently, on diverse factors such as the previous history of the sample, kinetic characteristics, and so on.

Therefore, it follows from our experimental data that the kinetic line of the I*h* ⟶ IX phase transformation changes smoothly to the line of the I*h* ⟶ II transition, which is consistent with the previously published data of [14, 16]. At the same time, the IX ⟶ VI phase transition occurs at a lower pressure than the II ⟶ VI transition (Fig. 1), with due regard for the kinetics of transitions (hysteresis).

3.2. Solid-Phase Amorphization

The variation of the elastic properties of ice in the process of solid-phase amorphization at 77 K was investigated by us in detail previously [37, 38]. Figure 4 gives experimentally obtained correlations for solid-phase amorphization at three temperatures, namely, 77, 125, and 130 K. One can see that the pattern of variation of the density and elastic properties does not vary qualitatively at different temperatures; it is only with the temperature rise that the amorphization pressure is observed to shift towards decreasing (Fig. 1). In view of the data of [37, 38], one can formulate the following singularities of the nonequilibrium scenario of solid-phase amorphization (Fig. 4): (1) as the pressure increases, the density and the bulk modulus of initial I*h* ice increase, and the velocity of transverse ultrasonic waves and the shear modulus decrease (Fig. 4); (2) the transformation of crystal into the amorphous phase begins as an abrupt and simultaneous variation of the density and elastic properties, similarly to phase transitions of the first kind; (3) the solid-phase amorphization is accompanied by a fairly extended "tail" of transformation (compare Figs. 2 and 4, and see Fig. 1); (4) prior to amorphization in the I*h* phase, an increase in the Poisson coefficient is observed up to anomalously high values of approximately 0.4 [38]. The shear elastic softening of the lattice of I*h* ice is of extreme importance for an understanding of the mechanism of solid-phase amorphization and will be treated below (Section 5).

3.3. Phase Transitions in the Vicinity of the Crystallization Line

At $T = 140$ K, the experimentally obtained pressure dependence of ρ and V_t (Fig. 4) turned out to be unusual. Two weak singularities in the behavior of ρ(*P*)

and $V_t(P)$ at pressures of 0.3 and 1.4 GPa, marked by arrows in Fig. 4, apparently should be associated with the I*h* ⟶ IX and IX ⟶ VI transitions, as a result of which impurities of the IX and VI phases emerge, respectively. These singularities are defined more clearly on the ρ(*P*) curve. However, the main structural transformation of I*h* ice occurs in the vicinity of 0.8 GPa. By the pattern of variation of ρ and V_t and by the value of pressure of this transition (Figs. 1 and 4), it would be natural to associate this transition with the solid-phase amorphization of I*h* ⟶ *hda*. However, the amplitude of the density jump and, especially, of the jump in the value of the transverse velocity of sound during this transition is much higher than in the case of I*h* ⟶ *hda* transformation (Fig. 4). Moreover, the final density of ice at P = 1.6 GPa is markedly higher than the density of both *hda* ice and the VI phase, and, from the standpoint of the transformation coordinates, this cannot be a phase transition to VI ice or to the distorted VI' phase. Obviously, the pattern observed at 140 K cannot be represented as a superposition of the I*h* ⟶ *hda* and I*h* ⟶ IX ⟶ VI transformations (see the dependence of ρ and V_t and of G for T = 130 and 150 K in Figs. 4 and 2, respectively).

The observed anomalous pattern of phase transformations at 140 K can be readily explained if we assume that the jump in ρ and V_t in the vicinity of 0.8 GPa corresponds to the phase transition to XII ice characterized by the density of 1.44 g/cm^3 [10]. Koza *et al.* [40, 41] have found recently that the I*h* ⟶ XII phase transition competes with solid-phase amorphization during transformations of I*h* ice in the entire low-temperature range; at the same time, the kinetic factors defining the type of transformation (I*h* ⟶ XII or I*h* ⟶ *hda*) were not exposed [40]. As was demonstrated later, the I*h* ⟶ XII phase transition is more probable at a high compression rate [41]. It has been found that the upper limit of the temperature of formation of XII ice corresponds to T = 150 K, which is consistent with our data.

The evolution of the sequence of transformations from I*h* ⟶ II(IX) ⟶ VI to I*h* ⟶ *hda* is given in Fig. 5, where the values of ρ and V_t are taken for different samples of ice at fixed values of pressure of 0.7 and 1.6 GPa. One can see in Fig. 5 that the high-temperature and low-temperature modes of transformations are clearly separated. Unfortunately, the accuracy of measurements and the number of experimental points prevent one from finding exact temperature dependences of these characteristics for samples of different phases. However, the values of both the density and the velocity of transverse ultrasound are registered fairly reliably for the phases identified as VI and *hda* ice. The variation of ρ and V_t for *hda* ice may be attributed to two reasons. Firstly, as was already discussed, a mixture of the *hda* and XII phases is formed in the low-temperature part of the phase diagram corresponding to solid-phase amorphization of I*h* ice [40, 41], with the content of the XII phase depending on the kinetic singularities of the experiment. Secondly, the properties of the *hda* phase may systematically depend on the amorphization temperature because, unlike the crystal lattice, an amorphous network cannot be a uniquely defined structure (in terms of short-range singularities). The measured characteristics of VI ice in the temperature range from 150 to 170 K (Fig. 5) are too high compared with the available data for VI ice [31–33, 47, 48]. While the deviation of the values of the velocity of transverse ultrasound could be associated with the presence of texture in samples of VI ice in view of the fact that its structure is of tetragonal symmetry [49] and, consequently, anisotropic, the deviation of the density toward increasing cannot be associated with the texture. It is natural to assume the presence of another, denser, phase at a high pressure, first of all, XII ice. In this case, XII ice may be treated as an indicator of the nonequilibrium scenario of transformations of I*h* ice (I*h* ⟶ XII phase transition), although direct structural investigations under pressure are no doubt required for unique identification of phases (or their mixtures).

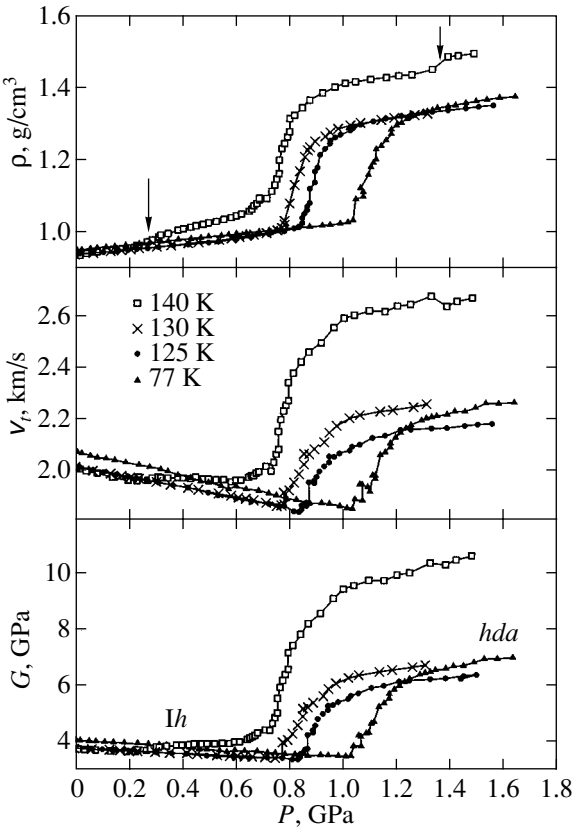

Fig. 4. Typical experimentally obtained dependences of the density, of the velocity of transverse ultrasound, and of the shear modulus during compression of I*h* ice, observed in the low-temperature range of nonequilibrium phase diagram (77 to 140 K). For T = 140 K, the arrows indicate the singularities of the density curve, which correspond to the I*h* ⟶ IX and IX ⟶ VI phase transitions occurring in respective phase impurities.

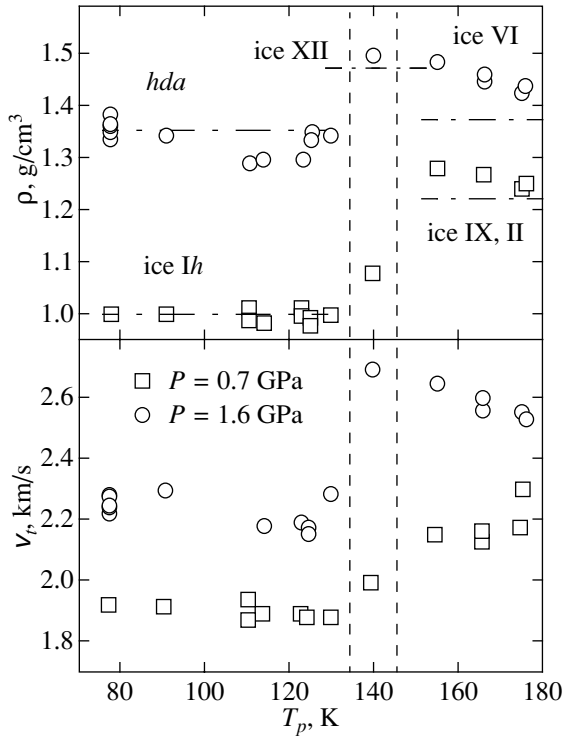

Fig. 5. Values of the density and of the velocity of transverse ultrasonic waves, taken for fixed values of pressure of 0.7 and 1.6 GPa from the results of experiments performed at different temperatures T_P. The horizontal dot-and-dash lines correspond to the density values interpolated or extrapolated to the respective pressures: for the I*h* and VI phases, by the formulas from [33]; for IX ice, by the density of the III phase from [33]; for *hda* ice, by the data of [14]; and for XII ice, by the data of [10].

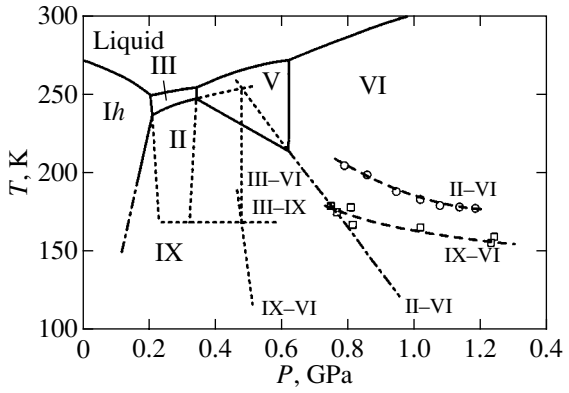

Fig. 6. A phase diagram for ice in which the experimentally obtained curves of (○) II ⟶ VI and (□) IX ⟶ VI phase transitions are presented, as well as the respective curves of thermodynamic equilibrium (see text). The solid curves correspond to the known interfaces.

4. II–VI AND IX–VI PHASE TRANSITIONS

The thermodynamic nature of IX ice and the pattern of the IX ⟶ VI phase transition are of importance from the standpoint of accurate interpretation of the crossover between the thermodynamic and nonequilibrium scenarios of transformations of I*h* ice. It appears that IX ice is a metastable phase [44], and, therefore, the I*h* ⟶ IX ⟶ VI phase transitions may be treated as nonequilibrium from the viewpoint of thermodynamics. Nevertheless, it is to be assumed that the mechanism of IX ⟶ VI phase transition is a diffusion one, because, firstly, it is accompanied by a substantial rearrangement of structure of ice and, in particular, of the oxygen sublattice, and, secondly, the pattern of abruptly increasing hysteresis for the IX ⟶ VI transition (Fig. 1) is typical of the diffusion mechanism.

We will analyze in more detail the thermodynamic correlations between the II, IX, and VI phases of ice. Obviously, for the arbitrary A, B, and C phases (with a uniquely defined structure and thermodynamic potentials), lines of thermodynamic equilibrium and a triple point may be introduced, even if they do not exist on the equilibrium *P–T* diagram, from the correlations $G_A = G_B$ and so on and $G_A = G_B = G_C$, where G_A is the thermodynamic potential of the A phase and so on. In treating the phase diagram of ice, we will assume for simplicity that the variations of volume, ΔV, and of entropy, ΔS, are constant over a certain region along the lines of phase equilibria, which causes little distortion of the real pattern of the equilibrium phase diagram for ice. It follows from the Clausius–Clapeyron equation $dT/dP = \Delta V/\Delta S$ that this simplification implies a constant slope of the phase boundary on the *P–T* diagram.

Jumps in volume for phase transformations of ice are known from [32, 33], namely, $\Delta V_{\mathrm{III}\to\mathrm{II}} = -0.35$ cm³/mol, $\Delta V_{\mathrm{II}\to\mathrm{V}} = -0.88$ cm³/mol, and $\Delta V_{\mathrm{II}\to\mathrm{VI}} = -1.85$ cm³/mol; these data are in good agreement with the results of other measurements [9, 31, 48]. It follows from the phase diagram of ice in [7–9] that $S_{\mathrm{III}} \approx S_{\mathrm{V}} \approx S_{\mathrm{VI}}$ or, more precisely, that the variation of entropy for the respective phase transitions is rather small, because the observed interfaces have close-to-vertical slopes (Fig. 6). From this correlation, it follows, in particular, that the slope of the II–VI interface is negative and approximately 2.1 times steeper than the slope of the II–V curve, because $\Delta V_{\mathrm{II}\to\mathrm{VI}}/\Delta V_{\mathrm{II}\to\mathrm{V}} = 2.1$. We extrapolate the II–III and II–VI interfaces to lower temperatures and easily find the coordinates of a virtual (i.e., not existing on the equilibrium phase diagram) triple point II–III–VI, namely, $P = 0.48 \pm 0.01$ GPa and $T = 255 \pm 3$ K (Fig. 6). Because $S_{\mathrm{III}} \approx S_{\mathrm{V}} \approx S_{\mathrm{VI}}$, the slope of the line of equilibrium for III and VI ice is almost vertical. The temperature of the III ⟶ IX phase transition is 170 K [44], with the jump in volume being 0.1% or less. Therefore, one can conclude that the III–IX equilibrium line is an almost horizontal line in the neighborhood of $T = 170$ K (Fig. 6). This enables one to approximate the coordinates of the virtual triple point III–IX–VI as 0.5 GPa and 173 K. The slope of the virtual interface IX–VI may be calculated directly. Proceeding from the estimates of $\Delta V_{\mathrm{IX}\to\mathrm{VI}} = \Delta V_{\mathrm{II}\to\mathrm{VI}} = \Delta V_{\mathrm{III}\to\mathrm{II}} + \Delta V_{\mathrm{II}\to\mathrm{VI}} = 2.2$ cm³/mol and $\Delta S_{\mathrm{IX}\to\mathrm{VI}} = \Delta S_{\mathrm{IX}\to\mathrm{III}} = 1.35$ J/K mol [50], we derive

$(dT/dP)_{IX \to VI}$ = 1600 K/GPa. As a result, it is possible to obtain the line of IX–VI phase equilibrium, as is shown in Fig. 6.

Therefore, in the temperature range of 150–180 K being treated, the IX–VI interface is shifted by 0.3–0.4 GPa toward lower pressures relative to the II–VI curve. The curve of the IX ⟶ VI phase transition obtained by us is shifted by approximately the same value on the pressure scale relative to the respective curve of the II ⟶ VI transition, where one must take into account the kinetic hysteresis for both phase transitions. It is natural to assume that the relative position of points of the IX ⟶ VI and II ⟶ VI phase transitions is governed by thermodynamic relations. At the same time, the results of our analysis serve as additional arguments to prove that IX ice is a metastable phase. Indeed, if IX ice had a region of stability on the phase diagram, this region would have to be located between the regions of either the I*h* and II phases or the II and VI phases. However, both these situations may be eliminated in view of our constructions (Fig. 6), in particular, of the position of the triple point II–IX–VI which may be obtained by crossing the equilibrium lines of IX–VI and II–VI. In any of the cases identified above, the formation of IX ice would have been observed at relatively high temperatures (>200 K).

The observed similarity between the structures of IX and VI ice, at least relative to the positions of oxygen atoms [51], may serve as an additional kinetic factor affecting the position of the IX ⟶ VI phase transition. Summing up, one can assume that the sequence of the I*h* ⟶ IX ⟶ VI phase transitions is due to the thermodynamic driving forces and apparently associated with the diffusion mechanism of transitions. Nevertheless, this sequence corresponds to nonequilibrium phase transitions, because IX ice is metastable and, therefore, defined by the kinetics as well or, to be more precise, by the ratio of the energy barriers for phase transitions between different phases.

5. MECHANISM OF SOLID-PHASE AMORPHIZATION

Ultrasonic investigations yield direct information about the acoustic part of the phonon spectrum in a solid, which is very important for explaining the mechanism of solid-phase amorphization of I*h* ice under pressure. The characteristic features of solid-phase amorphization of ice were identified in the previous section. Note that the I*h* ⟶ *hda* transformation is similar to phase transitions of the first kind, although the process of solid-phase amorphization, unlike phase transitions between crystalline modifications of ice, has an extended (up to 1.7 GPa) "tail" (Fig. 1) corresponding to gradual relaxation compaction. The density jump value for the I*h* ⟶ *hda* transition of about 20% measured by us coincides with the results of previous studies [12–14, 34, 35].

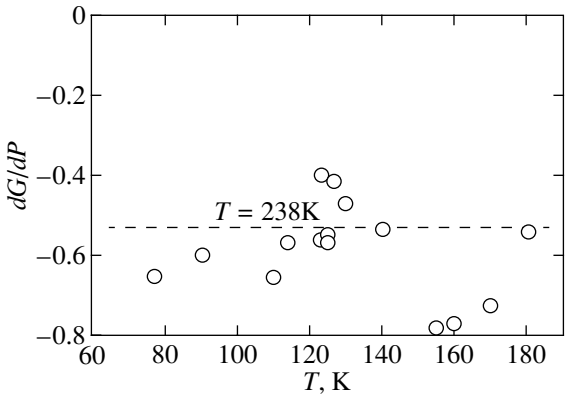

Fig. 7. Experimentally obtained values of the derivative of the shear modulus $(dG/dP)_T$. The horizontal line corresponds to the value of $(dG/dP)_T$ from [55] for T = 238 K.

Of key importance for the understanding of the mechanism of solid-phase amorphization of ice is the revealed decrease in the velocity of transverse ultrasonic waves $V_t(P)$ and, accordingly, in the shear modulus $G(P)$ up to the beginning of the I*h* ⟶ *hda* transition. The shear softening of I*h* ice prior to amorphization is accompanied by a density increase (~10%). The high value of the Poisson coefficient [38] at the moment of amorphization, i.e., the low value of the G/B ratio, likewise points to the shear softening of the lattice of ice under pressure. Therefore, the concept of instability of the ice lattice as the triggering mechanism of solid-phase amorphization receives direct proof from the ultrasonic measurements of the elastic properties.

Figure 7 gives the temperature dependence of the pressure derivative G'_P (Fig. 7). In spite of the considerable scatter of experimental points due to large errors in numerical differentiation, it is obvious that G'_P depends little on temperature. Therefore, the softening of the lattice upon compression of I*h* ice is primarily due to the singularities of its lattice geometry and of the interaction of atoms in the lattice, while the thermal oscillation of atoms is not so important in this case. While the mechanism of structural transformation at low temperatures is associated with dynamic reasons, the rise of temperature is accompanied by the activation of atomic diffusion and predomination of the thermodynamic scenarios of compaction of ice.

More detailed information about the components of the elastic constants tensor and about the phonon spectrum of crystalline I*h* ice under pressure is of special interest for the understanding of the mechanism of solid-phase amorphization. The data on the $G(P)$ correlation are insufficient in this case, because the shear modulus for a polycrystal is a characteristic that is averaged over different orientations of crystallites. However, in view of the fact that the pressure derivative G'_P is weakly dependent on temperature (Fig. 7), one can

assume that the pressure derivatives of the components of the elastic constant tensor do not vary strongly with temperature either, and, consequently, the low-frequency stability of I*h* ice may be analyzed using the data of [32, 33] obtained under pressure for the temperature of 238 K. The lattice will be mechanically stable if the elastic constant tensor of the compressed lattice is positive definite [19, 52–54]. For hexagonal I*h* ice ($P6_3/mmc$ space group), this implies three conditions of stability relative to shear strain, namely,

$$\mu_1 = (1/2)(c_{11} - c_{12}) > 0, \quad (1)$$

$$\mu_2 = c_{44} > 0, \quad (2)$$

$$\mu_3 = (1/2)(c_{11} + c_{12} + c_{33} - \sqrt{(c_{11} + c_{12} - c_{33})^2 + 8c_{13}^2}) > 0, \quad (3)$$

where c_{11}, c_{12}, c_{13}, c_{33}, and c_{44} are five basic constants describing the elastic constant tensor of hexagonal lattice of I*h* ice (in this case, $c_{66} = (1/2)(c_{11} - c_{12})$). Here, one more condition, according to which the bulk modulus is positive, is assumed to be valid. The interpolation of the data of [32, 33, 55] readily yields the following logarithmic derivatives with respect to pressure for shear elastic constants at $P = 0$: $\mu_1'/\mu_1 = -0.057$ GPa^{-1}, $\mu_2'/\mu_2 = -0.183$ GPa^{-1}, and $\mu_3'/\mu_3 = -0.216$ GPa^{-1}; i.e., the decrease in μ_2 and μ_3 is more intensive. However, the second derivatives μ_2 and μ_3 with respect to pressure are positive, and these elastic moduli vary little with pressure until approximately 1 GPa, while $\mu_1' < 0$, and the decrease in μ_1 rises rapidly with pressure. The extrapolated quantity μ_1 tends to zero at 1.5 GPa. With a pressure of approximately 1.1 GPa corresponding to amorphization of ice, the extrapolated decrease in the modulus μ_1 is ~60% relative to the initial value. For various procedures of solid-phase amorphization, the softening of elastic constants by 30–60% is typical [56]. The decrease in the moduli μ_2 and μ_3 with pressure is not so significant in our case, and the rate of decrease in the polycrystalline shear modulus is intermediate between the respective values for μ_1, μ_2, and μ_3.

The results of computer calculations of Tse *et al.* [27, 57] lend support to the assumed scenario of softening the elastic constants of I*h* ice. In particular, the method of molecular dynamics was used to demonstrate that the pressure-induced collapse of the lattice of I*h* ice begins with an abrupt decrease in the modulus μ_1. The softening of the elastic constants corresponds to the lattice instability with respect to acoustic phonon modes in the neighborhood of the center of the Brillouin zone. At the same time, for substances with a diamond-like structure, it is known, for example, that the lattice instability during compression occurs first on the boundary of the Brillouin zone; it must be emphasized that, with respect to oxygen atoms, I*h* ice has a short-range order with tetrahedral packing of atoms analogous to that of diamond-like semiconductors. Naturally, a rigorous calculation of the phonon spectrum of I*h* ice upon compression is of most interest for the understanding of the dynamic mechanism of solid-phase amorphization. However, simple reasoning analogous to that following from the analysis of stability of diamond-like lattices [19] may lead to the understanding of the reasons for the instability of I*h* ice under pressure. The instability of the ice lattice is due to the loose tetrahedral structure of ice. The shear elastic instability is associated with the negative contribution by pressure to the shear moduli [18, 19], which increases rapidly due to central repulsion between neighboring oxygen atoms.

Note that the presence of an unstable mode in the vibrational spectrum of crystal lattice is not a sufficient condition of solid-phase amorphization, because the unstable mode may correspond to the lattice transition to a new crystalline state. It is obvious that the factors disturbing the coherent motion of atoms, for example, the interaction of two soft modes (see the examples of softening of two or more phonon modes in [19] and [30]), may contribute to the disordering of an unstable lattice. One can mention the following singularities for I*h* ice which may contribute to solid-phase amorphization: (1) a high degree of disordering in the proton arrangement [58] or orientational disorder of H_2O [59], (2) the existence of two types of hydrogen bonds [60], and (3) a possible contribution of libration phonon modes [61] to the process of dynamic disordering of the ice lattice.

6. TRANSITION FROM THE THERMODYNAMIC TO NONEQUILIBRIUM SCENARIOS OF TRANSFORMATION DURING COMPRESSION OF I*h* ICE

Now, one can identify two main and interrelated characteristic features of the kinetics of structural transformations of I*h* ice upon a decrease in temperature: firstly, the transition from the thermodynamic to nonequilibrium scenario of structural transformations, which is the main subject of this study, and, secondly, the replacement of the diffusion mechanism of phase transitions by mechanisms caused by the dynamics of the lattice being softened with cooperative (to some degree) motion of atoms at the moment of rearrangement of structure.

It is natural to assume that the crossover between the crystal–crystal (II ⟶ IX phase transition) and crystal–amorphous phase modes of transformations of I*h* ice corresponds to the freezing of diffusion in the oxygen sublattice. This is suggested by the fact that the interface between the two modes is in the region of crystallization of amorphous *hda* ice at temperatures of 140–150 K (Fig. 1). In the same temperature range, a crossover was observed between the two-phase melting of ice emulsion, in which the nucleation of crystalline phases could be prevented, and the solid-phase amor-

phization as a single-phase process defined by the instability of the I*h* lattice [16] (see also Fig. 1). The general form of the curve of transformations of I*h* ice (Fig. 1) may be described as the intersection of the hysteresis curve of the I*h* ⟶ IX(II) phase transition and the instability curve, in good agreement with the results of model analysis of [18]. Naturally, this intersection is smoothed out by transition processes which are apparently of thermoactivation nature.

Unfortunately, the mechanism of the I*h* ⟶ XII phase transition remains unclear. The interpretation of structural transformation at 140 K as the I*h* ⟶ XII phase transition also needs to be confirmed. It is known [41] that this phase transition is observed below 150 K as a process competing with solid-phase amorphization. One can assume that the mechanism of the I*h* ⟶ XII phase transition, which is also associated with the lattice instability, apparently has a nature analogous to that of martensite phase transitions, and the choice between two channels of transformations is governed by the kinetics of experiment.

The diffusion of atoms in the oxygen sublattice develops above the crystallization temperature of the amorphous phases of ice, and, as was already mentioned, the thermodynamic correlations between the phases affect considerably the relative position of the points of phase transitions, as in the case of the IX ⟶ VI and II ⟶ VI transitions. However, nonequilibrium scenarios are possible in this case as well, if the temperature is not high. In the pressure range being treated, the thermodynamic driving forces proportional to the factor $\exp(\Delta G/kT)$ (where ΔG is the difference of the values of the Gibbs free energy between the phases) are fairly small for the phase transitions between the II and III phases of ice or between the II and IX phases, so that all of these phases are very close in density and in energy (31–31, 44–46]. At the same time, the kinetic barriers for the II–III or II–IX phase transitions are obviously not low, because these transitions are associated with considerable rearrangement of the oxygen sublattice. On the contrary, for the III–IX phase transition, the barriers are not high, because the III and IX phases are characterized by the same structure of the oxygen sublattices and by the disordered and ordered arrangement of protons, respectively. Indeed, IX ice was first produced upon cooling III ice [44–46]. If we assume that the I*h* ⟶ IX ⟶ VI sequence of phase transitions during compression proceeds by a nonequilibrium scenario (i.e., IX ice is a metastable phase), and the mechanism of these phase transitions is a diffusion one, then the reasons for which the nonequilibrium scenario becomes preferable are associated with the restrictions in the diffusion motion of atoms that arise during a temperature decrease. It is in a configuration space that these restrictions correspond to higher barriers, including the case of transition to a thermodynamically stable phase.

Therefore, the general tendency toward transition to nonequilibrium scenarios with decreasing temperature is associated with a gradual freezing of the motion of atoms and diffusion, and the triggering of the dynamic mechanisms of transformations is associated with the softening of the lattice and with the reduction of the respective energy barriers in the configuration space. Note that the complex pattern of crossover between the thermodynamic and nonequilibrium scenarios of structural transformations of ice is not unique. Previously, a similar crossover was observed under conditions of relieving high-pressure phases of silicon and germanium, where the transition also occurred from the mode of crystal–crystal transformations for phases with a stability region on the phase diagram to modes of the type of crystal–metastable crystalline phase, and then to the mode of crystal–amorphous phase. Further progress in the understanding of the nonequilibrium polymorphism of ice must be associated with detailed crystallographic and dynamic analysis of phase transitions between crystalline modifications and with computer simulation of various stages of the process of solid-phase amorphization.

ACKNOWLEDGMENTS

We are grateful to S.V. Popova for fruitful discussions. This study received financial support from the Russian Foundation for Basic Research (grant nos. 01-02-16557, 00-15-96593, and 00-15-99308).

REFERENCES

1. J. P. Poirier, Nature **299**, 683 (1982).
2. A. G. G. M. Tielens and L. J. Allamandola, in *Physical Processes in Interstellar Clouds*, Ed. G. E. Morfill and M. Scholer (Reidel, Dordrecht, 1987), p. 333.
3. M. J. Mumma, P. R. Weissman, and S. A. Stern, in *Protostars and Planets III*, Ed. by E. H. Levy, J. I. Lunine, and M. S. Matthews (Univ. of Arizona Press, Tucson, 1993), p. 1177.
4. P. Jenniskens and D. F. Blake, Science **265**, 753 (1994).
5. P. Jenniskens, D. F. Blake, M. A. Wilson, and A. Pohorille, Astrophys. J. **455**, 389 (1995).
6. P. Mehl and P. Boutron, J. Phys. (Paris), Colloq. **48**, C1-449 (1987).
7. P. W. Bridgman, Proc. Am. Acad. Arts Sci. **47**, 441 (1911).
8. P. V. Hobbs, *Ice Physics* (Oxford Univ. Press, London, 1974).
9. E. Yu. Tonkov, *High Pressure Phase Transformations* (Metallurgiya, Moscow, 1988; Gordon and Breach, Philadelphia, 1992), Vol. 2.
10. C. Lobban, J. L. Finney, and F. Kuhs, Nature **391**, 268 (1998).
11. O. Mishima and H. E. Stanley, Nature **392**, 164 (1998).
12. O. Mishima, L. D. Calvert, and E. Whalley, Nature **310**, 393 (1984).

13. O. Mishima, L. D. Calvert, and E. Whalley, Nature **314**, 76 (1985).
14. O. Mishima, J. Chem. Phys. **100**, 5910 (1994).
15. R. J. Hemley, L. C. Chen, and H. K. Mao, Nature **338**, 638 (1989).
16. O. Mishima, Nature **384**, 546 (1996).
17. J. W. Christian, *The Theory of Transformations in Metals and Alloys* (Pergamon, Oxford, 1975, 2nd ed.), Part 1.
18. V. V. Brazhkin and A. G. Lyapin, High Press. Res. **15**, 9 (1996).
19. A. G. Lyapin and V. V. Brazhkin, Phys. Rev. B **54**, 12036 (1996).
20. V. V. Brazhkin, Ye. V. Tat'yanin, A. G. Lyapin, *et al.*, Pis'ma Zh. Éksp. Teor. Fiz. **71**, 424 (2000) [JETP Lett. **71**, 293 (2000)].
21. R. J. Hemley, A. P. Jephcoat, H. K. Mao, *et al.*, Nature **334**, 52 (1988).
22. Y. Fujii, M. Kowaka, and A. Onodera, J. Phys. C **18**, 789 (1985).
23. E. G. Ponyatovsky and O. I. Barcalov, Mater. Sci. Rep. **8**, 147 (1992).
24. L. E. McNeil and M. Crimsditch, Phys. Rev. Lett. **68**, 83 (1992).
25. K. J. Kingma, C. Meade, R. J. Hemley, *et al.*, Science **259**, 666 (1993).
26. J. S. Tse and D. D. Klug, Phys. Rev. Lett. **67**, 3559 (1991).
27. J. S. Tse, J. Chem. Phys. **96**, 5482 (1992).
28. N. Binggeli and J. R. Chelikowsky, Phys. Rev. Lett. **69**, 2220 (1992).
29. N. Binggeli, N. R. Keskar, and J. R. Chelikowsky, Phys. Rev. B **49**, 3075 (1994).
30. M. Hemmati, A. Chizmeshya, G. H. Wolf, *et al.*, Phys. Rev. B **51**, 14 841 (1995).
31. G. H. Shaw, J. Chem. Phys. **84**, 5862 (1986).
32. R. E. Gagnon, H. Kiefte, M. J. Clouter, and E. Whalley, J. Phys. (Paris), Colloq. **48**, C1-29 (1987).
33. R. E. Gagnon, H. Kiefte, M. J. Clouter, and E. Whalley, J. Chem. Phys. **92**, 1909 (1990).
34. M. A. Floriano, Y. P. Handa, D. D. Klug, and E. Whalley, J. Chem. Phys. **91**, 7187 (1989).
35. A. Bizid, L. Bosio, A. Defrain, and M. Oumezzine, J. Chem. Phys. **87**, 2225 (1987).
36. E. Whalley, D. D. Klug, M. A. Floriano, *et al.*, J. Phys. (Paris) **48**, C1-429 (1987).
37. O. V. Stal'gorova, E. L. Gromnitskaya, and V. V. Brazhkin, Pis'ma Zh. Éksp. Teor. Fiz. **62**, 334 (1995) [JETP Lett. **62**, 356 (1995)].
38. E. L. Gromnitskaya, O. V. Stal'gorova, and V. V. Brazhkin, Zh. Éksp. Teor. Fiz. **112**, 200 (1997) [JETP **85**, 109 (1997)].
39. A. G. Garg, Phys. Status Solidi A **110**, 467 (1988).
40. M. Koza, H. Schober, A. Tölle, *et al.*, Nature **397**, 660 (1999).
41. M. Koza, H. Schober, T. Hansen, *et al.*, Phys. Rev. Lett. **84**, 4112 (2000).
42. E. P. Papadakis, Rev. Sci. Instrum. **47**, 805 (1976).
43. O. V. Stal'gorova, E. L. Gromnitskaya, D. R. Dmitriev, and F. F. Voronov, Prib. Tekh. Éksp. **39**, 115 (1996).
44. E. Whalley, J. B. R. Heath, and D. W. Davidson, J. Chem. Phys. **48**, 2362 (1968).
45. S. J. La Placa, W. C. Hamilton, B. Kamb, and A. Prakash, J. Chem. Phys. **58**, 567 (1973).
46. J. D. Londo, W. F. Kuhs, and J. L. Finney, J. Chem. Phys. **98**, 4878 (1993).
47. C. A. Tulk, R. E. Gagnon, H. Kiefte, and M. J. Clouter, J. Chem. Phys. **104**, 7854 (1996).
48. C. A. Tulk, R. E. Gagnon, H. Kiefte, and M. J. Clouter, J. Chem. Phys. **107**, 10 684 (1997).
49. B. Kamb, Science **150**, 205 (1965).
50. K. Nishibata and E. Whalley, J. Chem. Phys. **60**, 3189 (1974).
51. B. Minčeva-Šukarova, G. E. Slark, W. F. Sherman, and G. R. Wilkinson, J. Phys. (Paris), Colloq. **48**, C1-37 (1987).
52. D. C. Wallace, *Thermodynamics of Crystals* (Wiley, New York, 1972).
53. J. Wang, S. Yip, S. R. Phillpot, and D. Wolf, Phys. Rev. Lett. **71**, 4182 (1993).
54. J. Wang, J. Li, S. Yip, *et al.*, Phys. Rev. B **52**, 12627 (1995).
55. R. E. Gagnon, H. Kiefte, M. J. Clouter, and E. Whalley, J. Chem. Phys. **89**, 4522 (1988).
56. J. Koike, Phys. Rev. B **47**, 7700 (1993).
57. J. S. Tse, D. D. Klug, C. A. Tulk, *et al.*, Nature **400**, 647 (1999).
58. S. W. Peterson and H. A. Levy, Acta Crystallogr. **10**, 70 (1957).
59. W. P. Kuhs and M. S. Lehman, in *Water Science Reviews*, Ed. by F. Franks (Cambridge Univ. Press, Cambridge, 1985), Vol. 2.
60. J. Li and D. K. Ross, Nature **365**, 327 (1993).
61. J. S. Tse, M. L. Klein, and I. R. McDonald, J. Chem. Phys. **81**, 6124 (1984).

Translated by H. Bronstein

Journal of Experimental and Theoretical Physics, Vol. 94, No. 2, 2002, pp. 293–298.
Translated from Zhurnal Éksperimental'noĭ i Teoreticheskoĭ Fiziki, Vol. 121, No. 2, 2002, pp. 347–353.

SOLIDS
Structure

A Mixed Domain Structure in Ferrite–Garnet Films

M. L. Akimov, P. A. Polyakov, and N. N. Usmanov
Moscow State University, Moscow, 119899 Russia
e-mail: polyakov@magnetic.phys.msu.su
Received June 26, 2001

Abstract—A stable static mixed domain structure consisting of strip domains and a cylindrical magnetic domain (CMD) is obtained in $(Bi_{0.7}Lu_{0.3})_3(Fe_{0.8}Ga_{0.2})_5O_{12}$ ferrite–garnet films. An analytic theory of the mixed domain structure is constructed. An analytic solution is obtained for the shape of a distorted strip domain, which is in good agreement with experimental results. © *2002 MAIK "Nauka/Interperiodica".*

1. INTRODUCTION

It is well known that the magnetic domain ordering is energetically favorable in ferromagnetic films [1, 2]. An equilibrium domain structure is determined by the balance of many factors, of which the exchange interaction, magnetization, anisotropy, the shape of a magnetic sample, the energy of domain walls, the magnitude and direction of external magnetic field, temperature, defects, magnetostriction, and the structure of the surface are the most important ones. For a specific set of physical parameters, a magnetic sample is characterized by a definite type of magnetic domains. For example, the most widespread type of magnetic ordering in magnetic films with perpendicular anisotropy is either a strip (or labyrinth) domain structure or an array of cylindrical magnetic domains (CMDs) [3].

A mixed magnetic structure in an isotropic material seems to be energetically unfavorable; artificial implementation of such a structure will result in unstable structures that eventually transform into a uniform equilibrium magnetically ordered state. Nevertheless, the existence of a nonequilibrium nonstationary mixed magnetic structure is quite possible; moreover, it has apparently been obtained in the experiments carried out in [4, 5]. In these studies, an equilibrium strip structure in a $(BiTm)_3(FeGa)_5O_{12}$ ferrite–garnet film was exposed to a focused laser beam, which locally heated a cylindrical region inside a strip domain to a temperature higher than the Curie point, thus destroying the ferromagnetic medium in this region, which is equivalent to the formation of a mixed magnetic structure: a cylindrical domain inside a strip domain. This nonstationary mixed structure evolved with time as new regions of the film were heated. Hence, the radius of the effective cylindrical domain increased, thus generating a nonuniform magnetostatic stray field. Then, the magnetic field induced a disordered motion of various regions of the domain walls and distorted the original strip domain structure, increasing the deflection of the strip domain walls. After a time, as the temperature of the overheated region decreased, an inverse process occurred: the deflection of the strip domain decreased, and the equilibrium strip domain structure was recovered [4, 5]. In spite of the fact that the results of experiments [4, 5] are in good qualitative and quantitative agreement with the model concepts of [6] concerning the efficient generation of a mixed domain structure by a focused laser impulse, the authors of [4, 5] did not directly observe such a structure.

In the present paper, we demonstrate (both experimentally and theoretically) the existence of a quasi-equilibrium mixed domain structure representing a system of strip domains and a CMD; this structure is stable and may exist during an infinitely long period of time. The constructed analytic theory that describes this mixed structure is in good agreement with the experimental results presented in this paper.

2. DESCRIPTION OF THE EXPERIMENT

The aim of the experiment carried out is to obtain a concrete mixed domain structure consisting of an oriented strip structure and a CMD situated inside a strip domain. A mixed domain structure of a different type was considered in [1]. In that paper, the authors presented the results of investigating the magnetization of epitaxial ferrite–garnet films with orientation (210) and the diagram of the phase states of quasi-uniaxial magnetic films whose easy magnetization axis made an angle with a normal to the film surface. A single-domain state, an oriented strip domain structure, and an array of tilted CMDs of hexagonal type were the basic magnetic states. For certain values of the free energy, a set of magnetic structures consisting of tilted CMDs, dumbbell-shaped domains, and strip domains with a unified correlated period was implemented in these films of rhombic anisotropy. However, these structures were localized in different regions of the magnetic film.

In the present paper, we used a $(Bi_{0.7}Lu_{0.3})_3(Fe_{0.8}Ga_{0.2})_5O_{12}$ film with orientation (210) for the experimental observation of a mixed static domain configuration. We chose a sample with the fol-

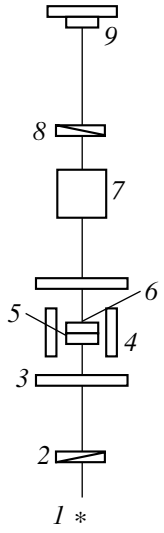

Fig. 1. Observation scheme; (*1*) light source, (*2*) polarizer, (*3*) bias field (H_b) coils, (*4*) planar field (H_x) coils, (*5*) sample, (*6*) pulse field (H_z) coil, (*7*) objective lens of the microscope, (*8*) analyzer, and (*9*) photographic camera.

lowing parameters in our experiment: a film thickness of $h \approx 13$ μm, an inclination angle of the easy magnetization axis of $\theta \approx 30°$, a saturation magnetization of $4\pi M_s \approx 60$ G, a dimensionless Hilbert decay parameter of $\alpha \approx 0.01$ (the dimensionless decay parameter was determined from the magnetic resonance linewidth), and a rhombic anisotropy field of $H \approx 1400$ Oe. The sample was fabricated in A.M. Balbashov's laboratory at the Moscow Power Institute.

The magnetic structure was observed through a polarization microscope in white light using the Faraday effect with amplitude resolution. Helmholtz coils were used to create a magnetic bias field H_b perpendicular to the sample surface. A planar pulse field was also generated by Helmholtz coils. A pulsed magnetic field H_z perpendicular to the film surface was generated by a planar coil. The minimal pulse rise and fall times were 7 and 40 ns, respectively. The sample was placed at the center of the coils. A G5-67 oscillator was used as a pulse generator, and a G3-33 oscillator, as a source of harmonic signals. The diagram of the experimental setup for the observation of the magnetic structure is shown in Fig. 1.

It was pointed out in [1] that the domain structure in a given type of film can be controlled either by a magnetic field directed perpendicular to the film surface or by a planar field.

A required magnetic state was achieved only by applying a magnetic field with allowance for the feature of the behavior of strip dynamic domains under magnetization. At the beginning of the experiment, a sample was demagnetized and had a strip domain structure. Then, a bias field of $H_b = 15$ Oe was applied to the sample. When the width of magnetic domains with the orientation of magnetization vector opposite to the external field decreased, the sample was exposed to five single rectangular pulses of magnetic field H_z with minimal rise and fall times. The amplitude of the pulsed field was $H_z = 5$ Oe, and the pulse duration was 7 μs. After this procedure, one could observe CMDs in the film. Then, single pulses of magnetic field H_x directed along the projection of the easy magnetization axis onto the film plane were applied to the sample. Pulses of triangular shape with a rise and fall time of 10 μs and an amplitude of $H_x = 7$ Oe facilitated the growth of CMDs into the strip domains. However, the growth of certain CMDs into a strip domain was hindered by the adjacent strip domains that had earlier grown from a CMD. Under the effect of the above single pulses, all CMDs except for one grew into strip domains. Thus, a structure consisting of strip domains and a CMD was obtained. Next, the bias field was decreased to $H_b = 6$ Oe, while the structure obtained was preserved.

Then, a series of sinusoidal pulses of a magnetic field perpendicular to the film surface were applied to the sample with a frequency of 30 Hz, and a final domain configuration was obtained when the field amplitude was reduced from 1 Oe to zero. The films of the type investigated may have large relaxation times after switching off external forces. Therefore, the structure obtained was photographed after a time interval necessary for establishing a stable domain configuration. Figure 2 shows a photograph of the mixed domain structure obtained. The width of the strip domain (the dark domain in the figure) in which a CMD is located is equal to 16 μm. The mean radius of the CMD is equal to 6.75 μm.

The CMD situated inside a strip domain bends the domain walls. The domain structure is stable; therefore, the magnitude of bending is preserved during the whole period of observation, which amounts to more than eight hours. It is known that, if the films of this type have a strip domain structure in the initial state, this structure is preserved under small variations of external conditions; moreover, the period of the strip structure is also preserved [7]. The magnetic structure under investigation also proves to be stable with respect to small variations of external magnetic fields. Since the configuration considered is obtained without local variations in the film parameters, its stability is determined by magnetostatic fields. The magnitude of bending is in good agreement with the results of calculations carried out in this work.

3. THE THEORY OF A MIXED DOMAIN STRUCTURE

To describe a mixed domain structure, we proceed from the general concepts of micromagnetism. For simplicity, we restrict the analysis to a single strip domain containing a cylindrical magnetic domain. This restriction is justified by the fact that, as is clear from experi-

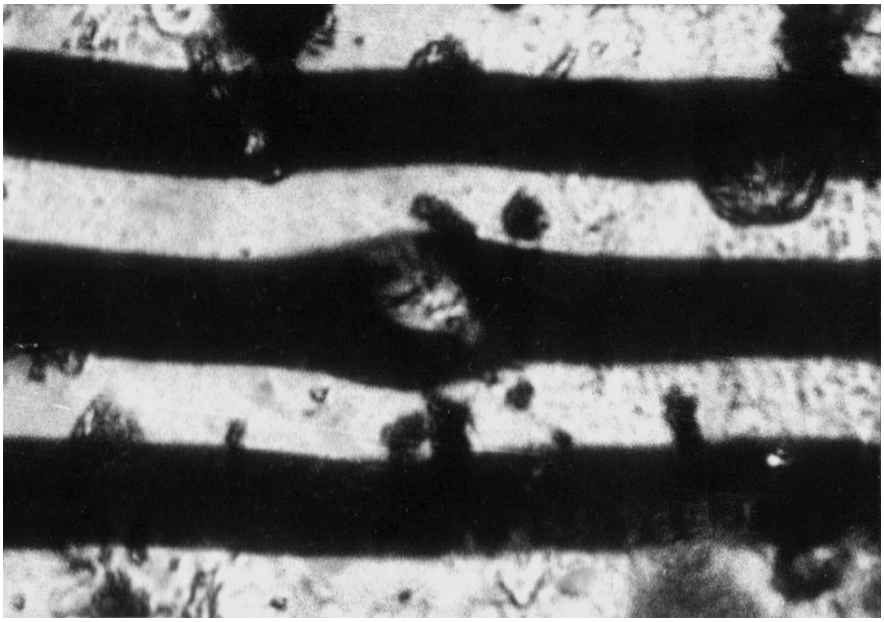

Fig. 2. Cylindrical magnetic domain in a strip domain structure.

ments, the effect of the next-nearest strip domains is negligible. This assumption allows us to construct an analytic solution for the mixed domain structure under consideration.

Consider an isolated strip domain that contains a cylindrical magnetic domain of radius R inside it. Figure 3 shows an isolated strip domain of width $w = 2a$ situated along the coordinate axis x in an infinite film of thickness h. The coordinate axis z is perpendicular to the film plane, while the axis y is perpendicular to the domain wall. The origin of coordinates is located at the center of the cylindrical domain. The magnetostatic stray field of the cylindrical domain distorts the shape of the strip domain; thus, the width of the latter domain depends on the coordinate x.

Suppose that a function $y(x)$ describes the bending of the wall of the strip domain. Then, the magnetostatic energy, considered as a functional of the unknown function $y(x)$, can be represented as

$$W = W_1 + W_2 + W_3 + W_4 + W_5. \quad (1)$$

Consider the individual terms of functional (1):

$$W_1 = -8\sigma^2 \int_{-A}^{A} dx \int_{a}^{y(x)} dy \int_{-A}^{A} dx' \int_{y(x')}^{b} dy' H(x, y, x', y')$$
$$-8\sigma^2 \int_{-A}^{A} dx \int_{a}^{y(x)} dy \int_{-A}^{A} dx' \int_{-b}^{-y(x')} dy' H(x, y, x', y')$$

is the variation of the magnetostatic energy due to the bending of the domain walls in two rectilinear strips that fringe the bent domain walls and are parallel to the x axis, as well as the variation of the energy of interaction between the surface magnetic charges of the above strips due to the bending of the domain walls. Here, b is the maximum of the function $y(x)$ that describes the distortion of the strip domain wall due to the magnetostatic stray field of the cylindrical domain, σ is the magnetostatic surface charge density equal to the normal component of the magnetization vector, A is a regularization parameter, and

$$H(x, y, x', y') = \frac{1}{\sqrt{(x - x'^2) + (y - y')^2}} - \frac{1}{\sqrt{(x - x')^2 + (y - y')^2 + h^2}},$$

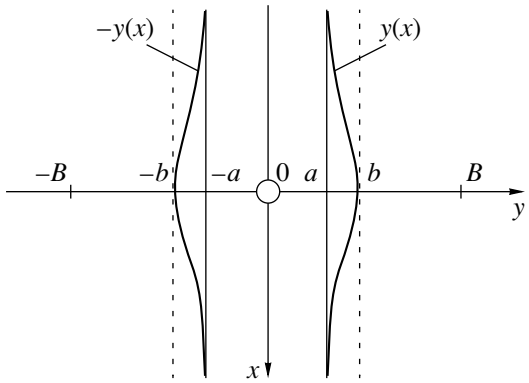

Fig. 3. Isolated strip domain with a cylindrical magnetic domain in the center (top view).

$$W_2 = -4\sigma^2 \int_{-R}^{R} dx_1 \int_{-\sqrt{R^2-x_1^2}}^{\sqrt{R^2-x_1^2}} dx_2 \times \left[\int_{-A}^{A} dx \int_{a}^{y(x)} dy \tilde{H}(x, x_1, y, x_2) - \int_{-A}^{A} dx \int_{y(x)}^{b} dy \tilde{H}(x, x_1, y, x_2) \right]$$

is the energy of interaction between the magnetic charges of the cylindrical domain and the surface magnetic charges of the strip domain, induced by the bending of the domain walls (hereupon, we neglect the distortion of the cylindrical domain itself), where

$$\tilde{H}(x, x_1, y, x_2) = \frac{1}{\sqrt{(x-x_1)^2 + (y-x_2)^2}} - \frac{1}{\sqrt{(x-x_1)^2 + (y-x_2)^2 + h^2}},$$

$$W_3 = 8\sigma^2 \int_{-A}^{A} dx \int_{-a}^{a} dy \int_{-A}^{A} dx' \int_{a}^{y(x')} dy' H(x, y, x', y') - 8\sigma^2 \int_{-A}^{A} dx \int_{b}^{B} dy \int_{-A}^{A} dx' \int_{a}^{y(x')} dy' H(x, y, x', y') - 8\sigma^2 \int_{-A}^{A} dx \int_{-B}^{-b} dy \int_{-A}^{A} dx' \int_{a}^{y(x')} dy' H(x, y, x', y')$$

is the variation of the magnetostatic energy of interaction between the upper and lower surfaces of the unbent strip domain with adjoining rectilinear strips that fringe the bent domain walls and are parallel to the x axis, as well as the variation of the energy of interaction between rectilinear semi-infinite planes with the strips that fringe the bent strip domain walls, where B is a regularization parameter;

$$W_4 = 2\sigma^2 \int_{-R}^{R} dx_1 \int_{-\sqrt{R^2-x_1^2}}^{\sqrt{R^2-x_1^2}} dx_2 \left[2 \int_{-A}^{A} dx \int_{b}^{B} dy \tilde{H}(x, x_1, y, x_2) - \int_{-A}^{-R} dx \int_{-a}^{a} dy \tilde{H}(x, x_1, y, x_2) - \int_{-R}^{R} dx \int_{-a}^{-\sqrt{R^2-x_1^2}} dy \tilde{H}(x, x_1, y, x_2) - \int_{-R}^{R} dx \int_{\sqrt{R^2-x_1^2}}^{a} dy \tilde{H}(x, x_1, y, x_2) - \int_{R}^{A} dx \int_{a}^{-a} dy \tilde{H}(x, x_1, y, x_2) \right]$$

is the energy of interaction of the magnetic charges of the cylindrical domain with the surface charges of the upper and lower parts of the unbent strip domain and with the semi-infinite planes that bound the isolated strip domain in a thin ferromagnetic film; and

$$W_5 = 2\sigma h H_z \int_{-A}^{A} dx \left(\int_{-y(x)}^{-a} dy + \int_{a}^{y(x)} dy \right) + \text{const}$$

is the variation of the magnetostatic energy of the strip domain in the external bias magnetic field, where H_z is a magnetic field parallel to the z axis and const stands for the terms independent of the domain wall bending.

Calculating the variational derivative of the magnetostatic energy functional (1) and equating it to zero, we obtain a nonlinear functional integral equation for the function $y(x)$; for relatively small degrees of bending of the domain walls, this equation can be linearized. Expanding the function $y(x)$ in series with respect to the points a and b within the integration limits, we obtain the equation

$$\int_{-A}^{A} dx' [P_1(x') + P_2(x')](y(x') - a) - (y(x') - a) f = \int_{-R}^{R} dx_1 \int_{-\sqrt{R^2-x_1^2}}^{\sqrt{R^2-x_1^2}} dx_2 \left(\frac{1}{\sqrt{(x-x_1)^2 + (a-x_2)^2}} - \frac{1}{\sqrt{(x-x_1)^2 + (a-x_2)^2 + h^2}} \right), \quad (2)$$

where $\psi = b - a$, $\nu = b + a$, $f = 4\ln(1 + h^2/4a^2)$,

$$P_1(x') = \frac{1}{\sqrt{(x-x')^2 + \psi^2}} - \frac{1}{\sqrt{(x-x')^2 + \psi^2 + h^2}},$$

and

$$P_2(x') = \frac{1}{\sqrt{(x-x')^2 + \nu^2}} + \frac{1}{\sqrt{(x-x')^2 + \nu^2 + h^2}}.$$

Equation (2) is a convolution-type linear integral equation; it can be solved by the Fourier transform technique [8]. Applying a cosine Fourier transform to Eq. (2), we obtain

$$\{K_0(y\psi) - K_0(y\sqrt{\psi^2 + h^2}) + K_0(y\nu)$$

$$- K_0(y\sqrt{\nu^2 + h^2}) + f\}(\tilde{y}(x') - a) = \int_0^\infty dx' \int_{-R}^{R} dx_1$$

$$\times \int_{-\sqrt{R^2 - x_1^2}}^{\sqrt{R^2 - x_1^2}} dx_2 \left(\frac{1}{\sqrt{(x' - x_1)^2 + (a - x_2)^2}} \right. \tag{3}$$

$$\left. - \frac{1}{\sqrt{(x' - x_1)^2 + (a - x_2)^2 + h^2}} \right) \cos(x'y),$$

where $(\tilde{y}(x') - a)$ is the Fourier image of the function $(y(x') - a)$.

Solving algebraic equation (3) and applying the inverse Fourier transform, we obtain the following expression for the magnitude of deformation of the domain wall due to the magnetostatic stray field of the cylindrical domain:

$$y(x) = a + \sqrt{\frac{2}{\pi}} \int_0^\infty \frac{N(y)\cos(xy)\,dy}{K_0(y\psi) - K_0(y\sqrt{\psi^2 + h^2}) + K_0(y\nu) - K_0(y\sqrt{\nu^2 + h^2}) + f}, \tag{4}$$

where

$$N(y) = \int_0^\infty dx' \int_{-R}^{R} dx_1$$

$$\times \int_{-\sqrt{R^2 - x_1^2}}^{\sqrt{R^2 - x_1^2}} dx_2 [P(x', x_1, x_2)] \cos(x'y),$$

and

$$P(x', x_1, x_2) = \frac{1}{\sqrt{(x' - x_1)^2 + (a - x_2)^2}}$$

$$- \frac{1}{\sqrt{(x' - x_1)^2 + (a - x_2)^2 + h^2}}.$$

For small deflections of the domain wall, we can assume that the denominator in the integrand in solution (4) is constant, which corresponds to the expansion of the Macdonald function $K_0(y)$ for small values of the argument [9]. As a result, we obtain the following analytic solution $y(x)$ that describes the distortion of the domain wall of an isolated strip domain due to the field of the cylindrical domain:

$$y(x) = a + \left\{ \ln \frac{h}{b - a} + \ln \frac{\sqrt{(b + a)^2 + h^2}}{b + a} + f \right\}^{-1}$$

$$\times \int_{-R}^{R} dx_1 \int_{-\sqrt{R^2 - x_1^2}}^{\sqrt{R^2 - x_1^2}} dx_2 \left[\frac{1}{\sqrt{(x - x_1)^2 + (a - x_2)^2}} \right. \tag{5}$$

$$\left. - \frac{1}{\sqrt{(x - x_1)^2 + (a - x_2)^2 + h^2}} \right].$$

Substituting $x = 0$ into Eq. (5), we obtain an equation for determining the maximum bending b of the strip domain wall. Thus, the theory developed solves the problem stated in this paper.

4. CONCLUSIONS AND COMPARISON WITH AVAILABLE EXPERIMENTAL RESULTS

The shape of deflection of a strip domain wall obtained in the experiment (Fig. 2) is in good agreement with the theoretical result represented in Fig. 4; thus, the theoretical model developed can be applied to describe the behavior of a quasi-equilibrium mixed configuration of magnetic domains (strip domains and CMDs).

The maximum bending of a strip domain wall calculated by formula (4) (Fig. 4) for the parameters corresponding to the experimental data (a strip domain width of $w = 16$ μm, a magnetic film thickness of $h = 13$ μm, and a mean radius of the CMD of $R = 6.75$ μm) is equal to 5.1 μm. The maximal bending of the strip domain wall obtained in the experiment with the above parameters is 3.9 μm. Thus, the value calculated by formula (4) is in good agreement with the experimental value of

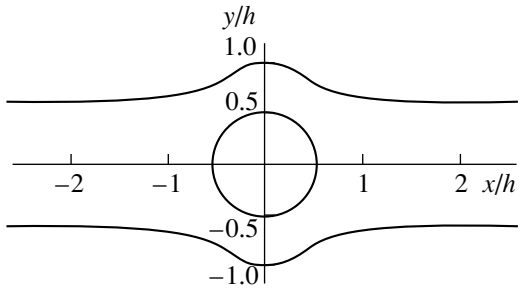

Fig. 4. The shape of the strip domain structure in the presence of a cylindrical magnetic domain in a thin ferromagnetic film.

the strip domain wall bending due to the stray field of the cylindrical domain.

REFERENCES

1. L. D. Landau and E. M. Lifshitz, *Course of Theoretical Physics*, Vol. 8: *Electrodynamics of Continuous Media* (Nauka, Moscow, 1992; Pergamon, New York, 1984).
2. S. V. Vonsovskiĭ, *Magnetism* (Nauka, Moscow, 1971; Wiley, New York, 1974).
3. A. H. Eschenfelder, *Magnetic Bubble Technology* (Springer-Verlag, Berlin, 1980; Mir, Moscow, 1983).
4. A. S. Logginov, A. V. Nikolaev, V. N. Onishchuk, and P. A. Polyakov, Pis'ma Zh. Éksp. Teor. Fiz. **66**, 398 (1997) [JETP Lett. **66**, 426 (1997)].
5. A. S. Logginov, A. V. Nikolaev, E. P. Nikolaeva, and V. N. Onishchuk, Zh. Éksp. Teor. Fiz. **117**, 571 (2000) [JETP **90**, 499 (2000)].
6. M. L. Akimov, Yu. V. Boltasova, and P. A. Polyakov, Radiotekh. Élektron. (Moscow) **46**, 504 (2001).
7. E. N. Il'icheva, A. V. Klushina, N. N. Usmanov, *et al.*, Vestn. Mosk. Univ., Ser. 3: Fiz., Astron. **35**, 59 (1994).
8. *Tables of Integral Transforms (Bateman Manuscript Project)*, Ed. by A. Erdelyi (McGraw-Hill, New York, 1954; Nauka, Moscow, 1969).
9. *Handbook of Mathematical Functions*, Ed. by M. Abramowitz and I. A. Stegun (Dover, New York, 1971; Nauka, Moscow, 1979).

Translated by I. Nikitin

Journal of Experimental and Theoretical Physics, Vol. 94, No. 2, 2002, pp. 299–306.
Translated from Zhurnal Éksperimental'noĭ i Teoreticheskoĭ Fiziki, Vol. 121, No. 2, 2002, pp. 354–362.

SOLIDS
Structure

Magnetic, Optical, and Electrical Properties of Solid Solutions $V_xFe_{1-x}BO_3$

N. B. Ivanova, V. V. Rudenko, A. D. Balaev, N. V. Kazak, V. V. Markov, S. G. Ovchinnikov*, I. S. Edel'man, A. S. Fedorov, and P. V. Avramov

Kirenskiĭ Institute of Physics, Siberian Division, Russian Academy of Sciences, Akademgorodok, Krasnoyarsk, 660036 Russia

** e-mail: sgo@iph.krasn.ru*

Received July 2, 2001

Abstract—Complex studies of magnetic, electrical, and optical properties of $V_xFe_{1-x}BO_3$ solid solutions are carried out in the entire range of concentrations between the extreme compounds VBO_3 and $FeBO_3$. A concentration semiconductor–insulator transition accompanied by a change in the magnetic structure is observed. It is found that the physical properties of the solid solution under investigation differ from those predicted in the model of a virtual crystal in the form of an aggregate of V and Fe centers taken with the weight of x and $1-x$, respectively. The systems of electron energy levels of the VB_6O_6 and FeB_6O_6 clusters are calculated from first principles using the Hartree–Fock method. The calculated electron structure forms the basis for simulating the optical absorption spectra, which are in good agreement with experimental results. A qualitative explanation is given for the entire body of data on electrical conductivity and magnetization. © *2002 MAIK "Nauka/Interperiodica".*

1. INTRODUCTION

Antiferromagnetic dielectric oxides of 3*d* metals have become the objects of intense studies as Mott–Hubbard dielectrics with strong electron correlations. Their alloying leads to the emergence of high-temperature superconductivity in copper oxides and the colossal magnetoresistance effect in manganese oxides. A number of borates ABO_3 of 3*d* metals (A = Fe, Cr, V, Ti) form another class of isostructural oxides with strongly differing electrical and magnetic properties [1–3]. Such a difference in the properties is apparently associated mainly with different occupancies of the 3*d* shell, which determines different types of exchange interactions in these compounds. Among these compounds, $FeBO_3$ has been studied comprehensively, while the data on other representatives of this class (especially solid solutions in which the consequences of competing exchange interactions may be manifested most clearly) are exceptionally scarce.

The VBO_3 and $FeBO_3$ compounds are, respectively, a ferromagnet (T_C = 32 K) and an antiferromagnet with weak ferromagnetism (T_N = 348 K). At T < 500 K, the former compound is a semiconductor and the latter is an insulator. Both compounds have the same crystal structure of a calcite of the rhombohedral system with the same lattice parameters a = 4.62 Å and c = 14.52 Å, which is apparently due to virtually identical ionic radii of V^{3+} and Fe^{3+} ions. The magnetic properties of VBO_3 and $FeBO_3$ are determined by an indirect 90° exchange through the O^{2-} anions; a considerable difference in these properties can be attributed to their different electron configurations (d^2 and d^5, respectively). The high value of T_N for $FeBO_3$ indicates the high-spin state of the Fe^{3+} ion. The magnetic moment of the V^{3+} ion in VBO_3, determined from the saturation magnetization in the ferromagnetic phase, is the sum of the spin and orbital magnetic moments and is approximately 6% lower than the theoretical value. It is unclear whether this discrepancy is a consequence of noncollinearity of the magnetic moments due to the Dzyaloshinski interaction or results from the effect of covalence.

In the present work, we analyze an aggregate of magnetic, electric, and optical properties of $V_xFe_{1-x}BO_3$ solid solutions in the entire concentration range between the extreme compounds.

2. SAMPLES AND PREPARATION TECHNOLOGY

Crystals of the mixed composition $V_xFe_{1-x}BO_3$ were grown by spontaneous crystallization from the solution–melt of the system Fe_2O_3–V_2O_3–B_2O_3–(20PbO + 30$PbFe_3$ wt %). We used compositions with the following relation between components:

$$(1-x)Fe_2O_3 - xV_2O_3 = 10\text{–}15 \text{ wt \%}, \quad x = 0.5\text{–}1.0,$$

$$B_2O_3 = 40\text{–}42.5 \text{ wt \%},$$

$$0.2PbO + 0.3PbF_2 = 42.5\text{–}50 \text{ wt \%}.$$

It should be noted that the value x is given in accordance with the concentration of components in the charge and is approximate.

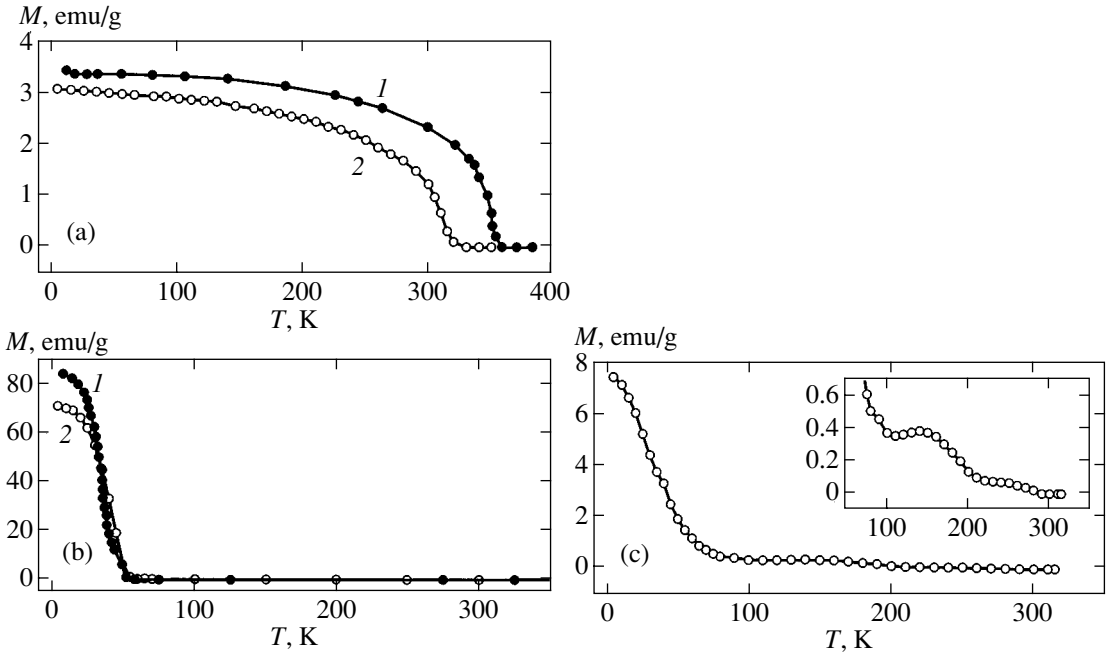

Fig. 1. Temperature dependence of magnetization in a magnetic field $H = 10$ kOe: (a) $FeBO_3$ (*1*), $V_{0.5}Fe_{0.5}BO_3$ (*2*); (b) VBO_3 (*1*), $V_{0.95}Fe_{0.05}BO_3$ (*2*); (c) $V_{0.6}Fe_{0.4}BO_3$. The inset to Fig. 1c shows the magnetization on a magnified scale.

The mixture of the initial components was placed in closed platinum crucibles having a volume of 100 cm^3 and was held at $T = 1000°C$ until the charge was diluted completely. Then the mixture was rapidly cooled to 800°C and held for 1 h.

Using this technology, we obtained crystals in the form of thin plates with a size of 4×4 mm and a thickness of about 0.1 mm, having a smooth and bright surface.

The $V_xFe_{1-x}BO_3$ samples with $x = 0.6$ were subjected to X-ray structural and chemical analyses; the former analysis revealed that the compound with a mixed composition has the same crystal lattice as the extreme compounds VBO_3 and $FeBO_3$, while the latter analysis confirmed the closeness of the concentration x of the substituent ion to that laid during synthesis. X-ray diffraction measurements carried out at 77 K revealed that the compound does not experience any phase transition.

3. EXPERIMENTAL RESULTS

The temperature and magnetic-field dependences of magnetization were measured with the help of a vibrating-coil magnetometer with a superconducting solenoid. Resistive measurements were made by a direct two-contact method using a teraohmmeter. Indium contacts were deposited using the surface wetting effect, and the sample temperature was controlled by its blasting with a gaseous nitrogen or air jet in a flow cryostat. We also obtained optical absorption spectra in the spectral region 4000–20 000 cm^{-1} in the temperature range 83–300 K.

The results of complex measurements showed that, in the concentration range $0 < x < 0.5$, the magnetic and electrical properties of solid solutions are close to those of the initial compound $FeBO_3$. Figure 1a shows by way of an example the temperature dependences of magnetization for $FeBO_3$ (curve *1*) and for a composition with $x = 0.5$ (curve *2*) in a magnetic field of 10 kOe. Since $FeBO_3$ is a well-studied compound, it was not investigated additionally in the present work, and the data of magnetization of $FeBO_3$ were borrowed from [4]. Surprisingly, both curves exhibit the same behavior and demonstrate close values of magnetic moment at $T = 4.2$ K in spite of the fact that half iron atoms are replaced by vanadium atoms. However, the value of T_N for the solid solution is considerably (approximately by 20 K) lower than for the initial compound.

While solid solutions remain close to $FeBO_3$ in the magnetic and electric respect in a wide concentration range of the substituent ion V^{3+}, the addition of small amounts of Fe to VBO_3 leads, on the contrary, to a rapid change in the nature of magnetic ordering. Although the curves describing the temperature dependence of magnetization for VBO_3 (curve *1*) [1] and for a composition with 5% Fe (curve *2*) have the same form typical of ferromagnets (Fig. 1b), the saturation magnetic moment for the solid solution at $T = 4.2$ K is 15% lower than for VBO_3.

For values of $x = 0.6$ and 0.75, the temperature dependences of magnetization are close and exhibit a

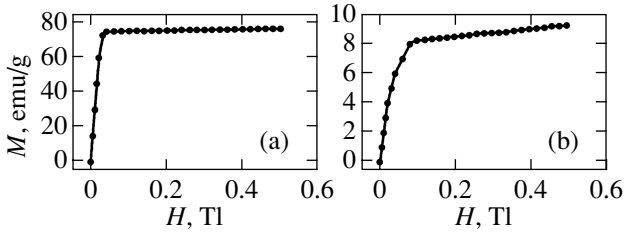

Fig. 2. Magnetization curves at T = 4.2 K for (a) $V_{0.95}Fe_{0.05}BO_3$ and (b) $V_{0.6}Fe_{0.4}BO_3$.

complex behavior. Figure 1c shows the temperature dependence of magnetization for a $V_{0.6}Fe_{0.4}BO_3$ sample. It can be seen from the figure that the function $M(T)$ decreases near T_C, which is typical of pure VBO_3, but the value of the saturation magnetization M_s amounts to only 10% of its value for the initial compound [1], although the vanadium concentration in the sample is 60%. In the vicinity of T = 150 K, the curve has a peak followed by a decay in $M(T)$, which also displays singularities. Such an unusual behavior of $M(T)$ was observed in [4, 5] for solid solutions of $Cr_xFe_{1-x}BO_3$ and was attributed to the existence of an intermediate magnetic structure.

Figure 2 shows the $M(H)$ curves at T = 4.2 K. It can be seen that the magnetization processes are different for samples with different compositions. For example, the tangent to the $M(H)$ curve in the region of strong fields for a sample with x = 0.95 is almost parallel to the abscissa axis (Fig. 2a). The samples with x = 0.5 are characterized by a weak paraprocess, while this process for an intermediate composition with x = 0.6 and 0.75 is strong (Fig. 2b).

As regards the electric properties of the samples, the samples with $0 < x < 0.5$ are insulators (see above), while the remaining compositions, which are closer to VBO_3, are conductors whose resistivity decreases by 9% upon an increase in temperature from 77 to 550 K. The electric properties of samples with x = 1 and 0.95 as well as of compositions with x = 0.6 and 0.75 are close; for this reason, Fig. 3 depicts only the dependences for the former compositions. It can be seen from Figs. 3a and 3b that the temperature dependence of the resistance of VBO_3 is close to a simple activation law with the activation energy E_a = 0.9 eV. At high temperatures, the composition $V_{0.6}Fe_{0.4}BO_3$ also displays activation conduction with a slightly higher value of E_a = 1.1 eV. However, at lower temperatures, the linear dependence of $\ln R$ on reciprocal temperature is violated for this composition. It can be seen in Fig. 3c that, in this temperature range, the resistance is described more correctly by the law [6]

$$R \propto \exp(Q/k_BT)^{1/4},$$

where Q is the quantity determined by the density of states at the Fermi level and by the rate of the decrease for the envelope of the wave function. This law is typical of hopping conduction with a varying jump length. Thus, this mechanism obviously dominates at low temperatures. Unfortunately, we cannot trace the concentration dependence of the absolute value of resistance for various samples since its variations are not very pronounced and the resistance cannot be measured pre-

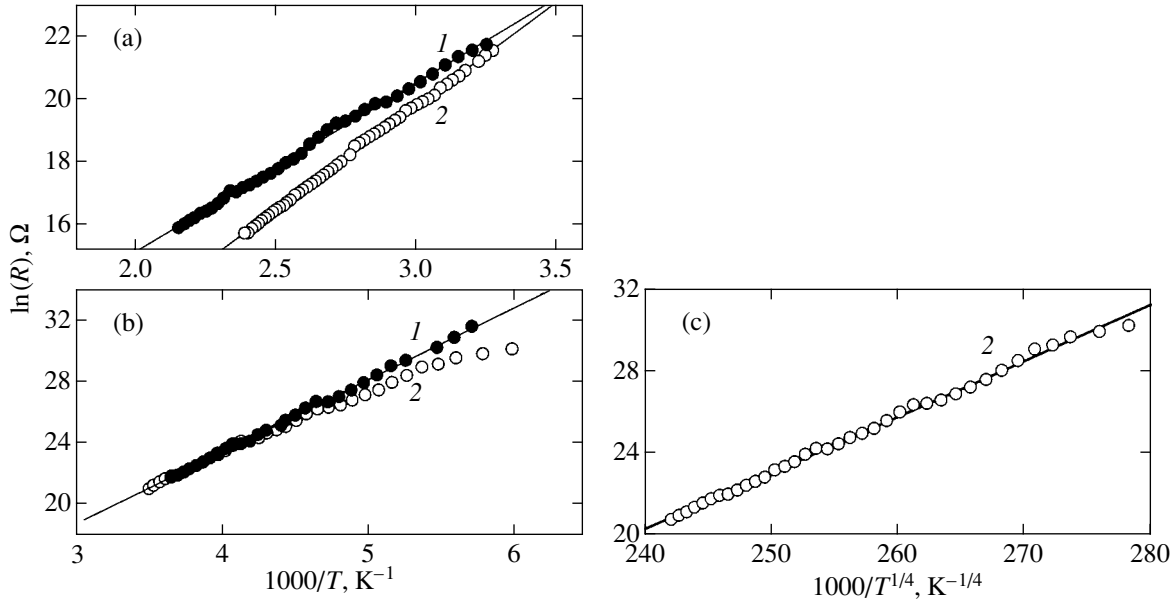

Fig. 3. Logarithm of resistance as a function of (a, b) reciprocal temperature $1000/T$ and (c) $1000//T^{1/4}$ for VBO_3 (*1*) and $V_{0.6}Fe_{0.4}BO_3$ (*2*) at (a) T > 300 K and (b, c) T < 300 K.

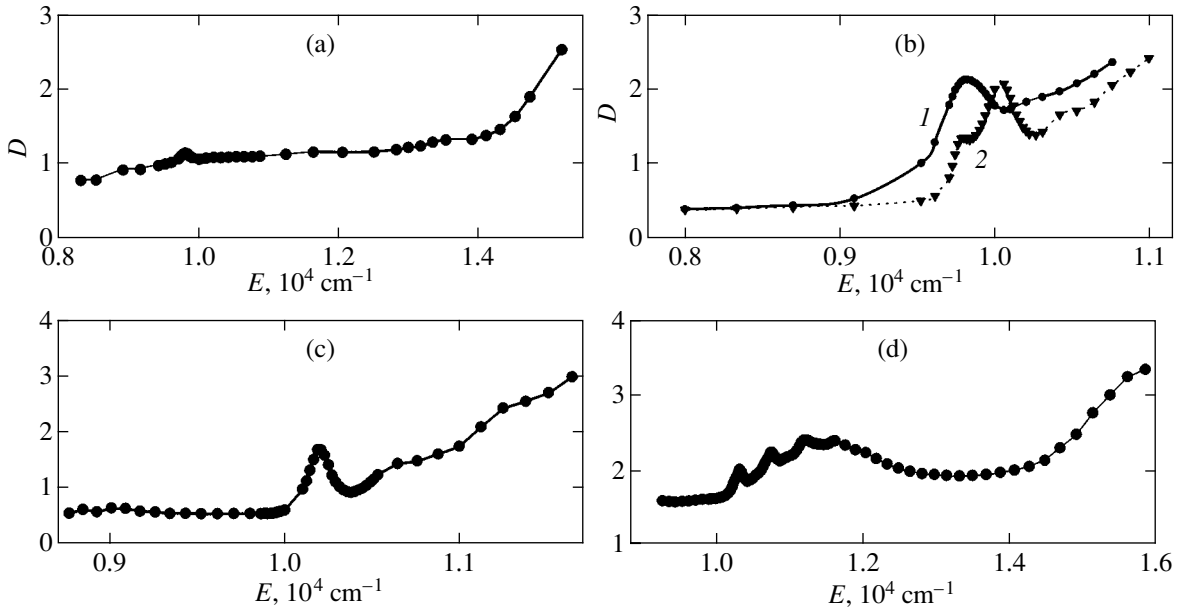

Fig. 4. Optical absorption curves at $T = 90$ K: (a) VBO_3; (b) $V_{0.75}Fe_{0.25}BO_3$ (curves *1* and *2* correspond to 300 and 90 K, respectively); (c) $V_{0.5}Fe_{0.5}BO_3$; and (d) $V_{0.25}Fe_{0.75}BO_3$.

cisely in view of the irregular geometrical shape of the samples.

The observed variation of the optical absorption spectrum $D = \ln(I_0/I)$ with x is also nontrivial by nature. Figure 4 shows the spectral characteristics for samples from the series $V_xFe_{1-x}BO_3$. For the VBO_3 crystal (Fig. 4a), an extremely weak temperature-independent peak can be seen at 9800 cm^{-1}. The absorption edge corresponds to approximately 16 000 cm^{-1}. For a $V_{0.75}Fe_{0.25}BO_3$ crystal (Fig. 4b), the absorption edge is strongly displaced to 11 000 cm^{-1}. In addition to the 9800-cm^{-1} peak typical of V^{3+}, a new peak with a clearly manifested temperature dependence appears. For a $V_{0.5}Fe_{0.5}BO_3$ sample (Fig. 4c), this peak remains, while the peak typical of V^{3+} vanishes. Figure 4d shows the absorption spectrum for a $V_{0.25}Fe_{0.75}BO_3$ sample, which obviously contains a series of bands typical of $FeBO_3$ [7]. In all publications devoted to the absorption spectra of $FeBO_3$ (see, for example, [8]), this series of bands is attributed for phonon–magnon repetitions of the lowest–frequency transition ${}^6A_{1g} \longrightarrow {}^4T_{1g}$ in Fe^{3+}. Thus, the temperature-dependent absorption peak observed near 10 000 cm^{-1} for intermediate concentrations of V and Fe cannot be attributed to single-ion transitions in V^{3+} and Fe^{3+}.

Apart from the emergence of the additional absorption peak, the nonmonotonic change in the position of the fundamental absorption band edge is also nontrivial: with decreasing x, the edge is displaced to the long-wave region, but as x approaches zero, it is abruptly shifted to the short-wave region as in the case of $FeBO_3$.

4. ONE-ELECTRON CALCULATIONS OF FeB_6O_6 AND VB_6O_6 CLUSTERS

In order to explain qualitatively the obtained experimental results, the knowledge of the electron structure is essential. Since borates (like other oxide dielectrics with localized *d* electrons) belong to the class of systems with strong electron correlations, the standard one-electron band calculations using the density functional method in the local dipole approximation (LDA) are inapplicable. In this situation, *ab initio* one-electron calculations of molecular orbitals (MO) for finite clusters provide incomplete, but rather valuable, information on the degree of hybridization of various cation and anion orbitals, the parameters of their splitting in the crystal field, and dipole matrix elements for interband transitions. In spite of the fact that the absolute values of electron energies cannot be correct if we disregard strong correlations, their difference can be rightfully used for a qualitative analysis of experimental data.

An analysis of the electron structure of the given compounds was carried out using the Hartree–Fock method with the help of the GAMESS package [9]. In view of the absence of metallic properties in both compounds, cluster methods of calculations could be applied. The necessity of taking into account the exchange effects exactly in order to explain the magnetic properties of Fe and V ions dictated the application of the Hartree–Fock method.

As a model, we chose the FeB_6O_6 (VB_6O_6) cluster (Fig. 5). The central Fe (V) atom is surrounded by an octahedron of oxygen atoms. In view of the small separation (1.42 Å) between the oxygen and boron atoms and strong hybridization of their orbitals, the boron

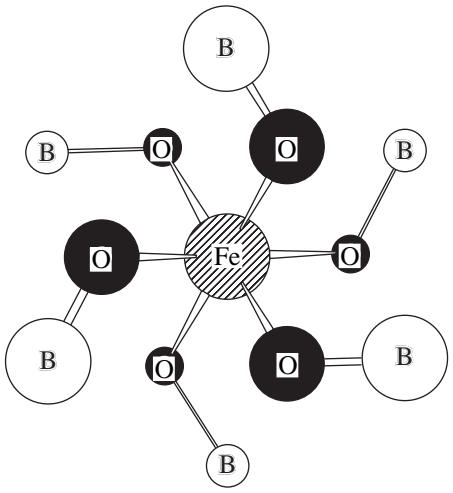

Fig. 5. Structure of the FeB_6O_6 (VB_6O_6) cluster being calculated.

atoms in the cluster had to be taken into account also. The chosen formula $Fe(V)B_6O_6$ of the cluster correctly describes the surroundings of the central metal atom in the first and second coordination spheres. In our calculations, we included the *s*, *p*, and *d* electrons of the cation; the *s* and *p* electrons of oxygen; and the *s* and *p* electrons of boron.

Since the effect of atoms from the next coordination spheres is disregarded in all cluster models, an additional charge *dZ* must be introduced into the cluster charge or *dZ* must be subtracted from the cluster charge. We chose the charge of the cluster under investigation equal to –3, since each boron atom has only one bond (with oxygen atoms), which corresponds to approximate occupancy of the *d* shell of the central atom of the metal.

The calculations for VB_6O_6 (even number of electrons) and for FeB_6O_6 (odd number of electrons) were carried out for a triplet and for a doublet, respectively. According to the results of calculations, the level corresponding to the highest occupied molecular orbital (HOMO) is formed by the *d* shell of the Fe (V) atom, which is weakly hybridized with other orbitals of the cluster. This is visually shown in Fig. 6 depicting the partial densities of states for both compounds. In these figures, the contributions from the *s*, *p*, and *d* electrons of the central metal atom; the *sp* shells of oxygen; and the *sp* shells of boron are presented successively from bottom to top. It can be seen that the *d* level for Fe lies much lower on the energy scale than in the shell of the V atom. This shift is apparently associated with the larger charge of the nucleus of the Fe atom, which lowers the energy of the *d* electron.

For both crystals, a weak *sp*–*d* hybridization of the *d* electrons of the cation and the *sp* states of the anion is observed. For VB_6O_6, a very small addition to the density of states from the 3*d* electrons can be seen in the energy range 1.1–1.3 eV, where the contributions from the *p*(V), *p*(O), *s*(B), and *p*(B) atomic orbitals dominate. In the HOMO region, one can see a very small contribution from the *p* orbitals of oxygen. The splitting of the HOMO peaks for VB_6O_6 by $\Delta E \approx 0.4$ eV corresponds to the splitting of the electron t_{2g} level due to the uniaxial crystal field component. For FeB_6O_6, the *p*–*d* hybridization is stronger than for vanadium, which is manifested in the larger height of the *d* peak of Fe in the partial density of states with an energy of 1.3 eV and the peak of the *d* states of oxygen in the HOMO. At the same time, strong hybridization of the *s* and *p* states of the cation with the *p* states of oxygen and *sp* states of boron takes place for both compounds; this hybridization determines the covalent component of the chemical bond as well as the optical absorption spectra.

The calculated energy levels and dipole matrix elements formed the basis for simulating the optical absorption spectra (Fig. 7). It can be seen that the absorption spectra for these compounds are completely

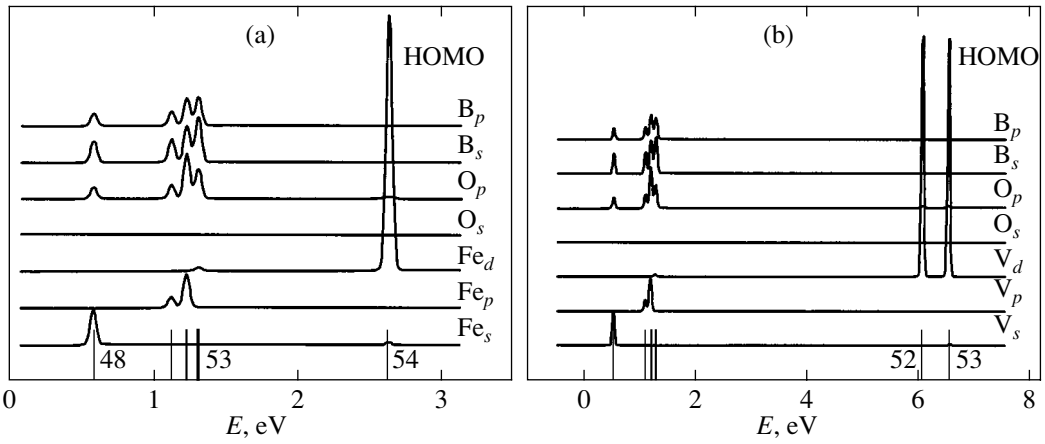

Fig. 6. Partial density of states for (a) FeB_6O_6 and (b) VB_6O_6 clusters. The lower scale shows the energy levels of molecular orbitals.

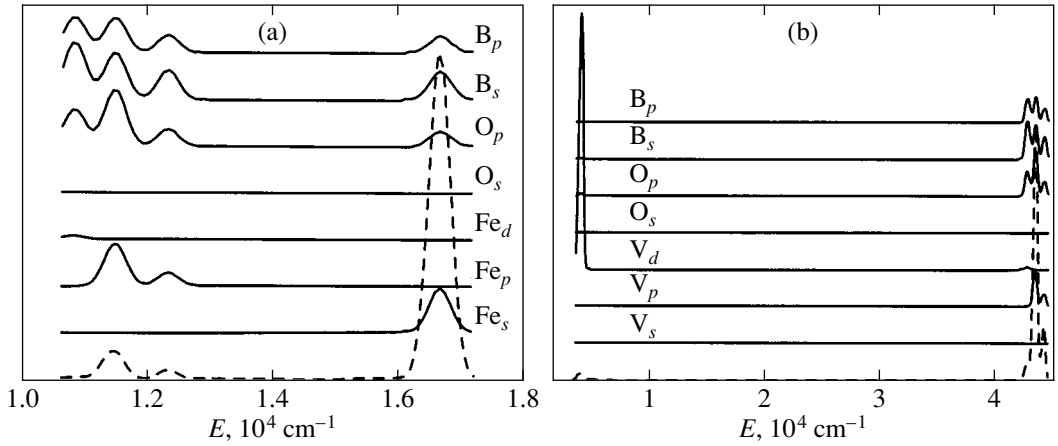

Fig. 7. Combined partial density of states relative to the HOMO level (solid curves) and optical absorption (dashed curves) for (a) FeB_6O_6 and (b) VB_6O_6 clusters.

different due to different positions of the *d* shell of the metal relative to other shells.

It can be seen from Fig. 7 that the optical absorption spectrum is determined by the dipole transitions from filled MO to partly filled HOMO. For FeB_6O_6, three absorption peaks repeating qualitatively the absorption spectrum of $FeBO_2$ [7] are observed in the energy range $(10–16) \times 10^3$ cm^{-1}: closely spaced peaks in the range $(1.1–1.25) \times 10^4$ cm^{-1} (Fig. 7a) correspond to the broad absorption peak for a $FeBO_3$ crystal with the center at 1.15×10^4 cm^{-1}, while the position of the peak at 1.65×10^4 cm^{-1} completely coincides with the experimental peak. Naturally, various types of interactions occurring in the crystal may lead to a renormalization of the spectrum. In view of the absence of fitting parameters in the calculations and the simplicity of the FeB_6O_6 cluster, we may conclude that the main contribution to partial densities of states and to the optical spectra is formed by the electron bonds in the first and second coordination spheres.

For VB_6O_6, high-intensity p–*d* transitions from the filled MO to the partly filled HOMO produce a high-intensity peak with an energy exceeding 4×10^4 cm^{-1}, which is beyond the range of our measurements. Weak *d*–*d* transitions allowed due to the cation–anion *p*–*d* hybridization lead to a low-intensity peak at 9800 cm^{-1}. A theoretical analysis leads to a similar low-intensity peak with the energy $\Delta E = 0.4$ eV, presented in Fig. 7b, which is determined by the splitting of the filled (band index $\lambda = 1$) and unfilled ($\lambda = 2$) parts of the t_{2g}orbitals in the crystal field. In this case, the intra-atomic Coulomb interaction between different orbitals in the t_{2g} configuration enhances this splitting. Indeed, the Hamiltonian of such an interaction can be written in the form

$$H^{12} = \varepsilon_1 n_{d1} + \varepsilon_2 n_{d2} + V_{12} n_{d1} n_{d2}, \qquad (1)$$

where $n_{d\lambda} = \sum c^{+}_{d\lambda\sigma} c_{d\lambda\sigma}$ is the operator of the number of *d* electrons at the λ level; $c_{d\lambda\sigma}$ is the annihilation operator for a *d* electron at the λ level with spin σ; and ε_1, ε_2, and V_{12} are the energies of molecular orbitals 1, 2 and the parameter of the Coulomb interaction between them. In the simplest mean-field approximation,

$$V_{12} n_{d1} n_{d2} \longrightarrow V_{12} n_{d1} \langle n_{d2} \rangle + V_{12} \langle n_{d1} \rangle n_{d2},$$

we obtain renormalized MO levels,

$$\tilde{\varepsilon}_1 = \varepsilon_1 + V_{12} \langle n_{d2} \rangle, \quad \tilde{\varepsilon}_2 = \varepsilon_2 + V_{12} \langle n_{d1} \rangle, \qquad (2)$$

and the transition energy

$$\Delta \tilde{E} = \varepsilon_2 - \varepsilon_1 + V_{12} (\langle n_{d1} \rangle - \langle n_{d2} \rangle). \qquad (3)$$

Since orbital 1 is filled ($\langle n_{d1} \rangle = 1$) and orbital 2 is empty ($\langle n_{d2} \rangle = 0$), the line in the absorption spectrum is determined not only by the splitting $\Delta E = \varepsilon_2 - \varepsilon_1$ in the crystal field, but also by the Coulomb interorbital matrix element. Considering that the typical value of V_{12} for 3*d* metal oxides is on the order of 1 eV, we obtain the shift of the theoretical peak depicted in Fig. 7b to the region of observable values.

5. DISCUSSION

The most adequate model of the electron structure of 3*d* metal borates, which describes the electric and magnetic properties on a unified basis, is the multiband Hubbard model taking into account different *d* orbitals explicitly as well as their interatomic overlapping and strong electron correlations $U \gg t$, where *t* is the jump integral. In this model, $FeBO_3$ with the $3d^5$ configuration for the Fe^{3+} ion is an analogue of the conventional orbital-nondegenerate Hubbard model with a half-filled band, in which the indirect exchange interaction $J \sim t^2/U$ through anions is of the antiferromagnetic type.

For VBO_3 with the d^2 configuration of the V^{3+} ion, we have one unfilled orbital in the t_{2g} shell, which, in the language of the Hubbard model, leads to a kinematic ferromagnetic exchange interaction. The separation between filled and unfilled t_{2g} orbitals (3) determines not only the peak in the optical absorption spectrum, but also the conduction activation energy $E_a \approx 0.9$ eV.

In solid solutions $V_xFe_{1-x}BO_3$, the average number of d electrons per cation is

$$n_d = 5(1-x) + 2x = 5 - 3x. \quad (4)$$

For a low Fe concentration in the range $2/3 < x < 1$, charge carriers are holes in t_{2g} states, which ensure the semiconductor-type conduction. The concentration $x_c = 2/3$ is critical in the sense that it corresponds to half the filling of the t_{2g} levels, i.e., to the t_{2g}^3 configuration. Considering that the e_g levels of d electrons lie above the t_{2g} levels by the cubic crystal field component, $10D_q \approx 3$–5 eV, we arrive at the conclusion that the t_{2g}^3 configuration is analogous to a half-filled band in the one-band Hubbard model, and strong electron correlations lead to the localization of charge carriers. Thus, a transition from the semiconductor-type conduction to the dielectric state occurs at concentration $x = x_c$. In view of composition disorder in solid solutions, the temperature dependence of the resistance near x_c at low temperatures is of the characteristic Mott type $\ln R \propto T^{1/4}$ corresponding to jumps with a varying jump length (see Fig. 3). As regards the magnetic properties, an additional integral of indirect exchange through the anions, which is responsible for the antiferromagnetic contribution as in the Hubbard model and for the additional scale in Fig. 1c, appears in the case of the half-filled t_{2g}^3 configuration. The approach described above corresponds to an averaged pattern. In the nonaveraged form, we can speak of the exchange integrals $I(V^{3+}$–$V^{3+})$ (ferromagnetic), $I(Fe^{3+}$–$Fe^{3+})$ (antiferromagnetic), and $I(V^{3+}$–$Fe^{3+})$ (antiferromagnetic). For $x \approx 0.5$ (including the range of $x \sim x_c$), the number of V^{3+}–Fe^{3+} pairs is maximum, and it is the interaction between such pairs which is apparently manifested in the form of the peak at $T = 150$ K (Fig. 1c).

In the other limiting case of a low vanadium concentration, the electron structure is determined by a superposition of the d^5 and d^4 configurations. The role of charge carriers may probably be played by holes from the e_g shell, but they are localized due to the small band width in view of weak cation–anion hybridization.

In order to interpret the optical absorption spectra in solid solutions, we calculate the spectrum of a virtual crystal consisting of independent absorbing $FeBO_3$ and VBO_3 centers using the formula

$$D(x) = xD(VBO_3) + (1-x)D(FeBO_3), \quad (5)$$

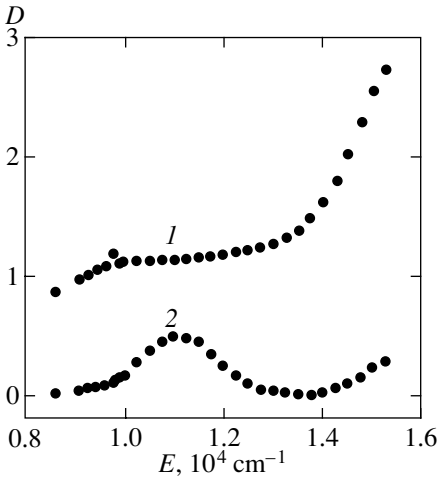

Fig. 8. Experimental absorption spectra for VBO_3 (*1*) and $FeBO_3$ (*2*) at $T = 300$ K.

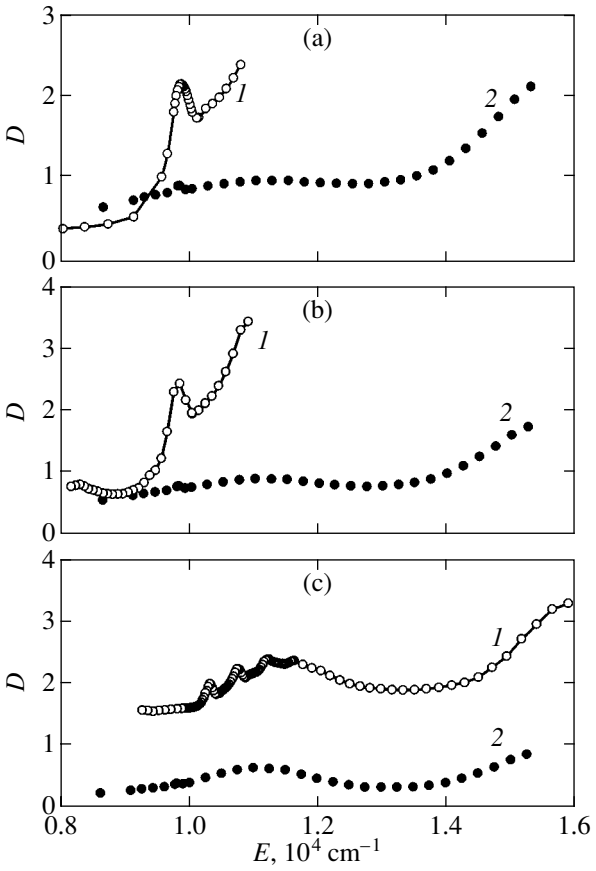

Fig. 9. Absorption spectra for (a) $V_{0.75}Fe_{0.25}BO_3$, (b) $V_{0.6}Fe_{0.4}BO_3$, and (c) $V_{0.25}Fe_{0.75}BO_3$: experimental curves *1* were obtained at $T = 300$ K (a, b) and $T = 90$ K (c); theoretical curves *2* correspond to $T = 300$ K.

where the $D(VBO_3)$ and $D(FeBO_3)$ spectra are taken from the experimental data for the initial single crystals (Fig. 8).

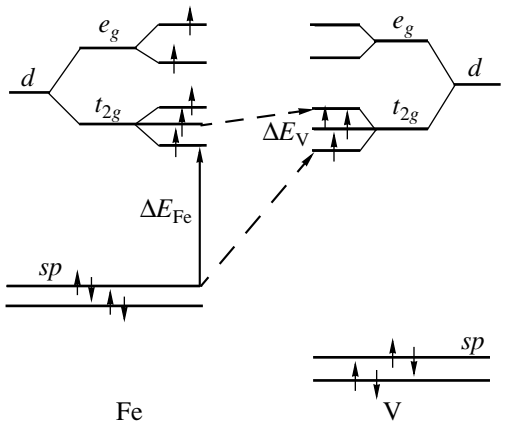

Fig. 10. Diagrams of molecular orbitals for $FeBO_3$ and VBO_3.

The experimental spectra with those calculated on the basis of formula (5) for the compositions $V_{0.75}Fe_{0.25}BO_3$, $V_{0.6}Fe_{0.4}BO_3$, and $V_{0.25}Fe_{0.75}BO_3$ are compared in Figs. 9a, 9b, and 9c, respectively. It can be seen from the figure that the positions of the experimental peaks are close to the corresponding peaks for the initial components, but the peak intensities are much higher than for the virtual crystal. The reason for the increase in the peak intensity is explained in Fig. 10 showing the diagrams of molecular orbitals for $FeBO_3$ and VBO_3, constructed on the basis of the numerical calculations of clusters in Section 4. The notation in the figure corresponds to the initial atomic orbitals of *d* electrons of the cation and the *sp* electrons of oxygen and boron; actually, molecular orbitals with small admixtures of states due to the *sp*–*d* hybridization are presented. Here, ΔE_{Fe} and ΔE_V are the energies of transitions between molecular orbitals of $FeBO_3$ and VBO_3, determining the absorption peaks at 11 000 and 9800 cm^{-1}, respectively. In addition to independent contributions to the spectrum in a solid solution (formula (5)), a mutual effect takes place when the unit cells of $FeBO_3$ and VBO_3 occupy neighboring positions. This effect is manifested in the enhancement of the *sp*–*d* hybridization, since the *sp* states of boron and oxygen belong simultaneously to the $FeBO_3$ and VBO_3 cells. This gives rise to additional optical transitions with energies ΔE_{Fe} and ΔE_V, which are depicted in Fig. 10 by inclined dashed lines and are responsible for the enhancement of peaks in the absorption spectrum as compared to the virtual crystal.

ACKNOWLEDGMENTS

The authors are grateful to A. F. Bovina who carried out X-ray measurements.

This work was supported by the Russian Foundation for Basic Research (project no. 99-02-17405).

REFERENCES

1. T. A. Bither, C. G. Frederick, T. E. Gier, *et al.*, Solid State Commun. **8**, 109 (1970).
2. H. Schmid, Acta Crystallogr. **17**, 1080 (1964).
3. B. Andlauer, J. Schneider, and W. Wettling, Appl. Phys. **10**, 189 (1976).
4. O. Müller, M. P. O'Horo, and J. F. O'Neill, J. Solid State Chem. **23**, 115 (1978).
5. M. P. O'Horo and O. Müller, J. Appl. Phys. **49**, 1516 (1978).
6. N. F. Mott, *Metal-Insulator Transitions* (Taylor & Francis, London, 1974; Nauka, Moscow, 1979).
7. V. N. Zabluda, A. V. Malakhovskiĭ, and I. S. Édel'man, Fiz. Tverd. Tela (Leningrad) **27**, 133 (1985) [Sov. Phys. Solid State **27**, 77 (1985)].
8. B. Andlauer, O. F. Schirmen, and J. Schneider, Solid State Commun. **13**, 1655 (1973).
9. M. W. Schmidt, K. K. Balridge, J. A. Boats, *et al.*, J. Comput. Chem. **14**, 1347 (1993).

Translated by N. Wadhwa

Journal of Experimental and Theoretical Physics, Vol. 94, No. 2, 2002, pp. 307–314.
Translated from Zhurnal Éksperimental'noĭ i Teoreticheskoĭ Fiziki, Vol. 121, No. 2, 2002, pp. 363–371.

SOLIDS
Structure

Calculations of the Complete Morphological Phase Diagram for Nonequilibrium Growth of a Spherical Crystal under Arbitrary Surface Kinetics

L. M. Martyushev[a, b, *], I. E. Kuznetsova[a], and V. D. Seleznev[b]

[a]*Institute of Industrial Ecology, Ural Division, Russian Academy of Sciences, Yekaterinburg, 620219 Russia*

[b]*Ural State Technical University, Yekaterinburg, 620002 Russia*

**e-mail: mlm@ecko.uran.ru*

Received July 6, 2001

Abstract—Complete morphological diagrams (with stable, metastable, and absolutely unstable regions) were calculated for the problem of morphology selection under the conditions of nonequilibrium growth of a spherical crystal taking into account arbitrary kinetic process rates at the boundary and a linear dependence of the growth rate on supersaturation. The consideration was performed by jointly using linear stability analysis and the principle of maximum entropy production. The principal difference between kinetically and diffusion-controlled crystal growth is the possibility of the coexistence of three or more morphological phases under the same conditions in the former case. It was shown that, at the transition point, the rate of accretion of the growing crystal mass increased in a jump. The jump value was studied as a function of the parameters of the problem. © *2002 MAIK "Nauka/Interperiodica".*

1. INTRODUCTION

Problems of structure formation under nonequilibrium crystallization conditions are extensively studied in view of their theoretical importance for the physics of open nonequilibrium systems. These problems are also of importance for practical applications in materials science. It has been found in many experimental and computer simulation studies that different morphological phases can coexist at the same thermodynamic parameters (for instance, supersaturation) that control nonequilibrium crystallization [1–5]. It has also been noted that the transition from one morphological phase to another is accompanied by a jump in either the crystal growth rate or its derivative [2–8]. Based on these observations, an analogy is often drawn between phase and morphological diagrams, and the concepts of first- and second-order morphological transitions are introduced [4, 8]. One of the most fundamental problems that arise in this context is the development of a theoretical apparatus that can be used in calculating and predicting the form of complete morphological diagrams (including metastable and labile region boundaries). No final solution to this problem has, however, been reported.

Based on an analysis of the problem of diffusion-controlled crystal growth from solutions, joint use of the principle of maximum entropy production and a linear morphological stability analysis was suggested in [9, 10] for the construction of morphological diagrams. The principal idea of these studies was that the use of the maximum entropy production principle [11] led to finding the binodal of a nonequilibrium morphological transition (the instability point with respect to small but finite perturbations) rather than the spinodal (the instability point with respect to infinitesimal perturbations). The maximum entropy production principle then becomes a complement rather than an alternative (as according to [12, 13]) to traditional perturbation theory and makes its own contribution to solving the problem of morphological selection. The strong point of the approach suggested in [9, 10] is the possibility of simple analytic calculations of morphological diagrams (with stable, unstable, and metastable regions), which allows the phenomenon of the coexistence of different morphological phases at the same thermodynamic parameters observed in many computer and physical experiments to be explained and described.

This approach was used in [9, 10] in considering the simplest problem of crystal growth on the assumption of infinitely fast kinetic processes on its surface. The purpose of this work was to apply the method suggested in [9, 10] to the problem of morphology selection in nonequilibrium growth of a spherical crystal with arbitrary surface kinetics. It was assumed that the growth rate was isotropic and linearly depended on supersaturation. This problem is an essential generalization of the one considered in [9, 10] and opened up the possibility in principle of describing numerous experimental data on the crystallization of quasi-isotropic systems.

1063-7761/02/9402-0307$22.00

2. LINEAR MORPHOLOGICAL STABILITY ANALYSIS

A linear stability analysis was earlier performed only for growth of spherical particles from melts [14]. As concerns growth of weakly distorted spherical particles from solutions, the problem has certain mathematical peculiarities and will therefore be briefly described.

The problem is formulated as follows.

(1) The most typical situation of isothermal-isobaric crystallization is considered; it is assumed that the solvent is completely displaced by the growing crystal. It is also assumed that the surface free energy and the kinetic coefficient are isotropic.

(2) The concentration field is described by the Laplace equation $\nabla^2 c = 0$; that is, it is assumed that the condition

$$\left|\frac{C_\infty - C_{\rm int}}{C - C_{\rm int}}\right| \le \left|\frac{C_\infty - C_0}{C - C_0}\right| \ll 1 \qquad (1)$$

is satisfied [15]. Here, C is the constant concentration of the solute in the crystal (in our approximation, the density of the crystal), and C_∞, $C_{\rm int}$, and C_0 are the concentrations of the solute far from the crystal and at the surface of an arbitrary type and the equilibrium concentration at a plane boundary, respectively.

(3) It is assumed than an arbitrary small distortion of the spherical particle can be represented as a superposition of spherical harmonics, and the behavior of a single spherical harmonic Y_{lm} is considered.

(4) The concentration in the solution satisfies the boundary conditions

$$c(\infty, t) = C_\infty, \qquad (2)$$

$$c(R + \delta Y_{lm}, t) = C_{\rm int}, \qquad (3)$$

$$V \equiv \dot R + \dot\delta Y_{lm} = \frac{D}{C}\frac{\partial c}{\partial r}\bigg|_{r = R + \delta Y_{lm}} = \beta\frac{C_{\rm int} - C_{\rm int\,eq}}{C}, \qquad (4)$$

where $\dot R \equiv dR/dt$, $\dot\delta \equiv d\delta/dt$, $R = R(t)$ is the radius of the sphere, t is the time, δ is the perturbation amplitude, V is the local growth rate, D is the diffusion coefficient, β is the kinetic crystallization coefficient, and $C_{\rm int\,eq} = C_{\rm int}(\beta \longrightarrow \infty)$ is the equilibrium solute concentration near the surface of an arbitrary type.

Boundary condition (4) is written on the assumption that the solute concentration is negligibly small compared with the crystal density; this assumption considerably simplifies the problem solution and is well satisfied for many real systems crystallizing from solutions. It is also assumed that the rate linearly depends on supersaturation, which is valid for the normal crystal growth mechanism or when supersaturation exceeds some critical value [16, 17].

Solving this problem in a linear approximation yields

$$C_{\rm int} = C_R + \frac{\delta Y_{lm} R_S^*}{2R^2}\frac{(C_\infty - C_0)(l-1)}{(1+\alpha\rho)(1+\alpha\rho(l+1))} \times [l + 2 + 2\alpha + l\alpha\rho], \qquad (5)$$

$$C_R = \frac{C_{R\,\rm eq} + C_\infty\alpha\rho}{1+\alpha\rho}, \qquad (6)$$

$$\dot R = \frac{C_\infty - C_{R\,\rm eq}}{C}\frac{D}{R(1+\alpha\rho)}, \qquad (7)$$

$$\dot\delta = \delta Y_{lm}\frac{D(C_\infty - C_0)(l-1)}{2CR^2(1+\alpha\rho)(1+\alpha\rho(l+1))} \times (2 - \rho(2 + (l+1)(l+2)) - \alpha\rho^2(l+1)(l+2)), \qquad (8)$$

where $\alpha = D/\beta R_S^*$, $R_S^* = 2\Gamma/\Delta$ is the critical nucleus radius, Γ is the surface tension coefficient, $\Delta = (C_\infty - C_0)/C_0$ is the relative supersaturation, $C_{R\,\rm eq} = C_0 + 2C_0\Gamma/R$ is the equilibrium solute concentration near a spherical surface, and $\rho = R_S^*/R$.

Using (8) and following [14, 15], it can be shown that infinitesimal perturbations increase when the radius of the crystal becomes larger than the critical radius (R_S^S),

$$R_S^S = 0.5R_S^*(1 + 0.5(l+1)(l+2)) \times \left[1 + \sqrt{1 + 2\alpha\frac{(l+1)(l+2)}{(1+0.5(l+1)(l+2))^2}}\right]. \qquad (9)$$

Equations (8) and (9) fully determine the stability of the growing spherical particle with respect to infinitesimal perturbations.

Equation (9) is, by definition, the equation of the spinodal of the stable (spherical) growth–unstable (dendrite-like, skeletal) growth morphological transition.

3. THERMODYNAMIC MORPHOLOGICAL STABILITY ANALYSIS

Let us apply the thermodynamic approach to analyzing the problem formulated above. Let $r^2 d\Omega dr$ be a volume element at distance $r \equiv r(\varphi, \theta, t) = R(t) + \delta(t)Y_{lm}(\varphi, \theta)$ from the center of the spherical crystal ($d\Omega$ is the solid angle). The Σ_S local entropy production of this solution volume element close to the surface then has the form [18]

$$\Sigma_S = j\nabla\mu r^2 dr d\Omega, \qquad (10)$$

where $\nabla\mu$ is the chemical potential gradient and j is the crystallizing component flux. We will restrict ourselves

to the dilute solution approximation, which is traditionally used in analyzing growth of crystals from solutions. According to [18], the $j\nabla\mu$ value can be written accurate to within a constant in the form

$$j\nabla\mu \sim D\frac{(\nabla c)^2}{c}. \tag{11}$$

Applying (4) allows the local entropy production in the volume element under consideration close to the surface to be written as

$$\Sigma_S \sim \frac{C^2V^2}{C_{\text{int}}D}r^2 dr d\Omega. \tag{12}$$

Following [9, 10], we can find the $\Delta\Sigma_S$ difference between the entropy productions in growth of perturbed and unperturbed spherical crystals. Using (12), we can write the equation for $\Delta\Sigma_S$ in the form

$$\Delta\Sigma_S \sim \frac{C^2}{D}\left\{\frac{V^2r^2}{C_{\text{int}}} - \frac{\dot{R}^2R^2}{C_R}\right\}dr d\Omega = \frac{C^2R\dot{R}}{C_RD} \times\left\{2Y_{lm}(R\dot{\delta} + \dot{R}\delta) - R\dot{R}\left(1 - \frac{C_R}{C_{\text{int}}}\right)\right\}dr d\Omega. \tag{13}$$

Equations (5)–(8) were used to numerically analyze (13). The results show that, at $Y_{lm}(\varphi, \theta) > 0$, the $\Delta\Sigma_S$ function increases in the $[R_S^*, R_S^S]$ interval of its possible variations as the crystal radius grows and passes zero at spherical crystal size R_S^b. It follows that, at crystal sizes larger than R_S^b, the entropy production at a perturbed surface is larger than the entropy production near the unperturbed crystal surface. Following [9, 10], the conclusion can be drawn that this point is the binodal of the morphological transition under study.

The plot of R_S^b variations depending on the parameter α value is shown in Fig. 1. This plot was constructed by numerically solving the $\Delta\Sigma_S = 0$ equation with the use of the MathCAD software. It follows from the results given in Fig. 1 that the R_S^b binodal radius decreases as α increases, most noticeably starting with $\alpha = 0.1$.

The principal difference between the present problem of morphology selection and that considered earlier [9, 10] is the absence of local equilibrium at the crystal–solution boundary in the general case. We cannot therefore use formulas of type (10) to calculate entropy production directly at the interphase boundary. Instead, the following equation should be used [18]:

$$\Sigma_S^{\text{int}} = j(\mu_{\text{int}} - \mu_{\text{eq}})r^2 d\Omega, \tag{14}$$

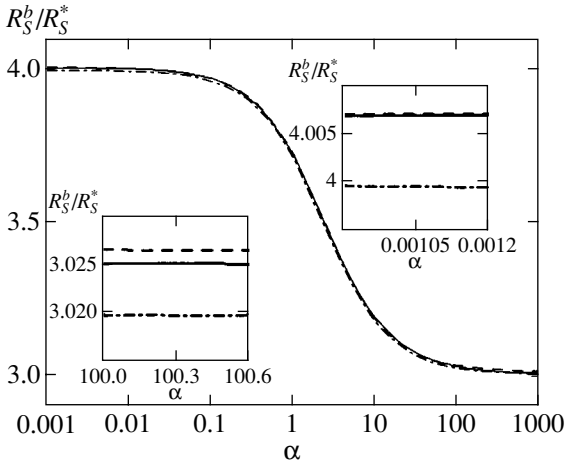

Fig. 1. R_S^b in R_S^* units as a function of parameter α. Solid curve corresponds to numerical solution of the $\Delta\Sigma_S = 0$ equation, where $\Delta\Sigma_S$ is defined by (13); dashed curve is numerical solution to the $\Delta\Sigma_S^{\text{int}} = 0$ equation; and dot-and-dash curve corresponds to analytic equation (17) for the binodal radius. The plots are given for $\Delta = 0.02$ and $l = 2$.

where μ_{int} and μ_{eq} are the chemical potentials of the solute with the C_{int} concentration and the $C_{\text{int eq}}$ equilibrium concentration, respectively.

Within an additive constant, the chemical potential in dilute solutions is related to the concentration as $\mu_{\text{int}} \sim \ln C_{\text{int}}$, and, for the flux, we have $j \sim CV$ (it is assumed that $C \gg c$). The $\Delta\Sigma_S^{\text{int}}$ difference between the entropy productions on the surface in growth of perturbed and unperturbed spherical crystals therefore takes the form

$$\Delta\Sigma_S^{\text{int}} \sim d\Omega C\left\{V(R + \delta Y_{lm})^2 \ln\frac{C_{\text{int}}}{C_{\text{int eq}}} - \dot{R}R^2 \ln\frac{C_R}{C_{R\,\text{eq}}}\right\} = d\Omega CR\left\{Y_{lm}(R\dot{\delta} + 2\dot{R}\delta)\ln\frac{C_R}{C_{R\,\text{eq}}} + R\dot{R}\ln\frac{C_{\text{int}}C_{R\,\text{eq}}}{C_RC_{\text{int eq}}}\right\}. \tag{15}$$

By analogy with the situation considered above, we can use (5)–(8) and (15) to determine the point at which $\Delta\Sigma_S^{\text{int}} = 0$. It does not follow from general nonequilibrium thermodynamics considerations that the binodals found by (13) and (15) should have equal values. What is more, numerical calculations show that the difference of these values becomes substantial at relative supersaturations exceeding 0.1 (see Fig. 2). At $\Delta < 0.1$, the solutions to the equations $\Delta\Sigma_S = 0$ and $\Delta\Sigma_S^{\text{int}} = 0$, however, coincide within 1% (see Fig. 1). It follows from the local maximum entropy production principle suggested in [9–11] that the presence in the system of perturbations of a sufficiently large amplitude causes the forma-

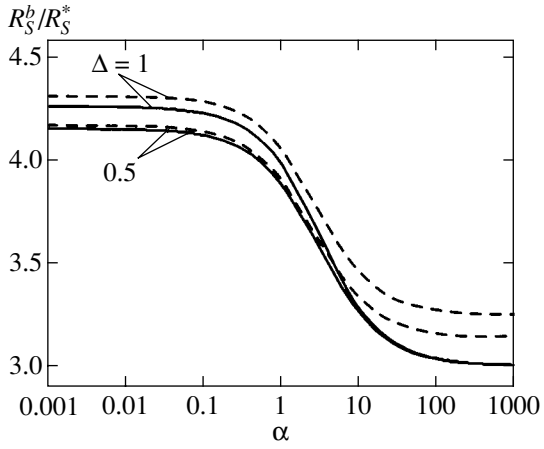

Fig. 2. Dimensionless binodal radii R_S^b/R_S^* as functions of parameter α at large supersaturations Δ. Solid curves correspond to numerical solutions of the $\Delta\Sigma_S = 0$ equation [see (13)], and dashed curves are numerical solutions to the $\Delta\Sigma_S^{\text{int}} = 0$ equation. The plots are given for $l = 2$.

tion of a state characterized by a local entropy production maximum. It appears that, in the absence of local equilibrium on the surface (that is, always except when crystal growth is diffusion-controlled) and at fairly large supersaturations, the determination of the binodal requires using expressions of type (15). A study of morphological transitions in this strongly nonequilibrium situation is a separate very interesting theoretical problem. It, however, follows from the results shown in Fig. 1 that the binodals found by both methods coincide in a fairly large region of supersaturations that are usually observed in experiments. At the same time, the approach based on (13) is less cumbersome and makes it possible to analytically obtain a fairly simple approximation to R_S^b, which is valid in the whole range of α variations and fairly accurately describes the numerical solution. For this reason, we only consider corollaries to the $\Delta\Sigma_S = 0$ equation in what follows.

As

$$1 - \frac{C_R}{C_{\text{int}}} = \delta Y_{lm}\Delta \times \frac{R_S^*(l-1)(l+2+2\alpha+\alpha l\rho)}{2R^2(1+\rho(\alpha+\Delta+\alpha\Delta))(1+\alpha\rho(l+1))},$$

(13) can be rewritten in the $\Delta \ll 1$ approximation in the form

$$\Delta\Sigma_S \sim 2l - \rho(l^3 + 2l^2 + l - 2 - 2\alpha(l+1)) - \rho^2\alpha l(l+1)^2. \quad (16)$$

In the $[R_S^*, R_S^S]$ interval of possible sphere radius variations, the $\Delta\Sigma_S$ function determined by (16) becomes positive starting with $R = R_S^b$,

$$R_S^b = (41)^{-1}R_S^*\{l^3 + 2l^2 + l - 2 - 2\alpha(l+1) + [(l^3 + 2l^2 + l - 2)^2 + 4\alpha^2(l+1)^2 + 4\alpha(l^4 + l^3 - l^2 + l + 2)]^{1/2}\}. \quad (17)$$

The R_S^b radius is shown by the dot-and-dash curve in Fig. 1. According to the insets in Fig. 1, the approximation that we use allows the exact numerical solution of the $\Delta\Sigma_S = 0$ equation to be described with high accuracy at low supersaturations. Indeed, the difference between the R_S^b value determined by (17) and that obtained by numerically solving the $\Delta\Sigma_S = 0$ equation does not exceed 3% at $\Delta \le 0.1$. The largest deviations for small perturbed harmonic numbers are observed for diffusion-controlled growth, and for large harmonic numbers, for kinetically controlled growth.

In the approximation of an infinitely fast surface kinetics ($\beta \longrightarrow \infty$), (17) becomes

$$R_S^{b\,\text{diff}} = (2l)^{-1}R_S^*[l^3 + 2l^2 + l - 2]. \quad (18)$$

The $R_S^{b\,\text{diff}}$ binodal radius coincides with that obtained in [10].

For kinetically controlled crystal growth ($\beta \longrightarrow 0$), the R_S^b binodal radius also tends to the $R_S^{b\,\text{kin}}$ asymptotic value,

$$R_S^{b\,\text{kin}} = 0.5R_S^*l(l+1). \quad (19)$$

The obtained spinodal (9) and binodal (17) equations were used to construct complete morphological diagrams.

4. MORPHOLOGICAL DIAGRAMS OF A SPHERICAL CRYSTAL GROWING UNDER NONEQUILIBRIUM CONDITIONS

The binodal and spinodal radii as functions of growth conditions are shown in Fig. 3 for various harmonics. Under diffusion-controlled conditions ($\alpha < 0.1$), metastable regions corresponding to different harmonics do not intersect. In the intermediate region ($0.1 < \alpha < 1$), the binodal of the $(l+1)$th harmonic and the spinodal of the lth harmonic approach each other, and, at $\alpha \approx 1$, they intersect; as a result, the metastable regions of neighboring harmonics overlap each other. A further increase in α can cause overlapping of three or more metastable regions. As a consequence, under intermediate and kinetically controlled spherical crystal growth conditions, the coexistence and development of a large number of crystals of different shapes (differ-

ent morphological phases) from a spherical nucleus is possible (for instance, for $\alpha = 150$, the coexistence of seven morphological phases is possible, and ten such phases can coexist if $\alpha = 500$).

The aforesaid is illustrated by the morphological diagrams shown in Figs. 4 and 5; these diagrams are constructed in the crystal size–supersaturation and surface tension–supersaturation variables for only two perturbed harmonics. A comparison of Fig. 4a with 4b and Fig. 5a with 5b shows that, whereas, at $\alpha = 0.001$, metastable regions do not intersect, the coexistence of three morphological phases (metastable spherical and two phases with developing perturbations corresponding to harmonics $l = 2$ and $l = 3$) is possible at $\alpha = 100$. It also follows from Fig. 4 that the binodal and spinodal radii sharply decrease as supersaturation grows.

Let us study crystal mass changes caused by the morphological transition from a spherical particle to a particle with developing perturbations. For this purpose, consider the difference between increments in the mass of a crystal (in other words, between substance fluxs from the solution to the crystalline surface) in the perturbed $(dN/dt)_p$ and unperturbed $(dN/dt)_n$ cases. As previously, mass changes will be calculated per unit time for volume element $r^2 d\Omega dr$ close to the surface of the crystal. Performing the calculations by analogy with what has been done above, we obtain

$$\begin{aligned}\left(\frac{dN}{dt}\right)_p - \left(\frac{dN}{dt}\right)_n &= (CVr^2 - C\dot{R}R^2)drd\Omega \\ &\sim (2\dot{R}\delta + R\dot{\delta})Y_{lm}drd\Omega \\ &\sim 2 - \rho(l(l+1) - 4\alpha) - \rho^2\alpha(l^2 + l + 2).\end{aligned} \tag{20}$$

This difference is an increasing function of crystal radius R and vanishes at

$$\begin{aligned}R_S^I &= 0.25R_S^* \\ &\times \{l(l+1) - 4\alpha + \sqrt{l^2(l+1)^2 + 16\alpha + 16\alpha^2}\}.\end{aligned} \tag{21}$$

The α dependences of the R_S^S, R_S^b, and R_S^I radii are shown in Fig. 6. No matter what conditions, the radius starting with which the mass of a crystal with a perturbed surface increases at a higher rate than that of an unperturbed crystal is always smaller than the binodal radius. As a consequence, the rate of mass accretion can only increase stepwise at the morphological transition point situated somewhere between R_S^b and R_S^S depending on the perturbation amplitude. Examples of the behavior of the rate of mass accretion and entropy production during a morphological transition directly at the binodal point are shown in Fig. 7. Note that the closer the crystal radius at which the morphological transition occurs to the spinodal radius, the larger the stepwise change in the rate of mass accretion. The question of whether this result is general in character or is determined by the boundary conditions that we use

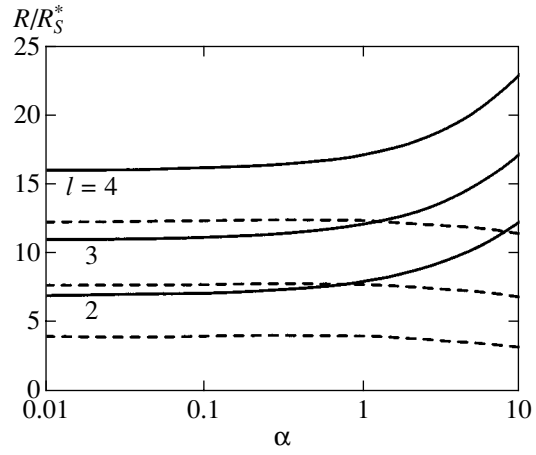

Fig. 3. Binodal and spinodal radii in R_S^* units as functions of α at various l values. Dashed curves are binodals, and solid curves are spinodals.

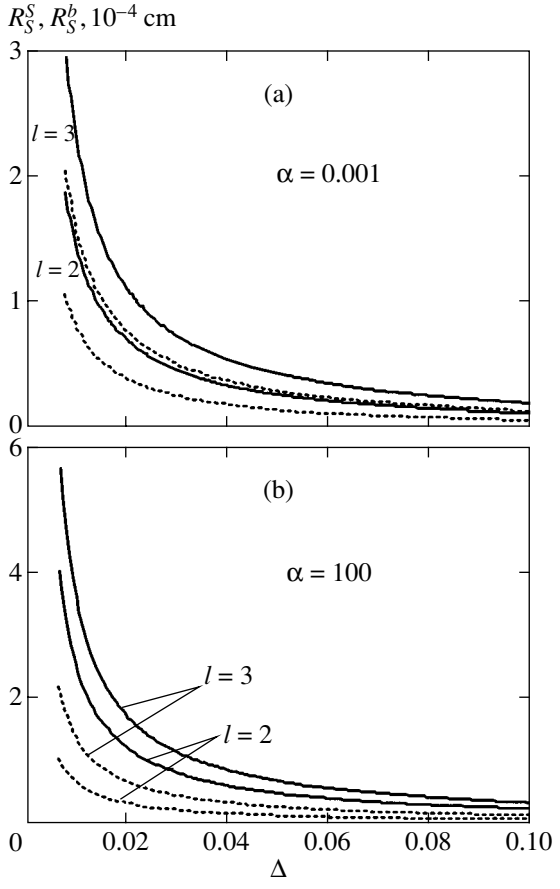

Fig. 4. Radii of morphological transition binodals R_S^b (dotted curves) and spinodals R_S^S (solid curves) as functions of relative supersaturation Δ. Stable growth is observed below the binodals, and absolutely unstable growth occurs above the spinodals; a metastable regions is situated between them. The plots are given for $\Gamma = 10^{-7}$ cm.

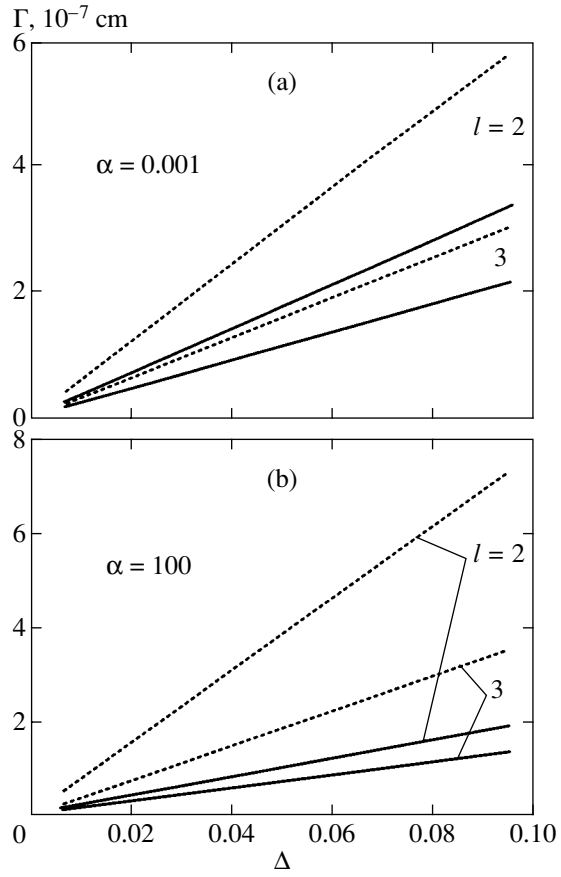

Fig. 5. Morphological phase diagram of stable (unstable) sphere growth in surface tension Γ—relative supersaturation Δ variables. Solid curves are spinodals, and dotted curves are binodals. Stable growth is observed above binodals, and absolutely unstable growth occurs below spinodals. Metastable regions are situated between them. The plots are given for $R = 5 \times 10^{-5}$ cm.

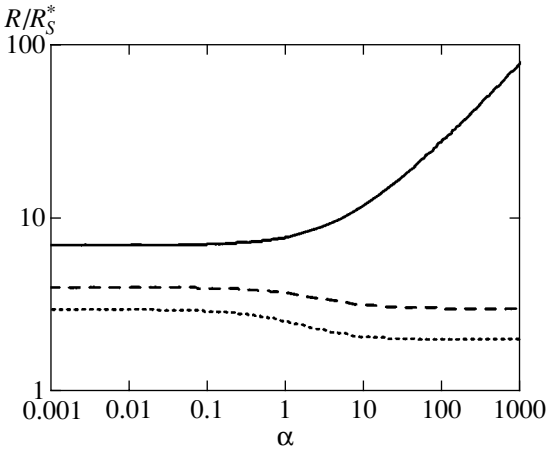

Fig. 6. Radii R_S^S (solid curve), R_S^b (dashed curve), and R_S^I (dotted curve) as functions of parameter α. The plots are given for $l = 2$.

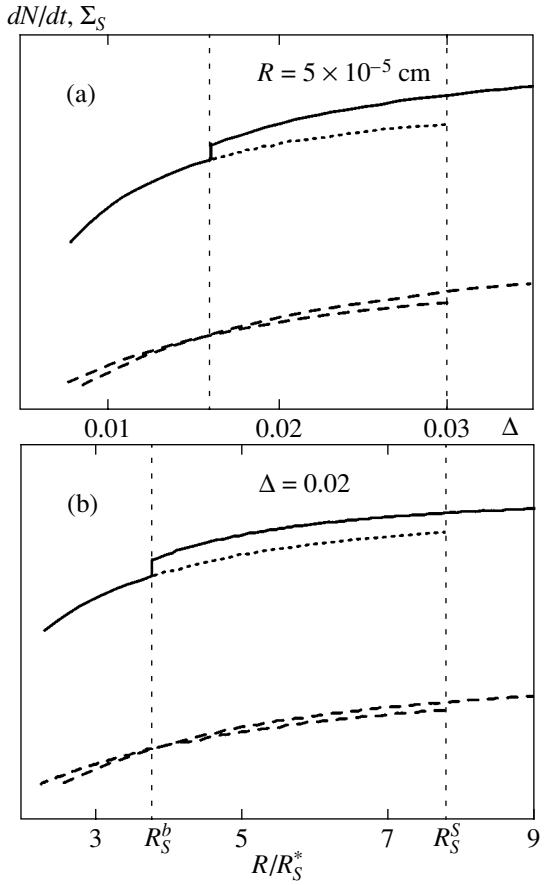

Fig. 7. Mass accretion rate dN/dt (solid and dotted curves refer to stable and metastable growth regions, respectively) and entropy production Σ_S (dashed curves) as functions of (a) supersaturation Δ and (b) crystal size R. The plots are given for α = 10 and $l = 2$.

(in particular, by the linear supersaturation dependence of the rate of crystal growth) and by the simplified solution model under consideration requires additional theoretical inquiries. Many experimental works [2–7] give evidence that the rate of crystal mass accretion increases with the thermodynamic force or with the crystal size. At the same time, an example of a morphological transition accompanied by a decrease in the growth rate was described in [8]. The results of this experiment are, however, very difficult to analyze because of a very special character of the system under consideration. Namely, the crystallization occurred from an anisotropic medium (from a smectic liquid crystal). As a result, changes in supercooling caused the appearance of numerous difficultly distinguishable anisotropic morphological phases.

The crystal size and supersaturation dependences of the rate of mass accretion near the morphological transition point constructed according to (17), (20), and (21) are shown in Figs. 8 and 9. Diagrams of the type shown in Fig. 8 are most convenient for interpreting experimental data on crystal mass changes during crystal growth when crystallization occurs from a solution

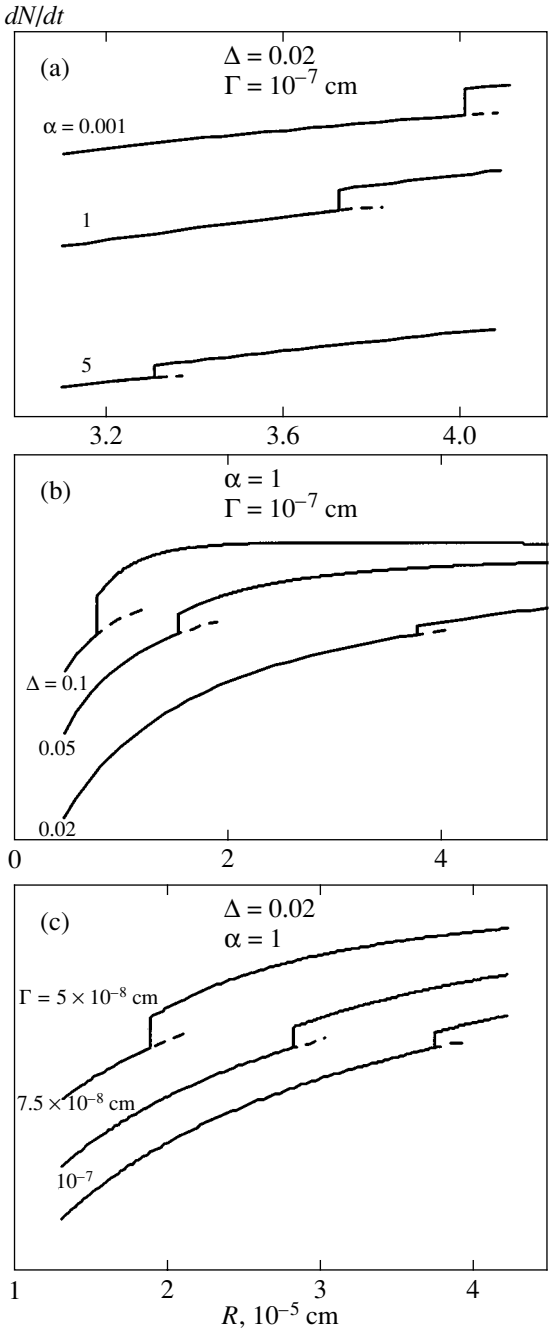

Fig. 8. Mass accretion rate dN/dt as a function of crystal size R close to the morphological transition point. The plots are given for $l = 2$.

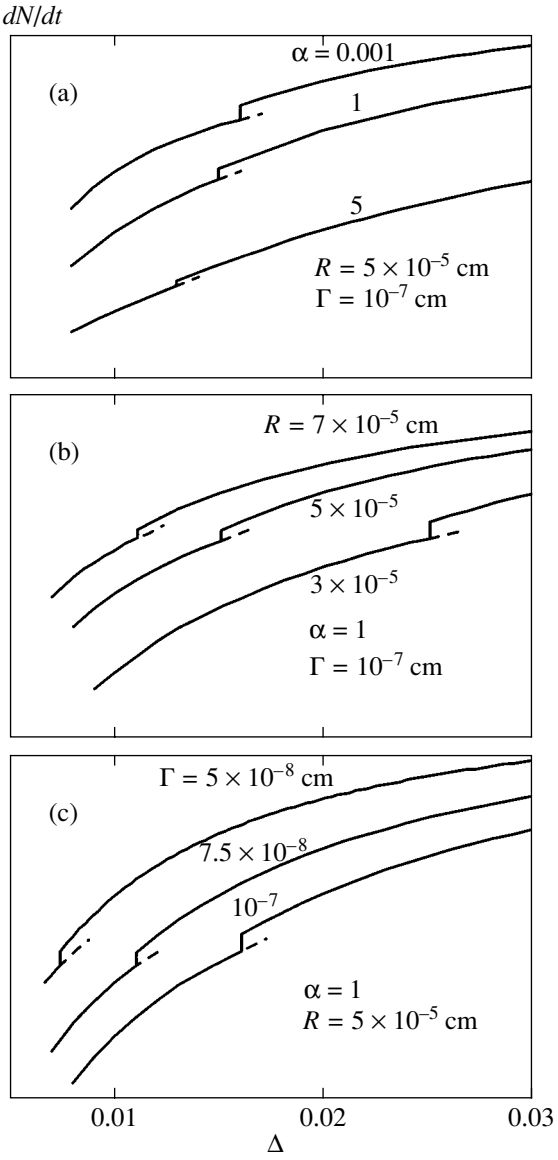

Fig. 9. Mass accretion rate dN/dt as a function of relative supersaturation Δ close to the morphological transition point. The plots are given for $l = 2$.

with certain initially set characteristics. Diagrams of the type shown in Fig. 9 are used in studies of growth rate and morphological phase type variations caused by changes in solution parameters at a constant crystal size.

An analysis of Figs. 8 and 9 shows that (a) the mass accretion rate jump decreases as the kinetic crystallization coefficient and supersaturation decrease or the crystal size and the perturbed harmonic number increase; (b) the rate jump shifts to lower supersaturations as the kinetic coefficient and surface tension decrease or the crystal size increases; and (c) the rate jump shifts to a smaller crystal size as the kinetic crystallization coefficient or surface tension decreases or supersaturation increases.

5. CONCLUSION

In this work, we considered the problem of morphology selection during nonequilibrium growth of a spherical crystal taking into account arbitrary kinetic process rates at the interface. For the first time, the complete morphological diagram (including stable, metastable, and absolutely unstable regions) was calculated

for different growth conditions with the use of the approach suggested in [9, 10]. The principal feature of the kinetically controlled growth in comparison to the diffusion-controlled process is the possibility of intersection of metastable regions corresponding to different perturbing harmonics and, as a consequence, the possibility of the coexistence of a large number of morphological phases under identical conditions. Another important peculiarity of the intermediate and kinetically controlled growth is a substantial broadening of the metastable region corresponding to the perturbing harmonic. This fact allows simpler quantitative experimental methods to be used to verify the theoretical approach suggested in [9, 10] and applied in this work to calculating the metastable behavior of a spherical particle growing from a solution under nonequilibrium conditions.

Because the problem considered in this work is fairly general in character, the results that we obtained can be very useful in other domains of science concerned with transitions between different structures under nonequilibrium conditions, especially, we believe, in handling biological morphogenesis problems [19].

REFERENCES

1. Y. Sawada, B. Perrin, P. Tabeling, *et al.*, Phys. Rev. A **43**, 5537 (1991).
2. O. Shochet, K. Kassner, E. Ben-Jacob, *et al.*, Physica A (Amsterdam) **187**, 87 (1992).
3. A. A. Shibkov, M. A. Zheltov, and A. A. Korolev, Priroda **9**, 12 (2000).
4. E. Ben-Jacob and P. Garik, Nature **343**, 523 (1990).
5. O. Shochet and E. Ben-Jacob, Phys. Rev. E **48**, R4168 (1993).
6. Mu Wang and Nai-ben Ming, Phys. Rev. Lett. **71**, 113 (1993).
7. S. K. Chan, H. H. Reimer, and M. J. Kahlweit, J. Cryst. Growth **32**, 303 (1976).
8. J. L. Hutter and J. Bechhoefer, Phys. Rev. E **59**, 4342 (1999).
9. L. M. Martiouchev and V. D. Seleznev, Dokl. Akad. Nauk **371** (4), 466 (2000) [Dokl. Phys. **45**, 129 (2000)].
10. L. M. Martiouchev, V. D. Seleznev, and I. E. Kuznetsova, Zh. Éksp. Teor. Fiz. **118**, 149 (2000) [JETP **91**, 132 (2000)].
11. H. Ziegler, in *Progress in Solid Mechanics*, Ed. by I. N. Sneddon and R. Hill (North-Holland, Amsterdam, 1963; Mir, Moscow, 1966), Vol. 4, Chap. 2.
12. M. E. Gliksman and S. P. Marsh, in *Handbook of Crystal Growth*, Ed. by D. T. Hurle (Elsevier, Amsterdam, 1993), Vol. 1B.
13. A. Hill, Nature **348**, 426 (1990).
14. S. Coriell and R. Parker, in *Proceedings of an International Conference on Grystal Growth, Boston, 1966*, Ed. by H. S. Peiser (Pergamon, Oxford, 1967; Mir, Moscow, 1968), p. 146.
15. W. W. Mullins and R. F. Sekerka, J. Appl. Phys. **34**, 323 (1963).
16. A. A. Chernov, E. I. Givargizov, Kh. S. Bagdasarov, *et al.*, in *Modern Crystallography* (Nauka, Moscow, 1980), Vol. 3.
17. V. A. Timofeeva, *Growth of Crystals from Solutions-Melts* (Nauka, Moscow, 1978).
18. S. R. de Groot and P. Mazur, *Nonequilibium Thermodynamics* (North-Holland, Amsterdam, 1962; Mir, Moscow, 1964).
19. B. N. Belintsev, Usp. Fiz. Nauk **141** (1), 55 (1983) [Sov. Phys. Usp. **26**, 775 (1983)].

Translated by V. Sipachev

Journal of Experimental and Theoretical Physics, Vol. 94, No. 2, 2002, pp. 315–328.
Translated from Zhurnal Éksperimental'noĭ i Teoreticheskoĭ Fiziki, Vol. 121, No. 2, 2002, pp. 372–387.

SOLIDS
Structure

Nonlinear Dynamics of Domain Walls with a Vortex Internal Structure in Magnetouniaxial Films with Planar Anisotropy

B. N. Filippov and L. G. Korzunin*
Institute of Metal Physics, Ural Division, Russian Academy of Sciences,
ul. S. Kovalevskoĭ 18, Yekaterinburg, 620219 Russia
**e-mail: filbor@imp.uran.ru*
Received July 20, 2001

Abstract—The nonlinear and generally unsteady dynamics of domain walls with a vortex internal structure in a constant magnetic field **H** is investigated on the basis of the numerical solution of the Landau–Lifshitz equation for a 2D distribution of magnetization **M** in magnetic films with planar anisotropy taking into account exactly the main interaction, including the dipole–dipole interaction. It is shown that in addition to field H_c (bifurcation field) above which the motion of a wall becomes unsteady and its internal structure experiences global dynamic changes, there exists a field H_0 separating two steady motions of the wall with different structures. The data clarifying the physical origin of the nonlinear dynamic rearrangement of the wall structure are presented. New rearrangement mechanisms associated with the generation and attenuation of vortices as well as their tunneling through the central surface of the wall are established. The existence of subperiod oscillations of the wall velocity in a static field in addition to the oscillations associated with the precession of **M** around the easy magnetization axis is predicted. The period T of dynamic variations of the wall structure is studied, and an empirical formula is proposed for describing the singular behavior of the $T(H)$ dependence near $H = H_c$ with the critical index depending on the film parameters. The bifurcation process is studied, and a nonlinear dependence of the critical field H_c on the film thickness and the saturation magnetization is established. The possibility of direct experimental investigation of the dynamic rearrangement of the internal structure of the wall is indicated. © *2002 MAIK "Nauka/Interperiodica".*

1. INTRODUCTION

The spin subsystem of magnetically ordered substances is very sensitive even to weak external effects. Under real conditions, this leads to nonlinear phenomena playing an important role in the physics of magnets. In particular, the dynamic properties of local formations of magnetization **M** such as domain walls play a fundamental role. The dynamic properties of domain walls can be described by the nonlinear Landau–Lifshitz equations [1].

In view of gyroscopic properties of elementary magnetic moments forming domain walls, the physical origin of the dynamic behavior of the walls cannot be reduced to a mechanical analogy. At the present time, the domain wall dynamics is successfully described by using the 1D model of magnetization distribution [2–4], leading to the classical structure of the walls with the rotation of magnetization in their planes (Bloch walls). However, the situation is complicated considerably for thin magnetic films in which the magnetization distribution is known to be non-one-dimensional (see, for example, [4, 5]) and the dipole–dipole interaction plays a significant role. For such films, only the wall dynamics in magnetically uniaxial films with transverse anisotropy and a large quality factor $Q = K/4\pi M_s^2$ (K is the magnetic anisotropy constant and M_s is the saturation magnetization) has been studied comprehensively [5, 7]. This is due to the fact that the dipole–dipole interaction in such films can be taken into account approximately.

We concentrate our attention on films with a planar anisotropy and a small Q factor. In these films, the dipole–dipole interaction plays the leading role in both static and dynamic properties of domain walls. For this reason, this interaction must be taken into account exactly whenever possible. It is due to the dipole–dipole interaction that the domain wall structure in such films is not one-dimensional and is of the asymmetric vortex type [8, 9]. At the present time, the existence of such walls has been confirmed experimentally [10–12]. As a domain wall with a vortex internal structure moves under the action of an external magnetic field **H** applied along the easy magnetization axis (EMA), the vortex in the wall is displaced towards one of the film surfaces. Clearly, the dynamic properties of such an object can be studied neither on the basis of the above-mentioned 1D models nor on the basis of the models developed for describing the dynamics of walls with transverse anisotropy. In the films under investigation, we in fact encounter a very interesting object from the viewpoint of nonlinear physics, viz., a topological soliton with internal degrees of freedom. The analysis of the wall dynamics in such films is of considerable practical

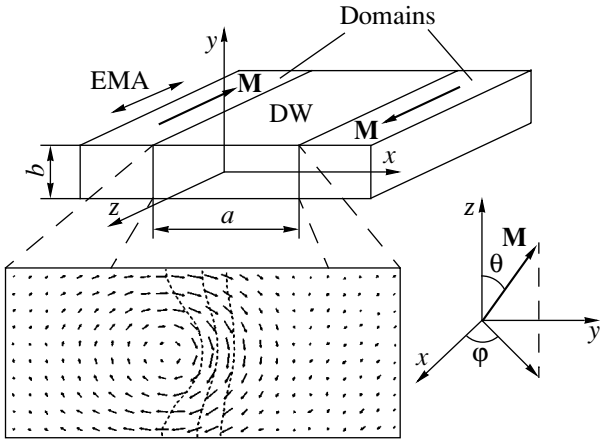

Fig. 1. Geometry of the problem and an example of equilibrium configuration of an asymmetric (one-vortex) Bloch wall. The arrows indicate the projections of relative magnetization **u** on the *xy* plane. The domain wall (DW) structure is obtained for basic films of thickness $b = 0.05$ μm.

importance in connection with the improvement of the heads for high-frequency recording (reading) of high-density information.

The first publication in which direct computational methods were used to consider dynamic transformations of the structure of a moving domain wall taking into account meticulously the main interactions in a 2D model of the distribution of magnetization **M** in the steady-state and unsteady modes belongs to Yuan and Bertram [13]. They proved that a transition from one mode to the other occurs at a certain value of the external magnetic field $H = H_c$ (H_c is the bifurcation, or critical, field). It was found that a dynamic rearrangement of the internal structure of the domain wall takes place for $H > H_c$. The mechanism of such a rearrangement includes the transformation of an asymmetric Bloch wall to an asymmetric Néel wall and back with simultaneous variation of the chirality of the domain wall vortex.

These results correspond to the motion of a domain wall away from the critical field. For this reason, the physical nature of the transition from a steady-state motion of the wall to an unsteady motion (the nature of the bifurcation process) occurring in this case and the effect of the magnetic properties of the film on this process remains unclear. The related questions whether or not the mechanism of the transition of the wall to the state of unsteady motion is universal and, if not, how the change in the film parameter may alter this mechanism call for further investigations. The parameters of the periodic rearrangement of the internal structure of the wall (in particular, its period) and the characteristics of possible subperiod oscillations of the dynamic structure of the walls have not been investigated either. Moreover, such oscillations were not detected earlier. The present article is devoted to the description of the results of such investigations carried out on the basis of direct numerical calculations in the framework of a 2D model of magnetization distribution using a rigorous micromagnetic approach. We propose an "empirical" formula for the period of the dynamic rearrangement of a domain wall, which clarifies the pattern of the nonlinear movement of domain walls with internal degrees of freedom in the range of fields $H > H_c$. We also describe the new mechanisms of nonlinear dynamic rearrangement of the wall structure, discovered by us and modifying considerably the concept of a bifurcation process.

2. FORMULATION OF THE PROBLEM AND METHODS OF ITS SOLUTION

Let us consider a magnetouniaxial film of thickness *b* with the plane of the surface parallel to the *xz* plane and with the EMA oriented along the *z* axis (Fig. 1). We assume that the magnetic state of the film corresponds to two domains with the saturation magnetizations $+\mathbf{M}_s$ and $-\mathbf{M}_s$ oriented along the $+z$ and $-z$ axes, respectively, for $x > -a/2$ and $x < a/2$. We also assume that a domain wall is located in region *V* having the rectangular cross section *D* in the *xy* plane and the size *a* along the *x* axis. Let the magnetization in *D* be $\mathbf{M} = \mathbf{M}(x, y)$, which corresponds to a 2D model of distribution of **M**.

In order to solve the problem, we first define the equilibrium configuration of a wall and then consider its evolution in time.

In the 2D model, the equilibrium configurations of a domain wall and the minimum energies γ_0 corresponding to them can be determined through a numerical minimization of the functional

$$\gamma_D = \iint_D \left\{ \frac{A}{M_s^2}\left[\left(\frac{\partial \mathbf{M}}{\partial x}\right)^2 + \left(\frac{\partial \mathbf{M}}{\partial y}\right)^2\right] - \frac{K}{M_s^2}(\mathbf{M}\cdot\mathbf{c})^2 - \frac{1}{2}\mathbf{M}\cdot\mathbf{H}^{(m)}\right\} dxdy \quad (1)$$

per unit length (along *z*). In formula (1), the first, second, and third terms in the braces are the densities of the exchange energy, magnetic anisotropy energy, and dipole–dipole (in the continual approximation) energy; *A* is the exchange parameter; **c** is a unit vector along the EMA; and $\mathbf{H}^{(m)}$ is the magnetostatic field which can be determined from the equations of magnetostatics with the conventional boundary conditions.

We will solve the problem using the constancy of the magnetization modulus ($\mathbf{M}^2 = \text{const}$) and the following conditions at the boundaries of the rated region:

$$\left[\mathbf{M}\times\frac{\partial \mathbf{M}}{\partial x}\right]_{y = \pm b/2} = 0, \quad (2)$$

$$M_z\big|_{x=\pm a/2} = \pm M_s,$$
$$M_x\big|_{x=\pm a/2} = M_y\big|_{x=\pm a/2} = 0. \quad (3)$$

To carry out numerical minimization, we divide the rated region D into small meshes by a rectangular network. The region V in this case is divided into parallelepipeds extended along the z axis, whose lateral faces are parallel to the coordinates planes xz and yz. We assume that meshes have a macroscopic but small size so that the direction of vector $\mathbf{u} = \mathbf{M}/\mathbf{M}_s$ can be regarded as constant at all points of each parallelepiped. Vector $\mathbf{u}$ = const along z (2D model). The orientation of $\mathbf{M}$ in domain D changes upon a transition from one mesh to another. The details of the model can be found in [14, 15].

We used networks with different number of meshes and with different ratios a/b. The maximum number of meshes was 90×30. A larger number of meshes would strongly increase the counting time without changing the results significantly. The a/b ratio was varied in the interval $1 \le a/b \le 6$. As the basis, we choose the parameters

$$A = 10^{-6}\ \text{erg/cm}, \quad K = 10^3\ \text{erg/cm}^3,$$
$$M_s = 800\ \text{Gs},$$

which are typical of permalloy films. The criterion determining the end of counting was chosen in accordance with [16].

By way of an example, Fig. 1 shows a stable structure known an asymmetric Bloch wall (which was predicted in [8]). Other 2D structures also exist but prove to be metastable except in some special cases (see [4, 14, 17]). Periodic structures with domain walls of this type were considered in [18].

Figure 1 shows the distribution of $\mathbf{u}$ in the xy plane perpendicular to the film surface and to the EMA. It can be seen that the component of $\mathbf{M}$ changes upon a transition from one domain to another so that a magnetization vortex is formed in the xy plane. The z component of $\mathbf{M}$ changes as we pass from a domain to its neighbor. On the central dashed curve ($y = y_0(x)$), the value of $u_z = 0$ (wall center). Thus, at different depths of the film, the wall center corresponds to different coordinates x. The asymmetry of this curve relative to the y axis is responsible for this wall being referred to as asymmetric. The other two curves are level lines M_z = const, between which the direction of $\mathbf{M}$ changes by approximately 60°.

An analysis of the nonlinear dynamics of the domain wall was based on the numerical solution of the Landau–Lifshitz equation written in the form

$$(1+\alpha^2)\frac{\partial \mathbf{u}}{\partial \tau} = -[\mathbf{u}\times\mathbf{h}_{\text{eff}}] - \alpha[\mathbf{u}\times[\mathbf{u}\times\mathbf{h}_{\text{eff}}]], \quad (4)$$

where $\tau = \gamma M_s t$, t is the real time, γ is the gyromagnetic ratio, α is the Hilbert damping parameter, and $\mathbf{h}_{\text{eff}}$ is the dimensionless effective field defined as

$$\mathbf{h}_{\text{eff}} = \mathbf{h}_e + \mathbf{h}^{(m)} - k_A(\mathbf{u}\cdot\mathbf{c})\mathbf{c} + \mathbf{h}, \quad (5)$$

where

$$\mathbf{h}_e = \frac{\partial^2 \mathbf{u}}{\partial \xi^2} + \frac{\partial^2 \mathbf{u}}{\partial \eta^2},$$
$$\mathbf{h}^{(m)} = \mathbf{H}^{(m)}/M_s, \quad h = \mathbf{H}/M_s,$$
$$k_A = 2K/M_s, \quad \xi = x/b_0,$$
$$\eta = y/b_0, \quad b_0 = \sqrt{A/M_s^2}.$$

Equation (4) was solved numerically taking into account conditions (2) and (3) by choosing the same spatial mesh as for the minimization of the γ_D functional. We used the predictor-corrector method [19]. At instant $\tau = 0$, the $\mathbf{u}_0$ distribution is defined, which is determined through the numerical minimization of the energy (1) of the domain wall. At the first stage, iteration u_{n+1} is defined in accordance with formula

$$\mathbf{u}^*_{n+1} = \mathbf{u}_n + \Delta\tau\mathbf{f}(\tau_n, \mathbf{u}_n) \quad (6)$$

(predictor), where

$$\mathbf{f}(\tau_n, \mathbf{u}_n) = -\frac{\Delta\tau}{1+\alpha^2}$$
$$\times([\mathbf{u}_n\times\mathbf{h}_{\text{eff}}(\mathbf{u}_n)] + \alpha[\mathbf{u}_n\times[\mathbf{u}_n\times\mathbf{h}_{\text{eff}}]]).$$

At the second stage, the procedure to the final determination of $\mathbf{u}_{n+1}$ is applied:

$$\mathbf{u}_{n+1} = \mathbf{u}_n + (\Delta\tau)\mathbf{f}(\tau_n, \mathbf{u}^*_{n+1}) \quad (7)$$

(corrector).

The time step $\Delta\tau$ is chosen to be either constant, or variable if the maximum angle of rotation of the magnetization vector in the meshes is bounded by a certain small number.

It is envisaged that, at any instant, random perturbations of any amplitude can be introduced and that the start is possible from any configuration of $\mathbf{M}$. This enables us to judge the stability of the obtained solutions.

In order to exclude the emergence of the wall at the boundary of the rated region V, we make allowance for a displacement of this region during the motion of the wall. The displacement of the "center of gravity" of the wall is traced thereby. For the wall "mass," we choose the quantity $u_x^4 + u_y^4$ assuming the highest values on the central line of the domain wall.

The procedure described above and aimed at the preliminary determination of the equilibrium distribution of $\mathbf{M}$ rapidly leads to stable solutions.

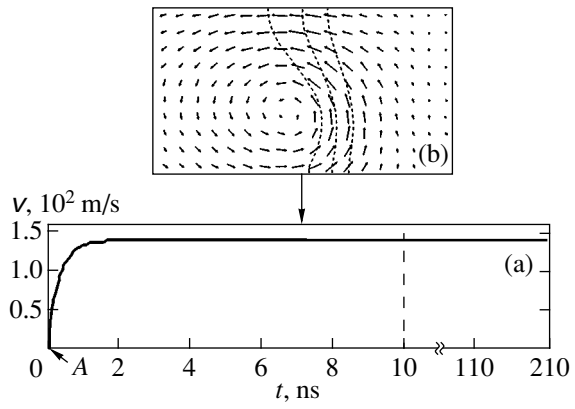

Fig. 2. (a) Dependence of the average (corresponding to the motion of the center of gravity) velocity of a domain wall on time t and (b) the instantaneous configuration of magnetization for steady motion of the wall. At the initial moment (A), the **M** configuration is identical to that depicted in Fig. 1. Basic films have the following parameters: $b = 0.05$ μm, $\alpha = 0.1$, and $H = 80$ Oe.

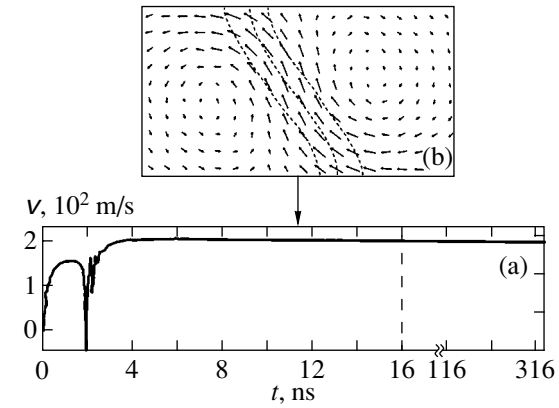

Fig. 3. The same as in Fig. 2 but for $H = 99$ Oe. For $0 < t < 2$ ns, the wall structure is similar to that in Fig. 2b.

3. ORIGIN OF DYNAMIC TRANSFORMATION OF THE DOMAIN WALL STRUCTURE

It was proved in [13] that there exists a certain critical value H_c of the external magnetic field. In fields $H < H_c$, the motion of a wall after the completion of the unsteady process associated with the application of the field is steady. The changes in its structure are reduced to the displacement of the magnetization vortex, which was initially localized at the center of the film, to one of the surfaces in the dynamic mode. The direction of the displacement depends on the direction of the external field **H** oriented along the EMA. We established that, under certain conditions, there also exists another mode of steady motion (see below). In fields $H > H_c$, the motion of the domain wall becomes complex (its velocity becomes variable), which is connected with a complex dynamic transformation of the internal structure of the wall.

In order to find the physical reasons for dynamic transformations of the internal structure of the wall, we calculated the instantaneous configurations of magnetization **M** for fields close to critical. We also determined the time dependences of the velocities for various points of the wall and of angle φ (see Fig. 1). The final data are displayed on a monitor in the form of videofilms which make it possible to trace the features of the dynamic changes in the wall structure. By way of an example, Figs. 2–4 show the time dependences of the mean velocities v of the walls (corresponding to the motion of the "center of gravity") and some instantaneous configurations of the wall. The results were obtained for basic films with $b = 0.05$ μm and $\alpha = 0.1$. It was found that the critical field H_c is approximately equal to 99.3 Oe.

Figures 2 and 3 correspond to a steady motion of the wall (after the completion of unsteady processes). A comparison of these figures indicates that the form of the steady motion changes as H approaches the field H_c. It can be seen that a wall moving steadily in the field $H = 80$ Oe has the asymmetric Bloch structure, while, in the field $H = 99$ Oe, the structure is completely different and is known as the asymmetric Néel structure [4]. Thus, in a certain field $H_0 < H_c$, the structure of a steadily moving wall may be rearranged. In the course of the rearrangement process, the steady motion of the wall is violated. In order to understand the reason for the emergence of this effect, it should be borne in mind that the motion of the wall indicates the magnetization rotation from its direction in one domain to the direction in another domain. Under the action of the field applied along the EMA, such a rotation is possible if additional magnetostatic fields are created, leading to the precession of **M** around the x axis (in the middle layers of the film) or around the y axis in the surface layers. The presence of these fields gradually distorts the domain wall structure and generally leads to an increase in the angle φ_a averaged over the film thickness. For a certain value of the field $H = H_0$, the structure of an antisymmetric Bloch wall cannot ensure any further increase in φ_a, and the wall undergoes an appropriate rearrangement. Field H_0 turns out to be a function of the parameters of the film and its thickness. An analogous rearrangement of the wall structure during its inertial motion was predicted in [4].

It follows from Fig. 4 that, in fields $H > H_c$, the velocity of the wall and its structure vary periodically with time. Among other things, it can be seen that an asymmetric Bloch wall a is transformed, through a state b with a displaced vortex, to an asymmetric Néel wall c which is again transformed (through a structure close to a simple Néel wall d) to the structure of an asymmetric Néel wall e, but with the slope of the central line opposite to that in the case c. This structure is transformed (through stage f) into an asymmetric Bloch structure (at point A) of type a, but with the opposite chirality. This completes the half-period of the change in the domain

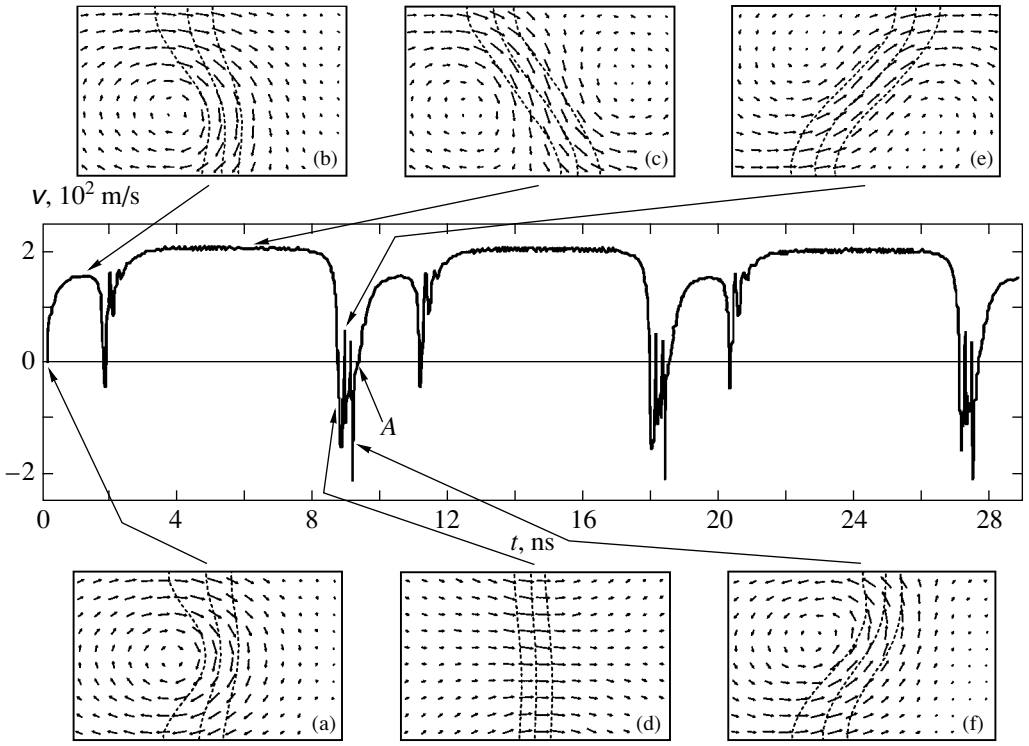

Fig. 4. Example of the time dependence of the average (in the above sense) velocity of a domain wall in the field region $H > H_c$ (unsteady motion) and instantaneous configurations (a)–(f) of the wall structure. Basic films with $b = 0.05$ μm, $\alpha = 0.1$, and $H = 100$ Oe are considered.

wall structure. During the second half-period, similar transformations take place and the wall structure becomes identical to case *a* by the end of this time interval.

In order to clarify the physical origin of the emergence of the unsteady motion of the wall and the dynamic rearrangement of its structure, we determined the angle $\varphi(t)$ for $H = 80$, 99, and 150 Oe. The $\varphi(t)$ dependence describes an additional (as compared to the equilibrium static state) emergence of magnetization from the *yz* plane, which is known to be connected [2, 3] with the formation of a magnetostatic field $H_x^{(m)}$ around which the magnetization precession takes place, causing the motion of the wall along *x*.

In the 2D model of **M** distribution under investigation, angle $\varphi(t)$ is a function of coordinate *y*. We made calculations for three values of $y = 0, \pm b/2$, i.e., for the central plane of the film and for its surfaces. For $H = 80$ Oe, when the first type of steady motion of the domain wall takes place, all three values of $\varphi(t)$ become time-independent after a certain short-term unsteady process and remain different in magnitude. For $H = 99$ Oe, when, in accordance with Fig. 3, we have a steady motion of the second type, the three $\varphi(t)$ curves converge and become time-independent after the rearrangement of an asymmetric Bloch wall into an asymmetric Néel wall. For $H > H_c$ (Fig. 5), angle $\varphi(t)$ increases indefinitely. Consequently, in fields $H > H_c$, the magnetization starts precessing around the EMA in addition to the other type of precession of **M** associated with the motion of the wall. As in the case of a domain wall with a 1D distribution of **M**, this leads to the situation where, during certain time intervals, the wall moves oppositely to the initial direction (backward motion of the wall). In this case, the motion of the wall remains unidirectional on the average over the period of velocity variation.

Thus, in spite of the fact that a domain wall can be regarded as a certain macroscopic object possessing an effective mass, its dynamic behavior differs radically from the behavior of other objects in view of the gyroscopic properties of elementary magnetic moments forming the wall. In contrast to the 1D model, the precession around the EMA emerging in a wall with a 2D distribution of **M** is nonuniform (see Fig. 5). Considering that the precession of **M** around the EMA emerges only as a result of violation of the balance of the torques (see, for example, [2]), we may conclude that the emergence of a nonlinear dynamic rearrangement of the wall structure is associated precisely with the violation of the balance of the torques in fields $H = H_c$ and higher.

Thus, the deep-rooted physical reason for the dynamic rearrangement of the domain wall structure is

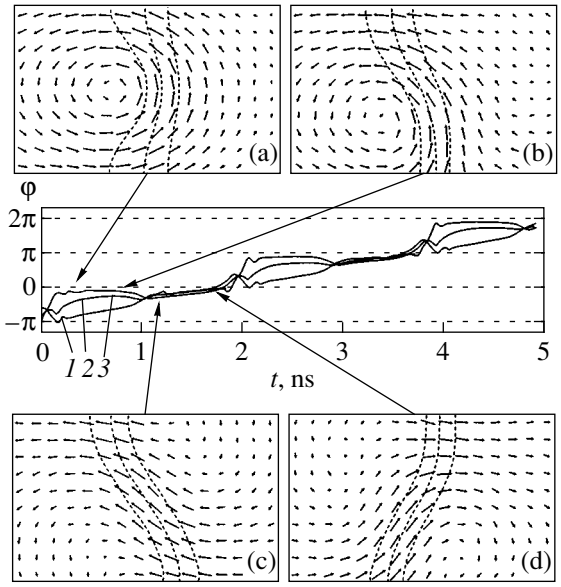

Fig. 5. Time dependence of angle φ in three planes of the film: $y = -b/2$ (*1*), $y = 0$ (*2*), and $y = b/2$ (*3*); (a)–(d) are instantaneous configurations of the wall. Basic films with $b = 0.05$ μm, $\alpha = 0.1$, and $H = 150$ Oe are considered.

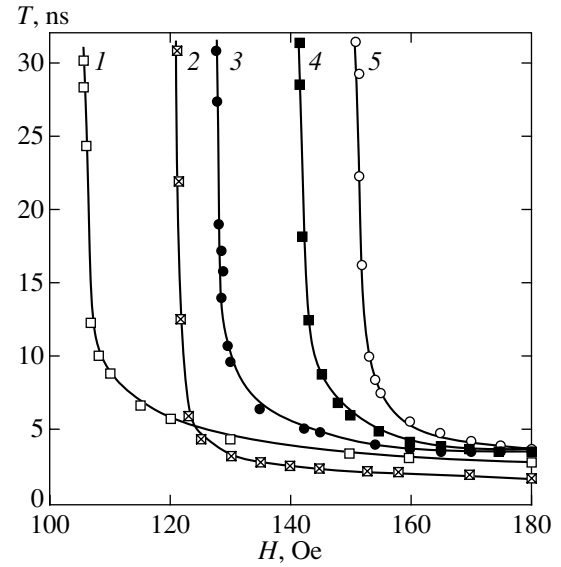

Fig. 6. Example of the field dependence of the period T of dynamic rearrangement of domain walls for films with $\alpha = 0.1$ and different parameters: $K = 10^5$ erg/cm^3, $b = 0.05$ μm (*1*); $b = 0.08$ μm (*2*); $b = 0.055$ μm (*3*); $K = 10^6$ erg/cm^3, $b = 0.05$ μm (*4*); $M_s = 900$ G, $b = 0.05$ μm (5). The missing parameters correspond to the basic values. Symbols correspond to the results of numerical experiments. Solid curves are plotted for better visualization.

the same for walls with 1D and 2D configurations of the **M** distribution.

The transformations of the wall structure described above were predicted for the first time in [13]. We will refer to such transformations as classical. In spite of the fact that the dynamic rearrangement of the wall structure is similar to that in [13], the velocity variation obtained by us is noticeably different. This is due to the fact that, in contrast to [13], our results were obtained in fields close to the bifurcation field. These differences indicate a considerable change in the behavior of the wall velocity with time as the external field approaches the value H_c. As the field H decreases (for $H > H_c$), the wall preserves the asymmetric Néel structure over longer and longer time intervals. Such a behavior of the domain wall matches the emergence of the second type of steady motion depicted in Fig. 3 in the field range $H < H_c$.

Despite the generality of the reasons for the emergence of bifurcation (for $H = H_c$) in different models of **M** distribution, the form of specific transformations of the domain wall structure upon a transition through point H_c is very sensitive to the distribution of **M** and to the variation of physical parameters of the film. For example, a change in the film thickness, damping, magnetizations, etc., may bring about completely different mechanisms of the dynamic transformation of the wall structure. In fields differing from H_c considerably, the mechanisms of dynamic wall transformation are also different. If, for instance, we increase the field to 350 Oe for the same film parameters as in the above discussion, the rearrangement of the internal structure of the domain wall occurs with the formation of three vortices. In still stronger fields, the state of deterministic chaos is attained. The experimental observation of the chaotic behavior of domain walls in yttrium garnet ferrite plates subjected to a varying magnetic field was reported in [20]. The existence of deterministic chaos in the behavior of domain walls in films with transverse anisotropy was reported, for example, in [21, 22].

4. DEPENDENCE OF THE PERIOD OF THE DYNAMIC TRANSFORMATION OF THE WALL INTERNAL STRUCTURE ON THE FILM PARAMETERS

An analysis of the period T of the dynamic rearrangement of the wall structure is important for determining the features of the nonlinear transitional dynamic behavior of a domain wall. This problem is not easy if only because the form of the rearrangement changes significantly with increasing field (see above). In this connection, we will consider in this section the results obtained in fields very close to the bifurcation field H_c.

By way of an example, Fig. 6 shows the period T for different film parameters. As expected, the period T increases indefinitely as H approaches H_c. An analysis shows that the types of this singularity are different for

different films. None of the curves obtained as a result of a numerical experiment matches the period

$$T = \frac{2\pi}{\omega_H}(1+\alpha^2)\left(1-\frac{H_c^2}{H^2}\right)^{-1/2}, \quad (8)$$

where $\omega_H = \gamma H$, which was determined in [2] (see also [23]) in the framework of a 1D model of the **M** distribution. According to our calculations, the exponent $s \neq 1/2$ varying with the film parameters should be used instead of the critical exponent 1/2 characterizing the behavior of the period of dynamic rearrangement of the internal structure of the wall in the vicinity of the singular point (point of bifurcation). By way of an example, the table presents the results of numerical experiments for a film with the basic parameters $b = 0.05$ μm and $\alpha = 0.1$. For the sake of comparison, the results obtained on the basis of the empirical formula

$$T = \frac{2\pi}{\omega_H}(1+\alpha^2)\left[\left(1-\frac{H_c^2}{H^2}\right)^{-s} + \frac{1}{5}\left(1-\frac{H_c^2}{H^2}\right)\right], \quad (9)$$

$$H \geq H_{c,}$$

and on the basis of formula (8) derived using the 1D model are also presented. It can be seen from the table that, for the critical exponent $s = 0.4$ and for the critical field $H_c = 99.3265$ Oe (this value is in accord with that obtained in [13]), formula (9) describes the results of the numerical experiments quite accurately. The relative error does not exceed 5%. On the other hand, the best results obtained for T on the basis of the 1D model of magnetization distribution (for $H_c = 99.3078$ Oe) differ significantly (up to 45%) from the results of the numerical experiment. These discrepancies are obviously due to completely different types of dynamic rearrangement of the domain wall structure in the cases of 1D and 2D models of magnetization distributions. New possible mechanisms of the wall structure rearrangement in the 2D model of the **M** distribution, which are associated, for example, with the formation, motion, and decay of magnetization vortices in the wall, must also affect the critical (bifurcation) field itself.

5. DEPENDENCE OF THE CRITICAL FIELD ON THE FILM PARAMETERS

The critical field is important not only as a parameter describing basic features of the nonlinear behavior of domain walls, but also for practical applications. By controlling its value, it is possible to optimize the high-frequency magnetization reversal of the films, which is necessary for the development of heads intended for hf recording and reading of high-density information. As a matter of fact, the wall mobility in weak fields ($H < H_c$) must be given by (see, for example, [4])

$$\mu = \gamma\delta/\alpha \quad (10)$$

Dependence of the period of dynamic rearrangement of a domain wall on the external magnetic field. The results of numerical experiments are compared with the results obtained on the basis of formula (9) proposed in this work and formula (8) for a 1D model

H, Oe	T, ns (numerical experiment)	T, ns (formula (9))	T, ns (formula (8))
99.33	171.684	166.244	171.704
99.35	77.854	77.630	124.531
99.37	59.280	60.698	102.569
99.40	46.910	49.223	84.239
99.50	33.530	34.934	58.330
100	19.680	20.351	30.698
102	11.640	11.774	15.488
104	9.524	9.434	11.674
106	8.344	8.166	9.727
108	7.534	7.379	8.494
110	6.981	6.776	7.721
115	5.906	5.787	6.218
120	5.194	5.149	5.352
130	4.330	4.329	4.298

(δ is the wall thickness), i.e., inversely proportional to the damping parameter α. It may appear that, by choosing substances with small values of α, we can attain high velocities. However, these arguments are valid only for fields $H < H_c$. In fields higher than H_c, the time-averaged translational velocity of the wall decreases due to its backward movements emerging in this case. In addition, 1D models [2] give

$$H_c = 2\pi M_s \alpha. \quad (11)$$

This means that the region of fields in which the velocity of a domain wall can be high becomes narrower upon a decrease in α. This means that we must choose some optimal values of α. The situation does not change radically if we go over to an analysis of 2D models of the **M** distribution in a wall.

Figure 7 shows the $H_c(\alpha)$ dependence obtained by us for basic films of thickness 0.05 μm. This dependence turned out to be almost linear. Insignificant deviations are observed only for small values of α. In order to find the reason for such deviations, we analyzed the dynamic rearrangement of a domain wall for small values of α. Figures 8 and 9 show examples of the time variation of the wall velocities and the corresponding instantaneous configurations of **M.** A new effect is observed: along with the main nonlinear periodic (with period T) velocity variations described in Section 3, additional oscillations of the wall velocity appear over fractions of period T (such oscillations will be referred to as subperiodic). Figure 9 shows the velocity v for the same film over a shorter time interval. The instanta-

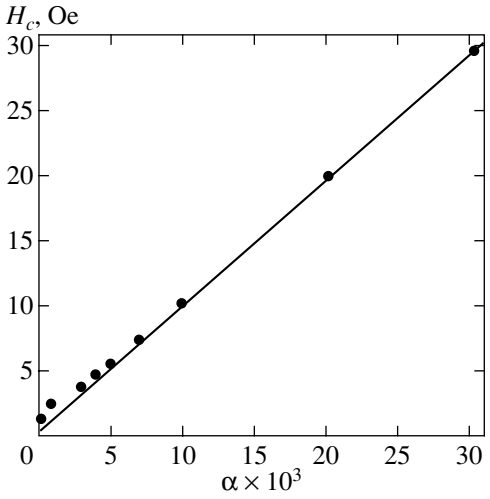

Fig. 7. Critical field as a function of the damping parameter α for basic films with $b = 0.05$ μm.

neous configurations of the magnetization in the wall corresponding to the minima and maxima of the velocity are also presented. An analysis of Fig. 9 shows that subperiodic oscillations are associated with vibrations of some parts of the walls relative to others. Such oscillations are excited every time when the wall structure is rearranged radically; namely, an asymmetric Bloch wall is reconstructed into an asymmetric Néel wall, etc. At this moment, sharp changes in local magnetostatic fields occur, whose nonuniformity is naturally commensurate with the inhomogeneities of the magnetization distribution in the wall. These results were obtained for fields $H > H_c$ very close to the critical field H_c. Similar oscillations also take place for $H < H_c$ [24]. The deviations of $H_c(\alpha)$ from a straight line, which are observed for small values of α, are apparently associated with these oscillations. Oscillations of the same origin are also observed in fields considerably exceeding H_c.

Thus, a decrease in damping for fixed H terminates the translational motion of the wall not only due to equalization of the time intervals during which the main and backward movements of the wall take place, but also due to the development of subperiod oscillations. These oscillations strongly affect the T(H) dependence also. This is demonstrated in Fig. 10 which shows that the smaller the damping parameter, the more gently sloping the $T(H)$ curve. This fact offers unique possibilities for experimental investigations of peculiarities of the nonlinear transitional wall dynamics (see Section 6).

The observed velocity oscillations are characterized by frequencies on the order of 10^{11} Hz, which are much higher than the frequencies associated with the precession of magnetization around the EMA (see above). These oscillations may lead, in addition to radiation

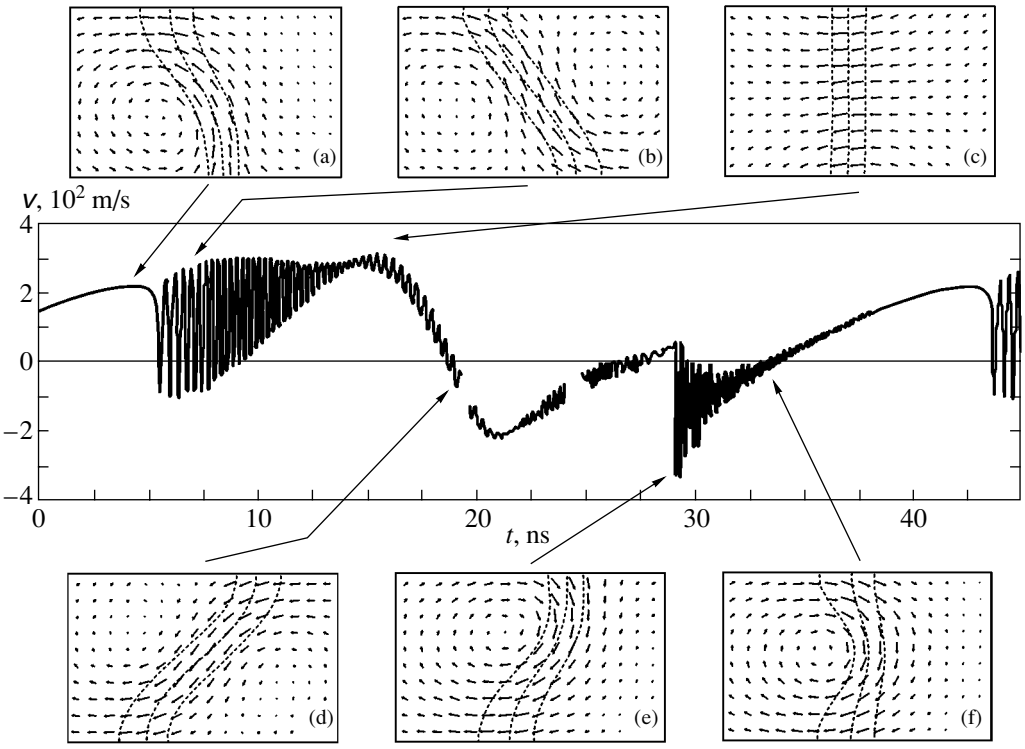

Fig. 8. Time dependence of the average (in the above sense) velocity for a film with the basic parameters and $b = 0.05$ μm, $\alpha = 0.001$, and $H = 5$ Oe. Instantaneous configurations (a)–(f) correspond to the main rearrangement of **M**.

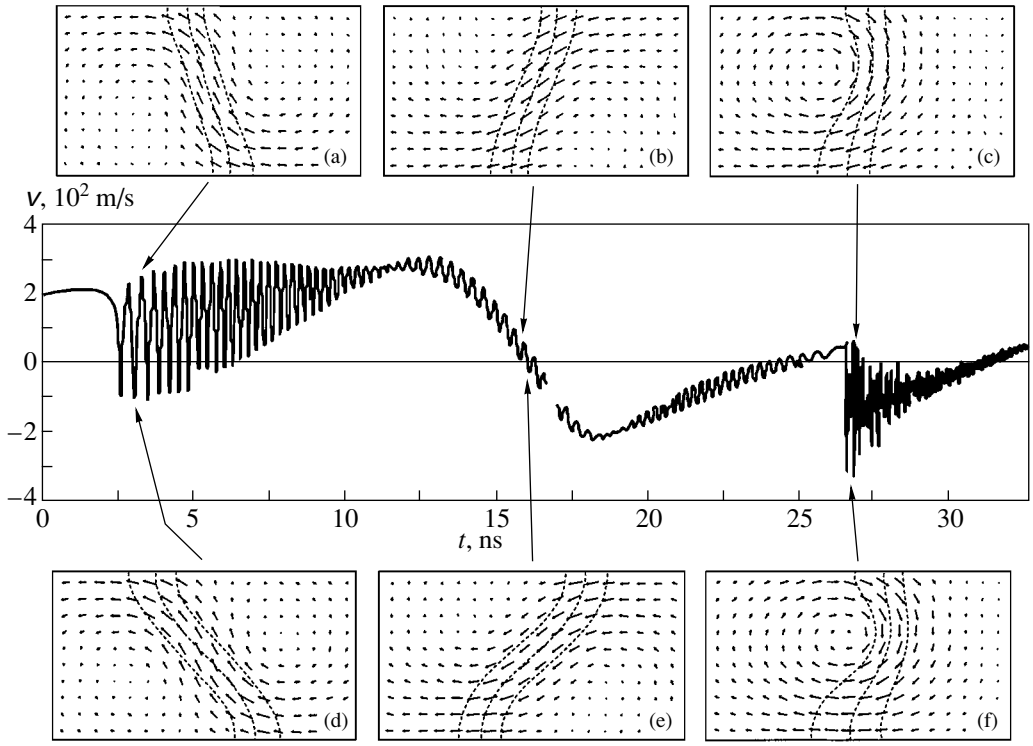

Fig. 9. The same dependence $v(t)$ as in Fig. 8, but for a shorter time interval. Instantaneous configurations (a)–(f) in this case illustrate the type of vibrations in the wall on various segments of *T*.

predicted in [25], to the magnetic-dipole emission of electromagnetic waves due to the motion of domain walls.

Returning to expression (11), we recall that H_c corresponds to the field H in which the torque associated with the magnetostatic field component $H_x^{(m)}$ assumes the maximum value. This is observed only for the maximum value of $H_x^{(m)} = H_{\max}$ which can be attained when the **M** configuration becomes close to that of a classical Néel wall (see Fig. 4d). In this case, the domain wall can be visualized as a plate magnetized to saturation in the transverse direction. If this plate is infinitely large, as is the case in the 1D model [2], we have

$$H_{\max} = 4\pi M_{av} = 2\pi M_s,$$

which leads precisely to expression (11). Here, M_{av} is the value of the M_x component averaged over the wall thickness. For a one-dimensional Néel rotation of vector **M** in the wall, we have $M_{av} = M_s/2$. Obviously a wall in a film can be likened to a finite-size plate; consequently, irrespective of the model describing the magnetization distribution, field H_c is a function of the film thickness; i.e.,

$$H_c = 4\pi M_s \alpha F(b), \qquad (12)$$

where $F(b)$ is a function depending on the wall thickness, such that the value of $4\pi M_s F(b)$ must approach $2\pi M_s$, viz., the value for an infinitely large sample, upon an increase in *b*. Consequently, the field H_c should increase with the film thickness. Such an increase was indeed observed [26], but in a very narrow region of *b*. In a wider region of *b*, contrary to expectations, we

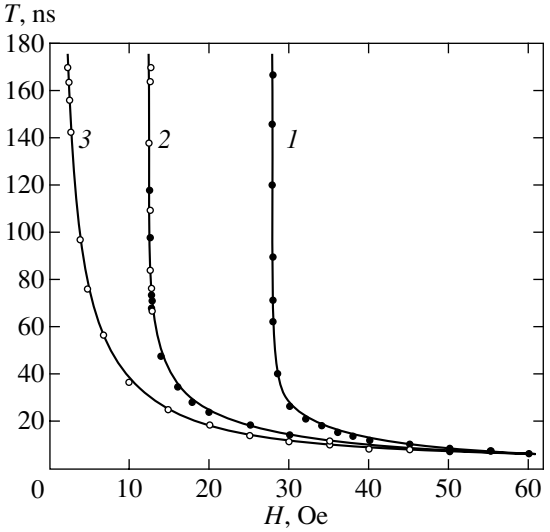

Fig. 10. Magnetic field dependence of the period of dynamic rearrangement of the wall structure for basic films with $b = 0.05$ μm and $\alpha = 0.001$ (*1*), 0.01 (*2*), and 0.03 (*3*). Symbols correspond to the results of numerical experiments, and solid curves are plotted for better visualization.

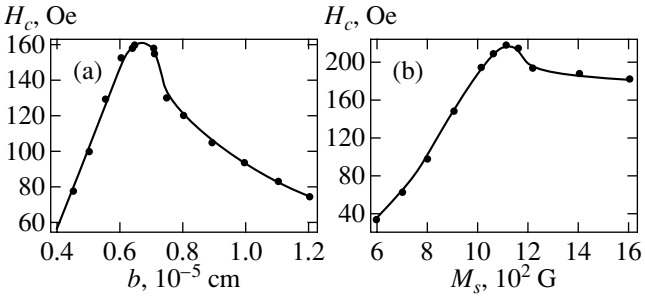

Fig. 11. Dependence of the critical field on (a) the film thickness and (b) the saturation magnetization for b = 0.05 μm, basic parameters, and $\alpha = 0.1$.

obtain a nonlinear and nonmonotonic dependence H_c(b) (Fig. 11a). Moreover, the $H_c(M_s)$ dependence is found to be nonmonotonic also (Fig. 11b). Both curves have nothing in common with those predicted by the 1D model of the **M** distribution [2] (see formula (11)).

In order to find the reasons for the observed behavior of field H_c, we analyzed the dynamic rearrangement of the domain wall structure upon a change in the film thickness and in the saturation magnetization. New mechanisms of the wall structure rearrangement were established. Let us consider two of such mechanisms to establish the reason for the above-mentioned nontrivial behavior of H_c as a function of the film thickness and M_s. Some instantaneous configurations illustrating new mechanisms of the rearrangement of the wall structure are given in Fig. 12.

Classical transformations described above and shown in Fig. 4 exist in films having a small thickness (approximately up to b = 0.064 μm). As the thickness increases, the mechanism of rearrangement changes. In films with b = 0.065–0.75 μm placed in fields close to critical, the rearrangement stages c, d, and e associated with the formation of Néel walls vanish (see Fig. 4). A vortex of an asymmetric Bloch wall (Fig. 12) located at the center of the film at a certain instant is displaced towards its lower surface (a). In this case, a new vortex of opposite chirality is generated at the upper surface; consequently, at a certain stage of dynamic rearrangement, the wall consists of two vortices located one above the other (b). Then both vortices are displaced downwards and the lower vortex ultimately disappears (c). The remaining upper vortex moves in the downward direction, passing through the middle of the film (d), and then a vortex configuration of magnetization (e) similar to case (a) but possessing the opposite chirality is formed. This completes the half-period of the formation of the wall structure. A similar rearrangement takes place during the next half-period, and we arrive at the initial domain wall structure.

In films of a large thickness $b > 0.075$ μm, the mechanism of the dynamic rearrangement of the wall is different. By way of an example, Fig. 12b shows the structural transformation for a wall moving in the field H = 103 Oe. In this case, a vortex of **M** moving downwards (a) starts gradually tunneling through the central line to the right part of the wall (b); ultimately a vortex with the previous chirality is formed on this side (c). Then, another vortex with the opposite chirality is generated at the upper surface to the left of the central line. At the next stage, this vortex grows and the magnetization configuration acquires the form depicted in Fig. 12b (d). Then the right vortex gradually disappears, while the left vortex moves downwards. This gives rise to the **M** configurations presented in Fig. 12b (e) and (f). The latter differs from the initial configuration (a) only in the chirality of the vortex. This completes the half-period. During the next half-period, similar transformations lead to structure (a).

Thus, in the thickness range b = 0.04–0.064 μm, the domain wall is transformed so that a structure of type (d) (Fig. 4) appears. In this case, the wall can be conditionally presented as a "plate" with the average magnetization perpendicular to the yz plane. The magnitude of this magnetization is determined by $H_{\max}$ and, hence, H_c. An increase in b leads to an increase in $H_{\max}$ and, accordingly, to an increase in H_c.

The subsequent decrease in the value H_c upon an increase in b (for b = 0.65 μm) is associated with a radical change in the type of rearrangement. In this case, the structure of type (d) (Fig. 4) is not formed. Instead, either a structure of type (b) (first-type mechanism in Fig. 12a) is formed after the displacement of the vortex to the lower surface for b = 0.65–0.75 μm, or the (b)-type structure (second-type mechanism in Fig. 12b) appears for $b > 0.75$ μm. In both cases, in contrast to structure (d) (Fig. 4), magnetostatic poles with alternating signs are formed on the surfaces of the wall. Such a fragmentation of poles on the surface of a domain wall perpendicular to x leads to a decrease in $H_{\max}$ and, hence in H_c. A further increase in the film thickness enhances the tendency to the pole fragmentation.

If we increase the saturation magnetization after fixing the value of b, the density of poles on the lateral surface of the wall increases in the case of the classical scenario of the domain wall rearrangement. This leads to an increase in the value of H_c. However, since the exchange length b_0 decreases with increasing M_s, the pole fragmentation on the planes of the wall perpendicular to x becomes possible. Consequently, starting from certain values of M_s, field H_c must decrease, which is indeed observed in our numerical experiments. An analysis shows that the wall rearrangement mechanisms appearing in this case are similar to those described above.

The nonmonotonic behavior of the critical field and the mechanisms of the dynamic rearrangement of the domain wall structure described above are also observed for films with parameters differing from the basic parameters.

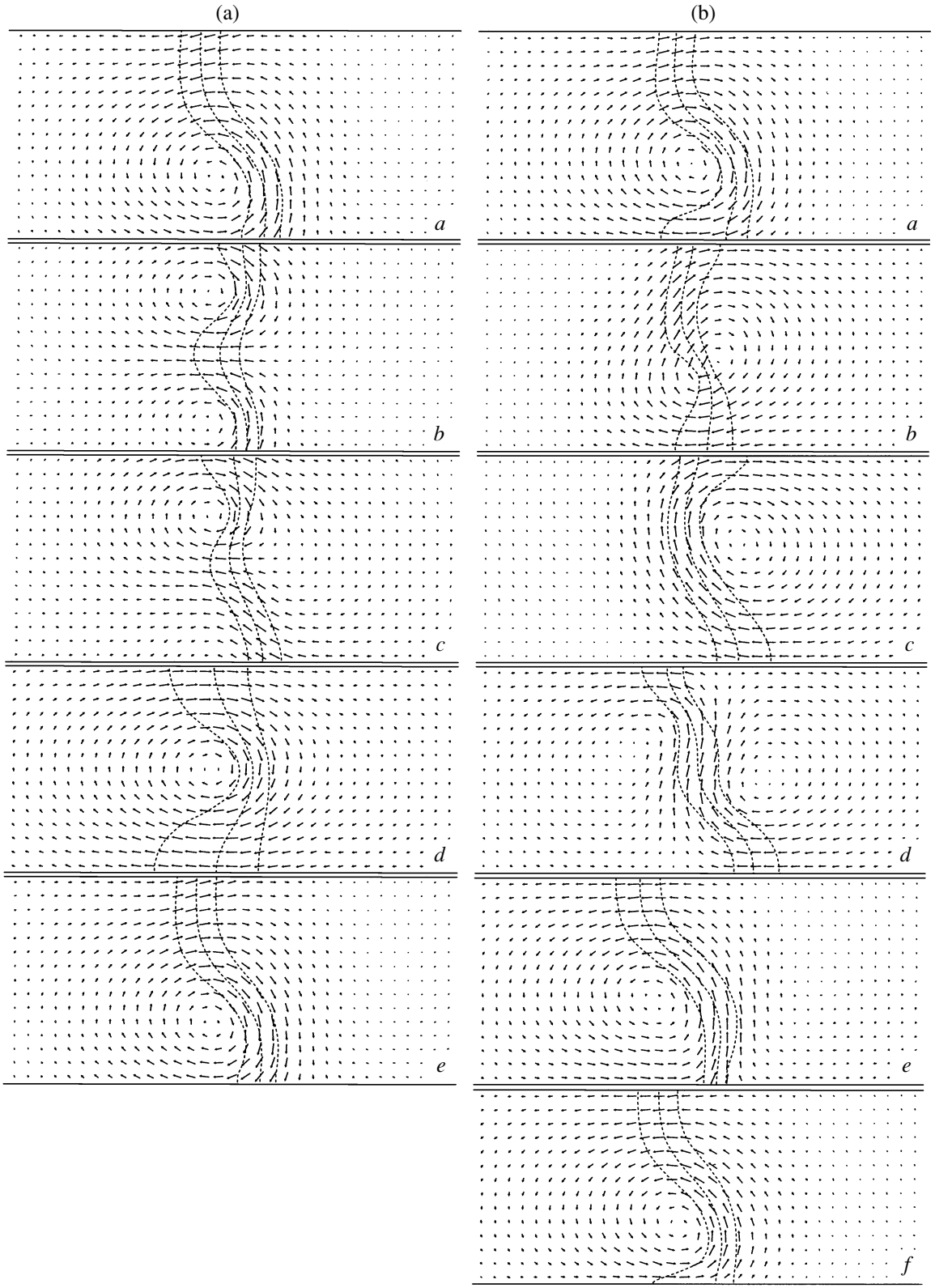

Fig. 12. Sequence of instantaneous configurations of the wall under the dynamic transformation of its structure in films with the basic parameters, $\alpha = 0.1$, $b = 0.07$ μm (a), $b = 0.1$ μm (b), and $H = 103$ Oe.

It can be seen that expression (11) for the critical field is independent of the anisotropy field. However, this is associated not with the 1D nature of the magnetization distribution, for which formula (11) was derived, but with the assumption that the shape of the wall remains virtually unchanged during its motion. It was demonstrated above that this assumption is incorrect in the general case for the model of a 2D distribution of **M** and the wall structure actually experiences considerable distortions. This means that, in addition to the torque associated with the magnetostatic fields, the torques associated with the exchange and anisotropic interactions also appear. Both these contributions to the torque, as well as the contribution associated with magnetostatic fields, are finite. This means that, in this case also, an increase in the external magnetic field must induce bifurcation leading to the emergence of a unsteady motion of the wall; i.e., in contrast to formula (11), field H_c must depend on the anisotropy field H_a and on the exchange field H_e. It was found that the dependence of the critical field on H_a is close to linear and its dependence on H_e is nonmonotonic.

6. DISCUSSION AND CONCLUSIONS

We investigated the nonlinear and generally unsteady dynamics of domain walls with a 2D magnetization distribution in magnetouniaxial films with an easy magnetization axis parallel to the surface. It is shown that there exist three field regions in which the dynamic behavior of domain walls is different and is in poor agreement with the predictions of a 1D model in many respects.

It is shown that the dynamic rearrangement of the wall structure occurs not only after a change from a steady-state to unsteady motion upon a transition though field H_c (bifurcation field) as predicted earlier [2, 13], but also as a result of the change in the type of steady motion upon a transition through field H_0 which is always smaller than field H_c.

It has been proved that the nature of bifurcation (transition from a steady to an unsteady behavior of the wall) is the same for walls with 1D and 2D distributions of magnetization. It is associated with the magnetization precession around the easy magnetization axis. In addition, the 1D models of the **M** distribution widely used earlier do not provide an adequate description of the domain wall dynamics in fields stronger than H_0 (field H_0 does not exist at all in 1D models). In particular, 1D models cannot lead to nonmonotonic dependences of the bifurcation field on the film thickness and on the saturation magnetization, which were observed by us in the framework of a 2D model.

It is only in low fields $H \ll H_0$ that the domain wall dynamics can be considered under the assumption of an invariable internal structure of the wall, as was done starting from [3]. In fields stronger than H_0 (and especially stronger than H_c), the structure of domain walls changes dramatically during their motion. The mechanisms of the dynamic structure rearrangement for domain walls change significantly upon the variation of the film parameters. Among other things, we predicted new mechanisms which are completely different as compared to the classical mechanism [13].

The rearrangement of the internal structure of domain walls strongly affects their velocities. It should be recalled that the wall velocity $\bar{v}$ averaged over a certain time interval (e.g., the time between two consecutive exposures) is usually measured in experiments [7, 27, 28]. As applied to the films under investigation, the velocity being measured as a function of the external magnetic field increases in many cases up to field H_c in accordance with the above-discussed theory (see below). However, in fields $H > H_c$, the averaged wall velocity $\bar{v}$ being measured starts decreasing upon a further increase in H due to periodic backward movements of the wall. It should be recalled that the period T of dynamic transformations of the wall decreases upon an increase in the external field (see table). The same nonmonotonic dependence of velocity was observed, for example, in [27]. True enough, the authors of [27] associated such a dependence with the nonlinear field dependence of the velocity of a domain wall in the region of its steady motion, which was predicted in [2] for films with a small Q factor and obtained on the basis of a 1D model of the magnetization distribution. However, more rigorous calculations made on the basis of a 2D model of magnetization distribution in [13] and in the present work do not confirm this conclusion. It is appropriate to recall in this connection the second type of steady motion of domain walls predicted by us (see Fig. 3). In this case, the wall velocity changes with time nonmonotonically (first decreases and then increases) upon a transition from the first to the second type of steady motion. If we again consider the above-mentioned method of the wall velocity measurements, we can formally arrive (under certain conditions) to a dependence $\bar{v}(H)$ resembling that predicted in [2]. However, first, it will be the time-averaged velocity for each fixed H, in contrast to [2]. Second, the above-mentioned transition may occur long before the emergence of unsteady motion of the wall. Consequently, the decrease in the time-averaged velocity as a function of H must give way to its further increase, which is not predicted in [2], but is observed experimentally [27] for CoNiFe films. In the present communication, we only consider films with a planar anisotropy. The nonmonotonic behavior of the domain wall velocity as a function of the field in films with a transverse anisotropy [28] is probably also connected with additional transformations of the domain wall structure, which have not been studied comprehensively as yet.

Returning to the nonmonotonic behavior of the domain wall velocity upon a transition through the

bifurcation field, we note that such a behavior (velocity maximum for $H = H_c$) provides a comparatively simple method of experimental investigation of the bifurcation field depending on film parameters.

The experiments carried out by us indicate for the first time the practical opportunity for not only experimental investigations of the above-mentioned averaged characteristics of unsteady motion of the wall, but also for a direct analysis of the time evolution of the wall velocity in the unsteady mode of motion. It can be seen from Fig. 10 that an increase in T is observed for all values of α; it is important, however, that the curves become more gently sloping upon a decrease in α. Along with comparatively low values of the fields (on the order of a few oersted) in which the dynamic rearrangement of domain walls takes place for small α, this circumstance is favorable for experimental investigations in our opinion. As a matter of fact, for large periods of dynamic transformations, high time resolutions are not required. It may appear that experiments should be carried out in the vicinity of the critical field, where the period T is quite large. If, however, we take films with $\alpha = 0.1$, the critical field in them is rather strong ($H_c = 99.3$ Oe for basic films). In the immediate vicinity of this field, the period T is large. For example, $T = 171.7$ ns for $H = 99.33$ Oe. It is difficult, however, to get into such a narrow region of the fields. If the field is increased just to 102 Oe, the period T decreases approximately to 11.6 ns. On the other hand, our numerical experiments show that, for $\alpha = 0.001$, the period T still remains large enough ($T = 80$ ns) even in a field of 5 Oe, which is approximately twice as large as the critical field. Consequently, in order to detect experimentally the regions of periodic variation of the velocity of the walls, a time resolution on the order of 10 ns is required. In addition, there exists a certain reserve for increasing T by decreasing H.

The experiments can be carried out, for example, on the basis of the method of high-speed photography in the double or triple flash mode. For a flash duration of about 1 ns, it is possible to determine the coordinate q of the instantaneous displacement of the wall as a function of time t.

It is very important to select appropriate films. Films with a small damping parameter (e.g., $\alpha = 0.001$) are preferable. It should be noted that, although we used for our calculations the permalloy films with the basic parameters described above, other films with a quality factor $Q \leq 1$ are also quite suitable. By way of an example, we varied M_s from 400 to 1600 G and K from 10^3 to 10^6 erg/cm^3 to observe a behavior resembling that described above. However, the selected films should not be too thick (not thicker than 0.2 μm for permalloy) since the dynamic behavior pattern for thicker films is very complicated.

ACKNOWLEDGMENTS

The authors are grateful to V.V. Volkov (Ioffe Physicotechnical Institute, Russian Academy of Sciences) for the discussion of possibilities of experimental verification of the results and to M.G. Chernikhovskaya for a number of valuable remarks which considerably improved the manuscript.

This work was partly supported by the Russian Foundation for Basic research (project no. 99-02-16279).

REFERENCES

1. L. D. Landau and E. M. Lifshitz, in *Collection of Works* (Nauka, Moscow, 1969), Vol. 1, p. 128.
2. N. L. Shryer and L. R. Walker, J. Appl. Phys. **45**, 5406 (1974).
3. W. Döring, Z. Naturforsch. A **3**, 372 (1948).
4. A. Hubert, *Theorie der Domanenwände in Geordneten Medien* (Springer-Verlag, Berlin, 1974; Mir, Moscow, 1977).
5. A. P. Malozemoff and J. C. Slonczewski, *Magnetic Domain Walls in Bubble Materials* (Academic, New York, 1979; Mir, Moscow, 1982).
6. V. V. Volkov, V. A. Bokov, and V. I. Karpovich, Fiz. Tverd. Tela (Leningrad) **24**, 2318 (1982) [Sov. Phys. Solid State **24**, 1315 (1982)].
7. V. G. Bar'yakhtar, B. A. Ivanov, and M. V. Chetkin, Usp. Fiz. Nauk **146**, 417 (1985) [Sov. Phys. Usp. **28**, 563 (1985)].
8. A. E. La Bonte, J. Appl. Phys. **40**, 2450 (1969).
9. A. Hubert, Phys. Status Solidi **32**, 519 (1969).
10. S. Tsukahara and H. Kavakatsu, J. Phys. Soc. Jpn. **32**, 1493 (1972).
11. J. N. Chapmen, G. R. Morrison, J. P. Jacubovics, *et al.*, J. Magn. Magn. Mater. **49**, 277 (1985).
12. M. R. Scheinfen, J. Unguris, R. J. Celotta, *et al.*, Phys. Rev. B **43**, 3395 (1991).
13. S. W. Yuan and H. N. Bertram, Phys. Rev. B **44**, 12 395 (1991).
14. B. N. Filippov and L. G. Korzunin, Fiz. Met. Metalloved. **75**, 49 (1993).
15. B. N. Filippov and L. G. Korzunin, IEEE Trans. Magn. **29**, 2563 (1993).
16. A. Aharoni, J. Appl. Phys. **39**, 861 (1968).
17. K. Ramstöck, W. Hartung, and A. Hubert, Phys. Status Solidi **155**, 505 (1996).
18. L. I. Antonov, E. V. Lukasheva, and E. A. Mukhina, Fiz. Met. Metalloved. **80**, 5 (1995).
19. G. I. Marchuk, *Methods of Numerical Mathematics* (Nauka, Moscow, 1989; Springer-Verlag, New York, 1975).
20. V. S. Gornakov, V. I. Nikitenko, I. A. Prudnikov, *et al.*, Phys. Rev. B **46**, 10 829 (1992).
21. E. E. Kotova and V. M. Chetverikov, Fiz. Tverd. Tela (Leningrad) **32**, 1269 (1990) [Sov. Phys. Solid State **32**, 748 (1990)].

22. R. A. Kosinski and A. Sukiennicki, J. Magn. Magn. Mater. **93**, 128 (1991).

23. B. N. Filippov and A. P. Tankeev, *Dynamical Effects in Ferromagnets with Domain Structure* (Nauka, Moscow, 1987).

24. V. N. Filippov, L. G. Korzunin, and F. A. Kassan-Ogly, Phys. Rev. B **64**, 104 412 (2001).

25. A. K. Zvezdin, Pis'ma Zh. Éksp. Teor. Fiz. **31**, 508 (1980) [JETP Lett. **31**, 478 (1980)].

26. B. N. Filippov and L. G. Korzunin, Fiz. Tverd. Tela (St. Petersburg) **38**, 2442 (1996) [Phys. Solid State **38**, 1343 (1996)].

27. D. S. Bartran and H. C. Bourne, IEEE Trans. Magn. **6**, 743 (1972).

28. V. A. Bokov and V. V. Volkov, Fiz. Tverd. Tela (St. Petersburg) **39**, 660 (1997) [Phys. Solid State **39**, 528 (1997)].

Translated by N. Wadhwa

Journal of Experimental and Theoretical Physics, Vol. 94, No. 2, 2002, pp. 329–335.
Translated from Zhurnal Éksperimental'noĭ i Teoreticheskoĭ Fiziki, Vol. 121, No. 2, 2002, pp. 388–395.

SOLIDS
Structure

Investigation of Magnetic Phase Transformations in a System of $Nd_{1-x}Ba_xMnO_{3-\delta}$ ($0 \le x \le 0.50$) Depending on the Conditions of Preparation

S. V. Trukhanov[a, *], I. O. Troyanchuk[a], D. D. Khalyavin[a], I. M. Fita[b], H. Szymczak[c], and K. Bärner[d]

[a]*Institute of Solid-State and Semiconductor Physics, Belarussian Academy of Sciences, ul. Brovki 17, Minsk, 220072 Belarus*
[b]*Donetsk Physicotechnical Institute, National Academy of Sciences of Ukraine, Donetsk, 341141 Ukraine*
[c]*Institute of Physics, Academy of Sciences, Warsaw, PL-02-668 Poland*
[d]*IY Physikalisches Institut, Göttingen, D37073 Germany*
**e-mail: truhanov@ifttp.bas-net.by*
Received August 22, 2001

Abstract—Investigations are performed of the crystal structure and magnetic and electromagnetic properties of single crystals ($0.23 \le x \le 0.34$) and polycrystals ($0 \le x \le 0.50$) of an $Nd_{1-x}Ba_xMnO_{3-\delta}$ system of solid solutions. It is found that, for samples prepared in the air, the maximal Curie temperature (T_C) does not exceed 150 K, while, in the case of polycrystalline samples in the concentration range of $0.34 \le x \le 0.50$, prepared in a reducing medium (a gaseous mixture of argon and carbon monoxide), T_C increases to 320 K. As a result of the reducing medium effect on the compositions, the type of the magnetic phase transition to the paramagnetic state changes from the first to second order. The electrical resistivity of reduced polycrystalline samples ($0.34 \le x \le 0.50$) decreases in magnitude and correlates with the behavior of magnetization. Both series of samples, prepared both in the air and in a reducing medium, exhibit a transition from the metal to dielectric state at a temperature below T_C. The temperature and field dependences of magnetization for the stoichiometric polycrystalline composition of $Nd_{0.50}Ba_{0.50}MnO_3$ are measured under conditions of hydrostatic pressure. It is demonstrated that the hydrostatic pressure induces in $Nd_{0.50}Ba_{0.50}MnO_3$ the transition from the antiferromagnetic to ferromagnetic state. Based on the measurement results, hypothetical magnetic phase diagrams are constructed for the system of solid solutions being treated, depending on the concentration of barium and the method of preparation. It is found that no T_C increase is observed in single crystals ($0.23 \le x \le 0.34$) such as is observed in polycrystals. It is assumed that the abrupt increase in T_C of polycrystalline samples prepared in a reducing medium is a result of the emergence of extended defects and microstresses in the crystal lattice. © *2002 MAIK "Nauka/Interperiodica".*

1. INTRODUCTION

$Ln_{1-x}D_xMnO_3$ manganites of rare-earth elements (Ln denotes ions of La, Pr, Nd, and the like, and D denotes ions of Ca, Sr, and Ba) with the perovskite structure have been attracting the attention of researchers in the field of physics of magnetic phenomena for well over 50 years [1]. Their unusual magnetic and electric properties became the subject of numerous experimental [2, 3] and theoretical [4, 5] investigations. However, it was much later that interest in these compounds increased sharply as a result of discovery of the effect of giant magnetoresistance [6] and, to a greater extent, of the metal–semiconductor and charge order–disorder phase transitions induced by a magnetic field [7, 8].

The investigation of compounds of this class is important both from the standpoint of fundamental research and from the practical standpoint. The nature of the magnetic and electric processes involved is still unclear and is the subject of extensive discussion. However, even today these compounds find wide application in magnetic recording of information as the active element of a readout device. Because of the high chemical stability, they are used as the electrode materials of high-temperature fuel cells and cathodes for CO_2 lasers.

$LaMnO_3$ is the best studied of all manganites. This compound has the perovskite structure and is characterized by an O^1 orthorhombically distorted ($c/\sqrt{2} < a \le b$) unit cell. The distortion of this type is typical of compounds containing Jahn–Teller ions [9]. In this case, these are Mn^{3+} ions (proceeding from the charge conservation law, $La^{3+}Mn^{3+}O_3^{2-}$). By its magnetic properties, $LaMnO_3$ is an *A*-type antiferromagnet with a small ferromagnetic component due to the Dzyaloshinski–Moriya interaction, and by its electric properties it is a

semiconductor [2]. The magnetic properties of this compound are fully defined by the spins of Mn ions, because the orbital magnetic moments are "frozen" in the crystal field of oxygen anions.

Stoichiometric $La^{3+}Mn^{3+}O_3^{2-}$ contains only Mn^{3+} ions with the electronic configuration $t_{2g}^3 e_g^1$ ($S = 2$). The substitution of Ln^{3+} ions by alkali-earth elements D^{2+} is accompanied by the formation of Mn^{4+} ions (t_{2g}^3, $S = 3/2$) and by the transition to the ferromagnetic metal state. In order to explain this behavior of substituted systems, Zener elaborated a special theory of indirect exchange interactions via charge carriers (in this case, the latter are e_g electrons). This form of interactions was given the name of double exchange [10, 11].

The double exchange is based on the real transition of an electron from a half-filled e_g orbital of an Mn^{3+} ion to a free e_g orbital of Mn^{4+}. Such a jump is energetically advantageous in the case of parallel arrangement of local spins S of Mn^{3+} and Mn^{4+} ions which are nearest neighbors. Therefore, the double exchange favors ferromagnetism and metallic type of conduction. However, numerous facts exist which cannot be interpreted within the double exchange theory [12].

Goodenough [13] formulated the basic principles of the theory of superexchange, a specific type of indirect exchange interaction. This theory is based on the virtual exchange of electrons between manganese ions and predicts the anisotropic pattern of exchange interactions. The interaction between Mn^{3+} and Mn^{4+} depends on the number of factors such as the Mn–O bond length, Mn–O–Mn bond angle, and the Mn^{3+}/Mn^{4+} ratio. Note that, in accordance with the theory of superexchange, the state of ferromagnetic order may not correlate with the behavior of electrical conductivity.

The presence of Mn^{3+} and Mn^{4+} ions is the determining factor for the formation of the magnetic and electric properties of manganites. Different methods may be used to vary the Mn^{3+}/Mn^{4+} ratio [14], namely, (1) the replacement of Ln^{3+} ions by D^{2+} ions (Ca, Sr, Ba, Pb, and Cd) in the *A* sublattice of perovskite; (2) the replacement of Mn ions by various metals; and (3) the removal of oxygen anions, which leads to the transition of Mn^{4+} ions to Mn^{3+} ions with a simultaneous decrease in their coordination.

It is known that, as the oxygen content decreases, the Curie temperature T_C and spontaneous magnetization decrease, as a rule, and the resistance increases. Anion-deficient compositions were prepared such as $La_{1-x}Ca_xMnO_{3-\delta}$ ($0 \le \delta \le 0.50$) [15, 16] and $Ln_{0.55}Ba_{0.45}MnO_{3-\delta}$ ($0 \le \delta \le 0.37$) [17]. A gradual transition was observed from ferromagnetism to the properties of spin glass or antiferromagnetic, and the electrical resistance increased considerably and assumed the semiconductor behavior. It is known that $La_{0.50}Ba_{0.50}MnO_3$ is a ferromagnet with $T_C \approx 350$ K [18], while $La_{0.50}Ba_{0.50}MnO_{2.75}$ is an antiferromagnet with the Néel temperature $T_N \approx 185$ K [19]. However, it has been reported recently [20] that, after being reduced in argon, a $Pr_{0.50}Ba_{0.50}MnO_{3-\delta}$ sample exhibits a considerable increase in T_C from 140 to 320 K and demonstrates the transition from the ferromagnetic to antiferromagnetic state at about 200 K, where a high magnetoresistance is developed. The reduced composition remained a semiconductor at a temperature below T_C, while the sample synthesized in the air performed at T_C a transition to the metal state. These unusual properties were interpreted using the Goodenough model, according to which the Mn^{3+}–O–Mn^{3+} exchange interaction is ferromagnetic in the case when static Jahn–Teller distortions are relieved. However, the sign of the Mn^{3+}–O–Mn^{3+} exchange interaction depends also on the coordination of ions. In an orbital disordered phase, the interaction between Mn^{3+} ions is ferromagnetic in octahedral positions and antiferromagnetic in pentahedral positions [21]. Therefore, the ferromagnetism should have decayed gradually with decreasing oxygen content, whereas a considerable increase in T_C was observed. It was to find the reason for the unusual behavior of the $Pr_{0.50}Ba_{0.50}MnO_{3-\delta}$ sample and to investigate the effect of oxygen deficiency on the magnetic and electric properties of manganites on the basis of other rare-earth elements that our study was performed. As a result, we have found that polycrystalline samples of $Nd_{1-x}Ba_xMnO_{3-\delta}$ ($0.34 \le x \le 0.50$) annealed in a reducing medium (a gaseous mixture of argon and carbon monoxide) also exhibit a two- to threefold increase in T_C (up to 320 K). However, unlike $Pr_{0.50}Ba_{0.50}MnO_{3-\delta}$, samples from the $Nd_{1-x}Ba_xMnO_{3-\delta}$ series at a temperature below T_C make a transition to the metal state. Single crystals ($0.23 \le x \le 0.34$) demonstrate no such behavior.

2. EXPERIMENT

Polycrystals of $Nd_{1-x}Ba_xMnO_3$ ($0 \le x \le 0.50$) were prepared using the conventional ceramic technology. Nd_2O_3 and Mn_3O_3 oxides and $BaCO_3$ carbonate (optically and spectroscopically pure) were mixed in the stoichiometric ratio and ground in an agate mortar with an addition of ethyl alcohol. For the removal of moisture, Nd_2O_3 was roasted in the air at 1000°C for one hour. Then, the oxide mixture was pressed into tablets 2 cm in diameter and 0.5 cm high. These tablets were twice annealed in the air at 1000 and 1200°C for one hour with subsequent grinding. The final synthesis was performed in the air at 1530°C for two hours. In order to produce compositions close to stoichiometric with respect to oxygen, samples with $x \le 0.20$ were quenched, and those with $x \ge 0.40$ were held for 100 hours in the air at 900°C with subsequent cooling to room temperature at a rate of 100 deg h^{-1}. Single crystals of $Nd_{1-x}Ba_xMnO_3$ ($0.23 \le x \le 0.34$) were pre-

pared by spontaneous crystallization from a solution in a B_2O_3–BaO–BaF_2 melt upon slow cooling from a temperature of 1150°C in the air in a platinum crucible. The chemical composition was determined by Auger electron spectroscopy in a PHI-660 scanning Auger spectrometer. The oxygen content of the compositions synthesized in the air was determined by thermogravimetric analysis. According to this investigation, all of the samples prepared in the air were stoichiometric with respect to oxygen. The crystal structure and the unit cell parameters were determined by the method of X-ray powder diffraction in K_α radiation of Cr, using a DRON-3 diffractometer. The investigations were performed at room temperature at angles in the range of $20° \le 2\theta \le 80°$. The prepared samples were annealed in a stream of argon at 900°C for 24 hours. In order to enhance the reduction effect, pellets of activated carbon were located alongside the samples. Activated carbon caused a decrease in the partial pressure of oxygen in accordance with the reaction

$$2C + O_2 \longrightarrow 2CO. \quad (1)$$

The oxygen content after annealing in a reducing medium was monitored by weighing the samples before and after reduction. We did not observe any significant decrease in the mass of samples after the reduction procedure. For example, according to the data of our measurements, the oxygen content in the case of a sample with $x = 0.50$ annealed in argon was close to 2.93. For monitoring the oxygen content, reduced samples were annealed in the air at 900°C for 12 hours. The value of the oxygen index of reduced sample, equal to $x = 0.50$ and calculated by the variation of the mass before and after annealing in the air, corresponds to 2.97. An OI-3001 vibrating-coil magnetometer was used for magnetic measurements. The magnetization was measured in the temperature range from 4 to 400 K. The Curie temperature was determined as the temperature corresponding to the minimum of the derivative of magnetization in a weak magnetic field. A miniature Be–Cu container was used to measure the magnetization under conditions of hydrostatic pressure. A mixture of mineral oil and kerosene was used as the pressure-transmitting medium. The pressure was graduated at low temperatures using a superconducting lead junction. The dynamic magnetic susceptibility was measured by a mutual-inductance bridge in the temperature range from 77 to 350 K. The field amplitude was 200 A/m, with the frequency of 1200 Hz. Electrical conductivity was measured by the standard four-probe technique in the temperature range from 77 to 350 K. Samples in the form of $10 \times 2 \times 2$ mm^3 bars without macrocracks were used to measure the electrical conductivity. A silver paste was used for contacts. The magnetoresistance was calculated in accordance with the equation

$$\mathrm{MR}(\%) = \{[\rho(H) - \rho(H = 0)]/\rho(H = 0)\} \times 100(\%), \quad (2)$$

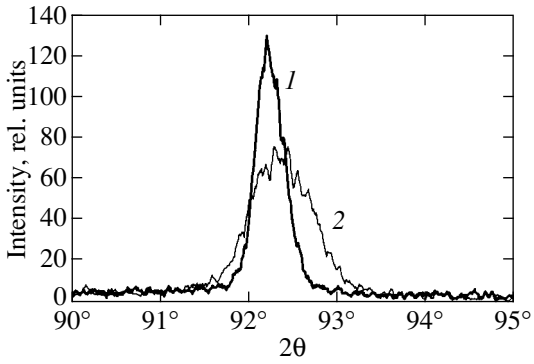

Fig. 1. X-ray reflections 211 for polycrystalline $Nd_{0.50}Ba_{0.50}MnO_{3-\delta}$ samples prepared (*1*) in the air and (*2*) in a reducing medium.

where MR(%) is the negative isotropic magnetoresistance in percent, $\rho(H)$ is the electrical resistivity in a magnetic field of 9 kOe, and $\rho(H = 0)$ is the electrical resistivity in zero magnetic field. The magnetic field was applied in parallel with the electric current in the sample.

3. RESULTS AND DISCUSSION

According to the results of X-ray analysis, the samples synthesized in the air are single-phase perovskites. The parameters were calculated [22] on the assumption of orthorhombic ($0 \le x \le 0.25$) and pseudocubic ($0.25 \le x \le 0.50$) symmetries of a unit cell. For example, for a polycrystalline sample with $x = 0.50$, the parameter is $a = 3.893$ Å ($V = 59.00$ Å^3). The polycrystalline samples annealed in argon were divided into two groups, namely, (1) those in the concentration range of $0.34 \le x \le 0.50$, in which the samples are single-phase perovskites, and (2) those in the range of $0 \le x \le 0.34$, in which the presence of the second phase was revealed. The X-ray photographs of polycrystalline samples annealed in a reducing medium exhibited characteristic features such as a clearly defined broadening of reflections and their shift towards greater angles (Fig. 1). The X-ray photographs of reduced samples were interpreted on the assumption of cubic symmetry of a unit cell. For example, the parameter for a polycrystalline sample with $x = 0.50$ annealed in a reducing medium is $a = 3.889$ Å ($V = 58.84$ Å^3). After annealing a compound of the same composition in the air, the parameter became $a = 3.887$ Å ($V = 58.76$ Å^3)). This behavior is unusual for the parameter of a reduced sample, because an increase in the unit cell volume was usually observed after reduction, this being attributed to the transition of a part of the Mn^{4+} ions to Mn^{3+} ions, which have a much greater effective ionic radius [23]. A similar behavior of the unit cell parameter was observed for reduced polycrystalline compositions from the $0.34 \le x \le 0.50$ range. All single crystals ($x = 0.23$, 0.25, 0.27, 0.30, 0.34) remained single-phase after reduction. In the case of single-phase samples, the type of unit cell symmetry

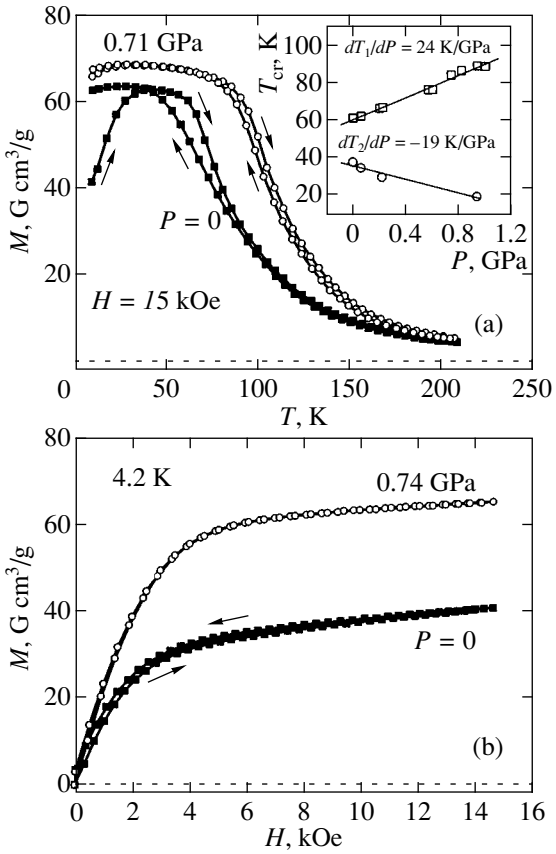

Fig. 2. The dependence of magnetization (a) on the temperature in a magnetic field of 15 kOe and (b) on the magnetic field at a temperature of 4.2 K under conditions of hydrostatic pressure $P = 0$ and $P = 0.74$ GPa for a stoichiometric polycrystalline sample with $x = 0.50$ prepared in the air. The arrows indicate the direction of variation of temperature in the process of measurement. Given in the inset is a linear interpolation of the temperatures of the emergence of ferro- (T_1) and antiferromagnetic (T_2) components as a function of applied hydrostatic pressure. The dotted lines indicate the magnetic contribution made by the Be–Cu container.

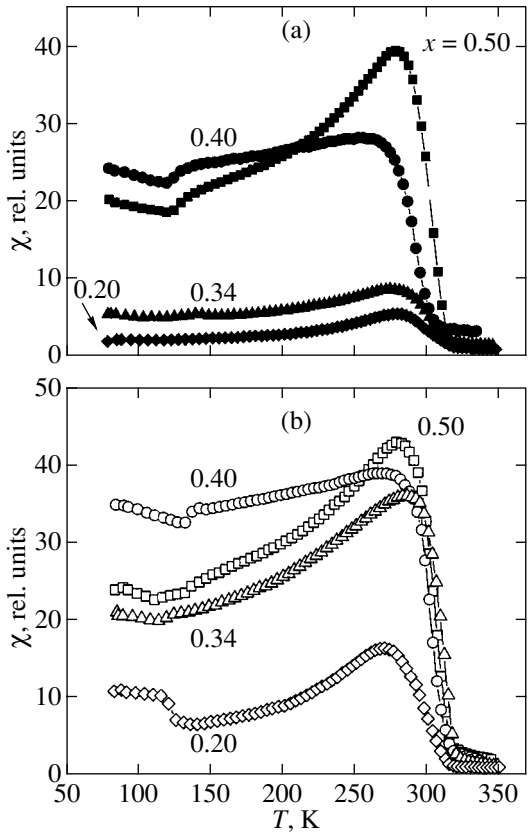

Fig. 3. The temperature dependence of dynamic magnetic susceptibility for polycrystalline $Nd_{1-x}Ba_xMnO_{3-\delta}$ samples with different values of the concentration of Ba ions (x = 0.20, 0.34, 0.40, 0.50), prepared (a) in a reducing medium and (b) annealed in the air afterwards.

remained unchanged. However, unlike polycrystals, the unit cell volume of reduced single crystals increased drastically. The Auger spectroscopy investigation of samples annealed in a reducing medium failed to reveal the presence of chemical elements other than Nd, Ba, Mn, and O.

Figure 2 gives the dependences of magnetization on temperature and magnetic field, measured at different hydrostatic pressures for a sample with $x = 0.50$ prepared in the air. In the case where no external hydrostatic pressure is present, the magnetization in a field of 1.5 T is approximately 40 G cm^3, while the magnetization under a pressure of 0.74 GPa increases to 62 G cm^3/g ($T = 4.2$ K). The external pressure brings about the disappearance of the field magnetization hysteresis, as well as causes a high rise of the Curie point, approximately at the rate of $dT_C/dP = 24$ K/GPa. Note that the value of the temperature of the onset of magnetic order depends strongly on the applied hydrostatic pressure. Shown in the inset of Fig. 2 is a linear interpolation of the critical temperatures of the emergence of ferro- (T_1) and antiferromagnetic (T_2) components as a function of hydrostatic pressure, prepared in a field of 100 Oe after cooling in zero field. The equations for the T_1 and T_2 straight lines are as follows:

$$T_1 = 60.97 + 2.92P, \quad T_2 = 36.22 - 1.83P.$$

In our opinion, such a behavior of the magnetization of a sample with $x = 0.50$ prepared in the air points to the presence of an antiferromagnetic component in the sample. A two-phase ferro-antiferromagnetic state was observed in $Pr_{1-x}Ca_xMnO_3$ compounds in the vicinity of ferromagnetic–antiferromagnetic concentration transitions [24]. The same singularities of the two-phase magnetic state are apparently inherent in the $Nd_{0.50}Ba_{0.50}MnO_3$ compound as well. The range of variation of dT_C/dP was determined experimentally to be 5 to 50 K GPa^{-1}. It has been found that the highest values of dT_C/dP correspond to compositions with the lowest values of T_C. Medvedeva *et al.* [25] attributed this to the competition between the double-exchange and superexchange interactions.

Figure 3 gives the results of measurement of the dynamic magnetic susceptibility as a function of tem-

perature for polycrystalline samples with the barium content in the range of $0.20 \le x \le 0.50$, prepared under reducing conditions and then annealed in the air. One can see that all of the reduced samples exhibit an increase in T_C up to approximately 310 K. However, the value of susceptibility and the steepness of transition to the paramagnetic state decrease gradually with decreasing concentration of Ba. Clearly defined in this plot is the low-temperature anomaly in the neighborhood of 125 K, which correlates with the temperature of the onset of magnetic order of stoichiometric samples. After annealing the same reduced samples in the air, the temperature of transition to the paramagnetic state increases slightly to 320 K, and the values of susceptibility in the high-temperature part of the samples with $x = 0.50$, 0.40, and 0.34 become almost equal. It will be remembered that a sample with $x = 20$ annealed in argon contains an impurity phase. One can see in the figures that the Curie temperature for samples prepared in argon is two–three times that for compounds prepared in the air. Note that the Curie temperature of compounds prepared in argon varies little with the barium concentration. A similar behavior was observed for a $La_{1-x}Pb_xMnO_3$ ($0.26 \le x \le 0.44$) system prepared in the air [26]. As was revealed by the measurements of magnetization, the spontaneous magnetic moment for samples prepared in a reducing medium is somewhat (approximately 10%) less than that for samples prepared in the air (Fig. 2). A sample with the concentration $x = 0.50$ prepared in the air exhibited a kink in magnetization at a temperature below T_C, which is characteristic of a smeared first-order phase transition; in the case of reduced samples, the transition to the paramagnetic state is smooth (Fig. 4), which corresponds to a second-order phase transition.

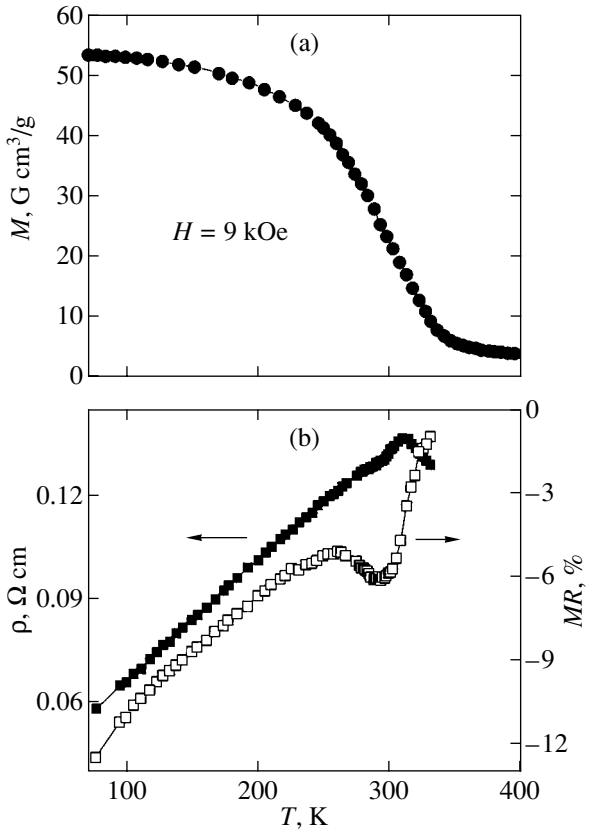

Fig. 4. The temperature dependence of (a) magnetization and (b) electrical resistivity and magnetoresistance measured in a magnetic field of 9 kOe (pointed by arrows) for a polycrystalline $Nd_{0.66}Ba_{0.34}MnO_{3-\delta}$ sample annealed in a reducing medium.

The temperature dependences of magnetization, electrical resistivity, and magnetoresistance for a sample with $x = 0.34$ annealed in argon are given in Fig. 4. One can see in the figures that the curves of electrical resistivity and magnetoresistance exhibit peaks in the vicinity of T_C. The increase in magnetoresistance with decreasing temperature is apparently due to intergranular effects, as in the case of other polycrystalline manganites. The temperature dependences of electrical conductivity and magnetoresistance of samples with a high content of barium ions ($0.34 \le x \le 0.50$) are similar to the dependences given in Fig. 4 for a sample with $x = 0.34$. In [20], the semiconductor behavior of $Pr_{0.50}Ba_{0.50}MnO_{3-\delta}$ prepared in argon was revealed. This difference is possibly due to different procedures for the preparation of samples employed for measurements.

Figure 5 gives magnetic phase diagrams of systems of $Nd_{1-x}Ba_xMnO_{3-\delta}$ samples prepared both in the air and in a reducing medium. The phase diagram for the system prepared in the air is based on the data given in [22]. The samples prepared in the air exhibit the classical sequence of concentration phase transformations, namely, antiferromagnetic dielectric–ferromagnetic dielectric–ferromagnetic metal, and, at $x \approx 0.5$, the antiferromagnetic phase appears again. However, samples with a low barium content are unstable in a reducing medium. In these conditions, they break down into a mixture of phases, one of which possesses a perovskite structure with a high barium content, and its magnetic properties are similar to the properties of single-phase samples with $x \ge 0.34$. Therefore, the phase diagram of reduced compositions starts with the value of $x = 0.34$. All of these compositions are ferromagnetics with the Curie point above room temperature. The value of electrical resistivity is small compared with that of the samples prepared in the air, and the metal–insulator transition is observed in the vicinity of T_C.

Magnetic measurements have revealed that single crystals annealed in argon are spin glasses with the freezing temperature of magnetic moments of about 40 K, i.e., they exhibit a behavior similar to that of reduced samples of the La–Ca–Mn–O [27] and La–Ba–Mn–O [28] systems. This is due to the fact that the single crystals have lost a significant fraction of oxygen as a result of annealing in the reducing medium and transformed to phases with a high deficiency of oxygen ions.

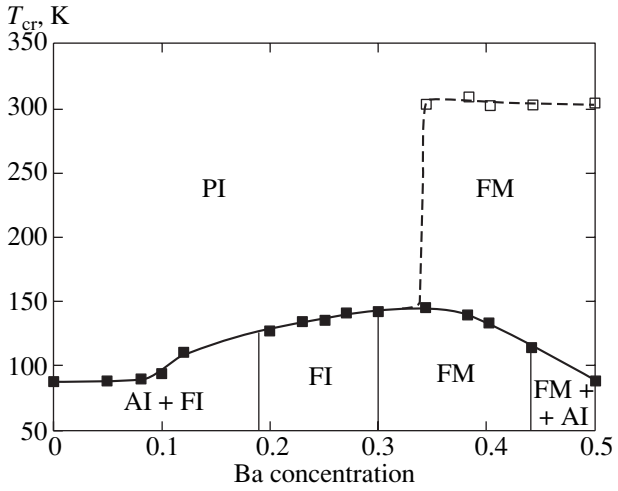

Fig. 5. The magnetic phase diagram for polycrystalline samples of two $Nd_{1-x}Ba_xMnO_{3-\delta}$ systems of solid solutions. The system prepared in the air is indicated by solid symbols, and that prepared in a reducing medium, by hollow symbols. AI denotes antiferromagnetic semiconductor; FI, ferromagnetic semiconductor; FM, ferromagnetic metal; and PI, paramagnetic semiconductor.

Apparently, an intensive exchange of oxygen with the ambient gas medium (which, in addition to Ar, contained Co, CO_2, and O_2) occurred in polycrystalline samples in the case of annealing in a reducing medium. We believe that the main result of this exchange was an abrupt increase in a certain type of extended defects and microstresses of the crystal lattice rather than the emergence of oxygen vacancies; in our opinion, it was this fact that brought about the change in the behavior of phase transformation from the first to second order, with an abrupt increase in T_C. The effect of this type of defects of crystal structure on the magnetic properties is, in all likelihood, similar to the effect of external hydrostatic pressure, which also causes an increase in T_C. The broadening of X-ray reflections is, in our opinion, a direct result and proof of the emergence of defects and microstresses in the sample. The emergence of microstresses may be due both to the formation of defects and to the crystal-structure phase transformations. Note that the phases obtained in argon are stable during heating in the air to 1250°C. Upon heating to 1350°C, the magnetic properties become the same as those of the initial samples prepared in the air. The high stability, under oxidizing conditions, of the samples annealed in a reducing medium supports the assumption that these samples do not contain a significant number of oxygen vacancies. However, this may be proof of the high stability of the resultant anion-deficient systems as well.

We did not observe a similar behavior for samples of manganites doped with calcium and strontium ions. This is apparently due to the specific features of the crystal structure of barium-containing samples or to the inadequate accuracy of the experiments performed. For example, $Ln_{0.50}Ba_{0.50}MnO_3$ samples (Ln = La, Pr, Nd, Sm, Eu, Gd) are characterized by the cubic symmetry of a unit cell, in spite of the very great difference between the ionic radii of the *A* sublattice of ABO_3 perovskite (for example, $r(Gd^{3+}) = 1.107$ Å and $r(Ba^{2+}) = 1.470$ Å [23]). It is possible that, in compositions such as $Nd_{0.50}Ba_{0.50}MnO_3$ prepared in the air, the Nd and Ba ions are partly ordered, which may have an effect on the processes of defect formation.

4. CONCLUSION

We have demonstrated that rare-earth neodymium manganites from an $Nd_{1-x}Ba_xMnO_3$ system of solid solutions, replaced by barium ions, may find themselves in different magnetic states without considerable changes in the chemical composition and unit cell parameters. It has been found that polycrystalline samples in the concentration range of $0.34 \le x \le 0.50$, prepared in a reducing medium (a gaseous mixture of argon and carbon monoxide), exhibit an increase in T_C and a variation of the pattern of the magnetic phase transition to the paramagnetic state. It has been demonstrated that the hydrostatic pressure induces the antiferromagnet–ferromagnet transition in $Nd_{0.50}Ba_{0.50}MnO_3$. Hypothetical magnetic phase diagrams have been constructed for the systems being treated, depending on the concentration of barium and the method of preparation. The experimental data obtained lead one to conclude that the magnetic and electric properties of substituted manganates may be largely defined by defects and microstresses in the crystal lattice. Further structure and spectroscopic studies are required to provide for a more detailed understanding of the properties of reduced $Ln_{1-x}Ba_xMnO_{3-\delta}$ manganites (Ln = Pr, Nd).

ACKNOWLEDGMENTS

This study received partial financial support from the Foundation for Basic Research of Belarus (project F99-264) and from DFG (Germany).

REFERENCES

1. G. H. Jonker and J. H. van Santen, Physica (Utrecht) **16**, 337 (1950).
2. G. Matsumoto, J. Phys. Soc. Jpn. **29**, 606 (1970).
3. G. Matsumoto, J. Phys. Soc. Jpn. **29**, 615 (1970).
4. K. Kubo, J. Phys. Soc. Jpn. **33**, 21 (1972).
5. K. Kubo, J. Phys. Soc. Jpn. **33**, 929 (1972).
6. R. von Helmolt, J. Wecker, B. Holzapfel, *et al.*, Phys. Rev. Lett. **71**, 2331 (1993).
7. K. Chabara, T. Ohno, M. Kasai, *et al.*, Appl. Phys. Lett. **63**, 1990 (1993).
8. Y. Tomioka, A. Asamitsu, Y. Moritomo, *et al.*, Phys. Rev. Lett. **74**, 5108 (1995).
9. J. B. Goodenough, Phys. Rev. **100**, 564 (1955).

10. C. Zener, Phys. Rev. **82**, 403 (1951).
11. P.-G. de Gennes, Phys. Rev. **118**, 141 (1960).
12. I. O. Troyanchuk, D. D. Khalyavin, E. F. Shapovalova, *et al.*, Phys. Rev. B **58**, 2422 (1998).
13. J. B. Goodenough, A. Wold, R. J. Arnott, and N. Menyuk, Phys. Rev. **124**, 373 (1961).
14. S. V. Trukhanov, I. O. Troyanchuk, F. P. Korshunov, *et al.*, Low Temp. Phys. **27**, 283 (2001).
15. I. O. Troyanchuk, D. D. Khalyavin, S. V. Trukhanov, *et al.*, Pis'ma Zh. Éksp. Teor. Fiz. **70**, 583 (1999) [JETP Lett. **70**, 590 (1999)].
16. I. O. Troyanchuk, S. V. Trukhanov, H. Szymczak, *et al.*, Zh. Éksp. Teor. Fiz. **120**, 183 (2001) [JETP **93**, 161 (2001)].
17. I. O. Troyanchuk, S. V. Trukhanov, D. D. Khalyavin, *et al.*, J. Magn. Magn. Mater. **208**, 217 (2000).
18. A. Barnabe, F. Millange, A. Maignan, *et al.*, Chem. Mater. **10**, 252 (1998).
19. V. Caignaert, F. Millange, B. Domenges, and B. Raveau, Chem. Mater. **11**, 930 (1999).
20. O. Troyanchuk, S. V. Trukhanov, H. Szymczak, *et al.*, J. Phys.: Condens. Matter **12**, L155 (2000).
21. K. R. Poeppelmeier, M. E. Leonowicz, and J. M. Longo, J. Solid State Chem. **44**, 89 (1982).
22. I. O. Troyanchuk, D. D. Khalyavin, S. V. Trukhanov, *et al.*, J. Phys.: Condens. Matter **11**, 8707 (1999).
23. R. D. Shannon, Acta Crystallogr. A **32**, 751 (1976).
24. M. M. Savosta, P. Novak, and M. Marysko, Phys. Rev. B **62**, 9532 (2000).
25. I. V. Medvedeva, K. Bäerner, G. H. Rao, *et al.*, Physica B (Amsterdam) **292**, 250 (2000).
26. L. K. Leung, A. H. Morrish, and C. W. Searle, Can. J. Phys. **47**, 2697 (1969).
27. J. M. Gonzalez-Calbet, E. Herrero, N. Rangavittal, *et al.*, J. Solid State Chem. **148**, 158 (1999).
28. H. L. Ju, J. Gopalakrishnan, and J. L. Peng, Phys. Rev. B **51**, 6143 (1995).

Translated by H. Bronstein

Journal of Experimental and Theoretical Physics, Vol. 94, No. 2, 2002, pp. 336–344.
Translated from Zhurnal Éksperimental'noĭ i Teoreticheskoĭ Fiziki, Vol. 121, No. 2, 2002, pp. 396–405.

SOLIDS
Structure

A Molecular Dynamics Study of the Microstructure of the Liquid–Gas Interphase Surface

D. I. Zhukhovitskiĭ

Associated Institute for High Temperatures, Russian Academy of Sciences, Moscow, 127412 Russia
e-mail: dmrzh@orc.ru

Received August 31, 2001

Abstract—Numerical experiments showed that the number-of-bonds distribution of particles that form a fairly large molten argon-like cluster was bimodal. This result was interpreted as a consequence of the formation of two "phases," namely, particles inside the cluster and a monolayer of particles lying above the others. Particle chains were shown to be formed near the surface of the cluster. Splitting off of separate particles from them was the most probable mechanism of vaporization. Model concepts that described the dependences observed in numerical experiments were developed. *© 2002 MAIK "Nauka/Interperiodica".*

1. INTRODUCTION

According to current views, a transition layer exists between coexisting gas and liquid. The basis for describing this layer was laid by Gibbs [1] and van der Waals [2]. Gibbs obtained thermodynamic relations between various macroscopic values characterizing the transition layer as a whole but did not consider its microscopic structure. The van der Waals theory assumed that the properties of one phase smoothly transformed into the properties of the other within a transition layer whose thickness noticeably exceeded the intermolecular distance; in this theory, the surface thermodynamic parameters were expressed in terms of the parameters that characterized this transition.

Modern approaches to describing the surface are based on the statistical mechanics apparatus [3]. The density functional method [4–6] is used most extensively. It is assumed in this method that the density is a continuous function of the coordinate normal to the interphase boundary. The characteristic transition layer thickness is usually of the order of four–five intermolecular distances. The modified van der Waals theory [7] and the mean field approximation within the framework of this theory [8] are also used.

Considerable advances in the description of the equilibrium properties of surfaces have been made by applying the density functional method and other approximations based on the assumption of a smooth transformation of one phase into the other. These approaches are, however, inapplicable to surface kinetics, for instance, to the description of undamped density correlations [9] and high self-diffusion coefficient values [10] observed in numerical experiments. These phenomena can be qualitatively explained following Frenkel [11], that is, by treating the transition layer as a set of elementary thermal excitations of the capillary wave type. Smooth coordinate dependences of values within the layer are then obtained by time averaging instantaneous values at a given point. This approach was further developed in [12–14]. It, however, uses macroscopic values (such as surface tension and density) to describe waves of microscopic lengths. The corresponding results are therefore purely qualitative in character and cannot be used in model verification.

To summarize, the problem of the microscopic structure of the transition layer remains unsolved. A wealth of data have been obtained by numerically simulating the interphase surface by the molecular dynamics [9, 15–17] and Monte Carlo [18, 19] methods. However, numerical experiments are as a rule performed to study time-averaged values. Studies of instantaneous configurations of systems comprising large numbers of particles are impeded by their complexity. The conclusion can only be drawn that the surface of a liquid is exceedingly uneven and strong surface fluctuations are noticeable.

In this work, we suggest a method for studying the microstructure of the interphase surface in numerical experiments. The method is based on determining number-of-bonds (number of nearest neighbors) distribution functions of particles constituting the system. The number of nearest neighbors is one of the fundamental values characterizing the state and structure of condensed substances. This number is sensitive to state and structural changes and, at the same time, is easy to determine in numerical experiments. The object of our molecular dynamics study was variously sized argon-like clusters present in supersaturated vapor at temperatures above the triple point of the corresponding substance. As distinguished from the plane condensed phase layer traditionally used in molecular dynamics calculations [9, 15–17], clusters are characterized by easily variable ratios between the numbers of particles on the surface and in the bulk, which makes them con-

1063-7761/02/9402-0336$22.00

venient objects of study. In addition, with clusters, we have no bottom wall, which, in traditional experiments, determines the interphase boundary profile and can influence the results of measurements.

Number-of-bonds distributions of particles in large clusters comprising no less than several hundred particles have a well-defined bimodal character and can be represented by the sum of two Gaussian exponential functions. The ratio between the modes is a cluster size function. The bimodal character of the distribution is evidence of the presence of two groups of particles or "phases" with sharply different properties. The particles that lie above the others and form a monolayer (surface particles) form fewer bonds than the other (internal) particles, which form the same number of bonds as particles in the continuous liquid. The number-of-bonds distributions of the surface and internal particles were found to exactly reproduce the modes observed for the cluster as a whole. This means that, at every time moment, there exists a very sharp boundary separating homogeneous gas from homogeneous liquid. The position of this boundary changes as time passes.

According to [20], small clusters containing less than ten particles predominantly occur in the state with the number of bonds equal to two; that is, the particles form virtual chains. Similar structures are also observed near the surface of large clusters; they play an important role in vaporization of clusters. It has been found that the most probable mechanism of vaporization from the surface of a liquid is the separation of particles from surface virtual chains.

The dependence of the number of bonds in a cluster on its size is interpreted using the two-phase cluster model comprising a nucleus of internal and a layer of surface particles. The limiting cases of small and large clusters can be related by a linear interpolation, which satisfactorily describes the size dependence observed in numerical experiments.

In Section 2, we describe the procedure for numerical simulation and the obtained number-of-bonds distribution functions. The two-phase cluster model is formulated in Section 3, and Section 4 contains a discussion of the results.

2. NUMBER-OF-BONDS DISTRIBUTION FUNCTIONS (NUMERICAL EXPERIMENT)

As mentioned in Introduction, variously sized clusters can conveniently be considered to study number-of-bonds distribution functions. We then reveal the dependence of the values of interest on the size of clusters, and the vapor–liquid interphase boundary is the limit of an infinitely large cluster. We used the method of molecular dynamics in a (*P*, *T*) ensemble. The numerical experiment procedure was described in detail in [21, 22]; it was as follows. The system to be simulated, which is a cluster placed into a vapor with fixed mean concentration and kinetic energy values, is contained in a spherical cell. The system is open, and particles that reach the cell boundary from the inside are removed, whereas vapor particles directed inside the cell and having a Maxwell velocity distribution are generated. A cluster is initialized in the center of the cell, and the values under study are recorded during its evolution. As distinguished from traditionally used microcanonical ensembles (e.g., see [23]), the (*P*, *T*) ensemble can conveniently be used to trace the whole spectrum of cluster sizes during a simulation experiment, from large clusters to very small ones. In addition, such a simulation corresponds with real experiment conditions.

It is assumed that the interaction of particles in the system is determined by the pair additive short-range potential function

$$u(r) = \begin{cases} v(r) - v(r_c), & r \le r_c, \\ 0, & r > r_c, \end{cases} \qquad v(r) = 4\epsilon\left(\frac{a^{12}}{r^{12}} - \frac{a^6}{r^6}\right), \tag{1}$$

where the cutoff radius $r_c = 2.5a$ and ϵ and a are the depth of the potential and the length scale, respectively. Potential function (1) with the cutoff radius specified above is often used to study argon-like systems. To decrease the effect of cluster temperature fluctuations, we used the modified Berendsen thermostat method described in [21, 22]. The temperature of the system was assumed to equal $0.75\epsilon/k_B$, where k_B is the Boltzmann constant, the radius of the cell was set equal to $R = 16a$, and vapor concentration n_v was varied in the range $(0.008–0.016)a^{-3}$. The critical cluster size was larger than or of the order of 10^3. The initial cluster size equaled 2500; during the evolution, the cluster completely vaporized.

The determination of the number-of-bonds distribution function required the bond concept to be defined. A particle will be assumed to have *b* bonds if *b* particles in the same cluster are situated at a distance not exceeding r_b from it. Clearly, selecting r_b should give a correct definition of the cluster size. According to the most frequently used Stillinger definition [23], a cluster is a set of particles each bonded with at least one particle from the same cluster. For a cluster to be observable, its size should not depend on r_b at least in a narrow range of r_b variations. The value suggested by Stillinger (it equals the distance to the point at which the potential function vanishes) does not satisfy this condition. As has been shown in [24], there exists such an r_b value at which the first and second derivatives of the dependence of the number of particles in a cluster (of particle size *g*) with respect to r_b equal zero; that is, in the vicinity of this r_b value, *g* is independent of r_b. Precisely this value will be used to determine the size of clusters and the number of

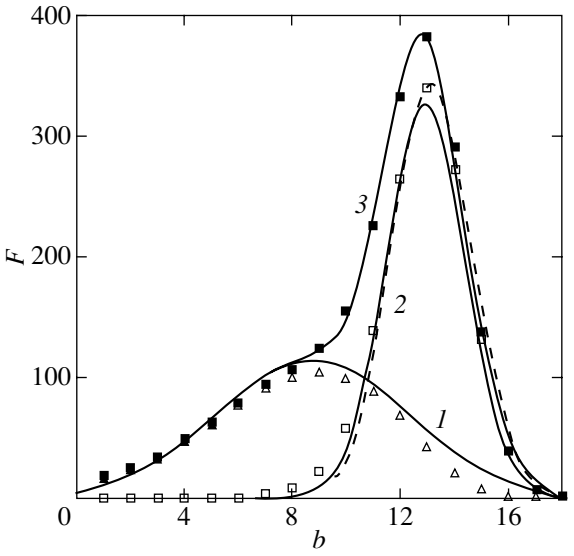

Fig. 1. Number-of-bonds distribution functions for a cluster comprising 2152 particles. Given by symbols are numerical simulation results for all particles constituting the cluster (solid squares), surface particles (open triangles), and internal particles (open squares). Solid curves *1* and *2* are the decomposition of numerical simulation results into two Gaussian components, and curve *3* is the sum of curves *1* and *2* [Eq. (3)]. The dashed curve is the number-of-bonds distribution function for the particle closest to the center of mass normalized with respect to the number of internal particles.

bonds per particle. For the numerical experiment parameters specified above, r_b = 1.65a. Note that the surface tension of a curved surface is similarly determined in classical thermodynamics; that is, in the vicinity of the surface of tension, the surface tension value does not depend on the position of this surface. It has also been shown in [24] that, if r_b is selected as described above, the g value determines the equimolar cluster radius R_e; namely, $g = R_e^3 n_l$, where n_l is the concentration of particles in the continuous liquid.

We define the number-of-bonds distribution function of a system of particles, $F(b)$, as the mean number of particles with b bonds. Then,

$$g = \sum_{b=1}^{\infty} F(b), \quad B = \sum_{b=1}^{\infty} bF(b) \tag{2}$$

are the number of particles in the cluster and the total number of bonds, respectively. The $F(b)$ value was determined during numerical simulations. Each vaporization process realization was repeated many times, and the $F(b)$ value was recorded in time intervals of $\tau_0/2$, where $\tau_0 = a\sqrt{M/24\epsilon}$ is the characteristic molecular dynamics time and M is the mass of a particle. Instantaneous $F(b)$ values were averaged for each cluster size g and then over the $g \pm 0.04g$ interval.

The F(b) values found for a cluster comprising 2152 particles are shown in Fig. 1. The $F(b)$ function can be represented by the sum of two Gaussian exponential functions,

$$F(b) = a_1 \exp\left[-\frac{(b-b_1)^2}{c_1^2}\right] + a_2 \exp\left[-\frac{(b-b_2)^2}{c_2^2}\right], \tag{3}$$

whose parameters were adjusted to obtain the best fit to the numerical experiment results; this gave a_1 = 113, a_2 = 326, b_1 = 8.78, b_2 = 12.93, c_1 = 5.00, and c_2 = 2.03. Figure 1 shows that this approximation is fairly accurate.

To determine the reason why the obtained distribution is bimodal, let us divide the particles in the cluster into two types, namely, internal and surface. Particle 1 with radius vector $\mathbf{r}_1$ (the origin is at the center of mass of the cluster) will be called internal if it forms more than four bonds and there exists at least one particle 2 with coordinate $\mathbf{r}_2$ such that the conditions

$$\mathbf{r}_2 \cdot \mathbf{r}_1 > r_1^2, \tag{4}$$

$$r_1^2 - \frac{(\mathbf{r}_2 \cdot \mathbf{r}_1)^2}{r_1^2} < \frac{1}{3n_l^{2/3}} \tag{5}$$

are satisfied. Condition (4) means that the projection of the radius vector of particle 2 onto the direction of the radius vector of particle 1 exceeds the length of the latter. Condition (5) limits the length of the projection of vector $\mathbf{r}_2$ onto the plane normal to $\mathbf{r}_1$. This condition corresponds to the model concept according to which a surface particle is situated in a vertex of a regular tetrahedron with edge length $n_l^{-1/3}$ equal to the mean distance between particles in the liquid, whereas the other particles that occupy the remaining tetrahedron vertices are internal.

The particles that are not internal will be called surface particles. It is shown below that surface particles with less than five bonds form virtual chains anchored to the surface of the cluster.

As the surface of clusters is essentially nonspherical, the simple condition of the largest distance between a surface particle and the center of mass of the cluster is insufficient. More exact conditions (4) and (5) identify particles 2 that can be situated outside a small neighborhood of particle 1 but lie within a solid angle with a vertex at the center of mass of the cluster and an axis passing through point $\mathbf{r}_1$ at a distance from the center of mass larger than r_1. If a microcavity is spontaneously formed within the cluster, the particles adjacent to this cavity are considered internal in accordance with (4) and (5). At the same time, when a deep hollow or a

sharp protuberance are formed on the surface of the cluster, surface particles correctly outline their contours.

Definition (4), (5) is heuristic in character. However, the related separation of particles into internal and surface usually corresponds with what is apparent. A typical shape of the cross section of a cluster is given in Fig. 2. The thickness of the cross section is of the order of the mean interparticle distance. The figure shows that the surface particles form a monolayer strongly curved by thermal fluctuations. Insignificant deviations from the monolayer structure arise because the particles shown in the figure do not lie in one plane. The number of bonds formed by internal particles is not less than ten, and particles with four or less bonds form virtual chains.

The obtained number-of-bonds distribution functions for surface $F_1(b)$ and internal $F_2(b)$ particles shown in Fig. 1 are satisfactorily described by the Gaussian exponential functions on the right-hand side of formula (3) (except for asymptotic behavior at large b, which cannot be Gaussian because of strong interparticle repulsion at $r < a$). We also calculated the $F_0(b)$ number-of-bonds distribution function for the particle closest to the center of mass (the central particle determined during simulations at every time step). This function is independent of the cluster size at $g > 300$ and can also be represented in the form of the Gaussian exponential function (dashed curve in Fig. 1)

$$F_0(b) = a_0 \exp[-(b - b_0)^2/c_0^2],$$

where

$$a_0 = \frac{\sum_{b=1}^{\infty} a_2 \exp[-(b - b_2)^2/c_2^2]}{\sum_{b=1}^{\infty} \exp[-(b - b_0)^2/c_0^2]} \approx 342$$

is the factor that normalizes the $F_0(b)$ distribution with respect to the number of internal particles, $b_0 = 13.19$, and $c_0 = 2.06$. The obtained parameters show that the distributions for the central and internal particles are almost indistinguishable; that is, the whole region occupied by internal particles is homogeneous. It also follows from the calculation results that, in accordance with the definition of bonds that we use, the number of bonds per particle in the continuous liquid equals 13.2.

The number-of-bonds distribution functions of surface and internal particles obtained for smaller clusters are plotted in Fig. 3. A comparison of Figs. 1 and 3 shows that the distributions have a well-defined bimodal character independent of size, but the ratio between the modes changes. The number of surface particles increases as g decreases, and the distribution maxima noticeably shift to the lower b values because of a decrease in the density of particles in small clusters.

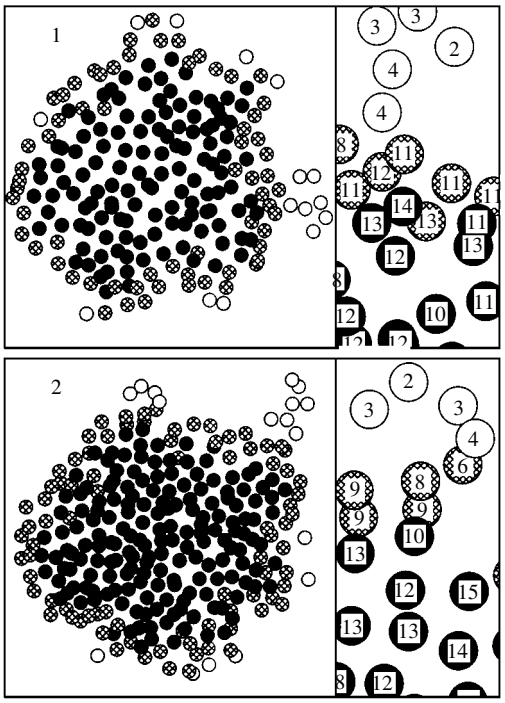

Fig. 2. Typical form of cluster cross sections at various cluster sizes g and layer thicknesses h: (*1*) $g = 1592$, $h = 1.39a$ and (*2*) $g = 2230$, $h = 1.57a$. Solid circles are internal particles, hatched circles are surface particles, and open circles are virtual chains; gas particles are not shown. Given at the right are fragments of cross sections with numbers of bonds formed by each particle.

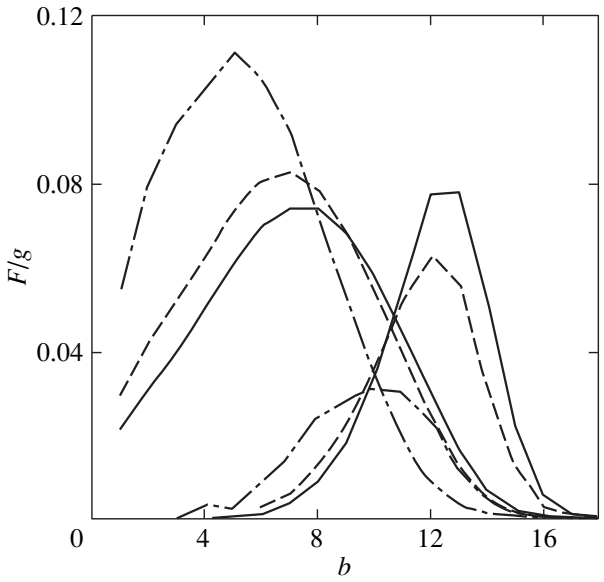

Fig. 3. Distribution functions for surface (left curves) and internal (right curves) cluster particles. The solid, dashed, and dot-and-dash curves correspond to $g = 316$, 198, and 72, respectively.

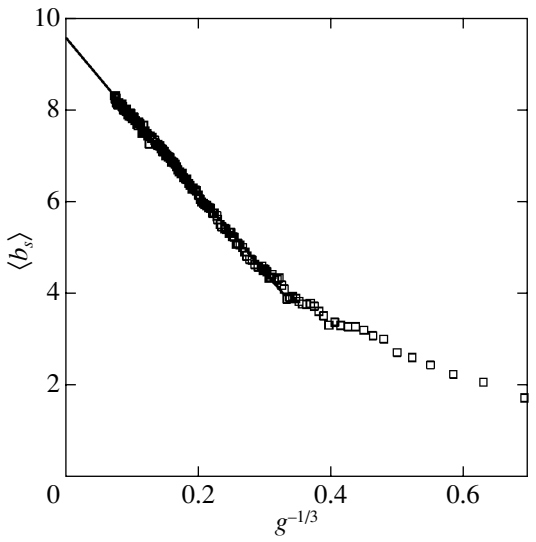

Fig. 4. Mean number of surface particle bonds in clusters of various sizes. Squares are numerical simulation data, and the straight line is the extrapolation to the plane surface.

Changing the size of clusters also changes the average number of bonds of surface particles,

$$\langle b_s \rangle = \frac{\sum_{b=1}^{\infty} bF_1(b)}{\sum_{b=1}^{\infty} F_1(b)}$$

(Fig. 4). In small clusters, the $\langle b_s \rangle$ value is insignificantly different from two; that is, surface particles predominantly form virtual chains. The $\langle b_s \rangle$ value increases in parallel with g, first slowly and then (at $g > 15$) at a higher rate. At $g > 27$, $\langle b_s \rangle$ linearly depends on $g^{-1/3}$. This circumstance allows the obtained dependence to be extrapolated to a plane gas–liquid interphase boundary ($g = \infty$), which gives $\langle b_s \rangle \approx 9.58$. Note that the $\langle b_s \rangle / b_0$ ratio is close to the corresponding ratio for the face of an ideal hexagonal crystal, which equals 9/12.

It follows from the aforesaid that particles constituting a cluster separate into two phases with sharply different properties, namely, the surface and internal phases. Consider a simplified model that allows these results to be interpreted.

3. THE TWO-PHASE CLUSTER MODEL

The numerical simulation results allow a cluster comprising two parts (phases), a nucleus and a surface layer, to be considered. For simplicity, we will use a spherically symmetrical model. As follows from numerical simulations, spherical cluster symmetry is strongly perturbed by thermal fluctuations, and the number of surface particles in a real cluster therefore exceeds the number of surface particles in a spherically symmetrical monolayer introduced in the model under consideration. For convenience of characterizing the cluster as a whole, model surface particles are assigned numbers of bonds different from the true numbers and the concept of the mean number of surface particles is introduced. This effective number can be related to the total number of particles g as follows. Consider a cluster with nucleus radius R_1 and outside surface layer radius R_2. Suppose that the concentration of particles in the nucleus coincides with concentration n_l in the continuous liquid and that the concentration of particles in the surface layer is ηn_l, where η is a model parameter. By the definition of the equimolar radius R_e for a cluster in a homogeneous vapor with the concentration n_v, we have

$$(R_e^3 - R_1^3)(\eta - 1) + (R_2^3 - R_e^3)\left(\eta - \frac{n_v}{n_l}\right) = 0. \qquad (6)$$

Using the notation

$$\lambda = \frac{R_2 - R_1}{r_l}, \quad r_l = \left(\frac{3}{4\pi n_l}\right)^{1/3}, \quad \delta = \eta\lambda - \frac{\lambda}{2}$$

and assuming that $\eta \gg n_v/n_l$, we can rewrite (6) in the form [25]

$$g = \left(\delta + \frac{\lambda}{2}\right)\beta + g_1, \quad g_0 = \left(\delta + \frac{\lambda}{2}\right)\beta, \qquad \beta = 3g_1^{2/3} + 3\lambda g_1^{1/3} + \lambda^2, \qquad (7)$$

where g_0 and $g_1 = (4\pi/3)R_1^3 n_l$ are the effective numbers of particles in the surface layer and cluster nucleus, respectively. The λ and δ parameters can be related to some thermodynamic value characterizing the cluster. For instance, if the chemical potential of the cluster is used, then δ is the Tolman length for a plane interphase boundary [24] and

$$n\lambda = \sigma + \frac{\lambda}{2} = \frac{4\pi}{3}\frac{\sigma r_l^2}{k_B T \ln(K_2/n_1)},$$

where σ is the surface tension coefficient of a plane surface of the liquid, T is the temperature, K_2 is the equilibrium dimerization constant, and n_1 is the concentration of monomers in saturated vapor. In addition, λ and δ determine the number of cluster particles,

$$z = \left(\delta + \frac{\lambda}{2}\right)(\lambda^2 + 3\lambda + 3) + 1, \qquad (8)$$

at which the nucleus contains a single particle (we set $g_0 = g$ at $g < z$). Usually, λr_l is of the order of the interparticle distance in the liquid, and z approximately equals the number of nearest neighbors [25].

Note that the model under consideration can also be applied to bubbles in liquids. It is assumed that vapor in

a bubble and the liquid are separated by a layer λr_l thick with the ηn_l concentration of particles. The first equation in (7) then becomes

$$g = (-\delta + \lambda/2)\beta + g_1,$$

where $g = (4\pi/3) R_e^3 n_l$ is the equimolar size of the bubble. The second equation in (7) remains unchanged. The bubble and cluster problems can therefore be combined as follows:

$$g = \left(\kappa\delta + \frac{\lambda}{2}\right)\beta + g_1, \quad g_0 = \left(\delta + \frac{\lambda}{2}\right)\beta, \qquad (9)$$

where $\kappa = 1$ for the cluster and $\kappa = -1$ for the bubble, in accordance with the sign of the radius of curvature of the corresponding surfaces.

Consider the size dependence of the total number of bonds in a cluster (B). This dependence can be described using the linear interpolation procedure for the thermodynamic potentials of clusters [25]. According to Fig. 4, $\langle b_s \rangle \approx 2$ in small clusters. It in turn follows from Fig. 5 that virtually all particles in such clusters are surface particles. The total number of bonds then linearly depends on the size of clusters, namely, $B = 2(g - 1) = 2(g_0 - 1)$. In a large cluster, the fraction of surface particles is negligibly small, and the gb_l number of bonds, where $b_l \approx b_0$ is the number of bonds of a particle in the continuous liquid, is proportional to the clusters size. The limiting cases of small and large clusters can be combined by the formula

$$B = 2(g_0 - 1) + b_l(g - g_0). \qquad (10)$$

Equations (10) and (7) can be used to calculate the size dependence of B for the two-phase cluster model. In particular, for $g \longrightarrow \infty$, we obtain

$$B = 3(2 - b_l)(\delta + \lambda/2)g^{2/3} + b_l g = -4\pi\alpha R_e^2 + b_l g,$$

where $\alpha = (3/4\pi r_l^2)(b_l - 2)(\delta + \lambda/2)$ is the "deficiency" in the number of bonds per unit surface area. It follows that surface particles in the two-phase cluster model can be assigned an arbitrary effective number of bonds b_{eff} satisfying the condition $2 < b_{\text{eff}} < b_l$. The $\delta + \lambda/2$ factor should then be replaced by $(\delta + \lambda/2)(b_l - 2)/(b_l - b_{\text{eff}})$. The g_0/g fraction of surface particles also increases $(b_l - 2)/(b_l - b_{\text{eff}})$ times. The applicability of the model is, however, limited at small g values at which the cluster does not contain internal particles.

It follows from (10) that the total number of bonds (B) can be used to determine the effective number of surface particles with two bonds,

$$g_0 = \frac{gb_l - B - 2}{b_l - 2}, \qquad (11)$$

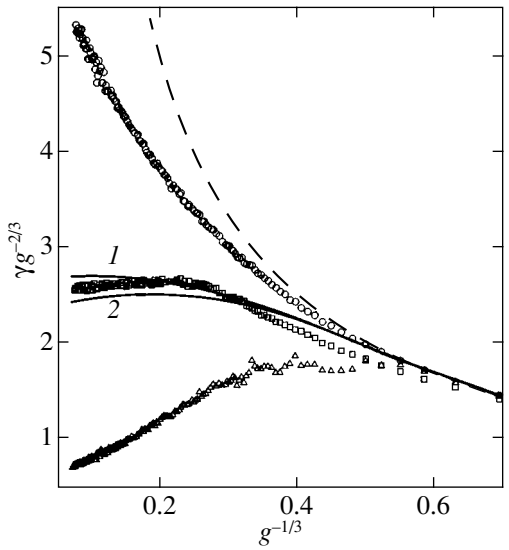

Fig. 5. Number of particles on the surface of a cluster as a function of its size: $\gamma = g_s$ (circles, the true number of surface particles), g_0 (squares, the effective number of particles), and g_{Vc} (triangles, the number of particles in virtual chains). Curves were calculated by (11) for (*1*) internal energy and (*2*) chemical potential parameters [24]; $\gamma = g_0$ (solid curves) and g (dashed curve, depicted for comparison).

along with the true number of surface particles

$$g_s = \sum_{b=1}^{\infty} F_1(b).$$

The numerical experiment data represented in the form of the size dependence of the g_0 effective number are shown in Fig. 5. The g_0 value was calculated using λ and δ obtained in [24] for an argon-like system with potential (1) parameters at the temperature that coincided with the temperature of our numerical experiments. The $\lambda = 2.124$ and $\delta = -0.175$ values describe the internal energy of the cluster, and $\lambda = 2.386$ and $\delta = -0.420$ describe its chemical potential. Figure 5 shows that these sets of parameters give close g_0 values, which are in satisfactory agreement with the numerical simulation data. The largest discrepancy is observed in the transition region, in which clusters contain several dozen particles. Naturally, the accuracy of describing simulation results can be noticeably improved by properly selecting λ and δ. The specific effective number of surface particles $g_0 g^{-2/3}$ is seen to tend to a constant value as $g \longrightarrow \infty$, and the true number of surface particles is noticeably larger than their effective number. Note that the $z = 13.3$ value corresponding to both pairs of λ and δ values [see (8)] is close to b_0. It follows that the two-phase cluster model can be used to describe the size dependence of the number of bonds in clusters, which is evidence for the applicability of this model also to describing the equilibrium properties of clusters.

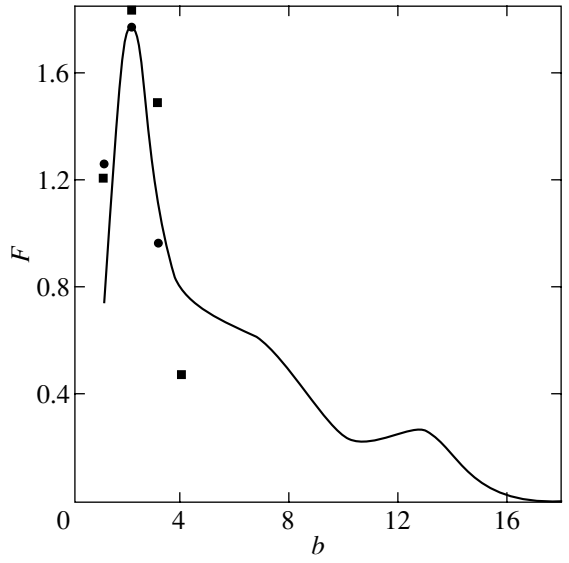

Fig. 6. Number-of-bonds distribution function for particles bonded with a vaporizing particle; the curve reproduces smoothed numerical simulation results; symbols are number-of-bonds distributions for small clusters, $g = 4$ (circles) and 5 (squares).

4. DISCUSSION

The numerical simulation results are evidence that a monolayer of particles separating two homogeneous phases is formed at the liquid–gas interphase boundary. The shape of this layer is substantially different from spherical (or plane for separation of macroscopic phases) and fluctuates as time passes. This allows us to claim the existence of a new surface phase. In the Gibbs theory, this phase is sometimes called "surface azeotrope" [3]. In the classical theory, the thermodynamic properties of curved surfaces are usually considered on the assumption that the Tolman length does not depend on surface curvature. In the two-phase cluster model, the thickness of the surface phase rather than the Tolman length is constant.

As mentioned in Section 2, part of the surface particles form virtual chains anchored to the cluster surface. In large clusters, the fraction of such particles relative to the total number of surface particles under the numerical experiment conditions is not large and amounts to 0.14 at $g = 2200$. But the bond energy between particles in virtual chains is minimum. It should therefore be expected that vaporizing particles separate precisely from virtual chains. The role played by virtual chains was studied by recording each vaporization event (using time steps of $\tau_0/2$) and determining the number-of-bonds distribution function for the particles that were bonded with the vaporized particle at the preceding step. We found that the form of the distribution function was virtually independent of g at $g > 500$. The results of averaging this function over the interval $1500 < g < 2500$ (Fig. 6) showed that the function contained three singularities corresponding to three vaporization mechanisms. The first one (a sharp maximum) was situated at the $b = 2$ number of bonds characteristic of virtual chains; this was evidence that such chains played the determining role in vaporization. The distribution function in Fig. 6 is normalized in such a way that its first maximum has the height equal to that of the number-of-bonds distribution function for the cluster comprising four particles. Figure 6 shows that the function under consideration is situated between the distribution functions for the clusters with four and five particles, $g = 4$ and 5. This circumstance leads us to conclude that the characteristic number of particles in a surface virtual chain is of the order of four. The number of bonds for virtual chain particles was therefore limited to four, as suggested in Section 2. The presence of particles with more than two bonds takes into account both the existence of branching points and admixtures of compact virtual chain states with the number of bonds larger than its minimum value [26].

The second singularity of the $F(b)$ function is situated at $b \approx \langle b_s \rangle$; it is likely to correspond to splitting off of vaporizing particles from surface particles (a small shift of this singularity to the left of $\langle b_s \rangle$ may be related to splitting off of particles predominantly from convex regions). The third singularity is a poorly defined maximum at $b \approx b_0$. It corresponds to direct splitting off of surface particles that do not form virtual chains from internal particles. Clearly, the third vaporization mechanism has a low probability.

The suggestion was made in [27] that vaporizing particles were split off from spontaneously formed convex liquid surface regions. The results of this work substantiate and refine this suggestion; indeed, surface virtual chains can be treated as the limiting case of protuberances.

It would be interesting to consider the size dependences of the number of surface particles g_s and the number of particles constituting virtual chains,

$$g_{vc} = \sum_{b=1}^{4} F_1(b),$$

per unit cluster surface (Fig. 5). At large g, the $g_{vc}g^{-2/3}$ value almost linearly depends on $g^{-1/3}$,

$$g_{vc}g^{-2/3} \approx C_1 + C_2 g^{-1/3},$$

where C_1 and C_2 are constants. According to classical nucleation theory [11], the rate of vaporization of particles from unit cluster surface is proportional to $\exp(8\pi\sigma r_l^2/3k_BTg^{1/3})$, where σ is taken to be independent of g in large clusters ($g > 300$). At large g, the exponent is smaller than one and

$$\exp\left(\frac{8\pi\sigma r_l^2}{3k_BTg^{1/3}}\right) \approx 1 + \frac{8\pi\sigma r_l^2}{3k_BTg^{1/3}}.$$

If vaporizing particles are only split off from virtual chains, the rate of vaporization should be proportional to $g_{vc}g^{-2/3}$, which gives

$$\frac{C_2}{C_1} = 8\pi\sigma r_l^2/3k_BT.$$

For the potential function cutoff radius and temperature used in our numerical experiments, we have $\sigma = 0.52\epsilon/a^2$ and $r_l = 0.68a$ [16]. This gives $C_2/C_1 = 2.48$, in agreement with the $C_2/C_1 \approx 3$ value obtained in numerical simulations (Fig. 5).

The size dependence of the g_s number of surface particles may be evidence of changes in the fractal dimension of the surface phase. It is likely that the same effect explains the size dependence of the $\langle b_s \rangle$ mean number of bonds of surface particles at large g (Fig. 4). Note that the g_s/g fraction of surface particles fairly slowly decreases as g increases. For instance, the cluster with $g = 37$ contains 90% surface particles (Fig. 5), and $g_s/g = 0.5$ at $g = 1000$. The extrapolation of these data to very large g values gives $g_s/g = 0.1$ at $g \sim 10^5$. The latter size can, we believe, be considered threshold; a cluster with this size acquires the properties of a macroscopic drop.

The analysis of the $g_s(g)$ and $g_{vc}(g)$ dependences given above is only qualitative in character. Topical problems are a detailed study of surface structures of the type of virtual chains (in particular, the refinement of their definition) and the determination of the fractal dimension of the surface phase.

When the size of a cluster decreases, approximations of $F_1(b)$ and $F_2(b)$ by Gaussian exponential functions (3) become less accurate, and distribution maxima shift to the left. This can be related to gradual disappearance of the nucleus of internal particles as g decreases. A nucleus can be assumed to form at $g > 200$, because increasing the size above this value has virtually no effect on the density of particles in the cluster center. It follows that the size range $z < g < 200$ is a transition region in which the nucleus of clusters is formed. According to its physical meaning, the two-phase cluster model (Section 3) should be applicable at $g > 200$. At $g < 200$, the results obtained using this model should be treated as extrapolation results. It is therefore not surprising that the largest discrepancies between these results and the numerical experiment data are observed at $7 < g < 20$.

It is natural to identify the number of bonds for an internal particle with the number of nearest neighbors in the liquid. As follows from the b_0 parameter value, it equals 13.19 under the conditions of our experiments. This number exceeds the number of nearest neighbors in hexagonal crystals (twelve), which is not surprising, because, in crystals, the concept of atomic shells rather than the r_b length parameter is used. With the r_b value used in this work, which approximately equals the distance to the first radial distribution function maximum in the liquid, the number of "nearest neighbors" in crystals increases to nineteen.

Strong cluster surface shape fluctuations in combination with the existence of a sharp boundary that separates homogeneous gas and liquid can be interpreted as capillary waves at the interphase boundary. From this point of view, the results obtained in this work substantiate the capillary-wave model of the boundary [12–14]. It follows from the simulation results that the internal transition layer thickness usually introduced in theory equals the thickness of the layer of surface particles, which is close to the mean interparticle distance. The total thickness is determined by averaging the position of the interphase boundary.

One of the difficulties of the theory of thermocapillary waves is the divergence of the spectrum of these waves [14]. This divergence may arise because thermocapillary waves are treated as macroscopic waves and the surface tension σ value for a plane surface is used. However, if the wavelength is of the order of the interparticle distance, a size correction to σ should be taken into account. Equation (9) may prove useful in solving this problem. The development of the capillary wave theory of the interphase boundary is a topical problem whose solution would allow not only the equilibrium but also the transport properties of the surface to be described.

ACKNOWLEDGMENTS

This work was financially supported by the Russian Foundation for Basic Research (projects nos. 00-15-96529 and 99-02-16094).

REFERENCES

1. J. W. Gibbs, in *The Collected Works of J. Willard Gibbs* (Yale Univ. Press, New Haven, 1948; Nauka, Moscow, 1982), Vols. 1, 2.
2. J. D. van der Waals, *Lehrbuch der Thermostatik*, Ed. by P. A. Kohnstamm (J. A. Barth, Leipzig, 1927; ONTI, Moscow, 1936), Parts I, II.
3. J. Rowlinson and B. Widom, *Molecular Theory of Capillarity* (Oxford Univ. Press, Oxford, 1982; Mir, Moscow, 1986).
4. X. C. Zeng and D. W. Oxtoby, J. Chem. Phys. **94**, 4472 (1991).
5. V. Talanquer and D. W. Oxtoby, J. Phys. Chem. **99**, 2865 (1995).
6. T. V. Bykov and X. C. Zeng, J. Chem. Phys. **111**, 3705 (1999); **111**, 10 602 (1999).
7. M. P. A. Fisher and M. Wortis, Phys. Rev. B **29**, 6252 (1984).
8. A. E. van Giessen, E. M. Blokhuis, and D. J. Bukman, J. Chem. Phys. **108**, 1148 (1998).
9. S. I. Anisimov, D. O. Dunikov, V. V. Zhakhovskii, and S. P. Malyshenko, J. Chem. Phys. **110**, 8722 (1999).

10. A. ten Bosch and D. I. Zhukhovitskiĭ, in *Proceedings of the First International Conference on Computational Nanoscience, Hilton, Head Island, South Carolina, USA, 2001*, p. 141.
11. Ya. I. Frenkel', *Kinetic Theory of Liquids: Collection of Selected Works* (Akad. Nauk SSSR, Moscow, 1959).
12. F. P. Buff, R. A. Lovett, and F. H. Stillinger, Phys. Rev. Lett. **15**, 621 (1965).
13. M.-D. Lacasse, G. S. Grest, and A. J. Levine, Phys. Rev. Lett. **80**, 309 (1998).
14. S. W. Sides, G. S. Grest, and M.-D. Lacasse, Phys. Rev. E **60**, 6708 (1999).
15. M. J. P. Nijmeijer, A. F. Bakker, C. Bruin, and J. H. Sikkenk, J. Chem. Phys. **89**, 3789 (1988).
16. M. J. Haye and C. Bruin, J. Chem. Phys. **100**, 556 (1994).
17. M. Mecke, J. Winkelmann, and J. Fischer, J. Chem. Phys. **107**, 9264 (1997).
18. J. K. Lee, J. A. Barker, and G. M. Pound, J. Chem. Phys. **60**, 1976 (1974).
19. G. A. Chapela, G. Saville, S. M. Thompson, and J. S. Rowlinson, J. Chem. Soc., Faraday Trans. 2 **8**, 1133 (1977).
20. D. I. Zhukhovitskiĭ, Zh. Éksp. Teor. Fiz. **113**, 181 (1998) [JETP **86**, 101 (1998)].
21. D. I. Zhukhovitskiĭ, Zh. Éksp. Teor. Fiz. **109**, 839 (1996) [JETP **82**, 451 (1996)].
22. D. I. Zhukhovitskiĭ, J. Chem. Phys. **103**, 9401 (1995).
23. F. H. Stillinger, Jr., J. Chem. Phys. **38**, 1486 (1963).
24. D. I. Zhukhovitskiĭ, Zh. Fiz. Khim. **75**, 1157 (2001).
25. D. I. Zhukhovitskiĭ, J. Chem. Phys. **101**, 5076 (1994).
26. D. I. Zhukhovitskiĭ, J. Chem. Phys. **110**, 7770 (1999).
27. V. V. Zhakhovskiĭ and S. I. Anisimov, Zh. Éksp. Teor. Fiz. **111**, 1328 (1997) [JETP **84**, 734 (1997)].

Translated by V. Sipachev

Journal of Experimental and Theoretical Physics, Vol. 94, No. 2, 2002, pp. 345–349.
Translated from Zhurnal Éksperimental'noĭ i Teoreticheskoĭ Fiziki, Vol. 121, No. 2, 2002, pp. 406–411.

SOLIDS
Electronic Properties

Anisotropy of the Raman Scattering Measured in the *xy* Plane of a Nontwinned $YBa_2Cu_3O_{7-x}$ Single Crystal

O. V. Misochko

Institute of Solid State Physics, Russian Academy of Sciences,
p/o Chernogolovka, Moscow oblast, 142432 Russia
e-mail: misochko@issp.ac.ru

Received July 10, 2001

Abstract—The temperature dependence of anisotropy of the phonon and electron Raman scattering components was studied by measurements in the *xy* plane of a nontwinned $YBa_2Cu_3O_{7-x}$ single crystal. It is shown that the sign of the orthorhombicity parameter $\gamma = (I_{yy} - I_{xx})/(I_{yy} + I_{xx})$ for the full-symmetry phonons (150, 340, and 435 cm^{-1} modes) generated by the displacements of ions in the CuO_2 plane is opposite to the sign of this parameter for the phonons generated by the out-of-plane barium and bridging oxygen displacements (120 and 500 cm^{-1} modes). In the superconducting state, the γ value decreases in the region of low frequencies, but the frequency renormalization of the 340 cm^{-1} mode measured in the *xx* and *yy* spectra is the same to within the experimental error. © *2002 MAIK "Nauka/Interperiodica".*

1. INTRODUCTION

The knowledge of how superconductivity modifies the Raman spectrum of a solid was provided by a pioneering work of Abrikosov and Fal'kovskiĭ [1], where it was demonstrated that the superconducting state features a new scattering channel related to breakage of the Cooper pairs. As a result, the electron Raman scattering spectrum exhibits a new peak at a frequency of $\Omega = 2\Delta$, whereas no scattering takes place in the region of $\Omega < 2\Delta$ for a superconductor with an isotropic gap of the *s* type even if such scattering was observed in the normal state.

Since the discovery of high-temperature superconductivity, Raman scattering has became one of the methods that provide information about basic parameters such as the superconducting gap width and symmetry, the energy and damping of the low-energy electron excitations in various regions of the Fermi surface, and the electron–phonon interaction characteristics [2]. The typical Raman spectrum of a high-temperature superconductor (HTSC) comprises a rather intense structureless electron continuum bearing relatively narrow phonon lines. In the normal state, the electron continuum extends up to frequencies exceeding 1 eV [3] and exhibits no maximum in the region of the $v_F q$ frequency (v_F is the velocity on the Fermi level, $q \approx 1/\delta$ is the transferred momentum, and δ is the optical penetration depth). Upon transition to the superconducting state, the electron continuum exhibits a polarization-dependent redistribution in the low-frequency region. Using the positions of the electron Raman scattering peaks (related to the Cooper pair breakage), it is possible to judge the superconducting gap width, anisotropy, and (in some cases) preferred symmetry [1, 2]. It should be noted that a relative change in the electron continuum intensity is usually small, which complicates accurate determination of the peak positions. In some HTSCs, additional information concerning the superconducting gap can be gained from the phonon renormalization effect related to the antiphase displacements of oxygen ions in the cuprate plane [4]. However, a large magnitude of the electron–phonon interaction related to corrugation of the CuO_2 planes and the crystal field asymmetry [5] is only partly responsible for the phonon mode "softening" in the superconducting state and does not indicate that this phonon plays any significant role in the formation of this state [6].

Although the real symmetry of an HTSC crystal is usually below tetragonal, convenient simplifications are offered by the groups of a higher symmetry providing a common description for various HTSC classes with an allowance for the circumstance that the tetragonal symmetry is dominating in most of the theoretical models employed. The simplification is justified by the fact that the high-temperature superconductivity takes place in CuO_2 cuprate layers with square lattices, in which deviations from the tetragonal symmetry are crystallographically small. In application to electron Raman scattering, this tetragonal approximation is confirmed by the fact that most of the HTSC crystals belonging to various classes (provided close degrees of doping) exhibit surprisingly like Raman scattering spectra measured in a coordinate system related to the directions of CuO bonds in the cuprate plane. In optimum-doped HTSCs, the $2\Delta/T_c$ values determined from the full- symmetry A_{1g} spectra and/or nondiagonal B_{2g} spectra are always smaller

(by approximately 30%) than the analogous values measured in the B_{1g} spectra [2].

In the case of B_{1g} symmetry, the excitations are measured in the $x'y'$ polarization probing predominantly a part of the Fermi surface near the principal axes [2] (here and below we use Porto's short notation αα for various scattering polarizations, where the first and the second symbols denote polarizations of the exciting and scattered light beams, respectively; the phonon wavevector for the spectra taken in the *xy* plane is always directed along the *z* axis). In the B_{2g} spectra measured in the *xy* polarization, a maximum contribution is from the Fermi surface regions along diagonals of the Brillouin zone. The polarized spectra with $e_i \parallel e_s$ give a full-symmetry component always containing an admixture of the *B* representations depending on the electric field vector orientation in the basal plane [2]. This fact indicates that the superconducting gap on the CuO_2 plane is anisotropic, reaching a maximum width for the reciprocal space directions coinciding with orientations of the CuO bonds in the cuprate plane. Moreover, the electron Raman scattering for $Bi_2Sr_2CaCu_2O_8$ in both normal and superconducting states obeys the selection rules for the tetragonal group [7]. This fact confirms that the main contribution to the scattering is from the electron states in the tetragonal CuO_2 plane. At the same time, a number of active phonons in the Raman spectrum of this crystal possess a pronounced anisotropy related to a one-dimensional modulation in the BiO planes [7].

We may expect that a different situation takes place in $YBa_2Cu_3O_{7-x}$ (YBCO) crystals containing one-dimensional chains representing conducting channels for the charge carriers. Although an orthorhombic character of the phonon spectra of YBCO was reported long ago [8], no detailed analysis of anisotropy of the phonon and electron Raman spectra was undertaken until now. Of special interest are the recent communications [9] concerning the *xy* anisotropic softening of the 340 cm^{-1} mode, from which it was concluded that the superconducting gap exhibits a considerable anisotropy in the *x* and *y* directions. However, a critical analysis of these results showed that the anisotropic softening results from incorrect processing of the experimental data and that the conclusion about a large (>20%) difference between the superconducting gap widths in the k_x and k_y directions in the *k* space is most likely misleading [10].

This paper analyzes in detail the manifestation of orthorhombicity (i.e., unequivalence of the *x* and *y* crystallographic directions) in YBCO single crystals as revealed by the Raman scattering spectra. Special attention is paid to separation of the electron and phonon scattering components and to analysis of the temperature dependence of the orthorhombicity parameter determined from a comparison of the Raman spectra measured for various polarizations.

2. EXPERIMENT, RESULTS, AND DISCUSSION

The Raman scattering spectra were measured in a twin-free *ab* basal plane of an YBCO crystal. The measurements were performed in a backscattering geometry in a temperature range from 10 K to room temperature. The oxygen chains were aligned in the *b* direction and a Cartesian coordinate system was selected so that $x \parallel a$, $y \parallel b$, and $z \parallel c$. Prior to mounting in a cryostat, the YBCO crystal was oriented using the Laue diffraction pattern. According to the results of magnetic measurements, the sample had a superconducting transition temperature of $T_c = 92$ K, which showed evidence of a nearly optimum doping level.

The Raman scattering spectra were measured with a triple spectrometer equipped with a multichannel detector. The spectra were excited with an Ar^+ laser ($\lambda = 488$ nm). In order to avoid overheating of the sample, the radiant power density did not exceed 10 W/cm^2. The excitation area (for a characteristic laser beam spot size of 100 μm) was monitored with a microscopic attachment, which allowed the same (to within 10 μm) twin-free region of a sample crystal to be studied in various experiments. The spectra were recorded for the same orientation (45° relative to the spectrometer entrance slit) of the electric field vector **E** in the scattered beam. This orientation, adjusted with the aid of a polarization attachment, eliminated the need for additional normalization related to the polarization dependence.

The Raman scattering spectrum of an YBCO crystal possessing the orthorhombic D_{2h} symmetry exhibits signals due to 15 active phonons. Ten of these possess a symmetry lower than that of the crystal lattice. Most clearly pronounced for nondiagonal phonons, the crystal orthorhombicity leads to a difference of the B_{2g} and B_{3g} mode frequencies. Removal of the tetragonal degeneracy is most clearly pronounced for the phonon modes of the out-of-plane ions, reaching up to 100 cm^{-1} for the nondiagonal modes of bridging oxygen [8]. Five full-symmetry phonons are detected in the polarized Raman scattering spectra at 120, 150, 340, 435, and 500 cm^{-1}. These phonons are generated by the axial displacements of metal (Ba and Cu2) and oxygen (O2, O3, and O4) ions [8]. Among the full-symmetry phonons, the 340 cm^{-1} mode (generated by the antiphase displacements of oxygen atoms from the CuO_2 plane) possesses special transformation properties and can be detected not only in the polarized *xx*, *yy*, and $x'x'$ spectra, but in the depolarized $x'y'$ spectrum as well. This fact indicates that the tensor

$$\begin{pmatrix} a & & \\ & b & \\ & & c \end{pmatrix}$$

of this mode has the elements $a \approx -b$ and $c \approx 0$, thus virtually coinciding with the tetragonal B_{1g} tensor

$$\begin{pmatrix} b & & \\ & -b & \\ & & 0 \end{pmatrix}.$$

In contrast to the in-phase displacements of the same oxygen atoms (corresponding to the 435 cm^{-1} mode), the antiphase displacements exhibit no mixing with the displacements of bridging oxygen O4 [5]. The activity of this mode is due to violated symmetry of the single CuO_2 plane (which is related to the asymmetry of chemical bonds and the crystal environment) and is mediated by the care transfer between oxygen ions in the CuO_2 plane [5, 11].

Figure 1 shows the Raman scattering spectra measured in various polarizations upon excitation of the *ab* basal plane of a nontwinned YBCO single crystal. The electron Raman scattering spectrum offers the most convincing evidence of crystal orthorhombicity: this spectrum shows a maximum intensity in the case when the electric field vector **E** is parallel to the oxygen chains (**E** ∥ **b**). The orthorhombicity is also manifested in the phonon scattering spectrum, where the relative intensities of phonon modes are different for the spectra measured in the *xx* and *yy* polarizations. It should be specially pointed out that the 340 cm^{-1} mode appears in the *x'x'* spectrum with a rather large intensity, which is indicative of the mixed symmetry ($A_{1g} + B_{1g}$) of this band measured in the tetragonal D_{4h} group basis. For a purely tetragonal B_{1g} symmetry, the mode cannot appear in the *x'x'* spectrum because the matrix elements are equal (in absolute value) and the B_{1g} tensor trace is zero. A deviation from the tetragonal symmetry for this phonon mode is also manifested by different intensities of this mode in the *xx* and *yy* spectra.

In order to evaluate the orthorhombicity of a crystal studied, we may separate the corresponding contribution in the Raman scattering spectra by subtracting the *xx* spectrum from the *yy* spectrum and normalizing the difference to the sum of these intensities, which yields the parameter $\gamma = (I_{yy} - I_{xx})/(I_{yy} + I_{xx})$. A plot of this orthorhombicity parameter versus frequency for two temperatures is presented in Fig. 2. As can be seen, the main contribution to γ in the entire frequency range studied is related to the electron scattering component, while the out-of-plane phonons produce an additional increase in the orthorhombicity. It is remarkable that the signs of the orthorhombicity parameter, determined by the difference of the diagonal elements of the full-symmetry tensor

$$\begin{pmatrix} a & & \\ & b & \\ & & c \end{pmatrix},$$

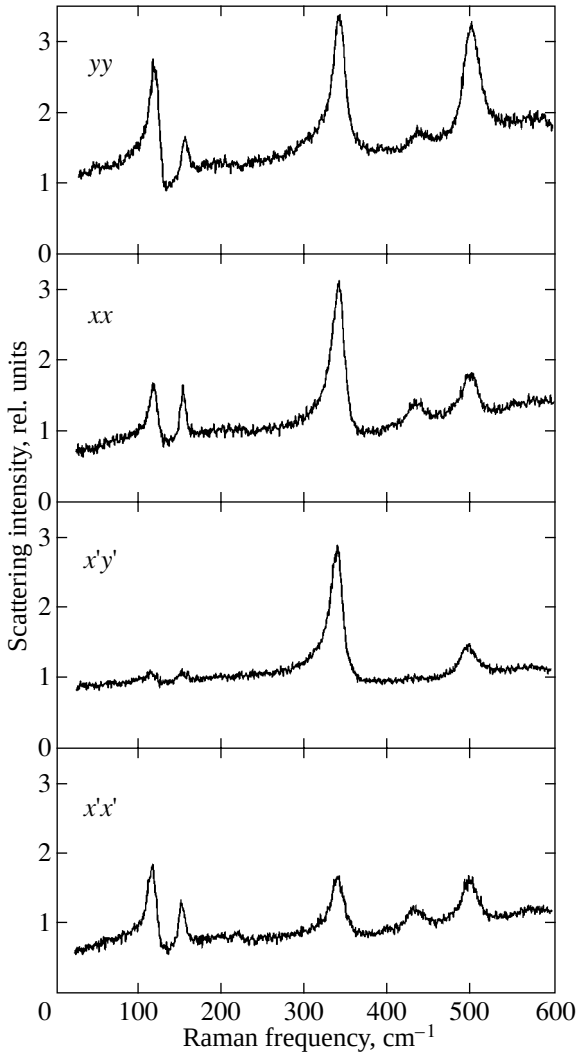

Fig. 1. The Raman scattering spectra measured at $T = 245$ K in various polarizations for $YBa_2Cu_3O_{7-x}$ single crystal excitation in the *ab* basal plane.

are opposite for the phonon modes generated by ion displacements from the CuO_2 plane and for the modes with dominating displacements of ions occurring outside the cuprate plane. This is clearly illustrated by a comparison between the 150, 340, and 435 cm^{-1} modes generated by ion displacements from the CuO_2 plane and the 120 and 500 cm^{-1} modes in which the out-of-plane ion displacements are dominating. In the former case, $b > a$ and the γ value exhibits minima, while the latter phonons are characterized by $b < a$ and give peaks in the orthorhombicity parameter spectrum.

It should be noted that, although the reported Raman spectra were not normalized to the light penetration depth in the sample, this cannot significantly influence the results because the optical penetration depth for the *yy* polarization ($E \parallel y$) is smaller than that for the *xx* polarization ($E \parallel x$). This implies that the ratio of the matrix elements b/a is greater than the ratio of the cor-

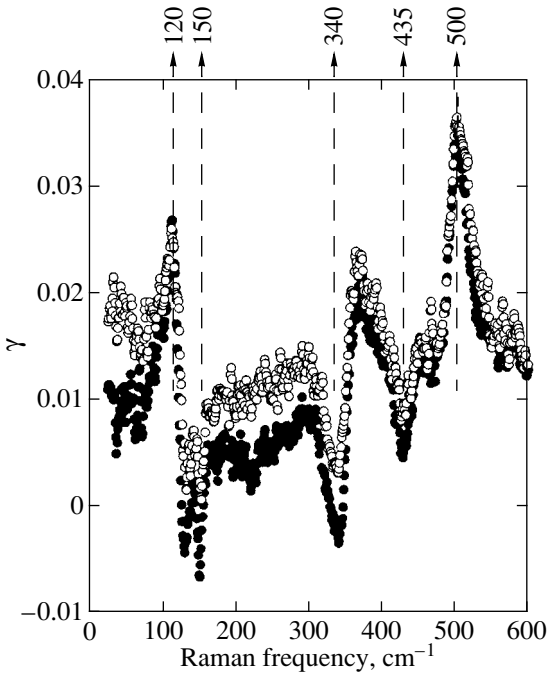

Fig. 2. The frequency dependence of the orthorhombicity parameter γ at two temperatures: (○) $T = 295$ K; (●) $T = 10$ K.

responding intensities; determined by the scattering cross section, the orthorhombicity parameter will only increase in magnitude while retaining the same sign. It is also interesting to note that the excitation of phonons in the CuO_2 plane leads to a decrease in the orthorhombicity parameter, whereby the γ value approaches zero in the given frequency range. This effect is most significant for the 150 and 340 cm^{-1} modes and less pronounced for the 435 cm^{-1} mode, which is probably explained by the mixing of displacements of the in-plane and bridging oxygen for this mode [11].

Since the orthorhombicity of the Ba mode (as well as that of the bridging oxygen mode) is due to the CuO chains and reflects additional electron transitions (allowed only for the **E** || **y** polarization) in the O4–Cu1–O1 chain complex, the resonance dependence of the scattering intensity suggests that the orthorhombicity parameter would decrease with increasing excitation wavelength [12]. For the 435, 340, and 150 cm^{-1} modes, the presence of oxygen chains results in a nonuniform corrugation of the CuO_2 plane (with O2 and O3 ions differently displaced along the *c* axis relative to the Cu ions). This nonconformity probably accounts for the anisotropy of the phonon response observed for various full-symmetry polarizations.

For an YBCO crystal in the superconducting state, the orthorhombicity parameter exhibits a maximum variation in the region of low frequencies. The transition into a superconducting state renders the crystal more "tetragonal," whereby the orthorhombicity parameter decreases. This is caused by stronger suppression of the electron scattering and by the superconductivity-induced growth in the phonon intensity for the *yy* polarization (although the latter effect is not as pronounced for the laser wavelength used in the experiment [13]). At the same time, no *xy* softening anisotropy for the 340 cm^{-1} mode is observed to within the experimental accuracy (see Fig. 3). The phonon line shape was fitted using a standard Fano formula, while the frequency and damping were not fixed for various polarizations. Even under these conditions, the frequency difference between the *xx* and *yy* polarizations fell within the experimental error (see Fig. 3); the frequency coincided with that observed in the *x'x'* spectra

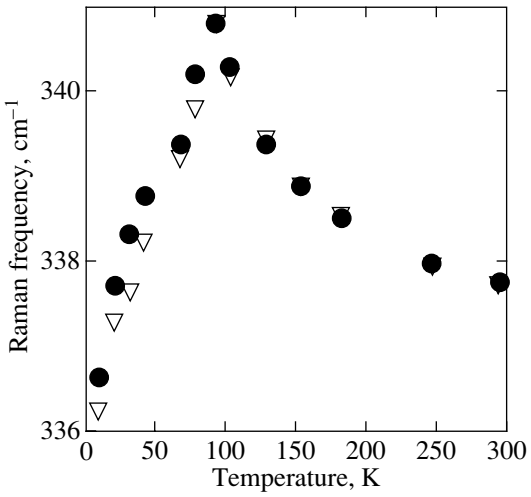

Fig. 3. The temperature variation of the 340 cm^{-1} mode frequency determined from the *xx* (▽) and *yy* (●) Raman scattering spectra.

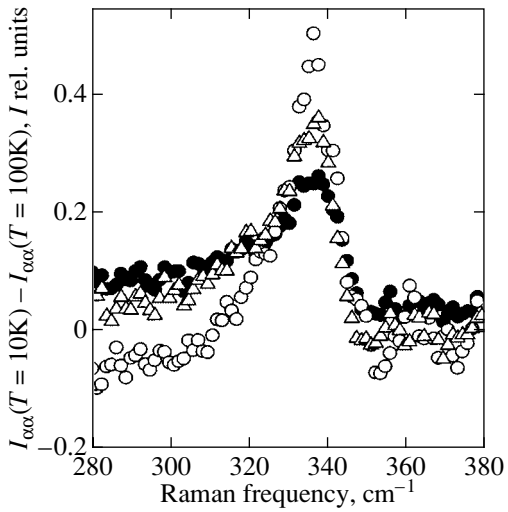

Fig. 4. Superconductivity-induced full-symmetry electron Raman scattering component determined from the *xx* (●), *yy* (○), and *x'x'* (△) Raman scattering spectra.

(not depicted in the figure). Simple physical considerations suggest that the frequency and damping for the seeding parameters of phonons in various polarizations must be identical [10]. The fitting parameters are the intensity of the electron continuum and the phonon line asymmetry: these quantities are different for various polarizations in both normal and superconducting states. However, a difference existing in the normal state is evidence of the orthorhombicity of the system studied, rather than of the *xy* anisotropy of the superconducting sate.

In addition, the positions of full-symmetry electron peaks presented in Fig. 4 (rather than the peak intensities [7]) coincide for the *xx*, *yy*, and *x*'*x*' spectra. This indicates (by analogy with the case of $Bi_2Sr_2CaCu_2O_8$ [6]) that the superconducting gap widths in the *x* and *y* directions coincide (at least to within a few percent). Note that this by no means implies that the gap is isotropic: the superconducting gap of an HTSC is anisotropic because the electron peak of the Raman scattering in the *x*'*y*' polarization in the superconducting state occurs at a higher frequency (approximately at 550 cm^{-1}) as compared to the full-symmetry peaks [2].

3. CONCLUSION

A comparative analysis of the Raman scattering spectra of a nontwinned $YBa_2Cu_3O_{7-x}$ single crystal showed that the orthorhombicity parameter possesses opposite signs for the phonons generated by ion displacements in the CuO_2 plane and the displacements of ions situated out of the cuprate planes. The contribution of the electron Raman scattering component to the orthorhombicity parameter dominates and coincides in sign with a contribution due to the out-of-plane phonons. To within the experimental accuracy, the frequency renormalization for the 340 cm^{-1} mode is identical in the *xx* and *yy* polarizations. This, together with the data on the electron Raman scattering, is indicative of the absence (to within the experimental accuracy) of differences between the superconducting gap width in the k_x and k_y directions in the reciprocal space.

ACKNOWLEDGMENTS

This study was supported by the Russian Foundation for Basic Research, project no. 01-02-16480.

REFERENCES

1. A. A. Abrikosov and L. A. Fal'kovskiĭ, Zh. Éksp. Teor. Fiz. **40**, 262 (1961) [Sov. Phys. JETP **13**, 179 (1961)].
2. M. Cardona, Physica C (Amsterdam) **317–318**, 30 (1999); D. Einzel and R. Hackl, J. Raman Spectrosc. **27**, 307 (1996).
3. D. Salamon, P. Abbanonte, Ran Liu, *et al.*, Phys. Rev. B **53**, 886 (1996).
4. R. M. Macfarlane, H. Rosen, and H. Seki, Solid State Commun. **63**, 831 (1987); S. L. Cooper, M. V. Klein, B. J. Pasol, *et al.*, Phys. Rev. B **37**, 5920 (1988).
5. É. I. Rashba and E. Ya. Sherman, Pis'ma Zh. Éksp. Teor. Fiz. **47**, 404 (1988) [JETP Lett. **47**, 482 (1988)]; Sverkhprovodimost: Fiz., Khim., Tekh. **2**, 91 (1989).
6. S. Y. Savrasov and O. K. Andersen, Phys. Rev. Lett. **77**, 4430 (1996); T. P. Devereaux, A. Virosztek, A. Zawadowski, *et al.*, Solid State Commun. **108**, 407 (1998).
7. O. V. Misochko and G. Genda, Physica C (Amsterdam) **288**, 115 (1997); O. V. Misochko, Int. J. Mod. Phys. B **14**, 1501 (2000).
8. C. Thomsen, M. Cardona, B. Gegenheimer, *et al.*, Phys. Rev. B **37**, 9860 (1988); V. D. Kulakovskiĭ, O. V. Misochko, and V. B. Timofeev, Fiz. Tverd. Tela (Leningrad) **31** (9), 220 (1989) [Sov. Phys. Solid State **31**, 1599 (1989)].
9. M. F. Limonov, A. I. Rykov, S. Tajima, and A. Yamanaka, Phys. Rev. Lett. **80**, 825 (1998); Phys. Rev. B **61**, 12 412 (2000).
10. T. Strohm, V. I. Belitsky, V. G. Hadjiev, and M. Cardona, Phys. Rev. Lett. **81**, 2180 (1998).
11. O. V. Misochko, E. I. Rashba, E. Ya. Sherman, and V. B. Timofeev, Phys. Rep. **194**, 393 (1990).
12. O. V. Misochko and E. Ya. Sherman, Zh. Éksp. Teor. Fiz. **99**, 330 (1991) [Sov. Phys. JETP **72**, 185 (1991)].
13. B. Friedl, C. Thomsen, H.-U. Habermeier, and M. Cardona, Solid State Commun. **78**, 291 (1991); O. V. Misochko, E. Ya. Sherman, N. Umesaki, *et al.*, Phys. Rev. B **59**, 11 495 (1999).

Translated by P. Pozdeev

Journal of Experimental and Theoretical Physics, Vol. 94, No. 2, 2002, pp. 350–355.
Translated from Zhurnal Éksperimental'noĭ i Teoreticheskoĭ Fiziki, Vol. 121, No. 2, 2002, pp. 412–417.

SOLIDS
Electronic Properties

The Evolution of the Optical Spectra of $LaMnO_3$ under Light *n*- and *p*-Type Doping and the Separation of Phases

N. N. Loshkareva[a, *], Yu. P. Sukhorukov[a], E. V. Mostovshchikova[a], L. V. Nomerovannaya[a], A. A. Makhnev[a], S. V. Naumov[a], E. A. Gan'shina[b], I. K. Rodin[b], A. S. Moskvin[c], and A. M. Balbashov[d]

[a]*Institute of Metal Physics, Ural Division, Russian Academy of Sciences, Yekaterinburg, 620219 Russia*
[b]*Moscow State University, Moscow, 119899 Russia*
[c]*Ural State University, Yekaterinburg, 620083 Russia*
[d]*Moscow Power Institute, Moscow, 105835 Russia*
**e-mail: loshkareva@imp.uran.ru*
Received March 15, 2001

Abstract—The optical absorption spectra of $LaMnO_3$ single crystals, pure and slightly doped with Ce and Sr (7%), were studied in the middle IR region. Ellipsometry measurements were performed in the visible region to determine real and imaginary permittivity parts. The energies of the onset of indirect transitions in $LaMnO_3$ at 293 and 80 K were found to be 0.30 and 0.40 eV, respectively. Impurity absorption bands corresponding to transition in hole and electron clusters were observed. The anomalous temperature dependence of IR absorption was explained by the existence of conducting droplets in the insulated doped crystal matrices at temperatures below the temperature of the appearance of a ferromagnetic contribution. The existence of such a contribution was proved by studying the equatorial Kerr effect. Because of the separation of phases, manganites slightly doped by a nonisovalent admixture can be treated as optically nonuniform media whose properties are similar to those of a composite system with metallic inclusions. *© 2002 MAIK "Nauka/Interperiodica".*

1. INTRODUCTION

Interest in doped manganites with perovskite structures of the $La_{1-x}A_xMnO_3$ type, where A = Cr^{2+}, Sr^{2+}, or Ba^{2+}, stems from the giant magnetoresistance that they exhibit. It is believed [1] that the separation of phases occurs in manganites at doping levels below the percolation threshold, which implies the coexistence of conducting ferromagnetic and insulating antiferromagnetic regions.

Various data are indicative of magnetic nonuniformity. The optical data [2] are, however, the only evidence of the existence of conduction regions (droplets). The resistance of slightly doped manganites (sample-average characteristic resistance) has an activation character below T_C, similarly to the resistance of composite systems with metallic inclusions [3]. In the pioneer work [2], proof for the existence of conducting (absorbing) regions in an insulating (transparent) matrix was obtained in a study of optical absorption by polycrystalline $La_{1-x}Ca_xMnO_3$ in the spectral region of light interactions with charge carriers (in the middle infrared region). In [4], these results were confirmed by measuring optical absorption by $La_{0.9}MnO_3$ and $La_{1-x}Sr_xMnO_3$ (x = 0.1) single crystals. Do metallic droplets exist at divalent ion concentrations lower than x = 0.1? How does *n*-type doping with tetravalent Ce ions affect the optical spectra? What is the optical spectrum of undoped $LaMnO_3$? Our goal is to answer these questions. Note that only data on crystals heavily doped with cerium are available [5].

Of a great many studies on the properties of manganites, quite a number are concerned with their optical properties. As a rule, the reflectance spectra of manganite polycrystalline samples or single crystals are recorded and processed according to Kramers and Kronig to obtain $\sigma(\omega)$ optical conductivity spectra (e.g., see [6]) or the absorption spectra of poly- or single-crystalline films on various substrates are studied. The absorption spectra of manganite single crystals were only reported in [4, 7], although precisely measurement of absorption by single crystals is a direct optical method.

2. PROCEDURE FOR MEASUREMENTS AND SAMPLES

In this work, we studied manganite single crystals in the IR region (0.08–0.8 eV). In the visible region (1.0–5.0 eV), we used ellipsometry to record the permittivity and optical conductivity $\sigma(\omega)$ spectra. The equatorial Kerr effect was studied in the spectral region of 1.5–3.8 eV at temperatures of 40 to 300 K in a 3 kOe magnetic field.

1063-7761/02/9402-0350$22.00

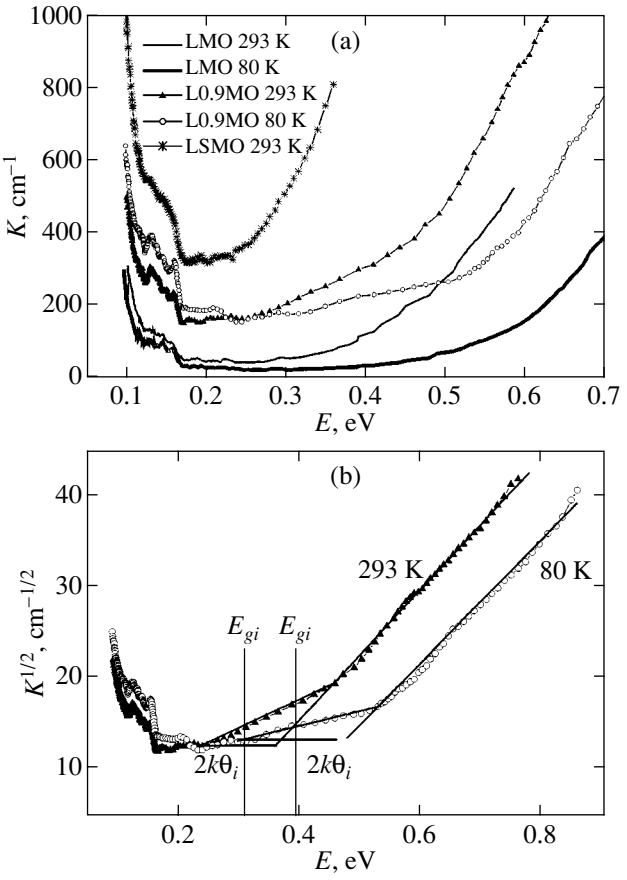

Fig. 1. (a) Absorption spectra of manganite single crystals at 293 and 80 K (the spectra of L0.9MO were taken from [6]) and (b) photon energy dependence of K for L0.9MO.

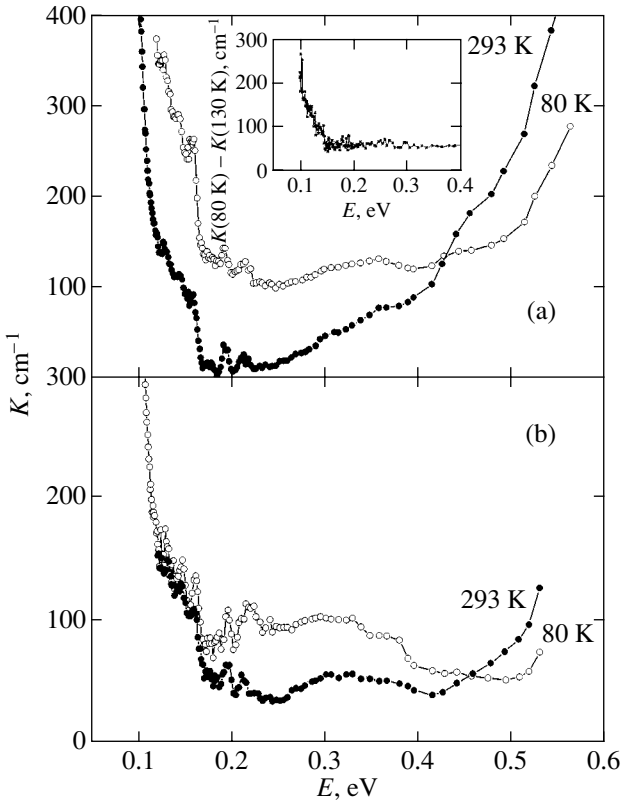

Fig. 2. Absorption spectra of (a) LCMO(air) and (b) LCMO(Ar) single crystals at 293 and 80 K. The difference of the spectra of LCMO(air) recorded at 80 and 130 K is shown in the inset.

The $LaMnO_3$ (LMO), $La_{0.93}Ce_{0.07}MnO_3$ [LCMO(Ar)], and $La_{0.93}Sr_{0.07}MnO_3$ (LSMO) single crystals were grown by the floating zone method under radiation heating [8] in argon; the $La_{0.93}Ce_{0.07}MnO_3$ [LCMO(air)] single crystal was grown in air. All crystals were orthorhombic at room temperature.

3. RESULTS AND DISCUSSION

Resistance ρ of all crystals has a semiconducting character in the temperature range 77–300 K, and the thermoelectromotive force is positive at 300 K. The largest resistance at room temperature is observed for LCMO(Ar) (2×10^3 Ω cm), and the lowest resistance, for LSMO (3 Ω cm). The $\rho_{300\,K}$ value for LMO and LCMO(air) equals 2×10^2 and 4×10^2 Ω cm, respectively. Magnetic measurements are evidence of the appearance of a ferromagnetic contribution in LMO, LCMO, and LSMO at T_C = 140, 135, and 125 K, respectively. The spontaneous magnetizations of LCMO(air), LCMO(Ar), LMO, and LSMO equal 4.3, 4.7, 6.5, and 44.7 G cm^3, respectively. The details of the magnetic and electric properties of the crystals require a separate discussion. The absorption spectra of LMO are shown in Fig. 1a in comparison with the spectra of the $La_{0.9}MnO_3$ (L0.9MO) single crystal taken from [4] and the spectrum of LSMO. The spectra of the LCMO(Ar) and LCMO(air) crystals are shown in Fig. 2. The temperature dependences of transmission (or the intensity of light that passed through the samples) are shown in Fig. 3. According to Figs. 1a and 2, undoped manganites and manganite doped with cerium have small absorption coefficient K values in the "transparency window," that is, in the region bounded by the beginning of the phonon spectrum on the side of low energies and the absorption band edge at about 2.0 eV on the side of high energies (Fig. 4).

The dependence of $\sqrt{K}$ on energy E is shown in Fig. 1b for $La_{0.9}MnO_3$ in the absorption band edge region. This dependence is evidence that the absorption band edge is related to indirect transitions. The $\sqrt{K}(E)$ dependence for $LaMnO_3$ has a similar shape. The E_{gi} energy of the onset of indirect transitions equals 0.30 ± 0.02 eV at 293 K and 0.40 ± 0.02 eV at 80 K for both samples. An analysis of these data and a comparison with the phonon spectra [9] show that La vacancies have a substantial influence on the relative contributions of various optical phonons that allow the indirect

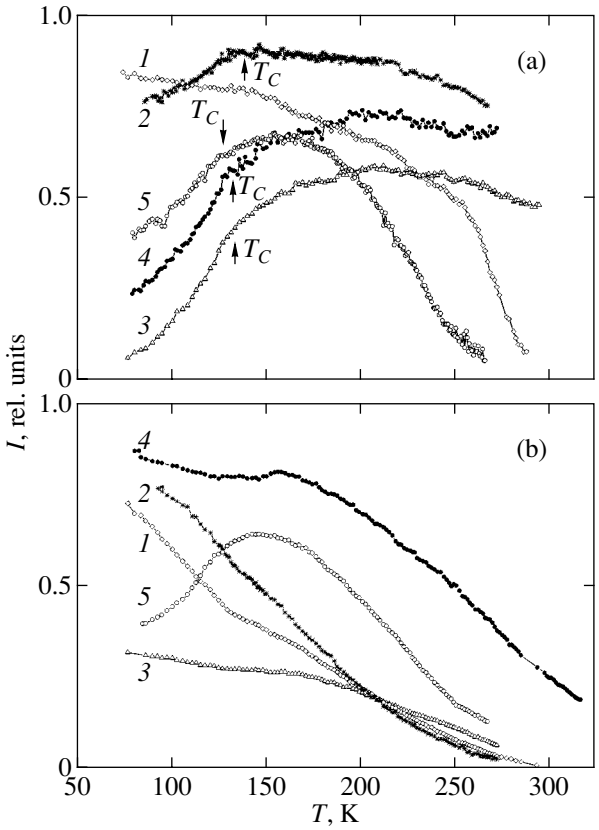

Fig. 3. Temperature dependence of transmission for (*1*) LMO, (*2*) L0.9MO, (*3*) LCMO(air), (*4*) LCMO(Ar), and (*5*) LSMO single crystals at (a) 0.14 and (b) 0.3 eV energies. Different scales are used to plot data on different compositions.

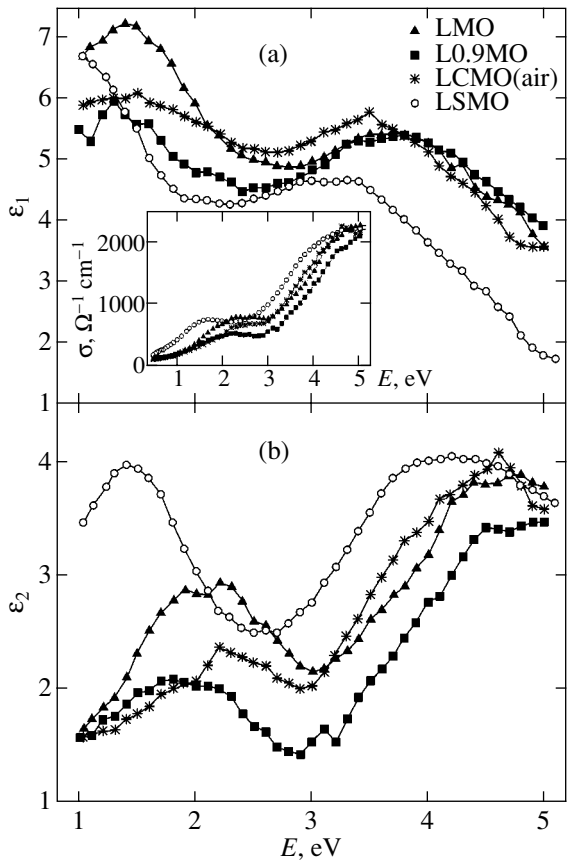

Fig. 4. (a) Real and (b) imaginary permittivity part spectra of LMO, L0.9MO, LCMO(air), and LSMO single crystals. Optical conductivity spectra are shown in the inset.

transition. In $LaMnO_3$ and $La_{0.9}MnO_3$, the most active phonons have wave numbers θ_i = 594 [9] and 287 cm^{-1}, respectively; both phonons have B_{3u} symmetry.

In the transparency window of a usual semiconductor, impurity absorption bands are observed, and, when free carriers appear, the absorption coefficient grows as energy decreases (the Drude contribution). In all samples studied in this work including "pure" LMO, a complex absorption band approximately at an energy of 0.14 eV is observed. In [4], this band was related to transitions in the hole pseudo-Jahn–Teller $[MnO_6^{8-}]_{JT}$ cluster in terms of the model of polar centers [10].

The presence of a band at an energy of about 0.14 eV in the spectra of pure LMO is evidence of the presence of hole centers in a low concentration. The energy positions of the narrow lines that constitute the band at approximately 0.14 eV do not change as a result of either doping or temperature changes. As follows from Figs. 1a and 2, the intensity of this band at room temperature increases as the sample is depleted of La and as a result of doping with Sr^{2+}. This is likely to be related to an increase in the number of hole clusters (Mn^{4+}). A decrease in resistance caused by *p*-type doping is in agreement with this suggestion. For instance, in the spectrum of L0.9MO, the intensity of the band at about 0.14 eV is higher and the resistance at 293 K is two orders of magnitude lower [4] than the corresponding characteristics of LMO.

Manganites with *n*-type doping (Ce) are partially electrically compensated; the crystal grown in argon is compensated to the greatest degree. When crystal growth occurs in air (in an oxygen-containing atmosphere), the formation of a large number of vacancies (Mn^{4+} ions) in the cation sublattices is more probable than in argon, because the atmosphere of argon is more reducing than air.

The thermoelectromotive force of samples doped with cerium (7%) remains positive. It can therefore be suggested that the fraction of vacancies in the cation sublattices of $LaMnO_3$ is approximately 7–8%. This estimate may be exaggerated, because the cerium valence may differ from four. Note that, according to the photoemission spectroscopy data on $La_{0.67}Ce_{0.33}MnO_3$ [11], the valence of cerium is larger than three but not four, and, generally, the concentration of additional electrons is lower than the concentration of cerium.

The temperature behavior of optical absorption in the low-frequency spectral region related to new phase nuclei (Fig. 3a) gives fundamentally important information about the character of phase separation in manganites.

In pure LMO, optical absorption near the 0.14 eV band decreases as temperature lowers (Fig. 1a). Figure 3a shows that transmission (the reverse of absorption) monotonically increases. The transmission of the other single crystals in this energy region also increases as temperature decreases. Conversely, below T_C, transmission decreases. The difference of the absorption spectra of LCMO(air) at temperatures below T_C (80 and 130 K) is shown in the inset in Fig. 2a. An increase in absorption when energy decreases is indicative of a contribution of free carriers. It follows that the normal (for a usual semiconductor) increase in transmission caused by cooling pure LMO (Fig. 3a) changes as a result of nonisovalent substitution to an anomalous decrease in transmission, which is naturally related to the appearance of a "metallic" contribution at temperatures below T_C. As shown by us in [2, 4], the possibility of detecting the contribution of free carriers in spectra is determined by the concentration of carriers in separate high-conductivity droplets, which give a quasi-Drude contribution against the background of a transparent (insulating) matrix. Indeed, if the sample were in the homogeneous dielectric state, light absorption would decrease with cooling because of a decrease in conductivity. The observed increase in absorption (decrease in transmission) as temperature lowers below T_C is therefore evidence of the presence of regions in which conductivity increases, as is characteristic of metals.

It follows that the optical data are evidence of a charge separation of phases in slightly doped manganites. Although the ferromagnetic contribution in LMO and L0.9MO manifests itself at close temperatures (of about 140 K), the smaller size and/or concentration of droplets in pure LMO prevent them from being detected in optical spectra.

To summarize, nonisovalent substitution and/or La vacancies result not only in the appearance of a band at 0.14 eV but also in a quasi-Drude increase in absorption. Such a behavior fully conforms to the concept of phase separation. For instance, in the polar center phase model [10], nonisovalent substitution in strongly correlated oxides is accompanied by the formation and growth of nuclei of a new variable-valence metallic phase, which, in the limiting case, consists of electron and hole clusters of the $[MnO_6^{10-}]_{JT}$ and $[MnO_6^{8-}]_{JT}$ types, respectively. The optical "portrait" of such a nucleus includes intracenter transitions and a quasi-Drude contribution of charge fluctuations.

An additional absorption band at an energy of about 0.3 eV is observed for crystals doped with Ce. This band is likely to be related to transitions in the $[MnO_6^{10-}]_{JT}$ pseudo-Jahn–Teller electron cluster [4]. The crystal doped with 7% Sr may also contain a band related to the electron center which is not resolved because of strong absorption. In [4], this band was observed in the spectrum of the $La_{0.9}Sr_{0.1}MnO_3$ single crystal. The simultaneous existence of hole and electron clusters in manganites, which, as a rule, have deviations from stoichiometry in all sublattices, can be related to the low disproportionation threshold for reactions of the type

$$2MnO_6^{9-} \longrightarrow [MnO_6^{8-}]_{JT} + [MnO_6^{10-}]_{JT},$$

where MnO_6^{9-} are the main clusters corresponding to Mn^{3+} ions.

The band corresponding to the electron center in the spectra of LMO and L0.9MO, possibly, lies higher in energy and is not resolved against the background of the absorption band edge. A broad band centered at 0.6 eV is observed in experiments on photoinduced absorption of $LaMnO_3$ [11].

As follows from the shape of the spectrum and the absorption coefficient value (Fig. 1a), the number of clusters and the contribution of free carriers in the crystal doped with Sr are substantially larger than in the crystals doped with Ce.

Light doping with Ce and Sr influences the energy position of the optical conductivity band at 2.0 eV (Fig. 4). This is especially clearly seen in the spectrum of the imaginary part of permittivity ε_2 (Fig. 4b). In pure LMO, the band maximum is situated at $\hbar\omega_{max} = 2.20$ eV and shifts to $\hbar\omega_{max} = 1.45$ eV as a result of *p*-type doping with Sr. In the L0.9MO crystal, the maximum of this band is situated at 1.85 eV. The opposite behavior of the band is observed under *n*-type doping with Ce. The band then shifts to the higher energies [$\hbar\omega_{max} = 2.35$ eV for LCMO(air)].

The reason for the observed shift of the band maximum in LSMO may be a considerable contribution of charge carriers to impurity absorption. The violation of a monotonic dependence of absorption at 0.6 eV in the crystal doped with Sr is evidence that the contribution of charge carriers to the absorption spectrum is still substantial at this energy value. In L0.9MO and *n*-type doped LCMO crystals, charge carries do not make a noticeable contribution at energies above 0.6 eV, as is seen from the absorption spectra (Figs. 1a and 2) and the monotonic temperature dependence of absorption (Fig. 3b).

The nature of the optical conductivity band at about 2.0 eV (inset in Fig. 4a) was discussed by various authors. One of the possible explanations is based on the one-electron band model [13]. Theoretical state density curves were used to interpret the optical conductivity spectra of $La_{0.7}Sr_{0.3}MnO_3$ in the ferromagnetic region; the conclusion was drawn that the band at about 2.0 eV was largely formed by $O(2p) - e_g(d) \longrightarrow e_g(d)$ interband transitions in the system of spin-upward

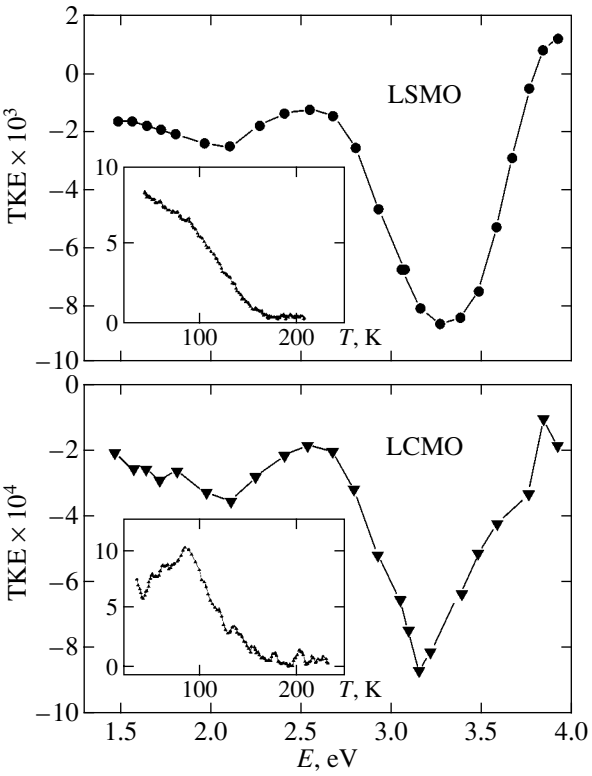

Fig. 5. Equatorial Kerr effect spectra of LSMO and LCMO single crystals at 40 K in a 3 kOe magnetic field. Temperature dependences of the Kerr effect are shown in the insets.

bands, and the band corresponding to an about 5.0 eV energy was a superposition of electronic transitions in both systems of spin bands [14]. The surprise is that light doping causes a large shift of the band related to the interband transition.

In the cluster model, the band at about 2.0 eV is naturally related to the ${}^5E_g$–${}^5T_{2g}$ *d*–*d* transition in Mn^{3+} ions, and an increase in ε_2 at energies higher than 3 eV, to the lower O2*p*–Mn3*d* charge transfer transition in $(MnO_6)^{9-}$ octahedral complexes. The crystal field is screened by hole density partly localized on surrounding oxygen ions in the sample doped with Sr and in L0.9MO. The partial screening of the negative charge of oxygen ions should decrease the crystal field splitting parameter and, hence, the ${}^5E_g$–${}^5T_{2g}$ transition energy. On the contrary, the electron doping must lead to an increase in the splitting parameter and the transition energy. A small displacement of the center of gravity of the band at 2.0 eV toward higher energies is indeed observed in the Ce-doped crystal.

The observation of the equatorial Kerr effect with temperature lowering (Fig. 5, inset) substantiates the existence of a ferromagnetic contribution in doped crystals. Figure 5 shows that, similarly to spontaneous magnetization, the Kerr rotation value is one order of magnitude larger for the crystal doped with Sr than for the Ce-containing sample. This is in close agreement with a larger absorption caused by charge carriers in the spectra of LSMO compared with LCMO. It follows that the optical and magnetooptical data lend support to the picture of phase separation in slightly doped manganites, in which "metallic" regions are characterized by ferromagnetic ordering. The positions of the low-energy (about 2.0 eV) band in the Kerr rotation spectra of the samples doped with Sr and Ce, in contrast to the ε_2 spectra (Fig. 4b), virtually coincide (Fig. 5). The difference between the equatorial Kerr effect spectra at energies higher than 2.5 eV is evidence of different ratios between Mn^{3+}, Mn^{4+}, and Mn^{2+} magnetically active ions in the single crystals doped with Sr and Ce. According to [15], the magnetooptical activity of manganese-based oxides (or manganese perovskites) is determined by the allowed electric dipole charge transfer transitions in the $(MnO_6)^{9-}$ and $(MnO_6)^{8-}$ octahedral complexes (3.5 and 4.3 eV, respectively) and the spin-allowed *d*–*d* transitions in the Mn^{3+} and Mn^{4+} ions (2.5 and 2.6, 3.1 eV, respectively). Transitions in Mn^{2+} ions should make an additional contribution to the equatorial Kerr effect spectrum of the Ce-doped single crystal.

Our experiments prove the existence of "metallic" ferromagnetic droplets, but do not allow the size and shape of the droplets to be estimated. The literature contains estimates of magnetic inhomogeneity sizes, but these estimates are to a great extent determined by the special features of the methods of study and the presence of twins in crystals. For instance, the neutron data on the twin-free $La_{0.94}Sr_{0.06}MnO_3$ crystal [17] show that ferromagnetic clusters formed as a result of charge segregation have the shape of platelets stretched along the [110] direction whose maximum size amounts to 17 Å. The results on twin crystals are explained by the existence of isotropic droplets.

4. CONCLUSION

To summarize, charge and magnetic separation of phases in manganites slightly doped with nonisovalent impurities makes these materials optically nonuniform; their properties are in a sense similar to those of composite systems with metallic inclusions [16]. Metallic ferromagnetic droplets are detectable by optical methods in crystals slightly *p*-type doped with Sr (7%) and *n*-type doped with Ce. The influence of doping with Ce on the optical spectra is much weaker than that of doping with strontium. The absorption edge of the initial $LaMnO_3$ crystal is related to indirect transitions, whose onset energy equals 0.30 and 0.40 eV at 293 and 80 K, respectively.

ACKNOWLEDGMENTS

The authors thank T.I Arbuzova, I.B. Smolyak, and N.I. Solin for providing the magnetic and electric data. This work was financially supported by INTAS-97-30252.

REFERENCES

1. E. L. Nagaev, Phys. Status Solidi B **186**, 9 (1994).
2. N. N. Loshkareva, Yu. P. Sukhorukov, S. V. Naumov, *et al.*, Pis'ma Zh. Éksp. Teor. Fiz. **68**, 89 (1998) [JETP Lett. **68**, 97 (1998)].
3. P. Sheng and D. Abeles, Phys. Rev. Lett. **28**, 34 (1972).
4. N. N. Loshkareva, Yu. P. Sukhorukov, É. A. Neĭfel'd, *et al.*, Zh. Éksp. Teor. Fiz. **117**, 440 (2000) [JETP **90**, 389 (2000)].
5. S. Das and P. Mandal, Z. Phys. B **104**, 7 (1997).
6. K. Takenaka, K. Iida, Y. Sawaki, *et al.*, J. Phys. Soc. Jpn. **68**, 1828 (1999).
7. N. N. Loshkareva, Yu. P. Sukhorukov, B. A. Gizhevskii, *et al.*, Phys. Status Solidi A **164**, 863 (1997).
8. A. M. Balbashov, S. G. Karabashev, Ya. M. Mukovskiy, *et al.*, J. Cryst. Growth **67**, 365 (1996).
9. I. Fedorov, J. Lorenzana, P. Dore, *et al.*, Phys. Rev. B **60**, 11 875 (1999).
10. A. S. Moskvin, Physica B (Amsterdam) **252**, 186 (1998).
11. J.-S. Kang, Y. J. Kim, B. W. Lee, *et al.*, J. Phys.: Condens. Matter **13**, 3779 (2001).
12. T. Mertelj, D. Kuscer, M. Kosec, and D. Mihailovic, Phys. Rev. B **61**, 15 102 (2000).
13. D. A. Papaconstantopoulos and W. E. Pickett, Phys. Rev. B **57**, 12 751 (1998).
14. L. V. Nomerovannaya, A. A. Makhnev, and A. Yu. Rumyantsev, Fiz. Met. Metalloved. **89**, 1 (2000).
15. E. A. Balykina, E. A. Ganshina, G. S. Krinchik, *et al.*, J. Magn. Magn. Mater. **117**, 259 (1992).
16. P. Sheng, Phys. Rev. Lett. **45**, 60 (1980).
17. M. Hennion, F. Moussa, G. Biotteau, *et al.*, Phys. Rev. B **61**, 9513 (2000).

Translated by V. Sipachev

Journal of Experimental and Theoretical Physics, Vol. 94, No. 2, 2002, pp. 356–366.
Translated from Zhurnal Éksperimental'noĭ i Teoreticheskoĭ Fiziki, Vol. 121, No. 2, 2002, pp. 419–430.

SOLIDS
Electronic Properties

Antimagnons in Ferrimagnets

I. F. Mirsaev and E. A. Turov*
Institute of Metal Physics, Ural Division, Russian Academy of Sciences, Yekaterinburg, 620219 Russia
**e-mail: turov@imp.uran.ru*
Received August 10, 2001

Abstract—Purely antiferromagnetic intrinsic oscillations of magnetic ions in a tetragonal ferrimagnet are considered. The magnetic ions occupy two double positions (forming four magnetic sublattices) so that the center of symmetry for each position is not a closed element. Not involving the total magnetization vector, the oscillations are not excited by the magnetic field; however, the oscillations can be excited by an alternating electric field or by a combination of a constant electric field and the alternating magnetic field of a certain frequency. This phenomenon is a dynamic manifestation of the magnetoelectric interaction. These oscillations, representing a new special type of spin waves (magnons), were called antimagnons. The intrinsic frequencies of antimagnons, as well as the corresponding susceptibilities, were determined. Quantitative estimates were obtained for a Mn_2Sb-based ferrimagnetic phase in both easy-axis and easy-plane orientation states. © *2002 MAIK "Nauka/Interperiodica".*

1. WHAT IS ANTIMAGNON?

Until recently, spin waves of three types were well known and extensively studied in magnetically ordered substances (magnets):

(a) A purely ferromagnetic mode in which the oscillatory variables are represented by two components of the total local magnetization vector $\mathbf{M}(\mathbf{r})$;

(b) A quasiferromagnetic mode, in which the oscillations involve, in addition to the two components of vector $\mathbf{M}$, components of the antiferromagnetic moment vector (or vectors) $\mathbf{L}$;

(c) A quasiantiferromagnetic mode featuring, in addition to the oscillations of vectors $\mathbf{L}$, the one-dimensional oscillations (one component) of the magnetization vector $\mathbf{M}$.

It is surprising that, until very recently, researchers did not pay attention to the fact that there is one more (i.e., the fourth) possible type of spin waves [1–4] (see also the remark in Appendix). We imply the purely antiferromagnetic oscillations not involving vector $\mathbf{M}$ and, hence, not excited by a magnetic field of the corresponding frequency.[1] Provided certain crystallographic and magnetic structure of a magnet featuring magnetoelectric interaction, oscillations of this type can be excited by an alternating electric field $\mathbf{E}(t)$. One of us predicted [1] that such purely antiferromagnetic oscillations can exist, in particular, in a purely ferromagnetic two-sublattice phase (magnetic structure). The main attention was paid to the problem of symmetry pertaining to this phenomenon.

Thus, excitation of the purely antiferromagnetic oscillations in a purely ferromagnetic phase presents, at first glance, a rather paradoxical situation. In order to distinguish these unusual electric-field-excited purely antiferromagnetic spin waves from the aforementioned spin waves, it was suggested [1] to term the new mode the "antimagnon waves" and refer to the corresponding quasiparticles as "antimagnons."

Recent reports made at EASTMAG-2001 [2, 3] were devoted to antimagnons excited in a magnet with four magnetic sublattices ($4c$ position of the D_{2h}^{16} group), including the cases of both a collinear purely ferromagnetic phase and weakly noncollinear magnetic structures (either with or without weak ferromagnetism). It was shown that the antimagnons can be excited by an alternating magnetic field $\mathbf{H}(t)$ provided that a constant electric field $\mathbf{E} = \mathbf{E}_0 = \text{const}$ is simultaneously applied. The corresponding antimagnon-electric ($\hat{\beta}$) and antimagnon-magnetic ($\hat{\delta}$) susceptibility tensors and the related thermal losses were calculated. These functions represent the linear response of the vector (or vectors) $\mathbf{L}$ to the applied electric or magnetic field of a given frequency. In the simple case of a two-sublattice ferromagnet, the spatial dispersion was taken into account in the form of the intrinsic oscillation frequency depending on the wavevector $\mathbf{k}$ [2].

The main results obtained previously [1–4] can be summarized as follows:

(i) The antimagnon frequency $\omega(k)$ usually falls within the optical (exchange) range. Situations were

[1] For fairness sake, we must point out that, calculating the antiferromagnetic resonance frequency in the two-sublattice model of an antiferromagnet in a constant magnetic field with a strength sufficient for the spin flip of the sublattice magnetization vectors, Gurevich and Melkov [5] found a solution corresponding to a mode that could not be excited by the magnetic field. However, data were presented neither on the crystallochemical and magnetic structures in which this effect can take place nor on the possible methods of exciting oscillations in this structure.

indicated when this frequency can be rather low (e.g., in the microwave range), which corresponds to a quasi-two-dimensional system featuring a weak exchange interaction between sublattices (atomic layers).

(ii) The most important sign of a magnet featuring antimagnons is the presence of magnetic ions (atoms) in the multiple site position with a center of symmetry not representing a closed element. This center permutes the magnetic ions (and, hence, magnetic sublattices) for one another.

(iii) The new susceptibilities (antimagnon-electric and antimagnon-magnetic), introduced in order to describe the excitation of antimagnons and related to the magnetoelectric interaction, differ in the intrinsic symmetry both from each other and from the conventional susceptibilities (electric, magnetic, and magnetoelectric). It should be noted that such a dynamic manifestation of the magnetoelectric interaction can also take place in a phase featuring no static magnetoelectric effect.

The previous investigations [1–3] considered the simplest possible examples demonstrating the existence of antimagnons and some related phenomena, but did not describe particular magnets featuring antimagnons. Only the phases (magnetic structures) in which all magnetic ions belonged to the same multiple site position were studied.

The main purpose of this study is to theoretically predict the existence and consider the features of antimagnons in a real ferrimagnet (characterized with respect to other properties), in which the magnetic ions occupy the positions of two types not connected by any symmetry transformation. The most appropriate structure of this kind might be offered by the yttrium iron garnet (YIG), in which the iron ions occupy the required two positions (*a* and *d*), one of which (*d*) possesses the aforementioned property (ii) necessary for the existence of antimagnons. Unfortunately, the magnetic structure of YIG comprising 20 sublattices [6] is too complicated for the first study of antimagnons in ferrimagnets. For this reason, we have selected a ferrimagnet possessing simpler crystal and magnetic structures, namely, the ferrimagnetic compound Mn_2Sb with a tetragonal crystal lattice. The tetragonal lattice is an important point, since previously [1–4] mostly the crystals possessing a rhombic symmetry were considered. It was interesting to know what can change upon going to uniaxial systems, in particular, to crystals possessing a major symmetry axis of the third, fourth, or sixth order.

However, Mn_2Sb has one disadvantage: this compound possesses a metallic conductivity that would certainly complicate the excitation of antimagnons by an electric field. This problem will be considered in the last section of our paper.

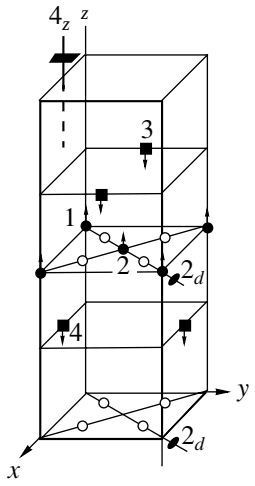

A schematic diagram of the unit crystal cell of Mn_2Sb. Only positions of the magnetic ions MnI (black circles) and MnII (black squares) in a magnetic structure of the easy axis type are indicated. In the text, we also consider an easy-plane state, whereby the magnetic moments are oriented as $\mathbf{M}_a \downarrow\uparrow \mathbf{M}_c \parallel \mathbf{H} \parallel y$. Open circles correspond to the centers of symmetry; also indicated are the rotation axes $4 \parallel z$ and $2_d \parallel [110]$.

2. CRYSTALLOCHEMICAL AND MAGNETIC STRUCTURES

The intermetallic compound Mn_2Sb (with the Curie point at $T_c = 550$ K) possesses a unit cell containing two pairs of magnetic Mn ions occupying (see the figure) positions *a* (MnI) and *c* (MnII). A characteristic feature is that ions in each pair are related via a center of symmetry [7, 8], so that both ion pairs possess the property (ii). Thus, below we will consider the properties of antimagnons in ferrimagnets using Mn_2Sb as an example.

The crystal lattice symmetry of the tetragonal ferrimagnet Mn_2Sb belongs to the $P4/nmm(D_{4h}^7)$ group. The neutron diffraction investigations [7] showed that the magnetic exchange structure of this compound comprises the (001) planes of MnI and MnII ions occupying various positions and, hence, possessing different magnetic moments.

As can be seen from the figure, Mn atoms in positions *a* [1(0, 0, 1/2) and 2(1/2, 1/2, 1/2)] and in positions *c* [3(0, 1/2, 1/2 + *z*) and 4(1/2, 0, 1/2 – *z*)] are actually related via the center of symmetry $\bar{1}$. In the interval of temperatures between 240 and $T_c = 550$ K, the atomic magnetic moments of Mn_2Sb are parallel to the crystallographic axis *c* (the easy magnetization axis state), whereas, in the interval $0 \text{ K} < T < 240$ K, these moments are perpendicular to axis *c* (the easy magnetization plane state) [7].

Note that, according to the figure, the magnetic exchange structure contains a group of atoms belonging to three layers MnII–MnI–MnII (four atoms per unit cell), which is repeated in every next period along the *z*

Table of transformations of the **M**, **L**, **H**, and **E** vectors

Γ_i	**H**, **E** **M**, **L**	$\bar{1}$ (–)	2_x(–)	2_y(–)	4_z(–)	4_z(+)
Γ_1	M_x, H_x	+1	+1	–1	M_y, H_y	
Γ_2	M_y, H_y	+1	–1	+1	$-M_x, -H_x$	
Γ_3	M_z, H_z	+1	–1	–1	M_z, H_z	
Γ_4	L_x, E_y	–1	–1	+1	$-L_y, -E_x$	$L_y, -E_x$
Γ_5	L_y, E_x	–1	+1	–1	L_x, E_y	$-L_x, E_y$
Γ_6	L_z	–1	+1	+1	$-L_z$	L_z
	E_z	–1	–1	–1	E_z	

Note: Given on the left of the double vertical line are the transformations for the *Pmmn* group (a subgroup of *P*4/*nmm*); symbols +1 and –1 indicate whether the function sign changes or not, respectively, under the action of the corresponding symmetry element; the right-hand part of the table gives the transformation rules for the elements $4_z(\mp)$ completing *Pmmn* to *P*4/*nmm*.

axis. Within each group of this type, the total magnetic moment is nonzero since the moments of MnI (position *a*) and MnII (position *c*) are different, amounting to $(2.13 \pm 0.20)\mu_B$ and $(3.87 \pm 0.40)\mu_B$, respectively. The magnetic moments of MnI and MnII layers are ordered antiparallel relative to each other in both easy axis and easy plane states, which is generally characteristic of a ferrimagnet. We will consistently consider both cases of the magnetic orientation.

The four-sublattice magnetic exchange structure of Mn_2Sb with the magnetizations $\mathbf{M}_n$ (n = 1, 2, 3, 4) is conveniently treated as combination of two-sublattice subsystems *a* and *c* with the basis set vectors of ferromagnetic $\mathbf{M}_\xi$ and antiferromagnetic $\mathbf{L}_\xi$ (ξ = *a*, *c*) moments:

$$\begin{aligned} \mathbf{M}_a &= \mathbf{M}_1 + \mathbf{M}_2, \quad \mathbf{L}_a = \mathbf{M}_1 - \mathbf{M}_2, \\ \mathbf{M}_c &= \mathbf{M}_3 + \mathbf{M}_4, \quad \mathbf{L}_c = \mathbf{M}_3 - \mathbf{M}_4. \end{aligned} \tag{1}$$

Shown in the figure are the independent crystal symmetry elements, including the center of symmetry $\bar{1}$, a fourth-order symmetry axis parallel to the *z* axis, and a diagonal binary axis of symmetry $2_d \parallel [110]$, which can be considered as generators of the *P*4/*nmm* group. In terms of these symmetry elements, the types of all positions can be coded by indicating the order of ion permutation: self-substitution ($1 \longleftrightarrow 1$, $2 \longleftrightarrow 2$, and $3 \longleftrightarrow 3$, $4 \longleftrightarrow 4$) versus one for another ($1 \longleftrightarrow 2$ and $3 \longleftrightarrow 4$). Accordingly, a symmetry element is provided with an index (+) or (–). As can be readily seen from the figure, the ion positions under consideration correspond to the following codes:

$$\begin{aligned} &(a)\ \ \bar{1}(-)4_z(-)2_d(+), \\ &(c)\ \ \bar{1}(-)4_z(+)2_d(-). \end{aligned} \tag{2}$$

Note that, if the binary axis $2_x = 2_d \times 4_z$ were used instead of the 2_d axis, both positions would be characterized by $2_x \equiv 2_x(-)$ and the codes of *a* and *c* would differ only by signs at the 4_z axis (minus versus plus).[2] Note that we deal here only with the permutation properties of the symmetry elements with respect to the position under consideration, irrespective of the magnetic exchange structure (ferro-, ferri-, or antiferromagnetic). In accordance with the above considerations, a necessary condition for the existence of antimagnons excited by the electric field is $\bar{1} \equiv \bar{1}(-)$. In the given (ii), this condition is satisfied for both positions.

3. THE TABLE OF TRANSFORMATIONS AND SPIN-WAVE REPRESENTATIONS

The calculation of intrinsic oscillation frequencies for a given ground state (phase) is simplified when it is known how the dynamic (oscillatory) variables are separated between the so-called spin-wave representations for this phase [4, 9–11].

In the case under consideration, this can be achieved in the following way. First, let us determine the spin-wave representations for the rhombic group *Pmmn*, which is a subgroup of the true tetragonal *P*4/*nmm* group since $4_z^2 = 2_z = 2_x \times 2_y$ (taking into account the fact that $2_z \equiv 2_z(+) = 4_z^2(\pm)$ for both positions). For this purpose, we will use a part of the table of transformations, presented below for the M_i and L_i components ($i = x, y, z$), acted upon by generators of the above subgroup $\bar{1}(-)2_x(-)2_y(-)$ that are the same for both positions *a* and *c* (see the top left part of the table). The right-hand part of the table indicates how the functions

[2] The notation (2) for the symmetry elements $g = g(+)$ and $g = g(-)$ was taken from the theory of antiferromagnetism [4], where the element $g(+)$ permutes the magnetic moments belonging to the same magnetic sublattice (or to the sublattices with parallel magnetizations), while $g(-)$ permutes the magnetic moments of sublattices with opposite magnetization orientations. In that theory, the antiferromagnetic structures $g(+)$ and $g(-)$ are referred to as the even and odd, respectively. Below we will call $g(+)$ and $g(-)$ the closed and open elements, respectively.

presented in the second column transform under the action of element 4_z for position *a*, $4_z(-)$ and *c*, $4_z(+)$. Thus we take into account the fact that the two one-dimensional representations Γ_1 and Γ_2 (or Γ_4 and Γ_5) have to be replaced by a single two-dimensional representation $\Gamma_{12}(M_x, M_y)$ or $\Gamma_{45}(L_x, L_y)$, since the functions $M_{\xi x}$ are mixed with $M_{\xi y}$ and the functions $L_{\xi x}$ are mixed with $L_{\xi y}$ ($\xi = a, c$). Note that the invariants in the rhombic symmetry group *Pmmn* can now be refined using an additional requirement of invariance with respect to elements $4_z(-)$ or $4_z(+)$.

3.1. Easy-Axis Phase $\Gamma_3(M_{\xi z})$ with $\mathbf{M}_a \downarrow\uparrow \mathbf{M}_c \parallel \mathbf{H} \parallel z$

We begin an analysis of the spin-wave representations for an easy-axis phase with $\mathbf{M}_a \downarrow\uparrow \mathbf{M}_c \parallel \mathbf{H} \parallel z$, the ground state of which is characterized by $\mathbf{M}_1 \downarrow\downarrow \mathbf{M}_2 \downarrow\uparrow \mathbf{M}_3 \uparrow\uparrow \mathbf{M}_4 \parallel z$. In terms of the *Pmmn* group (see the table), both positions possess the same spin-wave representations (for the algorithm, see [4, 9]):

$$\Gamma_{12}(\Delta M_{\xi x}, \Delta M_{\xi y}), \tag{3}$$

$$\Gamma_{45}(\Delta L_{\xi x}, \Delta L_{\xi y}). \tag{4}$$

Here, the sign Δ at *M* and *L* indicates that we deal with the oscillatory variables, although $\Delta M_i \equiv M_i$ and $\Delta L_i \equiv L_i$ ($i = x, y$). The same representations determine the independent modes upon taking into account the elements $4_z(\pm)$, since there are no symmetry elements mixing $\mathbf{M}_\xi$ with $\mathbf{L}_\xi$ (according to the table, these components transform differently as a result of inversion $\bar{1}$: $\bar{1}\,\mathbf{M} = \mathbf{M}$, $\bar{1}\,\mathbf{L} = -\mathbf{L}$. The products $M_{ai}M_{ci}$ and $L_{ai}L_{ci}$ ($i = x, y$), being independent invariants of the rhombic group *Pmmn* (factors of a product transform identically), form different combinations upon going to the tetragonal symmetry group *P*4/*nmm* to yield, respectively,

$$I_1 = M_{ax}M_{cx} + M_{ay}M_{cy}$$

and

$$I_2 = L_{ax}L_{cx} - L_{ay}L_{cy}.$$

The difference is related to dissimilar parity of the elements $4_z(-)$ and $4_z(+)$. The same factor accounts for the presence of an exchange invariant $\mathbf{M}_a \cdot \mathbf{M}_c$ and the absence of invariant $\mathbf{L}_a \cdot \mathbf{L}_c$. Note that it is the invariants I_1 and I_2 that connect the magnetic moment oscillations in positions *a* and *c*.

The table also indicates the rules of transformation for the other variables required for our description, namely, the vectors of magnetic (**H**) and electric (**E**) fields. Thus, the table contains all the symmetry-related information necessary for analysis of the problem under consideration.

It should also be noted that the spin-wave representation (3) corresponds to ferromagnons (the oscillatory variables include only components of the $\mathbf{M}_a$ and $\mathbf{M}_c$ vectors), while representation (4) corresponds to antimagnons (the oscillations involve only the $\mathbf{L}_a$ and $\mathbf{L}_c$ vectors).

3.2. Easy-Plane Phase $\Gamma_2(M_{\xi y})$ with $\mathbf{M}_a \downarrow\uparrow \mathbf{M}_c \parallel \mathbf{H} \parallel y$

Since the anisotropy in the basis plane *xy* is not taken into account, we can direct the magnetic field, for example, as $\mathbf{H} \parallel y$. In this case, the total magnetization $\mathbf{M} = \mathbf{M}_a + \mathbf{M}_c$, as well as the total magnetization for position *c* ($|\mathbf{M}_c| > |\mathbf{M}_a|$), will be parallel to the field **H**, so that

$$\mathbf{M} \uparrow\uparrow \mathbf{M}_c \uparrow\uparrow \mathbf{H} \parallel y \downarrow\uparrow \mathbf{M}_a. \tag{5}$$

In terms of the *Pmmn* group, we obtain (using the table) the following spin-wave representations for this phase:

$$\Gamma_{13}(\Delta M_{\xi x}, \Delta M_{\xi z}), \quad \Gamma_{46}(\Delta L_{\xi x}, \Delta L_{\xi z}). \tag{6}$$

Note that these representations are not mixed even after taking into account the elements $4_z(\pm)$ because of the different transformation properties of vectors **M** and **L**.

4. THERMODYNAMIC POTENTIAL AND EQUATIONS OF MOTION: EASY-AXIS PHASE

In what follows, we will consider the model of equal moduli in which

$$|\mathbf{M}_1| = |\mathbf{M}_2| = \frac{M_{a0}}{2}, \quad |\mathbf{M}_3| = |\mathbf{M}_4| = \frac{M_{c0}}{2},$$

and, hence,

$$\mathbf{M}_\xi^2 + \mathbf{L}_\xi^2 = M_{\xi 0}^2, \quad \mathbf{M}_\xi \cdot \mathbf{L}_\xi = 0, \quad \xi = a, c. \tag{7}$$

Assuming for the ground state that $\mathbf{M}_{a0} \downarrow\uparrow \mathbf{M}_{c0} \parallel \mathbf{H} \parallel z$, where **H** is the constant magnetic field, we can write the thermodynamic potential density in a bilinear homogeneous exchange approximation (taking into account the transformation rules for the basis set vectors $\mathbf{M}_\xi$ and $\mathbf{L}_\xi$ indicated in the table) in the following form:

$$\begin{aligned}\Phi &= \frac{1}{2}(A_a\mathbf{L}_a^2 + A_c\mathbf{L}_c^2) + B\mathbf{M}_a \cdot \mathbf{M}_c - M_z H_z \\ &- \frac{D_a}{M_0}M_z(E_xL_{ax} - E_yL_{ay}) - \frac{D_c}{M_0}M_z(E_xL_{cx} + E_yL_{cy}).\end{aligned} \tag{8}$$

Here, $A_a > 0$ and $A_c > 0$ are the exchange interaction constants for the ions in positions *a* and *c*, respectively, and $B > 0$ is the constant of exchange between these positions. Generally speaking, the expression for the potential (8) must also take into account exchange terms of the type $\mathbf{M}_a^2$ and $\mathbf{M}_c^2$; however, this would only lead, by virtue of the first condition (7), to renormalization of the A_a and A_c constants. In addition, expression (8) for the potential Φ includes the Zeeman

energy in the magnetic field $\mathbf{H} \parallel z$ and the magnetoelectric interaction represented by terms with the coefficients D_a and D_c.

As for the latter terms, it is important to take into account that these quantities involve the total magnetization $M_z = M_{az} + M_{cz}$, rather than the $\mathbf{M}_a$ and $\mathbf{M}_c$ values (z components). (In the ground state with $\mathbf{M} = \mathbf{M}_0 \parallel z$, the ratio $M_z/M_0 = 1$ is written only so as to check for the invariance.) It is evident that the expression (8) for Φ must also include the analogous terms with the total z projection of the antiferromagnetic vector $\mathbf{L} = \mathbf{M}_c - \mathbf{M}_a$ (possessing the same symmetry as that of $\mathbf{M}$, $\mathbf{M}_a$, and $\mathbf{M}_c$, since there are no symmetry elements relating the ions in positions a and c). It should be emphasized that we are speaking about the total antiferromagnetic moment vector $\mathbf{L}$, rather than about vectors corresponding separately to positions a and c. We have retained only terms containing the total projection M_z because, first, $\mathbf{L} \parallel \mathbf{M}$ for the field strengths H_z up to large values determined by the interposition exchange constant B and, second, it is the total magnetization $\mathbf{M}$ through which the magnetic field $\mathbf{H}$ acts upon the entire ferromagnetic structure (see, e.g., [5, section 3.3]). Under these conditions, we may assume that the terms involving $\mathbf{L}$ are included in the corresponding magnetoelectric terms involving $\mathbf{M}$. Strictly speaking, the coefficients in the two last terms should be written in the following form:

$$\begin{aligned} &d_{a1}M_{az}^0 + d_{a2}M_{cz}^0 \ \text{ or } \ D_a^M M_{0z} + D_a^L L_{0z}, \\ &d_{c1}M_{az}^0 + d_{c2}M_{cz}^0 \ \text{ or } \ D_c^M M_{0z} + D_c^L L_{0z}. \end{aligned} \tag{9}$$

The condition of equal moduli (7) implies that the longitudinal components $M_{\xi z}$ ($\xi = a, c$) are quadratic functions of the transverse components of vectors $\mathbf{M}_\xi$ and $\mathbf{L}_\xi$:

$$M_{\xi z} \approx M_{\xi z}^0 - \frac{1}{2M_{\xi 0}}(M_{\xi x}^2 + M_{\xi y}^2 + L_{\xi x}^2 + L_{\xi y}^2), \tag{10}$$

where $\xi = a, c$; $M_{az}^0 = -M_{a0}$ and $M_{cz}^0 = M_{c0}$ (see figure). As can be seen from relationships (10), the excitation of antimagnons (even due to the thermal motions) leads, as well as the excitation of usual magnons, to a decrease in the magnetization (longitudinal) for one position (M_{c0}) and an increase in the magnetization for another position (M_{a0}), the total magnetization (M_0) changing accordingly. Taking into account these relationships, we can separate in the thermodynamic potential (8) a quadratic (with respect to homogeneous oscillations of $L_{\xi x}$ and $L_{\xi y}$) part corresponding to the antimagnon modes:

$$\begin{aligned} \Phi_2 &= \frac{1}{2}\tilde{A}_a(L_{ax}^2 + L_{ay}^2) + \frac{1}{2}\tilde{A}_c(L_{cx}^2 + L_{cy}^2) \\ &- D_a(E_x L_{ax} - E_y L_{ay}) - D_c(E_x L_{cx} + E_y L_{cy}). \end{aligned} \tag{11}$$

Here, $\tilde{A}_a$ and $\tilde{A}_c$ are the exchange constants renormalized with an allowance for the interposition exchange constant B and the external magnetic field $\mathbf{H} \parallel \mathbf{M}_0 \parallel z$ ($\mathbf{M}_0 = \mathbf{M}_{a0} + \mathbf{M}_{c0}$):

$$\begin{aligned} \tilde{A}_a &= A_a + \frac{BM_{c0} - H_z}{M_{a0}}, \\ \tilde{A}_c &= A_c + \frac{BM_{a0} + H_z}{M_{c0}}. \end{aligned} \tag{12}$$

The quadratic forms in $M_{\xi x}$ and $M_{\xi y}$ determining the ferromagnetic modes for each position ξ can be separated from (11) (where any common terms are absent). This yields the known results (see [5]) not considered below.

In order to determine the oscillation frequencies and amplitudes for the antimagnons excited by the alternating electric field

$$E_{x,y}(t) \propto \exp(-i\omega t),$$

we will use the Landau–Lifshitz equations (applicable to the approximation of equal moduli) [4, 9]:

$$\begin{aligned} \dot{\mathbf{M}}_\xi &= \gamma\left(\mathbf{M}_\xi \times \frac{\partial \Phi}{\partial \mathbf{M}_\xi} + \mathbf{L}_\xi \times \frac{\partial \Phi}{\partial \mathbf{L}_\xi}\right), \\ \dot{\mathbf{L}}_\xi &= \gamma\left(\mathbf{M}_\xi \times \frac{\partial \Phi}{\partial \mathbf{L}_\xi} + \mathbf{L}_\xi \times \frac{\partial \Phi}{\partial \mathbf{M}_\xi}\right), \end{aligned} \tag{13}$$

where $\xi = a, c$ and γ is the absolute value of the magnetomechanical ratio. As can be seen from Eqs. (13), the purely antiferromagnetic mode $\Gamma_{45}(L_{\xi x}, L_{\xi y})$ of the $\Gamma_3(M_{\xi z})$ phase with $\mathbf{M}_{a0} \downarrow\uparrow \mathbf{M}_{c0} \parallel z$ is described by the equations

$$\begin{aligned} \dot{L}_{\xi x} + \Gamma L_{\xi x} &= -\gamma M_{\xi z}^0 \frac{\partial \Phi_2}{\partial L_{\xi y}}, \\ \dot{L}_{\xi y} + \Gamma L_{\xi y} &= \gamma M_{\xi z}^0 \frac{\partial \Phi_2}{\partial L_{\xi x}}, \end{aligned} \tag{14}$$

where $\xi = a, c$ and Γ is the Bloch damping parameter (introduced in the simplest way according to [12], assuming $\Gamma_a = \Gamma_c$).

5. INTRINSIC OSCILLATION FREQUENCIES AND SUSCEPTIBILITIES

Substituting expression (11) for Φ_2 into Eqs. (14), we obtain

$$\begin{aligned} L_{\xi x} &= \beta_{xx}^\xi E_x + \beta_{xy}^\xi E_y, \\ L_{\xi y} &= \beta_{yx}^\xi E_x + \beta_{yy}^\xi E_y. \end{aligned} \tag{15}$$

Here, $\hat{\beta}^\xi$ are the antimagnon-electric susceptibility tensors related to positions a and c, for which

$$\beta_{xx}^\xi = \frac{\omega_\xi \Omega_\xi}{\omega_\xi^2 - \tilde{\omega}^2}, \quad \beta_{xy}^\xi = -i\frac{\tilde{\omega}\Omega_\xi}{\omega_\xi^2 - \tilde{\omega}^2}, \tag{16}$$

where $\xi = a, c$ and the other components are determined from the relationships

$$\beta^a_{xx} = -\beta^a_{yy}, \quad \beta^a_{xy} = \beta^a_{yx}, \tag{17}$$

$$\beta^c_{xx} = \beta^c_{yy}, \quad \beta^c_{xy} = -\beta^c_{yx}. \tag{18}$$

The different signs in Eqs. (17) and (18) reflect the fact that the magnetoelectric interaction for the ions in positions a and c is described in the thermodynamic potential (8) by different invariants $M_z(L_{\xi x}E_x \mp L_{\xi y}E_y)$, where the signs minus and plus refer to positions a and c, respectively.

In expressions (16), the quantities

$$\omega_\xi = \gamma M_{\xi 0}\tilde{A}_\xi \tag{19}$$

determine the antimagnon resonance frequencies,

$$\Omega_\xi = \gamma M_{\xi 0}D_\xi \tag{20}$$

are the characteristic parameters (also having the dimensionality of frequency) of the magnetoelectric interaction, $\tilde{A}_\xi$ are exchange constants given by formulas (12), and $\tilde{\omega} = \omega + i\Gamma$ in (16) is the complex frequency taking into account the dissipation. Thus, expressions (16) and (19) describe two independent antimagnon modes, which correspond to positions a and c. According to Eqs. (15)–(18), these antimagnons are elliptically polarized. The polarization ellipses are different for positions a and c, being close to circles for $\omega \longrightarrow \omega_\xi$ (the formulas are omitted).

Now let us determine the thermal losses $Q = Q_a + Q_c$ related to the antimagnons excited by an electric field

$$\mathbf{E}(t) = \mathbf{E}_0\exp(-i\omega t).$$

Since the factors at E_x and E_y in the potential (11) play the role of the electric polarization, we can write [13]

$$Q_\xi = D_\xi\left(\overline{L_{\xi x}\frac{\partial E_x}{\partial t}} \mp \overline{L_{\xi y}\frac{\partial E_y}{\partial t}}\right), \tag{21}$$

where $\xi = a, c$ and the upper bar indicates averaging over a time $t \gg 2\pi/\omega$. Here and below, the signs minus and plus in the notation $(\mp)$ refer to positions a and c, respectively. Substituting Eqs. (15)–(18) into expression (21), we obtain

$$Q_\xi = -\frac{1}{2}\omega D_\xi \times[\beta''^\xi_{xx}|\mathbf{E}_0|^2 + i\beta'^\xi_{xy}(E_{0x}E^*_{0y} - E^*_{0x}E_{0y})], \tag{22}$$

where $\hat{\beta}^\xi = \hat{\beta}'^\xi + i\hat{\beta}''^\xi$ and

$$\beta'^\xi_{xy} = -\frac{\Omega_\xi\Gamma(\omega_\xi^2 + \omega^2)}{(\omega_\xi^2 - \omega^2)^2 + 4\omega^2\Gamma^2},$$
$$\beta''^\xi_{xx} = \frac{2\omega\omega_\xi\Omega_\xi\Gamma}{(\omega_\xi^2 - \omega^2)^2 + 4\omega^2\Gamma^2}. \tag{23}$$

Now we will consider the possibility of exciting antimagnons by an alternating magnetic field $\mathbf{H}(t)$. This may take place provided that a constant electric field $\mathbf{E} = \mathbf{E}_0$ is simultaneously applied in a certain direction [1–3]. In particular, this possibility is offered by invariants of the type

$$\frac{G}{M_0}(L_xE_{0x} \mp L_yE_{0y})H_z(t). \tag{24}$$

Note that there are magnetoelectric invariants of the type

$$(L_xH_x \mp L_yH_y)E_{0z}, \tag{25}$$

which also allow the field $\mathbf{H}$ to interact with L_x and L_y. However, this implies that the system in the field $\mathbf{E}_0 \parallel z$ also features invariants obtained from (25) by substituting $H_x \longrightarrow M_x$ and $H_y \longrightarrow M_y$. These invariants produce mixing of the ferromagnon (3) and antimagnon (4) modes, thus giving rise to a common quasiferromagnetic mode (M_x, M_y, L_x, L_y). The latter mode is just what will be excited by the field $\mathbf{H}(t) \perp z$.

The invariants (24) have to be substituted for the last two terms in expression (8). The corresponding invariants are obtained upon substituting

$$M_z \longrightarrow H_z(t) \propto \exp(-i\omega t), \quad D_\xi \longrightarrow G_\xi,$$
$$E_x \longrightarrow E_{0x}, \quad E_y \longrightarrow E_{0y}.$$

The corresponding solutions given by Eqs. (14) are now as follows:

$$L_{\xi x} = \delta^\xi_{xz}H_z, \quad L_{\xi y} = \delta^\xi_{yz}H_z, \tag{26}$$

where

$$\delta^\xi_{xz} = \frac{\Omega_\xi(\omega_\xi E_{0x} - i\tilde{\omega}E_{0y})}{M_0(\omega_\xi^2 - \tilde{\omega}^2)},$$
$$\delta^\xi_{yz} = \mp\frac{\Omega_\xi(\omega_\xi E_{0y} + i\tilde{\omega}E_{0x})}{M_0(\omega_\xi^2 - \tilde{\omega}^2)} \tag{27}$$

are components of the antimagnon-magnetic susceptibility tensor. Here, the parameters

$$\Omega_\xi = \gamma M_{\xi 0}G_\xi, \tag{28}$$

are determined, in contrast to the analogous quantities (20), by the constants G_ξ, while ω_ξ are the antimagnon resonance frequencies given by formulas (19).

It should be noted that tensors β_{ij} and δ_{ij} represent susceptibilities of a new type, differing in the intrinsic symmetry both from each other and from the conventional susceptibilities (electric κ_{ij}, magnetic χ_{ij}, and magnetoelectric α_{ij}). Indeed, the operators of spatial ($\bar{1}$) and temporal (1') inversion transform β_{ij} and δ_{ij} as the products L_iE_j and L_iH_j, respectively, whereas the conventional tensors κ_{ij}, χ_{ij}, and α_{ij} transform as P_iE_j, M_iH_j, and P_iH_j, respectively (where **P** is the polarization vector).

Thus, the above considerations show that, in the exchange approximation, each position (*a* and *c*) of the magnetic ions corresponds to its own antimagnon branch with the corresponding intrinsic oscillation frequency.

Now we will present the results of analogous calculations performed in the exchange approximation (with an allowance for the Zeeman energy at $\mathbf{H} \parallel \mathbf{M}_0 \parallel y$) for antimagnons in the easy-plane phase $\Gamma_2(M^0_{\xi y})$ (see Section 3.2). The initial quadratic form with respect to the oscillatory variables $L_{\xi x}$ and $L_{\xi z}$ for the antimagnon mode is

$$\Phi_2 = \frac{1}{2}\tilde{A}_a(L^2_{ax} + L^2_{az}) + \frac{1}{2}\tilde{A}_c(L^2_{cx} + L^2_{cz}) + D_aL_{az}E_y(t) - D_cL_{cz}E_y(t), \quad (29)$$

where $\tilde{A}_\xi$ are given by formulas (12) with H_z replaced by H_y. The last two terms in expression (29) are due to invariants of the type $(M_xE_x \mp M_yE_y)L_{\xi z}$ for $M_x = E_x = 0$.

Since the anisotropic terms in expression (29) are not taken into account, it is evident that the antimagnon resonance frequencies will again be represented by formulas (19) with the aforementioned replacement. Now, the antimagnon-electric susceptibilities $\hat{\beta}(\perp)$ for the easy-plane state can be expressed through the components of susceptibility $\hat{\beta}(\parallel)$ determined for the easy-axis phase:

$$\beta^\xi_{xy}(\perp) = -\beta^\xi_{xy}(\parallel), \quad \beta^\xi_{zy}(\perp) = \mp\beta^\xi_{xx}(\parallel). \quad (30)$$

Similar relationships take place for the antimagnon-magnetic susceptibility tensor components, which are obtained by replacing the two last terms in expression (29) by products of the type

$$\frac{G_\xi}{M_0}E_{0y}L_{\xi z}H_y(t). \quad (31)$$

The resulting antimagnon-magnetic susceptibilities $\hat{\delta}(\perp)$ for the easy-plane phase can be expressed through components of the $\hat{\delta}(\parallel)$ tensor (27) determined for the easy-axis state at $E_{0x} = 0$:

$$\delta^\xi_{xy}(\perp) = -\delta^\xi_{xz}(\parallel), \quad \delta^\xi_{zy}(\perp) = \delta^\xi_{yz}(\parallel). \quad (32)$$

Note that the invariants for $\mathbf{E}_0 \parallel z$ cannot be used instead of (31) in expressions for the easy-plane state (nor in those for the easy-axis state), because the former invariants relate the antimagnon mode Γ_{46} (for $\mathbf{H} \longrightarrow \mathbf{M}$) to the quasiferromagnetic Γ_{13} mode.

6. ANISOTROPY, ORIENTATIONAL PHASE TRANSITIONS, AND RELATIONSHIPS BETWEEN THE ANTIMAGNON MODES OF POSITIONS *a* AND *c*

The orientational phase transitions considered below are related to the magnetic anisotropy. These transitions were treated in sufficient detail both generally for ferrimagnets [6] and in particular for Mn_2Sb [14]. Determining the orientational ground states and the phase transition between these states, the anisotropy certainly influences the antimagnon spectrum as well. Taking into account the magnetically anisotropic relativistic interactions and their contributions to the spectrum, it would be inconsistent to employ an expression for Φ without the relativistic invariant

$$\Lambda(L_{ax}L_{cx} - L_{ay}L_{cy}). \quad (33)$$

This invariant, while not influencing the ground state, may significantly affect the spectrum by connecting the antimagnons of positions *a* and *c*, which are independent in the exchange approximation.

Now we will list the phase transitions related to the problem of antimagnons in ferrimagnets within the framework of a model studied. Note that this model, albeit based on a particular compound (Mn_2Sb), admits a rather broad variation of the parameters. This implies that the model is applicable to other ferrimagnets with similar crystal and magnetic structures.

The first one that we mention is the orientational phase transition from the easy-axis to easy-plane state occurring in cooled Mn_2Sb at $T = 240$ K, which is related to a temperature-induced change in the magnetic anisotropy. In a bilinear approximation, the anisotropic contribution to Φ determining the orientational ground state ($\mathbf{L}_\xi = 0$) is

$$\Phi^0_{an} = -\frac{1}{2}K_aM^2_{az} - \frac{1}{2}K_cM^2_{cz} + K_{ac}M_{az}M_{cz}. \quad (34)$$

Proceeding without violation of the antiparallel mutual orientation of magnetizations $\mathbf{M}_{a0}$ and $\mathbf{M}_{c0}$, the orientational phase transition from the easy-axis to easy-plane state and back is related to a change in the sign of the following combination of constants K_a, K_c, and K_{ac}:

$$K = K_aM^2_{a0} + K_cM^2_{c0} + 2K_{ac}M_{a0}M_{c0}, \quad (35)$$

whereby $K > 0$ corresponds to the easy-axis and $K < 0$, to the easy-plane state. The point $K = 0$ corresponds to the first-order phase transition, although no hysteresis takes place in the approximation (bilinear anisotropy) under consideration. The hysteresis appears when terms of a higher order are taken into consideration in the expression for Φ_{an}^0 [14].

A transition from the state $\mathbf{M}_{a0} \downarrow\uparrow \mathbf{M}_{c0} \parallel z$ to $\mathbf{M}_{a0} \downarrow\uparrow \mathbf{M}_{c0} \perp z$ may also take place under the action of an external field $\mathbf{H} \perp z$ (e.g., for $\mathbf{H} \parallel y$). The total magnetization $\mathbf{M}_0 = \mathbf{M}_{a0} + \mathbf{M}_{c0}$ gradually rotates within the interval of field strengths

$$0 < H_y < H_A = \frac{K}{M_0}. \tag{36}$$

The boundary values indicate two points of the second-order phase transition corresponding to the beginning ($H_y = 0$) and end ($H_y = H_A$) of the magnetization rotation.

In addition, there are two points of the second-order phase transition related to overcoming the exchange interaction between positions a and c (parameter B) in a field $\mathbf{H} \parallel \mathbf{M}$ (in the easy-axis and easy-plane states). The first point,

$$H \geq H_{B1} = B(M_{c0} - M_{a0}), \tag{37}$$

corresponds to the onset of deviation from collinear (antiparallel) orientation and the rotation of vectors $\mathbf{M}_{a0}$ and $\mathbf{M}_{c0}$ in the direction of $\mathbf{H}$ (the so-called angular phase). This rotation terminates at the point

$$H_{B2} = B(M_{c0} + M_{a0}), \tag{38}$$

where the spin flip takes place and a phase with $\mathbf{M}_{a0} \uparrow\uparrow \mathbf{M}_{c0} \parallel \mathbf{H}$ is formed at $H > H_{B2}$. With the magnetic anisotropy taken into account, additional terms H_{K1} and H_{K2} (different for the easy-axis and easy-plane states) appear in the right-hand parts of Eqs. (37) and (38), respectively.

Our task was to trace variation of the antimagnon frequencies during the above phase transitions, to determine whether the antimagnon modes exhibit softening in the vicinity of these points, and to establish the role of the interposition interaction (33) in these processes. Not dwelling on the details of analysis, we only present the results.

In the easy-axis state ($\Gamma_3(M_{\xi z})$ phase) corresponding to the interval of field strengths

$$0 \leq H_z < H_{B1} = B(M_{c0} - M_{a0}), \tag{39}$$

the system features antimagnons with the frequencies ω_1 and ω_2 given by the expressions

$$\omega_{1,2}^2 = \frac{1}{2}[\omega_c^2 + \omega_a^2 + 2\omega_\Lambda^2 \pm (\omega_c + \omega_a)\sqrt{(\omega_c - \omega_a)^2 + 4\omega_\Lambda^2}], \tag{40}$$

where

$$\begin{aligned} \omega_c &= \gamma[(A_c + K_c)M_{c0} + (B + K_{ac})M_{a0} + H_z], \\ \omega_a &= \gamma[(A_a + K_a)M_{a0} + (B + K_{ac})M_{c0} - H_z], \\ \omega_\Lambda^2 &= \gamma^2 \Lambda^2 M_{a0} M_{c0}. \end{aligned} \tag{41}$$

By the same token, the easy-plane state ($\Gamma_2(M_{\xi y})$ phase) corresponding to approximately the same interval of field strengths ($H_z \longrightarrow H_y$) features the antimagnons with

$$\omega_{1,2}^2 = \frac{1}{2}\left[\omega_c^2 + \omega_a^2 \pm \sqrt{(\omega_c^2 - \omega_a^2)^2 + \omega_\Lambda^4}\right], \tag{42}$$

where

$$\begin{aligned} \omega_c^2 &= \gamma^2(A_c M_{c0} + B M_{a0} + H_y) \\ &\times [(A_c - K_c)M_{c0} + B M_{a0} + H_y], \\ \omega_a^2 &= \gamma^2(A_a M_{a0} + B M_{c0} - H_y) \\ &\times [(A_a - K_a)M_{a0} + B M_{c0} - H_y], \\ \omega_\Lambda^4 &= \gamma^4 \Lambda^2 M_{a0} M_{c0} \\ &\times [(A_a - K_a)M_{a0} + B M_{c0} - H_y] \\ &\times [(A_c - K_c)M_{c0} + B M_{a0} + H_y]. \end{aligned} \tag{43}$$

An analysis of expressions (40)–(43) leads to the following conclusions:

(i) The bound a–c antimagnons possess different frequencies ω_1 and ω_2 in the easy-axis and easy-plane states, respectively. The difference is related both to the magnetic anisotropy and to the interaction (33) between positions a and c. The relative relativistic smallness of corrections is determined by the ratios K/A_ξ and $(\Lambda/A_\xi)^2$. An exception is offered by a particular structure with $\omega_a = \omega_c$, in which case the second ratio is replaced by Λ/A_ξ.[3]

(ii) Formulas (42) and (43) for the frequencies ω_1 and ω_2 are applicable in the case when the state with $\mathbf{M}_0 \perp z$ is obtained from the easy-axis state under the action of a field with $H_y > H_A$. As the field strength H_y decreases from the region of large fields, no one of the antimagnon frequencies goes to zero at the phase transition point $H_y = H_A$, although one of these frequencies exhibits a certain softening when this point is approached from above (ω_c decreases and ω_a increases

[3] This equality may, in principle, take place if initially $\omega_a > \omega_c$ at $H = 0$ and then ω_a decreases while ω_c increases with growing H. The magnetic field strength H at which the ω_a and ω_c values become equal must be smaller than that determined by condition (37), otherwise the aforementioned phase transition involving the rotation of $\mathbf{M}_{a0}$ and $\mathbf{M}_{c0}$ would begin. The estimates showed that this situation can hardly take place in Mn_2Sb.

with decreasing H_y), reaching a possible minimum at the point where the reverse transition begins.

(iii) Approximately the same behavior is observed at the phase transition points H_{B1} and H_{B2} bounding the angle phase for both $\mathbf{H} \parallel \mathbf{M}_0 \parallel z$ and $\mathbf{H} \parallel \mathbf{M}_0 \perp z$. The antimagnon frequencies $\omega_{1,2}^2$ do not go to zero at any of these points. Apparently, the phase transition at these points involves some other mode—a quasiferromagnetic mode Γ_{12} for the $\Gamma_3(M_{\xi z})$ phase or Γ_{13} for the $\Gamma_2(M_{\xi y})$ phase—and that mode exhibits softening (see, e.g. [4, Section 11.3]).

(iv) The points H_{B1} and H_{B2} exhibit an interesting feature: the antimagnon frequencies determined at these points in the exchange approximation are equal. This can be readily checked using the corresponding expressions.

Finally, there is an important (in our opinion, nontrivial) result concerning corrections to the antimagnon-electric susceptibility $\hat{\beta}$ given by formulas (16), related to the interaction term (33). For example, omitting for simplicity the magnetic anisotropy term, we obtain instead of formulas (16) the following expressions for the antimagnon-electric susceptibility tensor of the easy-axis phase $\Gamma_3(M_{\xi z})$:

$$\beta_{xx}^a = \frac{\omega_a \Omega_a}{\omega_a^2 - \tilde{\omega}^2}\left\{1 - \frac{\Lambda}{\tilde{A}_a}\frac{\Omega_c}{\Omega_a}\frac{\omega_a\omega_c + \tilde{\omega}^2}{\omega_c^2 - \tilde{\omega}^2}\right\},$$
$$\beta_{xy}^a = -i\frac{\tilde{\omega}\Omega_a}{\omega_a^2 - \tilde{\omega}^2}\left\{1 - \frac{\Lambda}{\tilde{A}_a}\frac{\Omega_c}{\Omega_a}\frac{\omega_a(\omega_a + \omega_c)}{\omega_c^2 - \tilde{\omega}^2}\right\}. \quad (44)$$

For position c, the susceptibilities β_{xx}^c and β_{xy}^c can be calculated using formulas (44) by substituting the indexes $a \longleftrightarrow c$. The other components (β_{yx}^ξ, β_{yy}^ξ) are obtained from the β_{xy}^ξ and β_{xx}^ξ values using relationships (17) and (18).

Thus, the corrections depend on the frequency $\tilde{\omega}$ and possess a resonance character, being maximum at the frequency ω_c in position a and at the frequency ω_a for position c. It is important to note that the corrections are linear with respect to interaction parameter Λ. At the resonance point, the relative magnitude of these corrections, determined by the ratio Λ/Γ, can probably be not small.

7. CONCLUSIONS AND QUANTITATIVE ESTIMATES

Let us summarize the above considerations. It is established that ferrimagnets (in particular, Mn_2Sb) containing magnetic ions connected to each other via the symmetry center $\bar{1}(-)$ can feature the spin waves of a new type termed antimagnons. These are oscillations of the purely antimagnon mode (not involving the total magnetization vector), which can be excited by an alternating electric field $\mathbf{E}(t)$ both in the presence and in the absence of a magnetic field. These oscillations can also be excited by an alternating magnetic field $\mathbf{H}(t)$, provided that a constant electric field $\mathbf{E}_0$ is simultaneously applied in a certain direction. The antimagnon-electric and antimagnon-magnetic susceptibility tensors β_{ij} [Eqs. (16)–(18) and (30)] and δ_{ij} [Eqs. (27) and (32)] describing these excitations exhibit a resonance dependence on the frequency of the exciting field. In contrast to a ferrimagnet with a single-position magnetic structure [1], the two-position material under consideration possess two antimagnon resonance frequencies, ω_a and ω_c (19), which correspond to the bound self-oscillations of a pair of magnetic moments in positions a and/or c. The presence of two antimagnon branches in the spectrum is related to the fact that $\bar{1} = \bar{1}(-)$ for both positions.

In the exchange approximation, the oscillations of vectors $\mathbf{L}_a$ and $\mathbf{L}_c$ are not interconnected, although, according to Eqs. (19) and (12), the exchange interaction between positions a and c determined by the parameter B influences the frequencies. In this approximation, equal frequencies ω_a and ω_c are obtained for the two (easy-axis and easy-plane) orientational states considered, given the corresponding field orientation ($\mathbf{H} \parallel z$ and $\mathbf{H} \perp z$, respectively). A difference between a and c frequencies in the easy-axis and easy-plane states arises on taking into account, first, the magnetic anisotropy and, second, the relativistic interposition interaction (33). This interaction links the oscillation components $\mathbf{L}_a$ and $\mathbf{L}_c$ into a unified system with the intrinsic frequencies ω_1 (40) and ω_2 (42) for the easy-axis and easy-plane states, respectively. Neither of the obtained antimagnon modes is soft (i.e., none goes to zero at the phase transition points). There are grounds to believe that the corresponding phase transitions involve the aforementioned quasiferromagnetic mode (not considered in this study), and just that mode turns out to be soft.

An important nontrivial result consists in establishing the resonance character of the effect of interposition interaction (33) upon the antimagnon-electric susceptibility $\hat{\beta}$.

An essential aspect of this study is that we have considered only homogeneous antimagnons representing an energy gap in the antimagnon spectrum, which are excited by a homogeneous electric field $\mathbf{E}(t)$. Although we believe that this restriction is justified for the first study of antimagnons in ferrimagnets, an urgent task in the further investigation of the antimagnon waves in ferrimagnets is making allowance for the spatial dispersion. This is necessary, first of all, for the description of

phenomena involving the interaction of antimagnons with the waves of other types (electromagnetic, elastic, etc.). The study of such phenomena is an important subsequent step in further analysis of the antimagnon problem. In addition, the conducting ferrimagnets are penetrated by the field $\mathbf{E}(t)$ to a finite depth as a result of the skin effect. Even this factor alone leads to an inhomogeneous field distribution, which results in the excitation of inhomogeneous antimagnons. Moreover, this situation implies the need for formulating and solving the problem of surface antimagnons.

Although the results obtained above are, generally speaking, also applicable to other types of magnets (including a two-position ferromagnet with four magnetic sublattices), it would be interesting to obtain some necessary quantitative estimates at least for Mn_2Sb.

First, we can use the molecular field theory [15] to express the exchange parameters A_ξ through the Curie point (T_c = 550 K):

$$A_\xi \approx 6N\frac{k_B T_c}{M_{\xi 0}^2}\left(\frac{S_\xi}{S_\xi + 1}\right). \quad (45)$$

Here, $N \approx 10^{22}$ cm^{-3} is the concentration of magnetic ions; k_B is the Boltzmann constant; $S_a = 3/2$, $S_c = 5/2$ are the atomic spins [14] and $M_{a0} \approx 400$ G, $M_{c0} \approx 700$ G are the magnetizations in positions *a* and *c*, respectively. Performing the calculations, we obtain

$$A_a \approx 1.7 \times 10^4, \quad A_c \approx 6.6 \times 10^3,$$

which yields, according to (19), the antimagnon frequencies

$$\omega_a \approx 1.2 \times 10^{14}\ \text{s}^{-1}, \quad \omega_c \approx 0.8 \times 10^{14}\ \text{s}^{-1}.$$

Note that the parameter *B* is significantly smaller than the A_ξ values and, hence, does not influence ω_ξ in order of magnitude. The same is valid for the anisotropy constants, which are smaller than A_ξ by 2–3 orders of magnitude [14].

Now we have to estimate the depth of penetration of the electric field $\mathbf{E}(t)$ at the frequency ω_ξ. Using experimental data [16] on the electric conductivity and the Hall effect, it is easy to show that the frequencies of interest in this study fall within the so-called classical absorption range (see, e.g., [17]) in which $\omega < 1/\tau$ (τ is the free path time) and the skin layer thickness is

$$\delta = \frac{c}{\sqrt{2\pi\sigma\omega}}, \quad (46)$$

where *c* is the velocity of light and σ is the specific electric conductivity. The calculation yields

$$\delta \approx 10^{-5}\ \text{cm}.$$

This estimate is much smaller than the electromagnetic wavelengths corresponding to the frequencies ω_ξ, thus pointing once again to the importance of considering the surface antimagnons. Although the above estimates were obtained using room-temperature parameters, the results would change only slightly for lower temperatures.

ACKNOWLEDGMENTS

This study was supported by the Russian Foundation for Basic Research, project no. 99-02-16268.

APPENDIX

This article was already written and prepared for publication when the authors found the paper by Yablonskii and Krivoruchko [18] (unfortunately, the source was previously unknown to the authors), in which the basic ideas concerning the existence of purely antiferromagnetic oscillations excited by an electric field were formulated before the same was done in [1]. Three earlier publications of the same researchers are cited in [18], in which they use an alternative, probably more adequate, term for the purely antiferromagnetic spin waves: electroactive waves, in contrast to the usual (magnetoactive) spin waves excited by a magnetic field. To our consolation, the problems considered in the above papers by Yablonskii and Krivoruchko do not overlap with the main content and results of our article. Not speaking of the dissimilar approaches employed, different types of magnets were studied: a two-position ferrimagnet in our case against antiferromagnets in [18]. Moreover, the materials belong different crystal symmetry classes, since the tetragonal structures were not considered in [18]. All the results obtained in our study are new as well.

REFERENCES

1. E. A. Turov, Pis'ma Zh. Éksp. Teor. Fiz. **73**, 92 (2001) [JETP Lett. **73**, 87 (2001)].
2. E. A. Turov and A. V. Kolchanov, in *Proceedings of the International Symposium on Magnetism, EASTMAG–2001, Yekaterinburg, 2001*; Fiz. Met. Metalloved. Suppl. **91–93**.
3. A. V. Kolchanov and E. A. Turov, in *Proceedings of the International Symposium on Magnetism, EASTMAG–2001, Yekaterinburg, 2001*; Fiz. Met. Metalloved. Suppl. **91–93**.
4. E. A. Turov, A. V. Kolchanov, V. V. Men'shenin, *et al.*, *Symmetry and Physical Properties of Antiferromagnets* (Fizmatlit, Moscow, 2001).
5. A. G. Gurevich and G. A. Melkov, *Magnetic Oscillations and Waves* (Nauka, Moscow, 1994), p. 84.
6. A. G. Gurevich, *Magnetic Resonance in Ferrites and Antiferromagnets* (Nauka, Moscow, 1973), p. 220.
7. M. K. Wilkinston, N. S. Gingrich, and C. G. Shull, J. Phys. Chem. Solids **2**, 289 (1957).

8. I. F. Mirsaev and E. A. Turov, Fiz. Met. Metalloved. **81**, 68 (1996).
9. E. A. Turov, A. V. Kolchanov, V. V. Men'shenin, *et al.*, Usp. Fiz. Nauk **168**, 1303 (1998) [Phys. Usp. **41**, 1191 (1998)].
10. Yu. A. Izyumov and N. A. Chernoplekov, *Neutron Spectroscopy. Series Neutrons and Solids*, Ed. by R. P. Ozerov (Énergoatomizdat, Moscow, 1983), Vol. 3, p. 101.
11. V. G. Bar'yakhtar, I. M. Vitebskiĭ, and D. A. Yablonskiĭ, Zh. Éksp. Teor. Fiz. **76**, 1381 (1979) [Sov. Phys. JETP **49**, 703 (1979)].
12. C. P. Slichter, *Principles of Magnetic Resonance* (Springer-Verlag, Berlin, 1978; Mir, Moscow, 1981).
13. L. D. Landau and E. M. Lifshitz, *Course of Theoretical Physics*, Vol. 8: *Electrodynamics of Continuous Media* (Nauka, Moscow, 1982; Pergamon, New York, 1984), Para. 96.
14. F. J. Darnell, W. H. Cloud, and H. S. Jarrett, Phys. Rev. **130**, 647 (1963).
15. C. P. Bean and D. S. Rodbell, Phys. Rev. **126**, 104 (1962).
16. J. H. Wijngaard and C. Haas, Phys. Rev. B **45**, 5395 (1992).
17. E. A. Pamyatnykh and E. A. Turov, *Principles of Electrodynamics of Material Media in Variable and Inhomogeneous Fields* (Nauka, Moscow, 2001).
18. D. A. Yablonskiĭ and V. N. Krivoruchko, in *Problems of Physical Kinetics and Solid State Physics* (Naukova Dumka, Kiev, 1990), p. 444.

Translated by P. Pozdeev

Journal of Experimental and Theoretical Physics, Vol. 94, No. 2, 2002, pp. 367–376.
Translated from Zhurnal Éksperimental'noĭ i Teoreticheskoĭ Fiziki, Vol. 121, No. 2, 2002, pp. 431–441.

SOLIDS
Electronic Properties

The Special Features of Ferromagnetism in Ordered Heusler Alloys

R. O. Zaĭtsev[a] and N. V. Terekhina[b]

[a]*Russian Research Center Kurchatov Institute, pl. Kurchatova 1, Moscow, 123182 Russia*
[b]*Thermal Instrument Research Institute State Scientific Center, Moscow, 129085 Russia*

Received May 31, 2001

Abstract—The electronic structure and magnetic properties of the Cu_2MnA, Ni_2MnA, Pd_2MnA, Co_2MnA, and Fe_2FeA compounds with cubic lattices, where A is a nontransition element anion (A = Al, In, Ge, As, Sn, Si, or Sb), are studied. An analysis is performed in terms of the generalized Hubbard model with an infinite electronic repulsion energy within the same atom. Equations for determining the spin magnetic susceptibility of the compounds are obtained. These equations are used to determine the conditions of ferromagnetic instability and to construct the phase diagram for the existence of ferromagnetic ordering. *© 2002 MAIK "Nauka/Interperiodica".*

1. INTRODUCTION

In this work, we establish the possibility of the rise of ferromagnetic instability in Me_2MnA ordered compounds depending on the *d* and *p* shell occupancies in transition element Me cations and nontransition element A anions.

The corresponding shell occupation numbers n_e, n_d, and n_p are related to the mean number of *d* electrons in the manganese shell by the electrical neutrality condition

$$\begin{aligned} n &= 2n_e + n_d + n_p = Z_p - 2 + 2\kappa_e + \kappa_d, \\ h &= 36 - n. \end{aligned} \tag{1}$$

Here, $\kappa_{e,d}$ is the number of *d* electrons in the incompletely occupied shell of the corresponding neutral atom, $Z_p - 2$ is the number of *p* electrons in the unoccupied shell of neutral atom A, and *h* is the mean number of holes.

2. THE MATTHIAS RULE

Ferromagnetic Heusler alloys can be divided into subgroups according to the total number of electrons in the incompletely occupied *n* shell. All these subgroups are listed in Table 1.

Note that the Curie temperature as a function of *n* has two maxima, at *n* = 27 and *n* = 30 (see Fig. 1).

Similar maxima were observed by Matthias [2] in studying the dependence of the superconducting transition temperature on *n*.

Note also (Fig. 1) that Table 1 is a continuation of the corresponding table for the A_3C superconducting compounds with the A15 structure [3].

The position of the Curie temperature maximum at *n* = 27 coincides with that of the minimum of the superconducting transition temperature.

We will show that these trends have the same physical nature and are caused by a sharp dependence of the scattering amplitude on the relative energy of electronic excitations.

3. EQUATIONS OF STATE

In this work, the rise of ferromagnetism in Heusler alloys is studied based on the concept of strong interactions between electrons of the same atom. The corresponding matrix elements (also called Hubbard energy) for copper, nickel, cobalt, iron, and manganese (equal to 20, 19, 18, 16.5, and 15 eV, respectively) exceed the

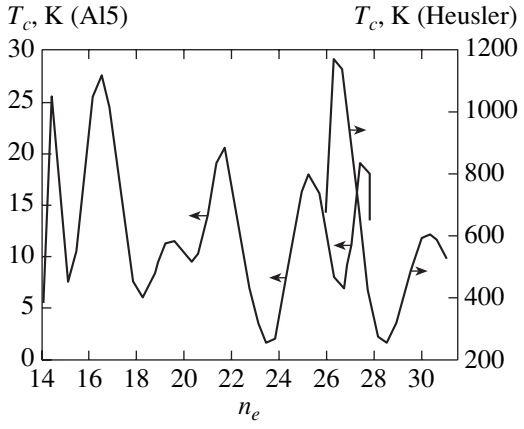

Fig. 1. Matthias rules. The scale on the left is for A15 superconductors. The right scale corresponds to ferromagnetic Heusler alloys.

Table 1

n	h	AB_2C (A and B are transition elements and C is a nontransition element)
26	10	Fe_2FeSi (380; $2 \times 1.51 + 2.15 = 5.17$), Co_2MnGa (694; 4.1)
27	9	Co_2MnSi (982; 5.1), Co_2MnGe (905; 5.1), Co_2MnSn (829; 5.1)
28	8	Ni_2MnGa (379; 4.2), Ni_2MnIn (323; 4.4)
29	7	Ni_2MnSn (344; 4.1), Pd_2MnGe (170; 3.2), Pd_2MnSn (189; 4.2)
30	6	Ni_2MnSb (360; 3.3), Pd_2MnSb (247; 4.4)
30	6	Cu_2MnAl (600; 3.6), Cu_2MnIn (520; 4.0), Au_2MnAl (258; 3.1)
31	5	Cu_2MnSn (530; 4.1)
32	4	Cu_2MnSb ($T_N = 380$); $h = h_d + h_p + 2h_e$

Note: Given in parentheses are the Curie temperature (in kelvins) and the mean saturation magnetic moment [1].

energy of electron transfer to neighboring atoms and are considered infinite in what follows.

Ideally, the unit cell of an ordered Heusler alloy consists of one FCC lattice of two transition elements and one FCC lattice containing Mn or Fe and nontransition element Me anions (see Fig. 2 and, e.g., [4]).

The cation positions at the origin and in the unit cell center (1/2, 1/2, 1/2) can conveniently be used as a basis.

We select three FCC cell vectors

$$\mathbf{a}_1 = \frac{1}{2}(\mathbf{e}_x + \mathbf{e}_y), \quad \mathbf{a}_2 = \frac{1}{2}(\mathbf{e}_y + \mathbf{e}_z), \quad \mathbf{a}_\mathbf{e} = \frac{1}{2}(\mathbf{e}_z + \mathbf{e}_x) \tag{2}$$

as three elementary translation vectors, were $\mathbf{e}_k$ is the unit vector in the orthogonal coordinate system. The system of basis cations forms a lattice of the NaCl type.

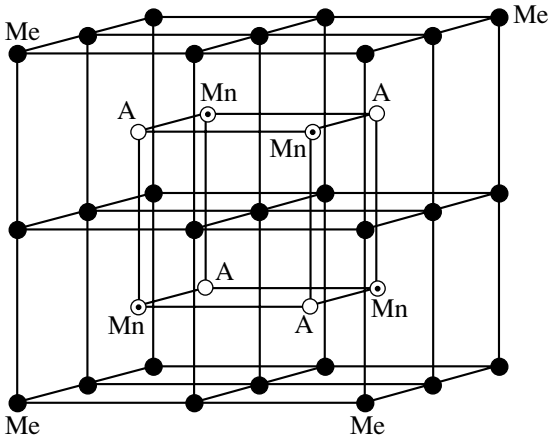

Fig. 2. Unit cell of ordered Heusler alloys (compounds Fe_2FeSi, Ni_2MnA: Me = Fe, Co, Ni, Cu, Pd, and Au; A = Al, Ge, In, Sn, Sb, As, Si, and Ga).

The elementary basis is augmented by cations with the coordinates (1/4, 1/4, 1/4) and anions with the coordinates (3/4, 3/4, 3/4).

We can conveniently pass to the hole representation $h_d = 10 - n_d$, $h_p = 6 - n_p$, and $h_e = 10 - n_e$. Next, it follows from Table 1 that the conditions of the rise of ferromagnetism should be studied in the fairly wide region

$$4 < 2h_e + h_d + h_p \le 10, \quad 3 < h_d \le 5, \quad 0 \le h_e \le 5, \quad 0 \le h_p \le 3. \tag{3}$$

The last three inequalities determine the regions where the bottom halves of hole shells, for which the tendency toward ferromagnetism is most probable (see below), are occupied.

The second inequality refers to Fe or Mn cations, in which the number of holes cannot be smaller than two or three.

The hybridization of the e and p states at a given $r_p = \epsilon_p - \epsilon_e$ energy difference is related to transitions between nearest neighbor cations and anions of the third and fourth FCC sublattices. The mean h_p numbers are then expressed in terms of normal coordinates and three energy spectrum branches as

$$h_p = [h_p] + g_p^2 f_p R_p K_p, \quad K_p = \sum_{\mathbf{p},\lambda} A_p^\lambda(\mathbf{p}) n_F(\xi^{(\lambda)}(\mathbf{p})). \tag{4}$$

The equations of state for the d and e hole excitations are written similarly,

$$h_d = [h_d] + g_d^2 f_d R_d K_d, \quad K_d = \sum_{\mathbf{p},\lambda} A_d^\lambda(\mathbf{p}) n_F(\xi^{(\lambda)}(\mathbf{p})),$$
$$h_e = [h_e] + g_e^2 f_e R_e K_e, \quad K_e = \sum_{\mathbf{p},\lambda} A_e^\lambda(\mathbf{p}) n_F(\xi^{(\lambda)}(\mathbf{p})). \tag{5}$$

Here and above, $[h_k]$ is the integral part. The other values calculated in the simplest zero-loop approximation [5, 6] for each $[h_k] \le h_k \le [h_k] + 1$ integer interval are listed in Table 2.

Generally, the $A_k^{(\lambda)}(\mathbf{p})$ normal coordinates are proportional to the diagonal minors of the inverse Green's function matrix,

$$\hat{G}_\omega^{-1}(\mathbf{p}) = \begin{pmatrix} i\omega - \epsilon_e & -\tilde{f}_e \tau^{e,d}(\mathbf{p}) & -\tilde{f}_e \tau^{e,p}(\mathbf{p}) \\ -\tilde{f}_d \tau^{d,e}(\mathbf{p}) & -i\omega - \epsilon_d & 0 \\ -\tilde{f}_p \tau^{p,e}(\mathbf{p}) & 0 & i\omega - \epsilon_p \end{pmatrix}, \tag{6}$$

Table 2

Δh_d	g_d^2	f_d	K_d	h_d	Γ_d
0…1	1	$(10 - 9h_d)/10$	$h_d/(10 - 9h_d)$	$10K_d/(1 + 9K_d)$	0
1…2	3/2	$(5 - 2h_d)/30$	$(h_d - 1)/(5 - 2h_d)$	$(1 + 5K_d)/(1 + 2K_d)$	–1/3
2…3	2	$(6 - h_d)/120$	$3(h_d - 2)/(6 - h_d)$	$6(1 + K_d)/(3 + K_d)$	–2/3
3…4	5/2	$(3h_d - 4)/200$	$8(h_d - 3)/(3h_d - 4)$	$4(6 - K_d)/(8 - 3K_d)$	–1
4…5	3	$(19h_d - 70)/150$	$25(h_d - 4)/(19h_d - 70)$	$10(10 - 7K_d)/(25 - 19K_d)$	–4/3
Δh_e	g_e^2	f_e	K_e	n_e	Γ_e
0…1	1	$(4 - 3n_e)/4$	$n_e/(4 - 3n_e)$	$4K_e/(1 + 3K_e)$	0
1…2	3/2	$(2 + n_e)/12$	$4(n_e - 1)/(2 + h_e)$	$2(2 + K_e)/(4 - K_e)$	–1/3
2…3	3/2	$(6 - n_e)/12$	$3(n_e - 2)/(6 - n_e)$	$6(1 + K_e)/(3 + K_e)$	+4/3
3…4	1	$(3n_e - 8)/4$	$4(n_e - 3)/(3n_e - 8)$	$4(3 - 2K_e)/(4 - 3K_e)$	+1
Δh_p	g_p^2	f_p	K_p	h_p	Γ_p
0…1	1	$(6 - 5h_p)/6$	$h_p/(6 - 5h_p)$	$6K_p/(1 + 5K_p)$	0
1…2	3/2	$(4 - h_p)/18$	$2(h_p - 1)/(4 - h_p)$	$2(1 + 2K_p)/(2 + K_p)$	–1/3
2…3	2	$(5h_p - 6)/36$	$9(h_p - 2)/(5h_p - 6)$	$6(3 - K_p)/(9 - 5K_p)$	–2/3

where

$$\omega = i(2n+1)\pi T, \quad \tilde{f}_k = g_k^2 f_k.$$

Using the convenient notation $E_k = i\omega - \epsilon_k$, we obtain

$$\begin{aligned} K_a &= T\sum_{\omega,\mathbf{p}} e^{i\omega\delta}\frac{E_dE_p}{\det_{\omega,\mathbf{p}}}, \\ \det_{\omega,\mathbf{p}} &= E_eE_pE_d - E_d\tilde{f}_e\tilde{f}_p\tau^{e,p}(\mathbf{p})\tau^{p,e}(\mathbf{p}) \\ &\quad - E_p\tilde{f}_e\tilde{f}_d\tau^{e,d}(\mathbf{p})\tau^{d,e}(\mathbf{p}), \end{aligned} \tag{7a}$$

$$\begin{aligned} K_d &= T\sum_{\omega,\mathbf{p}} e^{i\omega\delta}\frac{(E_eE_p - \tilde{f}_e\tilde{f}_p\tau^{e,p}(\mathbf{p})\tau^{p,e}(\mathbf{p}))}{\det_{\omega,\mathbf{p}}}, \\ K_p &= T\sum_{\omega,\mathbf{p}} e^{i\omega\delta}\frac{(E_eE_d - \tilde{f}_e\tilde{f}_d\tau^{e,d}(\mathbf{p})\tau^{d,e}(\mathbf{p}))}{\det_{\omega,\mathbf{p}}}. \end{aligned} \tag{7b}$$

The f_k end multipliers and the sums of the g_k^2 squares of fractional parentage coefficients determined for each integer interval of hole concentrations are summarized in Table 2.

The above equations of state correspond to the possibility of factorization into simple multipliers with the coefficients that are found from the general expressions for normal coordinates,

$$A_e = \frac{E_dE_p}{\det'_E},$$

$$\begin{aligned} \det'_E &= E_pE_d + E_eE_d + E_eE_p \\ &\quad - \tilde{f}_e\tilde{f}_p\tau^{e,p}(\mathbf{p})\tau^{p,e}(\mathbf{p}) - \tilde{f}_e\tilde{f}_d\tau^{e,d}(\mathbf{p})\tau^{d,e}(\mathbf{p}), \end{aligned} \tag{8}$$

$$A_d = \frac{(E_eE_p - \tilde{f}_e\tilde{f}_p\tau^{e,p}(\mathbf{p})\tau^{p,e}(\mathbf{p}))}{\det'_E},$$

$$A_p = \frac{(E_eE_d - \tilde{f}_e\tilde{f}_d\tau^{e,d}(\mathbf{p})\tau^{d,e}(\mathbf{p}))}{\det'_E}.$$

The A_e coefficient can be determined from the obvious relation $A_e = 1 - A_d - A_p$.

The problem is considerably simplified if integer magnetic moment values at which either K_d or K_p vanishes are considered.

In the limit of $\epsilon_d \longrightarrow \infty$ or $K_d \longrightarrow 0$, we have two spectrum branches, which are determined from the equation

$$\begin{aligned} &E_pE_e - \tilde{f}_e\tilde{f}_p\tau^{e,p}(\mathbf{p})\tau^{p,e}(\mathbf{p}) \\ &\approx -\frac{E_p}{\epsilon_d}\tilde{f}_e\tilde{f}_d\tau^{e,d}(\mathbf{p})\tau^{d,e}(\mathbf{p}). \end{aligned} \tag{9}$$

Passing to the $E_d \approx -\epsilon_d \longrightarrow -\infty$ limit yields

$$K_d = \frac{1}{\epsilon_d^2}\sum_{\mathbf{p},\lambda}\tilde{f}_e\tilde{f}_d\tau^{e,d}(\mathbf{p})\tau^{d,e}(\mathbf{p})A^{(-\lambda)}(\mathbf{p})n_F(\xi_d^{\lambda}(\mathbf{p})),$$

$$K_p = \sum_{\mathbf{p},\lambda} A^{\lambda}(\mathbf{p}) n_F(\xi_d^{\lambda}(\mathbf{p})),$$
$$K_e = \sum_{\mathbf{p},\lambda} A^{(-\lambda)}(\mathbf{p}) n_F(\xi_d^{\lambda}(\mathbf{p})), \quad (10)$$
$$A^{(\pm)}(\mathbf{p}) = \frac{1}{2}\left(1 \pm \frac{\mathrm{sgn}(r_p)}{\sqrt{1+ut_{\mathbf{p}}^2}}\right),$$
$$\xi_d^{\lambda}(\mathbf{p}) = \mathrm{sgn}\lambda \frac{|r_p|}{2}\sqrt{1+ut_{\mathbf{p}}^2} - \mu,$$

where $u = 4\tau^2 g_p^2 f_p g_e^2 f_e / r_p^2$, $\tilde{f}_d = g_d^2 f_d$, $\tilde{f}_e = g_e^2 f_e$, $r_p = \epsilon_p - \epsilon_e$, and $\mu = -(\epsilon_p + \epsilon_e)/2$.

In the $E_p \approx -\epsilon_p \longrightarrow -\infty$ limit, we obtain equations similar to (9) and (10) but with d replaced by p and p replaced by d. Assuming that multiparticle high-spin states may exist for e holes as well, the corresponding parameters can be obtained by replacing $d \longrightarrow e$ in Table 2.

The dependence on momentum $\mathbf{p}$ enters into the definition of excitation energies through the $t_{\mathbf{p}}^2$ function, which is proportional to $1 + \cos p_x \cos p_y + \cos p_y \cos p_z + \cos p_z \cos p_x$. We can therefore perform calculations using the known function for the density of FCC lattice states

$$\rho_0(z) = \sum_{\mathbf{p}} (z - \cos p_x \cos p_y - \cos p_y \cos p_z - \cos p_z \cos p_x).$$

It can be shown that, at $z \approx -1 + x$, the density of states corresponds to one-dimensional motion, $\rho_0 \approx 1/\sqrt{x}$. At high energies ($z \approx 3 - y$), the density of states corresponds to a three-dimensional isotropic spectrum, $\rho_0 \approx \sqrt{y}$.

It follows that, for simplicity of calculations, it is expedient to denote the $t_{\mathbf{p}}^2$ function by ϵ^2 and to assign it the semielliptic density of states

$$\rho(\epsilon) = \frac{4}{\pi}\sqrt{1-\epsilon^2} \quad \text{for} \quad 0 < \epsilon < 1. \quad (11)$$

4. FERROMAGNETIC INSTABILITY CONDITIONS

Calculations of the spin part of magnetic susceptibility will be performed by differentiating the equations of state written in the zero-loop approximation (the Hubbard I approximation).

After the diagonalization of the zeroth Hamiltonian corresponding to the nonoverlapping atomic states, the creation and annihilation operators take the form of expansions in all possible transitions between the N- and $(N+1)$-hole states (see [7]),

$$\hat{a}_{m,\sigma}^{+}(\mathbf{r}) = \sum_{\alpha} g_{\alpha}^{m,\sigma} \hat{X}_{\mathbf{r}}^{\alpha},$$
$$\hat{a}_{n,\sigma}(\mathbf{r}) = \sum_{\beta} g_{\beta}^{n,\sigma} \hat{X}_{\mathbf{r}}^{\beta}. \quad (12)$$

Here, indices α and β correspond to the mutually reverse $s \longrightarrow m$ transitions; that is, $\beta(m, s) = -\alpha(s, m)$. The $g_{\alpha}^{m,\sigma}$ values are called fractional parentage coefficients and are calculated below.

The equations for the n_m mean occupation numbers are found from the definition of the temperature Green's functions calculated for each pair of adjoint X operators (see [8]),

$$D^{\alpha,\beta}(\mathbf{r},\tau;\mathbf{r},\tau') = -\Theta(\tau-\tau')\langle X_{\mathbf{r}}^{\alpha}(\tau)_{\mathbf{r}} X_{\mathbf{r}'}^{\beta}(\tau')\rangle + \Theta(\tau'-\tau)\langle X_{\mathbf{r}'}^{\beta}(\tau')_{\mathbf{r}} X_{\mathbf{r}}^{\alpha}(\tau)\rangle. \quad (13)$$

The one-particle Green's function is calculated using the simplest zero-loop self-consistent field approximation. In this approximation, the Fourier components of the $D_{\omega}^{\alpha,\beta}(\mathbf{p})$ one-particle Green's function only differ from the so-called virtual Green's function $G_{\omega}^{\alpha,\beta}(\mathbf{p})$ by the f_{β} coefficients. The virtual Green's function in turn satisfies the Dyson-type equation

$$D_{\omega}^{\alpha,\beta}(\mathbf{p}) = G_{\omega}^{\alpha,\beta}(\mathbf{p}) f_{\beta},$$
$$\{\hat{G}_{\omega}^{-1}(\mathbf{p})\} = \{i\omega - \epsilon_m + \epsilon_s\}\delta(\alpha+\beta) - \Sigma_{\omega}^{\alpha,\beta}(\mathbf{p}). \quad (14)$$

Here, $\epsilon_m - \epsilon_s$ is the transition energy corresponding to transition number α and $\omega = T(2n+1)\pi$.

At given one-particle transition numbers $\beta(m, s)$, each f_{β} end multiplier by definition equals the sum of the mean occupation numbers of the initial and final states. On the other hand, the eigenenergy part is, in our approximation, the sum of the products of the end multiplier by the generalized matrix of jumps and the one-loop correction, which does not depend on either frequency or momentum,

$$f_{\alpha(s,m)} = n_s + n_m, \quad \Sigma^{\alpha,\beta}(\mathbf{p}) = f_{\alpha} t_{\beta}^{\alpha}(\mathbf{p}) + \Sigma^{\alpha,\beta},$$
$$t_{\beta}^{\alpha}(\mathbf{p}) = g_{\alpha}^{k,\sigma} t_s^k(\mathbf{p}) g_{\beta}^{s,\sigma}. \quad (15)$$

The n^m_{N+1} mean occupation numbers for final states m are found from the diagonal component at $\beta = -\alpha$,

$$\begin{aligned}\lim_{\delta\to 0+} D^{\alpha,\beta}(\mathbf{r},\tau;\mathbf{r},\tau+\delta)\\ = \lim_{\delta\to 0+} T\sum_{\omega,\mathbf{p}} D^{\alpha,\beta}_{\omega}(\mathbf{p})\exp(i\omega\delta)\\ = \langle X^{\beta(m,s)}_{\mathbf{r}} X^{\alpha(m,s)}_{\mathbf{r}}\rangle = \langle X^{m,s}_{\mathbf{r}} X^{s,m}_{\mathbf{r}}\rangle\\ = \langle X^{m,m}_{\mathbf{r}}\rangle = n^m_{N+1}.\end{aligned} \tag{16}$$

Equations (15) determine all $f(a(s, m)) = n_s + n_m$ end multipliers that appear in the definition of the diagonal components of the one-particle Green's function, which, in turn, is written via all possible end multipliers. The one-loop eigenenergy parts are not taken into account in the zero-loop approximation because they are considered independent of indices $\Sigma^{\alpha,\beta}$ and are therefore added to the chemical potential.

If we restrict our analysis to transitions between the high-spin N- and $(N + 1)$-hole states, we can conveniently use the projection of the spin of the $(N + 1)$-hole state with spin $S = (N + 1)/2$ instead of indices α and β (e.g., see [9]). The squares of the fractional parentage coefficients are then determined by the S spin value and its projection M,

$$\begin{aligned}|g_S(M)| = \sqrt{\frac{S+M}{2S}},\\ M = S, S-1, S-2, \ldots, -S.\end{aligned} \tag{17}$$

The mean occupation numbers present in the Green's function definition (14) are also determined from the total spin value and its projection. When a magnetic field is switched on, energy level splitting occurs, which determines corrections to mean occupation numbers. Suppose that the splitting of levels is equidistant, that is, that Zeeman splitting with some effective factor g occurs. We then have

$$\delta n_N(S_z) = n_N(0)\delta\exp\left(-\frac{E(S_z)}{T}\right) = -n_N(S_z)\delta\frac{E(S_z)}{T},$$

$$\delta E(S_z) = g\mu_B S_z \delta H.$$

After excluding the $n_N(0)g\mu_B/T$ factor that appears in this expression, we obtain relations that do not explicitly depend on magnetic field variations,

$$\begin{aligned}(S_z-1)\delta n_N(S_z) = S_z\delta n_N(S_z-1),\\ \delta n_N(-S_z) = -\delta n_N(S_z).\end{aligned} \tag{18}$$

It follows that these expressions allow all variations for given N to be expressed through a single variation, for instance, through the variation of occupation numbers with a minimum spin projection, namely, $\delta n_N(S_z) = S_z\delta n_N(S_z = 1)$ for even N and $\delta n_N(S_z) = 2S_z\delta n_N$ for odd N. The relation between the variations of the N- and $(N + 1)$-particle states can be expressed via the mean value of the diagonal component of the Green's function at a zero magnetic field value,

$$K_0 = \frac{T}{g^2}\lim_{\delta\to 0+}\sum_{\omega,\mathbf{p}}\sum_{\alpha,\beta} g_\alpha G^{\alpha,\beta}_{\omega}(\mathbf{p}) g_\beta f_\beta \exp(i\omega\delta),$$

where

$$g^2 = \sum_\alpha g^2_\alpha.$$

The expressions for K_d, K_p, and K_e are given by (7), (8), and (10).

To obtain equations for determining the end multipliers, let us average the T product of annihilation operator (12) by a linear combination of adjoint X operators with arbitrary coefficients $\gamma^{m,\sigma}_\alpha$,

$$\hat{Y}_{m,\sigma} = \sum_\beta \gamma^{m,\sigma}_\beta \hat{X}^\beta_{m,\sigma}.$$

$$\langle \hat{T}(\hat{a}_{n,\sigma}(\mathbf{r},\tau)\hat{Y}_{m,\sigma}(\mathbf{r}',\tau'))\rangle$$

$$= \sum_{\alpha,\beta} g^{n,\sigma}_\alpha \gamma^{m,\sigma}_\beta \langle \hat{T}(\hat{X}^\alpha_{\mathbf{r},\tau}\hat{X}^\beta_{\mathbf{r},\tau'})\rangle.$$

Here, we use the expansion of annihilation operator (12) with the known fractional parentage coefficients $g^{n,\sigma}_\beta$. After the passage to the $\tau' \longrightarrow \tau$, $\tau' > \tau$ limit, we obtain equations for determining all $(N + 1)$-particle occupation numbers n^s_{N+1}:

$$\begin{aligned}\sum_\alpha g^{k,\sigma}_{\alpha(m,s)} n^s_{N+1}\gamma^{k,\sigma}_{\alpha(s,m)} = T\lim_{\delta\to 0+}\sum_{\omega,\mathbf{p}}\sum_{\alpha,\beta} g^{k,\sigma}_{\alpha(m,s)}\\ \times D^{\alpha,\beta}_{\omega}(\mathbf{p})\gamma^{k,\sigma}_{\beta(s,m)}\exp(i\omega\delta).\end{aligned} \tag{19}$$

Let us substitute Green's function (14) written in the zero-loop approximation into these equations and take the variation of the resulting equations with respect to the applied magnetic field value,

$$\begin{aligned}\sum_\alpha g^{k,\sigma}_{\alpha(m,s)}\delta n^s_{N+1}\gamma^{k,\sigma}_{\alpha(s,m)} = T\sum_{\alpha,\beta} g^{k,\sigma}_{\alpha(m,s)}\\ \times\lim_{\delta\to 0+}\sum_{\omega,\mathbf{p}} G^{\alpha,\beta}_{\omega}(\mathbf{p})\exp(i\omega\delta)\delta f_\beta\gamma^{k,\sigma}_{\beta(s,m)}\\ + T\sum_{\alpha,\beta} g^{k,\sigma}_{\alpha(m,s)}\lim_{\delta\to 0+}\sum_{\omega,\mathbf{p}}\delta G^{\alpha,\beta}_{\omega}(\mathbf{p})\exp(i\omega\delta) f_\beta\gamma^{k,\sigma}_{\beta(s,m)}.\end{aligned} \tag{20}$$

It can be shown that, in the zero-loop approximation,

$$T\sum_{\alpha} g^{k,\sigma}_{\alpha(m,s)} \lim_{\delta \to 0+} \sum_{\omega,\mathbf{p}} G^{\alpha,\beta}_{\omega}(\mathbf{p}) \exp(i\omega\delta) = K_0 g^{k,\sigma}_{\beta(m,s)} \tag{21}$$

with the K_0 coefficient independent of number β.

In the $H \longrightarrow 0$ limit, the end multipliers prove to be independent of transition number β; that is, $\lim_{H \to 0} f_\beta = f_0$.

Suppose that the $\gamma^{k,\sigma}_{\alpha(s,m)}$ auxiliary coefficients satisfy the condition of orthogonality to the fractional parentage coefficients, $\sum_\alpha g^{k,\sigma}_{\alpha(m,s)} \gamma^{k,s}_{\alpha(s,m)} = 0$. The right-hand side of (20) is then transformed as follows:

$$\sum_{\alpha} g^{k,\sigma}_{\alpha(m,s)} \delta n^{s}_{N+1} \gamma^{k,\sigma}_{\alpha(s,m)} = K_0 \sum_{\alpha} g^{k,\sigma}_{\alpha(m,s)} \delta f^{s}_{\alpha} \gamma^{k,\sigma}_{\alpha(s,m)}. \tag{22}$$

Bearing in mind that, at a zero magnetic field, K_0 is the same value as in the equation of state, we obtain

$$\sum_{M=-S+1}^{M=S} b(S-M+1) g(S-M+1) \delta n_{N+1}(M) = K_0 \sum_{M=-S+1}^{M=S} b(S-M+1) g(S-M+1) \times \left\{ \delta n_{N+1}(M) + \delta n_N\left(M - \frac{1}{2}\right) \right\}. \tag{23}$$

Let us write all variations through the variation of occupation numbers with a minimum spin projection,

$$\sum_{M=-S+1}^{M=S} b(S-M+1) g(S-M+1) \times \frac{M}{1+N} \delta n_{N+1}\left(-\frac{1+N}{2}\right) = K_0 \sum_{M=-S+1}^{M=S} b(S-M+1) g(S-M+1) \times \left\{ \frac{M}{1+N} \delta n_{N+1}\left(-\frac{1+N}{2}\right) + \frac{(2M-1)}{2N} \delta n_N\left(-\frac{N}{2}\right) \right\}.$$

Taking into account the $\sum_k b_k g_k = 0$ orthogonality condition allows the sums over M to be reduced, and, after the substitutions $(N+1)/2 = S$ and $N/2 = S - 1/2$, we obtain

$$(1-K_0)\frac{1}{(-S)} \delta n_{N+1}(-S) = K_0 \frac{2}{1-2S} \delta n_N\left(-S + \frac{1}{2}\right).$$

This leads us to conclude that, for an arbitrary spin projection S_z, the variation of $(N+1)$-particle states is related to the corresponding variation of N-particle states as

$$(1-K_0)\frac{1}{S_z} \delta n_{N+1}(S_z) = K_0 \frac{2}{(2S_z - 1)} \delta n_N\left(S_z - \frac{1}{2}\right).$$

Put $S_z = 1$ for odd N. This gives

$$(1-K_0)\delta n_{N+1}(1) = 2K_0 \delta n_N\left(\frac{1}{2}\right). \tag{24a}$$

For even N, we can write $S_z = -1/2$. Therefore,

$$2(1-K_0)\delta n_{N+1}\left(\frac{1}{2}\right) = K_0 \delta n_N(1). \tag{24b}$$

It follows that all occupation number variations can be expressed through the $\delta n_{N+1}(1)$ or $\delta n_{N+1}(1/2)$ variation.

To eventually determine the ferromagnetic instability condition, let us write (20) for[1] $\gamma^{k,\sigma}_{\alpha(m,s)} = g^{k,\sigma}_{\alpha(s,m)}$.

In other words, we average the product of creation and annihilation operators (12),

$$\sum_{\alpha} g^{2}_{\alpha(m,s)} \delta n^{s}_{N+1} = \sum_{\alpha} g^{2}_{\alpha(m,s)} K_0 \delta f_\alpha + \sum_{\alpha} g^{2}_{\alpha(m,s)} f_\alpha \delta K_0. \tag{25}$$

Let us substitute the explicit expression for the fractional parentage coefficients [Eq. (17)] into the left-hand side of (25) and express all occupation number variations through the $\delta n^{(1)}_{N+1}$ or $\delta n^{(1/2)}_{N+1}$ variation.

After transforming the left-hand side, the equation of state takes the form

$$\sum_{k} g^{2}_{k} \delta n^{k}_{1+N} = \sum_{M=-S}^{S} \frac{S+M}{2S} M \delta n_{1+N}(1) = \frac{(1+S)(1+2S)}{6} \delta n_{1+N}(1) = K_0 \delta J + \tilde{f} \delta K_0. \tag{26}$$

Here, the notation $\tilde{f} = f_0 \sum_\alpha g^2_\alpha = f_0 g^2$ and $\delta J = \sum_\alpha g^2_\alpha \delta f_\alpha$ is used.

The K_0 diagonal components of the one-particle Green's function depend on invariant combinations of the $\sum_\alpha g^2_\alpha f_\alpha$ type. Both the variation of K_0 and the

[1] This relation in combination with all possible orthogonality conditions makes up a complete system of independent conditions that can be imposed on the $\gamma^{k,\sigma}_{\alpha(m,s)}$ coefficients.

whole right-hand side of (26) are therefore expressed through $\delta J = \sum_\alpha g_\alpha^2 \delta f_\alpha$.

Assume for definiteness that (N + 1)-particle states have integral spin S, and N-particle states have spin $S - 1/2$.

Let us write the variations for given projection M through the variation with a minimum projection and use explicit equation (17) for the fractional parentage coefficients. This gives

$$\delta J = \sum_{M=-S}^{S} \frac{S+M}{2S} \times \left[M\delta n_{1+N}(1) + 2\left(M - \frac{1}{2}\right)\delta n_N\left(\frac{1}{2}\right)\right].$$

Further, let us write the $\delta n_N(1/2)$ variation through $\delta n_{1+N}(1)$. Using formula (24a), we obtain

$$\delta J = \frac{1}{K_0}\sum_{M=-S}^{S} \frac{S+M}{2S} \times \left[MK_0 + \left(M - \frac{1}{2}\right)(1-K_0)\right]\delta n_{1+N}(1).$$

It remains to perform the summations

$$\sum_{M=-S}^{S} = 1 + 2S, \quad \sum_{M=-S}^{S} M^2 = \frac{S}{3}(1+S)(1+2S).$$

This eventually yields a general expression valid for occupations not exceeding one half:

$$\delta J = \frac{1+2S}{4K_0}[K_0 - \Gamma_d]\delta n_{N+1}(1), \tag{27a}$$

where

$$\Gamma_d = -\frac{2S-1}{3}$$

This formula is also valid for half-integer spins.

Substituting (27a) into (26) yields

$$\frac{1+2S}{4}(1-K_0)\delta n_{N+1}(1) = \tilde{f}_0 \sum_{s=0}^{p} \frac{\delta K_0}{\delta \tilde{f}_s}\frac{1+2S_s}{4K_s}[K_s - \Gamma_s]\delta n_{N(s)+1}(1),$$

where index s numbers various multiplets (in our problem, $s = p, d, e$).

We can conveniently introduce new variables $\delta y_k = (1 + 2S_k)\delta n_{N(k)+1}(1)/4$, which transforms the system of homogeneous equations into

$$(1-K_n)\delta y_n = \tilde{f}_n \sum_{s=0}^{p} \frac{\delta K_n}{\delta \tilde{f}_s}\frac{[K_s - \Gamma_s]}{K_s}\delta y_s.$$

A solution to this system exists, provided that

$$\det\left\{\delta_{n,s}(1-K_s) - \tilde{f}_n \frac{\delta K_n}{\delta \tilde{f}_s}\frac{[K_s - \Gamma_s]}{K_s}\right\} = 0. \tag{28}$$

If the shell is more than half-filled, the partially hole symmetry transformation $K_0 \longrightarrow 1 - K_0$ yields

$$\Gamma_d = \frac{2S-1}{3} + 1, \tag{27b}$$

where S is, as previously, the maximum spin for a given group of transitions.

In our three-component model, the condition of the rise of ferromagnetism is found from the equation

$$\det\begin{pmatrix} 1-K_e-R_{ee} & -R_{ed} & -R_{ep} \\ -R_{de} & 1-K_d-R_{dd} & -R_{dp} \\ -R_{pe} & -R_{pd} & 1-K_p-R_{pp} \end{pmatrix} = 0, \tag{29}$$

$$\text{where } R_{nm} = \tilde{f}_n \frac{\delta K_n}{\delta \tilde{f}_m}\left(1 + \frac{\gamma_m}{K_m}\right).$$

In the $T \longrightarrow 0$ limit, all possible R_{mn} matrix element products drop out of consideration, and the condition for the rise of ferromagnetism takes the form

$$1 = L_d\frac{(K_d - \Gamma_d)}{K_d(1-K_d)} + L_p\frac{(K_p - \Gamma_p)}{K_p(1-K_p)} + L_e\frac{(K_e - \Gamma_e)}{K_e(1-K_e)}. \tag{30}$$

Here, K_n are defined by (7) and (8), and the L_n values are their derivatives, $L_n = \tilde{f}_n(\delta K_n)/\delta \tilde{f}_n$.

In the limit of integer magnetic moment S_d or S_p values, we have

$$K_{d,p} \longrightarrow 0, \quad L_{d,p} \longrightarrow 0, \quad L_{d,p}/K_{d,p} \longrightarrow 1,$$

and, for integer S_d, we can therefore write

$$1 + \Gamma_d = L_p\frac{K_p - \Gamma_p}{K_p(1-K_p)} + L_e\frac{K_e - \Gamma_e}{K_e(1-K_e)}. \tag{31}$$

For integer S_p moments, we have the same relation but with p replaced by d and d replaced by p.

Consider the situation most favorable for meeting ferromagnetism condition (31), when the lower hybridization subband is filled and all L_n coefficients are positive.

In the $T = 0$ limit, two energy parameters $\epsilon_{p,e}$ can conveniently be replaced by

$$u = 4\frac{g_p^2 f_p g_e^2 f_e}{r_p^2}, \quad y = \sqrt{\frac{4\mu^2 - r_p^2}{u r_p^2}}. \tag{32}$$

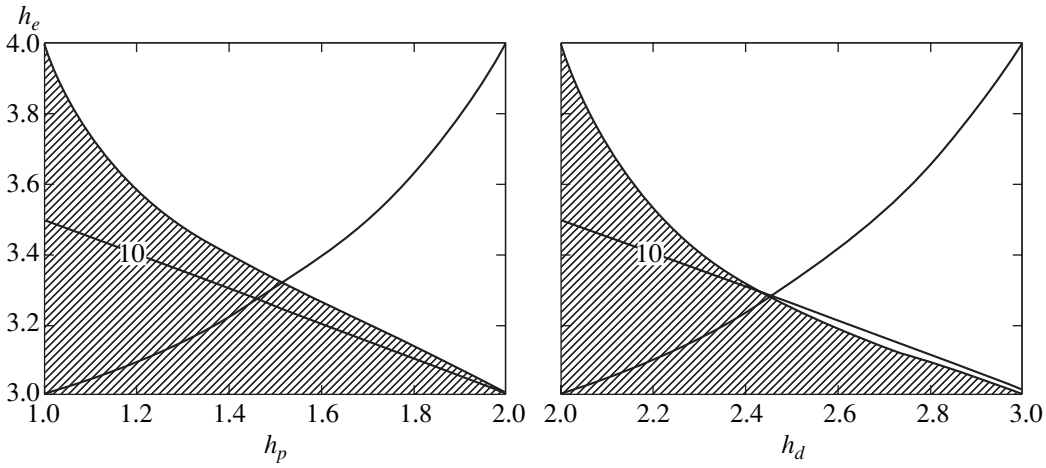

Fig. 3. Magnetic phase diagram of Fe_3Si at $T = 0$: $h_d = 2$ (at the left) and $h_p = 1$ (at the right). Ferromagnetic regions are hatched.

The transition to the integration with the use of the density of states (11) yields equations reducible to elliptic integrals of the first and second kind,

$$K_e(u, y) = \frac{1}{2}\int_y^1 \left[1 + \frac{\mathrm{sgn}(r_p)}{\sqrt{1+ux^2}}\right]\rho(x)dx,$$
$$K_p(v, y) = \frac{1}{2}\int_y^1 \left[1 - \frac{\mathrm{sgn}(r_p)}{\sqrt{1+ux^2}}\right]\rho(x)dx. \quad (33)$$

Differentiating these relations at given μ and r_p yields

$$L_e(u, y) = -\mathrm{sgn}(r_p)\frac{u}{4}\int_y^1 \frac{x^2}{(1+ux^2)^{3/2}}\rho(x)dx + \frac{y}{4}\left[1 + \frac{\mathrm{sgn}(r_p)}{\sqrt{1+uy^2}}\right]\rho(y), \quad (34)$$

$$L_p(u, y) = \mathrm{sgn}(r_p)\frac{u}{4}\int_y^1 \frac{x^2}{(1+ux^2)^{3/2}}\rho(x)dx + \frac{y}{4}\left[1 - \frac{\mathrm{sgn}(r_p)}{\sqrt{1+uy^2}}\right]\rho(y). \quad (35)$$

Equation (31) together with equations of state (10) determines the phase boundary in the space of two variables h_p and h_e at a given h_d integer value, $h_d = 2, 3, 4$. The phase boundary is a curve formed by the intersection between the phase surface and the electrical neutrality plane characteristic of each compound.

The same equations [(31)–(35)] but with p replaced by d and d replaced by p apply to integer h_p values, $h_p = 0, 1, 2, 3$.

At large total spin values, when $h_p = 3$ and $h_d = 4$, dimensionless amplitude Γ equals –1 and –4/3, and the boundary of the ferromagnetic region corresponds to filling the upper hybridization subband ($\lambda = +1$). In this region, relations (33) and (35) take the form

$$K_e(u, y) = 1 - \frac{1}{2}\int_y^1 \left[1 - \frac{\mathrm{sgn}(r_p)}{\sqrt{1+ux^2}}\right]\rho(x)dx,$$
$$K_p(v, y) = 1 - \frac{1}{2}\int_y^1 \left[1 + \frac{\mathrm{sgn}(r_p)}{\sqrt{1+ux^2}}\right]\rho(x)dx, \quad (36)$$

$$L_e(u, y) = -\mathrm{sgn}(r_p)\frac{u}{4}\int_y^1 \frac{x^2}{(1+ux^2)^{3/2}}\rho(x)dx - \frac{y}{4}\left[1 - \frac{\mathrm{sgn}(r_p)}{\sqrt{1+uy^2}}\right]\rho(y), \quad (37a)$$

$$L_p(u, y) = \mathrm{sgn}(r_p)\frac{u}{4}\int_y^1 \frac{x^2}{(1+ux^2)^{3/2}}\rho(x)dx - \frac{y}{4}\left[1 + \frac{\mathrm{sgn}(r_p)}{\sqrt{1+uy^2}}\right]\rho(y). \quad (37b)$$

Equations (36) and (37) actually determine continuations of phase curves (33)–(35), which reach the boundary corresponding to filling the lower hybridization subband.

5. PHASE DIAGRAM

As follows from the principal equation (31), ferromagnetic ordering exists in all regions corresponding to the onset of filling the lower hybridization subbands,

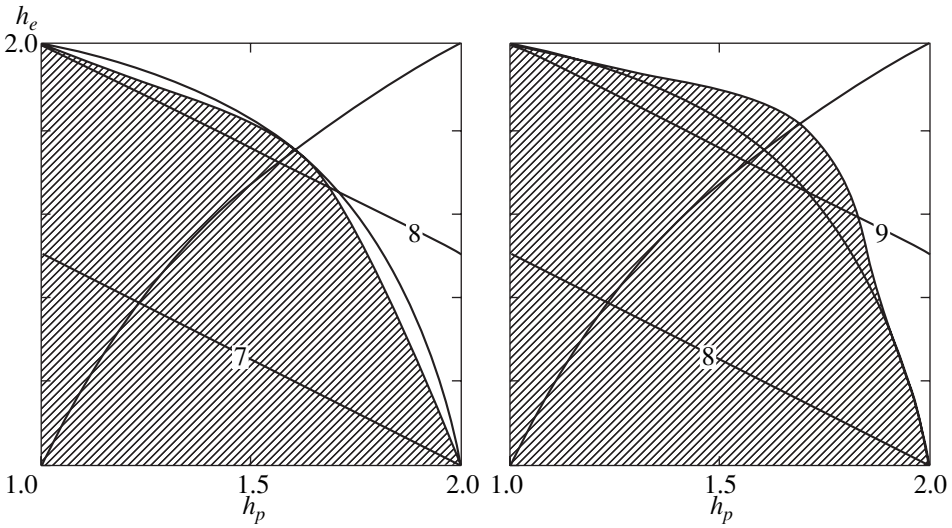

Fig. 4. Two characteristic phase diagrams for integer manganese cation spins at $h_d = 3 + 0$ (at the left) and $h_d = 4 + 0$ (at the right). Ferromagnetic regions are hatched.

for which dimensionless exchange scattering amplitudes Γ_k have signs opposite to those of variational derivatives L_k. In other words, when the *d*, *e*, and *p* shells are less than half filled, ferromagnetic instability exists in the regions where occupation numbers h_k slightly differ from their integer values $[h_k]$.

The three-dimensional phase diagram in the h_d, h_e, h_p variables that satisfies condition (31) is a combination of separate surfaces situated between electrical neutrality planes (3).

Fist, consider plane phase diagrams that intersect the $h_p + 2h_e + h_d = 10$ electrical neutrality plane corresponding to the Fe_3Si compound characterized by the high-spin states $2 < h_d < 3$ and $3 < h_e < 4$. The corresponding electrical neutrality plane is situated within the ferromagnetic instability region, which is always adjacent to the region of small deviations from integer values, $h_k - [h_k] \ll 1$.

This is illustrated by two phase diagrams for integer *d*-hole spins $S_d = 2$ and *p*-hole spins $S_p = 1$. In both diagrams, the electrical neutrality line intersects the ferromagnetic region in its broad part.

Table 2 shows that all ferromagnetic Heusler alloys except Fe_3Si contain the manganese cation with three to five holes in the incompletely occupied 3*d* shell as the central magnetic atom.

The measured magnetic moments do not strongly differ from the corresponding integer values. Considering a plane phase diagram at given integer $h_d = 3 + 0$ and $h_d = 4 + 0$ values will not therefore be meaningless. Taking into account the $h_d \geq 5$ region would not make sense, because the Γ_d scattering constant in this region is positive, and the region of the existence of ferromagnetism is virtually absent.

For the same reason, we considered all possible plane regions for which $0 < h_p < 3$ and $0 < h_e < 5$.

For each integer interval of h_p and h_e variations, we have a phase diagram topologically equivalent to one of the two phase diagrams shown in Fig. 4.

For integer $h_d = [h_d]$ occupation numbers, we have $r_d > 0$ and $u \longrightarrow 0$.

It follows that, in the whole region adjacent to finite integer hole variable h_d values, the region of the existence of ferromagnetism expands along the h_d and h_e variables, because the passage from $h_d = 3$ to $h_d = 4$ increases the $-\Gamma_d$ value from 1 to 4/3.

This is the reason why ferromagnetism exists in a broad concentration region of h_p and h_e values. The boundary at which ferromagnetic ordering disappears corresponds to the h_p and h_e values at which the exchange scattering amplitude is positive and so large that it compensates the contribution of Γ_d, which is large in magnitude. Accordingly, at $h_d = 3 + 0$, the ferromagnetism boundary lies within the region corresponding to complete filling of the lower hybridization subband ($\lambda = -1$) and touches its boundary curve $r_p = 0$ (see the left part of Fig. 4). If $h_d = 4 + 0$, the ferromagnetic ordering boundary at $r_p = \epsilon_p = \epsilon_e$ lies within the region corresponding to the onset of filling the upper hybridization subband ($\lambda = 1$) and can intersect this subzone at finite r_p values (see Fig. 4, right part).

The special features of ferromagnetism depending on the total number of holes were studied by calculating phase diagrams for various integer numbers of holes h_p in the incompletely occupied nontransition element shell (see Fig. 5, where characteristic phase diagrams for the completely occupied shell with $h_p = 0$ are shown). For these states, exchange scattering ampli-

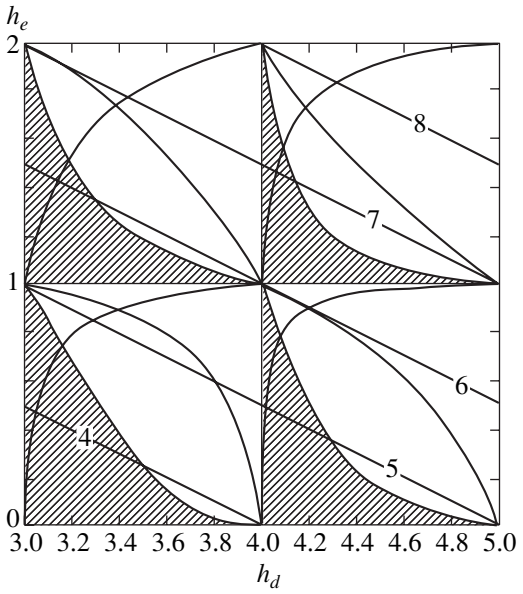

Fig. 5. Phase diagram for integer anion spins (at $h_p = 0$). Ferromagnetic regions are hatched.

tudes Γ_p do not exceed one in magnitude and therefore do not lead to ferromagnetism per se. For this reason, ferromagnetism only exists in a fairly narrow rage of h_d and h_e variations at all integer h_p. This difference can be noticed by comparing the phase diagrams shown in Figs. 4 and 5.

Note also that, at a given number of hole *p* states h_p, the $h = 2h_e + h_p + h_d$ electrical neutrality line only intersects one of the ferromagnetic regions, either that adjacent to $h_d = 3$ or the region adjacent to $h_d = 4$. More exactly, a ferromagnetic region with fixed $[h_d] = 3$ or $[h_d] = 4$ corresponds to each integer h_p value and a given parity of the total number of holes *h*.

According to Fig. 5, ferromagnetism exists in a fairly narrow region at $h_e < 1$ and $3 < h_p < 4$. The $2h_e + h_p + h_d = 4$ electrical neutrality line of Cu_2MnSb intersects this region.

The Cu_2MnSn compound with a magnetic moment of 4.1 can unambiguously be assigned to the region $4 < h_d < 5$, $0 < h_e < 1$, and $h_p = 0$, where there is a ferromagnetic region adjacent to $h_d = 4$. Here, the $2h_e + h_p + h_d = 5$ electrical neutrality line intersects the ferromagnetic region at the $h_e \sim 1$ number of holes, and ferromagnetism of Cu_2MnSn is therefore determined by the interaction of copper one-hole states and manganese three-hole states.

If the total number of holes exceeds 5, $h > 5$, the magnetic properties of Heusler alloys cannot be interpreted with the use of plane phase diagrams. It can, however, be claimed that the nonmonotonic dependence of the Curie temperature on the total number of hole states is determined by the possibility of exchange scattering amplitude sign changes in going from the center of the Brillouin zone to its boundary. In the language of hole variables, this leads to alternation of ferromagnetic and nonferromagnetic regions within a given integer interval of variations of each of the three hole variables.

This explains the observation that the Matthias rules originally discovered for superconducting compounds are also qualitatively applicable to Heusler ferromagnetic alloys.

ACKNOWLEDGMENTS

This work was financially supported by the Russian Foundation for Basic Research (project no. 98-02-17388).

REFERENCES

1. *Handbook of Physical Quantities*, Ed. by I. S. Grigoriev and E. Z. Meilikhov (Énergoatomizdat, Moscow, 1991; CRC Press, Boca Raton, 1997).
2. B. T. Matthias, Phys. Rev. **97**, 1 (1955).
3. R. O. Zaĭtsev and Yu. V. Mikhaĭlova, Zh. Éksp. Teor. Fiz. **118**, 654 (2000) [JETP **91**, 568 (2000)].
4. J. B. Goodenough, *Magnetism and the Chemical Bond* (Interscience, New York, 1963; Metallurgiya, Moscow, 1968).
5. J. Hubbard, Proc. R. Soc. London, Ser. A **281**, 401 (1964).
6. V. J. Emery, Phys. Rev. Lett. **58**, 2794 (1987).
7. R. O. Zaĭtsev, Zh. Éksp. Teor. Fiz. **112**, 2223 (1997) [JETP **85**, 1218 (1997)].
8. R. O. Zaĭtsev, Pis'ma Zh. Éksp. Teor. Fiz. **68**, 275 (1998) [JETP Lett. **68**, 295 (1998)].
9. D. T. Smirnov and Yu. F. Smirnov, *Theory of Optical Spectra of Transition-Metal Ions* (Nauka, Moscow, 1977).

Translated by V. Sipachev

Journal of Experimental and Theoretical Physics, Vol. 94, No. 2, 2002, pp. 377–386.
Translated from Zhurnal Éksperimental'noĭ i Teoreticheskoĭ Fiziki, Vol. 121, No. 2, 2002, pp. 442–452.

SOLIDS
Electronic Properties

Magnetization of Two-Dimensional Superconductors with Defects

V. A. Kashurnikov*, I. A. Rudnev, and M. V. Zyubin

Moscow Institute of Engineering Physics (Technical University), Kashirskoe sh. 31, Moscow, 115409 Russia
**e-mail: kash@cityline.ru*

Received July 4, 2001

Abstract—A new method is developed for numerical simulation of the magnetization of layered superconductors with defects that is based on the Monte Carlo algorithm. The minimization of the free energy functional of a two-dimensional vortex system enables one to obtain equilibrium configurations of vortex density and calculate the magnetization of a superconductor with arbitrary distribution of defects in a wide temperature range. Magnetization curves are obtained for the first time for a defective superconductor under conditions of cyclic variation of the external magnetic field for different temperatures. The magnetic induction profiles and the magnetic flux distribution inside a superconductor are calculated, which support the validity of Bean's model. It is demonstrated that the process of magnetization reversal is accompanied by the emergence of an annihilation wave, i.e., the motion of a zone with zero magnetic induction at the leading front of the incoming magnetic flux.

1. INTRODUCTION

The behavior of the magnetization M of type II superconductors as a function of external magnetic field H is of considerable interest. Given the dependence $M(H)$, one can determine both the fundamental parameters of a superconductor, for example, the upper and lower critical fields, and the quantities of practical importance, namely, the value of critical current J_c and the hysteresis loss in the superconductor. Quite a few papers are devoted to the theoretical description of the magnetization of defect-free superconductors (see, for example, the review [1]). In weak fields, the magnetization within the London model is well described by Fetter's formula [2]. In the vicinity of the upper critical field, Abrikosov's expression is valid [3]. The behavior of magnetization in the entire range of fields from H_{c1} to H_{c2} is described in [4, 5]; and, finally, Pogosov *et al.* [6] proposed a variational method enabling one to find, in a self-consistent manner, the dependence of magnetization of a type II superconductor on the magnetic field. At the same time, note that all of the proposed methods treat defect-free superconductors and do not make it possible to calculate (using a unified approach) a closed magnetization loop under conditions of cyclic variation of the magnetic field for superconductors with defects.

The analytical solution of the problem on the behavior of magnetization of high-temperature superconductors (HTSC) with an arbitrary preassigned arrangement of pinning centers is extremely complicated and calls for inclusion of numerous parameters; therefore, it is advisable to use numerical methods, including the Monte Carlo method. For example, in [7–12], the Monte Carlo method was used to investigate the phase transitions and dynamics of a two-dimensional vortex lattice. It has been demonstrated that, in the absence of defects, a phase transition of melting of a triangular lattice to vortex fluid is observed. In the presence of defects, the phase of "revolving lattice" arises between the phases of vortex crystal and vortex fluid. The vortex system in this phase is represented by lattice islands revolving around the pinning centers.

Attempts at performing the numerical calculation of the magnetization of a two-dimensional superconducting layer with defects under conditions of increasing and decreasing magnetic field were made by Reichhardt *et al.* [13] using the method of molecular dynamics. However, in the studies involving the use of the method of molecular dynamics, the effect of the boundary on the processes of magnetic flux penetration was ignored, and all calculations were performed for zero temperature.

In this paper, we present the results of numerical calculation of the magnetization of a quasi-two-dimensional HTSC plate with an arbitrary distribution of pinning centers. We have developed a method based on the Monte Carlo algorithm for a grand canonical ensemble, which involves a number of singularities reflecting the behavior of vortex systems in layered HTSC materials. This method enables one to obtain an equilibrium distribution of the vortex density upon variation of the external magnetic field H and to calculate the dependence of the magnetization M on H under conditions of arbitrary arrangement of pinning centers and different temperatures. Our approach is characterized by a number of fundamental differences compared with the known calculation techniques, namely, the most correct

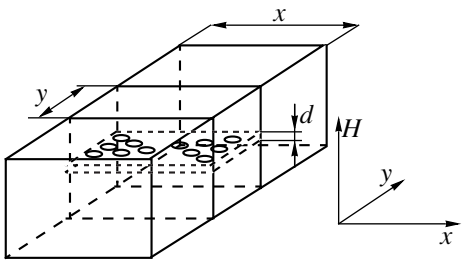

Fig. 1. The geometry of calculations.

inclusion of the effect of the plate boundary, a wide range of the working temperatures $0 < T < T_c$, and the possibility of allowing for any distribution of defects of any types.

2. THE MODEL AND CALCULATION PROCEDURE

We will treat a three-dimensional sample of an HTSC layered in the *xy* plane. The sample has a finite thickness in the *x* direction and infinite dimensions in the *y* and *z* directions (Fig. 1). It is placed in a magnetic field parallel to the *z* axis, which rules out the possibility of demagnetization effects. We will assume a weak interaction between layers in the HTSC and will treat, for calculations, only a quasi-two-dimensional *xy* plate of thickness *d*, which will simulate the superconducting layer; i.e., on the *z* axis we will "cut out" a layer of thickness *d* and treat this layer in what follows.

In the external magnetic field *H* inside the plate, we treat a two-dimensional system of Abrikosov vortices in the form of model classical particles with a long-range potential.

The Gibbs thermodynamic potential of a vortex system in such a plate will have the form

$$G = Nd\varepsilon - Nd\frac{\Phi_0 H}{4\pi} + d\frac{\Phi_0 H}{4\pi}\sum_i (e^{-x_i/\lambda} + e^{-(a-x_i)/\lambda})$$

$$+ \frac{1}{2}\sum_{i\neq j} U(r_{ij}) + \sum_i U_p(r_i) + U_{\text{surf}},$$

$$U(r_{ij}) = U_0 K_0\left(\frac{r_{ij}}{\lambda}\right),$$

where

$$\varepsilon = \left(\frac{\Phi_0}{4\pi\lambda}\right)^2\left(\ln\frac{\lambda_0}{\xi_0} + 0.52\right)$$

is the intrinsic vortex energy [6] (ξ_0 is the size of the vortex core at $T = 0$); $Nd\Phi_0 H/4\pi$ is the energy of interaction with the external field *H*;

$$U_0 = \frac{\Phi_0^2}{8\pi^2\lambda^2}d$$

is the pairwise vortex interaction;

$$d\frac{\Phi_0 H}{4\pi}(e^{-x_i/\lambda} + e^{-(a-x_i)/\lambda})$$

is the energy of interaction of the *i*th vortex with the Meissner currents flowing along the plate surface in the *y* direction; $U_p(r_i)$ is the energy of interaction of the *i*th vortex with the pinning centers; U_{surf} is the energy of interaction of the vortex system with the superconductor surface; $\Phi_0 = hc/2e$ is a magnetic flux quantum; *d* is the superconducting layer thickness; λ is the depth of the magnetic field penetration into the superconductor; and *N* is the number of vortices in the system.

The interaction between an individual vortex and the superconductor surface in a plate of width *a* ($-a/2 < x < a/2$) is conventionally represented as the vortex interaction with its mirror image (antivortex),

$$U_{\text{surf}}(x) = \frac{U_0}{2}\left\{2\sum_{j=1}^{\infty} K_0\left(\frac{2ja}{\lambda}\right)\right.$$

$$\left. - \sum_{j=0}^{\infty}\left[K_0\left(\frac{2x+ja}{\lambda}\right) + K_0\left(\frac{2(a-x)+ja}{\lambda}\right)\right]\right\}.$$

In order to investigate the behavior of a system with defects, pinning centers were introduced. In this case, the energy of interaction with a pinning center was selected in the model form

$$U_p(T, r) = -\alpha\frac{U_0(T)}{U_0(0)}\frac{1}{r/\xi + 1}\exp\left(-\frac{r}{2\xi}\right)$$

(α is a dimensionless parameter characterizing the depth of potential well of a defect). This choice of the dimensions and depth of pinning corresponds to the case where only one vortex may be secured on a pinning center.

The magnetic field induction in this geometry was calculated by the formula

$$B = \frac{N\Phi}{S} + \frac{2\lambda H}{a}(1 - e^{-a/\lambda}).$$

The latter expression includes the contribution of the Meissner currents. In addition, we have allowed for the fact that the flux carried by each vortex depends on the distance to the plate edge, i.e.,

$$\Phi(x) = \Phi_0\left(1 - \frac{2}{\pi}\int_{x/\lambda}^{\infty} K_0(y)y\arccos\left(\frac{x}{y\lambda}\right)dy\right).$$

The latter expression was derived with due regard for the vortex image at the boundary and for the system

geometry. Strictly speaking, the formula was derived for a semi-infinite superconductor. However, if the plate is fairly wide ($a \gg \lambda$), the effect of the second boundary may be ignored.

The algorithm developed for calculation differed considerably from the conventional Monte Carlo method for a canonical ensemble, which was previously employed in [7–12]. In the present approach, we have abandoned the use of a 3D mesh and assumed the phase space to be continuous. A unit change in the vortex position is not restricted to the mesh spacing; it is selected at random from the permissible domain, for example, the plate area. The configurations are selected in accordance with the Gibbs weight. In order to raise the counting efficiency, all vortex interactions in the system are tabulated depending on the distance with an accuracy of at least 1 Å; this rules out the possibility of errors characteristic of algorithms allowing for the 3D mesh.

In order to calculate the magnetization, one must deal with a grand canonical ensemble, i.e., take into account the production and annihilation of vortex filaments. The processes of creation and annihilation of vortices were allowed in a boundary strip of width λ along the y axis. In this manner, the magnetic flux penetration into the plate is simulated. The competition between repulsion on the part of the Meissner currents and attraction to the boundary brings about the emergence of a surface barrier (of the Bean–Livingston type) which is naturally included in this approach.

In addition, for a smooth description of the processes of magnetization reversal, vortices with oppositely directed currents (antivortices) are formally introduced into the treatment. For the principle of detailed balancing to be valid, the process of annihilation of a pair consisting of a vortex and an antivortex (annihilation), if they are spaced at a distance of the order of several ξ from one another, is added to the scheme in addition to the standard annihilation process. Therefore, as the sign of external magnetic field H changes, vortices are automatically replaced by antivortices; i.e., the process of magnetization reversal of the plate is simulated. This is especially important in the case of correct treatment of freezing of magnetic flux on defects and nonuniformities.

All in all, processes of four types are treated in the suggested Monte Carlo scheme, namely, the vortex motion, the production of a single vortex (or antivortex), the annihilation of a single vortex (antivortex), and the annihilation of a vortex–antivortex pair. The annihilation of a single vortex is likewise allowed only in the boundary strip λ, which corresponds in a real situation to the exit of magnetic flux only through the superconductor boundary.

For the principle of detailed balancing to be valid, all of the direct and inverse subprocesses are weighted in pairs. The probabilities of creation, P_c, and annihilation, P_a, are multiplied by $1/(N+1)$ and by N to include the variation of the number of vortices N before and after the process, respectively, so that the final probabilities have the form

$$P_c = \begin{cases} R_c/W_c, & R_c < W_c, \\ 1, & R_c > W_c, \end{cases}$$

$$P_a = \begin{cases} W_a/R_a, & (R_a > W_a,) \\ 1, & R_a < W_a, \end{cases}$$

$$R_c = \frac{a^* L_y}{N+1}, \quad R_a = \frac{a^* L_y}{N},$$

$$W_c = \exp(\beta^* \Delta E_1), \quad W_a = \exp(-\beta \Delta E_a),$$

$$\Delta E_1 = E_{N+1} - E_N, \quad \Delta E_2 = E_{N-1} - E_N.$$

Here, $W_{a,c}$ denote conventional Gibbs weights, and R is the ratio of the inversion probability to the respective vortex ($\sim 1/N$) and to the space point for the creation of vortex ($1/aL_y$) and for annihilation. This scheme of detailed balancing allows an arbitrary choice of R: this quantity may be multiplied by any constant factor (the same for R_a and R_c), which will not disturb the balance but will make possible to optimize the renewal of configurations.

The parameters of a real layered $Bi_2Sr_2CaCu_2O_8$ superconductor were used for simulation, namely, d = 0.27 nm, λ_0 = 180 nm, ξ_0 = 2 nm, and T_c = 84 K [14]. The calculations were performed for 5×3 μm plates. The size of the region being treated was selected such that, on the one hand, we could restrict ourselves to the first terms in the vortex–surface interaction and, on the other hand, the use of periodic boundary conditions would not bring about considerable errors in calculating the vortex interaction. The maximal range of variation of the external field H is limited only by the computer power and, accordingly, by the count time. In our calculations, the range of external field variation was $-0.12\ \text{T} \le H \le 0.12\ \text{T}$.

3. RESULTS AND DISCUSSION

3.1. Magnetization Curves M(H)

Figure 2 gives, by way of illustration, a typical magnetization loop at T = 5 K and the number of defects N_d = 100, obtained for increasing and decreasing external magnetic field. No vortices are produced or penetrate into the plate upon the initial increase in the external magnetic field. In the graph, this region corresponds to a straight line (up to point *1*). After reaching the field of superheating of the Meissner state, the vortices start entering the plate, with the magnetization decreasing (segment *1–3*). After H = 0.1 T, the external field decreases; however, the surface barrier prevents the vortices from leaving the plate. Therefore, the magneti-

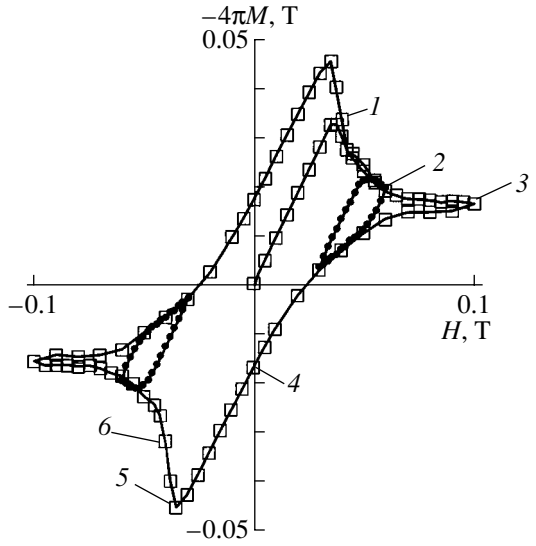

Fig. 2. A magnetization loop for $N_d = 100$ and $T = 5$ K. The dark circles indicate small magnetization loops formed upon variation of the direction of the external magnetic field.

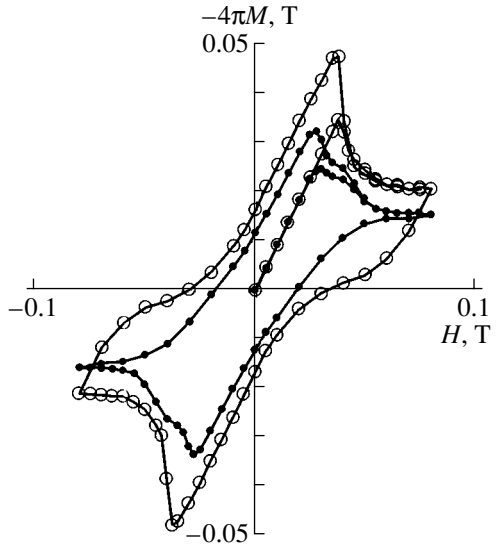

Fig. 3. Magnetization loops at $T = 1$ K (light circles) and 20 K (dark circles). The number of defects $N_d = 100$.

zation behavior becomes irreversible. When the external magnetic field decreases to zero, the surface barrier disappears, and a number of vortices leave the plate (segment *3–4*). However, residual magnetization exists, which is due to the presence of vortices secured on pinning centers. As the external magnetic field of opposite sign increases, the vortices remain secured on the pinning centers, and the surface barrier prevents antivortices from entering the sample (segment *4–5*). As the external magnetic field continues to increase, the antivortices penetrate into the plate and annihilate the vortices secured on the pinning centers; i.e., the plate experiences magnetization reversal (segment *5–6*). In the case of inverse variation of the external magnetic field, the pattern is repeated, and the magnetization curve closes. Note that one observes the closure both of the total magnetization curve and of small loops formed upon variation of the magnetic field direction (see Fig. 2). Therefore, the method developed by us enables one to correctly reproduce the real process of magnetization reversal of a superconductor in a unified calculation.

A temperature variation brings about a magnetization loop variation. Shown by way of example in Fig. 3 are two loops of magnetization $M(H)$ calculated at $T = 1$ and 20 K. As the temperature increases, one observes

(1) a reduction of the loop area,

(2) a decrease in the field corresponding to the beginning of the entry of vortices into the plate (superheating of the Meissner state), and

(3) the emergence of the field of reversibility of the magnetization loop.

We will trace the variation of magnetization loops with increasing number of pinning centers. For this purpose, we calculated the magnetization curves for a fixed temperature $T = 5$ K and different numbers of pinning centers. The depth of defects was selected such as to eliminate the process of thermal depinning and amounted to 0.1 eV. The pinning centers were arranged at random. The effect of defects on the behavior of magnetization varies as their number increases; in fact, the mechanism of irreversibility varies. One can see in Fig. 4 that, as the number of pinning centers increases,

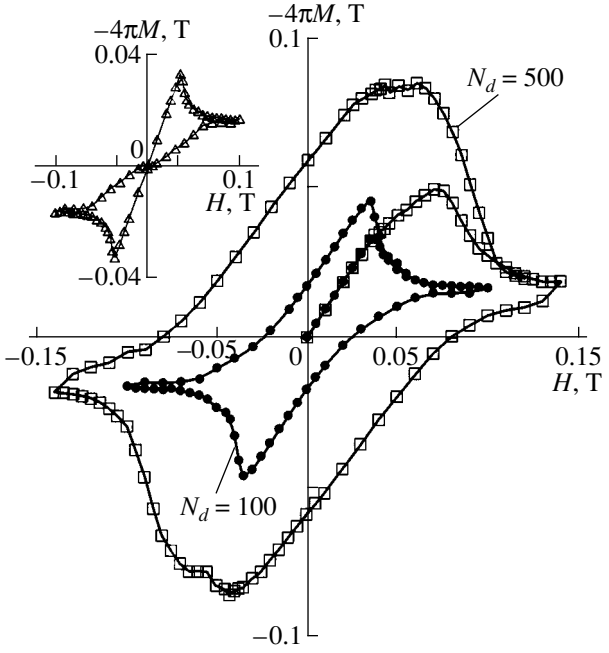

Fig. 4. Magnetization loops for different numbers of defects; $T = 5$ K. In the inset, a magnetization loop at $N_d = 0$ is given.

residual magnetization increases, as well as the loop area. With a large number of defects, the loop width is actually defined by residual magnetization; the latter, in turn, depends on the number of pinning centers. Therefore, one can conclude that, in the case of an "impure" sample, the irreversibility of magnetization is largely defined by the number of defects rather than by the surface barrier. The irreversibility of a magnetization loop due to surface barrier is significant only in the case of a low concentration of defects or of their complete absence (see the inset in Fig. 4).

An increase in the pinning hardness, namely, an increase in the number of pinning centers, leads to a considerable variation of the shape of the magnetization loop. Figure 5 gives the magnetization for the cases of N_d = 100, 250, 500, and 1000. A broadening of the magnetization loop is observed as the number of defects N_d increases from 100 to 250; on the contrary, with a very large number of defects N_d = 500 and 1000, the magnetization loop contracts. From the physical standpoint, this behavior of the $M(H)$ curves is associated with the fact that, as the pinning becomes stronger, the region penetrated by the magnetic flux front decreases, this leading both to a decrease in the magnetization and to a reduction of the area of the magnetization loop. One can compare magnetization loops with one another only under conditions in which the maximal field exceeds the field of penetration for all types of pinning being treated. By the field of complete penetration is meant the value of the external applied field at which the magnetic flux completely fills the superconductor. Evidently, the value of the field of complete penetration depends on the degree of imperfection of the superconductor. It is interesting to note that the slope of the branch of the magnetization curve corresponding to the fields somewhat exceeding H_{c1} likewise depends on the concentration of defects (see the inset in Fig. 5). Note that, at $H = H_{c1}$, the slope of the magnetization curve changes sign in the case of a small number of defects N_d = 100; in the case of strong pinning, N_d = 250 and 500, the slope only decreases compared with the initial diamagnetic segment of the curve. The slope sign varies at a higher value of the field H^*. For N_d = 1000, the sign of $dM(H)/dH$ in the calculated range of fields does not vary at all. This result is due to the strong repulsive interaction between surface pinned vortices and new incoming vortices which "try" to penetrate into the sample under conditions of increasing external magnetic field.

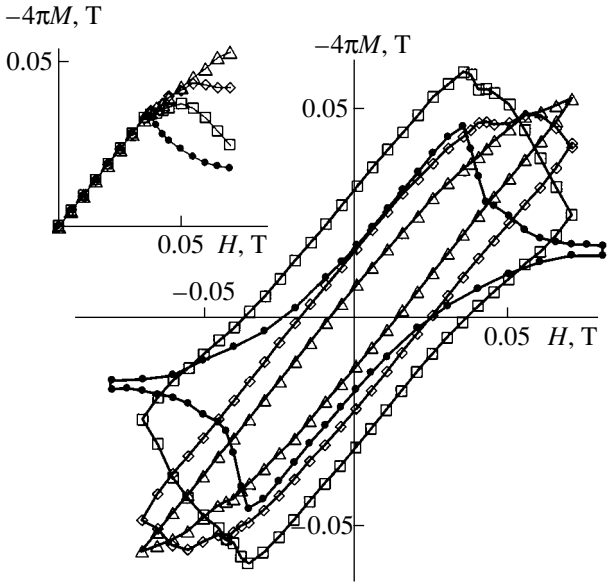

Fig. 5. Magnetization loops for different numbers of defects; N_d = (●) 100, (□) 250—a case of total penetration of magnetic field, and (◇) 500 and (△) 1000—cases of partial penetration of magnetic field. In the inset, initial segments of magnetization curves, which are not shown in the figure, are given.

3.2. Magnetic Flux Profiles

By calculating the equilibrium configuration of vortices, we can analyze the range of validity of Bean's model [15]. According to this model, the current density in hard (i.e., with strong pinning) superconductors may have only three values, namely, $-J_c$, 0, and J_c, where J_c is the critical current density independent of magnetic induction. This postulate leads to a number of results. In particular, from Bean's model there follows a linear decrease in magnetic induction inside a hard superconductor. Our method may be used to directly calculate the profiles of magnetic induction in a superconductor.

We will now give predicted profiles of magnetic flux for different cases. Figures 6a and 6b give magnetic flux profiles for plates with N_d = 100 and 500. One can see that, by and large, the flux profiles correspond to the concept of critical state in the superconductor volume according to Bean's model (the linear pattern of the $B(x)$ dependence), except for the Meissner regions in the vicinity of the surface. The linearity is also absent in the case of a low concentration of defects. As the magnetic field increases, the slope of the $B(x)$ curves varies; i.e., a decrease in the critical current density is observed. The dependence of the slope of the magnetic induction profile $dB(x)/dx$ on the external magnetic field correlates well with the same dependence of the width of the magnetization loop on H (Fig. 7), which points to the possibility of determining the critical flux density from the width of the magnetization loop of a hard superconductor. Note, however, that this procedure is incorrect in the case of a superconductor with weak pinning. Indeed, the magnetization loop given in the inset in Fig. 4 has a reversible pattern and a finite width. At the same time, the reversibility in this case is defined by surface, rather than bulk, pinning, and Bean's model is invalid.

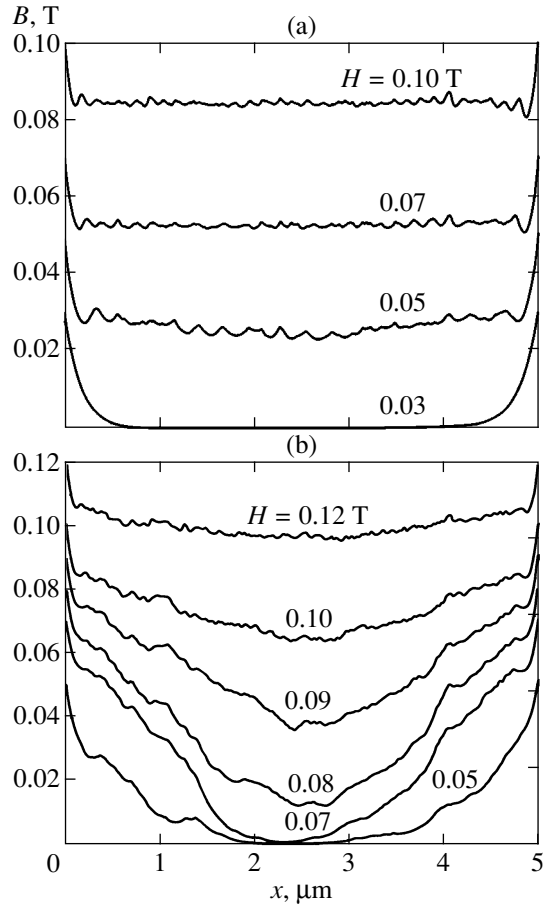

Fig. 6. Profiles of magnetic induction for different numbers of pinning centers N_d = (a) 100 and (b) 500.

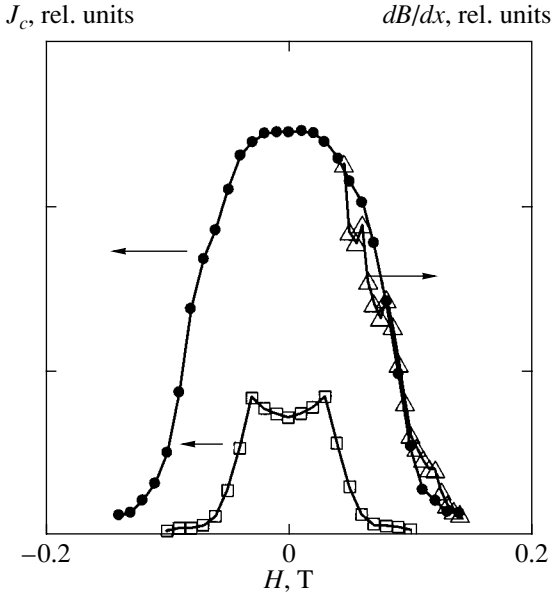

Fig. 7. The width of magnetization loop and the slope of magnetic induction profiles as functions of the intensity of external magnetic field. ΔM: N_d = (●) 500, (□) 100; dB/dx: N_d = (△) 500.

3.3. Penetration and Distribution of Magnetic Flux in Superconductors

The basic result of all calculations is the equilibrium configuration of the density of probability of finding vortices in the plate being treated at a preassigned temperature, external field, and selected configuration of defects. By adding up magnetic fields from each vortex, we can obtain a visual pattern of magnetic flux distribution in a superconductor at any point of its magnetization curve. For example, we will trace the flux distribution at points *1–6* of the magnetization curve in Fig. 2. The magnetic flux distribution is given in Fig. 8. The dark background corresponds to the absence of a magnetic field, and the white dots correspond to vortex magnetic fields.

Point *1* corresponds to the lower critical field of the given system (with due regard for the superheating of the Meissner state). At $H < H_{c1}$, the field does not penetrate into the superconductor except for strips of width λ at the plate edges. When H_{c1} is exceeded, one observes the entry of vortices into the plate and a gradual advance of the magnetic flux front deep into the superconductor. For the field value at which a complete penetration occurs, the magnetic flux takes up the entire plate (point *2*). The distribution of magnetic induction corresponds to Bean's model. A further increase in the external magnetic field leads to an increase in the magnetic induction in the plate. In this case, the vortices tend to form a triangular vortex lattice (point *3*). Point *4* corresponds to residual magnetization. Following the change of sign of the external magnetic field, vortices of opposite sign (antivortices) start to enter the plate (point *5*). The annihilation of vortices and antivortices results in the formation of a clearly defined region with zero magnetic induction at the incoming flux front; this region advances deep into the superconductor as the amplitude of the external magnetic field increases (point *6*). The effect of motion of a zone with zero magnetic induction from the edge of a superconducting plate toward its center was given by us the name of "annihilation wave." The annihilation wave arises each time when the sign of the external magnetic field is changed.

In order to trace the dynamics of magnetic flux penetration into superconductors with different defective states, we treated three cases, namely, 250 defects with U_{pin} = 100 meV, 250 defects with U_{pin} = 10 meV, and 10 defects with U_{pin} = 100 meV. We will refer to these cases as strong, moderate, and weak pinning, respectively.

We will treat the distribution of magnetic induction upon an increase in the magnetic field.

At first, for $0 < H < H_{c1}$, the magnetic flux does not penetrate into the plates except for fringe strips of width λ. Further patterns of flux distribution are given in Figs. 9a–9f.

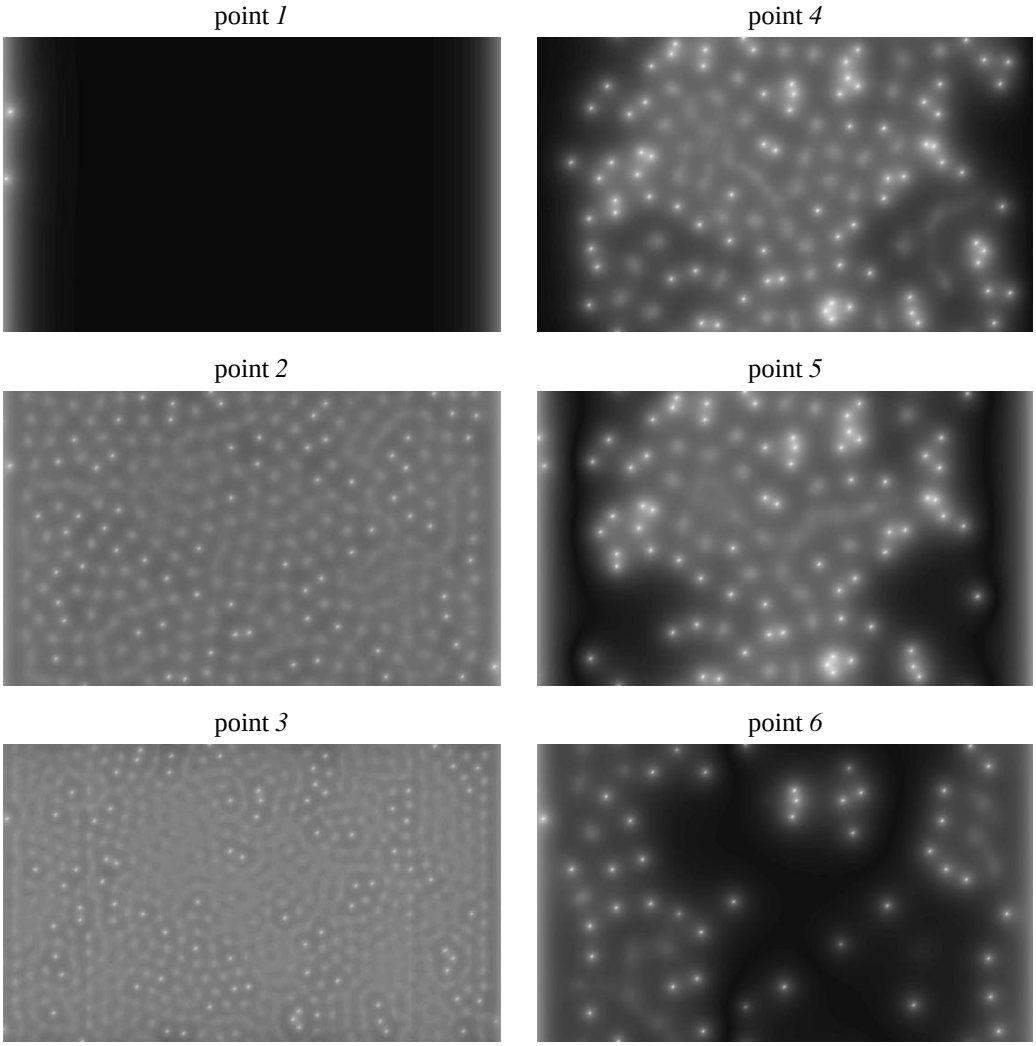

Fig. 8. The magnetic flux distribution for different external fields. Points *1–6* correspond to Fig. 2. The dark background corresponds to the absence of a magnetic field, and the white color corresponds to a vortex magnetic field.

In Fig. 9a, the external magnetic field $H = 0.0375$ T exceeds H_{c1}. The vortices start entering the superconductor. In the cases of strong and moderate pinning, the magnetic flux front moves gradually from the plate edges to its center. The magnetic flux line is curved, which reflects the local nonuniformity in the distribution of pinning centers. In the case of weak pinning, the magnetic flux fills the superconductor almost immediately.

In Fig. 9b, the magnetic field $H = 0.05$ T is the field of complete penetration for moderate pinning. In the case of strong pinning, the central part of the plate is still free of magnetic flux. For weak pinning, an increase in the vortex density is observed, with a tendency to formation of a triangular lattice.

In Fig. 9c, the magnetic field $H = 0.075$ T. The magnetic flux reaches the plate center in the case of strong pinning as well.

In Fig. 9d, the magnetic field $H = 0$. After the magnetic flux increases to $H = 0.08$ T and then decreases to zero, the magnetic flux pinning is observed in all three cases. It is significant that residual magnetization for strong and moderate pinning is formed by both pinned and free vortices owing to collective interaction; in the case of weak pinning, residual magnetization is defined only by pinned vortices.

In Fig. 9e, the magnetic field $H = -0.04$ T. After the change of direction of the external magnetic field, vortices of opposite sign start entering the plates. In the forefront, one can clearly see the regions of annihilation of vortices and antivortices or annihilation waves (indicated by white arrows). The velocity of motion of an annihilation wave is the higher, the weaker the pinning. In the case of weak pinning, the annihilation is almost instantaneous. The annihilation wave disappears when the external magnetic field exceeds the field of com-

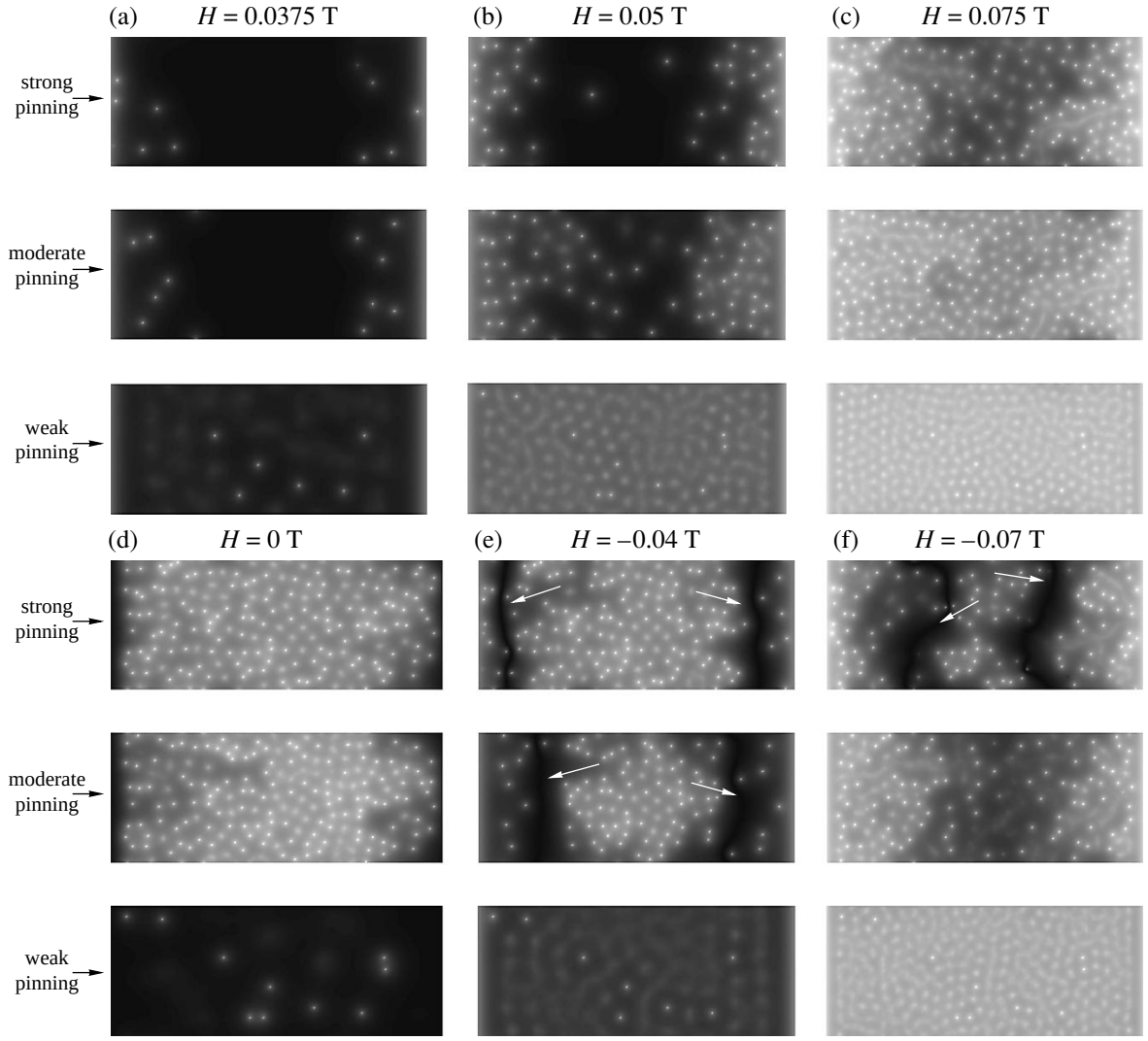

Fig. 9. The magnetic flux distributions for different external magnetic fields for the cases of strong, moderate, and weak pinning. White arrows indicate annihilation waves.

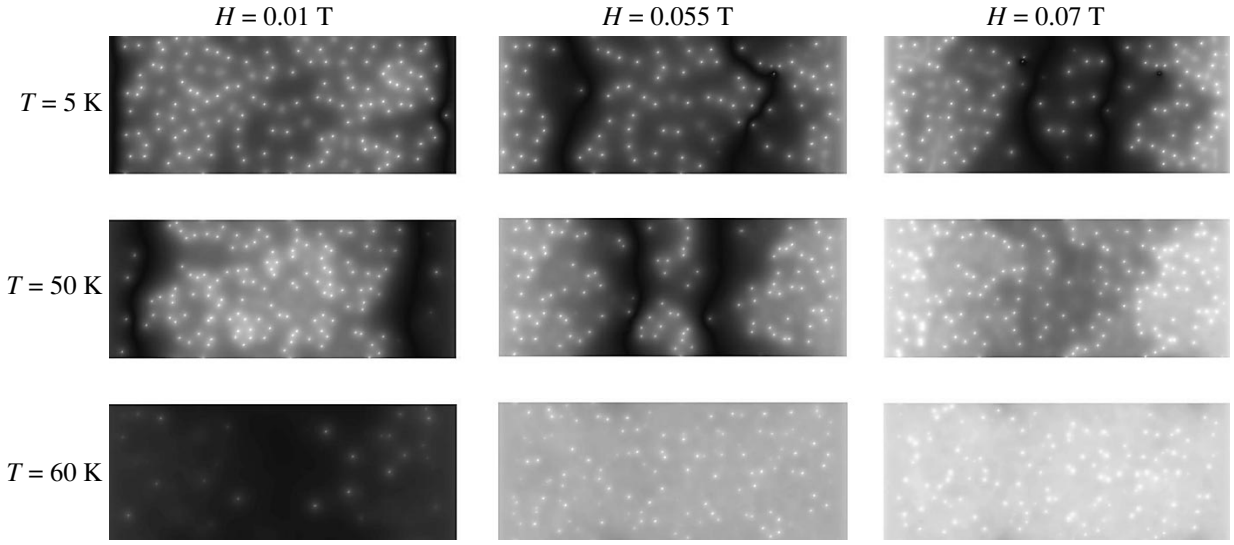

Fig. 10. The magnetic flux distributions for different external magnetic fields for three temperatures T = 5, 50, and 60 K; N_d = 250.

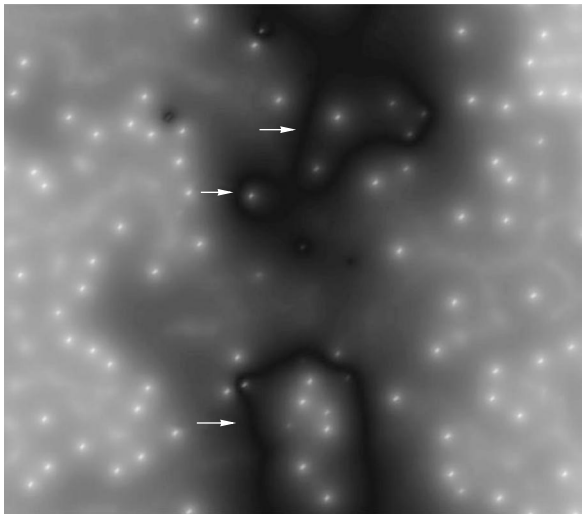

Fig. 11. The magnetic flux in a superconductor with a nonuniform distribution of pinning centers. White arrows indicate annihilation waves.

plete penetration (Fig. 9f). The next annihilation wave arises after the next change of sign of the external magnetic field. The velocity of an annihilation wave further depends on temperature. As the temperature increases, the velocity of the annihilation front is higher. Figure 10 gives the magnetic flux for three temperatures $T = 5$, 50, and 60 K.

In the case of a superconductor with a nonuniform distribution of defects, the annihilation front is highly distorted and may close around regions with a high local concentration of defects. In Fig. 11, one can see an annihilation wave encircling the region of an opposite-sign magnetic field pinned on defects.

Note that annihilation waves similar to those calculated by us were actually observed both during static measurements of magnetic flux penetration into an HTSC involving the use of scanning Hall probes and during dynamic magneto-optical investigations [16].

4. CONCLUSIONS

We have presented a new method for numerical calculation of magnetization curves and magnetic flux in a two-dimensional superconductor plate with defects of any type that is based on the Monte Carlo algorithm. The effect of the boundary has been included as correctly as possible, and the calculations have been performed in a wide temperature range. Given by way of illustration are the results of calculations of magnetization loops for different concentrations of defects and different temperatures. It has been demonstrated that the concentration of defects affects considerably the shape of the magnetization loop and that Bean's model of the critical state is valid in the case of high concentration of defects. Visual patterns of penetration and distribution of magnetic flux in two-dimensional superconductors have been calculated. It has been demonstrated that the process of magnetization reversal is accompanied by the motion of an annihilation wave, i.e., of a zone with zero magnetic induction.

In conclusion, note that it is still not clear how the results of calculation of magnetization obtained using a two-dimensional model will change upon transition to a three-dimensional model. Apparently, in spite of the clearly defined anisotropy of layered HTSCs, one cannot fully ignore the interaction between layers. The interaction between layers has an effect on the H–T phase diagram of the vortex lattice, as was pointed out, for example, in [17, 18]. Our preliminary data on calculation of magnetization in a three-dimensional case with due regard for electromagnetic and Josephson interactions between two-dimensional vortices in different layers are in qualitative agreement with the results given in the present paper. The three-dimensional case will be treated in detail in the process of further study.

ACKNOWLEDGMENTS

This study received financial support from the State scientific and technical program on "Topical Lines of Research in the Physics of Condensed State" (subprogram on superconductivity), from the Integratsiya target-oriented program (project nos. A0099 and A0133), and from the Russian Foundation for Basic Research (project no. 00-02-17803).

REFERENCES

1. E. H. Brandt, Rep. Prog. Phys. **58**, 1465 (1995).
2. A. L. Fetter, Phys. Rev. **147**, 153 (1966).
3. D. St. James, G. Sarma, and E. J. Thomas, *Type II Superconductivity* (Pergamon, Oxford, 1969; Mir, Moscow, 1970).
4. J. R. Clem, J. Low Temp. Phys. **18**, 427 (1975).
5. Z. Hao, J. R. Clem, M. W. Elfresh, *et al.*, Phys. Rev. B **43**, 2844 (1991).
6. V. V. Pogosov, A. L. Rakhmanov, and K. I. Kugel', Zh. Éksp. Teor. Fiz. **118**, 676 (2000) [JETP **91**, 588 (2000)].
7. M. E. Gracheva, V. A. Kashurnikov, and I. A. Rudnev, Pis'ma Zh. Éksp. Teor. Fiz. **66**, 269 (1997) [JETP Lett. **66**, 291 (1997)].
8. M. E. Gracheva, M. V. Katargin, V. A. Kashurnikov, and I. A. Rudnev, Fiz. Nizk. Temp. **23**, 1151 (1997) [Low Temp. Phys. **23**, 863 (1997)].
9. M. E. Gracheva, V. A. Kashurnikov, and I. A. Rudnev, Fiz. Nizk. Temp. **25**, 148 (1999) [Low Temp. Phys. **25**, 105 (1999)].
10. M. E. Gracheva, V. A. Kashurnikov, O. A.Nikitenko, and I. A. Rudnev, Fiz. Nizk. Temp. **25**, 1027 (1999) [Low Temp. Phys. **25**, 765 (1999)].

11. V. A. Kashurnikov, I. A. Rudnev, M. E. Gracheva, and O. A. Nikitenko, Zh. Éksp. Teor. Fiz. **117**, 196 (2000) [JETP **90**, 173 (2000)].
12. I. A. Rudnev, V. A. Kashurnikov, M. E. Gracheva, and O. A. Nikitenko, Physica C (Amsterdam) **332**, 383 (2000).
13. C. Reichhardt, C. J. Olson, J. Groth, *et al.*, Phys. Rev. B **52**, 10 441 (1995).
14. S. L. Lee, P. Zimmermann, H. Keller, *et al.*, Phys. Rev. Lett. **71**, 3862 (1993).
15. C. P. Bean, Phys. Rev. Lett. **8**, 250 (1962).
16. A. V. Eremin, O. S. Esikov, V. A. Kashurnikov, *et al.*, Supercond. Sci. Technol. **14**, 690 (2001).
17. J. Yeo and M. A. Moore, Phys. Rev. B **64**, 024 514 (2001).
18. K. Kadowaki *et al.*, Phys. Rev. B **64**, 094 521 (2001).

Translated by H. Bronstein

Journal of Experimental and Theoretical Physics, Vol. 94, No. 2, 2002, pp. 387–394.
Translated from Zhurnal Éksperimental'noĭ i Teoreticheskoĭ Fiziki, Vol. 121, No. 2, 2002, pp. 453–461.

SOLIDS
Electronic Properties

Effect of Symmetry of the Electron States of HTSC on the Current–Voltage Characteristics of *SIS* Junctions

S. O. Loiko, N. K. Fedorov*, and P. I. Arseev

Lebedev Physical Institute, Russian Academy of Sciences, Leninskiĭ pr. 53, Moscow, 119991 Russia
**e-mail: fedorov@lpi.ru*

Received July 19, 2001

Abstract—The current–voltage (*IV*) characteristics of *SIS* junctions are calculated in the framework of a multiband model with an anisotropic effective order parameter of HTSC. The results of calculations show that the shape of the *IV* characteristic and of the density of electron states changes significantly depending on the parameters of the model. A theoretical explanation is proposed for the experimentally observed *s*-like behavior of the *IV* characteristics of *SIN* and *SIS* junctions with BSCCO-type superconductors. The dependence of the superconducting peak asymmetry on the mutual arrangement of the bands is analyzed. The difference between the obtained results and the results of one-band models with the *s* and *d* symmetries of the order parameter is discussed. © *2002 MAIK "Nauka/Interperiodica".*

The lack of a generally accepted explanation of the pairing mechanism in high-temperature superconductors (HTSC) makes the interpretation of numerous experimental data (including the results of tunnel experiments) difficult. The complexity of the crystal structure of HTSC compounds also complicates the situation. In most cases, it is difficult to explain peculiarities in the tunnel characteristics within in the framework of the standard Bardeen–Cooper–Schrieffer (BCS) model. Such peculiarities include the variety of the subgap structure ranging from a linear *d*-type structure to a nearly planar structure of the *s* type [1], the asymmetry of superconducting peaks at the edge of the gap [2, 3], and nontrivial behavior of the tunnel density of states of *SIN* junctions and of the current–voltage characteristics of *SIS* junctions outside the gap region. In some experiments [4, 5], strongly suppressed (dI/dV) characteristics with very narrow peaks typical of *s*-type superconductors were obtained in the subgap region, which contradict at first glance the available data on strong anisotropy of the order parameter in the CuO_2 plane [6].

A large number of theoretical models have been proposed to explain the aggregate of experimental data. These include the models based on various features of the band structure (taking into account, for example, the closeness of the Van Hove singularities to the chemical potential [7, 8]), on the choice of the order parameter symmetry [8], and on the properties of the tunnel matrix element [9] in the one-band BCS scheme. Even the slave-boson approach [10] was used for explaining the asymmetry of the superconducting peaks and the inhomogeneity of the density of electron states in the normal state. A series of publications [11–14] is devoted to the role of inelastic scattering, including the inelastic scattering at antiferromagnetic spin fluctuations. The results of theoretical investigations show that the inclusion of Van Hove singularities and the use of the ($s + d$) symmetry of the order parameter are obviously essential for a correct explanation of the most experimentally observed properties of the tunnel conductance of HTSC. For this reason, the experimental investigation of the properties of the electron spectrum of high-temperature superconductors in the normal state is very important.

In our opinion, it is precisely the analysis of the crystal structure that makes it possible to explain a number of results of tunnel measurements in high-temperature superconductors. This paper aims at explaining the features of tunnel characteristics using the model with an anisotropic effective order parameter, which is based exclusively on the properties of the electron spectrum of HTSC [15]. The spectrum of the model in the problem under investigation corresponds to the band structure of compounds of the BiSrCaCuO (BSCCO) type. An important feature of this approach is that the initial electron–electron interaction leading to pairing is treated as isotropic in the CuO_2 plane. The anisotropy of the order parameter and of the excitation spectrum is determined by the symmetry properties of the crystal lattice. According to calculations, many features of the tunnel characteristics typical of HTSC compounds can be explained by using a rather universal approach which will be described below.

We analyze the problem of the effect of symmetry in the initial bands of the superconductor on the current–voltage characteristics of *SIS* junctions. Let us consider the electron system of the CuO_2 plane with a model Hamiltonian of the form

$$H = \varepsilon_{z^2}\sum_{i,\sigma} c^+_{i,\sigma}c_{i,\sigma} + \varepsilon_d\sum_{i,\sigma} d^+_{i,\sigma}d_{j,\sigma}$$

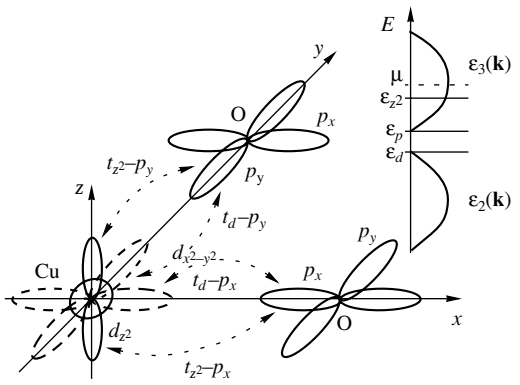

Fig. 1. Schematic diagram of atomic orbitals in the CuO_2 plane and transitions between these orbitals included in Hamiltonian (1). The inset shows schematically the arrangement of energy bands and levels corresponding to Hamiltonian (4).

$$
\begin{aligned}
&+\varepsilon_p\sum_{i,\sigma}(p_x^+(i,\sigma)p_x(i,\sigma)+p_y^+(i,\sigma)p_y(i,\sigma))\\
&+\sum_{i,j,\sigma}(t_{z^2-p_x}^{i,j}c_{i,\sigma}^+p_x(j,\sigma)+\text{H.c.})\\
&+\sum_{i,j,\sigma}(t_{z^2-p_y}^{i,j}c_{i,\sigma}^+p_y(j,\sigma)+\text{H.c.})\\
&+\sum_{i,j,\sigma}(t_{d-p_x}^{i,j}d_{i,\sigma}^+p_x(j,\sigma)+\text{H.c.})\\
&+\sum_{i,j,\sigma}(t_{d-p_y}^{i,j}d_{i,\sigma}^+p_y(j,\sigma)+\text{H.c.})\\
&+U_{z^2}\sum_i c_{i\downarrow}^+c_{i\downarrow}c_{i\uparrow}^+c_{i\uparrow}+U_d\sum_i d_{i\downarrow}^+d_{i\downarrow}d_{i\uparrow}^+d_{i\uparrow}.
\end{aligned}
\tag{1}
$$

Here, $c_{i,\sigma}^+$ and $d_{i,\sigma}^+$ are the creation operators for electrons with spin σ on the d_{z^2} and $d_{x^2-y^2}$ orbitals of the ith site of copper; $p_x^+(i,\sigma)$ and $p_y^+(i,\sigma)$ are the creation operators for electrons with spin σ on the p_x and p_y orbitals of the ith site of oxygen (Fig. 1); ε_p, ε_d, and ε_{z^2} are the energies of the p levels of oxygen and of the $d_{x^2-y^2}$ and d_{z^2} levels of copper, respectively, measured from the chemical potential ($\mu = 0$); and $t_{z^2-p_x}^{i,j} = t_{z^2-p_y}^{i,j} \equiv t_{z^2-p}$ and $t_{d-p_x}^{i,j} = -t_{d-p_y}^{i,j} \equiv t_{d-p}$ are the matrix elements of one-particle transitions between the d_{z^2} and $d_{x^2-y^2}$ orbitals of copper and the p orbitals of oxygen. For the sake of simplicity, we assume that superconductivity is associated with the isotropic attraction $U_{z^2} < 0$ of electrons on the d_{z^2} orbital. It should be noted that a more complicated account of the isotropic superconducting interaction would not lead to a considerable difference from the case considered here. We also assume the presence of the isotropic effective electron–electron interaction U_d on the $d_{x^2-y^2}$ orbital of copper.

Introducing new operators $a_{\mathbf{k},\sigma}^{(\beta)}$ ($\beta = 1, 2, 3$) in the $\mathbf{k}$ representation in accordance with the formulas

$$
\begin{aligned}
d_{\mathbf{k},\sigma} &= C_d^{(1)}a_{\mathbf{k},\sigma}^{(1)}+C_d^{(2)}a_{\mathbf{k},\sigma}^{(2)}+C_d^{(3)}a_{\mathbf{k},\sigma}^{(3)},\\
p_x(\mathbf{k},\sigma) &= C_{p_x}^{(1)}a_{\mathbf{k},\sigma}^{(1)}+C_{p_x}^{(2)}a_{\mathbf{k},\sigma}^{(2)}+C_{p_x}^{(3)}a_{\mathbf{k},\sigma}^{(3)},\\
p_y(\mathbf{k},\sigma) &= C_{p_y}^{(1)}a_{\mathbf{k},\sigma}^{(1)}+C_{p_y}^{(2)}a_{\mathbf{k},\sigma}^{(2)}+C_{p_y}^{(3)}a_{\mathbf{k},\sigma}^{(3)},
\end{aligned}
\tag{2}
$$

we diagonalize the Hamiltonian term describing one-particle transitions between the $d_{x^2-y^2}$ orbitals of copper and the p orbitals of oxygen. The coefficients C_d and $C_{p_x(p_y)}$ in formulas (2) have the form

$$
\begin{aligned}
C_d^{(1)} &= 0,\\
C_d^{(\alpha)} &= \frac{\varepsilon_p-\varepsilon_\alpha}{\sqrt{(\varepsilon_p-\varepsilon_\alpha)^2+t_x^{\,2}+t_y^{\,2}}},\\
C_{p_x(p_y)}^{(1)} &= \frac{it_{y(x)}}{\sqrt{t_x^{\,2}+t_y^{\,2}}},\\
C_{p_x(p_y)}^{(\alpha)} &= \pm\frac{t_{x(y)}}{\sqrt{(\varepsilon_p-\varepsilon_\alpha)^2+t_x^{\,2}+t_y^{\,2}}},
\end{aligned}
$$

where $\alpha = 2, 3$ and

$$
t_{x(y)} = t_{d-p}\sin\frac{k_{x(y)}}{2}.
$$

Similarly, the matrix element of a transition between the d_{z^2} orbitals of copper and the p orbitals of oxygen in the $\mathbf{k}$ representation can be written in the form

$$
\tilde{t}_{x(y)} = t_{z^2-p}\sin\frac{k_{x(y)}}{2}.
$$

Since the matrix elements $t_{d-p}^{i,j}$ and $t_{z^2-p}^{i,j}$ depend on the indices of different sites, the quantities $t_{x(y)}$ and $\tilde{t}_{x(y)}$ must be functions of $\mathbf{k}$. Operators $a_{\mathbf{k},\sigma}^{(1)+}$, $a_{\mathbf{k},\sigma}^{(2)+}$, and $a_{\mathbf{k},\sigma}^{(3)+}$ are the creation operators for electrons with spin σ and quasimomentum $\mathbf{k}$ in the bands formed by hybridized p orbitals of oxygen and $d_{x^2-y^2}$ orbitals of copper, having the dispersion relation

$$
\begin{aligned}
\varepsilon_1 &= \varepsilon_p,\\
\varepsilon_{2(3)}(\mathbf{k}) &= \frac{\varepsilon_p+\varepsilon_d}{2}\mp\frac{1}{2}\sqrt{(\varepsilon_p-\varepsilon_\alpha)^2+4(t_x^2(\mathbf{k})+t_y^2(\mathbf{k}))}.
\end{aligned}
\tag{3}
$$

As a result of transformation (2), the system Hamiltonian in the mean-field approximation assumes the form

$$\begin{aligned} H = &\sum_{\mathbf{k},\sigma} \varepsilon_{z^2} c^+_{\mathbf{k},\sigma} c_{\mathbf{k},\sigma} + \sum_{\mathbf{k},\sigma,\beta} \varepsilon_\beta a^{(\beta)+}_{\mathbf{k},\sigma} a^{(\beta)}_{\mathbf{k},\sigma} \\ &+ \sum_{\mathbf{k},\sigma,\beta} (W_\beta(\mathbf{k}) c^+_{\mathbf{k},\sigma} a^{(\beta)+}_{\mathbf{k},\sigma} + \text{H.c.}) \\ &- \sum_{\mathbf{k}} (\Delta_{z^2} c^+_{-\mathbf{k},\downarrow} c^+_{\mathbf{k},\uparrow} + \text{H.c.}) \\ &- \sum_{\mathbf{k},\beta,\gamma} (\Delta_{\beta\gamma} a^{(\beta)+}_{-\mathbf{k},\downarrow} a^{(\gamma)+}_{\mathbf{k},\uparrow} + \text{H.c.}), \end{aligned} \tag{4}$$

where

$$\begin{aligned} W_1(\mathbf{k}) &= \frac{\tilde{t}_x t_y + \tilde{t}_y t_x}{\sqrt{t_x^2 + t_y^2}}, \\ W_\alpha(\mathbf{k}) &= \frac{t_y \tilde{t}_y - t_x \tilde{t}_x}{\sqrt{(\varepsilon_p - \varepsilon_\alpha)^2 + t_x^2 + t_y^2}}, \quad \alpha = 2, 3, \end{aligned} \tag{5}$$

and new order parameters

$$\Delta_{\beta\gamma}(\mathbf{k}) = C_d^{(\beta)}(\mathbf{k}) C_d^{(\gamma)}(-\mathbf{k}) \Delta_d, \quad \beta, \gamma = 1, 2, 3, \tag{6}$$

have been introduced, in which

$$\begin{aligned} \Delta_d &= -\frac{1}{N} U_d \sum_{\mathbf{k}} \langle d_{\mathbf{k},\uparrow} d_{-\mathbf{k},\downarrow} \rangle, \\ \Delta_{z^2} &= -\frac{1}{N} U_{z^2} \sum_{\mathbf{k}} \langle c_{\mathbf{k},\uparrow} c_{-\mathbf{k},\downarrow} \rangle. \end{aligned} \tag{7}$$

The arrangement of the energy bands corresponding to Hamiltonian (4) is shown in the inset to Fig. 1. In the framework of a realistic description of BSCCO-type compounds [16], it is assumed that the chemical potential μ and the z^2 level of copper lie close to the middle of the upper band $\varepsilon_3(\mathbf{k})$. The remaining parameters of the problem are chosen in such a way that

$$\begin{aligned} &\varepsilon_d < \varepsilon_p, \quad \varepsilon_p - \varepsilon_d \ll t_{d-p}, \\ &t_{z^2-p} \ll |\varepsilon_d|, |\varepsilon_p|, \quad |\Delta_d| < \Delta_{z^2} \ll |\varepsilon_d|, |\varepsilon_p|. \end{aligned}$$

Since, in the following, we will be interested in the energy range near the chemical potential (on the order of several Δ_{z^2}), we can disregard the two lower bands $\varepsilon_1(\mathbf{k})$ and $\varepsilon_2(\mathbf{k})$ taking into account the relation between parameters and confine our analysis to the upper band $\varepsilon_3(\mathbf{k})$ only. In addition to one-particle transitions included in Hamiltonian (1), we can take into account the additional hybridization of the d_{z^2} orbital with the atoms surrounding the CuO_2 plane, including BiO and SrO complexes of the BSSCO-type compounds as well as direct transitions between the d_{z^2} orbitals of different copper atoms. In this connection, we assume that the initial z^2 band is characterized by the dispersion relation

$$\varepsilon_{z^2}(\mathbf{k}) = \varepsilon_{z^2} + t_{z^2}(\cos k_x + \cos k_y)$$

with a width much smaller than for the $\varepsilon_2(\mathbf{k})$ and $\varepsilon_3(\mathbf{k})$ bands. Thus, in the chosen approximation, the initial problem can be reduced to a two-band model in which the initial band $\varepsilon_{z^2}(\mathbf{k})$ and the $\varepsilon_3(\mathbf{k})$ band with the one-particle hybridization $W_3(\mathbf{k})$ between these bands and the order parameters Δ_{z^2} and $\Delta_{33}(\mathbf{k})$ in them are considered.

We introduce the following time Green's functions:

$$\begin{aligned} G_{z^2}(\mathbf{k}; t, t') &= -i\langle T c_{\mathbf{k},\sigma}(t) c^+_{\mathbf{k},\sigma}(t') \rangle, \\ g_{\sigma\sigma'} F^+_{z^2}(\mathbf{k}; t, t') &= -i\langle T c^+_{-\mathbf{k},\sigma}(t) c^+_{\mathbf{k},\sigma'}(t') \rangle, \\ G_{z^2,3}(\mathbf{k}; t, t') &= -i\langle T c_{\mathbf{k},\sigma}(t) c^{(3)+}_{\mathbf{k},\sigma}(t') \rangle, \\ g_{\sigma\sigma'} F^+_{z^2,3}(\mathbf{k}; t, t') &= -i\langle T a^{(3)+}_{-\mathbf{k},\sigma}(t) c^+_{\mathbf{k},\sigma'}(t') \rangle, \end{aligned}$$

where $\hat{g} = i\hat{\sigma}^y$. Using the equations of motion for operators $a^{(3)}_{\mathbf{k},\sigma}$ and $c_{\mathbf{k},\sigma}$ and passing to the frequency representation, we obtain the following system of equations for the z^2 Green's functions:

$$\begin{aligned} &(\omega - \varepsilon_{z^2}(\mathbf{k})) G_{z^2}(\mathbf{k}, \omega) \\ &- W_3(\mathbf{k}) G^+_{z^2,3}(\mathbf{k}, \omega) + \Delta_{z^2} F^+_{z^2}(\mathbf{k}, \omega) = 1, \end{aligned} \tag{8a}$$

$$\begin{aligned} &(\omega - \varepsilon_3(\mathbf{k})) G_{z^2,3}(\mathbf{k}, \omega) \\ &- W_3(\mathbf{k}) G^+_{z^2}(\mathbf{k}, \omega) + \Delta_3(\mathbf{k}) F^+_{z^2,3}(\mathbf{k}, \omega) = 0, \end{aligned} \tag{8b}$$

$$\begin{aligned} &(\omega + \varepsilon_{z^2}(\mathbf{k})) F^+_{z^2}(\mathbf{k}, \omega) \\ &+ W_3(\mathbf{k}) F^+_{z^2,3}(\mathbf{k}, \omega) + \Delta^+_{z^2} G_{z^2}(\mathbf{k}, \omega) = 0, \end{aligned} \tag{8c}$$

$$\begin{aligned} &(\omega + \varepsilon_3(\mathbf{k})) F^+_{z^2,3}(\mathbf{k}, \omega) \\ &+ W_3(\mathbf{k}) F^+_{z^2}(\mathbf{k}, \omega) + \Delta^+_3(\mathbf{k}) G^+_{z^2,3}(\mathbf{k}, \omega) = 0, \end{aligned} \tag{8d}$$

where

$$\Delta_3(\mathbf{k}) \equiv \Delta_{33}(\mathbf{k}) = \Delta_d \frac{(\varepsilon_p - \varepsilon_3)^2}{(\varepsilon_p - \varepsilon_3)^2 + t_x^2 + t_y^2}. \tag{9}$$

Henceforth, we will use the quasiparticle density of states in the z^2 band,

$$N(\omega) = -\frac{1}{\pi} \int \text{Im} G^R_{z^2}(\omega, \mathbf{k}) \frac{d^3k}{(2\pi)^3}. \tag{10}$$

The retarded Green's function is obtained by the solution of the system of equations (8) and has the form

$$G^R_{z^2}(\omega, \mathbf{k}) = \frac{u^2_{-,\mathbf{k}}}{\omega - E_-(\mathbf{k}) + i0} + \frac{u^2_{+,\mathbf{k}}}{\omega - E_+(\mathbf{k}) + i0} + \frac{v^2_{-,\mathbf{k}}}{\omega + E_-(\mathbf{k}) + i0} + \frac{v^2_{+,\mathbf{k}}}{\omega + E_+(\mathbf{k}) + i0},$$

where the coherence factors are defined as

$$u^2_{\pm,\mathbf{k}} = \mp\frac{(E_\pm + \varepsilon_{z^2})(-E^2_\pm + \varepsilon^2_3 + \Delta^2_3) + W^2_3(E_\pm - \varepsilon_3)}{2E_\pm(E^2_+ - E^2_-)},$$

$$v^2_{\pm,\mathbf{k}} = \mp\frac{(E_\pm - \varepsilon_{z^2})(-E^2_\pm + \varepsilon^2_3 + \Delta^2_3) + W^2_3(E_\pm + \varepsilon_3)}{2E_\pm(E^2_+ - E^2_-)}.$$

The dispersion relations for two branches of the excitation spectrum have the form

$$\begin{aligned} E^2_\pm(\mathbf{k}) &= [\varepsilon^2_{z^2}(\mathbf{k}) + \Delta^2_{z^2} + \varepsilon^2_3(\mathbf{k}) \\ &+ \Delta^2_3(\mathbf{k}) + 2W^2_3(\mathbf{k})]/2 \\ &\pm \{(\varepsilon^2_{z^2}(\mathbf{k}) + \Delta^2_{z^2} - \varepsilon^2_3(\mathbf{k}) - \Delta^2_3(\mathbf{k}))^2 \\ &+ 4W^2_3(\mathbf{k})[(\Delta_{z^2} - \Delta_3(\mathbf{k}))^2 \\ &+ (\varepsilon_{z^2}(\mathbf{k}) + \varepsilon_3(\mathbf{k}))^2]\}^{1/2}/2. \end{aligned} \quad (11)$$

The system of equations (8a)–(8d) can be reduced to the system of two equations for Green's functions G_{z^2} and F_{z^2} with the effective order parameter defined by the formula

$$\Delta_{z^2}(\mathbf{k}) = \frac{\Delta_3(\mathbf{k})W^2_3(\mathbf{k})}{\varepsilon^2_3(\mathbf{k}) + \Delta^2_3(\mathbf{k})} + \Delta_{z^2}. \quad (12)$$

The sign of the order parameter $\Delta_3(\mathbf{k})$ from (9) is determined by the sign of the parameter Δ_d from (7), which can be positive or negative depending on the type of interaction U_d (repulsion or attraction). The value of $\Delta_d = 0$ if $U_d = 0$ or for $U_d > U_d^{\text{crit}} > 0$, where U_d^{crit} is a certain critical value of repulsion on the $d_{x^2-y^2}$ orbital of copper, for which superconductivity in the system is completely suppressed. It can be seen from formula (12) that, in the case of a nonzero interaction U_d on the $d_{x^2-y^2}$ orbital ($\Delta_d \neq 0$), the order parameter depends on quasimomentum, while, in the case of repulsion, $\Delta_3(\mathbf{k})/\Delta_{z^2} < 0$ ($U_d > 0$), the quantity $\Delta_{z^2}(\mathbf{k})$ changes its sign.

The approach considered above explains the strong anisotropy of the order parameter as a consequence of the symmetry properties of the one-particle matrix element of the interband hybridization $W_3(\mathbf{k})$ [15], which has nodes along the diagonals of the Brillouin zone due to the difference between the types of symmetry of the initial bands. In this case, the branch $E_-(\mathbf{k})$ of the excitation spectrum vanishes at points located on lines in the $\mathbf{k}$ space [6] at which the effective order parameter $\Delta_{z^2}(\mathbf{k})$ is equal to zero. It should be noted that the initial interaction is regarded as isotropic; i.e., the effect considered above does not depend on the origin of the pairing mechanism. In addition, the above-mentioned approach does not require a strong anisotropy of the spectrum and, hence, can be used for various types of high-temperature superconductors. The model proposed in [17] also leads to formulas of the type (11), (12), but it is based on the exotic condition of the interaction sign reversal in various regions of the Fermi surface.

The diagonalization of the one-particle part of Hamiltonian (1) leads to the problem with anisotropic attraction in energy bands. The effective order parameters in the bands may have nodes, but possess no pure *d* or (*s* + *d*) symmetry since their anisotropy is determined by the band representations of the space symmetry group of the lattice [15, 18, 19].

The formulated model of the order parameter anisotropy makes it possible to obtain the (*dI*/*dV*) characteristics of *SIS* junctions for superconductors of the BSCCO type. Taking into account the crystal structure of these compounds, we will assume that tunneling along the *c* axis occurs mainly through the d_{z^2} orbitals of copper in the CuO_2 plane (and through the apical oxygen which is not included explicitly in the model under investigation). For break junctions, we assume that the matrix element of tunneling is independent of momentum ($T_{\mathbf{kp}} = T = \text{const}$) in view of the random formation of bonds between the d_{z^2} orbitals on both sides of the junction. Thus, tunneling between two superconductors (CuO_2 layers) is treated as proceeding through a number of point contacts.

The expression for the dependence of the quasiparticle tunnel current on the voltage applied to the junction in this case assumes the standard form

$$I(V) = 4e|T|^2 \int_{-\infty}^{\infty} [n(\omega) - n(\omega - eV)] \times N(\omega)N(\omega - eV)d\omega, \quad (13)$$

where

$$n(\omega) = \left[\exp\left(-\frac{\omega}{T}\right) + 1\right]^{-1}$$

is the Fermi distribution function and $N(\omega)$ is defined by formula (10). All calculations were made for temperature $T = 0$. An important aspect of this approach is that $N(\omega)$ is not the average density of states in the con-

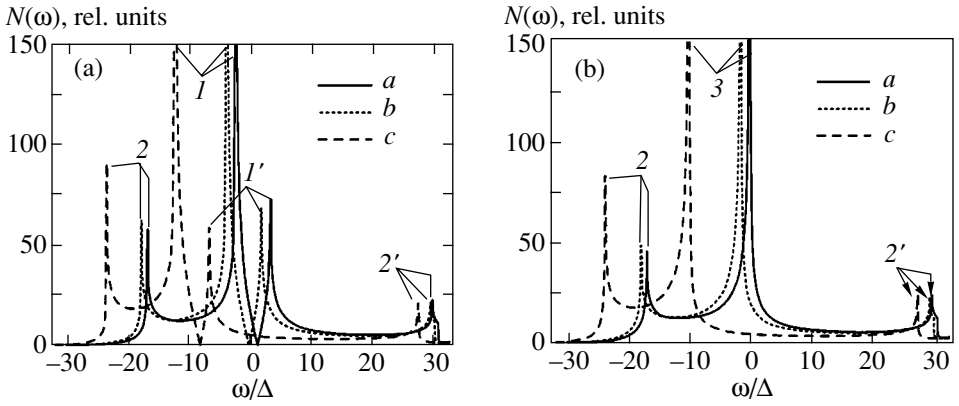

Fig. 2. Normal density of states in the z^2 band: t_{z^2} = 1.5 (a) and 0 (b) for ε_{z^2} = 0 (curves *a*), –1.5 (curves *b*) and –10 (curves *c*). Peaks *1* and *1'* are associated with the Van Hove singularities of the initial z^2 band, peaks *2* and *2'* are formed by the Van Hove singularities in the $\varepsilon_3(\mathbf{k})$ band, and peaks *3* are connected with the ε_{z^2} level.

duction band (as in the one-band BCS model), but is a partial density on the d_{z^2} orbital.

In order to find the density of states $N(\omega)$ and the tunnel conductance dI/dV in accordance with the chosen approximation, we used the values of parameters from the strong coupling model, which correspond to the calculations of the band structure of HTSC [20]. If all parameters are measured in the units of Δ_{z^2} and the position of energy levels is measured from the chemical potential, we have t_{d-p} = 75, t_{z^2-p} = 15, ε_d = –75, and ε_p = –50. In all calculations, we assumed the existence of a finite relaxation constant γ = 0.05. The parameter determining the width of the initial $\varepsilon_{z^2}(\mathbf{k})$ band is t_{z^2} = 1.5.

For the chosen values of the parameters, we analyzed the behavior of the characteristics $N(\omega)$ and dI/dV depending on the intensity of interaction between electrons on the $d_{x^2-y^2}$ orbital of copper and on the position of the center (ε_{z^2}) of the initial z^2 band relative to the chemical potential (Figs. 2–4). The obtained dependences were compared with cases of one-band model of the *s*- and *d*-types of symmetry of the order parameter (accordingly, Δ = const and $\Delta \propto (\cos k_x - \cos k_y)$).

Figure 2a shows the $N(\omega)$ curves calculated for the normal state (Δ_{z^2} = 0). These curves display split peaks associated with the Van Hove singularities of the initial $\varepsilon_{z^2}(\mathbf{k})$ band for various positions of its center relative to the chemical potential, as well as the next peaks formed by singularities of the $\varepsilon_3(\mathbf{k})$ band. Figure 2b shows the same curves in the case when the $\varepsilon_{z^2}(\mathbf{k})$ spectrum is replaced by a dispersionless level (t_{z^2} = 0).

Figure 3a presents the $N(\omega)$ dependences in the superconducting state for the case when the z^2 band is far away from the chemical potential (ε_{z^2} = –10). It can be seen from the figure that if there is electron–electron repulsion on the $d_{x^2-y^2}$ orbital (Δ_d = –0.5), the density of quasiparticles is similar to that calculated in a model with the *d* symmetry of the order parameter (in particular, it is a linear function of ω in the vicinity of ω = 0). If there is no interaction on the $d_{x^2-y^2}$ orbital, the distance between the superconducting peaks and their height increase. According to analytical estimations, $N(\omega) \propto \omega^{3/2}$ for very small frequencies. Similar results can also be obtained in the one-band model with a nontrivial spectrum and an effective order parameter of some symmetry. It was noted above taking into account the above approximations that the diagonalization of the one-particle part of Hamiltonian (1) leads to the one-band model with anisotropic pairing. In this case, the symmetry of the corresponding order parameter can be approximated by an (*s* + *d*)-type symmetry.

If the center of the initial z^2 band is close to the chemical potential (see Figs. 3b and 3c), the difference between the *a* and *b* curves (with and without taking into account repulsion) disappears due to the dominant role of the Van Hove singularities on energy scales on the order of Δ_{z^2}. In both cases, the behavior of the density of quasiparticles becomes of the *s* type. The calculated density of states demonstrates the asymmetry of peaks, which is associated with the distribution of Van Hove singularities in the normal density of states (see Fig. 2). The Van Hove singularity closest to the chemical potential increases the height of the corresponding peak in the density of states in the superconducting state. A comparison of Figs. 3b and 3c shows that, for a certain intermediate value of ε_{z^2}, the specular switch-

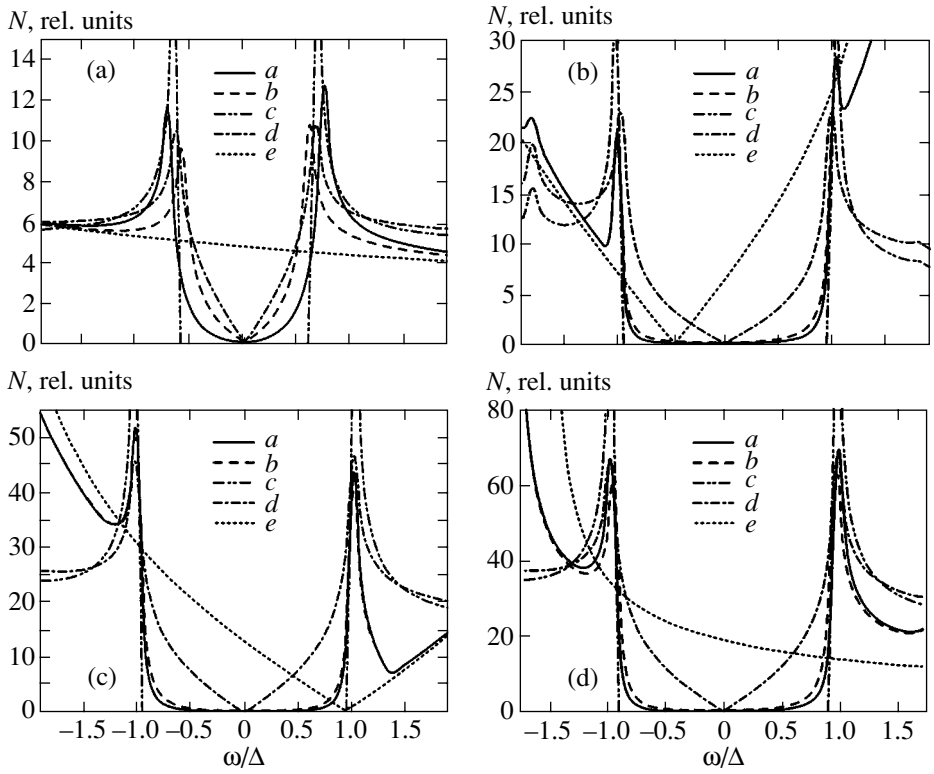

Fig. 3. Density of states in the normal and superconducting states in the z_2 band: (a) $\varepsilon_{z^2} = -10$, $t_{z^2} = 1.5$; (b) $\varepsilon_{z^2} = -1.5$, $t_{z^2} = 1.5$; (c) $\varepsilon_{z^2} = 0$, $t_{z^2} = 1.5$; (d) $\varepsilon_{z^2} = -1.5$, $t_{z^2} = 0$. Curves *a* are plotted in the absence of interaction on the $d_{x^2-y^2}$ orbital ($U_d = 0$), curves *b* take into account the repulsion on the $d_{x^2-y^2}$ orbital ($U_d > 0$), curves *c* are plotted in a model with the *s* symmetry of the order parameter, curves *d* are plotted, in a model with the *d* symmetry of the order parameter, and curve *e* illustrates the normal density of states.

ing of the asymmetry of peaks, which is associated with the model spectral structure, takes place.

The curves presented in Fig. 3a show that the distance between the superconducting peaks is smaller than $2\Delta_{z^2}$ even if we disregard the repulsion on the $d_{x^2-y^2}$ orbital for a large distance between the ε_{z^2} level and the chemical potential ($\varepsilon_{z^2} = -10$). As the ε_{z^2} level approaches the chemical potential, the distance between the superconducting peaks increases, and the position of the peaks on the $N(\omega)$ curve for $\varepsilon_{z^2} = 0$ corresponds to the parameter Δ_{z^2}. In this case, the height of the peaks increases significantly. The distance between the peaks changes as a result of the displacement of the ε_{z^2} level relative to the chemical potential for the fixed values of the remaining parameters. However, a more detailed analysis of this phenomenon requires the solution of the self-consistent model spectrum structure equations for order parameters as functions of the parameters of the problem as well as the determination of the interaction constants U_{z^2} and U_d taking into account the specific mechanism of pairing, which is beyond the scope of the present paper. The dependence of the distance between the superconducting peaks on the position of the chemical potential in the model with the ($s + d$) symmetry of the order parameter was also discovered theoretically in [13].

A comparison of the $N(\omega)$ dependences determined in the model under investigation with one-band models with the *s*- and *d*-types of symmetry of the order parameter was carried out taking into account the location of the Van Hove singularities associated with the initial $\varepsilon_{z^2}(\mathbf{k})$ band. A noticeable (on the scales of energy higher than Δ_{z^2}) asymptotic tendency of model densities of states of the *s* and *d* types to the density of states in the given problem, calculated for both the normal and the superconducting state (see Fig. 3c), was observed.

A comparison of the results presented in Figs. 3b and 3d shows that, as the width of the initial z^2 band determined by the parameter t_{z^2} decreases ($t_{z^2} = 1.5$ in Fig. 3b and $t_{z^2} = 0$ in Fig. 3d), the heights of the superconducting peaks increases, since the singularity in the

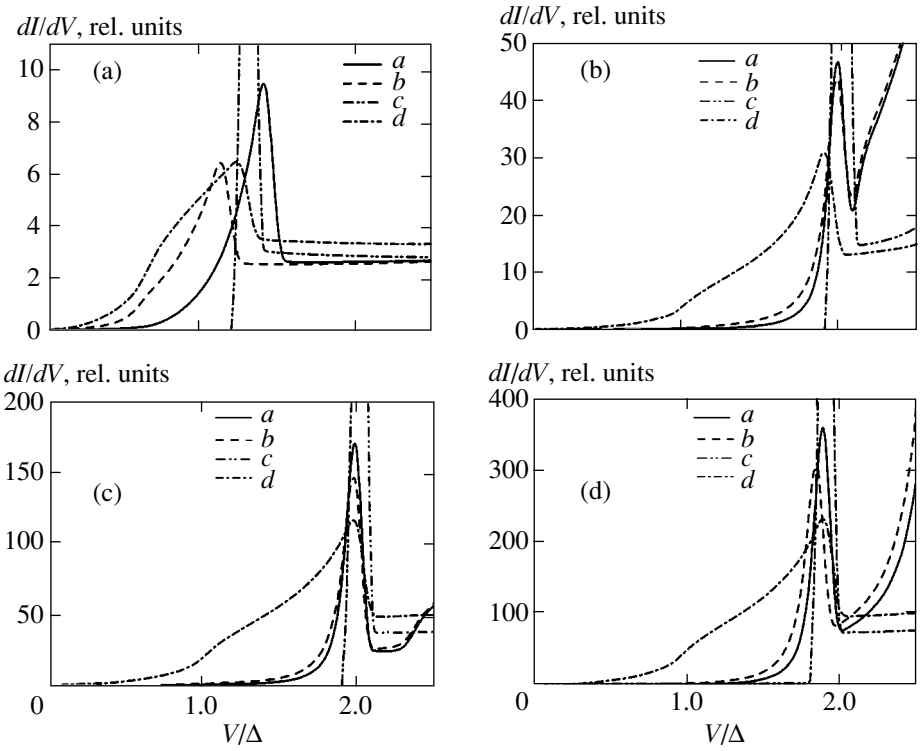

Fig. 4. (*dI*/*dV*) characteristics for (a) $\varepsilon_{z^2} = -10$, $t_{z^2} = 1.5$; (b) $\varepsilon_{z^2} = -1.5$, $t_{z^2} = 1.5$; (c) $\varepsilon_{z^2} = 0$, $t_{z^2} = 1.5$; (d) $\varepsilon_{z^2} = -1.5$, $t_{z^2} = 0$. Curves *a* are plotted in the absence of interaction on the $d_{x^2-y^2}$ orbital ($U_d = 0$), curves *b* take into account the repulsion on the $d_{x^2-y^2}$ orbital ($U_d > 0$), curves *c* are plotted in a model with the *s* symmetry of the order parameter, and curves *d* are plotted in a model with the *d* symmetry of the order parameter.

normal density of states in this case is displaced towards the chemical potential (see Fig. 2).

Figure 4 shows the (*dI*/*dV*) characteristics for an *SIS* junction, which were calculated using formula (13) using the determined $N(\omega)$ dependences for three positions of the ε_{z^2} level relative to the chemical potential ($\varepsilon_{z^2} = -10$, -1.5, and 0), which can be in model correspondence with different HTSC families. The common feature of these characteristics is (when repulsion is taken into account) that the superconducting peak emerges at lower voltages and is lower, but the curve at low voltages lies higher than in the absence of interaction on the $d_{x^2-y^2}$ orbital of copper. If the center of the initial z^2 band lies far away from the chemical potential ($\varepsilon_{z^2} = -10$), the (*dI*/*dV*) characteristics are similar to those calculated in a model with the *d* symmetry of the order parameter (Fig. 4a). As the ε_{z^2} level approaches the chemical potential, the curves tend to the dependences obtained in the model with the *s* symmetry of the order parameter (Figs. 4b and 4c). For low voltages ($V < \Delta_{z^2}$), the *IV* characteristic of an *SIS* junction is strongly suppressed. In analogy with the $N(\omega)$ dependences, the (*dI*/*dV*) characteristics exhibit extremely narrow superconducting peaks. This corresponds to a number of experimentally observed results for BSCCO-type compounds, e.g., optimally doped [4], overdoped [5], and underdoped [21] $Bi_2Sr_2CaCu_2O_{8+\delta}$.

Thus, the electron density of states and current–voltage characteristics of *SIS* junctions are calculated in the framework of the multiband HTSC model with an anisotropic effective order parameter. We took into account the hybridization between the p_x and p_y orbitals of oxygen and the $d_{x^2-y^2}$ orbitals of copper in the CuO_2 plane and assumed the presence of electron–electron attraction on the d_{z^2} orbital of copper. The performed calculations demonstrate the possibility of explaining the results of experimental measurements of the electron density of states and the tunnel properties of *SIN* and *SIS* junctions (e.g., *s*-type characteristics of BSCCO-type compounds) on the basis of the model taking into account the structure of the electron spectrum of HTSC. It is important to note that anisotropy of the order parameter and of the excitation spectrum is explained exclusively by the symmetry of the crystal lattice and atomic orbitals and does not depend on the nature of pairing.

The main result of this work is that for a strongly anisotropic order parameter $\Delta(\mathbf{k})$ (12) (including *d*-type parameters) and in the presence of zero points in the excitation spectrum of a superconductor, even the simple inclusion of the real band structure of the HTSC in a wide range of variation of the model parameter leads to the experimentally observed [4, 5, 21] *s*-type behavior of the current–voltage characteristics of *SIN* and *SIS* junctions. A comparison of the curves calculated for various values of the parameters of the problem under investigation and in the simplest cases of models with the *s* and *d* symmetries of order parameters indicates a strong dependence of both the density of states and the (dI/dV) characteristics on the electron band structure of high-temperature superconductors. These characteristics also depend on the crystal lattice symmetry and on the presence of an additional interaction between electrons, which was introduced in the model on the $d_{x^2-y^2}$ orbital of copper. The above analysis necessitates the inclusion of the band structure of HTSC for interpreting of the results of tunnel experiments.

ACKNOWLEDGMENTS

The authors are grateful to B. A. Volkov, E. G. Maksimov, and Ya. G. Ponomarev for numerous discussions in the course of the research.

This work was supported by the Russian Foundation for Basic Research (project no. 99-02-16449).

REFERENCES

1. Z. Yusof, J. F. Zasadzinski, L. Coffey, and N. Miyakawa, Phys. Rev. B **58**, 514 (1998).
2. K. Kouznetsov and L. Coffey, Phys. Rev. B **54**, 3617 (1996).
3. C. Renner and O. Fischer, Phys. Rev. B **51**, 9208 (1995).
4. Ya. G. Ponomarev, Chong Soon Khi, Kim Ki Uk, *et al.*, Physica C (Amsterdam) **315**, 85 (1999).
5. M. Suzuki, T. Watanabe, and A. Matsuda, Phys. Rev. Lett. **82**, 5361 (1999).
6. M. R. Norman, M. Randeria, H. Ding, and J. C. Campuzano, Phys. Rev. B **52**, 615 (1995).
7. J. Y. T. Wei, C. C. Tsuei, P. J. M. van Bentum, *et al.*, Phys. Rev. B **57**, 3650 (1998).
8. A. J. Fedro and D. D. Koelling, Phys. Rev. B **47**, 14 342 (1993).
9. M. Ledvij and R. A. Klemm, Phys. Rev. B **51**, 3269 (1995).
10. W. Rantner and X.-G. Wen, Phys. Rev. Lett. **85**, 3692 (2000).
11. P. Monthoux, A. V. Balatsky, and D. Pines, Phys. Rev. B **46**, 14 803 (1992).
12. N. Bulut and D. J. Scalapino, Phys. Rev. B **45**, 2371 (1992).
13. Yung-mau Nie and L. Coffey, Phys. Rev. B **59**, 11 982 (1999).
14. K. Schlenga, R. Kleiner, G. Hechtfischer, *et al.*, Phys. Rev. B **57**, 14 518 (1998).
15. P. I. Arseyev, N. K. Fedorov, and B. A. Volkov, Solid State Commun. **100**, 581 (1996).
16. P. Entel and J. Zielinski, Phys. Rev. B **42**, 307 (1990).
17. R. Combescot and X. Leyronas, Phys. Rev. Lett. **75**, 3732 (1995).
18. G. E. Volovik and L. P. Gor'kov, Zh. Éksp. Teor. Fiz. **88**, 1412 (1985) [Sov. Phys. JETP **61**, 843 (1985)].
19. A. N. Vasil'chenko and A. V. Sokol, Zh. Éksp. Teor. Fiz. **96**, 377 (1989) [Sov. Phys. JETP **69**, 213 (1989)].
20. O. Jepsen, O. K. Andersen, I. Dasgupta, and S. Savrasov, J. Phys. Chem. **59**, 1718 (1998).
21. Y. DeWilde, N. Miyakawa, P. Gaptasarma, *et al.*, Phys. Rev. Lett. **80**, 153 (1998).

Translated by N. Wadhwa

Journal of Experimental and Theoretical Physics, Vol. 94, No. 2, 2002, pp. 395–402.
Translated from Zhurnal Éksperimental'noĭ i Teoreticheskoĭ Fiziki, Vol. 121, No. 2, 2002, pp. 462–470.

SOLIDS
Electronic Properties

Dielectric Relaxation and Ferroelectricity in $Cd_2Nb_2O_7$ Pyrochlore

N. N. Kolpakova[a,*], P. Charnetzki[b], W. Nawrochik[b], P. P. Syrnikov[a], and A. O. Lebedev[a]

[a]*Ioffe Physicotechnical Institute, Russian Academy of Sciences, St. Petersburg, 194021 Russia*
**e-mail: kolpakova@shupop.ioffe.rssi.ru*
[b]*Institute of Physics, Mickiewicz University, 61-614 Poznan, Poland*

Received July 24, 2001

Abstract—The dielectric dispersion of $Cd_2Nb_2O_7$ pyrochlore in a weak electric field was studied in a broad frequency range (100 Hz to 13 MHz) using the crystal samples slowly cooled (0.5 K/min) in the temperature interval from 300 to 80 K. As the temperature decreased down to T_c = 196 K and T_{max} ~ 190 K, the dielectric permittivity exhibited deviation from the Curie–Weiss law. It is suggested that this behavior is related to the development of a short-range correlation between microscopic polar regions formed at $T \longrightarrow T_{max}^{+}$. The local order parameter $q(T) \sim \langle P_i P_j \rangle^{1/2}$ was calculated using the permittivity $\varepsilon'(T)$ measured at various frequencies. The variation of this parameter is compared to that of the spontaneous polarization $P_s(T)$ determined from the measurements of a pyroelectric current in the external electric field E_{dc} = 0.95 kV/cm. In the frequency range from 100 Hz to 13 MHz, the dispersion of the dielectric response in the temperature region of 180–192 K is characteristic of a relaxator ferroelectric featuring a glasslike behavior. The parameters of this state were determined, including the activation energy of the polarization fluctuations ($E_a \approx 0.01$ eV), the relaxation rate at $T \longrightarrow \infty$ ($f_0 = 1.9 \times 10^{12}$ Hz), and the polarization fluctuation freezing temperature (T_f = 183 K). In $Cd_2Nb_2O_7$ pyrochlore, in contrast to the known relaxator ferroelectrics of the PMN type studied previously, this state coexists with the normal ferroelectric state appearing at T_c. © *2002 MAIK "Nauka/Interperiodica".*

1. INTRODUCTION

In the large family of pyrochlores (belonging to the cubic space group O_h^7–$Fd3m$), the compound $Cd_2Nb_2O_7$ is the most interesting object featuring numerous phase transitions and involved dielectric behavior [1, 2]. With respect to the electric properties, pyrochlores of the $A_2^{2+}B_2^{5+}O_7$ type containing Cd^{2+} ($4d^{10}$) ions represent insulators, provided that cation B is Nb^{5+} ($4d^0$), Ta^{5+} ($5d^0$), or Sb^{5+} ($4d^{10}$) [1], and metals if cation B represents Re^{5+} ($5d^2$) or Os^{5+} ($5d^3$) [3, 4].

In common for the compounds $Cd_2Nb_2O_7$ and $Cd_2Ta_2O_7$ are the same ion radii of cations B (0.64 Å for Nb^{5+} and Ta^{5+}) [5] and the identical room-temperature lattice parameters (10.372 Å) [6]. Both these compounds are characterized by the same (albeit rather seldom) limiting case of the deformed coordination polyhedra $(BO_6)^{n-}$ and $(AO_8)^{n-}$, whereby the octahedron around ion B exhibits a maximum distortion, while the polyhedron around ion A is close to a regular cube [5, 7, 8]. The structure stability on both cases is provided by the dynamic displacements of Cd^{2+} ions relative to the central position in the $(CdO_8)^{n-}$ polyhedra [6]. Despite the identical structural features of the two pyrochlores, these compounds are different with respect to susceptibility toward a symmetry decrease and structural phase transitions.

In the temperature interval from 10 to 300 K, $Cd_2Nb_2O_7$ exhibits a sequence of five phase transitions: extrinsic ferroelastic (below T_s = 205 K)–intrinsic ferroelectric–ferroelastic (below T_c = 196 K)–incommensurate phase (below T_{inc} = 85 K)– commensurate phase (below T_{com} = 46 K)–glassy state (below T_g = 18 K) [2]. In the same interval, $Cd_2Ta_2O_7$ exhibits a single phase transition (at 204 K) [9].

The dielectric behavior of $Cd_2Nb_2O_7$ in the ferroelectric state (4 K < T < T_c) is characterized by the following features:

(a) A maximum value of the permittivity $\varepsilon'(T)$ for frequencies below 1 MHz is observed at a temperature T_{max} within the interval 180–192 K [2, 10–14], which is below the temperature of the ferroelectric phase transition (T_c = 196 K).

(b) In the temperature interval from 180 to 192 K (i.e., below the ferroelectric phase transition), $Cd_2Nb_2O_7$ exhibits a polydisperse dielectric relaxation typical of the so-called relaxator (disordered) state of the system [10, 11, 15], whereby ε'_{max} increases, while ε''_{max} and T_{max} decrease, with decreasing frequency. In the vicinity of T_{max}, neither the domain structure notice-

ably changed [13, 16, 17] nor did the values of heat capacity [16, 18, 19], spontaneous polarization [14, 20], and refractive index significantly vary [21]; the crystal symmetry did not decrease either [10, 22, 23].

(c) Below T_c, the domains of the ferroelectric phase coexist with the domains of the preceding ferroelastic phase (observed at $T_c < T < T_s$). The latter domains gradually decrease in size on cooling below 180 K, to become indistinguishable by optical methods in the region of 150 K [13, 16, 17, 22].

(d) Far from T_c (at $T_g \ll T_c$) the system features a disordered glassy state [24].

Manifestations of the above states in the relaxation processes, as well as evolution of these states with the temperature and their relation to the ferroelectric properties, are still unclear because of a complicated dielectric response of $Cd_2Nb_2O_7$. The relaxator behavior of this compound is also insufficiently substantiated, which is explained by a relatively weak frequency dependence of ε'_{max} and T_{max} as compared to that observed in the relaxator dielectrics with perovskite (O_h^1–$Pm3m$) structures such as $Pb(Mg_{1/3}Nb_{2/3})O_3$ (PMN) and $Pb(Sc_{1/2}Ta_{2/3})O_3$ (PST) [15, 25]. Elucidation of these questions is of a fundamental importance in the physics of relaxator ferroelectrics and the physics of disordered states in highly symmetric condensed media.

The purpose of this study was to reveal the possible additional characteristic features in the relaxation processes in $Cd_2Nb_2O_7$ in the temperature region of 180–192 K providing evidence for the relaxator behavior of the system and elucidating a relationship between the relaxator and ferroelectric states of the system.

As is well known, the relaxator ferroelectrics are characterized, in addition to the properties mentioned in point (b) above, by deviation of the temperature dependence of ε' from the Curie–Weiss law in the paraelectric phase, by a decrease in the relaxation rate with decreasing temperature (deviation from the Arrhenius law), by the absence of a macroscopic spontaneous polarization at temperatures below T_{max} (in a sample cooled in zero electric field $E_{dc} = 0$), by the coexistence of microscopic polar regions at temperatures significantly higher than T_{max}, etc. [15, 26–28]. The results of our investigations presented below indicate that $Cd_2Nb_2O_7$ pyrochlore exhibits all features of the dielectric behavior typical of ferroelectrics of the PMN type.

We have studied the $Cd_2Nb_2O_7$ samples by the dielectric spectroscopy method in a broad range of frequencies (100 Hz to 13 MHz) and temperatures (80–300 K). The temperature and frequency dependences of the complex dielectric permittivity were analyzed from the standpoint of modern notions about features of the relaxator ferroelectricity [26–28]. Previously, the dielectric dispersion was studied in a much narrower frequency range (500 Hz to 1 MHz) [10–12, 14], which hindered elucidation of the nature of relaxation processes developed in the narrow temperature interval in the region of T_c.

2. EXPERIMENTAL METHODS

Taking into account that the same sequence of phase transitions is observed in both single crystals and ceramics of $Cd_2Nb_2O_7$ [2, 10–14], we employed the ceramic samples. An advantage of using ceramic samples in the study of dielectric properties consists in the relatively simple sample preparation and in the possibility of obtaining samples possessing any desired dimensions. The samples of $Cd_2Nb_2O_7$ ceramics were prepared by a standard procedure [5, 14, 29, 30]. The relative density of ceramic disks with a diameter of 10 mm and a thickness of about 2 mm was 94–96% of the theoretical value. An analysis of the samples by the method of X-ray powder diffraction at room temperature (DRON-2 diffractometer, CuK_α radiation, Ni filter) confirmed the pyrochlore structure and showed the absence of other phases in the samples studied.

The dielectric measurements were performed on plane-parallel plate samples with either Au electrodes deposited in vacuum or Ag-paste electrodes applied to the parallel surfaces. The permittivity $\varepsilon'(T)$ and losses $\varepsilon''(T)$ of the samples were measured in a weak electric field ($E_{ac} \approx 2$ V/cm) with the aid of an HP-4192A capacitive bridge. The frequency dependences were studied in a range from 100 Hz to 13 MHz, using a set of frequencies in each decade equal to f_m, $3f_m$, $5f_m$, and $7f_m$ (where f_m is the lower decade frequency). The measurements were performed on the samples slowly cooled at a rate of 0.5 K/min. The sample temperature at each point was stabilized to within ±0.1 K.

The spontaneous polarizations $P_s(T)$ were calculated by integrating the temperature dependence of the pyroelectric current measured with the aid of a Keithley 6514 System Electrometer in the course of heating the sample at a rate of 1 K/min in a relatively weak electric field ($E_{dc} \sim$ 0.95 kV/cm). The constant field E_{dc} was applied to the sample at a room temperature, and the sample was cooled at an arbitrary rate down to 90 K. This field changes neither the dielectric permittivity of $Cd_2Nb_2O_7$ pyrochlore in the region of T_c nor the size of domains in the ferroelectric phase at $T < T_c$ (the ferroelectric domains in this compound begin to change only in the field with a strength of $E_{dc} \geq 4$ kV/cm [12, 17, 30]), while decreasing the permittivity in the region of T_{max} [11, 12]. At the same time, it is known that this field is capable of changing the long-range interaction between microscopic polar regions in the relaxator ferroelectrics at $T \ll T_{max}$ [31].

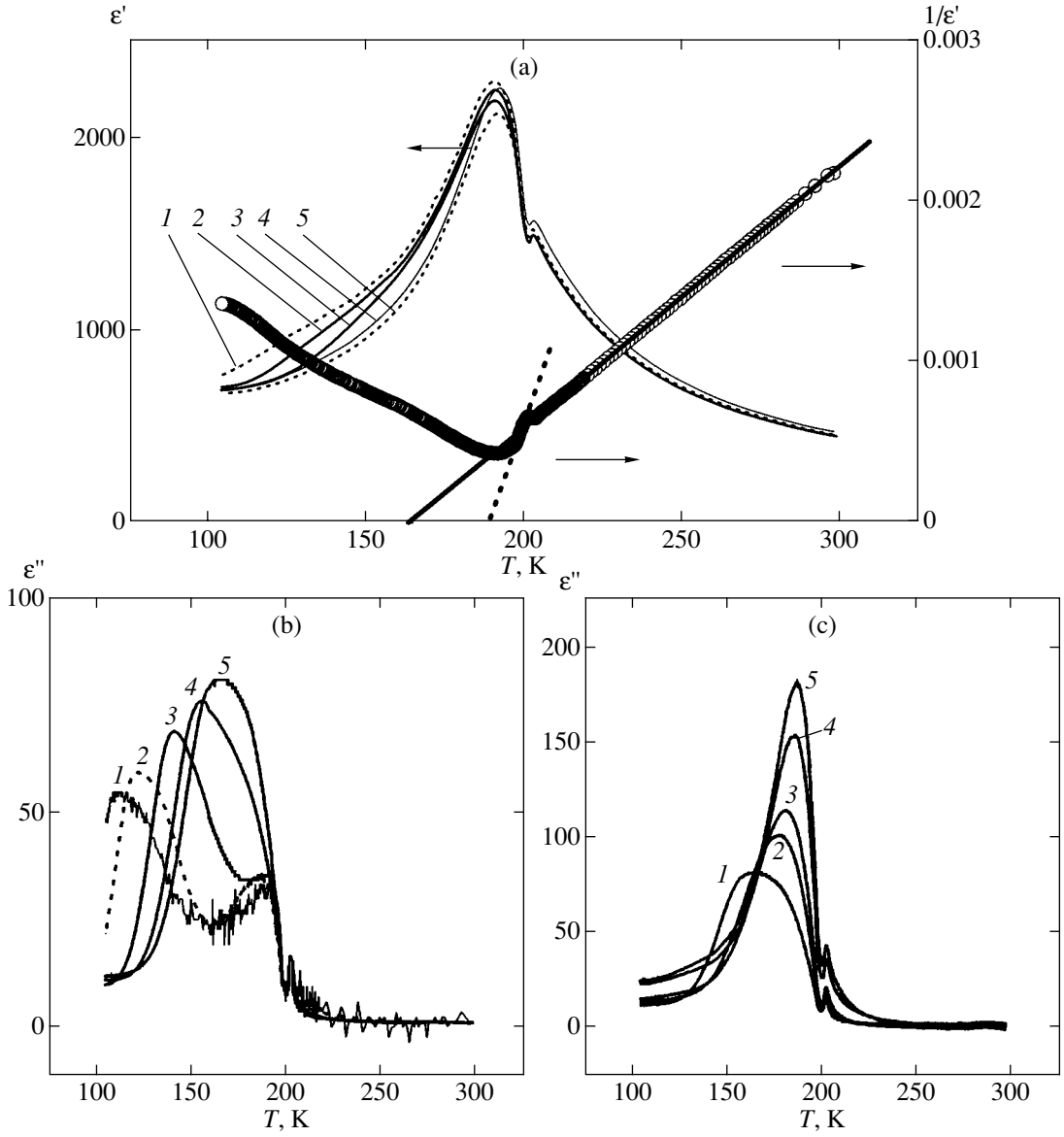

Fig. 1. The experimental temperature dependences of ε', ε'', and 1/ε' measured at various frequencies on the samples of $Cd_2Nb_2O_7$ ceramics slowly cooled (0.5 K/min) in an alternating electric field $E_{ac} \approx 2$ V/cm ($E_{dc} = 0$): (a) ε'(T) measured at 0.5 (*1*), 10 (*2*), 100 (*3*), 5000 (*4*), and 13000 kHz (*5*) and the 1/ε'(T) curve for 5 kHz; (b) ε''(T) measured at 0.5 (*1*), 5 (*2*), 100 (*3*), 500 (*4*), and 1000 kHz (*5*); (c) ε''(T) measured at 1000 (*1*), 3000 (*2*), 5000 (*3*), 10000 (*4*), and 13000 kHz (*5*). The straight lines in Fig. 1a show the approximation of 1/ε'(T) by the Curie–Weiss law at 5 kHz in a broad temperature interval above T_s (solid line) and in the interval $T_c < T < T_s$ (dashed line).

3. RESULTS AND DISCUSSION

3.1. Temperature and Frequency Dependences of the Complex Dielectric Permittivity

Previously, it was reported that $Cd_2Nb_2O_7$ can feature several relaxation processes at $T < T_c$ (i.e., in the ferroelectric state), which was explained by the presence of ferroelectric domains of various types and by changes in the structure of these domains [2, 10–14, 18, 22, 30]. However, neither the nature of relaxation processes observed in the region of T_c was elucidated, nor was a relation between these processes and the ferroelectric behavior of the system established. For this reason, our analysis of the temperature and frequency dependences of the dielectric response was aimed primarily at clarifying these questions.

Figure 1 shows the experimental curves of ε'(T), ε''(T), and 1/ε'(T) measured at several fixed frequencies in the range from 100 Hz to 13 MHz. The phase transition at T_s = 203.5 K is manifested by clearly pronounced anomalies on the ε'(T) and ε''(T) curves. It should be noted that small changes (between 201 and 206 K) in the temperature of this phase transition rela-

tive to the value (T_s = 205 K) most typical of the given pyrochlore were also reported previously for both single crystals and ceramics [11–14, 17, 21]. Note that, in most cases, the value of $T_c \approx 195$–196 remained virtually unchanged. It was suggested that the observed changes in T_s are related to the presence of uncontrolled impurities in the samples, which leads to a local breakage of the ideal pyrochlore structure [18, 19, 21, 32]. On the whole, elucidating the reasons for the observed behavior of T_s and T_c in $Cd_2Nb_2O_7$ would require a deeper analysis.

The phase transition at T_c = 196 K corresponds to a small bending in the $\varepsilon'(T)$ curve (Fig. 1a) and to a clear anomaly in the $\varepsilon''(T)$ curve at frequencies below 500 kHz (Fig. 1b, curves *1–4*). Above 500 kHz, the T_c determines a limiting shift of the intense anomaly in the $\varepsilon''(T)$ curve toward higher temperatures (Fig. 1b, curves *4* and *5*; Fig. 1c, curves *1–5*). In the entire frequency range studied, the maxima in the $\varepsilon'(T)$ and $\varepsilon''(T)$ curves are observed at $T < T_c$. As the frequency increases from 100 Hz to 13 MHz, the permittivity $\varepsilon'(T)$ in the region of T_c decreases, whereas the losses $\varepsilon''(T)$ tend to grow. This behavior is characteristic of a normal ferroelectric phase transition and the related relaxation of the domain wall oscillations in a weak electric field E_{ac} [33].

The behavior of $\varepsilon'(T)$ and $\varepsilon''(T)$ at $T < T_c$ observed with decreasing frequency—namely, the dispersion of ε'_{max} and ε''_{max} in a broad range of frequencies (100 Hz to 13 MHz), the shift of ε'_{max} and ε''_{max} toward lower temperatures, a relatively small variation in ε'_{max} at a strong change in ε''_{max}, the broadening of $\varepsilon'(T)$ in the region of ~150 K (Fig. 1a), and the asymmetric anomaly in $\varepsilon''(T)$ in the region of ~150 K at frequencies below 1 MHz (Fig. 1b)—is evidence that several dielectric relaxation processes occur simultaneously in the ferroelectric phase of $Cd_2Nb_2O_7$.

The process developed in the region of 180–192 K is characterized by an increase in ε'_{max} and by a slow shift of T_{max} toward lower temperatures with decreasing frequency (from T_{max} = 191.6 K at 12 MHz to 189 K at 100 Hz). Simultaneously, another relaxation process is developed in the region of ~150 K (Fig. 1a). This process was repeatedly mentioned [2, 10, 11, 14, 18], but the nature of this feature remains unclear. The maximum in the $\varepsilon''(T)$ curve, in contrast to the ε'_{max} value, rapidly decreases with decreasing frequency and shifts toward lower temperatures. This variation is nonmonotonic, being determined by different processes at frequencies above 1 MHz (Fig. 1c) and below this value (Fig. 1b). One of these processes dominates in the temperature region of 180–192 K (below the characteristic temperature $T_f \sim 182$ K, the characteristic ε'' value becomes virtually independent of the frequency; see Fig. 1c, curves *2–5*).

At a frequency of 1 MHz, the $\varepsilon''(T)$ curve exhibits strong broadening, becomes asymmetric (toward $T > T_{max}$), and changes curvature in the regions of T_c and $T \sim 175$ K. This variation implies that, in addition to the relaxation of domains and the aforementioned process dominating at 180–192 K, a considerable contribution to the dielectric losses at a frequency of 1 MHz is provided by another relaxation process dominating at a lower temperature (in the region of ~150 K). Below 1 MHz, the $\varepsilon''(T)$ curves shows two clear anomalies: a relatively weak anomaly in the region of the phase transition at T_c and a strong one at ~150 K. The ε''_{max} peak corresponding to the latter anomaly more rapidly shifts toward lower temperatures than does ε''_{max} observed in the region of 180–192 K. However, this study is not aimed at elucidating the relaxation process developed at 150 K. The behavior of the dielectric response observed in the region of 180–192 K is generally characteristic of the relaxator ferroelectrics [26, 27]. Below, we will analyze the dielectric response of the compound studied in terms of the models describing the relaxator ferroelectrics.

Before proceeding with the discussion of our experimental results, let us point out another special feature in the dielectric behavior of $Cd_2Nb_2O_7$. In the region of T_{max}, the $\varepsilon'(T)$ and $\varepsilon''(T)$ curves are rather broad for both ceramic and single crystal samples [10–14, 30]. At the same time, significant broadening of the dielectric curves for the ceramics in comparison to those of the single crystals in the region of T_{max}, as well in the vicinity of T_s and T_c (second-order phase transitions [17, 18, 21, 22]), was neither observed in our experiments nor reported by other researchers. These facts indicate that the behavior of $Cd_2Nb_2O_7$ in the region of T_{max} is determined by the internal properties of this compound, rather than by the quality of the samples studied. Moreover, a broad maximum in the $\varepsilon'(T)$ and $\varepsilon''(T)$ curves at T_{max} is characteristic of the relaxator ferroelectrics [15, 25–27].

3.2. Deviations from the Curie–Weiss Law in the Paraelectric Phase

The temperature dependence of the inverse dielectric permittivity of $Cd_2Nb_2O_7$ (Fig. 1a) in the paraelectric phase ($T > T_c$) exhibits two regions separated by the phase transition at $T = T_s$. Both in a broad range of temperatures above T_s and in the interval $T_c < T < T_s$, the behavior of $1/\varepsilon'$ is described by the Curie– Weiss law $1/\varepsilon'(T) = [(T - \theta)/C]$. However, the Curie constants C and the Curie–Weiss temperatures θ in the two temperature intervals are not the same. At first glance, this difference can be related to a weak anomaly (break) on the $\varepsilon'(T)$ curve at T_s. However, it will be shown below that the relaxator state in the vicinity of T_{max} may also influ-

ence the C and θ values in the aforementioned temperature intervals. Evaluation of these parameters above and below T_s at a frequency of 5 kHz yields $C = 0.61 \times 10^5$ and 0.18×10^5 K and [theta] = 161 and 188 K, respectively. For the comparison, we have also determined the Curie constant and the Curie–Weiss temperature in the region of $T > T_s$ at a frequency of 12 MHz: $C = 0.64 \times 10^5$ K; θ = 160 K.

The ε'(T) curve calculated using the C and θ values determined from the slope of 1/ε'(T) in the interval $T_c < T < T_s$ significantly deviates from the experimental curve observed for the paraelectric phase at $T > T_s$ (Fig. 2). If the parameters C and θ are determined from the slope of 1/ε'(T) in the broad temperature interval above T_s, the calculated ε'(T) curve deviates from the experimental plot on approaching the ferroelectric phase transition ($T \longrightarrow T_c^+$). A reason for which the empirical parameters fail to describe the variation of permittivity in the region of the ferroelectric phase transition consists in that the behavior of ε'(T) in the vicinity of T_s and above this temperature (i.e., in the interval for which the parameters C and θ were calculated) is determined by the superposition of processes related to the ferroelectric and ferroelastic phase transitions. The contribution of the latter process can be ignored only at temperatures above ~250 K (Figs. 1a and 1c). Actually, the behavior of the dielectric permittivity of $Cd_2Nb_2O_7$ in the paraelectric phase should be described using the C and θ values calculated in a broad temperature interval above 250 K (i.e., at temperature significantly higher than T_{max}, T_c, and T_s).

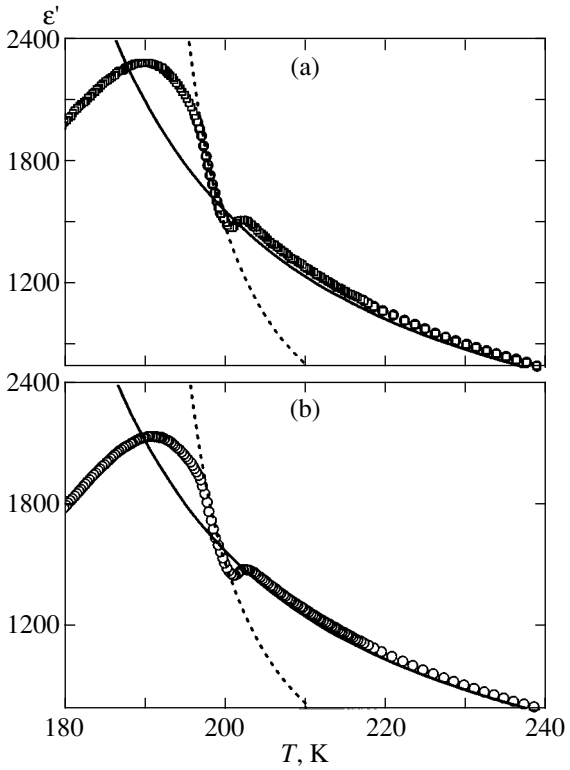

Fig. 2. The plots of ε'(T) for (a) 1 kHz and (b) 3 MHz: (open circles) experiment; (solid curve) the Curie–Weiss relationship ε'(T) = [C/(T – θ)] calculated by formula (1) for $C = 0.61 \times 10^5$ K and θ = 161 K ($T > T_s$); (dashed curve) the Curie–Weiss relationship calculated for $C = 0.18 \times 10^5$ K and θ = 188 K ($T_c < T < T_s$).

The Curie constants calculated in the interval of temperatures above T_s for various frequencies are smaller as compared to the values reported for $Cd_2Nb_2O_7$ (~1.2×10^5 K) [12–14, 20, 33] and the values characteristic of most ferroelectrics of the displacement type [33]. One possible reason for this discrepancy in the Curie constants can be related to the fact that previous ε'(T) measurements were performed on the samples cooled and heated at a higher rate (3 to 10 K/min). It was shown [10, 19] that a decrease in the sample heating rate leads to a significant decrease in the dielectric permittivity far from the phase transition temperature and especially in the region of T_{max}, T_c, and T_s. Also previously observed was a continuous decrease in ε'(T) either in the course of multiply repeated cooling–heating cycles in the region of T_{max} or upon keeping the sample for a prolonged time at a fixed temperature in the region of 180–192 K; the system did not attain an equilibrium state even after a 3-h period of time [16, 19, 20]. At the same time, the values of T_{max}, T_c, and T_s exhibited no variation with decreasing cooling/heating rate and with repeated cooling–heating cycles. After heating the sample up to room temperature followed by cooling at the same rate, both the initial ε'(T) value and the shape of this curve were reproduced. All the above facts are indicative of a nonequilibrium character of processes in the vicinity of T_{max} and in the region of 180–192 K, suggesting that these processes start at a temperature much higher than T_{max}. These features are generally typical of a relaxator ferroelectric featuring a glasslike behavior [31, 34]. Thus, the phase transitions at T_s and T_c take place on the background of rapidly developing nonequilibrium processes in the system. This may account both for a change in the C and θ values with decreasing cooling rate and for the different character of this variation observed above T_s (i.e., far from T_c) and on approaching T_c ($T_c < T < T_s$). Apparently, the same factors may account for a small variation of C and θ with the probing field frequency in the temperature interval above T_s. The Curie constant of $Cd_2Nb_2O_7$ above T_s was reported to decrease during uniaxial [35] and hydrostatic compression [36]. For example, when the uniaxial pressure was increased up to 1.5 MPa, the C value first rapidly dropped from 1.2×10^5 to 0.6×10^5 K and then varied only slightly [35].

Figure 2 shows the temperature dependence of the dielectric permittivity of $Cd_2Nb_2O_7$ at two frequencies approximated by the Curie–Weiss relationship

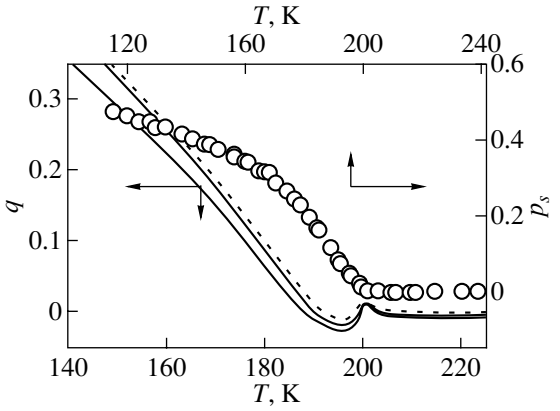

Fig. 3. Plots of the order parameter q (solid and dashed curves) measures at a probing field frequency of 1, 3000, and 12 000 kHz (left to right, respectively) and the reduced spontaneous polarization p_s (open circles) in $Cd_2Nb_2O_7$. The $q(T)$ curve was calculated by formula (1) using deviations from the Curie–Weiss law determined at the corresponding frequencies (E_{dc} = 0); the $p_s(T)$ curve was constructed using data on the pyroelectric current measured in an external electric field of E_{dc} ~ 0.95 kV/cm.

$\varepsilon'(T) = [C/(T - \theta)]$. A strong deviation from the Curie–Weiss law is observed on approaching T_c and T_{max}; the difference increases with decreasing frequency and temperature. In the region of T_{max}, the experimental $\varepsilon'(T)$ curve lies above the $C/(T - \theta)$ function calculated for $C = 0.61 \times 10^5$ K, θ = 161 K and below this function calculated for $C = 0.18 \times 10^5$ K, θ = 188 K. As was noted above, the calculated $\varepsilon'(T)$ values are smaller than the experimental ones as a result of using "understated" parameters C and θ. The fact is that the C and θ values were determined in the interval of temperatures featuring processes related not only to the ferroelectric phase transition, but to the ferroelastic phase transition and the nonequilibrium state as well (rather than at $T > 250$ K).

A decrease in the dielectric permittivity accompanied by deviation from the Curie–Weiss law in the region of T_{max} (as revealed by comparing the experimental curve to that calculated for $C = 0.18 \times 10^5$ K and θ = 188 K) can be interpreted by analogy with the behavior of spin glasses [37] and relaxator ferroelectrics of the PMN type [26–28]. It is suggested that microscopic polar regions may appear in these systems far from the phase transition temperature. A strong correlation developed between these local regions with decreasing temperature may significantly suppress the dielectric permittivity. Indirect evidence for the formation of microscopic polar regions far from T_c and T_s in $Cd_2Nb_2O_7$ is provided by behavior of the permittivity in response to changes in the regime of temperature scanning (see above), by the microscopic (11–15 nm in size) polar clusters observed in the ferroelectric phase [38], and by the impossibility of establishing a long-range order in the orientation of Cd–O–Cd dipole chains in the $(CdO_8)^{n-}$ sublattice in the pyrochlore structure [6, 22, 39].

Deviation of the dielectric permittivity from the Curie–Weiss law, the ambiguous behavior of $\varepsilon'(T)$ in the vicinity of T_c and T_{max} related to the use of two sets of parameters C and θ, and the uncertainty in determining the C and θ values in the temperature interval above T_s (see the considerations above)—all these facts suggest that the parameters C and θ in $Cd_2Nb_2O_7$ are temperature-dependent, which reflects the appearance of local polar regions in the system at high temperatures. Under these conditions, we can describe deviations from the Curie–Weiss law with the aid of the Sherrington–Kirkpatrick relationship [37]

$$\varepsilon' = c[1 - q(T)]/[T - \theta(1 - q(T))], \qquad (1)$$

where $q(T)$ is the local order (spin or dipole glass) parameter. Description of the experimental $\varepsilon'(T)$ curves in the range of frequencies from 100 Hz to 13 MHz using relationship (1) with $C = 0.61 \times 10^5$ K and θ = 161 K provides for a good coincidence (Figs. 2a and 2b). This implies that we can explain the dielectric behavior of $Cd_2Nb_2O_7$ in terms of a model involving the development of a correlation between microscopic polar regions with decreased temperature and reduced thermal disorder. In this case, a change in the permittivity on approaching T_c and T_{max} is determined as $\Delta\varepsilon' \sim q(T) \sim \langle P_i P_j \rangle^{1/2}$ [33], where P_i and P_j are the polarization vector components of the adjacent clusters.

Figure 3 shows the $q(T)$ curves calculated for several frequencies by formula (1) using the deviation of $\varepsilon'(T)$ from the Curie–Weiss law (by analogy with the case of spin and dipole glasses [26, 37]). The higher the frequency, the greater the deviation from the Curie–Weiss law. This is characteristic of the spin and dipole glasses [37] and the relaxator ferroelectrics featuring a glasslike behavior [26–28]. As the temperature increases from 140 to 190 K, the q value decreases almost linearly, not going to zero at the characteristic temperature T_f ~ 182 K (see also Fig. 1c). At all frequencies, the further decrease in q exhibits a tendency of delay to higher temperatures. However, the phase transitions taking place at T_s and T_c hinder the analysis of q at high temperatures and the determination of a T_d value at which the local polarization disappears and $q(T)$ goes to zero (T_d is always higher than T_c) [28]. In contrast to the q value, the reduced polarization $p_s = P_s(T)/P_s$ (100 K) exhibits a nonlinear variation in the temperature interval from 140 to 190 K and goes to zero at a certain temperature above T_c, these changes taking place within a rather narrow temperature interval (Fig. 3).

The phase transition temperature (T_c = 200 K) determined from the temperature dependence of the reduced polarization in the external field with a strength of 0.95 kV/cm is higher than the value (T_c = 196 K) determined from the temperature dependence of the permit-

tivity obtained in our experiments and reported in [11–14, 19, 20], as well as from data on the domain structure variation [16, 17] and the lattice dynamics [22]. As is well known, a field strength of about 1 kV/cm does not affect the permittivity of $Cd_2Nb_2O_7$ in the vicinity of T_c, but decreases this value in the vicinity of T_{max} [11, 12, 17, 30]. On the other hand, the applied electric fields with E_{dc} up to 15 kV/cm do not change T_c of this compound [11, 12, 30, 38]. Apparently, the shift of $p_s(T)$ toward higher temperatures in a relatively weak electric field E_{dc} is related to the fact that the ferroelectric phase features, in addition to the reversible polarization typical of the normal ferroelectric, a local polarization of microscopic clusters (with a size of 11–15 nm [38]) characteristic of a relaxator ferroelectric. The latter polarization determines behavior of the system in the external electric field at temperatures above T_c.

3.3. Decrease in the Dielectric Relaxation Rate at 190 K

Figure 4 shows a change in the inverse temperature of the maximum permittivity ($1/T_{max}$) in the region of 190 K as a function of the frequency. As can be seen, the dielectric relaxation rate characterizing the process in this interval nonlinearly decreases with decreasing temperature, which is typical of relaxator dielectrics [26, 27]. The dispersion was modeled by the empirical Vogel–Fulcher relationship [40]

$$f = f_0 \exp[-E_a/k(T - T_f)], \qquad (2)$$

where f_0 is a factor related to the nature of the relaxation mechanism (and determining the relaxation rate at $T \longrightarrow \infty$), E_a is the relaxation activation energy, k is the Boltzmann constant, T is the absolute temperature, and T_f is the characteristic polarization fluctuation freezing temperature. A good coincidence with the experimental data was obtained in the frequency range from 1 to 13 MHz for $E_a \approx 0.01$ eV, $T_f = 183$ K, and $f_0 = 1.9 \times 10^{12}$ Hz. The polarization fluctuation activation energy (E_a) and the preexponential factor (f_0) for $Cd_2Nb_2O_7$ are on the same order of magnitude as the analogous values in relaxator dielectrics of the PMN type [26, 27], being characteristic of a thermoactivated process. The T_f value is close to a temperature at which the dielectric losses in $Cd_2Nb_2O_7$ become frequency-independent (Fig. 1c). According to [41], this implies that behavior of the system below T_f becomes nonergodic.

Deviation of the experimental points from the calculated curve in the frequency range from 100 Hz to 1 MHz is probably related to a superposition of the process dominating at 190 K and another process dominating at 150 K (Figs. 1b and 1c). For this reason, approximation of the experimental data in terms of the Vogel–Fulcher relationship in the entire frequency range studied (100 Hz to 13 MHz) yields physically unreasonable values of the activation energy E_a in the region of 190 K

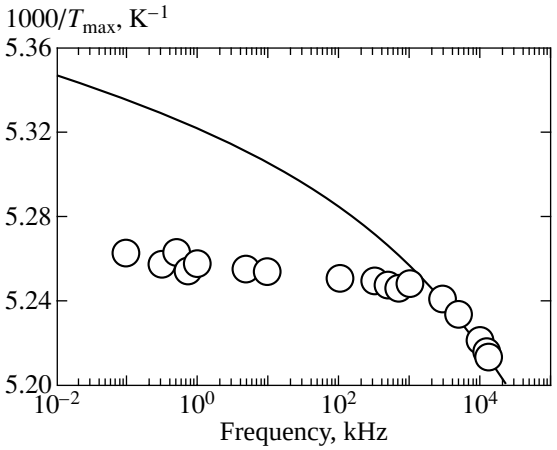

Fig. 4. The plot of the inverse temperature of maximum permittivity in the region of 180–192 K versus frequency: (open circles) experiment; (solid curve) calculation by the Vogel–Fulcher relationship (2).

and the polarization fluctuation freezing temperature T_f ($f_0 \sim 10^{13}$ Hz): $E_a = 0.003$ eV, $T_f = 189$ K. Provided that the factor $f_0 \sim 10^{13}$ Hz determining the nature of the relaxation mechanism does not change, a good coincidence of the experimental and calculated curves can be obtained only for certain E_a and T_f values, which restricts the possibility of varying these parameters.

4. CONCLUSION

In order to elucidate the nature of a polydisperse dielectric response of $Cd_2Nb_2O_7$ in the temperature region of 180–192 K and the influence of a relaxation process taking place in this region on the dielectric behavior of the system during the ferroelectric phase transition ($T_c = 196$ K), we have studied this pyrochlore by dielectric spectroscopy methods in a broad range of frequencies (from 100 Hz to 13 MHz) and temperatures (from 80 to 300 K). The temperature and frequency dependences of the complex dielectric permittivity of the system were analyzed taking into account the modern notions about features of relaxator ferroelectricity, based on the Curie–Weiss, Vogel–Fulcher, and Sherrington–Kirkpatrick relationships [26–28]. We have demonstrated that the dispersion of the dielectric response in $Cd_2Nb_2O_7$ in the frequency range from 100 Hz to 13 MHz in the temperature region of 180–192 K is characteristic of a relaxator ferroelectric featuring a glasslike behavior. The parameters of this state were determined, including the activation energy of the polarization fluctuations ($E_a \approx 0.01$ eV), the relaxation rate for $T \longrightarrow \infty$ ($f_0 = 1.9 \times 10^{12}$ Hz), and the polarization fluctuation freezing temperature ($T_f = 183$ K). In $Cd_2Nb_2O_7$ pyrochlore, in contrast to the known relaxator ferroelectrics of the PMN type studied previously [26, 27], this state coexists with the normal ferroelectric state appearing at T_c.

ACKNOWLEDGMENTS

This study was supported by the Russian Foundation for Basic Research (project no. 00-02-16900) and by the J. Mianowski Fund.

REFERENCES

1. M. A. Subramanian, G. Aravamudan, and G. V. Subba Rao, Prog. Sol. St. Chem. **15**, 55 (1983).
2. N. N. Kolpakova, I. L. Shul'pina, M. P. Shcheglov, *et al.*, Ferroelectrics **240**, 265 (2000).
3. A. W. Sleight, J. L. Gillson, J. F. Weiher, and W. Bindloss, Sol. St. Comm. **14**, 357 (1974).
4. P. C. Donohue, J. M. Longo, R. D. Rosenstein, and L. Katz, Inorg. Chem. **4**, 1152 (1965).
5. F. Brisse, D. J. Stewart, V. Seidl, and O. Knop, Can. J. Chem. **50**, 3648 (1972).
6. K. Lukaszewicz, A. Pietraszko, J. Stepien-Damm, and N. N. Kolpakova, Mater. Res. Bull. **29**, 987 (1994).
7. R. A. McCauley, J. Appl. Phys. **51**, 290 (1980).
8. N. N. Kolpakova, A. Pietraszko, S. Waplak, and L. Szczepanska, Sol. St. Comm. **79**, 707 (1991).
9. A. M. Sleight and J. D. Bierlein, Sol. St. Comm. **18**, 163 (1976).
10. N. N. Kolpakova, M. Wiesner, G. Kugel, and P. Bourson, Ferroelectrics **190**, 179 (1997); **201**, 107 (1997).
11. Ch. Ang, R. Guo, A. S. Bhalla, and L. E. Cross, J. Appl. Phys. **87**, 7452 (2000).
12. V. A. Isupov and G. I. Tarasova, Fiz. Tverd. Tela (Leningrad) **25**, 1018 (1983) [Sov. Phys. Solid State **25**, 587 (1983)]; Fiz. Tverd. Tela (Leningrad) **25**, 1013 (1983) [Sov. Phys. Solid State **25**, 584 (1983)].
13. F. M. Salaev, L. S. Kamzina, N. N. Kraĭnik, *et al.*, Fiz. Tverd. Tela (Leningrad) **25**, 163 (1983) [Sov. Phys. Solid State **25**, 89 (1983)].
14. S. L. Swartz, C. A. Randall, and A. S. Bhalla, J. Am. Ceram. Soc. **72**, 637 (1989).
15. D. Viehland, M. Wuttig, and L. E. Cross, Ferroelectrics **120**, 71 (1991).
16. N. N. Kolpakova, I. L. Shul'pina, L. Szczepanska, and P. Piskunowich, Pis'ma Zh. Tekh. Fiz. **23** (24), 64 (1997) [Tech. Phys. Lett. **23**, 972 (1997)].
17. Z. G. Ye, N. N. Kolpakova, J.-P. Rivera, and H. Schmid, Ferroelectrics **124**, 275 (1991).
18. N. N. Kolpakova, M. Wiesner, I. L. Shul'pina, *et al.*, Ferroelectrics **185**, 131 (1996).
19. N. N. Kolpakova, L. Szczepanska, I. L. Shul'pina, *et al.*, Ferroelectrics **190**, 173 (1997).
20. G. A. Smolenskiĭ, N. N. Kolpakova, S. A. Kizhaev, *et al.*, Fiz. Tverd. Tela (Leningrad) **26**, 989 (1984) [Sov. Phys. Solid State **26**, 604 (1984)].
21. P. P. Markovin, R. V. Pisarev, E. S. Sher, and B. N. Shermatov, Fiz. Tverd. Tela (Leningrad) **25**, 3642 (1983) [Sov. Phys. Solid State **25**, 2096 (1983)].
22. N. N. Kolpakova, S. Waplak, and W. Bednarski, J. Phys.: Condens. Matter **10**, 9309 (1998).
23. A. Kuster, Dissertation, Doctor der Naturwissenschaften (Eberhard-Karls-Universität zu Tübingen, Tübingen, Germany, 1992).
24. N. N. Kolpakova, B. Hilczer, and M. Wiesner, Phase Transit. **47**, 113 (1994).
25. F. Chu, I. M. Reaney, and N. Setter, J. Appl. Phys. **77**, 1671 (1995).
26. D. Viehland, S. J. Jang, L. E. Cross, and M. Wuttig, Phys. Rev. B **46**, 8003 (1992); Philos. Mag. B **64**, 335 (1991).
27. D. Viehland and J.-F. Li, J. Appl. Phys. **75**, 1705 (1994).
28. G. Burns and F. H. Dacol, Sol. St. Comm. **48**, 853 (1983); Phys. Rev. B **28**, 2527 (1983).
29. E. Aleshin and R. Roy, J. Am. Ceram. Soc. **45**, 18 (1962).
30. V. A. Isupov, G. I. Golovshchikova, and I. E. Myl'nikova, Ferroelectrics **8**, 507 (1974).
31. D. Viehland, J. F. Li, S. J. Jang, *et al.*, Phys. Rev. B **46**, 8013 (1992).
32. I. L. Shul'pina, N. N. Kolpakova, M. P. Shcheglov, and A. O. Lebedev, Pis'ma Zh. Tekh. Fiz. **25** (14), 26 (1999) [Tech. Phys. Lett. **25**, 561 (1999)].
33. F. Jona and G. Shirane, *Ferroelectric Crystals* (Pergamon, New York, 1962), p. 29.
34. E. V. Colla, E. Yu. Koroleva, N. M. Okuneva, and S. B. Vakhrushev, Ferroelectrics **184**, 209 (1996).
35. N. N. Kolpakova, R. Margraf, and M. Polomska, J. Phys.: Condens. Matter **6**, 2787 (1994).
36. N. Yasuda, S. Fujimoto, K. Tanaka, and T. Hachiga, J. Phys. D **17**, 2069 (1984).
37. D. Sherrington and S. Kirkpatrick, Phys. Rev. Lett. **35**, 1792 (1975).
38. Ch. Ang, L. E. Cross, R. Guo, and A. S. Bhalla, Appl. Phys. Lett. **77**, 732 (2000).
39. A. W. Sleight, Inorg. Chem. **7**, 1704 (1968).
40. H. Vogel, Z. Phys. **22**, 695 (1921); G. Fulcher, J. Am. Ceram. Soc. **8**, 339 (1925).
41. E. Courtens, Phys. Rev. Lett. **52**, 69 (1984).

Translated by P. Pozdeev

Journal of Experimental and Theoretical Physics, Vol. 94, No. 2, 2002, pp. 403–410.
Translated from Zhurnal Éksperimental'noĭ i Teoreticheskoĭ Fiziki, Vol. 121, No. 2, 2002, pp. 471–479.

SOLIDS
Electronic Properties

Kinetics of Brownian Particle Trapping by Randomly Distributed Traps of Various Sizes

Yu. A. Makhnovskiĭ[a, *], A. M. Berezhkovskiĭ[b], and I. V. Grigor'ev[a, c, **]

[a]*Topchiev Institute of Petrochemical Synthesis, Russian Academy of Sciences, Leninskii pr. 29, Moscow, 117912 Russia*
[b]*Center for Information Technology, National Institutes of Health Bethesda, MD 20892 USA*
[c]*Permanent address: Karpov Institute of Physical Chemistry, ul. Vorontsovo Pole 10, Moscow, 103064 Russia*
**e-mail: yuam@ips.ac.ru*
***e-mail: grigorjev@ips.ac.ru*
Received August 2, 2001

Abstract—Diffusion of a particle in a medium in the presence of absorbing traps of various size is considered. A theory describing the kinetics of particle trapping in the entire interval of time is suggested. Analytical relations for the probability of a particle survival in situations when many-body effects are weak and when they dominate are obtained. It is shown that polydispersity of traps leads to the slowdown of particle trapping and to attenuation of many-body effects inherent in the problem. © *2002 MAIK "Nauka/Interperiodica"*.

1. INTRODUCTION

Processes in which transformation and loss of active particles is controlled by diffusion are widespread throughout physics, chemistry, and biology. Among them are, for example, absorption of optical and magnetic excitations in solid [1], fast chemical reactions [2], quenching of fluorescence [3], and ligand binding to proteins [4]. The study of kinetics of diffusion-controlled processes leads to the problem of survival of a Brownian particle in a medium with randomly distributed traps [5, 6].

The simplest model of spatially noncorrelated spherical traps of identical radius, which was first considered in the classical work by Smoluchowski [7], is best studied. Smoluchowski's approach is based on the approximation that ignores the mutual influence of traps on the loss of particles. Later, the original one-body theory was elaborated in order to take into account many-body effects, which are inherent in the problem (see the recent monographs [8, 9] and references therein). Although an exact solution was obtained only in the one-dimensional case [10], a quite satisfactory understanding of the process kinetics has been achieved for the space of arbitrary dimension in the entire interval of time. In particular, for the most important three-dimensional case, the following facts have been established:

(i) Particle trapping always proceeds slower than is predicted by the time dependence of the survival probability found by Smoluchowski,

$$P_{Sm}(t; b) = \exp(-4\pi bcDt - 8b^2c\sqrt{\pi Dt}), \qquad (1)$$

where b and c are the radius and concentration of traps, and D is the particle diffusion coefficient. At the initial stage of the process, Eq. (1) provides a good approximation, and taking into account many-body effects only yields a correction that reflects the trapping slowdown at this stage [11].

(ii) At the final stage, the process goes much slower than at the beginning. This so-called fluctuation slowdown occurs due to the fact that the long-time kinetics is determined by the survival of particles that remain, from the very beginning, in fluctuation voids not containing traps. The asymptotic behavior of the exact solution to the problem at $t \longrightarrow \infty$,

$$-\ln P_\infty(t) \approx \frac{5}{3}(2\pi^4)^{2/5}(c^{2/3}Dt)^{3/5}, \qquad (2)$$

was found in [10, 12–14] on the basis of the optimal fluctuation method suggested by Lifshits in [15] for the calculation of the density "tail" of a quantum particle in the field of randomly distributed scatterers.

However, the model of traps with various radii, which is important for many applications, is less understood. We are aware of only several attempts to take into account the polydispersity of traps in the kinetics of diffusion-controlled reactions [16–19]. In these studies, many-body effects were neglected, and the emphasis was placed on determining the rate constant in the steady-state case on the basis of data obtained by computer simulation.

In this paper, we suggest a many-body theory of Brownian particle trapping by polydisperse traps. The theory not only provides a description of the process on the same completeness and accuracy level as those available for identical traps, but also demonstrates new features introduced by the polydispersity factor in the reaction kinetics. While developing the theory, we generalized the approach to the analysis of many-body

effects in the kinetics of diffusion-controlled reactions suggested in [11] and successfully used to study the influence of trap clustering [20] and an external field [21] on the particle trapping rate. The main idea of this approach is in the representation of the particle survival probability as the mean of an appropriate Brownian motion functional over all factors that cause the probabilistic properties of the process. For identical traps, there are two such factors—the stochasticity of the Brownian motion and a random distribution of traps. In the problem considered here, there exists one more probabilistic factor—the random size of traps. We show that the new factor, along with the random distribution of traps and the random nature of the Brownian motion, leads to the process slowdown. Moreover, the polydispersity of traps manifests itself at the initial stage of the process, while the fluctuations studied earlier cause substantial deviations in the kinetics only at asymptotically long times.

In Section 2, it is shown how the additional probabilistic factor can be taken into account, and a general expression for the particle survival probability (for a given distribution of traps in size) is obtained as a path-integral. Comparing this expression with the similar one for identical traps (Section 3), we will see that, at a fixed concentration and volume fraction of traps, their polydispersity at least does not deteriorate the conditions of particle survival. This effect is most pronounced at the initial stage of the process, where the mean-field approximation is applicable. An analysis of the mean-field dependence (Section 4) shows that the trapping process is the fastest when the traps are identical, and it is the slower the greater the size spread. In Section 5, we use the cumulant expansion of the survival probability to derive a correction to the mean-field dependence due to many-body effects. This correction reflects the slowdown of particle trapping at the initial stage of the process. Finally, in Section 6, we discuss the kinetics of particle trapping at the final stage of the process and show that in this case the fluctuation slowdown (2) takes place as in the case of identical traps. Although the polydispersity of traps does not modify the dependence characterizing the kinetics at the final stage of the process, it leads to the decrease in the fraction of particles trapped at this stage. This observation clearly demonstrates that the polydispersity of traps attenuates many-body effects.

2. STATEMENT OF THE PROBLEM AND AN APPROACH TO ITS SOLUTION

Consider a point particle that diffuses in a medium with randomly distributed static traps. The concentration of traps is assumed to be c. As in the conventional model, we assume that the traps are perfectly absorbing spheres (i.e., a particle is absorbed as soon as it touches the trap) uniformly distributed in space. However, in contrast to the conventional model, we assume that the traps are different in size; more precisely, the radius of the trap ξ is a random variable (continuous or discrete) described by the probability density $f(\xi)$ normalized to unity:

$$\int_{b_{\min}}^{b_{\max}} f(\xi)d\xi = 1, \tag{3}$$

Here, $b_{\min}$ and $b_{\max}$ are the minimal and maximal radius of the traps. The distribution of radii can also be described by the set of moments $\overline{\xi^k}$ ($k = 1, 2, \ldots$):

$$\overline{\xi^k} = \int_{b_{\min}}^{b_{\max}} \xi^k f(\xi)d\xi. \tag{4}$$

We assume that the volume fraction of the traps

$$\phi = \frac{4}{3}\pi c\overline{\xi^3}$$

is small, i.e., $\phi \ll 1$. The problem is to find the time dependence of a particle survival probability, $P(t)$, that determines the process kinetics and to exhibit the effect of trap polydispesrity. We assume that the concentration and the volume fraction of traps ("the volume of the absorbing phase") are always the same.

First, we consider the simplest model in which a Brownian particle starts from the origin and moves along a Wiener trajectory W_t in the presence of a single trap of radius ξ centered at the point $\mathbf{r}$. In order to describe the particle survival, we introduce the quantity $P(t|W_t|\mathbf{r}|\xi)$ that is equal to unity if the particle survives during the time t and to zero if the particle is trapped. The survival condition is formulated in a very simple form if we consider the process from the particle's point of view. Then, the particle is at rest at the point $\mathbf{r}$, and the trap center moves along the trajectory W_t. Then, the trap covers the region $\omega_\xi(W_t)$ that is a tube of radius ξ with the trajectory W_t as its axis. In the theory of stochastic processes, this ξ neighborhood is called the Wiener sausage [22, 23]. The particle survives if and only if the region $\omega_\xi(W_t)$ does not contain the point $\mathbf{r}$. This means that

$$P(t|W_t|\mathbf{r}|\xi) = 1 - I(\mathbf{r}; \omega_\xi(W_t)),$$

where $I(\mathbf{r}; \omega)$ is the indicator function that is equal to unity if $\mathbf{r}$ belongs to ω and is zero otherwise. Notice that the volume of the region $\omega_\xi(W_t)$ can be written in the form

$$v_\xi(W_t) \equiv v[\omega_\xi(W_t)] = \int I(\mathbf{r}; \omega_\xi(W_t))d\mathbf{r}. \tag{5}$$

When there are many traps such that the location and radius of each of them is fixed and equal to $\mathbf{r}_k$ and ξ_k for the kth trap, respectively, then the survival of the particle is characterized by the quantity

$$\prod_k P(t|W_t|\mathbf{r}_k|\xi_k) = \prod_k [1 - I(\mathbf{r}_k; \omega_{\xi_k}(W_t))]. \tag{6}$$

So far, we have not considered randomness. Actually, we deal with a randomly moving particle and a random distribution of traps of random sizes. This means that the survival probability $P(t)$ is the mean average of (6) over various realizations of trajectories W_t, trap locations $\{\mathbf{r}_k\}$, and their radii $\{\xi_k\}$.

First, we find the average over the trap size, which we will denote by a bar. Then, we find the average over the trap distribution. Taking into account that the trap centers have the Poisson distribution, this can be done by the conventional method (an auxiliary volume Ω containing $N = c\Omega$ trap centers is introduced that then tends to infinity):

$$P(t|W_t) = \lim_{\Omega\to\infty}\frac{1}{\Omega^N}\int_\Omega\ldots\int\overline{\prod_{\Omega k=1}^{N}[1-I(\mathbf{r}_k;\,\omega_k(W_t))]d\mathbf{r}_k}$$
$$= \lim_{\Omega\to\infty}\left[1-\frac{1}{\Omega}\int_\Omega\overline{I(\mathbf{r};\,\omega_\xi(W_t))d\mathbf{r}}\right]^N \qquad (7)$$
$$= \exp\left[-c\int\overline{I(\mathbf{r};\,\omega_\xi(W_t))}d\mathbf{r}\right] = \exp[-c\overline{v}_\xi(W_t)].$$

In the derivation of the last formula in (7), we used relation (5).[1] This formula shows that the survival probability of a particle that moves along a fixed trajectory in a medium with various traps is simply the product of the probabilities to avoid its absorption by traps of each type. Indeed, the probability for the particle to avoid the traps of radius ξ with the concentration $cf(\xi)d\xi$ is equal to the part of the configurations of such traps whose centers are at a distance greater than ξ from W_t. Since the positions of traps are independent of each other, this part is

$$\exp[-cv_\xi(W_t)f(\xi)d\xi].$$

Finally, averaging $P(t|W_t)$ over the trajectories of the particle W_t, which is denoted by angle brackets, we obtain the following expression for the particle survival probability:

$$P(t) = \langle\exp[-c\overline{v}_\xi(W_t)]\rangle. \qquad (8)$$

This is the fundamental relation for our approach. In its derivation, we actually passed from the conventional model of a point particle and spherical traps to the equivalent model of a spherical particle and point traps. In these terms, taking into account the polydispersity of traps means that we must take into account the random size of the particle, ξ. Under this approach, the key role is played by the partial mean of the Wiener sausage volume $\overline{v}_\xi(W_t)$, and the problem is essentially reduced to the analysis of statistical properties of this random variable, which describes the Brownian motion of a random-radius particle in the space free of traps.

3. THE GENERAL INEQUALITY

For monodisperse traps of radius b, the probability density

$$f(\xi) = \delta(\xi - b)$$

and, as it should be, Eq. (8) is reduced to the expression for the survival probability obtained in [11], where trapping by identical traps was considered:

$$P(t;\,b) = \langle\exp[-cv_b(W_t)]\rangle. \qquad (9)$$

Let us compare the survival probabilities in the case of polydisperse (8) and identical (9) traps assuming that the concentration and the volume fraction of traps are the same in both cases, i.e.,

$$\overline{\xi^3} = b^3 \qquad (10)$$

for any $f(\xi)$. It can be shown that $v_\xi(W_t)$ is a concave function of ξ^3 for any trajectory W_t. Then, by the well-known Jensen's inequality [24], the expected value of the concave function of a random variable does not exceed the function of the expected value of this variable. In our case, this means that for any trajectory

$$v_b(W_t) \geq \overline{v}_\xi(W_t);$$

hence, trapping by different traps proceeds, at any rate, no faster than that by identical traps (this is true for all time intervals), i.e.,

$$P(t) \geq P(t;\,b). \qquad (11)$$

It will be demonstrated below that (11) turns into a strict inequality at the initial stage of the process and turns into an equality at its final stage.

4. THE MEAN-FIELD APPROXIMATION

The principal difficulty in the kinetics analysis based on the representation of the survival probability in form (8) is related to the fact that there are no means to obtain an analytical estimate of the integral over Wiener trajectories. As in the case of identical traps [11], the simplest and the most effective way to overcome this difficulty is to invoke the mean-field approximation, which neglects fluctuations of the Wiener sausage volume. At the initial process stage, the applicability of this approximation is justified by the fact that up to asymptotically long times the main contribution to

[1] According to the definition of the survival probability, $P(0) = 1$. Generally, (7) does not satisfy this condition, since in its derivation we took into account the particles that started from the region occupied by a trap. However, it can be readily shown that the correct normalization is obtained if the proper volume of the particle is excluded from the Wiener sausage volume (in (7), integration must be performed over the domain $r \geq \xi$), i.e., if the volume is counted from its value at $t = 0$ as is done below.

the survival probability is made by typical trajectories, which determine the mean (over trajectories) value of the Wiener sausage volume. Using the dependence of the mean Wiener sausage volume $\langle v_b(W_t)\rangle$ on time (see [25]),

$$\langle v_b(W_t)\rangle = 4\pi bDt + 8b^2\sqrt{\pi Dt}, \tag{12}$$

it is easy to show that, in this approximation, Eq. (9) is reduced to the Smoluchowski formula (1).

In the case of polydisperse traps, the functional $\overline{v_\xi}(W_t)$ is the key quantity. It is a linear combination of Wiener sausage volumes corresponding to different radii of particles that move along the same trajectory W_t. The mean-field approximation, which ignores fluctuations of the random variable $\overline{v_\xi}(W_t)$, is equivalent to neglecting volume fluctuations of each Wiener sausage. Under this approximation, the mean of the exponent in Eq. (8) can be replaced by the exponent of the mean, and the kinetics of the process is determined by the total mean value of the Wiener sausage volume $\langle \overline{v_\xi}(W_t)\rangle$:

$$P_{mf}(t) = \exp[-c\langle \overline{v_\xi}(W_t)\rangle]. \tag{13}$$

Substitution of Eq. (12) into Eq. (13) yields the following formula for the mean-field solution:

$$P_{mf}(t) = \exp(-4\pi\bar{\xi}cDt - 8\overline{\xi^2}c\sqrt{\pi Dt}). \tag{14}$$

This formula is a generalization of the Smoluchowski result (1) for polydisperse traps. It implies that, in the mean-field approximation, the probability of a particle survival among traps of various radii is equal to the product of the probabilities to avoid the reaction with identical traps of each radius. The latter are described by the Smoluchowski formula. This is quite natural, since the mean-field approximation neglects the mutual influence of traps both of the same and of different radii (i.e., many-body effects).

Let us show that, at the initial stage of the process, when the mean-field approximation is applicable, the general Eq. (11) turns into a strict inequality. Comparing the survival probabilities (1) and (14) under condition (10), we see that, by virtue of the well-known inequality between the moments of the positive definite random variable [24], we have

$$\sqrt[3]{\overline{\xi^3}} \geq \sqrt{\overline{\xi^2}} \geq \bar{\xi} \tag{15}$$

(the equality sign corresponds to the case when ξ takes only a single value with a nonzero probability, i.e., when the size of all traps is identical). The mean Wiener sausage volumes satisfy the inequality

$$\langle v_b(W_t)\rangle > \langle \overline{v_\xi}(W_t)\rangle. \tag{16}$$

Hence, for the survival probabilities, we have

$$P_{mf}(t) > P_{Sm}(t;\, b). \tag{17}$$

Note that the greater the fluctuations in the distribution of traps in size, the stronger the inequalities (15)–(17). Thus, at the initial stage (when the majority of particles are trapped), the process proceeds the most fast for identical traps and slows down as the trap size spread becomes greater.

Formula (14) makes it possible to estimate the average survival time of a Brownian particle as

$$\langle t\rangle = \int_0^\infty t\left[-\frac{dP(t)}{dt}\right]dt = \int_0^\infty P(t)dt. \tag{18}$$

The main contribution to integral (18) is made by rather small time values, where the mean-field approximation is applicable. Hence, the substitution of (14) into (18) yields a rather accurate estimate

$$\begin{aligned}\langle t\rangle_{mf} &= \langle t\rangle_0\left[1 - \sqrt{3\Phi}\exp\left(\frac{3\Phi}{\pi}\right)\mathrm{erfc}\sqrt{\frac{3\Phi}{\pi}}\right] \\ &\approx \langle t\rangle_0(1 - \sqrt{3\Phi}),\end{aligned} \tag{19}$$

where $\mathrm{efrc}(z)$ is the complementary error function [26], and the main term of expansion $\langle t\rangle_0$ and the effective volume fraction of traps Φ are determined by

$$\langle t\rangle_0 = \frac{b^2}{D}\frac{1}{3\phi}\frac{\sqrt[3]{\overline{\xi^3}}}{\bar{\xi}}, \quad \Phi = \frac{\overline{\xi^2}^2}{\overline{\xi^3}\bar{\xi}}\phi. \tag{20}$$

In accordance with the conclusion made in the preceding section, $\langle t\rangle_0$ and, consequently, the mean survival time of a particle increase as the trap size spread increases. We also note that, by virtue of the Schwarz inequality [24],

$$\overline{\xi^2}^2/(\overline{\xi^3}\bar{\xi}) < 1,$$

the effective volume fraction of traps Φ is less than the actual one, $\Phi < \phi$.

5. REFINING THE MEAN-FIELD DEPENDENCE

Particles are always trapped more slowly than predicted by the mean-field dependence (14). Indeed, by the well-known inequality

$$\langle e^{-x}\rangle \geq e^{-\langle x\rangle},$$

we have

$$P(t) \geq P_{mf}(t) \tag{21}$$

for all t, and the equality is true only for $t = 0$. In order to derive a correction to (14) that reflects this slowdown (for time values where the mean-field approximation is applicable), it is convenient to represent, on the basis of

the general expression (8), the logarithm of the survival probability as the expansion in the cumulants of the random variable $\overline{v_\xi}(W_t)$:

$$\ln P(t) = \sum_{n=1}^{\infty} \frac{(-c)^n}{n!} K_n(t). \quad (22)$$

Here, the n cumulant $K_n(t)$ is a rational function of the volume moments $\overline{v_\xi}(W_t)$ of orders not exceeding n (see [24]). The first cumulant, which is equal to the total mean value of the Wiener sausage volume,

$$K_1(t) = \langle \overline{v_\xi}(W_t) \rangle,$$

is easily found from (12). The second cumulant is the variance of $\overline{v_\xi}(W_t)$,

$$K_2(t) = \sigma^2(t).$$

It is calculated for $t \gg b_{\max}^2/D$ by the method suggested in [25] (the calculation is outlined in the Appendix):

$$\sigma^2(t) \approx 16\pi^2 Dt \overline{\xi}^{2^2} \ln\left(\frac{Dt}{b_{\text{eff}}^2}\right), \quad (23)$$

where

$$b_{\max} \geq b_{\text{eff}} \geq b_{\min}.$$

Comparing this formula with the well-known formula of the variance of the volume visited by a Brownian particle of radius b in the course of the time $t \gg b^2/D$ [25],

$$\sigma^2(t) \approx 16\pi^2 b^4 Dt \ln(Dt/b^2),$$

we note that when the particle radius is random, the variance of the Wiener sausage volume, as well as its mean value (see inequality (16)), is less than in the case of a fixed radius (however, the estimate of the relative fluctuation $K_2(t)/K_1^2(t)$ shows that a random value of the particle can lead both to an increase and decrease of this quantity).

The approximation of series (22) by its first term corresponds to the mean-field approximation (see (13)). In the case under consideration, when the volume fraction of traps is small, $\phi \ll 1$, this term is much greater than the sum of all other terms at times when the majority of particles are trapped; then, the mean-field dependence (14) provides a good approximation. Retaining the second term in expansion (22) refines Eq. (14), making it possible to take into account fluctuations of the Wiener sausage volume (many-body effects) and reflect the slowdown of the kinetics corresponding to inequality (21). Under this approximation, we have

$$P(t) \approx P_{mf}^c(t) = \exp\left[-c\langle \overline{v_\xi}(W_t)\rangle + \frac{1}{2}c^2\sigma^2(t)\right] \approx P_{mf}(t)\left(1 + \frac{3}{2}\Phi\frac{t}{\langle t\rangle_0}\ln\frac{Dt}{b_{\text{eff}}^2}\right). \quad (24)$$

The mean-field approximation gives the first two terms in the expansion of $\langle t\rangle$ in the small parameter ϕ (see Eq. (19)). Formula (24) yields the next term of this expansion, which reflects (in the first approximation) many-body effects. Substituting (24) into (18) and estimating the corresponding integral up to the linear terms (in ϕ), we obtain

$$\langle t\rangle_{mf}^c \approx \langle t\rangle_0\left(1 - \sqrt{3\Phi} + \frac{3}{2}\Phi\ln\frac{1}{\phi}\right). \quad (25)$$

This formula is a generalization of the result by Mattern and Felderhof in [27] obtained for identical traps to the case of polydisperse traps. Note that (1) $\langle t\rangle_{mf}^c > \langle t\rangle_{mf}$, as it must be according to inequality (21); (2) at the initial stage of the processes, the trap polydispersity leads to an attenuation of many-body effects, since the effective volume fraction of traps Φ decreases as the trap size spread becomes greater.

6. LONG-TIME ASYMPTOTIC BEHAVIOR

Taking into account a finite number of terms in expansion (22) refines the mean-field dependence at rather short times where the subsequent terms are small compared to the first one. Since $K_j(t)$ increase with time, this procedure becomes useless at long times.

As in the case of identical traps [10, 12–14], the long-time behavior of the process is determined by rare fluctuations of the Wiener sausage volume, which manifest themselves in the kinetics due to fluctuations in the arrangement of traps. We show that the asymptotic behavior of $P(t)$ in our model is exactly the same as the behavior in the model with identical traps. This fact follows from the obvious inequality

$$P(t; b_{\min}) \geq P(t) \geq P(t; b_{\max}). \quad (26)$$

According to (2), the probabilities $P(t; b_{\min})$ and $P(t; b_{\max})$, which describe the survival of particles among identical traps of radii $b_{\min}$ and $b_{\max}$, respectively, as $t \longrightarrow \infty$ are the same (with a logarithmic accuracy). Hence, the asymptotic behavior of $\ln P(t)$ as $t \longrightarrow \infty$ is also described by (2). Note that this result can be obtained directly from the general Eq. (8). Indeed, at large time (see the similar reasoning in [11] for identical traps), the major contribution to $P(t)$ is made by multiply self-intersecting trajectories generating Wiener sausages, the volume of which is much less than the mean one.

Thus, as $t \longrightarrow \infty$, the general inequality (11) turns into an equality. However, we stress that, although the polydispersity of traps does not lead to a change in dependence (2), it results in a decrease in the fraction of particles trapped in the fluctuation regime. To show this, we introduce the characteristic time t^* such that $P_{mf}(t^*) = P_\infty(t^*)$:

$$t^* \approx \frac{5^{5/2}\pi^3}{54\sqrt{\phi}}\sqrt{\frac{\overline{\xi^3}}{\overline{\xi}^3}}\langle t\rangle_0. \tag{27}$$

At $t \ll t^*$, the probability of survival is described by the mean-field solution $P_{mf}(t)$ (14); for $t \gg t^*$, it is described by the fluctuation asymptotic dependence $P_\infty(t)$ (2). Estimating the fraction of particles $\epsilon = P(t^*)$ that are trapped in the asymptotic mode (2), we obtain

$$\epsilon = (\epsilon_m)^{\sqrt{\overline{\xi^3}/\overline{\xi}^3}}, \tag{28}$$

where

$$\epsilon_m = \exp\left[-\frac{5^{5/2}\pi^3}{54\sqrt{\phi}}\right] \ll 1$$

is the fraction of particles whose trapping is described by the nonexponential kinetics (2) in the case of identical traps. We see that, as fluctuations of the trap size increase, ϵ becomes substantially less than ϵ_m. This and the fact that was mentioned in the analysis of the initial stage of the process (see the remark at the end of the preceding section) lead to the conclusion that the polydispersity of traps always contributes to the attenuation of many-body effects.

APPENDIX

According to the definition of variance,

$$\sigma^2(t) = \int_{b_{\min}}^{b_{\max}}\int [\langle v_\xi(W_t)v_{\xi'}(W_t)\rangle - \langle v_\xi(W_t)\rangle\langle v_{\xi'}(W_t)\rangle] f(\xi)f(\xi')d\xi d\xi', \tag{A.1}$$

in order to calculate it, we have to find $\langle v_\xi(W_t)\rangle$ and $\langle v_\xi(W_t)v_{\xi'}(W_t)\rangle$. The mean value of the Wiener sausage volume for a particle of fixed radius, $\langle v_\xi(W_t)\rangle$ (see formula (12) in the main part of the paper), is immediately obtained from definition (5) with regard for the fact that

$$\langle I(\mathbf{r};\ \omega_\xi(W_t))\rangle = q(r, \xi;\ t),$$

where $q(r, \xi;\ t)$ is the probability for a particle to be trapped in time t by a trap of radius ξ such that the trap is initially at the distance $r > \xi$ from the particle:

$$q(r, \xi;\ t) = \frac{\xi}{t}\operatorname{erfc}\left(\frac{r-\xi}{2\sqrt{Dt}}\right). \tag{A.2}$$

In order to find $\langle v_\xi(W_t)v_{\xi'}(W_t)\rangle$, we write, on the basis of definition (5),

$$\langle v_\xi(W_t)v_{\xi'}(W_t)\rangle = \int_{r\ge\xi}\int_{r'\ge\xi'}\langle I(\mathbf{r};\ \omega_\xi(W_t))I(\mathbf{r}';\ \omega_{\xi'}(W_t))\rangle d\mathbf{r}d\mathbf{r}'. \tag{A.3}$$

The quantity $\langle I(\mathbf{r};\ \omega_\xi(W_t))I(\mathbf{r}';\ \omega_{\xi'}(W_t))\rangle$ is the fraction of trajectories that start from the origin and visit at time t both the ξ neighborhood of the point $\mathbf{r}$ and the ξ' neighborhood of the point $\mathbf{r}'$. It is easy to see that this quantity can be written as

$$\langle I(\mathbf{r};\ \omega_\xi(W_t))I(\mathbf{r}';\ \omega_{\xi'}(W_t))\rangle = q(r, \xi;\ t) + q(r', \xi';\ t) - q(\mathbf{r}, \xi;\ \mathbf{r}', \xi';\ t), \tag{A.4}$$

where the first two terms are the probabilities for the particle starting from the origin to be trapped at time t by a single trap located at the point $\mathbf{r}$ (of radius ξ) or at the point $\mathbf{r}'$ (of radius ξ'). The third term is the probability for the particle to be trapped in the presence of both traps described above.

The probability for a particle to be trapped by a single trap is known (see (A.2)). Attempts to calculate this quantity for two arbitrarily located traps fail. However, we need only the integral of this quantity over various configurations of traps. For times

$$t \gg (\xi + \xi')^2/D,$$

the major contribution to this integral is made by configurations with traps rather far apart,

$$|\mathbf{r}' - \mathbf{r}| \gg \xi + \xi'.$$

For such configurations, the probability of a particle to be trapped can be determined approximately by representing it in terms of the known probabilities of being trapped by a single trap.

For this purpose, we represent the probability $q(\mathbf{r}, \xi;\ \mathbf{r}', \xi';\ t)$ as a sum of the conditional probabilities

$$q(\mathbf{r}, \xi;\ \mathbf{r}', \xi';\ t) = q(\mathbf{r}, \xi;\ t|\mathbf{r}', \xi') + q(\mathbf{r}', \xi';\ t|\mathbf{r}, \xi), \tag{A.5}$$

where $q(\mathbf{r}, \xi;\ t|\mathbf{r}', \xi')$ is the probability of the particle to be trapped at the time t by a trap of radius ξ located at the point $\mathbf{r}$ under the condition that there is one more trap of radius ξ' located at the point $\mathbf{r}'$; $q(\mathbf{r}', \xi';\ t|\mathbf{r}, \xi)$ is defined similarly. These conditional probabilities

approximately satisfy the following system of integral equations:

$$\begin{aligned} &q(\mathbf{r}, \xi; t) - q(\mathbf{r}, \xi; t|\mathbf{r}', \xi') \\ &\approx \int_0^t \frac{\partial q(\mathbf{r}', \xi'; t'|\mathbf{r}, \xi)}{\partial t'} q(|\mathbf{r} - \mathbf{r}'|, \xi; t - t')dt', \\ &q(\mathbf{r}', \xi'; t) - q(\mathbf{r}', \xi'; t|\mathbf{r}, \xi) \\ &\approx \int_0^t \frac{\partial q(\mathbf{r}, \xi; t'|\mathbf{r}', \xi')}{\partial t'} q(|\mathbf{r}' - \mathbf{r}|, \xi'; t - t')dt'. \end{aligned} \tag{A.6}$$

The approximation is such that we place the starting point of the particle that arrives at the time t' in the ξ (ξ') neighborhood of the point $\mathbf{r}$ ($\mathbf{r}'$) just at the point $\mathbf{r}$ ($\mathbf{r}'$).

Using the Laplace transformation

$$\mathcal{L}\{f(t)\} = \int_0^\infty f(t)\exp(-st)dt,$$

it easy to find a solution to system (A.6) and the Laplace transforms of $q(\mathbf{r}, \xi; \mathbf{r}', \xi'; t)$ (A.5) and $\langle I(\mathbf{r}; \omega_\xi(W_t))I(\mathbf{r}'; \omega_{\xi'}(W_t))\rangle$ (A.4). We assume that the equations obtained are true not only for traps that are far apart but also for all configurations satisfying the condition

$$|\mathbf{r}' - \mathbf{r}| > \xi + \xi'.$$

The resulting error does not exceed the accuracy of our computation. Taking into account the fact that

$$\mathcal{L}\{q(r, \xi; t)\} = s^{-1}(\xi/r)\exp\left[-\sqrt{s(r-\xi)^2/D}\right],$$

we obtain, after some straightforward algebraic manipulations,

$$\begin{aligned} &\mathcal{L}\{\langle v_\xi(W_t)v_{\xi'}(W_t)\rangle\} \approx 4\pi\xi\xi' \\ &\times [\mathcal{L}\{\langle v_\xi(W_t)\rangle\}J(\xi; s) + \mathcal{L}\{\langle v_{\xi'}(W_t)\rangle\}J(\xi'; s)], \end{aligned} \tag{A.7}$$

where

$$\begin{aligned} &\mathcal{L}\{\langle v_z(W_t)\rangle\} = (4\pi Dz/s^2)(1 + \sqrt{sz^2/D}), \\ &J(z; s) \\ &= \int_{\xi+\xi'}^\infty \frac{\exp[-\sqrt{s/D}(2R - \xi - \xi')]}{1 - (\xi\xi'/R^2)\exp[-\sqrt{s/D}(2R - \xi - \xi')]} \\ &\times \left\{\frac{R}{z}\exp\left[\sqrt{\frac{s}{D}}(R - z)\right] - 1\right\}dR. \end{aligned} \tag{A.8}$$

Expanding (A.7) into a series in small s, we find the main terms of the long-time asymptotic behavior $\langle v_\xi(W_t)v_{\xi'}(W_t)\rangle$ neglecting linear and higher order terms with respect to time. Substituting these terms into (A.1), we arrive at Eq. (23) in the main part of the paper. An accurate estimate of this computation shows that the error does not exceed $b_{\max}^4 Dt$ by the order of magnitude.

ACKNOWLEDGMENTS

We thank V.Yu. Zitserman for useful discussions of the results. Yu.A. Makhnovskiĭ is also grateful to L.V. Bogachev for the discussion of issues concerning the subject of this paper.

This work was supported in part by the Russian Foundation for Basic Research, project nos. 00-03-32989 and 99-01-00298, and by Deutsche Forschungsgesellshaft, project no. 436 RUS 113/534.

REFERENCES

1. V. M. Agranovich and M. D. Galanin, *Electronic Excitation Energy Transfer in Condensed Matter* (Nauka, Moscow, 1978; North-Holland, Amsterdam, 1982).
2. A. A. Ovchinnikov, S. F. Timashev, and A. A. Belyĭ, *Kinetics of Diffusion-Controlled Chemical Processes* (Khimiya, Moscow, 1986).
3. A. Szabo, J. Phys. Chem. **93**, 6929 (1989).
4. J. A. McCammon and S. C. Harvey, *Dynamics of Proteins and Nucleic Acids* (Cambridge Univ. Press, Cambridge, 1987).
5. A. S. Mikhaĭlov and I. V. Uporov, Usp. Fiz. Nauk **144**, 79 (1984) [Sov. Phys. Usp. **27**, 695 (1984)].
6. F. den Hollander and G. H. Weiss, in *Contemporary Problems in Statistical Physics*, Ed. by G. H. Weiss (SIAM, Philadelphia, 1994), p. 147.
7. M. von Smoluchowski, Phys. Z. **17**, 557 (1916); **17**, 585 (1916).
8. E. Kotomin and V. Kuzovkov, *Modern Aspects of Diffusion-Controlled Reactions* (Elsevier, Amsterdam, 1996).
9. A. S. Sznitman, *Brownian Motion, Obstacles and Random Media* (Springer-Verlag, Berlin, 1998).
10. B. Ya. Balagurov and V. G. Vaks, Zh. Éksp. Teor. Fiz. **65**, 1939 (1973) [Sov. Phys. JETP **38**, 968 (1973)].
11. A. M. Berezhkovskiĭ, Yu. A. Makhnovskiĭ, and R. A. Suris, Khim. Fiz. **8**, 833 (1989); A. M. Berezhkovskii, Yu. A. Makhnovskii, and R. A. Suris, Chem. Phys. **137**, 41 (1989); J. Stat. Phys. **65**, 1025 (1991).
12. M. D. Donsker and S. R. S. Varadhan, Commun. Pure Appl. Math. **28**, 525 (1975).
13. A. A. Ovchinnikov and Ya. B. Zeldovich, Chem. Phys. **28**, 215 (1978).
14. P. Grassberger and I. D. Procaccia, J. Chem. Phys. **77**, 6281 (1982).
15. I. M. Lifshits, Usp. Fiz. Nauk **83**, 617 (1964) [Sov. Phys. Usp. **7**, 549 (1965)].
16. P. M. Richards, J. Chem. Phys. **85**, 3520 (1986).

17. C. A. Miller and S. Torquato, Phys. Rev. B **40**, 7101 (1989).
18. L. Zheng and Y. C. Chiew, J. Chem. Phys. **93**, 2658 (1990).
19. J. A. Given, J. Blawzdzievicz, and G. Stell, J. Chem. Phys. **93**, 8156 (1990).
20. Yu. A. Makhnovskii, D.-Y. Yang, A. M. Berezhkovskii, *et al.*, Phys. Rev. E **58**, 4340 (1998); A. M. Berezhkovskii, Yu. A. Makhnovskii, L. V. Bogachev, and S. A. Molchanov, Phys. Rev. E **47**, 4564 (1993).
21. Yu. A. Makhnovskii, M. E. Maslova, and A. M. Berezhkovskii, J. Chem. Phys. **108**, 6431 (1998).
22. M. A. Leontovitsch and A. N. Kolmogorov, Phys. Z. Sowjetunion **4**, 1 (1933).
23. M. Kac, Rocky Mt. J. Math. **4**, 511 (1974).
24. W. Feller, *An Introduction to Probability Theory and Its Applications* (Wiley, New York, 1968; Mir, Moscow, 1984), Vol. 2.
25. A. M. Berezhkovskiĭ, Yu. A. Makhnovskii, and R. A. Suris, J. Stat. Phys. **57**, 333 (1989).
26. *Handbook of Mathematical Functions*, Ed. by M. Abramowitz and I. A. Stegun (National Bureau of Standards, Washington, 1964; Nauka, Moscow, 1979).
27. K. Mattern and B. U. Felderhof, Physica A (Amsterdam) **135**, 505 (1986).

Translated by A. Klimontovich

Journal of Experimental and Theoretical Physics, Vol. 94, No. 2, 2002, pp. 411–418.
Translated from Zhurnal Éksperimental'noĭ i Teoreticheskoĭ Fiziki, Vol. 121, No. 2, 2002, pp. 480–488.

SOLIDS
Electronic Properties

Electron and Hole Spectra of Silicon Quantum Dots

V. A. Burdov
Lobachevskiĭ State University, pr. Gagarina 23, Nizhni Novgorod, 603600 Russia
e-mail: burdov@phys.unn.runnet.ru
Received August 6, 2001

Abstract—In the framework of perturbation theory, the first several one-particle energies and wave functions for electrons and holes (six for each) in spherical silicon quantum dots are obtained in the envelope function approximation (**kp** method). It is shown that the model of an isotropic dispersion relation with the mean reciprocal effective mass is applicable for the ground state of holes in the valence band. Anisotropy of the dispersion relation, which takes place for bulk semiconductors, becomes significant for the electron ground state in the conduction band as well as for all excited (both electron and hole) states. © *2002 MAIK "Nauka/Interperiodica".*

1. INTRODUCTION

Optical properties of various heterostructures with semiconductor quantum dots which can be used for obtaining radiation in the near-IR range and even in the visible part of the spectrum have been investigated both experimentally and theoretically in recent years. Silicon is one of the most promising materials for optoelectronics in view of its abundance. In this connection, it would be interesting to calculate the band structure of silicon quantum dots.

The band structure of silicon quantum dots was calculated earlier using various methods including the method of pseudopotential [1], the tight-binding model [2, 3], and the local density approximation [4]. All these methods are rather complicated and involve cumbersome computer calculations. Their application is justified for very small crystallites (with a size smaller than one or two nanometers), when the effective mass approximation fails to provide satisfactory results.

The effective mass approximation (or the **kp** method) itself was also used for calculating the electron structure of silicon nanocrystals of a slightly larger size (exceeding two or three nanometers) [3, 5–7]. However, these calculations, as well as those made in [1, 2, 4], were mainly aimed at determining the energy of the basic transition in quantum dots, i.e., the transition from the lower level of the conduction band to the upper level of the valence band. The models of the envelope function Hamiltonian used in this case for calculating the two ground states in the valence band and in the conduction band were insufficiently accurate (this will be discussed in greater detail below) and require considerable corrections.

In this work, we will carry out an analysis of the electron and hole spectra of spherical (of radius R) silicon quantum dots in the envelope function approximation. We will assume that the size of crystallites is not small enough to transgress the validity of our calculations. We will calculate the energies of not only the ground states in the valence band and in the conduction band, but also of several excited states and the wave functions of all these states, which is required, for example, for determining the probabilities of various interband and intraband transitions.

2. VALENCE BAND

2.1. Computational Technique

It is well known (see, for example, [8]) that, in the envelope function approximation, the Hamiltonian in the valence band disregarding the spin-orbit interaction (which is rather weak in silicon) is a 3×3 matrix operator owing to the triple degeneracy of the spectrum at the Γ point. The diagonal elements of this matrix have the form

$$\hat{H}_{jj} = \hat{H}_0 + \hat{V}_{jj} = -\frac{\hbar^2}{2m_0}\frac{L+2M}{3}\hat{\mathbf{k}}^2 + \frac{\hbar^2}{2m_0}\frac{L-M}{3}(\hat{\mathbf{k}}^2 - 3\hat{k}_j^2), \quad (1)$$

while the nondiagonal elements are given by

$$\hat{H}_{ij} = \hat{V}_{ij} = -\frac{\hbar^2}{2m_0}N\hat{k}_i\hat{k}_j. \quad (2)$$

In expressions (1) and (2), m_0 is the mass of a free electron; $\hat{\mathbf{k}} = -i\nabla$ is the wave vector operator; and numbers L, M, and N are dimensionless empirical parameters, which are equal to 6.8, 4.43, and 8.61, respectively [9]. Hamiltonian $\hat{H}_0$ is the result of averaging over all directions of any diagonal element.

1063-7761/02/9402-0411$22.00

The problem involves the solution of the matrix equation

$$\hat{H}_{ij}F_j(\mathbf{r}) = \mathscr{E}F_i(\mathbf{r}), \quad (3)$$

where $F_j(\mathbf{r})$ is the envelope function and $\mathscr{E}$ is the energy. We assume that a quantum dot is in a layer of a wideband material (e.g., SiO_2) so that the potential barriers both for holes and for electrons can be regarded as infinitely high. In accordance with these assumptions, the values of envelope functions at the boundary must vanish.

It was mentioned above that the calculations made in [5–7] are apparently insufficiently rigorous. For example, the spectrum for the valence band was calculated either by using the Luttinger Hamiltonian [5] (when the initial 6×6 Hamiltonian splits into two: 4×4 and 2×2), which is hardly justified for silicon in view of the smallness of spin-orbit splitting, or by using a model of the dispersion relation in which anisotropy is determined by two effective masses [7], which requires an additional substantiation. In [3], a 6×6 Hamiltonian was used, but the energy of the ground state alone was calculated. For this reason, a more detailed and comprehensive analysis of the hole and electron states is required.

We will try to solve the eigenfunction and eigenvalue problem (3) in the framework of perturbation theory choosing the Hamiltonian

$$\hat{H}_{ij}^{(0)} = \delta_{ij}\hat{H}_0 \quad (4)$$

as the zeroth approximation. In this case, all nondiagonal elements (2) and anisotropic terms $\hat{V}_{ij}$ in the diagonal elements are regarded as perturbations.

It should be noted that anisotropy in silicon is quite strong; in particular, the nondiagonal elements $\hat{V}_{ij}$ are comparable in order of magnitude with $\hat{H}_0$ and, hence, can hardly be treated as small. However, we must take into account the specific form of the perturbation: it cannot bind "neighboring" states of the unperturbed Hamiltonian (e.g., *s* and *p*, *p* and *d*, etc.) and binds only states of the same parity. The criterion of applicability of perturbation theory is hence the smallness of the matrix elements of a perturbation relative to the energy of the corresponding allowed transition, equal to the energy difference, say, between the *d* and *s* states, which is quite large indeed.

The perturbation theory series in this case can be constructed almost in the conventional way (see, for example, [10]). A specific feature of our problem is that each energy level in the valence band has three times higher degeneracy due to the matrix form of Eq. (3). We will seek the envelope functions in the form of an expansion in the basis of the eigenfunctions $|\alpha\rangle$ of the unperturbed Hamiltonian $\hat{H}_0$:

$$F_j(\mathbf{r}) = \sum_\alpha C_{j\alpha}|\alpha\rangle. \quad (5)$$

We will denote by Greek letters the states of the unperturbed problems and by Roman letters the index of the Bloch function in the valence band, which changes from 1 to 3. The explicit form of eigenfunctions $|\alpha\rangle$ is well known: their radial component is a first-kind spherical Bessel function $j_l(\mu_l^n r/R)$, where μ_l^n is the *n*th root of the given function; the angular component will henceforth be chosen in the form of a superposition of spherical harmonics $Y_{lm}(\theta, \varphi)$ taken with the same number *l*, but with different numbers *m*. Substituting expansion (5) into Eq. (3), we ultimately obtain the following equation for determining energy $\mathscr{E}$ and the expansion coefficients $C_{j\alpha}$:

$$(\mathscr{E} - E_\beta)C_{i\beta} = \sum_\alpha \sum_j C_{j\alpha}V_{ij}^{\beta\alpha}, \quad (6)$$

where E_β are the eigenvalues of operator $\hat{H}_0$ in state $|\beta\rangle$ and $V_{ij}^{\beta\alpha} = \langle\alpha|\hat{V}_{ij}|\beta\rangle$. After this, the solution of Eqs. (6) is carried out in the standard manner and leads to the following results.

2.2. Energies and Wave Functions of Holes in the Valence Band

We start with calculating the corrections to the ground 1*s* state of the unperturbed problem. While determining the first-order corrections to the energy value and the regular wave functions in the zeroth approximation, we confine the summation over α in Eqs. (5) and (6) only to the 1*s* state. It turns out that the first-order corrections to energy are equal to zero and that the energy value itself,

$$\mathscr{E}_{0h} = -\frac{\hbar^2\pi^2}{2m_hR^2}, \quad (7)$$

does not change and nor do the wave functions

$$\Psi_{0(1)} = v_x(\mathbf{r})|0\rangle, \quad \Psi_{0(2)} = v_y(\mathbf{r})|0\rangle, \quad \Psi_{0(3)} = v_z(\mathbf{r})|0\rangle. \quad (8)$$

Here, $v_x(\mathbf{r})$, $v_y(\mathbf{r})$, and $v_z(\mathbf{r})$ are the Bloch functions corresponding to the Γ point of the Brillouin zone, and $|0\rangle$ is the function of the 1*s* state of the unperturbed Hamiltonian $\hat{H}_0$. In formula (7), we have introduced the effective mass of a hole,

$$m_h = \frac{3m_0}{L + 2M}.$$

A nonzero correction to energy appears in the second order when the $1d$ and $2s$ states are taken into account in Eqs. (5) and (6) of the unperturbed problem (the remaining d and s states make a much smaller contribution). However, this correction does not exceed a few percent and hence will not be taken into account.

The spin-orbit interaction is usually taken into account in an analysis of the hole spectrum of semiconductors with the structure of diamond or zinc blende. According to calculations, the spin-orbit splitting of the $1s$ level occurs in a quantum dot as in the case of a bulk semiconductor: the fourfold degenerate (taking spin into account) level ascends to the top of the valence band by $\Delta/3 \approx 0.015$ eV, while the doubly degenerate level descends by $2\Delta/3$ to the bulk of the band. However, the spin-orbit splitting is of the same order of smallness as the second-order correction, and, hence, the spin-orbit splitting is not taken into account either.

Thus, expressions (7) and (8) remain valid to a high degree of accuracy; consequently, the ground state of holes is correctly described by an isotropic model with the effective mass m_h equal approximately to $0.19m_0$ even in the presence of a strong anisotropy of the spectrum.

Let us now calculate corrections to the $1p$ states. In this case, we will also confine our analysis to first-order corrections to energies, which are now nonzero, and construct the regular functions of the zeroth approximation. Solving Eq. (6) without taking spin into account, we find that, in the first order, the ninefold degenerate level splits into four levels, the highest of which is triply degenerate and has the energy

$$\mathscr{E}_{1h} = -\frac{\hbar^2\mu_1^2}{2m_hR^2}\left(1 - \frac{2(2N + L - M)}{5(L + 2M)}\right), \tag{9}$$

where the factor in front of the parentheses is the energy value for the $1p$ state and μ_1 is the smallest root of the spherical Bessel function $j_1(x)$. In this case, the correction is quite significant and amounts exactly to half the initial value E_{1h} according to estimates. The value of energy $\mathscr{E}_{1h}$ becomes very close to energy $\mathscr{E}_{0h}$ (the difference between the two values is on the order of 2%).

Since the energy $\mathscr{E}_{1h}$ remains triply degenerate, the choice of wave functions is ambiguous as before. In particular, these functions can be chosen in the form

$$\begin{aligned}
\Psi_{1(1)} &= \frac{v_y(\mathbf{r})|x\rangle - v_x(\mathbf{r})|y\rangle}{\sqrt{2}},\\
\Psi_{1(2)} &= \frac{v_x(\mathbf{r})|z\rangle - v_z(\mathbf{r})|x\rangle}{\sqrt{2}},\\
\Psi_{1(3)} &= \frac{v_z(\mathbf{r})|y\rangle - v_y(\mathbf{r})|z\rangle}{\sqrt{2}},
\end{aligned} \tag{10}$$

where $|x\rangle$, $|y\rangle$, and $|z\rangle$ are the real normalized wave functions of $1p$ states, which are transformed like coordinates x, y, and z.

The next energy level is doubly degenerate and has the energy

$$\mathscr{E}_{2h} = -\frac{\hbar^2\mu_1^2}{2m_hR^2}\left(1 - \frac{4(N - L + M)}{5(L + 2M)}\right) \tag{11}$$

and the wave functions

$$\begin{aligned}
\Psi_{2(1)} &= \frac{1 + \sqrt{3}}{\sqrt{6(2 + \sqrt{3})}} v_x(\mathbf{r})|x\rangle\\
&+ \frac{1}{\sqrt{6(2 + \sqrt{3})}} v_y(\mathbf{r})|y\rangle - \sqrt{\frac{2 + \sqrt{3}}{6}} v_z(\mathbf{r})|z\rangle,\\
\Psi_{2(2)} &= \frac{1 + \sqrt{3}}{\sqrt{6(2 + \sqrt{3})}} v_x(\mathbf{r})|x\rangle\\
&- \sqrt{\frac{2 + \sqrt{3}}{6}} v_y(\mathbf{r})|y\rangle + \frac{1}{\sqrt{6(2 + \sqrt{3})}} v_z(\mathbf{r})|z\rangle.
\end{aligned} \tag{12}$$

The correction to energy turns out to be smaller than in the previous case, but is still significant (more than 30%) and positive; i.e., the $\mathscr{E}_{2h}$ level is located closer to the top of the valence band as compared to the unperturbed energy value.

The remaining two levels obtained as a result of splitting of the $1p$ state are shifted to the bulk of the valence band relative to E_{1h}. One (triply degenerate) level increases the energy by almost 40%, while the other (nondegenerate) level, by 100%. We will not give here the expressions for the energies and wave functions of these four states since they lie quite deep in the valence band and the results obtained for these states may turn out to be too rough for several reasons. In particular, the quadratic approximation for elements of the matrix operator (1), (2) is in all probability insufficient for such energy values; the $1p1f$ hybridization, which was disregarded by us here, may also noticeably affect the position of the levels.

The splitting of the $1p$ level is found to be very strong, and the approximation with an isotropic dispersion relation is obviously inapplicable in this case. It should be noted that, in spite of the large values of first-order corrections, higher orders of perturbation theory do not lead to significant modifications (the corresponding corrections amount to a few percent according to estimates). We also disregard the spin-orbit coupling which gives corrections for the $1p$ states which are two orders of magnitude smaller than for the $1s$ state. The spin-orbit interaction will be neglected everywhere in the subsequent analysis.

The $1d$ state is characterized by fifteenfold degeneracy; it should be borne in mind, however, that the E_{0h}

level of the 2*s* state lies very close to the 1*d* energy level E_{2h}. For this reason, the 2*s* state must also be taken into account while solving the secular equation obtained from Eq. (6) in the first order of perturbation theory. Thus, the total number of unknown coefficients is equal to eighteen.

As a result of the solution of the given system of equations, we obtain seven different energy values, from which four levels (two triply degenerate, one nondegenerate, and one doubly degenerate) appear as a result of splitting of the 1*d* level, while three triply degenerate levels appear as a result of the 1*d*2*s* hybridization. As before, we will only write the expressions for energy levels displaced more strongly towards the top of the valence band as compared to their unperturbed values and, hence, located not very deep in the valence band.

The uppermost level is the triply degenerate energy level obtained as a result of the 1*d*2*s* hybridization,

$$\mathscr{E}_{3h} = -\frac{\hbar^2}{2m_h R^2}\frac{\mu_2^2 + 4\pi^2}{2} + \frac{\hbar^2\mu_2^2}{2m_0 R^2} \times\left(\frac{12\sqrt{2}\pi N}{\sqrt{15}\mu_2(4\pi^2 - \mu_2^2)} - \frac{N + 2L - 2M}{14}\right), \tag{13}$$

and characterized by the largest correction (slightly exceeding 50%) relative to the energy of the 1*d* level. The parameter μ_2 in this expression is the first root of the spherical Bessel function $j_2(x)$. The wave functions will be chosen as follows:

$$\Psi_{3(1)} = \frac{1}{\sqrt{2}} \times\left(v_x(\mathbf{r})|200\rangle - \frac{v_y(\mathbf{r})|xy\rangle + v_z(\mathbf{r})|xz\rangle}{\sqrt{2}}\right),$$

$$\Psi_{3(2)} = \frac{1}{\sqrt{2}} \times\left(v_y(\mathbf{r})|200\rangle - \frac{v_x(\mathbf{r})|xy\rangle + v_z(\mathbf{r})|yz\rangle}{\sqrt{2}}\right), \tag{14}$$

$$\Psi_{3(3)} = \frac{1}{\sqrt{2}} \times\left(v_z(\mathbf{r})|200\rangle - \frac{v_x(\mathbf{r})|xz\rangle + v_y(\mathbf{r})|yz\rangle}{\sqrt{2}}\right),$$

where $|200\rangle$ is the wave function of the 2*s* state.

The next (in the direction to the bulk of the valence band) is also the triply degenerate level

$$\mathscr{E}_{4h} = -\frac{\hbar^2\mu_2^2}{2m_h R^2}\left(1 - \frac{6N}{7(L + 2M)}\right), \tag{15}$$

which has a correction slightly smaller than 50% relative to the E_{2h} energy (the factor in front of the parentheses). This level is obtained as a result of splitting of the unperturbed 1*d* level without an "admixture" the 2*s* state. The three wave functions corresponding to energy (15) have the form

$$\Psi_{4(1)} = \frac{(3N/2 + L - M)v_x(\mathbf{r})(|x^2 - y^2\rangle + \sqrt{3}|3z^2 - r^2\rangle) + 3N(v_y(\mathbf{r})|xy\rangle - v_z(\mathbf{r})|xz\rangle)}{\sqrt{18N^2 + (3N + 2L - 2M)^2}},$$

$$\Psi_{4(2)} = \frac{(3N/2 + L - M)v_y(\mathbf{r})(|x^2 - y^2\rangle - \sqrt{3}|3z^2 - r^2\rangle) + 3N(v_z(\mathbf{r})|yz\rangle - v_x(\mathbf{r})|xy\rangle)}{\sqrt{18N^2 + (3N + 2L - 2M)^2}}, \tag{16}$$

$$\Psi_{4(3)} = \frac{(3N + 2(L - M))v_z(\mathbf{r})|x^2 - y^2\rangle + 3\sqrt{3}N(v_y(\mathbf{r})|yz\rangle - v_x(\mathbf{r})|xz\rangle)}{\sqrt{54N^2 + (3N + 2L - 2M)^2}},$$

where $|xy\rangle$, $|xz\rangle$, $|yz\rangle$, $|x^2 - y^2\rangle$, and $|3z^2 - r^2\rangle$ are the functions of the 1*d* state.

It should be noted that expressions (13)–(16) are not exact even in the first approximation; however, a more rigorous inclusion of the discarded terms would improve the accuracy of the result only by a few percent, rendering expressions (13)–(16) much more cumbersome. Taking into account the fact that we disregard the second-order corrections, which also amount to a few percent, the presentation of expressions (13)–(16) in a simpler form is quite justified.

Finally, the last level whose value of energy will be given here is doubly degenerate and is obtained from the 1*d* level,

$$\mathscr{E}_{5h} = -\frac{\hbar^2\mu_2^2}{2m_h R^2}\left(1 - \frac{3N + 4L - 4M}{7(L + 2M)}\right), \tag{17}$$

and the wave functions of the two degenerate states can be chosen in the form

$$\Psi_{5(1)} = \frac{1+\sqrt{3}}{\sqrt{6(2+\sqrt{3})}} v_x(\mathbf{r})|yz\rangle + \frac{1}{\sqrt{6(2+\sqrt{3})}} v_y(\mathbf{r})|xz\rangle - \sqrt{\frac{2+\sqrt{3}}{6}} v_z(\mathbf{r})|xy\rangle,$$
$$\Psi_{5(2)} = \frac{1+\sqrt{3}}{\sqrt{6(2+\sqrt{3})}} v_x(\mathbf{r})|yz\rangle - \sqrt{\frac{2+\sqrt{3}}{6}} v_y(\mathbf{r})|xz\rangle + \frac{1}{\sqrt{6(2+\sqrt{3})}} v_z(\mathbf{r})|xy\rangle. \quad (18)$$

The correction to the E_{2h} level slightly exceeds 30%.

3. CONDUCTION BAND

3.1. Computational Technique

The analysis of the electron spectrum and wave functions in the conduction band of silicon can be carried out in the same way as for the valence band, i.e., using perturbation theory. As the zeroth approximation, we can take, as before, the Hamiltonian operator averaged over all directions, the basis of its eigenfunctions, and the spectrum of eigenvalues.

It is well known that, in the conduction band of silicon, energy minima are located symmetrically relative to each of the X points on the boundary of the Brillouin zone. At the X points proper, energy branches intersect, giving rise to double degeneracy of the spectrum at each of the three physically nonequivalent X points (sixfold degeneracy in the whole).

The electron spectra in the conduction band of silicon are usually analyzed using the model of constant-energy surfaces in the form of an ellipsoid of revolution in the **k** space with two effective masses m_l and m_t (longitudinal and transverse). However, such a representation is valid only for not very high energies in the vicinity of any of the six minima. Considering that the energy difference between an X point and the point of minimum amounts to only 0.115 eV [11], while the size quantization energies in the system under investigation is several times higher, we conclude that the model of a constant-energy surface in the form of an ellipsoid of revolution is inapplicable in this case.

Instead, we must write the **kp** Hamiltonian of the problem in the vicinity of each of the three X points rather than in the vicinity of the energy minimum as was done in [11, 12]. This will enable us to considerably extend the energy range under investigation. For the sake of definiteness, we choose one of the three X points, say, that corresponding to the z direction [001] and calculate the electron spectrum in the vicinity of this point. Naturally, the spectrum at the other two X points will be the same.

In view of double degeneracy of the Bloch states at each X point, the Hamiltonian of the problem has the form of a 2×2 matrix operator [11, 12] with the elements

$$\hat{H}_{11} = \hat{H}_{22} = \frac{\hbar^2}{2m_t}(\hat{k}_x^2 + \hat{k}_y^2) + \frac{\hbar^2}{2m_l}\hat{k}_z^2,$$
$$\hat{H}_{12} = \hat{H}_{21}^\dagger = \hbar^2\left(\frac{1}{m_t} - \frac{1}{m_0}\right)\hat{k}_x\hat{k}_y + i\frac{\hbar^2 k_0}{m_l}\hat{k}_z, \quad (19)$$

where the values of m_t and m_l are respectively 0.19 and 0.92 of the free electron mass; $k_0 = 0.144(2\pi/a)$ is the distance from an X point to the nearest energy minimum in the **k** space; $a = 0.543$ nm is the lattice constant; and the values of **k** and energy are reckoned from the X point.

Averaging matrix (19) over directions, we obtain the zeroth-approximation Hamiltonian in form (4), where operator $\hat{H}_0$ is now equal to $\hbar^2\hat{\mathbf{k}}^2/2m_e$, and m_e is the effective isotropic electron mass obtained as a result of averaging of reciprocal effective masses:

$$\frac{1}{m_e} = \frac{1}{3}\left(\frac{1}{m_l} + \frac{2}{m_t}\right).$$

All the terms which do not appear in the averaged Hamiltonian $\hat{H}_{ij}^{(0)}$ will be regarded as a perturbation. In particular, the diagonal elements of the matrix perturbation operator have the form

$$\hat{V}_{11} = \hat{V}_{22} = \frac{\hbar^2}{6}\left(\frac{1}{m_t} - \frac{1}{m_l}\right)(\hat{\mathbf{k}}^2 - 3\hat{k}_z^2),$$

while the nondiagonal elements of the perturbation operator coincide with $\hat{H}_{12}$ and $\hat{H}_{21}$.

The basis of envelope eigenfunctions of the unperturbed problem in the conduction band is exactly the same as the hole basis in the zeroth approximation for the valence band, while the spectrum differs only in the value of the effective mass, which is now equal to $0.26m_0$. Accordingly, as was done in the hole spectrum calculations, we will classify electron states in the basis of Hamiltonian $\hat{H}_0$ and solve the problem using again expansion (5) and the equation for the expansion coefficients (6) in which the summation over j is now carried out from 1 to 2.

3.2. Electron Spectrum and Wave Functions in the Conduction Band

We begin with corrections to the ground 1*s* state. In contrast to the hole Hamiltonian (1), (2), the nondiagonal elements of Hamiltonian (19) contain terms linear in $\hat{k}_z$. For this reason, the 1*s* and 1*p* states can be mixed. A preliminary analysis shows that the splitting of the 1*p* level without taking into account its coupling with the 1*s* state is quite strong as on the valence band, and the lowest of the split *p* levels virtually overlaps with the 1*s*

level. In the valence band, a perturbation could not couple the *s* and *p* states; for this reason, the *s* and *p* levels were obtained independently. In the conduction band, a perturbation may couple the *s* and *p* states; for this reason, the *s* and *p* states start interacting with one another upon convergence.

In view of what has been said above, we will seek the regular functions in the zeroth approximation (5) in the form of superpositions of the wave functions of the 1*s* and 1*p* states. In this case, Eq. (6) leads to a system of equations for the expansion coefficients of 8×8 dimension, which splits into four 2×2 systems from which only two are different, while the other two are completely identical to the first equations. This indicates double degeneracy of each of the four obtained levels, which is apparently a consequence of complete symmetry of two valleys relative to the *X* point in a bulk semiconductor. The 1*s* state is mixed with the p_z state, and the p_x and p_y states mix with each other.

The ground state in the conduction band is obtained as a result of the sp_z hybridization and has the energy

$$\mathscr{E}_{0e} = \frac{E_e + E_{1e} - V}{2} - \sqrt{\left(\frac{E_{1e} - E_e - V}{2}\right)^2 + U^2}, \quad (20)$$

where E_e and E_{1e} are the energies of the 1*s* and 1*p* states, and *U* and *V* are the absolute values of matrix elements, which are defined as

$$U = \frac{\hbar^2 k_0}{m_l}\left|\langle 0|\hat{k}_z|z\rangle\right| = \frac{\hbar^2 k_0}{m_l}\frac{2\pi\mu_1}{\sqrt{3}R(\mu_1^2 - \pi^2)},$$
$$V = \left|\langle z|\hat{V}_{11}|z\rangle\right| = \frac{\hbar^2}{R^2}\left(\frac{1}{m_t} - \frac{1}{m_l}\right)\frac{2\mu_1^2}{15}. \quad (21)$$

The wave functions can be chosen in the form

$$\Phi_{0(1)} = \cos(\lambda)u_{1z}(\mathbf{r})|0\rangle + \sin(\lambda)u_{2z}(\mathbf{r})|z\rangle,$$
$$\Phi_{0(2)} = \cos(\lambda)u_{2z}(\mathbf{r})|0\rangle - \sin(\lambda)u_{1z}(\mathbf{r})|z\rangle, \quad (22)$$

where $u_{1z}(\mathbf{r})$ and $u_{2z}(\mathbf{r})$ are the Bloch functions at the *X* point and angle λ is defined by the relations

$$\cos(2\lambda) = \frac{(E_{1e} - E_e - V)/2}{\sqrt{(E_{1e} - E_e - V)^2/4 + U^2}},$$
$$\sin(2\lambda) = \frac{U}{\sqrt{(E_{1e} - E_e - V)^2/4 + U^2}}.$$

Here and below, we will not write expressions for second-order energy corrections since these expressions, as in the case of the valence band, are quite cumbersome, as a rule, and the values of corrections do not exceed a few percent.

The p_x and p_y energy levels split very strongly. The upper split level ascends to a considerable height, and its position is of no interest for our analysis. The level split in the downward direction is located next to the ground state and has the energy

$$\mathscr{E}_{1e} = \frac{\hbar^2\mu_1^2}{2m_eR^2}\left(1 - \frac{2m_e}{5m_t} - \frac{2m_e}{15m_l} + \frac{8m_e}{15m_0}\right), \quad (23)$$

which decreases relative to the unperturbed value by approximately 45%. We choose the wave functions in the form

$$\Phi_{1(1)} = \frac{u_{1z}(\mathbf{r})|x\rangle + u_{2z}(\mathbf{r})|y\rangle}{\sqrt{2}},$$
$$\Phi_{1(2)} = \frac{u_{1z}(\mathbf{r})|x\rangle - u_{2z}(\mathbf{r})|y\rangle}{\sqrt{2}}. \quad (24)$$

The next level $\mathscr{E}_{2e}$ is also obtained as a result of the sp_z hybridization as the second solution of the 2×2 system:

$$\mathscr{E}_{2e} = \frac{E_e + E_{1e} - V}{2} + \sqrt{\left(\frac{E_{1e} - E_e - V}{2}\right)^2 + U^2}. \quad (25)$$

The wave functions corresponding to this level are written in the form

$$\Phi_{2(1)} = \cos(\lambda)u_{1z}(\mathbf{r})|z\rangle + \sin(\lambda)u_{2z}(\mathbf{r})|0\rangle,$$
$$\Phi_{2(2)} = \cos(\lambda)u_{2z}(\mathbf{r})|z\rangle - \sin(\lambda)u_{1z}(\mathbf{r})|0\rangle. \quad (26)$$

It should be noted that the dependence of energies $\mathscr{E}_{0e}$ and $\mathscr{E}_{2e}$ on the size of a quantum dot is described by a more complex function than R^{-2} (it is intermediate between R^{-2} and R^{-1} due to the presence of terms linear in $\hat{k}_z$ in the Hamiltonian of the perturbation).

Let us now consider the 1*d* state. In view of the closeness of the 2*s* state, we again construct the regular wave functions in the zeroth approximation and calculate the first-order energy corrections taking into account in expansion (5) the wave functions of the 1*d* and 2*s* states and neglecting the effect of all the remaining corrections. It should be noted from the very outset that, in contrast to calculations for the valence band, the 1*d* and 2*s* states can now mix with the 1*p* states and, hence, we must also include in expansion (5) the functions of the 1*p* states. However, our calculations show that such a hybridization has virtually no effect on the position of the levels: the shifts turn out to be no larger than the second-order corrections which are disregarded. For this reason, the hybridization of the 1*d* and 2*s* states with the 1*p* states will also be neglected to simplify the form of the final expressions.

As a result, we find that the 2*s* state is hybridized with the $|xy\rangle$ and $|3z^2 - r^2\rangle$ states, but the state obtained due to the interaction of the $|xz\rangle$ and $|yz\rangle$ states possesses the lowest energy

$$\mathscr{E}_{3e} = \frac{\hbar^2\mu_2^2}{2m_eR^2} \times\left(1 - \frac{2(m_l - m_t)}{7(2m_l + m_t)} - \frac{6m_l}{7m_0}\frac{m_0 - m_t}{2m_l + m_t}\right). \quad (27)$$

The wave functions corresponding to this doubly degenerate energy value can be written in the form

$$\Phi_{3(1)} = \frac{u_{1z}(\mathbf{r})|xz\rangle - u_{2z}(\mathbf{r})|yz\rangle}{\sqrt{2}},$$
$$\Phi_{3(2)} = \frac{u_{1z}(\mathbf{r})|yz\rangle - u_{2z}(\mathbf{r})|xz\rangle}{\sqrt{2}}. \quad (28)$$

The splitting of the d_{xz} and d_{yz} states generates one more energy level; however, like the level of the $d_{x^2-y^2}$ state, it possesses a high energy since it lies above the unperturbed state. For this reason, these states will not be considered here.

The two states resulting from the 2*sd* hybridization (the third hybridized state also splits to a considerable height and is not considered by us) possess a slightly higher energy. However, one must solve a cubic equation for determining the energy of these two states. An explicit analytic solution of this equation cannot be obtained. For this reason, we carry out its numerical solution, which gives

$$\mathscr{E}_{4e} = \bar{E} - 0.481E_{2e}, \quad \mathscr{E}_{5e} = \bar{E} - 0.45E_{2e}, \quad (29)$$

where $\bar{E} = (E_{0e} + 2E_{2e})/3$. The corresponding wave functions can be written in the form

$$\Phi_{4(1)} = u_{1z}(\mathbf{r})(0.765|3z^2 - r^2\rangle - 0.181|200\rangle) + 0.618u_{2z}(\mathbf{r})|xy\rangle,$$
$$\Phi_{4(2)} = u_{2z}(\mathbf{r})(0.765|3z^2 - r^2\rangle - 0.181|200\rangle) + 0.618u_{1z}(\mathbf{r})|xy\rangle,$$
$$\Phi_{5(1)} = u_{1z}(\mathbf{r})(0.519|3z^2 - r^2\rangle + 0.741|200\rangle) - 0.425u_{2z}(\mathbf{r})|xy\rangle, \quad (30)$$
$$\Phi_{5(2)} = u_{2z}(\mathbf{r})(0.519|3z^2 - r^2\rangle + 0.741|200\rangle) - 0.425u_{1z}(\mathbf{r})|xy\rangle.$$

The energy levels (27) and (29) obtained from the 1*d* and 2*s* levels of the unperturbed problem have close energy values, the difference in the values of $\mathscr{E}_{3e}$ and $\mathscr{E}_{4e}$ being smaller than one percent, and the energy $\mathscr{E}_{5e}$ differs from these values by approximately 4%.

The dependence of the energies of electrons and holes on the quantum dot radius is shown in the figure. The energy in the figure is reckoned from the top of the valence band. Two dashed lines mark the forbidden gap for bulk silicon, whose width is taken at 1.1 eV. Both in the valence band and in the conduction band, the first six energy levels are indicated. The difference in energies $\mathscr{E}_{0h}(R)$ and $\mathscr{E}_{1h}(R)$ is insignificant (a few percent); for this reason, these two curves in the figure virtually merge into one. A similar situation takes place for the energy levels $\mathscr{E}_{3h}(R)$ and $\mathscr{E}_{4h}(R)$ as well as for the $\mathscr{E}_{3e}(R)$ and $\mathscr{E}_{4e}(R)$ curves in the conduction band (the difference in this case is still smaller). The $\mathscr{E}_{5e}(R)$ curve, which also merges with the previous two upon an increase in the radius, lies slightly higher than the $\mathscr{E}_{3e}(R)$ and $\mathscr{E}_{4e}(R)$ energy levels.

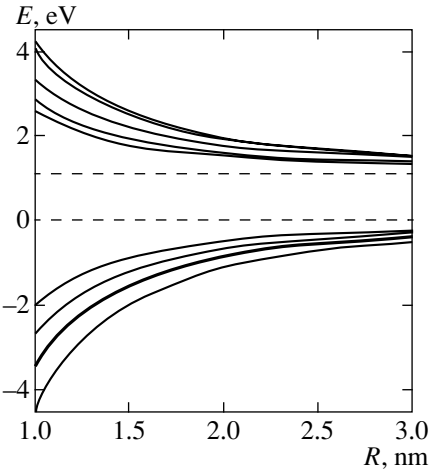

Dependence of the energy of the first six hole and electron levels on the quantum dot radius. The dashed lines mark the boundaries of the forbidden gap for bulk silicon. The region of negative energy values corresponds to the valence band, while the region above the upper dashed line corresponds to the conduction band.

The energies of all levels except $\mathscr{E}_{0e}(R)$ and $\mathscr{E}_{2e}(R)$ decrease with increasing radius of the quantum dot in proportion to R^{-2}. It was noted above, however, that the energies of the ground and the second excited state in the conduction band exhibit a certain intermediate (not power) dependence between R^{-2} and R^{-1}, which is determined by the sp_z hybridization.

It should be emphasized once again in conclusion that each energy level in the conduction band is sixfold and not doubly degenerate. The wave functions of the remaining four states can be obtained from those given above simply by changing the notation of the coordinate axes.

It should also be noted that since all (both electron and hole) states remain degenerate, a certain arbitrariness exists in the choice of the wave functions for these states. For example, they can be written as a superposition of these functions (corresponding to a given energy level) whose expressions were given above.

ACKNOWLEDGMENTS

The author is grateful to D.I. Tetel'baum for numerous fruitful discussions of this article.

This work was supported by the Russian Foundation for Basic Research (project no. 00-02-17488).

REFERENCES

1. L.-W. Wang and A. Zunger, J. Chem. Phys. **100**, 2394 (1994); A. Franceschetti and A. Zunger, Phys. Rev. B **62**, 2614 (2000).
2. J. P. Proot, C. Delerue, and G. Allan, Appl. Phys. Lett. **61**, 1948 (1992); E. Martin, C. Delerue, G. Allan, and M. Lannoo, Phys. Rev. B **50**, 18 258 (1994); C. Delerue, M. Lannoo, and G. Allan, Phys. Rev. Lett. **84**, 2457 (2000).
3. Y. M. Niquet, C. Delerue, G. Allan, and M. Lannoo, Phys. Rev. B **62**, 5109 (2000).
4. B. Delley and E. F. Steigmeier, Appl. Phys. Lett. **67**, 2370 (1995).
5. T. Takagahara and K. Takeda, Phys. Rev. B **46**, 15 578 (1992).
6. D. Babic, R. Tsu, and R. F. Greene, Phys. Rev. B **45**, 14 150 (1992).
7. J. B. Khurgin, E. W. Forsythe, G. S. Tompa, and B. A. Khan, Appl. Phys. Lett. **69**, 1241 (1996).
8. A. I. Anselm, *Introduction to Semiconductor Theory* (Nauka, Moscow, 1978; Prentice-Hall, Englewood Cliffs, 1981).
9. M. Voos, Ph. Uzan, C. Delalande, *et al.*, Appl. Phys. Lett. **61**, 1213 (1992).
10. L. D. Landau and E. M. Lifshitz, *Course of Theoretical Physics*, Vol. 3: *Quantum Mechanics: Non-Relativistic Theory* (Nauka, Moscow, 1989, 4th ed.; Pergamon, New York, 1977, 3rd ed.).
11. A. A. Kopylov, Fiz. Tekh. Poluprovodn. (Leningrad) **16**, 2141 (1982) [Sov. Phys. Semicond. **16**, 1380 (1982)].
12. A. A. Kopylov and A. N. Pikhtin, Fiz. Tekh. Poluprovodn. (Leningrad) **11**, 867 (1977) [Sov. Phys. Semicond. **11**, 510 (1977)].

Translated by N. Wadhwa

Journal of Experimental and Theoretical Physics, Vol. 94, No. 2, 2002, pp. 419–430.
Translated from Zhurnal Éksperimental'noĭ i Teoreticheskoĭ Fiziki, Vol. 121, No. 2, 2002, pp. 489–503.

SOLIDS
Electronic Properties

The Dielectric Response of Quantum Paraelectrics Containing Dipole Impurities

S. A. Prosandeev[a,*] and V. A. Trepakov[b]

[a]*Rostov State University, Rostov-on-Don, 344090 Russia*
**e-mail: pros@ic.ru*

[b]*Ioffe Physicotechnical Institute, Russian Academy of Sciences, St. Petersburg, 194021 Russia*

Received July 23, 2001

Abstract—The presence of even a very small concentration of slowly reoriented dipole impurities in a quantum paraelectric leads to strong changes in the dielectric response of the sample. This is manifested by the appearance of a giant dielectric susceptibility, colossal frequency dispersion, and several peaks in the temperature dependence of the susceptibility; in addition, the temperature dependence of the relaxation time deviates from exponential. The experimental results are presented for $KTaO_3$ samples slightly or moderately doped with lithium. General relationships between the dielectric response and the concentration of impurities, the temperature, and the frequency are established. A theory is proposed which qualitatively explains the observed complex phenomena and sometimes quantitatively describes the results with high precision. © *2002 MAIK "Nauka/Interperiodica".*

1. INTRODUCTION

An analysis of the dielectric susceptibility of perovskite-like oxides $KTaO_3$ and $SrTiO_3$, usually treated within the framework of the Curie–Weiss theory, suggests that these substances must behave as ferroelectrics when the temperature approaches absolute zero. However, the experimental behavior of the soft TO-mode frequency ω_c significantly deviates from that predicted by the Curie–Weiss law [1]. In order to explain the discrepancy, Rechester [2] and Khmel'nitskiĭ and Shneerson [3] suggested a quantum-mechanical treatment of the critical lattice TO mode with an allowance for the soft mode dispersion. Somewhat later, Vaks [4] developed this idea using a more realistic model of the lattice dynamics in perovskitelike crystals. It was demonstrated that, provided the square critical frequency at $T = 0$ is positive ($\omega_c^2 > 0$), the behavior of the soft mode frequency in the region of small temperatures ($T \ll \hbar\omega_c/2k_B$) is qualitatively close to that predicted by Barrett [5]: $\omega_c^2 \propto T^{3/2}\exp(-\hbar\omega_c/2k_BT)$ (note that the preexponential term in the Barrett formula [5] is independent of the temperature). However, when $\omega_c^2 < 0$ at $T = 0$, the soft mode frequency goes to zero at a certain temperature. In this case, behavior of the soft mode frequency near the phase transition on the paraelectric phase side was shown to obey the relationship $\omega_c^2 \propto T^2 - T_c^2$, which is significantly different both from the Barrett formula and from the Curie–Weiss law.

Recently, Farhi *et al.* [6] thoroughly measured the phonon frequencies in a low-temperature branch of the phonon spectrum of $KTaO_3$ by the method of inelastic phonon scattering. These data allowed the temperature variation of the critical mode frequency to be calculated with high precision [7]. It was established that, owing to the quantum effects, ferroelectric phase transitions take place neither in $SrTiO_3$ nor in $KTaO_3$, both compounds remaining in the paraelectric state at low temperatures. In other words, the quantum oscillations break the dipole order. For this reason, the crystals under consideration are called quantum paraelectrics. The increase in the dielectric susceptibility of quantum paraelectrics at low temperatures exhibits saturation (see, e.g., the review [8]).

At the same time, slowly reoriented dipole impurities introduced into a quantum paraelectric crystal significantly modify behavior of the dielectric permittivity and lead to the appearance of new structural effects and phase transitions [1, 9]. For example, very small lithium impurity concentrations on the order of 1% in potassium tantalate give rise to strong anomalies in the dielectric characteristics of the samples. In particular, the permittivity exhibits a sharp frequency dependence typical of relaxators, rather than soft-mode systems. The low-temperature phase state of such samples is referred to as a dipole glass. It should be emphasized that the very small impurity concentrations by no means correspond to the magnitude of the observed effects, that is, the impurity as such could not lead to such large changes in the dielectric susceptibility. This is indicative of a strong interaction of impurities with the crystal lattice, in particular, with the soft lattice mode.

In this study, we have developed a consistent theory of the soft-mode systems interacting with reoriented

dipole impurity centers. It will be shown that this interaction leads to very strong changes in the dielectric response of a quantum paraelectric, which are manifested by the appearance of a giant dielectric susceptibility, colossal frequency dispersion, several peaks in the temperature dependence of the susceptibility, and deviation of the temperature dependence of the relaxation time from exponential. We give a quantitative description of these phenomena in the case when the concentration of slowly reoriented dipole impurities exhibiting a linear interaction with the order parameter (polarization) is not too large, that is, insufficient to induce a normal ferroelectric phase transition.

The models taking into account the interaction of relaxators with soft modes were previously developed for description of the complex dynamics of a crystal lattice of KDP [4, 10], $KTaO_3$:Li (with a lithium concentration of $x > 0.02$) [9, 11, 12], $SrTiO_3$:Ca [13, 14], and $PbTiO_3$ and $KNbO_3$ [15]. In this study, the theory of such interactions is developed based on the fact that adding impurities leads to renormalization of the soft mode as a result of the impurity-mode interaction. This interaction is just what accounts for the appearance of intense peaks in both imaginary and real parts of the dielectric permittivity, with a strong frequency dispersion. After formulation of the theory, the results will be applied to interpretation and treatment of the experimental data. It will be demonstrated that the results of such treatment provide new information about the characteristics of impurity centers in the crystals studied. For example, it will be shown that the potential barrier of the lithium impurity in $KTaO_3$, which was previously considered as independent of the temperature, actually drops quite rapidly with the temperature. This leads to a conclusion of the self-localized character of this impurity (of the polaron type) in the crystals.

The experiments were performed with $K_{1-x}Li_xTaO_3$ (KLT) crystals with a lithium concentrations of $x = 0.006$ and 0.043. The samples were grown by a spontaneous crystallization method described, for example, in [16]. The lithium impurity concentration in the crystals was determined by the method of plasma emission spectroscopy possessing a sensitivity threshold of $x = 3 \times 10^{-5}$ with respect to lithium. The selected high-quality colorless transparent single crystal samples were preliminarily annealed in air for three hours at 400 K. Examination of the samples in an optical microscope with crossed polarizers showed that the crystals contained no visible impurities and boundaries characteristic of the possible twins [17]. The measurements were performed on thin ⟨100⟩-oriented single crystal plates with dimensions $3 \times 3 \times 0.2$ mm provided with gold electrodes deposited onto opposite polished surfaces. The complex dielectric permittivity components $\varepsilon'(T, f)$ and $\varepsilon''(T, f)$ were measured with the aid of a Hewlett-Packard Model 4192 analyzer operating in the frequency range from 100 Hz to 1 MHz. The samples were placed into a computer-controlled flow helium cryostat, which allowed the permittivity measurements to be performed in a temperature range from 5 to 300 K at a temperature variation rate of ±(10–100) mK/s.

2. A MODEL OF IMPURITY-FREE QUANTUM PARAELECTRIC

A starting point of the theory was selecting a Hamiltonian for the system of independent phonons. An appropriate Hamiltonian, proposed in [18, 19], was written in a special coordinate system with one of the axes directed along the wavevector and the other two lying in the perpendicular plane. In this coordinate system, the Hamiltonian is diagonal at the center of the Brillouin zone because the crystal possesses a cubic symmetry. We have strictly considered only a small region in the vicinity of the Brillouin zone, assuming that the other part of this zone does not significantly contribute to the temperature dependence of the critical mode frequency because of a relatively large energy of the critical oscillations outside the central region of the Brillouin zone. This approximation is justified by a very strong dispersion of critical oscillations observed in oxides of the perovskite family. For this reason, the elements of the dynamic matrix and the perturbation potential were expanded into series with respect to the wave vector and only the first terms of this expansion were taken into consideration.

The final equation for determining the soft mode frequency is as follows [4]:

$$\omega_c^2(T) = \omega_{c0}^2 + \frac{3\hbar\lambda^2}{8\pi^2} \times \sum_i \int \frac{d^3k}{(2\pi)^3} D_{\mathbf{k}i} \frac{n(\omega_{\mathbf{k}i})}{2\omega_{\mathbf{k}i}} - g_T(T); \quad (1)$$

where the integral is taken over the Brillouin zone. Here, λ is a coefficient relating the permittivity of a confined crystal to the soft mode frequency $\varepsilon = \lambda/\omega_c^2$ (in terms of the theory of metals, this coefficient can be considered as the squared plasma frequency);

$$D_{\mathbf{k}i} = \left[b_{11} n_\perp^2 \left|\mathbf{x}_{\mathbf{k}i}^{(2)}\right|^2 + \frac{b_{12}}{3}(1 + n_1^2)\left|\mathbf{x}_{\mathbf{k}i}^{(1)}\right|^2 \right] - \frac{\lambda(g_{11} + 2q_{12})^2}{6\pi v_c}\left(\left|\mathbf{x}_{\mathbf{k}i}^{(1)}\right|^2 + \left|\mathbf{x}_{\mathbf{k}i}^{(2)}\right|^2\right); \quad (2)$$

n_1, n_2, and n_3 are the unit vector components along the wave vector; $n_\perp = \sqrt{1 - n_1^2}$; q is the electrostriction constants; b are the electric nonlinearity constants; and $\mathbf{x}_{\mathbf{k}i}$ are the TO components of the phonon modes. The model constants S_t, V_t, A_t, S_a, V_a, A_a, and A_l estimated from the experimental data were reported elsewhere [4, 7]. Our task is to calculate the temperature dependence of

the squared critical mode frequency $\omega_c^2(T)$ (determined by the anharmonic corrections) at the center of the Brillouin zone. As can be seen, the right-hand part of Eq. (1) depends on the critical frequency and, hence, should be determined using a self-consistent procedure. Such a procedure has never been performed thus far using real values of the parameters determined from experimental data (preliminary results were reported at the conference [7]). For this reason, we attempted at analyzing the results of calculations so as to assess the influence of the method employed and the effect of some parameters.

Figure 1 shows the results of our calculations of the soft mode frequency in $KTaO_3$ as a function of the temperature by the above formula. In contrast to the estimates reported in [4], our data were obtained taking into account the self-consistent phonon frequency in the intrinsic energy part, the anisotropy of the dispersion relation, and the interaction of optical and acoustic modes; we also employed the electrostriction and elastic corrections derived in [4]. It was found that large values of the wavevector introduce a significant contribution to the final result despite a relatively large phonon energy. This fact can be explained by the density of states being much greater for large wavevectors than for small ones. In connection with this, the radius of truncation of the wavevector used in the Vaks theory should be considered as a fitting parameter. A comparison of the theoretical results to the experimental data shows that a good coincidence is observed for a truncation radius of 0.43.

In order to provide for a quantitative agreement between theory and experiment, we used the plasma frequency $\sqrt{\lambda} = 4.7 \times 10^{13}$ Hz instead of 4.0×10^{13} Hz experimentally determined in [20]. There are both theoretical and experimental grounds for this selection. We have also calculated the temperature dependence of the critical oscillation frequency by integrating the final expressions over the entire Brillouin zone. In contrast to the experiment, the temperature dependence of the critical frequency calculated in this way is nonlinear (quadratic) at temperatures above 25 K, although the absolute value of the frequency at 80 K coincides with the experimental data even without a change in the experimental plasma frequency. In principle, the experimentally observed linear relationship could be obtained assuming that the nonlinear electrostatic coefficients depend in a certain manner on the temperature [21]. However, in that case, it would be impossible to justify the scheme employed in the region of small wavevectors.

Thus, the Vaks model is capable of describing the experimental data, provided that the radius of truncation of the wavevector and the plasma frequency are properly selected. On the other hand, this model is at variance with experiment in describing the temperature behavior by integrating the corrections to Hamiltonian

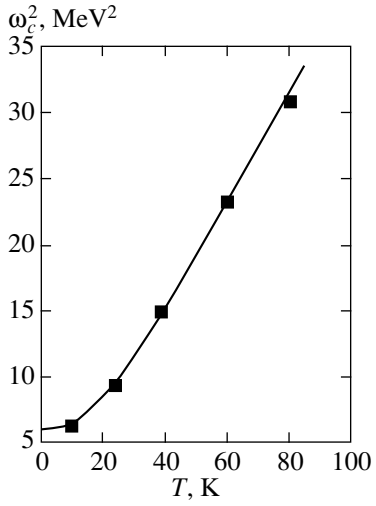

Fig. 1. The temperature variation of the soft-mode frequency in $KTaO_3$. A comparison of the experimental data (black squares) taken from [6] with our theoretical calculation (solid curve).

over the entire Brillouin zone. Apparently, the model can be improved further by providing a more precise description of the phonon spectrum and the anharmonic interaction constants at large wavevectors, as well as by taking in to account the temperature dependence of these quantities. This task was fulfilled within the framework of the theory of anharmonically polarized oxygen ions [22], but this theory did not take into account anharmonicity of another nature.

3. RELAXATORS RELATED TO THE SOFT MODE

3.1. Interaction between the Dipole Clusters and the Soft Mode

In order to describe a system of dipoles interacting with the soft mode, we propose a Hamiltonian consisting of several parts, including the self-consistent phonon Hamiltonian (H_{ph}) presented in the preceding section, a Hamiltonian of the Ising model (describing the dipole impurities), and a cross term responsible for the coupling of dipoles to the lattice polarization. In addition, we took into account the interaction between dipole impurities, including the interaction between clusters composed of these impurities. A reason for the appearance of clusters will be considered below (in a section devoted to the percolation approach).

The total Hamiltonian for the problem under consideration is as follows:

$$H = H_{ph} - 2E\sum_{i,n}\mu_n s_{in}^z - \lambda_n P_h \sum_{i,n} s_{in}^z$$
$$-\frac{1}{2}\sum_{i\neq j,n} J_{ijnn} s_{in}^z s_{jn}^z - \frac{1}{2}\sum_{i,j,n\neq 1} J_{ij1n}(s_{i1}^z s_{jn}^z + s_{in}^z s_{j1}^z), \quad (3)$$

where μ_n is the dipole moment of the nth cluster (index n = refers to single dipole impurities); λ_n is the constant of the nth cluster coupling to polarization; J_{ijnm} is the integral of interaction between ith and jth ions belonging to the nth and mth clusters; and s_{in}^z is the quasi-spin operator. Solving the problem for a polarization-dependent local field on the dipoles, we obtain

$$\chi_d = K_1 + K_2\chi_0, \tag{4}$$

where χ_0 is the lattice susceptibility,

$$K_1 = \frac{4M_1^2 n_1 G_1}{\varepsilon_0} + 4\sum_{m\neq 1}\frac{\mu_m^2 n_m F_m}{\varepsilon_0},$$

$$K_2 = 2M_1\Lambda_1 n_1 G_1 + 2\sum_{m\neq 1}\mu_m\lambda_m n_m F_m,$$

$$F_m = \frac{f_m}{1 - J_{mm} f_m},$$

$$f_m = [4(1 - i\omega\tau_m)k_B T]^{-1}, \tag{5}$$

$$M_1 = \mu_1 + \sum_{m\neq 1} J_{1m} n_m \mu_m F_m,$$

$$\Lambda_1 = \lambda_1 + \sum_{m\neq 1} J_{1m}\lambda_m n_m F_m,$$

$$G_1 = F_1\left[1 - n_1 F_1\left(\sum_{m\neq 1} J_{1m}^2 n_m F_m\right)\right]^{-1},$$

and n_m is the concentration of the mth clusters. The lattice susceptibility can be determined from the condition of stable free energy:

$$\alpha p + \beta p^3 + \gamma p^5 - \sum_n \lambda_n\langle s_n^z\rangle - E - e = 0,$$

where e is a random field created by lithium (impurity) atoms. The macroscopic polarization is obtained by averaging:

$$P_0 = \int_{-\infty}^{\infty} f(e)p(e)de,$$

where [9]

$$f(e) = \frac{1}{\sqrt{2}\delta}\exp\left(-\frac{e - E_0 P_0}{2\delta^2}\right).$$

Taking the derivative of P_0 with respect to E, we find

$$\chi_0 = \int_{-\infty}^{\infty}\frac{B(T,\omega)}{A(T, p(e)) - Q(T,\omega)} f(e)de, \tag{6}$$

where

$$B = 1 + K_2, \quad A(T, p) = (\alpha + 3\beta p^2 + 5\gamma p^4)\varepsilon_0,$$
$$Q = \varepsilon_0\sum_{m\neq 1}\lambda_m^2 n_m F_m + \varepsilon_0\Lambda_1^2 n_1 G_1. \tag{7}$$

Finally, an expression for the total susceptibility can be written in the following form:

$$\chi = \chi_o + \chi_d = K_1 + (1 + K_2)\chi_2$$
$$= K_1 + \int_{-\infty}^{\infty}\frac{B^2(T,\omega)}{A(T, p(e)) - Q(T,\omega)} f(e)de. \tag{8}$$

As can be seen, the susceptibility increases due to the interaction of dipole impurities with the soft mode, which leads to a decrease in the denominator in (8). The effect grows with increasing interaction constant and impurity concentration and with decreasing frequency of the measurements. This is also accompanied by an increase in the effective dipole moment of the impurity (M_1 substituted for μ_1) and in the dipole–polarization coupling constant (Λ_1 substituted for λ_1). An additional averaging has to be performed over the impurity relaxation times and potential barrier heights. Note that the first term in (8) is much smaller than the second and can be ignored in the case of small impurity concentrations.

The above consideration referred to the interaction of dipole clusters with the soft mode. Virtually the same conclusions are derived from an analysis of the interaction of clusters with single impurities. Thus, the single impurities play the role of a soft mode.

Previously, researchers analyzed only the second contribution (χ_d) in expression (8) [9]. This implies that the phase transitions in dilute solid solutions of virtual ferroelectrics were considered as resulting from an effective (indirect) interaction of dipoles via the soft mode, while the influence of dipoles upon this soft mode was ignored. However, it is seen that this contribution is also significant and has to be taken into account in the interpretation of experimental data. At temperatures above the critical value, the interaction of dipoles with the soft mode can actually be ignored for two reasons. First, the term $A(T, p)$ at such a temperature becomes large due to the anharmonic effects described in the preceding section, and, hence, the relatively small term $Q(T, p)$ can be ignored. Second, $Q(T, p)$ additionally decreases (as T^{-1}) with increasing temperature, which leads to vanishing of the dipole–phonon coupling at sufficiently high temperatures. Since $A(T, 0) \sim T - T_c$ for large T values, the susceptibility at these temperatures obeys the Curie–Weiss law. As the temperature decreases, the growing dipole–phonon interaction leads to a deviation from the Curie–Weiss law. This behavior will be described below.

Here, it should be noted that, besides the above low-temperature effects, the virtual ferroelectrics exhibit an

additional deviation from the Curie–Weiss law, which is caused by the quantum effects. Indeed, the systems at high temperatures obey the classical statistics in which the potential height in the temperature dependence of the relaxation time (described by the Arrhenius law) is measured from the potential well bottom. At low temperatures, the quantum statistics is operative and the potential has to be measured from the ground state energy level in the well. Thus, the transition from classical to quantum statistics is accompanied by acceleration of the relaxation processes. In the general case, it is also necessary to take into account the possible tunneling of impurities between various noncentrosymmetric states, which leads to the same consequences.

In the locally inhomogeneous solid solutions, there is another factor leading to a deviation from the Curie–Weiss law, which is related to finiteness of the polar regions in disordered crystals. As a result, the correlation radius and, hence, the lattice susceptibility exhibit saturation below the temperature at which the correlation radius equals the size of the polar regions. This factor results in the behavior of the temperature dependence of the dielectric susceptibility being the same as in quantum paraelectrics, whereby the susceptibility saturates below a certain temperature.

The interaction of the impurity dipoles with the soft mode leads to an effective dispersion of the soft mode frequency due to the dependence of Q on ω. This dispersion is significantly enhanced as compared to the case of an isolated relaxator and leads to a strong frequency dispersion of the permittivity in the temperature region of the dielectric susceptibility maximum.

Assuming the dipole impurities to be ordered on the nanoscale, we may suggest that the influence of the mean square polarization upon $A(T, p)$ would reduce the rate of the susceptibility growth with decreasing temperature. An estimate is provided by a linear relationship between the polarization and random internal field in the clusters: $\langle p^2 \rangle = K\varepsilon_0^2\chi_0^2$, where χ_0 is the initial lattice susceptibility and K is a constant coefficient. According to this estimate, the mean square polarization becomes especially large near the susceptibility maximum (and then saturates for the reasons considered above).

3.2. Small Impurity Concentrations

In the case of small impurity concentrations, we may ignore the probability of formation of percolation clusters or the presence of clusters of some other nature. For this reason, each lithium ion is characterized by a single mean relaxation time related to the impurity hopping between two nearest potential wells. As demonstrated below (see Section 3.4), deviations from the mean are mostly determined by the Gaussian distribution of the potential barrier heights near the mean value. This scatter is probably related to the random fields created by the surrounding impurities and defects. Thus, in the case of very small impurity concentrations considered here, for which the distances between impurity ions are significantly greater than the correlation radius of fluctuations in the ferroelectric order parameter of the matrix, we can restrict the consecration to a much simpler scheme as compared to that described above.

Here, this simplified scheme is studied theoretically and illustrated by the results of experimental investigations for a lithium concentration of $x = 0.006$. At this concentration, the impurity ions are spaced by approximately 5.5 lattice constants of the matrix, whereas the fluctuation correlation radius in potassium tantalate even at very low temperatures is on the order of 3.7 lattice constants. This estimate by no means implies that the impurity clusters are not formed at all. Based on the percolation calculations presented below, it will be demonstrated that the random distribution of impurities over lattice sites is just what accounts for the formation of a small number of small clusters even in the case under consideration. However, these clusters probably do not play any significant role in the lattice dynamics. Indeed, the experimental data available for the indicated impurity concentration show that the temperature dependences of both real (see Fig. 2a) and imaginary parts of the dielectric permittivity exhibit a single relaxation peak attributed to the hopping of lithium impurity ions between nearest-neighbor potential wells.

Before proceeding with the case of a small lithium ion concentration in the potassium tantalate lattice, it should be noted that below we will also consider the case of intermediate impurity concentrations for which lithium ions occur at a relatively small mean distance from each other, although the lithium ion displacements in the lattice are not fully ordered because of their random distribution (the order can be induced by applying an external electric field in the course of cooling of a sample). The case of intermediate impurity concentrations will be illustrated by the data for KLT with a lithium concentration of $x = 0.043$.

Now let us consider in more detail the case of a small concentration of lithium ions in the lattice of potassium tantalate. This system will be described in terms of a simplified Hamiltonian representing isolated impurity dipoles interacting with the soft mode (the full Hamiltonian includes the intrinsic energy of the matrix lattice):

$$H = -2E\sum_i \mu s_i^z - \lambda P_h \sum_i s_i^z, \qquad (9)$$

where notation is the same as above, but only isolated impurity dipoles of a single type are considered.

Figure 2a shows the experimental temperature dependence of the real part of the dielectric permittivity in a KLT crystal with $x = 0.006$. This lithium content can be considered as small [1], since this value is lower as compared to the lower critical concentration ($x_{cr} = 0.01$) at which the KLT crystal features a transition to the

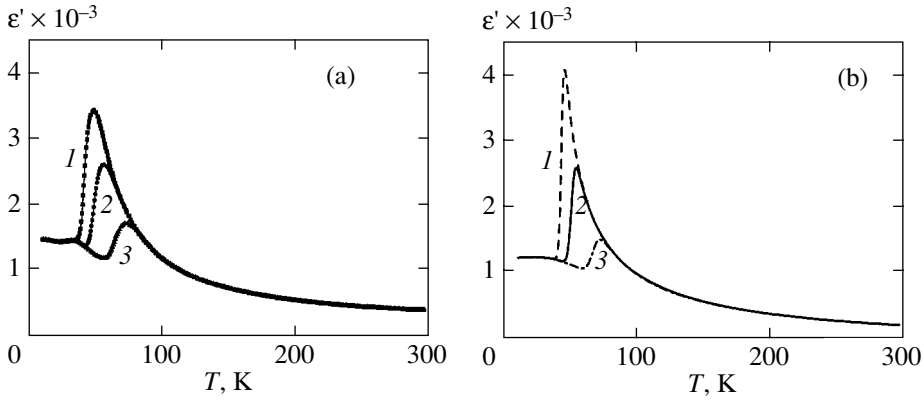

Fig. 2. (a) Experimental and (b) theoretical temperature dependences of the real part of the complex dielectric permittivity in KLT ($x = 0.006$) for various frequencies: (*1*) 400 Hz; (*2*) 11 kHz; (*3*) 1 MHz.

polar glass state. The dipole moment of the impurity was selected based on independent experimental data: $\mu = 0.6e$ Å [23]. The dipole–lattice coupling constant $\lambda_1 = 0.12\mu_1/3\varepsilon_0$ was selected so as to provide for a good fit of theory to experiment and proved to be close to purely theoretical estimates [24]. The impurity potential barrier height U and the relaxation time τ_0 at high temperatures were determined using the Arrhenius law: $U = 908$ K; $\tau_0 = 2 \times 10^{-13}$ s. The soft mode frequency was described by the Barrett formula

$$\omega_c^2 \propto T_s \coth(T_s/T) - T_0$$

with $T_0 = 0$ K and $T_s = 44$ K, which ensured a good reproduction of the high-temperature part of the susceptibility. A relatively large value of the saturation temperature T_s agrees with the results of investigation of the giant Raman scattering [25]. The value of $K = 5.6 \times 10^{-6}$ was determined from the condition of a good fit of theory to experiment in the region of the permittivity maximum. A comparison of the results of theoretical calculations (Fig. 2b) and experimental measurements (Fig. 2a) shows a good qualitative and semiquantitative coincidence of the data for various frequencies. A reasonable agreement between theory and experiment was observed for the imaginary part of the complex permittivity as well.

3.3. Intermediate Impurity Concentrations

Now let us proceed to an analysis of the case of intermediate concentrations of lithium ions in KLT. We have studied the samples with a lithium concentration of $x = 0.043$. The results of experimental investigations showed that the temperature dependences of both real and imaginary parts of the complex permittivity at such impurity concentrations (above the lower critical boundary, but below the level $x = 0.06$ at which the ferroelectric phase transition takes place [26]) exhibit two peaks (Fig. 3). In connection with this, a theoretical description of the experimental results was based on a more complicated Hamiltonian of the type

$$H = -2E\sum_i \mu_1 s_{i1}^z - 2E\sum_i \mu_2 s_{i2}^z - \lambda_1 P_h \sum_i s_{i1}^z - \lambda_2 P_h \sum_i s_{i2}^z. \quad (10)$$

Figure 3 shows the experimental temperature dependences of both real and imaginary parts of the complex permittivity in comparison with the results of our theoretical calculations for KLT with $x = 0.043$. As can be seen, there is a good agreement between theoretical and experimental data. The relaxation times and potential barriers heights used in the calculations were determined based on the Arrhenius representation of the experimental data. We obtained $\tau_0 = 9 \times 10^{-13}$ s and $U = 914$ K for the first relaxator and $\tau_0 = 1.36 \times 10^{-15}$ s and $U = 2695$ K for the second relaxator. The constant factor $K = 5.6 \times 10^{-6}$ was the same as that in the case of small concentrations. The coupling constants ($\lambda_1 = 0.05$ and $\lambda_2 = 0.025$) were smaller as compared to those for small concentrations, which is probably explained by the soft mode hardening (related to the random fields) with increasing impurity concentration.

Let us discuss the nature of two relaxators experimentally observed in KLT with an intermediate impurity concentration. It was suggested [27] that the first peak is related to the relaxation of isolated lithium ions, while the second peak reflects the relaxation of ion pairs. However, this interpretation encounters significant difficulties: the preexponential factor in the temperature dependence of the relaxation time for the second relaxator is too small to correspond to a cluster character of the impurity dynamics. Below (see Section 3.5), we will demonstrate that this factor should be corrected so as to take into account that the mean potential barrier height is a function of the temperature.

According to the results of the *ab initio* calculations [28–30], a potential barrier for the impurity hopping

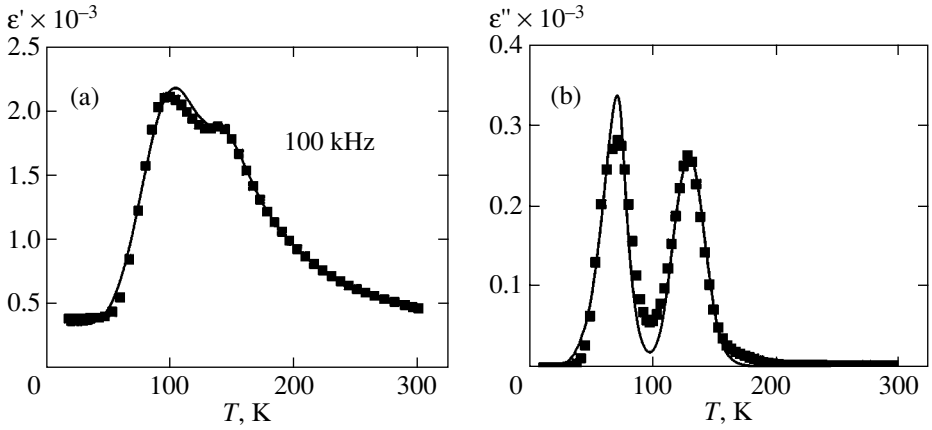

Fig. 3. A comparison of the theoretical (solid curves) and experimental (black squares) temperature dependences of (a) real and (b) imaginary parts of the complex permittivity for KLT with $x = 0.043$.

with the dipole moment rotation through 90° is significantly lower than a barrier for the dipole rotation through 180°. For this reason, we may suggest that some of the lithium ions occurring close to each other are strongly correlated and, hence, contribute to the dielectric permittivity in pairs. In such pairs, the (z, z) configuration is energetically favorable while the (x, x) and (x, $-x$) configurations possess greater energies. Hence, only two states, (z, z) and ($-z$, $-z$), separated by a 180° barrier are important for lithium ion dynamics in such pairs, which corresponds to the ideas of Doussineau *et al.* [27].

3.4. The Frequency Dependence of the Dielectric Permittivity

Studying the frequency dependence of the dielectric permittivity, we established the fact that the Debye description is insufficient to explain the experimental data. In the Debye description of the dielectric function, even with an allowance for the dipole interaction with the soft mode, the relaxation peak width in the imaginary part of the frequency dependence of the susceptibility is smaller than that observed in experiment. For this reason, we attempted at searching for an appropriate function describing a distribution of the impurity barrier heights. Assuming that this distribution is described by a Gauss function, the agreement between theory and experiment in the region of relatively high frequencies can be significantly improved.

However, the region of low frequencies still exhibits some discrepancy. Apparently, the region of intermediate lithium concentrations under consideration features an additional contribution in the low-frequency range. This can be related to the cooperative phenomena (e.g., the cluster contribution) and/or the contributions from the dipoles occurring in an additional electric (deformation) field of the surrounding ions. We have established that, at a temperature of about 140 K, the additional contribution in the entire frequency range studied can be described by a constant (Fig. 4). However, at lower temperatures, this contribution has to be described by a function that can be considered as constant only at low frequencies, while sharply decreasing in the region of high frequencies. In the region of saturation, the low-frequency contribution (constant value) increases with decreasing temperature, while the width of this region gradually narrows. Elucidating the microscopic nature of this contribution would require additional investigations. Analogous results were obtained in the region of still lower temperatures featuring a rapid relaxation process.

Upon fitting the parameter of the potential barrier distribution function, we obtained a mean halfwidth of this distribution of about 200 K. This result is quite reasonable if we take into account that the dipole impurities in the intermediate concentration range occur in a random field generated by the surrounding impurity ions. We may expect that the width of the potential barrier distribution function would decrease when the dipoles are ordered as a result of local or global polarization or under the action of an external electric field.

3.5. The Temperature Dependence of the Potential Barrier Height for Lithium Impurity in $KTaO_3$

It is usually accepted that the relaxation time obeys the Arrhenius law:

$$\tau = \tau_0 \exp(-U/k_B T), \tag{11}$$

where the potential barrier height U is assumed to be independent of the temperature. In the case of intermediate impurity concentrations under consideration (see Section 3.3), both relaxation processes must be described by formula (11) with the corresponding potential barriers and preexponential factors.

Using the general expressions obtained in Section 2, we established that the mean values of the potential barriers in the system studied linearly decrease with the temperature. Figure 5 shows the experimental values of

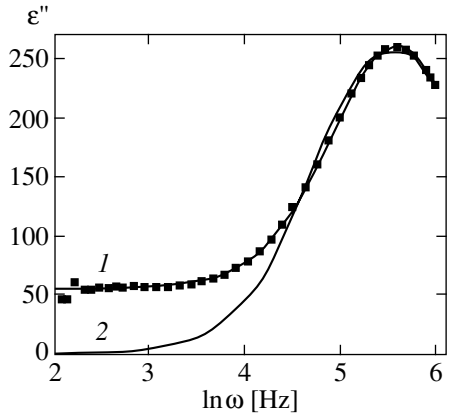

Fig. 4. A comparison of the theoretical (solid curves) and experimental (black squares) frequency dependences of the imaginary part of the complex permittivity for KLT with $x = 0.043$. The calculations were performed (*1*) with and (*2*) without taking into account the additional low-frequency contribution. $T = 140$ K.

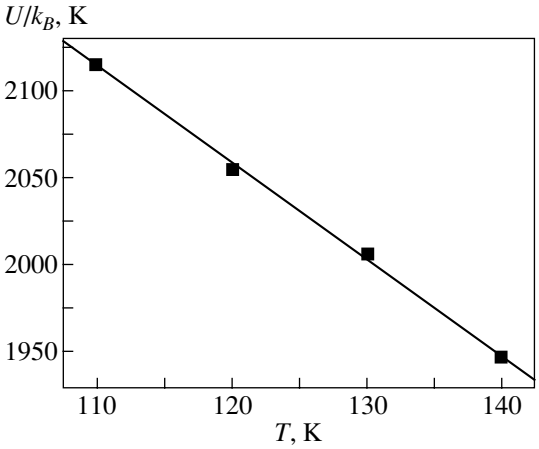

Fig. 5. Temperature dependence of the mean value of the potential barrier for the slow relaxation in KLT with $x = 0.043$. Black squares represent the values calculated from the frequency dependence of the permittivity; solid line shows the best linear approximation $U = U_0 - 5.5k_BT$.

the mean potential barrier height for the slow relaxation component. A similar plot, but with approximately half the rate of the barrier height decrease with the temperature, was obtained for the fast relaxation component. It should be emphasized that the experimental data were processed without assuming a certain analytical expression for the temperature dependence of the potential barrier. The result is essentially an experimental fact.

A linear dependence of the potential barrier height on the temperature is known for polarons [31]. However, we relate the relaxation process studied to neither electrons nor polarons for the reasons indicated below. We believe that the observed relaxation proceeds by hopping of the lithium ions between nearest potential wells, while the existence of these wells is related to the fact that large displacements of the impurity ions significantly influence the positions of the surrounding matrix atoms. The shifted matrix atoms create deep potential wells for the lithium ions, so that the corresponding energy of the lithium impurity is mostly due to the self-localization of lithium ions in one of the noncentrosymmetric positions related to polarization of the surrounding ions [28–30]. We believe that the potential barrier of lithium exhibits a certain "trembling" in response to the dynamics of surrounding ions. The amplitude of these vibrations increases with the temperature, thus leading to a decrease in the mean effective potential barrier. In this respect, a lithium ion in the $KTaO_3$ lattice may be called an ion polaron—by analogy with the electron polaron; however, it should be recalled that the observed relaxation is by no means related to the electron polarons.

A linear temperature dependence of the potential barrier in formula (11) results in that the preexponential factor determined from the Arrhenius plot describing the temperature dependence of the relaxation time is significantly (by several orders of magnitude) smaller than the experimental value. Indeed,

$$\begin{aligned}\tau &= \tau_0 \exp\left(-\frac{U_0 - \xi k_B T}{k_B T}\right) \\ &= \tau_0 e^{-\xi} \exp\left(-\frac{U_0}{k_B T}\right) = \tau_0^* \exp\left(-\frac{U_0}{k_B T}\right),\end{aligned} \tag{12}$$

where $\tau_0^* = \tau_0 e^{-\xi}$. This conclusion is explained by the fact that the preexponential factor determined from the Arrhenius plot for the second relaxator at intermediate lithium concentrations (see above) falls within the region of electron relaxation rates, rather than within the region of reasonable ion relaxation rates. A correction based on the linear temperature dependence of the potential barrier height leads to relaxation times quite acceptable for the ion relaxation. This fact is just what gives grounds for not relating the observed relaxation processes to the electron polarons.

It should be emphasized that the linear temperature dependence of the potential barrier, established using the experimental data on the frequency dependence of the imaginary part of the dielectric permittivity, cannot be derived from the Arrhenius plot (i.e., from the temperature dependence of the relaxation time) because this linear dependence leads only to an effective decrease in the preexponential factor in the Arrhenius relationship.

3.6. Deviations from the Curie–Weiss Law

The interaction of lithium dipoles with the soft mode in the case of small impurity concentrations gives rise to an interesting kinetic phenomenon, whereby the temperature dependence of the dielectric permittivity deviates from the Curie–Weiss law. Note that the direction of this deviation is the same as that for the fre-

quently employed Vogel–Fulcher empirical relationship. Taking this into account, we can propose an alternative interpretation of the experimental data for dilute solid solutions of ferroelectrics in which the temperature dependence of the mean relaxation time deviates from the Arrhenius law.

It is commonly accepted that a deviation from the Arrhenius law and fitting to the Vogel–Fulcher relationship are due to the "freezing" of dipoles at a certain (nonzero) temperature T_g. Unlike this, an increase in the relaxation time with decreasing temperature and the related deviation from the Arrhenius law in our case are related to an increase in dielectric permittivity of the medium. Indeed, the dipole relaxation proceeds in a dielectric medium, while the medium is sensitive with respect to changes in the dipole orientation. Apparently, the interaction between these subsystems is mediated by the local electric and deformation fields. It should be noted that below we will restrict the consideration to the case of small lithium concentrations, when the system features a single relaxation process.

To a first approximation, a local electric field E_l on the impurity dipoles linearly depends on the polarization of the matrix:

$$E_l = E + \frac{\lambda}{2\mu}P_h. \tag{13}$$

On the other hand, the local electric field E_h on the host lattice ions linearly depends on the dipole polarization: $E_h = E + \lambda P_d/2\mu + e$, where e is the random electric (deformation) field. Writing as above the free energy of the lattice

$$F_h = F_{h0} + \frac{\alpha(T)p^2}{2} + \frac{\beta p^4}{4} + \frac{\gamma p^6}{6} - E_h p,$$

we can express the macroscopic polarization as

$$P_h = \int_{-\infty}^{\infty} def(e)p(e),$$

where $f(e)$ is the random field distribution function. Using the condition of thermodynamic equilibrium of the lattice, we obtain

$$p(e) = E_h/A(T), \quad A(T) = \alpha(T) + 3\beta p^2 + 5\gamma p^4.$$

Below, we will employ an approximate estimate

$$\langle 3\beta p^2\rangle = K/\varepsilon_0^2\alpha^2,$$

where K is a constant factor. Substituting the expression for polarization into formula (13), we obtain

$$E_l = \left(1 + \frac{\lambda}{2\mu A(T)}\right)E + \frac{1}{A(T)}\left(\frac{\lambda}{2\mu}\right)^2 P_d. \tag{14}$$

In the relaxation time approximation, we can write

$$\frac{dP_d}{dt} = -\frac{1}{\theta}(P_d - \bar{P}_d), \tag{15}$$

where θ is the initial relaxation time and $\bar{P}_d = n_d\mu^2 E_l/Nk_BT$ [32]. Finally, formula (13) yields

$$\frac{dP_d}{dt} = \frac{n_d\mu^2}{Nk_BT\theta}\left(1 + \frac{\lambda}{2\mu A(T)}\right)E - \frac{1}{\theta}\left(1 - \frac{n_s\lambda^2}{4Nk_BT\alpha}\right)P_d. \tag{16}$$

A well known solution to this equation is

$$\tau = \frac{\theta_0\exp(U/k_BT)}{1 - n_d\lambda^2/4Nk_BTA(T)} = \theta_0\exp\left(\frac{U}{k_BT}\right)\frac{4 + r\chi_\infty(4 + r\chi)}{4 + r\chi_\infty(4 + r\chi_\infty)} \approx \theta_0\exp\left(\frac{U}{k_BT}\right)\frac{4 + r\chi}{4 + r\chi_\infty} \approx \theta_0\exp\left(\frac{U}{k_BT}\right)\frac{\chi}{\chi_\infty}, \tag{17}$$

where $\chi_\infty = A^{-1}(T)$.

In the first equality (17), the numerator in the right-hand part corresponds to the Arrhenius law, while the denominator exhibits a critical dependence on the temperature. This is just what leads to a deviation from the Arrhenius law, which is usually interpreted as the critical retardation of relaxators near the second-order phase transition. However, no phase transition may take place in our case, and, moreover, a change in the dielectric susceptibility is not directly related to the behavior of relaxators. This change is mostly due to the temperature-affected behavior of the soft mode related to anharmonicity of the thermal oscillations of atoms in the matrix.

The temperature dependence of the dielectric permittivity in KLT with $x = 0.006$ was treated in terms of the relationship

$$\ln\frac{1}{\tau} = C - \frac{U}{k_BT} + \ln\left(1 - \frac{B}{T[T_s\coth(T_s/T) - T_0]}\right), \tag{18}$$

which is readily derived from the first equality (17) by substituting the Barrett formula for the soft mode frequency. The results of fitting are presented in Fig. 6. The values of parameters determined from this fitting procedure are consistent both with the known experimental data and with the results of theoretical calculations. In particular, the constant of coupling of the lithium dipoles to the soft mode determined from these data is about 0.1, in good agreement with the previous theoretical estimates [9, 11, 24]. The good fit of theory to experiment observed in Fig. 6 is evidence for the validity of our description. However, at still lower temperatures, the quantum effects begin to play a more sig-

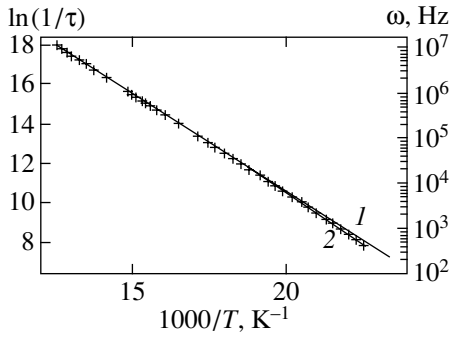

Fig. 6. A comparison of the theoretical (solid curves) and experimental (crosses) temperature dependences of the relaxation time in $KTaO_3$:Li. The calculations were performed using (*1*) the Arrhenius law and (*2*) the proposed model.

nificant role and the experimental data deviate from the Arrhenius law in the other direction, corresponding to a decrease in the relaxation time (calculated by quantum-mechanical methods) as compared to the classical value (given by the Arrhenius law). As noted above, an important role in this region belongs to the tunneling processes [33].

The aforementioned effect is small in the sense that it takes into account the temperature dependence of the preexponential factor in the Arrhenius relationship (11), related to the temperature dependence of the dielectric permittivity. At the same time, the Arrhenius relationship implies the temperature dependence of the exponent in (11). If the temperature dependence of the dielectric permittivity is a smooth function of the temperature, a deviation from the Arrhenius law is very difficult to observe in experiment. However, it was found that this effect is readily observed in the case of small lithium concentrations; moreover, the values of parameters obtained by treating the experimental data in terms of the model of relaxators interacting with the soft mode agree well with the theoretical estimates.

At first glance, it might seem that explanations of the effects studied in this and preceding sections are contradictory. Indeed, in both cases we are dealing with the temperature dependence of the potential barrier of lithium ions. In the first case, it was demonstrated that this behavior is described by a linear function of the temperature, whereas, in the second case, the function is essentially nonlinear (logarithmic). However, it must be emphasized that these cases refer to essentially different effects. The first is explained by "trembling" of the potential barrier in response to the dynamics of surrounding ions and is determined by the mean square of the order parameter. In contrast, the second effect is due to the interaction of dipoles with the ferroelectric order parameter mediated by the local fields and is determined directly by the order parameter. In addition, the first effect related to the potential "trembling" (leading to a linear temperature dependence of the potential barrier height) is not manifested in the Arrhenius plot because this implies no deviations from a linear relationship between the logarithm of the relaxation time and the inverse temperature. Therefore, a small deviation from the Arrhenius law observed for a small lithium impurity concentration in KLT ($x = 0.006$) is entirely due to the interaction of lithium dipoles with the soft mode.

As noted above, the effect considered in this section is small. Being observed at small impurity concentrations, this effect is hardly manifested at the intermediate concentration interval, at least in the frequency range studied. This can be theoretically explained by the fact that, as the impurity concentration grows, the constant of coupling of the lithium dipoles (relaxators) to the soft mode decreases, while the soft mode frequency grows due to random electric fields and stresses. Thus, on the one hand, the interaction of relaxators with the soft mode leads to an increase in the dielectric permittivity, while, on the other hand, the random fields introduced by the impurities lead to a decrease in the permittivity. As a result, the permittivity increases with the impurity concentration in the region of the peak (or peaks) and decreases in the adjacent region.

Thus, the effect described in this section is readily observed for very small lithium concentrations, in which case the impurity ions can be considered as independent relaxators interacting only with the soft mode but not with each other. This is just what explains the effect observed in the region of small concentrations ($x = 0.006$) where only one significant relaxation process takes place, while being weak in the region of intermediate concentrations ($x = 0.043$), at least in the frequency range studied. In any case, this effect is weak as compared to that considered in the preceding section.

3.7. Percolation Description

Here, we will take into account that the lithium impurity ions are randomly distributed over the corresponding sites in the A sublattice of $KTaO_3$. Some of these ions are closely spaced from each other, while some others are rather distant. The closely spaced ions may form clusters characterized by a common direction of their dipole moments acquired as a result of the indirect interaction through the soft mode. The problem of determining the interaction radius can be solved by comparing the magnitude of the indirect interaction to the potential barrier height. Thus, the task is to describe the statistics of such clusters composed of impurity ions.

The problem is conveniently solved using percolation theory, according to which the macroscopic means are described in terms of power functions determined by the critical indexes. One of the usually calculated parameters is the so-called cluster size s or, in fact, the number of impurities in the cluster. As the temperature

decreases, the cluster size grows because the indirect interaction between impurities increases as a result of further softening of the soft mode responsible for this interaction. The increase in the interaction magnitude implies an increase in the radius of interaction of the individual impurity ions, which leads, in particular, to coalescence of the initial relatively small clusters into clusters of a greater size. In fact, the formation of very big clusters is unlikely because a potential barrier for the coalescence of small clusters, involving the rotation of their dipoles in the same direction, is rather large.

In order to take into account the real situation, whereby the dipole moments of large clusters cannot be rotated in the random fields (viscosity) existing in the system, we introduce a restriction on the size of clusters that can merge together. For simplicity, we used the condition

$$s_i s_j < \text{const}, \tag{19}$$

where s_i and s_j are the dimensions of clusters to be combined. By comparing the theory to experiment, we have determined the constant in (19) that provided for the best coincidence with the available data.

The calculation procedure was as follows. The cubic lattice was divided into blocks, each containing several lattice sites. The impurities were distributed over blocks and then over sites in each block with the aid of a random number generator. The block size was approximately equal to the maximum correlation radius r_c in a given temperature interval, which can be readily estimated using the relationship $r_c \propto 1/\omega_c$ (ω_c is the critical frequency). The coefficient of proportionality in this relationship, representing the rate of variation of the soft mode frequency depending on the wavevector, can be determined from experiment [34]. The division into blocks was necessary in order to determine whether the impurity belongs to a given cluster by checking the distances between impurities occurring in the adjacent blocks. Otherwise it would be necessary to check for all distances in the ion pairs, which can significantly increase the required computational time.

In the first step, the calculation was performed for a relatively high temperature and a given maximum distance at which lithium ions are considered as belonging to a cluster. The interaction radius was assumed to be proportional to the correlation radius, with the proportionality coefficient selected so as to obtain a correct temperature of the percolation phase transition using a comparison between theory and experiment in a broad concentration range. As a result, ions belonging to different clusters were determined and the statistical means were calculated. As the temperature decreased, the correlation radius increased as $1/\sqrt{T - T_c}$ (if the quantum effects were taken into account, this relationship became more involved: $1/\sqrt{T_s \coth(T_s/T) - T_0}$, where T_s is the saturation temperature and T_0 is the critical Curie–Weiss temperature determined by extrapolation from the side of large T values). The interaction radius and the cluster size also increased with decreasing temperature. Thus, all the cluster characteristics were determined as functions of the temperature in the same calculation.

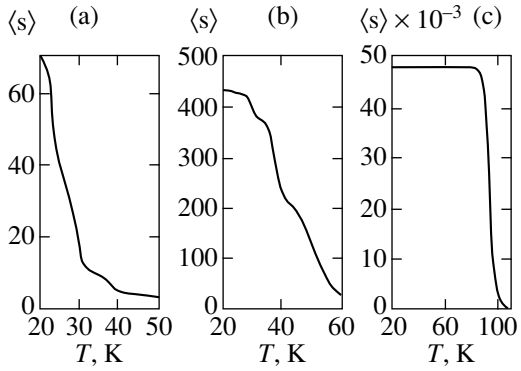

Fig. 7. Plots of the mean cluster size (mean number of lithium ions in the cluster) versus temperature in KLT with x = 0.008 (a), 0.022 (b), and 0.063 (c).

The results of calculations of the mean cluster size (i.e., of the number of ions in the cluster) are presented in Fig. 7. As can be seen from these data, the mean cluster size grows with decreasing temperature in accordance with the above assumptions. As a result, we have established that clusters formed for a lithium concentration of 0.6% are composed of several tens of impurity ions, while the lithium concentrations of 2% and 6% lead to the appearance of clusters containing several hundred and several thousand impurity ions, respectively. These results are in good agreement with the experimental data on the second harmonic generation [35].

4. CONCLUSION

It is commonly accepted that individual slowly relaxing impurity centers contribute to the dielectric susceptibility of substances, this contribution being dependent on the frequency of the applied electric field and on the temperature. If the impurity concentration is below the so-called critical value, the corresponding contribution to the total dielectric susceptibility of the system must be relatively small. The experimental data presented above and reported by other researchers indicate that small impurity concentrations in quantum ferroelectrics give rise to large macroscopic effects. We have demonstrated that these effects are due to the interaction of dipole impurities with the soft mode. Thus, the dynamics of impurity atoms and the soft mode are no longer independent.

The new phenomena related to the temperature and frequency dependences of the dielectric permittivity of KLT crystals with small and moderate lithium concentrations were explained within the framework of a common approach. These results, albeit resembling to a cer-

tain extent the analogous findings in the polaron theory (where the electron subsystem coupled to the lattice oscillations changes the kinetic, optical, and some other properties), are not related to the electron polarons. In connection with this, we propose the new term "ion polaron," which implies that light lithium ions appear to be "trapped" due to the lattice polarization created by the same ions. In this context, we can explain a linear decrease in the mean potential barrier observed for the first time in processing the frequency dependence of the imaginary part of the dielectric permittivity. This effect is due to the impurity potential barrier "trembling" caused by the dynamics of surrounding atoms. We have demonstrated that this effect leads to significantly underestimated values of preexponential factors in the Arrhenius relationship, determined from the temperature dependence of the relaxation time. As a result, the values of the preexponential factor may even fall within the interval of "electron" relaxation. However, corrections determined using the experimental data on the frequency dependence of the dielectric permittivity yield values typical of ion oscillations.

ACKNOWLEDGMENTS

The authors are grateful to P.P. Syrnikov for kindly providing the KLT crystals and to M.E. Savinov for his help in conducting the measurements. One of the authors (S.A.P.) is grateful to M.D. Glinchuk and A.V. Turik for fruitful discussions of results.

This study was supported by the Russian Foundation for Basic Research, project nos. 00-02-16875, 01-02-16029, and 01-02-17799.

REFERENCES

1. U. T. Höchli, K. Knorr, and A. Loidl, Adv. Phys. **39**, 405 (1990).
2. A. B. Rechester, Zh. Éksp. Teor. Fiz. **60**, 782 (1971) [Sov. Phys. JETP **33**, 423 (1971)].
3. D. E. Khmel'nitskiĭ and V. L. Shneerson, Fiz. Tverd. Tela (Leningrad) **13**, 832 (1971) [Sov. Phys. Solid State **13**, 687 (1971)].
4. V. G. Vaks, *Introduction to the Microscopic Theory of Ferroelectricity* (Nauka, Moscow, 1973).
5. J. H. Barrett, Phys. Rev. **86**, 118 (1952).
6. F. Farhi, A. K. Tagantsev, R. Currat, *et al.*, Eur. Phys. J. B **15**, 615 (2000).
7. S. A. Prosandeev, W. Kleemann, and J. Dec, Integr. Ferroelectr. **32**, 979 (2001).
8. O. E. Kvyatkovskiĭ, Fiz. Tverd. Tela (St. Petersburg) **43**, 1345 (2001) [Phys. Solid State **43**, 1401 (2001)].
9. B. E. Vugmeister and M. D. Glinchuk, Rev. Mod. Phys. **62**, 993 (1990).
10. A. Bussmann-Holder and K. H. Michel, Phys. Rev. Lett. **80**, 2173 (1998).
11. V. S. Vikhnin, Fiz. Tverd. Tela (Leningrad) **26**, 1495 (1984) [Sov. Phys. Solid State **26**, 552 (1984)].
12. S. A. Prosandeev, V. A. Trepakov, M. E. Savinov, and S. E. Kapphan, J. Phys.: Condens. Matter **13**, 719 (2001).
13. W. Kleemann, J. Dec, Y. G. Wang, *et al.*, J. Phys. Chem. Solids **61**, 167 (2000).
14. S. A. Prosandeev, W. Kleemann, and J. Dec, J. Phys.: Condens. Matter **13**, 5957 (2001).
15. Y. Girshberg and Y. Yacoby, J. Phys.: Condens. Matter **11**, 9807 (1999).
16. V. Trepakov, F. Smutny, V. Vikhnin, *et al.*, J. Phys.: Condens. Matter **7**, 3765 (1995).
17. D. Rytz and H. J. Scheel, J. Cryst. Growth **59**, 486 (1982).
18. J. D. Axe, J. Harada, and G. Shirane, Phys. Rev. B **1**, 1227 (1970).
19. V. G. Vaks, Zh. Éksp. Teor. Fiz. **54**, 910 (1968) [Sov. Phys. JETP **27**, 486 (1968)].
20. G. Shirane, R. Nathans, and V. J. Minkiewicz, Phys. Rev. **157**, 396 (1967).
21. G. V. Belokopytov, Ferroelectrics **168**, 69 (1998).
22. R. Migoni, H. Bilz, and D. Bauerle, Phys. Rev. Lett. **37**, 1155 (1976).
23. A. V. Turik and A. G. Khasabov, J. Phys.: Condens. Matter **13**, 1323 (2001).
24. S. A. Prosandeev and A. I. Riabchinski, J. Phys.: Condens. Matter **8**, 505 (1996).
25. H. Vogt, J. Phys.: Condens. Matter **7**, 5913 (1995).
26. S. R. Andrews, J. Phys. C **18**, 1357 (1985).
27. P. Doussineau, Y. Farssi, C. Frenos, *et al.*, Europhys. Lett. **24**, 415 (1993).
28. M. Exner, C. R. A. Catlow, H. Donnerbers, and O. Schrimer, J. Phys.: Condens. Matter **6**, 3379 (1994).
29. R. I. Eglitis, A. V. Postnikov, and G. Borstel, Phys. Rev. B **55**, 12 976 (1997).
30. I. Tupicyn, A. Dejneka, V. Trepakov, *et al.*, Ferroelectrics **237**, 9 (2000).
31. Yu. A. Firsov, *Polarons* (Nauka, Moscow, 1975).
32. G. I. Skanavi, *Physics of Dielectrics* (Gostekhizdat, Leningrad, 1949).
33. W. Kleemann, S. Kütz, and D. Rytz, Europhys. Lett. **4**, 239 (1987).
34. W. Prusseit-Elffroth and F. Schwabl, Appl. Phys. A: Solids Surf. **A51**, 361 (1990).
35. S. A. Prosandeev, V. S. Vikhnin, and S. Kapphan, Eur. Phys. J. B **15**, 469 (2000).

Translated by P. Pozdeev

Journal of Experimental and Theoretical Physics, Vol. 94, No. 2, 2002, pp. 431–433.
Translated from Zhurnal Éksperimental'noĭ i Teoreticheskoĭ Fiziki, Vol. 121, No. 2, 2002, pp. 504–507.

SOLIDS
Electronic Properties

On the Possibility of a Radical Decrease in the Strength of Many-Body Interactions in the Organic Metal α-$(BETS)_2KHg(SCN)_4$

S. I. Pesotskiĭ[a, b, c, *], R. B. Lyubovskiĭ[a, c], W. Biberacher[b], M.V. Kartsovnik[b], V. I. Nizhankovskiĭ[c], N. D. Kushch[a], H. Kobayashi[d], and A. Kobayashi[e]

[a]*Institute for Problems in Chemical Physics, Russian Academy of Sciences, Chernogolovka, Moscow oblast, 142432 Russia*
**e-mail: pesot@icp.ac.ru*
[b]*Walther Meissner Institute, D-85748 Garching, Germany,*
[c]*International Laboratory of High Magnetic Fields and Low Temperatures, Wroclaw, 53529, Poland*
[d]*Institute for Molecular Science, Okazaki 444, Japan*
[e]*Research Center for Spectrochemistry, Graduate School of Science, University of Tokyo 113, Japan*

Received August 23, 2001

Abstract—Behavior of the de Haas–van Alphen (dHvA) oscillations depending on the angle between the magnetic field direction and the perpendicular to conducting layers in the quasi-two-dimensional organic metal α-$(BETS)_2KHg(SCN)_4$ was studied in detail. The angular dependence of the dHvA oscillation amplitude exhibits a series of minima (at $\pm 43.2°$, $\pm 64.6°$, and $\pm 72.0°$) related to the "zero spin" effect, through which it is possible to estimate the splitting factor. An analysis of this value suggests that many-body interactions in the compound studied are either absent or at least radically weakened. *© 2002 MAIK "Nauka/Interperiodica".*

In the past decade, the family of isostructural quasi-two-dimensional organic metals of the α-$(ET)_2MHg(XCN)_4$ type (where ET = bis(ethylenedithio)tetrathiafulvalene; M = K, Tl, Rb, NH_4; and X = S, Se) has become an object of extensive investigation in the physics of organic conductors [1]. The main reason is that the Fermi surface of these metals features the coexistence and interaction of the corrugated open sheets characteristic of quasi-one-dimensional electron systems and the corrugated cylinder typical of a quasi-two-dimensional metal. As a result, a number of phenomena were simultaneously observed in this system that are typical of quasi-one- and -two-dimensional systems.

An example is offered by the quantum oscillations of various types (related to the closed orbits) and a phase transition of the Peierls type (accompanied by nesting of the open sheets of the Fermi surface) observed in the compounds with M = K, Tl, Rb and X = S at $T \le 10$ K [1]. The nature of a state below the transition temperature is still unclear, but recent extensive investigations of the phase diagram of these systems [2, 3] provided convincing evidence that this is a state with the spin density wave. The other metals of the aforementioned family retain their Fermi surfaces down to very low temperatures [1], and one of these compounds, α-$(ET)_2NH_4Hg(SCN)_4$, passes into the superconducting state at $T \approx 1$ K [4].

Quite recently, the quasi-two-dimensional organic metals α-$(BETS)_2KHg(SCN)_4$ and α-$(BETS)_2NH_4Hg(SCN)_4$, isostructural to the ET-based analogs from the above family, were synthesized using another organic molecule—bis(ethylenedithio)tetraseleniumfulvalene (BETS) differing from ET by selenium atoms partly substituted for sulfur atoms. Taking into account that the conductivity of the ET-based metals is provided by overlap of the atomic orbitals of sulfur in the conducting layer, we may expect that this substitution will significantly influence the properties of new complexes. Indeed, the organic metals α-$(BETS)_2KHg(SCN)_4$ and α-$(BETS)_2NH_4Hg(SCN)_4$ exhibited neither the Peierls transition nor the superconducting transition with decreasing temperature [5]. An analysis of the Shubnikov–de Haas oscillations in these metals suggested that the main factor suppressing the transitions is the partial weakening of the Coulomb electron–electron repulsion [5].

Based on the thorough investigation of the de Haas–van Alphen (dHvA) oscillations in the organic metal α-$(BETS)_2KHg(SCN)_4$, we propose a model explaining suppression of the low-temperature transitions by fully absent or radically weakened electron–electron and electron–phonon interactions.

We have studied single crystal samples of α-$(BETS)_2KHg(SCN)_4$ weighing 120–150 μg. The dHvA effect was observed using the method described elsewhere [6], according to which the magnetization varia-

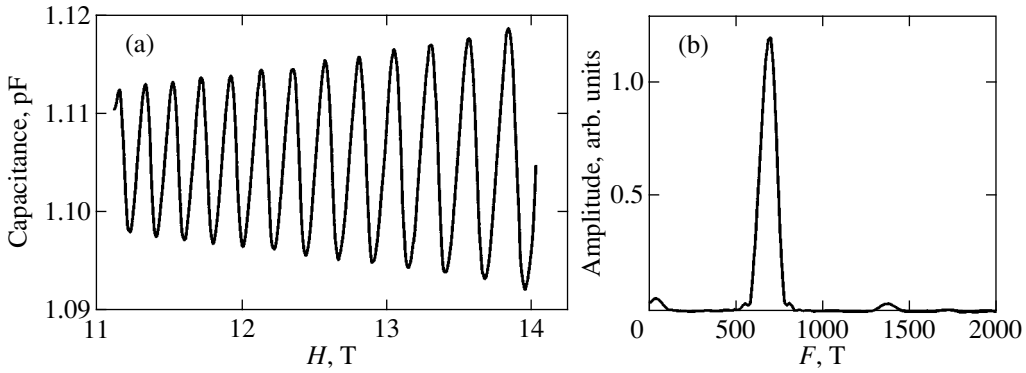

Fig. 1. Examples of (a) the torque oscillations observed in α-$(BETS)_2KHg(SCN)_4$ at $T = 0.45$ K and $\theta = 12.6°$ and (b) the Fourier spectrum of these oscillations.

tions were monitored by the torque of a capacitive magnetometer. The field strength was varied from 0 to 14 T at a temperature fixed within the interval from 0.45 to 1.3 K.

The dHvA oscillations were observed for various directions of the applied magnetic field (an example is presented in Fig. 1a. The oscillation spectrum shows a single fundamental frequency (Fig. 1b) depending on the angle θ between the magnetic field direction and the perpendicular to conducting layers in the sample. This dependence is described by a relationship typical of the metal with a cylindrical Fermi surface:

$$F(\theta) = F(0)/\cos\theta \approx 675\ [\mathrm{T}]/\cos\theta.$$

The quantity $F(0) \approx 675$ T, determining the area of the cylinder cross section by the conducting plane, agrees well with the results obtained in [5], while being about 20% greater than the value theoretically predicted by Seo *et al.* [7]. The cyclotron mass of the charge carriers related to the cylindrical part of the Fermi surface was calculated using the temperature dependence of the dHvA oscillation amplitude. For the field parallel to the cylinder axis, this quantity amounted to

$$\mu = m^*/m_0 = 1.09 \pm 0.02,$$

where m^* is the effective mass of electron and m_0 is the free electron mass.

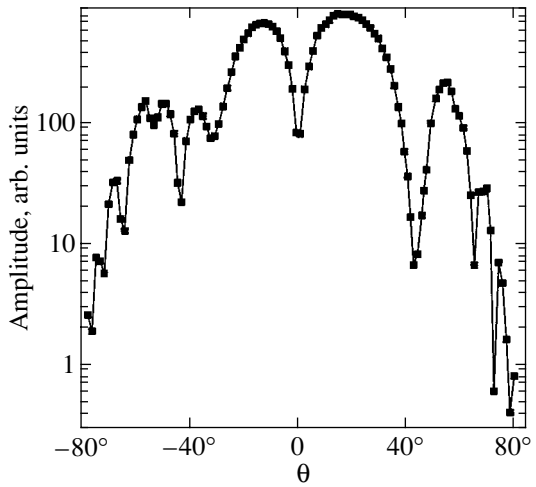

Fig. 2. The angular dependence of the de Haas–van Alphen oscillation amplitude in α-$(BETS)_2KHg(SCN)_4$ at $T = 0.45$ K.

The angular dependence of the dHvA oscillation amplitude (Fig. 2), exhibits several minima. The minimum at $\theta = 0$ is related to certain features of the experimental method employed [6]. The nature of the minima at $\theta = -32.3°$ and $-54°$ is still not completely clear. However, these minima are most probably related to corrugation of the cylindrical Fermi surface. The minima at $\theta = \pm 43.2°$, $\pm 64.6°$, and $\pm 72.0°$ represent the so-called "zero spin" effect related to the magnetic-field-induced splitting of the Landau levels [8]. The spin "zeros" take place under the condition

$$\cos(\pi\mu pg/2) = 0,$$

where p is the harmonic number and g is the g factor. The existence of three spin "zeros," under the assumption that the effective mass of an electron is related to the angle θ by a relationship $\mu(\theta) = \mu(0)/\cos\theta$ typical of the metals with a cylindrical Fermi surface, allows us to calculate with good precision the splitting factor for the first harmonic:

$$S = \frac{g\mu(0)}{2} = \frac{(2n+1)\cos\theta_n}{2} = 1.09 \pm 0.03$$

(here, θ_n are the positions of spin "zeros"; $n = 1, 2, 3$). Thus, to within the experimental error,

$$S \approx \mu(0). \quad (1)$$

The influence of many-body interactions on the splitting factor is described by the expression [8]

$$S = \frac{g\mu(0)}{2} = \frac{\mu_c(0)g_s(1+\gamma)}{2(1+\gamma')}, \quad (2)$$

where $\mu_c(0)$ is the relative band mass that depends only on the law of dispersion; g_s is the g factor determined from the EPR data (for the known organic metals, $g_s \approx 2$ [1]); and γ and γ' are the electron–electron correction constants for the effective mass and the g factor, respectively. Calculated from the temperature dependence of the dHvA oscillation amplitude, an expression for the effective mass $\mu(0)$ taking into account the many-body interactions is as follows [8]:

$$\mu(0) = \mu_c(0)(1 + \gamma)(1 + \lambda), \quad (3)$$

where λ is the electron–phonon correction constant for the electron mass.

The most natural way to satisfy condition (1) with an allowance for relationships (2) and (3) is to assume that $\gamma = \gamma' = \lambda = 0$, which implies that the many-body interactions are absent or very weak. In this case, the effective mass is equal to the band mass. Generally speaking, condition (1) could also be satisfied with a random combination of three constants and the corresponding band mass. Evidence for this variant is the theoretical estimate of the band mass $\mu_c(0) \approx 0.6$ [7]. However, it was previously demonstrated that condition (1) is satisfied for the isostructural complex α-$(BETS)_2TlHg(SeCN)_4$ [9] and, which is more important, for the complex κ-$(BETS)_2GaCl_4$ [10] possessing different crystal and electron structures. The situation when three different compounds meet the condition (1) as a result of a random combination of the aforementioned constants is unlikely. Therefore, the assumption about a radical weakening of the many-body interactions in α-$(BETS)_2KHg(SCN)_4$ seems to be justified. In this case, it is easy to explain the absence of both superconducting and Peierls transitions in the organic metal studied.

ACKNOWLEDGMENTS

This study was supported by the Russian Foundation for Basic Research (project no. 00-02-04019), DFG, NWO, and the Federal Scientific-Technological Program “Physics of Quantum and Wave Processes.”

REFERENCES

1. J. Wosnitza, *Fermi Surface of Low Dimensional Metals and Superconductors* (Springer-Verlag, Berlin, 1996); M. V. Kartsovnik and V. N. Laukhin, J. Phys. I **6,** 1753 (1996); J. Singleton, Rep. Prog. Phys. **63**, 1111 (2000).
2. M. V. Kartsovnik, W. Biberacher, E. Steep, *et al.*, Synth. Met. **86**, 1933 (1997).
3. P. Christ, W. Biberacher, M. V. Kartsovnik, *et al.*, Pis’ma Zh. Éksp. Teor. Fiz. **71**, 437 (2000) [JETP Lett. **71**, 303 (2000)]; D. Andres, M. V. Kartsovnik, W. Biberacher, *et al.*, submitted to Phys. Rev. Lett. (2001).
4. H. H. Wang, K. D. Carlson, U. Geiser, *et al.*, Physica C (Amsterdam) **166**, 57 (1990).
5. S. A. Ivanov, C. H. Mielke, T. Coffey, *et al.*, Phys. Rev. B **55**, 4191 (1997).
6. P. Christ, W. Biberacher, H. Müller, and K. Andres, Solid State Commun. **98**, 451 (1994).
7. D. K. Seo, M. H. Whangbo, B. Fravel, and L. K. Montgomery, Solid State Commun. **100**, 191 (1996).
8. D. Shoenberg, *Magnetic Oscillations in Metals* (Cambridge Univ. Press, Cambridge, 1984).
9. S. I. Pesotskiĭ, R. B. Lyubovskiĭ, V. I. Nizhankovskiĭ, *et al.*, Zh. Éksp. Teor. Fiz. **117**, 604 (2000) [JETP **90**, 527 (2000)].
10. S. I. Pesotskiĭ, R. B. Lyubovskiĭ, M. V. Kartsovnik, *et al.*, Zh. Éksp. Teor. Fiz. **115**, 205 (1999) [JETP **88**, 114 (1999)].

Translated by P. Pozdeev

Journal of Experimental and Theoretical Physics, Vol. 94, No. 2, 2002, pp. 434–445.
From Zhurnal Éksperimental'noĭ i Teoreticheskoĭ Fiziki, Vol. 121, No. 2, 2002, pp. 508–520.

NONLINEAR PHYSICS

A Turbulence Model in Unbounded Smooth Shear Flows: The Weak Turbulence Approach¶

G. D. Chagelishvili[a, b, *], R. G. Chanishvili[a], T. S. Hristov[c], and J. G. Lominadze[a]

[a]*Department of Theoretical Astrophysics, Abastumani Astrophysical Observatory, Tbilisi, 380060 Georgia*
[b]*Space Research Institute, Russian Academy of Science, Moscow, 117810 Russia*
[c]*University of California, Irvine, CA 92697-3975, USA*
**e-mail: georgech123@yahoo.com*

Received June 7, 2001

Abstract—We discuss a new concept of the subcritical transition to turbulence in unbounded smooth (noninflectional) spectrally stable shear flows. This concept (the so-called bypass transition) follows from considering the nonnormality of the linear dynamics of vortex disturbances in shear flows and is most easily interpreted by tracing the evolution of spatial Fourier harmonics (SFHs) of the disturbances. The key features of the concept are as follows: the transition of the flow by only finite-amplitude vortex disturbances despite the fact that the phenomenon is energetically supported by a linear process (the transient growth of SFHs); the anisotropy of processes in the **k** space; the onset of chaos due to the dynamical (not stochastic) process—nonlinear processes that close the transition feedback loop by the angular redistribution of SFHs in the **k** space. The evolution of two-dimensional small-scale vortex disturbances in a parallel flow with a uniform shear is analyzed within the weak turbulence approach. This numerical test analysis is carried out to prove the most problematic statement of the concept, the existence of a positive feedback caused by the nonlinear process. Numerical calculations also show the existence of a threshold: if the amplitude of the initial disturbance exceeds the threshold value, the self-maintenance of disturbances becomes realistic. The latter is a characteristic feature of the flow transition to the turbulent state and its maintenance. © *2002 MAIK "Nauka/Interperiodica".*

1. INTRODUCTION

Shear flows are permanently interesting because they are widespread both in the terrestrial and astrophysical environment (galaxies, stars, jets, planet atmospheres, oceans, etc.) and in the laboratory and industry (tokamaks, MHD facilities, etc.). Some simple and important hydrodynamic shear flows (e.g., the Couette flow) remain insensitive to infinitesimal disturbances at any Reynolds numbers but become turbulent at finite disturbances even at moderate (subcritical) Reynolds numbers. Moreover, the transition to turbulence occurring in such flows strongly depends not only on the amplitude of the initial disturbances but also on their type and spectrum. The physics of these facts was not explained even one decade ago [1–6].

Specific features of shear flows rigorously established recently [7] led to difficulties in studying linear phenomena in the framework of the canonical modal analysis, i.e., the technique where all the disturbed quantities are expanded in Fourier integrals in time. The point is that the operators arising in this approach are not self-adjoint [8]. Their eigenfunctions are not orthogonal to each other, which yields a strong interference among them. As a result, even if all the imaginary parts of all eigenfrequencies are negative and the eigenfunctions monotonically decay with time (i.e., the flow is spectrally stable), a particular solution can reveal a large relative growth over a finite time interval. The analysis of separate eigenfunctions and eigenfrequencies is therefore not sufficient to arrive at definite conclusions on the linear evolution of disturbances. In addition, taking the interference into account usually leads to insurmountable complications. This has given impetus to the so-called nonmodal analysis as a tool for describing the evolution of disturbances in smooth shear flows (i.e., those without the inflection point), primarily in a parallel flow with a uniform shear of velocity. Within this approach, the temporal behavior of the spatial Fourier harmonics (SFHs) of disturbances is studied without any spectral expansion in time. Being an optimal tool, the nonmodal analysis considerably simplifies the mathematical description of the processes and is capable of revealing the key phenomena that escape perception in the modal approach (in particular, the phenomena caused by the nonnormality of the linear dynamics). Many new unexpected results on time evolution of both the vortex mode [9–17] and acoustic wave [18, 19] disturbances have already been obtained within this approach; it was also successfully applied to the study of the MHD waves [20–22]. New linear mechanisms of the mutual transformation of wave modes [23–25] and conversion of vortices to waves [26–29] have been discovered. A new concept of the subcritical transition to turbulence in smooth shear

¶This article was submitted by the authors in English.

flows (those without the inflection point) has been formulated [30–37]. The latter, named the bypass transition, is the subject of our analysis.

According to this concept, the subcritical transition to turbulence that occurs in spectrally stable shear flows is caused by the interplay among four (linear and nonlinear) basic phenomena. The transition scenario based on this concept is presented in detail (in qualitative terms) in Section 2. In Section 2, we also consider the philosophical problem of turbulence, i.e., how a completely deterministic and causal system can have chaotic solutions. In Section 3, we give numerical test calculations to prove the most problematic statement of the concept—the existence of a positive nonlinear feedback. The subsequent results of numerical calculations are also presented in Section 3. We have restricted ourselves to the investigation of the action of nonlinearity for a two-dimensional symmetric disturbance (which is quite simple and most suitable for testing) in the weak turbulence approximation. In reality, the shear flow turbulence has a three-dimensional (3D) nature. However, from the discussion presented in Section 4, it follows that nonlinear processes should more easily cope with the mission of the positive feedback in the actual 3D case than in the 2D one. The weak turbulence equation for a 2D vortex mode disturbance in a parallel flow with a uniform shear is derived in the Appendix.

2. SCENARIO OF THE SUBCRITICAL TRANSITION TO TURBULENCE

Vortex mode (aperiodic/nonoscillating) disturbances are the creator of turbulence in the unbounded, parallel flow with a constant shear rate and a uniform density that we consider here. Therefore, the presented scenario involves disturbances of only this type. The nonmodal formalism allows the following specific features in the evolution of SFHs to be revealed:

(a) The wave number of a SFH along the axis orthogonal to the flow velocity (i.e., along the flow shear) varies in time; in the linear approximation, there is a drift of a SFH in the wave-number space, i.e., in the **k** space.

Actually, in a parallel flow with uniform shear (cf. [9–28]),

$$\mathbf{U}_0 = (Ay, 0, 0) \tag{1}$$

(where A is a shear parameter that is assumed to be positive), disturbances cannot have the form of a simple plane wave because of the effect of the shearing background on the wave crests. The SFH wave numbers are then time-dependent: if a SFH with the wave numbers k_x, $k_y(0)$, and k_z is initially disturbed,

$$\begin{aligned} v_x(0) &= \tilde{v}_x(k_x, k_y(0), k_z, 0) \\ &\times \exp(ik_x x + ik_y(0)y + ik_z z), \end{aligned} \tag{2}$$

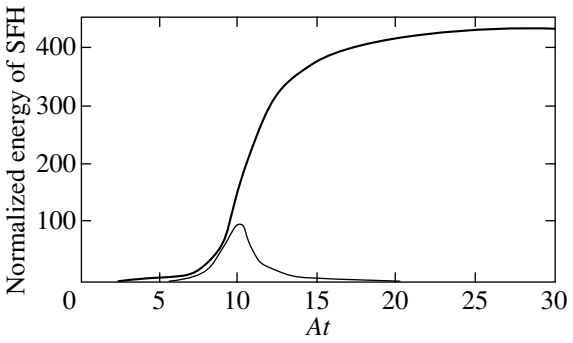

Fig. 1. Time evolution of the normalized energy of 2D and 3D SFHs defined in the linear stage and in the inviscid case (i.e., with only processes (a) and (b) involved). Thin solid line corresponds to a 2D SFH with the parameters $k_y(0)/k_x = 10$, $k_z = 0$, $\tilde{v}_x(0)/\tilde{v}_y(0) = -10$, and $\tilde{v}_z(0) = 0$. The bold solid line corresponds to a 3D SFH with the parameters $k_y(0)/k_x = 10$, $k_z/k_x = 1$, $\tilde{v}_x(0)/\tilde{v}_y(0) = -5$, and $\tilde{v}_z(0)/\tilde{v}_y(0) = -5$. Here, $\tilde{v}_x(0)$, $\tilde{v}_y(0)$, and $\tilde{v}_z(0)$ are the components of the SFH velocity at $t = 0$. k_x, $k_y(0)$, and k_z are related to the wave numbers of the SFH (see Fig. 2).

then the evolution of its phase for $t > 0$ is determined by the equations

$$v_x(t) \propto \exp(ik_x x + k_y(t)y + ik_z z), \tag{3}$$

$$k_y(t) = k_y(0) - k_x At \tag{4}$$

that describe the linear drift of the SFH in the wave-number space.

The values of the spatial characteristics (i.e., k_x, $k_y(t)$, and k_z) define the energy exchange intensity between SFHs and the background flow to a greater extent. Therefore, the linear drift leads to a variation in the intensity of this exchange.

(b) Not all SFHs can draw energy from the shear; only the SFHs that are located in a certain region of the **k** space (called the amplification region below) are amplified. Moreover, each SFH is amplified during a limited time interval until it leaves the amplification region as a result of the linear drift. In addition, the presence of SFHs in this region imposes conditions mainly on the direction (and not the magnitude) of their wave vector. Therefore, the process of the energy exchange between vortex mode disturbances and the shear flow has a pronounced anisotropic character in the **k** space. The physics of this process is described in detail in [38].

Therefore, vortex mode disturbances at the linear stage of the evolution are pumped by the background shear flow and grow within a limited time interval, i.e., exhibit a transient growth. There is an essential difference between the transient growths of 2D and 3D SFHs [16–20], which can be seen by comparing the evolution of their energy, as in Fig. 1. This figure shows time evolution of the normalized energy of 2D and 3D SFHs.

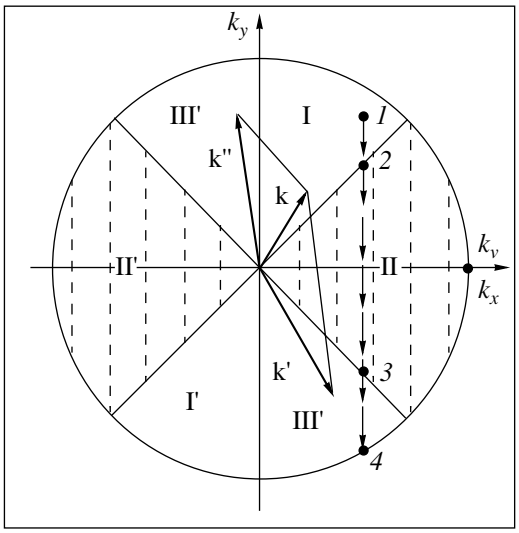

Fig. 2. A conventional separation of regions of the action of the basic physical processes that are responsible for the onset of turbulence/chaos in accordance with the bypass transition. The energy exchange between the disturbances and the background flow is essential (a transient growth takes place) in regions II(II') dashed by vertical lines; nonlinear processes (e.g., of the type $\mathbf{k}' + \mathbf{k}'' \longrightarrow \mathbf{k}$) and the linear drift are effective in all regions I(I'), II(II'), and III(III') inside the circle $\sqrt{k_x^2 + k_y^2} < k_v$. The viscous dissipation of SFHs dominates outside the circle $\sqrt{k_x^2 + k_y^2} > k_v$.

It corresponds to the linear dynamics of separate SFHs in the inviscid case (i.e., when only processes (a) and (b) are at work).

The amplification region in the **k** space is much wider for 3D SFHs than for 2D ones. Moreover, in contrast to 2D SFHs, the energy of 3D SFHs does not decrease after passing the amplification region (3D SFHs do not return energy to the flow) but saturates and approaches a value that may be much higher than their initial value. In reality, however, a viscous dissipation becomes efficient as $|k_y(t)| \longrightarrow \infty$ and (if no new phenomena, e.g., nonlinear phenomena, are involved) converts the energy of SFHs into heat. We list the viscous dissipation as item (c).

Thus, the nonmodal approach demonstrates not only the possibility of the algebraic/transient growth of SFHs of vortex mode disturbances in shear flows, but also the anisotropic properties of linear processes in the wave-number space. This anisotropy is also observed in nonlinear processes.

(d) Nonlinear processes, apart from the usual fragmentation of the disturbance scale, are also responsible for the angular redistribution of SFHs in the **k** space; i.e., they could "supply" SFHs to the amplification region, closing a feedback loop of the transition to turbulence. In a forced shear flow, the nonlinear terms do not contribute to the energy transfer between the mean flow and disturbances.

Processes (a) and (b) are quantitatively analyzed and well acknowledged in papers devoted to the nonmodal approach. The existence of a positive feedback (caused by the nonlinear processes) has been checked using model equations [34, 35]. In Section 3, we prove it using the Navier–Stokes equation in the weak turbulence approach.

It is plausible that the angular redistribution of SFHs in the **k** space is the main process caused by the nonlinearity. The nonlinear processes then indirectly favor the energy extraction by SFHs from the shear flow (the SFH scale decrease to the dissipative scale should be ensured by the linear drift of SFHs in the **k** space).

The scenario of the subcritical transition to turbulence (called the bypass transition) is based on the interplay of the linear and nonlinear basic phenomena itemized above. In presenting this scenario, we schematically describe these processes in the plane k_z = const (which is parallel to the plane $k_x k_y$). It is obvious that the boundaries of the **k** space regions where phenomena (b) and (c) occur are vague. We fix the regions where these phenomena are operative for clarifying the analysis. The viscous dissipation becomes essential for harmonics with the wave numbers satisfying the inequality

$$\sqrt{k_x^2 + k_y^2} > k_v,$$

where the value of k_v depends on the Reynolds number. As follows from Fig. 1, the real growth of the disturbance energy occurs when the ratio $|k_y(t)/k_x|$ reaches moderate values (the dashed region in Fig. 2). We can therefore separate three regions inside the circle

$$\sqrt{k_x^2 + k_y^2} < k_v:$$

I(I'), II(II'), and III(III'). We now discuss what happens to a SFH of the vortex mode disturbance injected into region I(I'), for instance, at point 1 (see Fig. 2). The wave number of the SFH varies in time, thereby leading to a drift in the direction marked by the arrows. After a certain moment, when the harmonics passes point 2, its energy starts to grow. This growth is transient and lasts until the SFH leaves the amplification region II(II') (point *3* in Fig. 2). Continuing its drift, the harmonics then reaches point 4, where the dissipative processes are switched on and convert the disturbance energy into heat. Consequently, if the nonlinear phenomena are inefficient, nothing interesting can occur as regards the transition, and the disturbances eventually disappear. A permanent extraction of the shear energy by disturbances is necessary for their maintenance. This is possible in the case of the permanent existence of disturbances in regions I(I') and II(II') that can be provided by nonlinear processes, in particular, by the three-wave processes

$$\mathbf{k}' + \mathbf{k}'' \longrightarrow \mathbf{k}$$

(see Fig. 2), four-wave processes

$$\mathbf{k}' + \mathbf{k}'' + \mathbf{k}''' \longrightarrow \mathbf{k},$$

five-wave processes, etc. This means a predominant transfer of the disturbance energy by the nonlinear processes from region III(III') to regions I(I') and II(II'). However, there are no restrictions on the reverse transfer (from regions I(I') and II(II') to region III(III')). But, as is shown in Section 3, the nonlinear processes ensure a preferential transfer of the disturbance energy to the amplification region.

The reproduction of disturbances in region I(I') depends on both the amplitude and the spectrum of the initial disturbances. The nonlinear decay processes are insignificant at low amplitudes and are not able to resist the linear drift of SFHs in the **k** space. As a result, low-amplitude disturbances are damped without any trace, i.e., without inducing the transition to turbulence. The higher the initial disturbance amplitude, the more noticeable nonlinear effects occur. At a certain amplitude (which evidently depends on the initial disturbance spectrum and the Reynolds number), nonlinear processes can compensate the action of the linear drift, thereby ensuring the permanent return of SFHs to the amplification region (this is justified by simulations in Section 3). This eventually ensures a permanent extraction of energy from the background flow and the maintenance of disturbances. Therefore, a certain threshold must occur in accordance with the scenario discussed here.

Any theory aiming at explaining the transition to turbulence must distinctly answer the question of how a completely deterministic and causal system can have chaotic solutions. In accordance with the above scenario, the onset of turbulence/chaos occurs because of dynamical (not stochastic) processes and can be explained as follows.

We assume that we initially have a spatially localized vortical disturbance with sufficiently regular features: a package of spatial Fourier harmonics. In general, a disturbance of some physical variable, e.g., velocity can be represented as

$$\mathbf{v}(\mathbf{r}, t) = \int d\mathbf{k} |\tilde{\mathbf{v}}(\mathbf{k}, t)| \exp[i\varphi(\mathbf{k}, t) + i\mathbf{k} \cdot \mathbf{r}], \quad (5)$$

where $|\tilde{\mathbf{v}}(\mathbf{k}, t)|$ and $\varphi(\mathbf{k}, t)$ are real functions of **k** and *t*. We assume that the initial phase, $\varphi(\mathbf{k}, 0)$, is a weakly varying function of **k**. In this case, the initial disturbance $\mathbf{v}(\mathbf{r}, 0)$ is regular and sufficiently smooth in space.

What kinds of processes govern the phase evolution at any point of the **k** space?

We consider processes at an arbitrarily chosen point in the **k** space inside the package. Following the scenario, the SFH that happens to be at the point at the initial moment of time leaves this point because of the linear drift. But this loss is compensated by the linear and nonlinear processes: a portion of energy arrives as the result of the linear drift; portions of energy are transferred from numerous points of the **k** space as a result of the nonlinear decay processes (three-wave, four-wave, etc.) described above. The total energy of the SFH at the chosen point is composed of these portions. Naturally, all these portions have their own phases. It is clear that the Fourier harmonic phase at the point must be a certain sum of these phases. It is evident that the phase $\varphi(\mathbf{k}, t)$ becomes a strongly varying function of **k** with the passage of time, because the phases of SFHs at neighboring points of the **k** space can differ from each other by any value. Consequently, an initially regular disturbance becomes more and more irregular, thereby tending to chaotic behavior.

3. THE WEAK TURBULENCE APPROACH

In accordance with the above scenario, nonlinear processes do not contribute to the energy transfer between the mean flow and perturbations. They result in (i) the fragmentation of the disturbance scale, i.e., the energy transfer from large scales to smaller ones and finally to dissipative ones, and (ii) the angular redistribution of SFHs in the **k** space. It must be noted that the energy transfer to small dissipative scales also occurs because of the linear drift of SFHs (process (a)), which could be even more operative than the nonlinear fragmentation of the disturbance scale. We again emphasize that the main role of the nonlinear processes in the presented scenario consists in (ii) rather than (i), because in doing so they could supply SFHs to the amplification region, closing the feedback loop of the transition to turbulence. The existence of a positive nonlinear feedback is the most problematic statement of the concept. It has been verified using model equations [34, 35]. In this section, we attempt to prove it using the Navier–Stokes equation. We performed numerical calculations for a 2D symmetric vortex mode disturbance in the weak turbulence approximation. As we see in what follows, the 2D symmetric disturbance is most suitable for testing the existence of a positive nonlinear feedback.

The weak turbulence equation describing the evolution of the energy spectral density of a 2D disturbance is derived in the Appendix,

$$\frac{\partial E_{\mathbf{k}}}{\partial t} + \nabla_{\mathbf{k}}(\mathbf{V}E_{\mathbf{k}}) - \frac{2Ak_xk_y}{k_x^2 + k_y^2}E_{\mathbf{k}} + \nu(k_x^2 + k_y^2)E_{\mathbf{k}} = \hat{N}E_{\mathbf{k}}, \quad (6)$$

where

$$\nabla_{\mathbf{k}} = (\partial/\partial k_x, \partial/\partial k_y),$$

$$\mathbf{V} = (-Ak_x, 0),$$

and $E_{\mathbf{k}}$ is the energy density of the 2D vortex mode disturbances at a fixed point of the **k** space. (In other words, $E_{\mathbf{k}}$ is the spectral density of energy.) The term $\hat{N}E_{\mathbf{k}}$ is defined by Eq. (A.36). As can be seen from Eq. (6)

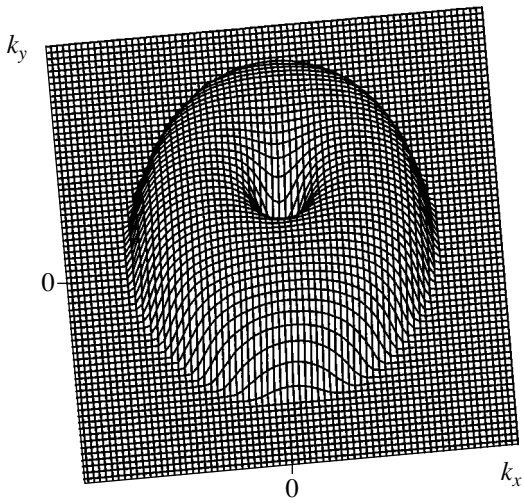

Fig. 3. The spectral density distribution of the disturbance energy in the k_xk_y plane for the time instant $t = 0$, i.e., initial conditions for the numerical solution of Eq. (6). The absence of SFHs with large wave numbers is related to the action of viscosity. SFHs with small wave numbers are also absent, because we consider small-scale disturbances.

(and as described in Section 2), the energy spectral density ($\partial E_{\mathbf{k}}/\partial t$) changes because of the following reasons.

(1) The linear drift of SFHs in the wave-number space (the second term on the left-hand side). This term does not cause a variation in the total disturbance energy,

$$\int d\mathbf{k}\nabla_{\mathbf{k}}(\mathbf{V}E_{\mathbf{k}}) = 0,$$

but results in a transfer of SFHs from the amplification region to the attenuation one.

(2) The energy exchange between disturbances and the background flow (the third term on the left-hand side). Assuming that $A > 0$, we can state that the 2D SFHs for which $k_y(t)/k_x > 0$ gain energy from the background flow and their amplitude increases, whereas the amplitudes of SFHs for which $k_y(t)/k_x < 0$ decrease.

(3) The viscosity (the last term on the left-hand side), which transforms the disturbance energy into heat and which is significant for large wave numbers.

(4) The nonlinear three-wave processes (the term on the right-hand side), leading to the energy exchange between different SFHs [39–41]. It is easy to show that

$$\int d\mathbf{k}\hat{N}E_{\mathbf{k}} = 0,$$

i.e., the nonlinear term leads only to the energy redistribution in the **k** space (not to a change in the total disturbance energy).

The conditions for wave vectors ($\mathbf{k}' + \mathbf{k}'' = \mathbf{k}$) and frequencies ($\omega_1 + \omega_2 = \omega$) are usually imposed on three-wave processes in the weak turbulence equations [39–41]. Because both conditions cannot be simultaneously satisfied for waves with certain wave vectors, the restriction of three-wave processes arises. Moreover, these conditions cause the existence of some completely nondecaying spectra. The vortex mode disturbances considered here are aperiodic ($\omega_1, \omega_2, \omega = 0$) and therefore automatically satisfy the second condition ($\omega_1 + \omega_2 = \omega$). Hence, there are no forbidden three-wave processes for SFHs in our case. However, they have different probabilities. For example, the probability of the processes $\mathbf{k}' + \mathbf{k}' = \mathbf{k}$ is equal to zero, although it is not forbidden in principle. Therefore, the nonlinear term in Eq. (6) is equal to zero if a single SFH mode is disturbed. This explains the following well-known fact: a single SFH mode is an exact solution of the complete incompressible Navier–Stokes equation, while a superposition of modes is usually not.

The net effect of all three-wave processes depends on two factors: the probability with which different decay acts occur (the coefficients of $E_{\mathbf{k}'}E_{\mathbf{k}''}$ and $E_{\mathbf{k}}E_{\mathbf{k}''}$ in Eq. (A.36)) and the distribution of SFHs in the **k** space (the values of $E_{\mathbf{k}'}E_{\mathbf{k}''}$ and $E_{\mathbf{k}}E_{\mathbf{k}''}$). If the spectral density of energy is increased in the first and third quarters of the **k** space at the cost of the second and fourth ones, we can say that the three-wave processes lead to the preferential transfer of SFHs to the amplification region, i.e., lead to the regeneration of SFHs, which can gain shear energy (lead to positive feedback). This trend of nonlinear processes can be revealed by showing their asymmetry in the **k** space with respect to the K_x axis. To proceed, we consider the initial 2D disturbance with the highest possible symmetry with respect to the K_x axis (see Fig. 3). In this case, processes (a) and (c) are symmetric with respect to K_x and process (b) is asymmetric because it results in removal of SFHs from the first and third quarters of the **k** space to the second and fourth ones; process (b) is therefore asymmetric in the opposite direction to nonlinear process (d). That is why the symmetric 2D disturbance presented in Fig. 3 is most suitable for determining the trend of the nonlinear transfer of SFHs.

3.1. Results of the Numerical Calculation of the Weak Turbulence Equation

We consider the 2D initial disturbance with the spectral density of energy that is symmetric in the **k** space (see also Fig. 3),

$$E_{\mathbf{k}}(t=0) = \begin{cases} B\{\arctan(\beta_1(k_v^2 - k_x^2 - k_y^2)) \\ \times \arctan(\beta_2(k_x^2 + k_y^2 - k_0^2))\}^2 \\ \text{for } k_v^2 > k_x^2 + k_y^2 \text{ and } k_x^2 + k_y^2 > k_0^2, \\ 0 \quad \text{for } k_v^2 < k_x^2 + k_y^2 \text{ and } k_x^2 + k_y^2 < k_0^2, \end{cases} \quad (7)$$

where B defines the value of the initial disturbance energy; k_0 and $k_\nu = 1/\sqrt{A\nu}$ are the minimum and maximum values of the disturbance wave vectors, respectively; and β_1 and β_2 denote the sharpness of the disturbance boundaries in the **k** space. The calculations are carried out at $\beta_1 = 0.07$, $\beta_2 = 0.8$, $k_0 = 0.3$, and $k_\nu = 10$ (i.e., $A = 1$ and $\nu = 0.01$). The absence of SFHs with large wave numbers is justified by the action of viscosity. SFHs with small wave numbers are also absent, because we consider small-scale disturbances. The evolution of $E_{\mathbf{k}}$ was numerically investigated for a short time interval ($At \le 1$) because of two reasons. First, Eq. (6) is obtained in the weak turbulence approximation, and it is therefore correct only for a relatively short time interval ($t \lesssim 1/A$). Second, the trend of nonlinear processes is revealed even for such short time intervals.

Initially, we tried to answer the question of what the redistributing action of the nonlinear term $\hat{N}E_{\mathbf{k}}$ in the **k** space is—specifically, whether the term $\hat{N}E_{\mathbf{k}}$ transfers disturbance energy to the amplification region. For 2D disturbances, the amplification region covers the first and third quarters of the k_xk_y plane (where $k_xk_y > 0$) and the attenuation region covers its second and fourth quarters (where $k_xk_y < 0$). Introducing polar coordinates $\varphi = \arctan(k_y/kx)$ and $k = \sqrt{k_x^2 + k_y^2}$, we can say that the angle φ between 0 and $\pi/2$ corresponds to the amplification region, and between $-\pi/2$ and 0 to the attenuation one.

Obviously, the value and sign of $\hat{N}E_{\mathbf{k}}$ depend on φ and k. Taking the integral over k, we obtain the function that describes the nonlinear redistribution of energy only in φ,

$$\Psi(\varphi, t) \equiv \int dk k \hat{N} E_{\mathbf{k}}. \qquad (8)$$

It is easy to see that if the conditions

$$\Psi(\varphi, t)|_{0 < \varphi < \pi/2} > 0, \quad \Psi(\varphi, t)|_{-\pi/2 < \varphi < 0} < 0 \qquad (9)$$

are satisfied, we can unambiguously state that the nonlinear processes transfer the disturbance energy to the amplification region, thereby realizing a positive feedback.

We thus determine the dependence of Ψ on φ. The result of our calculations at the instance time $At = 0.1$ is shown in Fig. 4. It is seen that conditions (9) are satisfied; i.e., the nonlinear three-wave processes lead to the preferential energy transfer to the amplification region. Because we used a symmetric initial disturbance (with SFHs having the same weight in the amplification and attenuation regions), we can conclude that the nonlinear three-wave processes do have the tendency to transfer SFHs to the amplification region. This conclusion can be considered as a numerical confirmation (in the weak turbulence approximation) of the suggestion given in (4).

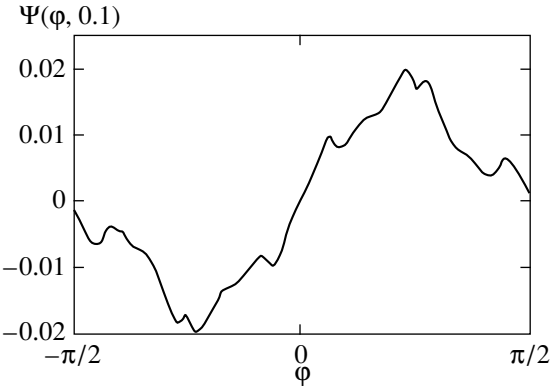

Fig. 4. The phase factor $\Psi(\varphi, t)$ (see Eq. (8)) for different $\varphi = \arctan(k_y/k_x)$ at $At = 0.1$. It can be seen that the nonlinear term $\hat{N}E_{\mathbf{k}}$ results in a transfer of the 2D SFH energy from the attenuation region $-\pi/2 < \varphi < 0$ to the amplification one $0 < \varphi < \pi/2$.

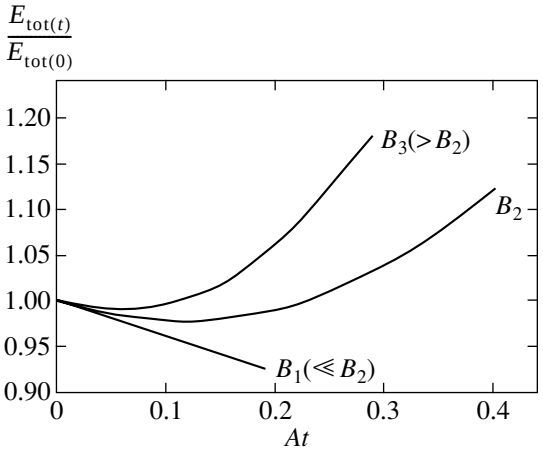

Fig. 5. The disturbance normalized total energy vs. time. Each curve corresponds to a different amplitude of the initial disturbance (i.e., to a different value of the initial disturbance energy), $B_1 \ll B_2 < B_3$ (see Eq. (7)). The first is well-suited to low values of $B = B_1$ at which the effect of nonlinear processes can be ignored. In this case, the total energy of the disturbance is gradually decreasing. For the other two values $B = B_2$ and B_3 (with $B_1 \ll B_2 < B_3$), the effect of nonlinear processes is significant and the initial decrease in the total energy of disturbances is replaced by its growth.

Figure 5 presents the disturbance normalized total energy $E_{\text{tot}}(t)/E_{\text{tot}}(0)$ vs. time, where

$$E_{\text{tot}}(t) = \int d\mathbf{k} E_{\mathbf{k}}.$$

The three curves correspond to different values of the parameter B (see Eq. (7)), i.e., to different values of the initial disturbance energy $\int d\mathbf{k} E_{\mathbf{k}}$. The first curve pertains to low values of $B = B_1$ at which the effect of non-

linear processes can be ignored. As seen from Fig. 5, the total disturbance energy gradually decreases if nonlinear processes are negligible. For the other two values $B = B_2$ and B_3 (with $B_1 \ll B_2 < B_3$), at which the effect of nonlinear processes is significant, the initial decrease in the total energy is replaced by its growth. The higher the initial energy, the sooner the growth begins. The results shown in Fig. 5 can be explained only by the nonlinear transfer of energy of the disturbances to the amplification region. The following arguments may prove this conclusion.

Only the unstable and dissipation processes ((b) and (c)) lead to changing the total disturbance energy. Viscosity (process (c)) always causes a decrease in the disturbance energy. As for process (b), its net effect depends on the distribution of the energy spectral density in the amplification and attenuation regions. If the weight of SFHs in the amplification region is heavier than that in the attenuation region, the net effect of process (b) causes an increase in the total energy of the 2D disturbance. Vice versa, if the "weight" of SFHs is "heavier" in the attenuation region, process (c) causes a decrease in the total energy. It follows from the above argument that, in accordance with Eq. (6), the total energy of 2D disturbances can become higher only if the weight of SFHs in the amplification region is heavier than that in the attenuation region. In addition, the weight must be so much heavier that the net effect of the third term in Eq. (6) dominates over that of the viscous term.

Initially, the SFHs of the 2D disturbance considered here (see Eq. (7) and Fig. 3) have the same weight in the amplification and attenuation regions. If we assume that the effect of nonlinear processes is negligible, the disturbance is transferred to the attenuation region with time by the linear drift. This causes an increase in the weight of SFHs in the attenuation region toward higher values than in the amplification region, and the total energy of the disturbance under study must therefore begin to decrease. It is the temporal history that can explain the $B = B_1$ curve run in Fig. 5. The behavior of the curves with $B = B_2$ and B_3, namely, the fact that the initial decrease in the total disturbance energy is replaced by its growth, thus unambiguously indicates that, beginning with a certain time instant (which occurs the earlier the larger the disturbance amplitude), the weight of SFHs in the amplification region dominates over the weight of SFHs in the attenuation one. This fact can be explained only by the preferential transfer of SFHs to the amplification region caused by the nonlinear processes. It also follows from Figure 5 that there exists some threshold B_{th} for the initial disturbances. If $B > B_{th}$ (e.g., B_2, $B_3 > B_{th}$), the initial decrease in the total disturbance energy is replaced by its growth, which must eventually lead to the self-maintenance of disturbances. We did not calculate the threshold because of the following simple reasons. In our calculations, the threshold must appear at large times $At \gg 1$, where the weak turbulence approach becomes invalid. In addition, we made calculations for a definite disturbance, and the calculation of the threshold in the particular case would not enrich the theory; much more important is the establishment of the threshold existence.

4. DISCUSSION

The aim of this paper was to prove the existence of a positive nonlinear feedback, the most problematic statement of the bypass transition to turbulence. We performed numerical calculations for the 2D case in the weak turbulence approximation. The results of calculations shown in Fig. 4 describe the preferential nonlinear transfer of the disturbance energy to the amplification region, and the results in Fig. 5 provide evidence for the preferential transfer that can crucially change the temporal history: the total disturbance energy decrease can be replaced by its growth at certain amplitudes. This behavior makes the self-maintenance of the disturbance realistic. This is in turn the characteristic feature of the flow transition to the turbulent state and its maintenance.

We can therefore conclude that our numerical test calculations prove the existence of a positive nonlinear feedback in the 2D case. In reality, the shear flow turbulence has a 3D nature (cf. [6]). However, the qualitative analysis in Section 2 implies that nonlinear processes easier cope with the positive feedback in the actual 3D case than in 2D one. Indeed, we refer to the case discussed in Section 2, where SFHs of incompressible vortical 3D disturbances are initially in region I(I') (see Fig. 2) and then drift along the k_y axis, thus falling in the amplification region II(II'). They are amplified and reach region III(III') because of the drift. In contrast to 2D SFHs (see Fig. 1), 3D SFHs do not become weaker after leaving the amplification region. The spectral energy density of 3D disturbances must therefore be higher in region III(III') than in region I(I'). Combining this fact with the preferential nonlinear transfer of the SFH energy to the amplification region, we conclude that the positive nonlinear feedback must be more easily realized in the 3D case than in the 2D one.

In accordance with the bypass transition to turbulence, the transient growth of disturbances is a key element of the subcritical transition. (The flow is spectrally stable.) At the same time, triggering the nonlinear positive feedback nonlinear regeneration of the SFH that can draw the mean flow energy is a necessary step to the transition. These facts require the existence of a sufficiently high level of initial disturbances in the system for the subcritical transition. It is obvious that finite disturbances can be produced by external forces. For instance, a pair of oblique waves with small but finite amplitudes were used in [42, 43] as the initial condition in numerical simulations of the transition. However, finite disturbances must also have an intrinsic fluctuation origin according to [44, 45]. (These results shed

new light on the fluctuation background of the vortex mode fluctuations in laminar Couette flow.) Namely, according to [44, 45], the background of the vortex mode fluctuations in a certain subspace of the wavenumber space is sufficiently strong at high Reynolds numbers and the level of its spectral energy density by far exceeds the level of the white noise. This must in turn trigger a nonlinear positive feedback and lead to the transition. The reality of this time history should be proved by direct numerical simulation.

ACKNOWLEDGMENTS

Our research was supported by the INTAS (grant GE-97 no. 0504).

APPENDIX

Derivation of the Weak Turbulence Equation

We let the *x* axis of a Cartesian coordinate system lie along the velocity of the mean flow and the *y* axis along the flow velocity shear, $\mathbf{U}_0(Ay, 0, 0)$. The fluid is assumed to be incompressible. Considering that the disturbed variables are independent of the *z* coordinate, the continuity equations and the equation of motion for the disturbances are given by

$$\frac{\partial v_x}{\partial x} + \frac{\partial v_y}{\partial t} = 0, \tag{A.1}$$

$$\left(\frac{\partial}{\partial t} + Ay\frac{\partial}{\partial x}\right)v_x + Av_y + v_x\frac{\partial v_x}{\partial x} + v_y\frac{\partial v_x}{\partial y} = -\frac{\partial P}{\partial x}, \tag{A.2}$$

$$\left(\frac{\partial}{\partial t} + Ay\frac{\partial}{\partial x}\right)v_y + v_x\frac{\partial v_y}{\partial x} + v_y\frac{\partial v_y}{\partial y} = -\frac{\partial P}{\partial y}, \tag{A.3}$$

where v_x and v_y are the respective disturbance velocities in the Cartesian coordinate system along the *x* and *y* axes and *P* is the pressure disturbance normalized by the undisturbed density of the fluid ρ_0. The action of viscosity in the weak turbulence equation is taken into account in the end. It is significant that we consider disturbances with the characteristic length scale much less than the distance between the flow boundaries. This allows us to neglect the boundary effects.

To simplify subsequent transformations, we introduce a coordinate system x_1y_1, with its origin and the x_1 axis coinciding with those of xy and the y axis convecting with the mean flow. This is equivalent to changing the variables as

$$x_1 = x - Ayt, \quad y_1 = y, \quad t_1 = t, \tag{A.4}$$

$$\frac{\partial}{\partial x} = \frac{\partial}{\partial x_1}, \quad \frac{\partial}{\partial y} = \frac{\partial}{\partial y_1} - At_1\frac{\partial}{\partial x_1}, \quad \frac{\partial}{\partial t} = \frac{\partial}{\partial t_1} - Ay\frac{\partial}{\partial x_1}. \tag{A.5}$$

In terms of the new variables, Eqs. (A.1)–(A.3) can be rewritten as

$$\frac{\partial}{\partial x_1}v_x + \left(\frac{\partial}{\partial y_1} - At_1\frac{\partial}{\partial x_1}\right)v_y = 0, \tag{A.6}$$

$$\frac{\partial v_x}{\partial t} + Av_y + v_x\frac{\partial v_x}{\partial x_1} + v_y\left(\frac{\partial}{\partial y_1} - At_1\frac{\partial}{\partial x_1}\right)v_x = -\frac{\partial P}{\partial x_1}, \tag{A.7}$$

$$\frac{\partial v_y}{\partial t} + v_x\frac{\partial v_x}{\partial y_1} + v_y\left(\frac{\partial}{\partial y_1} - At_1\frac{\partial}{\partial x_1}\right)v_y = -\left(\frac{\partial}{\partial y_1} - At_1\frac{\partial}{\partial x_1}\right)P. \tag{A.8}$$

Substitution (A.4) is not a physical transition to a new coordinate system, because in Eqs. (A.6)–(A.8) (as well as in Eqs. (A.1)–(A.3)), the quantities v_x and v_y are components of the disturbance velocity in the Cartesian coordinate system *xy*. The coefficients of the original set of linear equations (A.1)–(A.3) depend on the spatial coordinate *y*. As a result of the transformation, this spatial inhomogeneity is changed to a temporal one (Eqs. (A.7) and (A.8)).

The disturbed variables can be Fourier decomposed with respect to the Eulerian (laboratory) coordinates (*x*, *y*) and the Lagrangian (convected) coordinates (x_1, y_1),

$$\begin{Bmatrix} v_x \\ v_y \\ P \end{Bmatrix} = \int_{-\infty}^{\infty} dk_x dk_y \begin{Bmatrix} \hat{v}_x(k_x, k_y, t) \\ \hat{v}_y(k_x, k_y, t) \\ \hat{P}(k_x, k_y, t) \end{Bmatrix} \times \exp(ik_x x + ik_y y), \tag{A.9}$$

$$\begin{Bmatrix} v_x \\ v_y \\ P \end{Bmatrix} = \int_{-\infty}^{\infty} dk_{1x} dk_{1y} \begin{Bmatrix} \tilde{v}_x(k_{1x}, k_{1y}, t_1) \\ \tilde{v}_y(k_{1x}, k_{1y}, t_1) \\ \tilde{P}(k_{1x}, k_{1y}, t_1) \end{Bmatrix} \times \exp(ik_{1x}x_1 + ik_{1y}y_1). \tag{A.10}$$

The two Fourier representations in Eqs. (A.9) and (A.10) are different, although they coincide at the initial moment ($t = 0$) because $x \equiv x_1$ and $y \equiv y_1$. This difference is manifested in the dynamics of SFHs in the wavenumber space. The wave vector $\mathbf{k}_1$ of a particular SFH is constant in time in the convected coordinates, while it varies in laboratory coordinates. Each of these two methods has its advantages. In the linear theory,

Eq. (A.10) is convenient in studying the real spatial Fourier harmonics moving with them. However, in analyzing the weak turbulence equation (thus assuming the excitation of many degrees of freedom), it is impossible to follow the evolution of each Fourier harmonics. In the latter case, it is more convenient to study what occurs to the energy at a fixed point of the **k** space, i.e., to describe the variation of the spectral density of the disturbance energy at a fixed point of the **k** space.

In spite of this, expansion (A.10) is also useful for intermediate transformations.

To derive the weak turbulence equation, we insert expansion (A.10) in (A.6)–(A.8),

$$\begin{aligned} &k_{1x}\tilde{v}(k_{1x}, k_{1y}, t) \\ &+ (k_{1y} - k_{1x}At)\,\tilde{v}_y(k_{1x}, k_{1y}, t) = 0, \end{aligned} \tag{A.11}$$

$$-\left(\frac{k_{1y}}{k_{1x}} - At\right)\frac{\partial \tilde{v}_y(\mathbf{k}_1, t)}{\partial t} - 2A\tilde{v}_y(\mathbf{k}_1, t)$$

$$+ \int d\mathbf{k}_1' d\mathbf{k}_1''\left\{\delta(\mathbf{k}_1' + \mathbf{k}_1'' - \mathbf{k}_1)\left(\frac{k_{1y}'}{k_{1x}'} - At\right)\right.$$

$$\left.\times\, \tilde{v}_y(\mathbf{k}_1', t) ik_{1x}''\left(\frac{k_{1y}''}{k_{1x}''} - At\right)\tilde{v}_y(k_1'', t)\right\} \tag{A.12}$$

$$+ \int d\mathbf{k}_1' d\mathbf{k}_1''\left\{\delta(\mathbf{k}_1' + \mathbf{k}_1'' - \mathbf{k}_1)\,\tilde{v}_y(\mathbf{k}_1', t) ik_{1x}''\left(\frac{k_{1y}''}{k_{1x}''} - At\right)\right.$$

$$\left.\times\left[-\left(\frac{k_{1y}''}{k_{1x}''} - At\right)\right]\tilde{v}_y(\mathbf{k}_1'', t)\right\} = -ik_{1x}\tilde{P},$$

$$\frac{\partial \tilde{v}_y(\mathbf{k}_1 t)}{\partial t} + \int d\mathbf{k}_1' d\mathbf{k}_1''\left\{\delta(\mathbf{k}_1' + \mathbf{k}_1'' - \mathbf{k}_1)\right.$$

$$\left.\times\left[-\left(\frac{k_{1y}'}{k_{1x}'} - At\right)\tilde{v}_y(\mathbf{k}_1', t)\right] ik_{1x}''\tilde{v}_y(\mathbf{k}_1'', t)\right\} \tag{A.13}$$

$$+ \int d\mathbf{k}_1' d\mathbf{k}_1''\left\{\delta(\mathbf{k}_1' + \mathbf{k}_1'' - \mathbf{k}_1)\,\tilde{v}_y(\mathbf{k}_1', t)\right.$$

$$\left.\times ik_{1x}''\tilde{v}_y(\mathbf{k}_1'', t)\left(\frac{k_{1y}''}{k_{1x}''} - At\right)\right\} = -ik_{1x}\left(\frac{k_{1x}}{k_{1x}} - At\right)\tilde{P}.$$

Eliminating $\tilde{P}$ from these equations gives a symmetric equation for v_y

$$(k_{1x}^2 + k_{1y}^2)\frac{\partial \tilde{v}(k_{1x}, k_{1y}, t)}{\partial t} - 2Ak_{1x}k_{1y}(t)\,\tilde{v}_y(k_{1x}, k_{1y}, t)$$

$$+ \frac{i}{2}\int d\mathbf{k}_1' d\mathbf{k}_1''\left\{\delta(k_{1x}' + k_{1x}'' - k_{1x})\delta(k_{1y}' + k_{1y}'' - k_{1y})\right. \tag{A.14}$$

$$\times k_{1x}[k_1''^2(t) - k_1'^2(t)]\left(\frac{k_{1y}''}{k_{1x}''} - \frac{k_{1y}'}{k_{1x}'}\right)$$

$$\left.\times\, \tilde{v}_y(k_{1x}', k_{1y}', t)\,\tilde{v}_y(k_{1x}'', k_{1y}'', t)\right\} = 0,$$

where

$$k_{1y}(t) = k_{1y} - k_{1x}At, \quad k_1^2(t) = k_{1x}^2 + k_{1y}^2(t).$$

Introducing the function

$$C_{\mathbf{k}} = [k_{1x}^2 + k_{1y}^2(t)]\,\tilde{v}_y(\mathbf{k}_1, t), \tag{A.15}$$

we rewrite Eq. (A.14) in a more convenient form (cf. [39–41])

$$i\frac{\partial C_{\mathbf{k}_1}}{\partial t} = \int d\mathbf{k}_1' d\mathbf{k}_1'' V_{\mathbf{k}_1\mathbf{k}_1'\mathbf{k}_1''} C_{\mathbf{k}_1'} C_{\mathbf{k}_1''}, \tag{A.16}$$

where

$$V_{\mathbf{k}_1\mathbf{k}_1'\mathbf{k}_1''} = \delta(\mathbf{k}_1' + \mathbf{k}_1'' - \mathbf{k}_1)\frac{k_1'^2(t) - k_1''^2(t)}{k_1'^2(t)k_1''^2(t)} \tag{A.17}$$

$$\times (k_{1x}' + k_{1x}'')\left(\frac{k_{1y}'}{k_{1x}'} - \frac{k_{1y}''}{k_{1x}''}\right).$$

We note that $C_{\mathbf{k}}$ is related to the vorticity of the spatial Fourier harmonics.

Supposing that many degrees of freedom (modes) are excited, we use the random phase approximation (cf. [39]), which can be expressed by

$$\begin{aligned} \langle C_{\mathbf{k}_1} C_{\mathbf{k}_1'}\rangle &= n_{\mathbf{k}_1}(t)\delta(\mathbf{k}_1 + \mathbf{k}_1') \\ &\equiv n(k_{1x}, k_{1y}, t)\delta(\mathbf{k}_1 + \mathbf{k}_1'), \end{aligned} \tag{A.18}$$

where $\langle \ldots \rangle$ denotes the phase average.

To use the methods of the weak turbulence theory, we expand $C_{\mathbf{k}}$ as

$$C_{\mathbf{k}_1} = C_{\mathbf{k}_1}^{(0)} + C_{\mathbf{k}_1}^{(1)} + \ldots, \tag{A.19}$$

where

$$C_{\mathbf{k}_1}^{(0)} \gg C_{\mathbf{k}_1}^{(1)} \tag{A.20}$$

and

$$\frac{\partial C_{\mathbf{k}_1}^{(0)}}{\partial t} = 0, \tag{A.21}$$

which means that the nonlinearity is taken into account within perturbation theory. Using Eqs. (A.19)–(A.21), it follows from (A.16) that

$$C^{(1)}_{\mathbf{k}_1} = -i\int d\mathbf{k}'_1 d\mathbf{k}''_1 \left\{ C^{(0)}_{\mathbf{k}'_1} C^{(0)}_{\mathbf{k}''_1} \int_0^t dt' V_{\mathbf{k}_1\mathbf{k}'_1\mathbf{k}''_1} \right\}. \quad \text{(A.22)}$$

We next use the relations between higher correlations accepted in the weak turbulence theory,

$$\left\langle C^{(0)}_{\mathbf{k}_1} C^{(0)}_{\mathbf{k}'_1} C^{(0)}_{\mathbf{k}''_1} \right\rangle = 0, \quad \text{(A.23)}$$

$$\begin{aligned}
&\left\langle C^{(0)}_{\mathbf{k}_1} C^{(0)}_{\mathbf{k}'_1} C^{(0)}_{\mathbf{k}''_1} C^{(0)}_{\mathbf{k}'''_1} \right\rangle = \left\langle C^{(0)}_{\mathbf{k}_1} C^{(0)}_{\mathbf{k}'_1} \right\rangle \left\langle C^{(0)}_{\mathbf{k}''_1} C^{(0)}_{\mathbf{k}'''_1} \right\rangle \\
&+ \left\langle C^{(0)}_{\mathbf{k}_1} C^{(0)}_{\mathbf{k}''_1} \right\rangle \left\langle C^{(0)}_{\mathbf{k}'_1} C^{(0)}_{\mathbf{k}'''_1} \right\rangle + \left\langle C^{(0)}_{\mathbf{k}_1} C^{(0)}_{\mathbf{k}'''_1} \right\rangle \left\langle C^{(0)}_{\mathbf{k}'_1} C^{(0)}_{\mathbf{k}''_1} \right\rangle \\
&= n_{\mathbf{k}_1} n_{\mathbf{k}''_1} \delta(\mathbf{k}_1 + \mathbf{k}'_1)\delta(\mathbf{k}''_1 + \mathbf{k}'''_1) \quad \text{(A.24)} \\
&\quad + n_{\mathbf{k}_1} n_{\mathbf{k}'_1} \delta(\mathbf{k}_1 + \mathbf{k}''_1)\delta(\mathbf{k}'_1 + \mathbf{k}'''_1) \\
&\quad + n_{\mathbf{k}_1} n_{\mathbf{k}'_1} \delta(\mathbf{k}_1 + \mathbf{k}'''_1)\delta(\mathbf{k}'_1 + \mathbf{k}''_1).
\end{aligned}$$

As can easily be seen, we then have

$$\begin{aligned}
&\frac{\partial n_{\mathbf{k}_1}}{\partial t}\delta(\mathbf{k}_1 + \mathbf{k}'''_1) \\
&= -i\int d\mathbf{k}'_1 d\mathbf{k}''_1 (V_{\mathbf{k}_1\mathbf{k}'_1\mathbf{k}''_1} \left\langle C_{\mathbf{k}_1} C_{\mathbf{k}'_1} C_{\mathbf{k}''_1} \right\rangle \\
&\quad + V_{\mathbf{k}'''_1\mathbf{k}'_1\mathbf{k}''_1} \left\langle C_{\mathbf{k}_1} C_{\mathbf{k}'_1} C_{\mathbf{k}'''_1} \right\rangle) \\
&\approx -i\int d\mathbf{k}'_1 d\mathbf{k}''_1 (V_{\mathbf{k}_1\mathbf{k}'_1\mathbf{k}''_1} (\left\langle C^{(0)}_{\mathbf{k}_1} C^{(0)}_{\mathbf{k}''_1} C^{(1)}_{\mathbf{k}'''_1} \right\rangle \quad \text{(A.25)} \\
&\quad + \left\langle C^{(1)}_{\mathbf{k}'_1} C^{(0)}_{\mathbf{k}''_1} C^{(0)}_{\mathbf{k}'''_1} \right\rangle + \left\langle C^{(0)}_{\mathbf{k}'_1} C^{(1)}_{\mathbf{k}''_1} C^{(0)}_{\mathbf{k}'''_1} \right\rangle) \\
&\quad + V_{\mathbf{k}'''_1\mathbf{k}'_1\mathbf{k}''_1} (\left\langle C^{(0)}_{\mathbf{k}'_1} C^{(0)}_{\mathbf{k}''_1} C^{(1)}_{\mathbf{k}'''_1} \right\rangle + \left\langle C^{(1)}_{\mathbf{k}'_1} C^{(0)}_{\mathbf{k}''_1} C^{(0)}_{\mathbf{k}'''_1} \right\rangle \\
&\quad + \left\langle C^{(0)}_{\mathbf{k}'_1} C^{(1)}_{\mathbf{k}''_1} C^{(0)}_{\mathbf{k}'''_1} \right\rangle) \}.
\end{aligned}$$

In view of (A.22) and (A.24), this becomes

$$\begin{aligned}
&2\int d\mathbf{k}'_1 d\mathbf{k}''_1 \psi_{\mathbf{k}'_1\mathbf{k}''_1} \left\{ \delta(\mathbf{k}_1 - \mathbf{k}'_1 - \mathbf{k}''_1)\delta(\mathbf{k}_1 + \mathbf{k}'''_1) \right. \\
&\times \left(n_{\mathbf{k}_1} n_{\mathbf{k}''_1} \int_0^t dt' \psi_{\mathbf{k}'_1\mathbf{k}''_1} + 2 n_{\mathbf{k}_1} n_{\mathbf{k}''_1} \int_0^t dt' \psi_{-\mathbf{k}'_1\mathbf{k}''_1} \right) \quad \text{(A.26)} \\
&\quad + \delta(\mathbf{k}_1 + \mathbf{k}'_1 + \mathbf{k}''_1)\delta(\mathbf{k}_1 + \mathbf{k}'''_1) \\
&\left. \times \left(n_{\mathbf{k}'_1} n_{\mathbf{k}''_1} \int_0^t dt' \psi_{\mathbf{k}'_1\mathbf{k}''_1} + 2 n_{\mathbf{k}_1} n_{\mathbf{k}''_1} \int_0^t dt' \psi_{\mathbf{k}_1\mathbf{k}''_1} \right) \right\},
\end{aligned}$$

where

$$\psi_{\mathbf{k}'_1\mathbf{k}''_1}(t) \equiv \left(\frac{1}{\mathbf{k}''^2_1(t)} - \frac{1}{\mathbf{k}'^2_1(t)} \right)(k'_{1x} + k''_{1x}) \left(\frac{k'_{1y}}{k'_{1x}} - \frac{k''_{1y}}{k''_{1x}} \right).$$

Changing the variables in the second part of the integral as

$$\mathbf{k}'_1 \longrightarrow -\mathbf{k}'_1 \text{ and } \mathbf{k}''_1 \longrightarrow -\mathbf{k}''_1$$

and taking into account that

$$\psi_{-\mathbf{k}'_1, -\mathbf{k}''_1} = -\psi_{\mathbf{k}'_1\mathbf{k}''_1}, \quad \text{(A.27)}$$

we continue the transformations as

$$\begin{aligned}
\frac{\partial n_{\mathbf{k}_1}}{\partial t} &= 4\int d\mathbf{k}'_1 d\mathbf{k}''_1 \delta(\mathbf{k}_1 - \mathbf{k}'_1 - \mathbf{k}''_1)\psi_{\mathbf{k}'_1\mathbf{k}''_1} \\
&\times \left(n_{\mathbf{k}'_1} n_{\mathbf{k}''_1} \int_0^t dt' \psi_{\mathbf{k}'_1\mathbf{k}''_1} - 2 n_{\mathbf{k}_1} n_{\mathbf{k}''_1} \int_0^t dt' \psi_{\mathbf{k}_1 - \mathbf{k}''_1} \right).
\end{aligned} \quad \text{(A.28)}$$

Inserting the expressions for $\psi_{\mathbf{k}'_1\mathbf{k}''_1}$ and $\psi_{\mathbf{k}_1 - \mathbf{k}''_1}$ (see Eq. (A.26)) in the time integrals and integrating, we obtain

$$\begin{aligned}
&\int_0^t dt' \psi_{\mathbf{k}'_1\mathbf{k}''_1} = \frac{1}{A}(k'_{1x} + k''_{1x}) \left(\frac{k'_{1y}}{k'_{1x}} - \frac{k''_{1y}}{k''_{1x}} \right) \\
&\times \left\{ \frac{1}{k''^2_{1x}} \arctan \frac{At}{1 + (k''_{1y}/k''_{1x})((k''_{1y}/k''_{1x}) - At)} \right. \quad \text{(A.29)} \\
&\left. - \frac{1}{k'^2_{1x}} \arctan \frac{At}{1 + (k'_{1y}/k'_{1x})((k'_{1y}/k'_{1x}) - At)} \right\},
\end{aligned}$$

$$\begin{aligned}
&\int_0^t dt' \psi_{\mathbf{k}_1 - \mathbf{k}''_1} = \frac{1}{A}(k_{1x} - k''_{1x}) \left(\frac{k_{1y}}{k_{1x}} - \frac{k''_{1y}}{k''_{1x}} \right) \\
&\times \left\{ \frac{1}{k''^2_{1x}} \arctan \frac{At}{1 + (k''_{1y}/k''_{1x})((k''_{1y}/k''_{1x}) - At)} \right. \quad \text{(A.30)} \\
&\left. - \frac{1}{k^2_{1x}} \arctan \frac{At}{1 + (k_{1y}/k_{1x})((k_{1y}/k_{1x}) - At)} \right\}.
\end{aligned}$$

As mentioned above, it is convenient to obtain the equation for the energy density at a fixed point of the **k** space in order to construct the weak turbulence theory. For this, we use Eqs. (A.4)–(A.5) to transform Eqs. (A.28)–(A.30) to the new variables k_x and k_y,

$$\langle v^2\rangle = \langle v_x^2 + v_y^2\rangle = \int d\mathbf{k}_1(\tilde{v}_x^2 + \tilde{v}_y^2)$$
$$= \int d\mathbf{k}_1 \tilde{v}_y^2(k_{1x}, k_{1y}, t)\left(1 + \frac{k_{1y}^2(t)}{k_{1x}^2(t)}\right) \quad \text{(A.31)}$$
$$= \int d\mathbf{k}_1 \frac{n(k_{1x}, k_{1y}, t)}{k_{1x}^2[k_{1x}^2 + k_{1y}^2(t)]} = \int d\mathbf{k}\frac{n(k_x, k_y + k_x At, t)}{k_y^2(k_x^2 + k_y^2)},$$

where

$$k_x \equiv k_{1x}, \quad k_y \equiv k_{1y}(t) = k_{1y} - k_{1x}At. \quad \text{(A.32)}$$

On the other hand,

$$\langle v^2\rangle = \int d\mathbf{k}\,\hat{v}_x^2(k_x, k_y, t) + \hat{v}_y^2(k_x, k_y, t)$$
$$= \int d\mathbf{k}E(\mathbf{k}, t) \equiv \int d\mathbf{k}E_{\mathbf{k}}, \quad \text{(A.33)}$$

whence

$$E_{\mathbf{k}} = \frac{n(k_x, k_y + k_x At, t)}{k_x^2(k_x^2 + k_y^2)}. \quad \text{(A.34)}$$

$E_{\mathbf{k}}$ is the energy density of the 2D vortex mode disturbances at a fixed point of the **k** space. In other words, this is the spectral density of energy.

Inserting integrals (A.29) and (A.30) in Eq. (A.28), changing the variables in accordance with (A.4), and using (A.34), we obtain the equation for the spectral density of the disturbance energy at a fixed point in the **k** space,

$$\frac{\partial E_{\mathbf{k}}}{\partial t} + \nabla_{\mathbf{k}}(\mathbf{V}E_{\mathbf{k}}) - \frac{2Ak_xk_y}{k_x^2 + k_y^2}E_{\mathbf{k}}$$
$$+ \nu(k_x^2 + k_y^2)E_{\mathbf{k}} = \hat{N}E_{\mathbf{k}}, \quad \text{(A.35)}$$

where

$$\nabla_{\mathbf{k}} = (\partial/\partial k_x, \partial/\partial k_y), \quad \mathbf{V} = (-Ak_x, 0),$$

and

$$\hat{N}E_{\mathbf{k}} = \frac{4}{A}\int d\mathbf{k}_1' d\mathbf{k}_1'' \delta(\mathbf{k}_1 - \mathbf{k}_1' - \mathbf{k}_1'')$$
$$\times (k'^2 - k''^2)(k_y'k_y'' - k_x''k_x')^2$$
$$\times\left\{\frac{1}{k^2}\left(\frac{1}{k_{1x}''^2}\arctan\frac{At}{1 + (k_y''/k_x'')((k_y''/k_x'') + At)}\right.\right.$$
$$\left.\left. - \frac{1}{k_{1x}'^2}\arctan\frac{At}{1 + (k_y'/k_x')((k_y'/k_x') + At)}\right)E_{\mathbf{k}'}E_{\mathbf{k}''}\right.$$
$$+ 2\frac{1}{k'^2}\left(\frac{1}{k_x''^2}\arctan\frac{At}{1 + (k_y''/k_x'')((k_y''/k_x'') + At)}\right.$$
$$\left.\left. - \frac{1}{k_x^2}\arctan\frac{At}{1 + (k_y/k_x)((k_y/k_x) + At)}\right)E_{\mathbf{k}}E_{\mathbf{k}''}\right\}. \quad \text{(A.36)}$$

In the derivation of Eqs. (A.35) and (A.36), the viscosity term was omitted. It was then added in Eq. (A.35) (the fourth term on the left-hand side).

REFERENCES

1. S. A. Orszag and L. C. Kells, J. Fluid Mech. **96**, 159 (1980).
2. A. S. Monin and A. M. Yaglom, *Statistical Fluid Mechanics* (MIT Press, Cambridge, 1971).
3. D. D. Joseph, *Stability of Fluid Motions* (Springer-Verlag, Berlin, 1976).
4. U. Frisch and S. A. Orszag, Phys. Today **43**, 24 (1990).
5. F. Hussain, T. Kambe, K. Kuwahara, *et al.*, Fluid Dyn. Res. **7**, 51 (1991).
6. *Hydrodynamic Instabilities and the Transition to Turbulence*, Ed. by H. L. Swinney and J. P. Gollub (Springer-Verlag, Berlin, 1981).
7. S. C. Reddy, P. J. Schmid, and D. S. Hennington, SIAM J. Appl. Math. **53**, 15 (1993).
8. L. N. Trefethen, A. E. Trefethen, S. C. Reddy, *et al.*, Science **261**, 578 (1993).
9. K. Moffatt, in *Atmospheric Turbulence and Radio Wave Propagation*, Ed. by A. M. Yaglom and V. I. Tatarskiĭ (Nauka, Moscow, 1967).
10. S. Marcus and W. H. Press, J. Fluid Mech. **79**, 525 (1977).
11. A. D. D. Craik and W. O. Criminale, Proc. R. Soc. London, Ser. A **406**, 13 (1986).
12. V. A. Gorodtsov, Izv. Akad. Nauk SSSR, Mekh. Zhidk. Gaza, No. 2, 941 (1988).
13. J. G. Lominadze, G. D. Chagelishvili, and R. A. Chanishvili, Pis'ma Astron. Zh. **14**, 856 (1988) [Sov. Astron. Lett. **14**, 364 (1988)].
14. L. H. Gustavsson, J. Fluid Mech. **224**, 241 (1991).
15. S. C. Reddy and D. S. Henningson, J. Fluid Mech. **252**, 209 (1993).
16. K. M. Butler and B. F. Farrell, Phys. Fluids A **4**, 1637 (1992).
17. B. F. Farrell and P. J. Ioannou, Phys. Fluids A **5**, 1390 (1993).
18. G. D. Chagelishvili, G. R. Khujadze, J. G. Lominadze, *et al.*, Phys. Fluids **9**, 1955 (1997).
19. G. D. Chagelishvili, A. D. Rogava, and I. N. Segal, Phys. Rev. E **50**, R4283 (1994).
20. G. D. Chagelishvili, T. S. Christov, R. G. Chanishvili, *et al.*, Phys. Rev. E **47**, 366 (1993).
21. S. A. Balbus and J. H. Hawley, Astrophys. J. **400**, 610 (1992).
22. S. H. Lubow and H. C. Spruit, Astrophys. J. **445**, 337 (1995).
23. G. D. Chagelishvili, A. D. Rogava, and D. G. Tsiklauri, Phys. Rev. E **53**, 6028 (1996).

24. G. D. Chagelishvili and O. G. Chkhetiani, Pis'ma Zh. Éksp. Teor. Fiz. **62**, 301 (1995) [JETP Lett. **62**, 314 (1995)].
25. A. D. Rogava and S. M. Mahajan, Phys. Rev. E **55**, 1185 (1997).
26. G. D. Chagelishvili, A. G. Tevzadze, G. Bodo, *et al.*, Phys. Rev. Lett. **79**, 3178 (1997).
27. A. D. Rogava, G. D. Chagelishvili, and S. H. Mahajan, Phys. Rev. E **57**, 7103 (1998).
28. A. G. Tevzadze, Phys. Plasmas **5**, 1557 (1998).
29. G. D. Chagelishvili, A. G. Tevzadze, G. Bodo, *et al.*, in *Proceedings of Eight European Turbulence Conference, Barcelona, 2000*, Ed. by C. Dopazo *et al.*, p. 737.
30. L. Broberg and U. Brosa, Z. Naturforsch. Teil A **43**, 697 (1988).
31. G. D. Chagelishvili, R. G. Chanishvili, and J. G. Lominadze, in *Proceedings of the Joint Varenna-Abastumani International School & Workshop on Plasma Astrophysics, 1988*, ESA SP–285, Vol. I, p. 261.
32. G. D. Chagelishvili, R. G. Chanishvili, and J. G. Lominadze, in *High Energy Astrophysics: American and Soviet Perspectives* (National Academy Press, Washington, 1991), p. 55.
33. G. D. Chagelishvili, R. G. Chanishvili, J. G. Lominadze, *et al.*, in *Proceedings of the Fourth International Conference on Plasma Physics and Controlled Nuclear Fusion, 1993*, ESA SP-351, p. 23.
34. T. Gebhardt and S. Grossmann, Phys. Rev. E **50**, 3705 (1994).
35. J. S. Baggett, T. A. Driscoll, and L. N. Trefethen, Phys. Fluids **7**, 833 (1995).
36. D. S. Henningson and S. C. Reddy, Phys. Fluids **6**, 1396 (1994).
37. J. S. Baggett and L. N. Trefethen, Phys. Fluids **9**, 1043 (1997).
38. G. D. Chagelishvili, R. G. Chanishvili, and J. G. Lominadze, Pis'ma Zh. Éksp. Teor. Fiz. **63**, 481 (1996) [JETP Lett. **63**, 543 (1996)].
39. V. E. Zakharov, in *Basis of Plasma Physics*, Ed. by A. A. Galeev and R. N. Sudan (Énergoatomizdat, Moscow, 1984; North-Holland, Amsterdam, 1984), Vol. 2.
40. V. N. Tsytovich, *Nonlinear Effects in Plasma* (Nauka, Moscow, 1967).
41. R. C. Davidson, *Methods in Nonlinear Plasma Physics (*Academic, New York, 1972).
42. P. J. Schmid and D. S. Henningson, Phys. Fluids A **4**, 1986 (1992).
43. S. Berlin, M. Weigel, and D. S. Henningson, J. Fluid Mech. **393**, 23 (1999).
44. G. D. Chagelishvili and G. R. Khujadze, Zh. Éksp. Teor. Fiz. **112**, 1664 (1997) [JETP **85**, 907 (1997)].
45. G. D. Chagelishvili, G. R. Khujadze, and J. G. Lominadze, in *Proceedings of the Eight European Turbulence Conference, Barcelona, 2000*, Ed. by C. Dopazo *et al.*, p. 67.

Journal of Experimental and Theoretical Physics, Vol. 94, No. 2, 2002, pp. 446–452.
Translated from Zhurnal Éksperimental'noĭ i Teoreticheskoĭ Fiziki, Vol. 121, No. 2, 2002, pp. 521–527.

MISCELLANEOUS

Coherent Repopulating Hyperfine-Structure Levels by Pulsed Resonance Fields and the Quantum Computer Problem

D. F. Zaretskiĭ* and S. B. Sazonov

Russian Research Center Kurchatov Institute, Moscow, 123182 Russia

**e-mail: zaretsky@imp.kiae.ru*

Received July 5, 2001

Abstract—A new method of polarization of atoms and nuclei by pulsed bichromatic resonance radio-frequency fields is proposed to produce an initial state of a quantum computer constructed with the use of cubits representing impurity atoms in a solid matrix having the hyperfine structure. It is shown that this method can provide strong polarization without using ultralow temperatures. The problem is considered for the interaction of three- and four-level systems with bichromatic and two-phase fields. *© 2002 MAIK "Nauka/Interperiodica".*

1. INTRODUCTION

The problem of creation of a quantum computer is a topical problem attracting the attention of many researchers [1–3]. The search for physical systems that can be used as information media for quantum calculations is actively pursued. A solid medium containing two-level nuclear spin systems is one of the main candidates for the development of such systems [4]. On the one hand, a two-level system can carry one bit of quantum information. On the other hand, a variety of algorithms for quantum calculations can be realized by exciting this system by pulses of resonance high-frequency fields with specified parameters and using various mechanisms of the interaction between these systems. Such a two-level system is called a cubit. It has been proved that any quantum calculation algorithm can be represented as a sequence of transformations of the state of individual cubits and operations with pairs of the interacting cubits, when the result of the action of the field on one of the cubits in the pair depends on the state of another cubit (the CNOT operation) [5].

Before the action of the field, a cubit quantum system is in the state $|\Psi(0)\rangle$, which represents a superposition of the eigenstates of the Hamiltonian of the system interacting with a permanent magnetic field. For a two-level system, this state is written as $|\Psi(0)\rangle = a(0)|0\rangle + b(0)|1\rangle$. After irradiation by a pulses of duration t of the oscillating field, which is perpendicular to a permanent field and is much weaker than the permanent field, the system performing Rabi oscillations will be found in the state $|\Psi(t)\rangle$, which is $|\Psi(t)\rangle = a(t)|0\rangle + b(t)|1\rangle$ for a two-level system. Similar processes occur in nuclear magnetic resonance, and the description presented above is equivalent to the formalism used for the description of NMR [6].

One of the problems encountered in the development of a quantum computer is the creation of the initial state in which cubits are in the lower energy state $|\Psi(0)\rangle$. Such a state can be produced by cooling solids down to microkelvin temperatures, which is, however, a technically complicated problem.

Earlier [7], we considered repopulating a system consisting of the hyperfine-structure components of the ground state of an atom and of its excited level upon the interaction with laser fields. This effect underlies the well-known optical phenomenon of coherent population trapping. In addition, we proposed theoretically the procedure of polarization of the Zeeman levels of the nuclear spin of an impurity atom in a magnetically ordered crystal matrix or of the hyperfine-structure levels of an impurity in the ground state in dielectrics upon the interaction with a bichromatic radio-frequency wave [8]. We have shown that this method provides, under certain conditions, a substantial repopulating of the quantum-system levels. We believe that these methods can be used for creation of a quantum computer based on nuclear spins of impurities in solid matrices without their cooling down to ultralow temperatures. We propose to use two levels of a three-level or a four-level system of nonequidistant hyperfine-structure levels as a cubit, which interacts with a pulsed resonance coherent bichromatic or two-phase field. The polarization of such a system of quantum levels is considered assuming that all the levels are populated before the field action, i.e., the system is in the state of the type $|\Psi(0)\rangle$ with nonzero a(0) and b(0).

2. THREE-LEVEL NONEQUIDISTANT SYSTEM IN A BICHROMATIC RESONANCE HIGH-FREQUENCY FIELD

The Hamiltonian of a system of quantum levels in a field has the form

$$H(t) = H_0 + V(t), \quad (1)$$

where H_0 is the Hamiltonian of the quantum system interacting with fields that are stationary during the pulse and $V(t)$ is the operator of interaction of this system with the oscillating field. Assuming that $H_0 \gg V(t)$, we will perform calculations using time-dependent perturbation theory. We assume that the distances between the levels are smaller than kT and all the levels are populated differently in the general case before the HF field switching. Let us assume that the time of interaction of the system with the field is shorter than all relaxation times, namely, the longitudinal and transverse relaxation times. This condition allows us to study the interaction process in terms of the amplitudes, assuming that the system is in the state described by a wave function representing a superposition of the eigenfunctions of the Hamiltonian H_0, which also includes weak stationary perturbations which make the hyperfine-structure levels nonequidistant:

$$\Psi(t) = \sum b_i(t)F_i. \quad (2)$$

Here, $b_i(t)$ are the population amplitudes for the ith level, which satisfy the initial conditions

$$b_i(0) = A_i \exp(i\alpha_i), \quad (3)$$

where A_i is the amplitude of the initial population of the ith level,

$$A_i^2 = |b_i(0)|^2, \quad (4)$$

and α_i is the amplitude of the initial population of the ith level. Because the interaction time is assumed to be shorter than all the relaxation times, no stochastic perturbations of the system are present during the interaction. In addition, we assume that the period of Rabi oscillations is also shorter than all the relaxation times. This means that the interaction of an impurity center, an ion or an atom with a thermostat is much weaker than the interaction with the external field. Therefore, we should first find the probabilities of repopulating the levels of the system caused by the external field during the pulse and then average them over an ensemble of impurity centers or atoms. In this case, the amplitudes $b_i(t)$ are always proportional to constant phase factors $\exp(i\alpha_i)$ and can be written in the form

$$b_i(t) = a_i(t)\exp(i\alpha_i), \quad (5)$$

the functions $a_i(t)$ being independent of α_i at any time and equal to

$$a_i(0) = A_i \quad (6)$$

for $t = 0$. The wave eigenfunctions F_i can be redetermined as

$$F_i = F_i'\exp(-i\alpha_i), \quad (7)$$

where the functions F_i' are independent of phases α_i and are also the eigenfunctions of the Hamiltonian H_0.

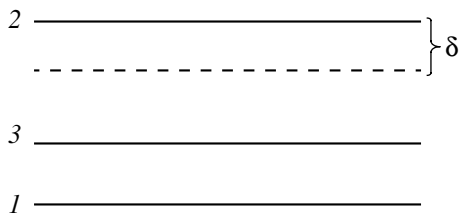

Fig. 1. System of three nonequidistant levels.

As a result, expression (2) takes the form

$$\Psi(t) = \sum \alpha_i(t)F_i'.$$

It follows from this that the coherent repopulation of the levels is independent of the initial phases of the population amplitudes if these phases are constant during the interaction. The system of equations for the amplitudes $a_i(t)$ can be obtained from the Schrödinger equation for the wave function $\Psi(t)$:

$$i\hbar\frac{d\Psi(t)}{dt} = H(t)\Psi(t). \quad (8)$$

Consider the interaction of a system of three nonequidistant levels with a bichromatic field of the form

$$H(t) = H_1\cos(\omega_1 t + \varphi_1) + H_2\cos(\omega_2 t + \varphi_2). \quad (9)$$

The components of the bichromatic field are coherent with each other, their phases φ_i and their relative phase $\Delta_\varphi = \varphi_2 - \varphi_1$ remaining constant during the interaction. Below we assume that $\varphi_1 = 0$ and $\varphi_2 = \Delta_\varphi$. The system of levels interacting with the field is shown in Fig. 1. We will assume that the first component with the frequency ω_1 is resonant to the transition between levels 1 and 3, while the second component is resonant with the frequency ω_2 to the transition between levels 2 and 3. The third level is common and lies between levels 2 and 3.

The system of equations of the time-dependent perturbation theory for the amplitudes $a_i(t)$ in the resonance approximation has the form

$$\begin{aligned}\frac{da_1}{dt} &= -iV_{13}a_3,\\ \frac{da_2}{dt} &= -iV_{23}a_3,\\ \frac{da_3}{dt} &= -iV_{31}a_1 - iV_{32}a_2,\end{aligned} \quad (10)$$

where V_{ij} are the matrix elements of the operators of interaction with the field components that are resonant to the corresponding transition. We assume in (10) and below that $\hbar = 1$.

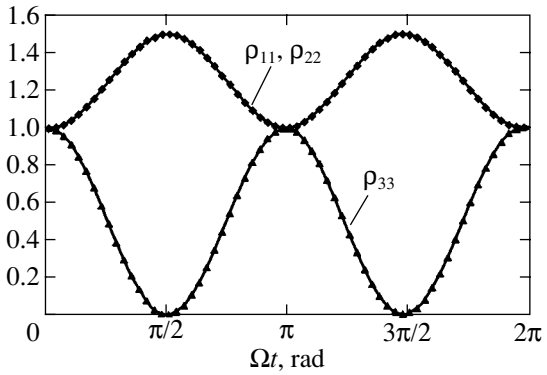

Fig. 2. Level populations in a three-level system after the interaction with pulses of the bichromatic field of different durations; $\Delta_\varphi = \pi$.

In the general case, the solution of the system of equations (10) for the case when all the levels are populated for $t = 0$ has the form

$$a_1(t) = \frac{V_2A_- + V_1A_+\cos(\Omega t)}{\Omega^2} - \frac{iV_1A_3\sin(\Omega t)}{\Omega},$$

$$a_2(t) = \left[\frac{V_2A_+\cos(\Omega t) - V_1A_-}{\Omega^2} - \frac{iV_2A_3\sin(\Omega t)}{\Omega}\right] \times \exp(-i\Delta_\varphi),$$

$$a_3(t) = A_3\cos(\Omega t) - \frac{iA_+\sin(\Omega t)}{\Omega}, \qquad (11)$$

$$A_+ = A_2V_2\exp(i\Delta_\varphi) + A_1V_1,$$

$$A_- = A_1V_2 - A_2V_1\exp(i\Delta_\varphi).$$

Here, Ω is the frequency of Rabi oscillations,

$$\Omega^2 = V_1^2 + V_2^2,$$

where V_1 and V_2 are the real parts of matrix elements. They are proportional to the strengths of the corresponding components of the bichromatic field H_i:

$$V_{13} = V_1, \quad V_{23} = V_2\exp(-i\Delta_\varphi).$$

To estimate the degree of the level repopulation, we will pass from amplitudes to populations:

$$\rho_{ii} = |a_i(t)|^2.$$

For all $A_i = 1$ and equal V_i, we have

$$\rho_{11} = 1 - \frac{\cos\Delta_\varphi}{2} + \frac{\cos\Delta_\varphi\cos^2(\Omega t)}{2} + \frac{\sin(\Omega t)\sin\Delta_\varphi[1 - \cos(\Omega t)]}{\sqrt{2}},$$

$$\rho_{22} = 1 - \frac{\cos\Delta_\varphi}{2} + \frac{\cos\Delta_\varphi\cos^2(\Omega t)}{2} - \frac{\sin(\Omega t)\sin\Delta_\varphi[1 + \cos\Omega t]}{\sqrt{2}}, \qquad (12)$$

$$\rho_{33} = 1 + \cos\Delta_\varphi\sin^2(\Omega t) + \frac{\sin\Delta_\varphi\sin(2\Omega t)}{\sqrt{2}}.$$

Figure 2 demonstrated the repopulation of the levels for $\Delta_\varphi = \pi$ upon irradiation by pulses of different durations. Note that for $\Omega t = \pi/2, 3\pi/2$, the intermediate level 3 is completely deleted. Therefore, the situation can be produced in a subsystem consisting of two levels, for example, of the first and third levels, when the lower level is populated, whereas the upper level is empty, which corresponds to the initial state of a cubit.

This can be achieved differently by using pulsed fields of duration exceeding the Rabi period but shorter than all relaxation times. If the duration of the high-frequency pulse is greater than the Rabi period Ω^{-1}, the population can be determined by averaging over Rabi oscillations. For the averaged populations after the termination of the field pulse, we obtain

$$\overline{\rho_{11}} = \frac{V_2^2|A_-|^2}{\Omega^4} + \frac{V_1^2|A_+|^2}{2\Omega^4} + \frac{V_1^2A_3^2}{2\Omega^2},$$

$$\overline{\rho_{22}} = \frac{V_1^2|A_-|^2}{\Omega^4} + \frac{V_2^2|A_+|^2}{2\Omega^4} + \frac{V_2^2A_3^2}{2\Omega^2}, \qquad (13)$$

$$\overline{\rho_{33}} = \frac{A_3^2}{2} + \frac{|A_+|^2}{2\Omega^2}.$$

Consider the typical situation. Let the relation $|A_+|^2 = 0$ be fulfilled. This can take place, for example, when $\Delta_\varphi = \pi$ and

$$V_1 = \frac{V_2A_2}{A_1}. \qquad (14)$$

Then, the averaged populations are described by the expressions

$$\overline{\rho_{11}} = A_1^2 + \frac{A_2^2A_3^2}{2(A_1^2 + A_2^2)},$$

$$\overline{\rho_{22}} = A_2^2 + \frac{A_1^2A_3^2}{2(A_1^2 + A_2^2)}, \qquad (15)$$

$$\overline{\rho_{33}} = \frac{A_3^2}{2}.$$

One can see from (15) that, after irradiation by the field pulse, the population of the level 3 decreases by half. After repeated irradiation by N pulses, by preliminarily changing V_i according to (14), the population of this

level will decrease by a factor of 2^N. In this way, the middle common level can be virtually completely deleted.

Therefore, the levels 1 and 3 will form a two-level subsystem, which can be used as a cubit of the information medium prepared in the initial state. By switching then only the component of the field that resonantly couples the levels 1 and 3, we can realize the calculation algorithms of a quantum computer. Of course, the levels should by nonequidistant strongly enough, at least so that the action of the remaining field component on the transition between the levels 2 and 3 could be neglected.

3. THREE-LEVEL WEAKLY NONEQUIDISTANT SYSTEM IN A TWO-PHASE RESONANCE HIGH-FREQUENCY FIELD

Consider now the interaction of the three-level weakly nonequidistant system (Fig. 1) with a two-phase resonance field, which represents two coherent waves of the same frequency resonant to the transition between the levels 1 and 3 and shifted in phase with respect to each other:

$$H(t) = H_1\cos(\omega t) + H_2\cos(\omega t + \Delta_\varphi). \quad (16)$$

If the levels are weakly nonequidistant ($\delta \ll \omega$), one should take into account the influence of both field components (16) on the transition between the levels 1 and 3, to which both components are resonant, and on the transition between the levels 2 and 3, to which both components are detuned by the quantity δ.

The system of equations of the time-dependent perturbation theory for the population amplitudes, which is similar to (10), has the form

$$\begin{aligned}\frac{da_1}{dt} &= -iW^*a_3,\\ \frac{da_2}{dt} &= -iW\exp(i\delta t)a_3,\\ \frac{da_3}{dt} &= -iWa_1 - iW^*\exp(-i\delta t)a_2.\end{aligned} \quad (17)$$

Here, W is the matrix element of interaction with the field (16), which consists of two terms:

$$W = V_1 + V_2\exp(-i\Delta_\varphi). \quad (18)$$

Let us represent it in the form

$$\begin{aligned}W &= \Omega_0\exp(i\alpha/2),\\ \Omega_0 &= (V_1^2 + V_2^2 + 2V_1V_2\cos\Delta_\varphi)^{1/2},\\ \alpha &= -2\arctan[V_2\sin\Delta_\varphi/(V_2 + V_1\cos\Delta_\varphi)].\end{aligned} \quad (19)$$

Let us overdetermine the amplitude $a_2(t)$ as

$$a_2'(t) = a_2(t)\exp(-i\delta t). \quad (20)$$

By substituting (20) into (17), we obtain the system of equations

$$\begin{aligned}\frac{da_1}{dt} &= -iW^*a_3,\\ \frac{da_2'}{dt} &= -iWa_3 - i\delta a_2',\\ \frac{da_3}{dt} &= -iWa_1 - iW^*a_2'.\end{aligned} \quad (21)$$

The quantity Ω_0 in (19) determines the repopulation rate and depends, in the case of a two-phase field, not only on the field strength but also on the phase difference Δ_φ. It follows from (19) that for

$$\cos\Delta_\varphi = -\frac{V_1^2 + V_2^2}{2V_1V_2} \quad (22)$$

we have $\Omega_0 = 0$, and, hence, no repopulating will occur. Note that, for $V_1 = V_2$, we have $\alpha = -\Delta_\varphi$.

The system of linear differential equations (21) corresponds to the characteristic equation

$$k^3 + i\delta k^2 + 2k\Omega_0^2 + i\delta\Omega_0^2 = 0. \quad (23)$$

We will solve this equation approximately under the condition that the deviation from the equidistant level spacing Δ is less than Ω_0. Let us introduce a small parameter $\eta = \delta/\Omega_0$. We obtain the following approximate expressions for the level populations in the case of equal initial populations for all the levels ($A_i = 1$):

$$\begin{aligned}\rho_{11} &= [8 - 4\cos\alpha\sin^2X - 8\sqrt{2}\sin(\alpha/2)\\ &\times \sin X\cos Y + 8\sin\alpha\cos X\sin Y + \eta R_{11}]/8,\\ R_{11} &= -\cos(\alpha/2)[\cos(2X) + 3]\\ &- \sqrt{2}\sin\alpha\sin(2X) + 4\cos(\alpha/2)\cos X\cos Y\\ &- 2\sqrt{2}\cos\alpha\sin X\sin Y\\ &+ \sqrt{2}\sin\alpha\sin X\cos Y - 4\sin(\alpha/2)\cos X\sin Y,\\ \rho_{22} &= [8 - 4\cos\alpha\sin^2X + 8\sqrt{2}\sin(\alpha/2)\\ &\times \sin X\cos Y - 8\sin\alpha\cos X\sin Y + \eta R_{22}]/8,\\ R_{22} &= \cos(\alpha/2)[5 - \cos(2X)]\\ &- \sqrt{2}\sin\alpha\sin(2X) - 4\cos(\alpha/2)\cos X\cos Y\\ &+ 2\sqrt{2}\cos\alpha\sin X\sin Y + 3\sqrt{2}\sin\alpha\sin X\cos Y\\ &- 4\sin(\alpha/2)\cos X\sin Y,\\ \rho_{33} &= [8 + 8\cos\alpha\sin^2X + \eta R_{33}]/8,\\ R_{33} &= 2\cos(\alpha/2)[\cos(2X) - 1]\\ &+ 2\sqrt{2}\sin\alpha\sin(2X) - 4\sqrt{2}\sin\alpha\sin X\cos Y\\ &+ 8\sin(\alpha/2)\cos X\sin Y.\end{aligned} \quad (24)$$

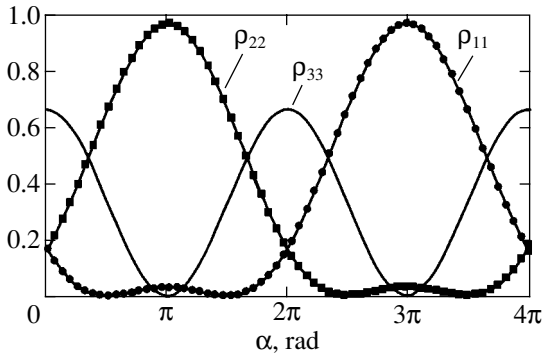

Fig. 3. Level populations in a weakly nonequidistant three-level system for different phases α after irradiation by the π/2 pulse of the two-phase field.

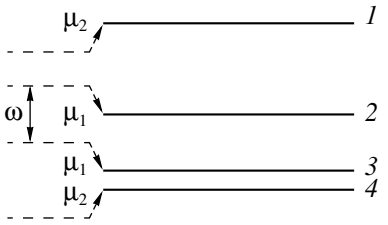

Fig. 4. System of four nonequidistant levels.

Here, $X = \sqrt{2}\,\Omega_0 t$ and $Y = \delta t/4$. Figure 3 shows the level populations as functions of α after irradiation by the π/2 pulse ($X = \pi/2$) for $\eta \ll 1$. One can see that for $\alpha = 3\pi$, using the π/2 pulse, we can prepare the system in the state in which only the lower level is populated. At the same time, the same pulse produces the inverse population in a subsystem consisting of two levels 1 and 3 when α is close to 3π/2, which can be used as a cubit.

4. FOUR-LEVEL SYSTEM IN A TWO-PHASE RESONANCE HIGH-FREQUENCY FIELD

The level repopulation in the system of four nonequidistant hyperfine-structure levels caused by the field (16) can be considered similarly. It has been shown in paper [9] that particles with the spin 3/2 having four energy levels also can used as carriers of the quantum information. It has been shown that in this case the CNOT operation can be performed for one particle, using two pairs of levels of this particle as two coupled cubits, rather than for two particles with the help of the interparticle interactions.

The system of equations for the population amplitudes of the four-level system shown in Fig. 4 has the form

$$\frac{da_1}{dt} = -i\sqrt{3}W\exp(i\delta t)a_2,$$

$$\frac{da_2}{dt} = -i\sqrt{3}W^*\exp(-i\delta t)a_1 - 2iWa_3, \qquad (25)$$

$$\frac{da_3}{dt} = -2iW^*a_2 - i\sqrt{3}W\exp(-i\delta t)a_4,$$

$$\frac{da_4}{dt} = -i\sqrt{3}W^*\exp(i\delta t)a_3.$$

The deviation from the equidistant level spacing in (25) or the detuning of the field (16) from the resonance, equal to it, is $\delta = \mu_1 + \mu_2$ (see Fig. 4). The nonequidistant system of levels shown in Fig. 4 corresponds to that of the Zeeman levels of the nucleus with the spin 3/2 of an impurity atom in a solid matrix, which appears due to the quadrupole interaction of the nucleus with the electric crystal field. We solve the system of equations (25) similarly to (17), by introducing the amplitudes

$$a_1' = \exp(-i\delta t)a_1, \quad a_4' = \exp(-i\delta t)a_4.$$

The characteristic fourth-degree equation is decomposed in this case into two quadratic factors:

$$[k(k+i\delta) + 3\Omega_0^2 + 2i\Omega_0(k+i\delta)][k(k+i\delta) + 3\Omega_0^2 - 2i\Omega_0(k+i\delta)] = 0. \qquad (26)$$

As in the three-level case, we solve this problem approximately for $\delta < \Omega_0$. By introducing the small parameter $\eta = \delta/\Omega_0$, we obtain, in the case of the initial conditions $A_i = 1$,

$$\begin{aligned}
\rho_{11} &= [8(4 - \sqrt{3}\cos\alpha) + 2Z_1\sin(6X) \\
&\quad - 6Z_2\sin(2X) - \sqrt{3}\eta\sin\alpha\sin(6X) \\
&\quad + 3\sqrt{3}\eta\sin\alpha\sin(2X) + \eta Q \\
&\quad + Z_6\cos(4X)\cos(2Y) - Z_3\sin(4X)\sin(2Y) \\
&\quad - Z_7\cos(2X)\sin(2Y) + Z_4\sin(2X)\cos(2Y)]/32, \\
\rho_{22} &= [8(4 + \sqrt{3}\cos\alpha) - 6Z_1\sin(6X) \\
&\quad + 2Z_2\sin(2X) + 3\sqrt{3}\eta\sin\alpha\sin(6X) \\
&\quad - \sqrt{3}\eta\sin\alpha\sin(2X) - \eta Q - Z_6\cos(4X)\cos(2Y) \\
&\quad + Z_3\sin(4X)\sin(2Y) - Z_8\cos(2X)\sin(2Y) \\
&\quad + Z_5\sin(2X)\cos(2Y)]/32, \\
\rho_{33} &= [8(4 + \sqrt{3}\cos\alpha) + 6Z_1\sin(6X) \\
&\quad - 2Z_2\sin(2X) - 3\sqrt{3}\eta\sin\alpha\sin(6X) \\
&\quad + \sqrt{3}\eta\sin\alpha\sin(2X) - \eta Q - Z_6\cos(4X)\cos(2Y) \\
&\quad + Z_3\sin(4X)\sin(2Y) + Z_8\cos(2X)\sin(2Y)
\end{aligned} \qquad (27)$$

$$- Z_5 \sin(2X)\cos(2Y)]/32,$$

$$\rho_{44} = [8(4 - \sqrt{3}\cos\alpha) - 2Z_1\sin(6X)$$

$$+ 6Z_2\sin(2X) + \sqrt{3}\eta\sin\alpha\sin(6X)$$

$$- 3\sqrt{3}\eta\sin\alpha\sin(2X) + \eta Q$$

$$+ Z_6\cos(4X)\cos(2Y) - Z_3\sin(4X)\sin(2Y)$$

$$+ Z_7\cos(2X)\sin(2Y) - Z_4\sin(2X)\cos(2Y)]/32,$$

where

$$Z_1 = \sin(3\alpha/2) + (2\sqrt{3} - 3)\sin(\alpha/2),$$

$$Z_2 = 3\sin(3\alpha/2) - (2\sqrt{3} + 1)\sin(\alpha/2),$$

$$Z_3 = 4(3 - 2\sqrt{3})\cos(\alpha/2)$$

$$- 12\cos(3\alpha/2) + 2\sqrt{3}\eta\cos\alpha,$$

$$Z_4 = 12\sin(3\alpha/2) + 4(3 + 2\sqrt{3})\sin(\alpha/2)$$

$$+ 4\sqrt{3}\eta\sin\alpha,$$

$$Z_5 = 12\sin(3\alpha/2) + 4(3 + 2\sqrt{3})\sin(\alpha/2)$$

$$- 4\sqrt{3}\eta\sin\alpha,$$

$$Z_6 = 8\sqrt{3}\cos\alpha - \eta Q,$$

$$Z_7 = 16\sqrt{3}\sin\alpha$$

$$+ 2\eta[3\sin(3\alpha/2) + \sqrt{3}\sin(\alpha/2)],$$

$$Z_8 = 16\sqrt{3}\sin\alpha - 2\eta(\sqrt{3} + 3)\sin(\alpha/2),$$

$$Q = (2\sqrt{3} + 3)\cos(\alpha/2) - 3\cos(3\alpha/2),$$

$$X = \Omega_0 t, \quad Y = \delta t/4.$$

Figure 5 shows the level populations as functions of α after irradiation by the $\pi/2$ pulse ($X = \pi/2$) for $\eta \ll 1$. For $\alpha \approx 3\pi/2$, the subsystem of levels 2 and 3 and the subsystem of levels 1 and 4 will be in the state in which their corresponding lower levels are populated, whereas the upper levels are empty. For $\alpha \approx 5\pi/2$, on the contrary, these subsystems will be inverted.

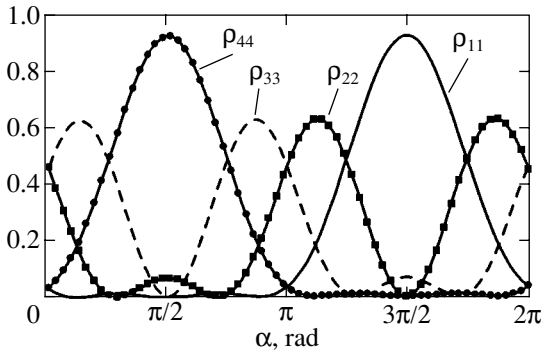

Fig. 5. Level populations in a weakly nonequidistant four-level system for different phases α after irradiation by the $\pi/2$ pulse of the two-phase field.

5. CONCLUSIONS

The results obtained in this paper show that the systems of hyperfine-structure levels used as cubits of the information solid medium in a quantum computer can be rapidly polarized by short pulses of a bichromatic or two-phase field without cooling to ultralow temperatures. Note once more that all the effects of coherent repopulation occur if the pulse duration is shorter than the longitudinal and transverse relaxation times and the interaction with the field is stronger than the interaction of the spin system with the thermostat.

The procedures of application of the bichromatic or two-phase field have some special features. Thus, a quantum system can be polarized by the bichromatic field by using pulses of duration exceeding the period of Rabi oscillations. In this case, to obtain a high degree of polarization, it is necessary to produce a series of pulses by changing the component strength in a proper way before each new pulse. This method cannot be applied for a system of weakly nonequidistant levels. When the system is polarized by the two-phase field, a substantial effect can be achieved using one pulse whose duration should be, however, comparable with the Rabi period. The two-phase field can be used in the case of weakly nonequidistant levels as well.

Note that when the system is polarized by short pulses of the bichromatic or two-phase field, whose duration is comparable with the Rabi period, a cubit state can be changed by changing only the phase difference of the field components, the pulse duration being fixed.

We believe that we deal with quite solvable technical problems, concerning both the preparation of the initial state of a quantum computer and, probably, the construction of algorithms for quantum calculations. It should be emphasized once more that the method for polarizing impurity centers in a solid matrix proposed here allows one first of all to obtain the ground state of a system of cubits representing the hyperfine-structure levels in these centers. If the wavelength of the resonance field greatly exceeds the distance between the centers, then the ground state of the cubit system for quantum calculations can be obtained in a macroscopic volume. The cubits in a solid matrix are coupled by the dipole–dipole interaction. This coupling should be taken into account in the construction of the algorithm for quantum calculations. The application of this method, taking into account magnetic interactions in the cubit system, requires a separate analysis.

REFERENCES

1. D. P. DiVincenzo, Science **270** (5234), 255 (1995).
2. B. W. Schumacher, Phys. Rev. A **51**, 2738 (1995).
3. A. L. Chuang, D. V. Lejung, and S. Lloyd, Kvant. Komp. **1**, 130 (1999).
4. S. Lloyd, Science **261** (5128), 1569 (1993).
5. A. Barenco, C. H. Bennett, R. Cleve, *et al.*, Phys. Rev. A **52**, 3457 (1995).
6. J. D. Macomber, *The Dynamics of Spectroscopic Transitions* (Wiley, New York, 1976).
7. D. F. Zaretskiĭ and S. B. Sazonov, Pis'ma Zh. Éksp. Teor. Fiz. **60**, 682 (1994) [JETP Lett. **60**, 699 (1994)].
8. D. F. Zaretskiĭ and S. B. Sazonov, Zh. Éksp. Teor. Fiz. **111**, 1236 (1997) [JETP **84**, 682 (1997)].
9. A. R. Kessel' and V. L. Ermakov, Zh. Éksp. Teor. Fiz. **117**, 517 (2000) [JETP **90**, 452 (2000)].

Translated by M. Sapozhnikov